NUCLEAR INSTRUMENTS & METHODS

A JOURNAL ON ACCELERATORS, INSTRUMENTATION
AND TECHNIQUES IN NUCLEAR PHYSICS

EDITOR: K. SIEGBAHN – UPPSALA

VOLUME 8

JULY 1960 — SEPTEMBER 1960

NORTH-HOLLAND PUBLISHING COMPANY — AMSTERDAM

PRINTED IN THE NETHERLANDS
DRUKKERIJ MEIJER N.V. WORMERVEER AND AMSTERDAM

NUCLEAR INSTRUMENTS AND METHODS 8 (1960) 1–10; NORTH-HOLLAND PUBLISHING CO.

FIELDS EXCITED BY BEAM CURRENTS IN CIRCULAR ACCELERATORS†

J. VAN BLADEL

Midwestern Universities Research Association

and

Department of Electrical Engineering, University of Wisconsin, Madison, Wisconsin

Received 7 March 1960

Formulas are given for the electric and magnetic fields in a circular accelerator of arbitrary cross section, excited by a non-scalloping beam of particles. Both steady-state and step-function transients are considered.

1. Introduction

The purpose of the present paper is to give general formulas for the electric and magnetic fields inside a beam-excited toroidal accelerator of arbitrary cross section. The configuration is shown in fig. 1. Some simplifying features will be introduced in the course of the analysis. It will be assumed, in particular:

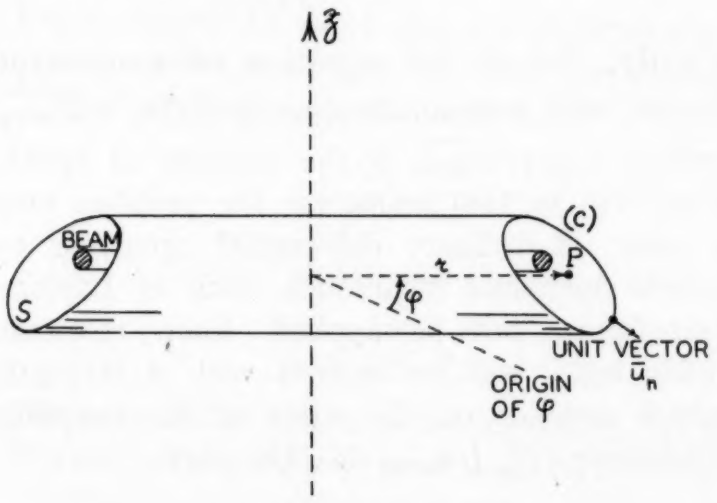

Fig. 1

(a) that the toroidal structure is bounded by a surface of revolution,

(b) that the beam current is circular, i.e., that the particles follow circular orbits (scalloping orbits are excluded),

(c) that the angular velocity Ω of all particles is the same,

(d) that the relative charge density distribution in a meridian plane is independent of the plane. (An azimuthal variation of the charge density will be allowed.)

With such a specialized beam, the volume charge density will be

$$\rho = \pi(r,z)\, g\,(\varphi - \Omega t) \tag{1}$$

and the current density

$$\boldsymbol{j} = \pi(r,z)\, g\,(\varphi - \Omega t)\, r\Omega \boldsymbol{u}_\varphi \tag{2}$$

where $\boldsymbol{u}_\varphi$ is the unit vector in the azimuthal direction.

2. General Formulas

Let us consider a ring-like cavity, which is not necessarily of revolution, and the current and charge densities $\boldsymbol{j}$ and ρ which it contains. We are going to express the fields in terms of their expansions in electric and magnetic eigenvectors as:

$$\mathbf{e}(\mathbf{r},t) = \sum_m \sum_n \sum_p A_{mnp}(t)\, \mathbf{f}_{mnp}(\mathbf{r}) + \sum_m \sum_n \sum_p B_{mnp}(t)\, \mathbf{e}_{mnp}(\mathbf{r}) \tag{3}$$

$$\mathbf{h}(\mathbf{r},t) = \sum_m \sum_n \sum_p C_{mnp}(t)\, \mathbf{g}_{mnp}(\mathbf{r}) + \sum_m \sum_n \sum_p D_{mnp}(t)\, \mathbf{h}_{mnp}(\mathbf{r}) + c_0 \mathbf{h}_0 \tag{4}$$

$$\mathbf{j}(\mathbf{r},t) = \sum_m \sum_n \sum_p J_{mnp}(t)\, \mathbf{f}_{mnp}(\mathbf{r}) + \sum_m \sum_n \sum_p K_{mnp}(t)\, \mathbf{e}_{mnp}(\mathbf{r}) \tag{5}$$

$$\rho(\mathbf{r},t) = \varepsilon_0 \sum_m \sum_n \sum_p Q_{mnp}(t)\, \phi_{mnp}(\mathbf{r})\,. \tag{6}$$

† AEC Research and Development Report. Research supported by the Atomic Energy Commission, Contract No. AT (11-1)-384.

In these equations, the unknowns are the time-dependent coefficients A, B, C and D. Coefficients J, K and Q, on the other hand, can be calculated once $\boldsymbol{j}$ and ρ are given. The various eigenvectors which appear in the formulas are defined as follows:

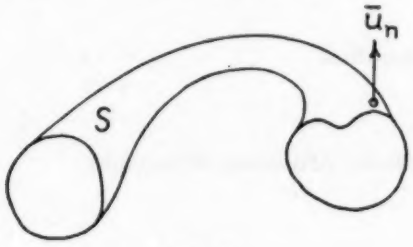

Fig. 2

1. The irrotational electric eigenvectors $\boldsymbol{f}_{mnp}$ derive from scalar potentials ϕ_{mnp}, where

$$\nabla^2\phi_{mnp} + \lambda'_{mnp}\phi_{mnp} = 0 \quad \phi_{mnp} = 0 \text{ on } S\,. \tag{7}$$

2. The solenoidal electric eigenvectors $\mathbf{e}_{mnp}$ are given by

$$-\operatorname{curl}\operatorname{curl}\mathbf{e}_{mnp} + \lambda''_{mnp}\mathbf{e}_{mnp} = 0$$

$$\boldsymbol{u}_n \times \mathbf{e}_{mnp} = 0 \text{ on } S\,. \tag{8}$$

3. The irrotational magnetic eigenvectors $\boldsymbol{g}_{mnp}$ derive from scalar potentials ψ_{mnp}, where

$$\nabla^2\psi_{mnp} + \mu_{mnp}\psi_{mnp} = 0\,, \quad \frac{\partial\psi_{mnp}}{\partial n} = 0 \quad \text{on} \quad S\,. \tag{9}$$

4. The solenoidal magnetic eigenvectors $\boldsymbol{h}_{mnp}$ are simply curl $\mathbf{e}_{mnp}$. They have the same eigenvalues λ''_{mnp} as $\mathbf{e}_{mnp}$.

5. The "magnetostatic" eigenvector $\boldsymbol{h}_0$ is tangent to S, and has vanishing curl and divergence.

To find equations for the unknown coefficients, we substitute the expansions in the four Maxwell's equations and, by well-known methods[1]), obtain

$$A_{mnp} = -\frac{Q_{mnp}}{\lambda'_{mnp}}$$

$$\left(\text{from which } \varepsilon_0\frac{\mathrm{d}A_{mnp}}{\mathrm{d}t} + J_{mnp} = 0 \quad \text{follows}\right) \tag{10}$$

[1]) J. C. Slater, Microwave Electronics (Van Nostrand Co., Inc., 1950) Chs. 3 and 4;
or J. van Bladel, On Helmholtz' Theorem in multiply-bounded and multiply-connected Regions, to appear in the June 1960 issue of the Journal of the Franklin Institute.

$$\frac{\mathrm{d}C_0}{\mathrm{d}t} = \frac{\mathrm{d}C_{mnp}}{\mathrm{d}t} = 0$$

$$\left(\text{with } C_{mnp} = \frac{\iint_s \psi_{mnp}\,(\boldsymbol{h}\cdot\boldsymbol{u}_n)\,\mathrm{d}S}{\iiint_v |\,\boldsymbol{g}_{mnp}\,|^2\,\mathrm{d}V}\right) \tag{11}$$

$$B_{mnp} = -\mu_0\frac{\mathrm{d}D_{mnp}}{\mathrm{d}t} \tag{12}$$

$$\varepsilon_0\frac{\mathrm{d}B_{mnp}}{\mathrm{d}t} + K_{mnp} = \lambda''_{mnp}\,D_{mnp}\,. \tag{13}$$

The coefficients C_0 and C_{mnp} are time-independent, and do not interest us. Furthermore, they are, and remain, zero if the beam is injected in a region where the fields are initially zero. Coefficients B and D are of particular importance, because of the possibility of resonance. The latter becomes evident when we write the differential equation for D, by use of eqs. (12) and (13), as

$$\frac{\mathrm{d}^2D_{mnp}}{\mathrm{d}t^2} + \frac{\lambda''_{mnp}}{\varepsilon_0\mu_0}D_{mnp} = \frac{\iiint_v \boldsymbol{j}\cdot\mathbf{e}_{mnp}\,\mathrm{d}V}{\varepsilon_0\mu_0\iiint_v |\,\mathbf{e}_{mnp}\,|^2\,\mathrm{d}V}\,. \tag{14}$$

Clearly, this is the equation of a resonant circuit with resonant frequency $(c/2\pi)\sqrt{\lambda''_{mnp}}$ (where $c = 1/\sqrt{\varepsilon_0\mu_0}$ is the velocity of light). Eqs. (10) to (14) transform the problem into a series of ordinary differential equations to which the usual techniques, such as Laplace transforms, can be applied. Each resonant mode $\mathbf{e}_{mnp}$ will be excited with a strength which depends on the value of the coupling coefficient $\iiint_v \boldsymbol{j}\cdot\mathbf{e}_{mnp}\,\mathrm{d}V$. The part

$$\sum_m\sum_n\sum_p A_{mnp}(t)\,\boldsymbol{f}_{mnp}(\boldsymbol{r})$$

of the electric field is rather trivial. It is simply the (non-retarded) electric field which would be found if the boundary were metallized, and the field calculated as an electrostatic field with sources corresponding to the instantaneous value of ρ.

At this point there is little else one could say to advance the analysis. More interesting results can be obtained by specializing the physical configuration in the manner described in the introduction.

3. Volumes of Revolution

In a volume of revolution, the eigenvectors take a particularly simple form because of the possibility of separation of the azimuthal dependence. More precisely[2])

1. The irrotational electric eigenvectors are the gradient of

$$\phi_{mnp} = \begin{Bmatrix} \sin m\varphi \\ \cos m\varphi \end{Bmatrix} \alpha_{mnp}(r,z) \tag{15}$$

where α_{mnp} is an eigenfunction of

$$\frac{\partial^2\alpha}{\partial r^2} + \frac{1}{r}\frac{\partial\alpha}{\partial r} + \frac{\partial^2\alpha}{\partial z^2} + \left(\lambda'_{mnp} - \frac{m^2}{r^2}\right)\alpha = 0 \qquad \alpha = 0 \quad \text{on} \quad C\,. \tag{16}$$

2. The solenoidal electric eigenvectors are of the form

$$\mathbf{e}_{mnp} = \begin{Bmatrix} \sin m\varphi \\ \cos m\varphi \end{Bmatrix} \mathbf{c}_{mnp}(r,z) + \begin{Bmatrix} \cos m\varphi \\ -\sin m\varphi \end{Bmatrix} \frac{r}{m} \operatorname{div} \mathbf{c}_{mnp}\, \mathbf{u}_\varphi \tag{17}$$

where $\mathbf{c}(r,z)$ is a meridian vector, with divergence (in the r, z plane)

$$\operatorname{div} \mathbf{c} = \frac{\partial c_r}{\partial r} + \frac{c_r}{r} + \frac{\partial c_z}{\partial z}$$

and satisfying the eigenvector problem

$$\nabla^2\mathbf{c} + \mathbf{u}_r\left(\frac{2}{r}\operatorname{div}\mathbf{c}\right) + \left(\lambda''_{mnp} - \frac{m^2}{r^2}\right)\mathbf{c} = 0 \quad \text{with} \begin{Bmatrix} \mathbf{u}_n \times \mathbf{c} = 0 \\ \operatorname{div}\mathbf{c} = 0 \end{Bmatrix} \quad \text{on} \quad (C) \tag{18}$$

where $$\nabla^2\mathbf{c} = \left(\frac{\partial^2 c_r}{\partial r^2} + \frac{1}{r}\frac{\partial c_r}{\partial r} + \frac{\partial^2 c_r}{\partial z^2} - \frac{c_r}{r^2}\right)\mathbf{u}_r + \left(\frac{\partial^2 c_z}{\partial r^2} + \frac{1}{r}\frac{\partial c_z}{\partial r} + \frac{\partial^2 c_z}{\partial z^2}\right)\mathbf{u}_z\,.$$

These formulas are valid when m is different from zero, i.e., when there is azimuthal dependence. The φ-independent modes, on the other hand, split into two simple families:

(a) "circular" modes $\beta_{0np}\mathbf{u}_\varphi$ where

$$\frac{\partial^2\beta}{\partial r^2} + \frac{1}{r}\frac{\partial\beta}{\partial r} + \frac{\partial^2\beta}{\partial z^2} + \left(\lambda''_{0np} - \frac{1}{r^2}\right)\beta = 0 \qquad \beta = 0 \quad \text{on} \quad (C) \tag{19}$$

(b) "meridian" modes curl $[\delta_{0np}\mathbf{u}_\varphi]$ where

$$\frac{\partial^2\delta}{\partial r^2} + \frac{1}{r}\frac{\partial\delta}{\partial r} + \frac{\partial^2\delta}{\partial z^2} + \left(\lambda'''_{0np} - \frac{1}{r^2}\right)\delta = 0 \qquad \frac{\partial}{\partial n}(r\delta) = 0 \quad \text{on} \quad (C)\,. \tag{20}$$

The irrotational magnetic modes, which do not appear in expansion (4), will not be listed here The solenoidal magnetic modes, on the other hand, are simply curl $\mathbf{e}_{mnp}$, curl $[\beta_{0np}\mathbf{u}_\varphi]$ and $\delta_{0np}\,\mathbf{u}_\varphi$.

To find the expansion coeffients A, B D, we expand the periodic volume charge distribution ρ in a Fourier series. More precisely, we write

$$g\,(\varphi - \Omega t) = \sum_{m=1}^{\infty} P_m \cos\,(m\varphi - m\Omega t + \phi_m) + g_{\mathrm{av}} \tag{21}$$

where the amplitude P_m and the phase ϕ_m are given, and g_{av} is the D.C., non-fluctuating part of the space charge. By introducing this expansion in (10) to (14), we find:

1. $$A_{0np} = -\frac{1}{\varepsilon_0\lambda'_{0np}} \frac{\iint_S \pi(r,z)\,\alpha_{0np}(r,z) r\,\mathrm{d}r\,\mathrm{d}z}{\iint_S \alpha^2_{0np}(r,z) r\,\mathrm{d}r\,\mathrm{d}z}\, g_{\mathrm{av}} = L_{0np} g_{\mathrm{av}}\,. \tag{22}$$

[2]) For more details, see J. Van Bladel, Sets of Eigenvectors for Volumes of Revolution, to appear shortly in the IRE Transactions on Microwave Theory and Techniques.

$$2. \qquad A_{mnp} = -\frac{1}{\varepsilon_0 \lambda'_{mnp}} \frac{\iint_S \pi(r,z)\, \alpha_{mnp}(r,z) r \, dr \, dz}{\iint_S \alpha^2_{mnp}(r,z) r \, dr \, dz} P_m \begin{Bmatrix} \sin (m\Omega t - \phi_m) \\ \cos (m\Omega t - \phi_m) \end{Bmatrix} = L_{mnp} P_m \begin{Bmatrix} \sin (m\Omega t - \phi_m) \\ \cos (m\Omega t - \phi_m) \end{Bmatrix}. \quad (23)$$

The sines and cosines in the brackets correspond to the sines and cosines in formula (15). Coefficients L can be calculated when ρ is given. They depend solely on the cross-sectional (i.e., meridian) distribution of the space charge.

$$3. \qquad \frac{d^2 D_{0np}}{dt^2} + \frac{\lambda''_{0np}}{\varepsilon_0 \mu_0} D_{0np} = \frac{\Omega}{\varepsilon_0 \mu_0} \frac{\iint_S \pi(r,z)\, \beta_{0np}(r,z) r^2 \, dr \, dz}{\iint_S \beta^2_{0np}(r,z) r \, dr \, dz} g_{av} = M_{0np} g_{av}. \quad (24)$$

D_{0np} is the expansion coefficient of the circular modes described in eq. (19). The meridian modes are not excited, because their eigenvectors are perpendicular to the current density $\boldsymbol{j}$.

$$4. \qquad \frac{d^2 D_{mnp}}{dt^2} + \frac{\lambda''_{mnp}}{\varepsilon_0 \mu_0} D_{mnp} = \frac{\Omega}{\varepsilon_0 \mu_0} \frac{\iint_S \pi(r,z)\, \operatorname{div} \mathbf{c}_{mnp} \frac{r^3}{m} \, dr \, dz}{\iint_S \left[(\mathbf{c}_{mnp})^2 + \frac{r^2}{m^2} (\operatorname{div} \mathbf{c}_{mnp})^2 \right] r \, dr \, dz} \begin{Bmatrix} \cos (m\Omega t - \phi_m) \\ -\sin (m\Omega t - \phi_m) \end{Bmatrix} P_m$$

$$= M_{mnp} \begin{Bmatrix} \cos (m\Omega t - \phi_m) \\ -\sin (m\Omega t - \phi_m) \end{Bmatrix} P_m. \quad (25)$$

The upper and lower terms in the bracket correspond to the upper and lower terms in (17). Coefficients M depend solely on the meridian distribution of the space charge. Factors $\lambda''_{0np}/\varepsilon_0\mu_0$ and $\lambda''_{mnp}/\varepsilon_0\mu_0$ are the squares of the resonant angular frequencies of the cavity. We shall henceforth denote them by ω^2_{0np} and ω^2_{mnp}.

To find the actual field distribution in the cavity, we should solve for the D_{mnp}, B_{mnp} and insert the results in expansions (3) and (4). Two cases are of particular interest.

A. STEADY STATE

The term g_{av} gives rise to electrostatic and magnetostatic fields. These fields will be omitted, for our main interest lies in the time-dependent terms, which consist of:

(a) a non-resonant part of the electric field

$$\sum_{m=1}^{\infty} \sum_n \sum_p A_{mnp}(t)\, \mathbf{f}_{mnp}(\mathbf{r}) = \sum_{m=1}^{\infty} P_m \cos (m\varphi - m\Omega t + \phi_m) \left[\sum_n \sum_p L_{mnp} \operatorname{grad} \alpha_{mnp} \right]$$

$$+ \sum_{m=1}^{\infty} P_m \sin (m\varphi - m\Omega t + \phi_m) \frac{m}{r} \left[- \sum_n \sum_p L_{mnp} \alpha_{mnp} \right] \boldsymbol{u}_\varphi. \quad (26)$$

The first summation is a meridian vector made out of waves travelling in step with the space-charge waves. The second summation is a circular vector made out of waves travelling 90° out of phase with the space-charge waves.

(b) a resonant part of the electric field

$$\sum_{m=1}^{\infty} \sum_n \sum_p B_{mnp}(t)\, \mathbf{e}_{mnp}(\mathbf{r}) = \sum_{m=1}^{\infty} P_m \cos (m\varphi - m\Omega t + \phi_m)\, \mu_0 m\Omega \left[\sum_n \sum_p \frac{M_{mnp}}{\omega^2_{mnp} - m^2\Omega^2} \mathbf{c}_{mnp} \right]$$

$$+ \sum_{m=1}^{\infty} P_m \sin (m\varphi - m\Omega t + \phi_m)\, \mu_0 r\Omega \left[\sum_n \sum_p - \frac{M_{mnp}}{\omega^2_{mnp} - m^2\Omega^2} \operatorname{div} \mathbf{c}_{mnp} \right] \boldsymbol{u}_\varphi. \quad (27)$$

The first and second summations represent meridian and circular vectors respectively.

(c) the magnetic field, which consists of a resonant part only. To express the latter explicitly, we notice that

$$\boldsymbol{h}_{mnp}(\boldsymbol{r}) = \operatorname{curl} \boldsymbol{e}_{mnp} = \begin{Bmatrix} \cos m\varphi \\ -\sin m\varphi \end{Bmatrix} \left[\frac{m}{r} (\boldsymbol{u}_\varphi \times \boldsymbol{c}_{mnp}) + \operatorname{curl} \left(\boldsymbol{u}_\varphi \frac{r}{m} \operatorname{div} \boldsymbol{c}_{mnp} \right) \right] + \begin{Bmatrix} \sin m\varphi \\ \cos m\varphi \end{Bmatrix} \operatorname{curl} \boldsymbol{c}_{mnp} . \tag{28}$$

The first term, which is a meridian vector, will, for reasons of conciseness, be written as

$$\boldsymbol{d}_{mnp} \begin{Bmatrix} \cos m\varphi \\ -\sin m\varphi \end{Bmatrix} .$$

The second term, which is a circular vector, can then be shown to be

$$- \begin{Bmatrix} \sin m\varphi \\ \cos m\varphi \end{Bmatrix} \frac{r}{m} \operatorname{div} \boldsymbol{d}_{mnp} .$$

With this notation, we find that

$$\sum_m \sum_n \sum_p D_{mnp}(t)\, \boldsymbol{h}_{mnp}(\boldsymbol{r}) = \sum_{m=1}^{\infty} P_m \cos (m\varphi - m\Omega t + \phi_m) \left[\sum_n \sum_p \frac{M_{mnp}}{\omega_{mnp}^2 - m^2\Omega^2} \boldsymbol{d}_{mnp} \right]$$

$$+ \sum_{m=1}^{\infty} P_m \sin (m\varphi - m\Omega t + \phi_m) \left[\sum_n \sum_p \frac{M_{mnp}}{\omega_{mnp}^2 - m^2\Omega^2} \operatorname{curl} \boldsymbol{c}_{mnp} \right] . \tag{29}$$

B. STEP-FUNCTION TRANSIENTS

Let us assume, as a convenient idealization, that the charge density (21) is suddenly injected in the accelerator at time $t = 0$, no charge being present before that time. We now find:

(a) a non-resonant part of the electric field, which is (26) augmented by a term

$$g_{\mathrm{av}} \sum_n \sum_p L_{0np} \operatorname{grad} \alpha_{0np} \tag{30}$$

(b) a resonant part of the electric field, which is (27) augmented by

$$- \sum_{m=1}^{\infty} \mu_0 P_m \sin (m\varphi + \phi_m) \sum_n \sum_p \frac{\omega_{mnp} M_{mnp} \sin \omega_{mnp} t}{\omega_{mnp}^2 - m^2\Omega^2} \boldsymbol{c}_{mnp}$$

$$- \sum_{m=1}^{\infty} \mu_0 m\Omega P_m \cos (m\varphi + \phi_m) \sum_n \sum_p \frac{M_{mnp} \cos \omega_{mnp} t}{\omega_{mnp}^2 - m^2\Omega^2} \boldsymbol{c}_{mnp}$$

$$- \mu_0 g_{\mathrm{av}} \sum_n \sum_p \frac{M_{0np}}{\omega_{0np}} \sin \omega_{0np} t \cdot \beta_{0np} \boldsymbol{u}_\varphi + \sum_{m=1}^{\infty} \mu_0 P_m r\Omega \sin (m\varphi + \phi_m) \sum_n \sum_p \frac{M_{mnp} \cos \omega_{mnp} t}{\omega_{mnp}^2 - m^2\Omega^2} (\operatorname{div} \boldsymbol{c}_{mnp})\, \boldsymbol{u}_\varphi$$

$$- \sum_{m=1}^{\infty} \mu_0 P_m \frac{r}{m} \cos (m\varphi + \phi_m) \sum_n \sum_p \frac{M_{mnp} \sin \omega_{mnp} t}{\omega_{mnp}^2 - m^2\Omega^2} (\operatorname{div} \boldsymbol{c}_{mnp})\, \boldsymbol{u}_\varphi . \tag{31}$$

(c) a resonant part of the magnetic field, which is (29) augmented by

$$g_{av} \sum_n \sum_p \frac{M_{0np}}{\omega_{0np}^2} (1 - \cos \omega_{0np} t) \operatorname{curl} (\beta_{0np} \mathbf{u}_\varphi) - \sum_{m=1}^{\infty} P_m \cos (m\varphi + \phi_m) \sum_n \sum_p \frac{M_{mnp} \cos \omega_{mnp} t}{\omega_{mnp}^2 - m^2\Omega^2} \mathbf{d}_{mnp}$$

$$- \sum_{m=1}^{\infty} P_m \sin (m\varphi + \phi_m)\, m\Omega \sum_n \sum_p \frac{M_{mnp} \sin \omega_{mnp} t}{\omega_{mnp}^2 - m^2\Omega^2} \frac{\mathbf{d}_{mnp}}{\omega_{mnp}}$$

$$- \sum_{m=1}^{\infty} P_m \sin (m\varphi + \phi_m) \sum_n \sum_p \frac{M_{mnp} \cos \omega_{mnp} t}{\omega_{mnp}^2 - m^2\Omega^2} \operatorname{curl} \mathbf{c}_{mnp}$$

$$- \sum_{m=1}^{\infty} P_m \cos (m\varphi + \phi_m)\, m\Omega \sum_n \sum_p \frac{M_{mnp} \sin \omega_{mnp} t}{\omega_{mnp}^2 - m^2\Omega^2} \frac{\operatorname{curl} \mathbf{c}_{mnp}}{\omega_{mnp}} . \tag{32}$$

These various formulas have been obtained under the assumption that no actual resonance took place, i.e. that $m\Omega$ was not equal to any of the ω_{mnp}. In case of resonance, the fields will build up to infinite values; that is, as long as we maintain the assumption of perfectly conducting walls. In reality, however, the walls have some resistance, and the build-up will be limited by the Q of the cavity. This phenomenon will be examined in more detail later on. The finite conductivity of the walls is also responsible for the decay of the transient terms, and the ultimate convergence of the fields to the values predicted by steady-state analysis.

C. PARTICULAR CASES

1. The fields excited by a very narrow beam (a beam which can be assimilated to a fine line) are of particular importance. They have the nature of a Green's function, and allow computation by simple integrations of the fields excited by a smeared-out distribution $\pi(r,z)$. We represent the line density of the beam as:

$$\Lambda = \Lambda_{\max}\, g\, (\varphi - \Omega t) \qquad \text{Clb m}^{-1} . \tag{33}$$

where g is a function which has a maximum value equal to one. Let furthermore $r_0 z_0$ be the location of the beam in the meridian plane. To find the fields excited by such a beam, it suffices to replace, in formulas (22) to (32), the L and M by their values

$$L_{0np} = - \frac{r_0 \alpha_{0np}(r_0,z_0)}{\varepsilon_0 \lambda'_{0np} \iint_S \alpha_{0np}^2(r,z) r\, dr\, dz} \Lambda_{\max} \tag{34}$$

$$L_{mnp} = - \frac{r_0 \alpha_{mnp}(r_0,z_0)}{\varepsilon_0 \lambda'_{mnp} \iint_S \alpha_{mnp}^2(r,z) r\, dr\, dz} \Lambda_{\max} \tag{35}$$

$$M_{0np} = \frac{\Omega}{\varepsilon_0 \mu_0} \frac{r_0^2 \beta_{0np}(r_0,z_0)}{\iint_S \beta_{0np}^2(r,z) r\, dr\, dz} \Lambda_{\max} \tag{36}$$

$$M_{mnp} = \frac{\Omega r_0^3}{m \varepsilon_0 \mu_0} \frac{\operatorname{div} \mathbf{c}_{mnp}(r_0,z_0)}{\iint_S \left[(\mathbf{c}_{mnp})^2 + \frac{r^2}{m^2} (\operatorname{div} \mathbf{c}_{mnp})^2 \right] r\, dr\, dz} \Lambda_{\max} . \tag{37}$$

We shall not rewrite all the formulas for the narrow beam explicitly, but will restrict ourselves to those which give the steady-state resonant parts of the electric and magnetic field:

$$\mathbf{e}(\mathbf{r},t) = \Lambda_{\max}\frac{r_0\beta^2}{\varepsilon_0}\sum_{m=1}^{\infty} P_m \cos(m\varphi - m\Omega t + \phi_m)\sum_n\sum_p \frac{\mathbf{c}_{mnp}(r,z)\ \mathrm{div}\ \mathbf{c}_{mnp}(r_0,z_0)}{\left(\lambda''_{mnp} - \frac{m^2\beta^2}{r_0^2}\right)\iint_S\left[(\mathbf{c}_{mnp})^2 + \frac{r^2}{m^2}(\mathrm{div}\ \mathbf{c}_{mnp})^2\right] r\,dr\,dz}$$

$$- \Lambda_{\max}\frac{rr_0\beta^2}{\varepsilon_0}\sum_{m=1}^{\infty}\frac{P_m}{m}\sin(m\varphi - m\Omega t + \phi_m)\sum_n\sum_p \frac{\mathrm{div}\ \mathbf{c}_{mnp}(r,z)\ \mathrm{div}\ \mathbf{c}_{mnp}(r_0,z_0)}{\left(\lambda''_{mnp} - \frac{m^2\beta^2}{r_0^2}\right)\iint_S\left[(\mathbf{c}_{mnp})^2 + \frac{r^2}{m^2}(\mathrm{div}\ \mathbf{c}_{mnp})^2\right] r\,dr\,dz}\mathbf{u}_\varphi \quad (38)$$

$$\mathbf{h}(\mathbf{r},t) = \Lambda_{\max}\frac{r_0^2\beta}{(\varepsilon_0\mu_0)^{3/2}}\sum_{m=1}^{\infty}\frac{P_m}{m}\cos(m\varphi - m\Omega t + \phi_m)\sum_n\sum_p \frac{\mathbf{d}_{mnp}(r,z)\ \mathrm{div}\ \mathbf{c}_{mnp}(r_0,z_0)}{\left(\lambda''_{mnp} - \frac{m^2\beta^2}{r_0^2}\right)\iint_S\left[(\mathbf{c}_{mnp})^2 + \frac{r^2}{m^2}(\mathrm{div}\ \mathbf{c}_{mnp})^2\right] r\,dr\,dz}$$

$$+ \Lambda_{\max}\frac{r_0^2\beta}{(\varepsilon_0\mu_0)^{3/2}}\sum_{m=1}^{\infty}\frac{P_m}{m}\sin(m\varphi - m\Omega t + \phi_m)\sum_n\sum_p \frac{\mathrm{curl}\ \mathbf{c}_{mnp}(r,z)\ \mathrm{div}\ \mathbf{c}_{mnp}(r_0,z_0)}{\left(\lambda''_{mnp} - \frac{m^2\beta^2}{r_0^2}\right)\iint_S\left[(\mathbf{c}_{mnp})^2 + \frac{r^2}{m^2}(\mathrm{div}\ \mathbf{c}_{mnp})^2\right] r\,dr\,dz}. \quad (39)$$

The parameter $\beta = v/c = r_0\,\Omega/c$ measures the velocity of the beam in terms of the velocity of light.

2. The formulas for the narrow beam can be extended to include the fields of a point charge Q. Let the origin of azimuths be chosen at the initial position of the particle. The volume charge density is then

$$\rho = Q\frac{\delta(r - r_0)\,\delta(z - z_0)\,\delta(\varphi - \Omega t)}{r}$$

while

$$g = \delta(\varphi - \Omega t) = \frac{1}{2\pi} + \sum_{m=1}^{\infty}\frac{1}{\pi}\cos(m\varphi - m\Omega t)\,.$$

We shall consequently replace g_{av} by $1/2\pi$, P_m by $1/\pi$, and set $\phi_m = 0$ in all our formulas. The values of the L and the M can be obtained from equations (34) to (37) by replacing $\Lambda_{\max}$ by Q/r_0.

4. The Straight Tube with Periodic Currents

The formulas for the resonant parts of the fields all exhibit a factor $\omega_{mnp}^2 - m^2\Omega^2$ in the denominator. This indicates the possibility of resonance, because $m^2\Omega^2 = m^2\,v^2/r_0^2 = m^2\beta^2\,c^2/r_0^2$ can become as large as desired provided the location of the beam is sufficiently close to the axis, i.e., the inner radius is sufficiently small. To prove that this possibility of resonance is a curvature effect, we shall now present formulas for the electric and magnetic fields in a straight tube. We shall restrict ourselves to narrow beams with charge density

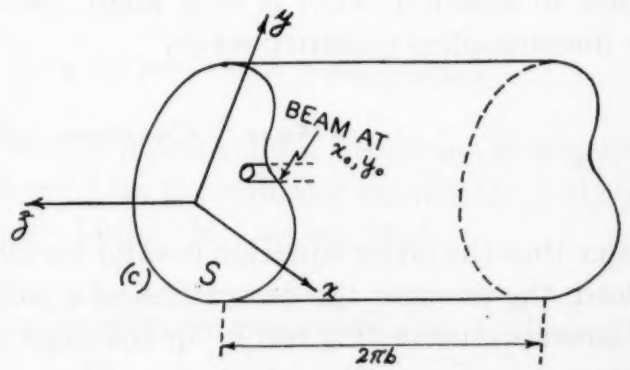

Fig. 3

$$\Lambda = \Lambda_{\max}\,g\left(\frac{z}{b} - \frac{vt}{b}\right) = \Lambda_{\max}\left[g_{\mathrm{av}} + \sum_m P_m\cos\left(\frac{mz}{b} - \frac{mvt}{b} + \phi_m\right)\right]. \quad (40)$$

The period of the beam is $2\pi b$ and the velocity v, We shall neglect the contribution of the D.C. component g_{av}, and consider the steady-state time-dependent part only. By well-known methods[1]), one obtains

$$\mathbf{e}(\mathbf{r},t) = -\frac{A_{\max}}{\varepsilon_0}\sum_{m=1}^{\infty} P_m \cos\left(\frac{mz}{b} - \frac{mvt}{b} + \phi_m\right)\sum_n\sum_p \frac{\mathscr{E}_{znp}(x_0y_0)\ \mathrm{grad}\ \mathscr{E}_{znp}(xy)}{\left[k_{np}^2 + \frac{m^2}{b^2}(1-\beta^2)\right]\iint_S \mathscr{E}_{znp}^2\,\mathrm{d}x\,\mathrm{d}y}$$

$$+ A_{\max}\frac{1-\beta^2}{\varepsilon_{0b}}\sum_{m=1}^{\infty} mP_m \sin\left(\frac{mz}{b} - \frac{mvt}{b} + \phi_m\right)\sum_n\sum_p \frac{\mathscr{E}_{znp}(x_0y_0)\,\mathscr{E}_{znp}(xy)}{\left[k_{np}^2 + \frac{m^2}{b^2}(1-\beta^2)\right]\iint_S \mathscr{E}_{znp}^2\,\mathrm{d}x\,\mathrm{d}y}\,\mathbf{u}_z \qquad (41)$$

$$\mathbf{h}(\mathbf{r},t) = -\frac{\beta A_{\max}}{(\varepsilon_0\mu_0)^{1/2}}\sum_{m=1}^{\infty} P_m \cos\left(\frac{mz}{b} - \frac{mvt}{b} + \phi_m\right)\sum_n\sum_p \frac{\mathscr{E}_{znp}(x_0y_0)\ (\mathbf{u}_z \times \mathrm{grad}\ \mathscr{E}_{znp})}{\left[k_{np}^2 + \frac{m^2}{b^2}(1-\beta^2)\right]\iint_S \mathscr{E}_{znp}^2\,\mathrm{d}x\,\mathrm{d}y} \qquad (42)$$

where $\beta = v/c = v\sqrt{\varepsilon_0\mu_0}$, and

$$\nabla_{xy}^2\,\mathscr{E}_{znp} + k_{np}^2\,\mathscr{E}_{znp} = 0 \qquad \text{with} \qquad \mathscr{E}_{znp} = 0 \quad \text{on} \quad (C)\,. \qquad (43)$$

All eigenvalues k_{np}^2 are positive and the factors $k_{np}^2 + (m^2/b^2)\ (1-\beta^2)$, which appear in the denominator, never become zero. One might wonder whether there is a threshold value of the curvature at which the possibility of resonance will appear. The answer is that this possibility will arise even for the slightest curvature, provided the value of the azimuthal quantum number m is sufficiently high. Consider again eq. (18) in which the eigenvalue λ''_{mnp} appears. There will be a resonance each time $m^2\beta^2/r_0^2$ exceeds λ''_{mnp} or, better said, as soon as $m^2\beta^2/r_0^2$ exceeds the lowest eigenvalue λ''_{m00} corresponding to quantum number m. For the lowest eigenvector $\mathbf{c}_{m00}$, the first and second order derivatives of $\mathbf{c}$ are of order $|\,\mathbf{c}\,|/D$ and $|\,\mathbf{c}\,|/D^2$ respectively, where D is a typical cross-sectional dimension. In the limit of small curvature, i.e., when D/r is small, the eigenvector equation (18) goes over into

$$\left(\frac{\partial^2 c_r}{\partial r^2} + \frac{\partial^2 c_r}{\partial z^2}\right)\mathbf{u}_r + \left(\frac{\partial^2 c_z}{\partial r^2} + \frac{\partial^2 c_z}{\partial z^2}\right)\mathbf{u}_z + \left(\lambda''_{m00} - \frac{m^2}{r^2}\right)\mathbf{c} = 0$$

or

$$\nabla^2\,\mathbf{c}_{m00} + \left(\lambda''_{m00} - \frac{m^2}{r^2}\right)\mathbf{c} = 0\,.$$

When, in addition, mD/r is very small, the term m^2/r^2 becomes negligible and, to higher orders in the dimensionless quantity mD/r,

$$\nabla^2\mathbf{c}_{mnp} + \lambda''_{mnp}\mathbf{c}_{mnp} = 0 \qquad \text{with} \quad \left.\begin{array}{l} \mathbf{u}_n \times \mathbf{c}_{mnp} = 0 \\ \dfrac{\partial c_r}{\partial r} + \dfrac{\partial c_z}{\partial z} = 0 \end{array}\right\} \quad \text{on} \quad (C)\,. \qquad (44)$$

Notice that the latter equation is valid for all quantum numbers n and p. The higher these numbers, indeed, the stronger the derivatives of $\mathbf{c}$ will be as compared with $|\,\mathbf{c}\,|/r$ and $|\,\mathbf{c}\,|/r^2$. We have now obtained an interesting result. In the limit of vanishing values of the parameter mD/r, the eigenvectors $\mathbf{c}_{mnp}$ are independent of m. They approach, in a smooth fashion, the eigenvectors of the Helmholtz equation (44). These eigenvectors are simply $\mathrm{grad}\,\mathscr{E}_{znp}$ and $\mathbf{u}_z \times \mathrm{grad}\,\mathscr{H}_{znp}$, where $\mathscr{E}_{znp}$ is given by eq. (43), and $\mathscr{H}_{znp}$ is an eigenfunction of

$$\nabla_{xy}^2\mathscr{H}_{znp} + \mu_{np}^2\mathscr{H}_{znp} = 0\,, \quad \frac{\partial\mathscr{H}_{znp}}{\partial n} = 0 \quad \text{on} \quad (C)\,. \qquad (45)$$

The eigenvalues λ''_{mnp} approach k_{np}^2 and μ_{np}^2. They are of order $1/D^2$, so that the denominator $\lambda''_{mnp} - m^2/r_0^2$ remains positive: there is no danger of resonance. One checks easily that the electric and magnetic fields in the curved tube, as given by (26), (27), (28), approach the electric and magnetic fields of the straight tube, as given by (41) and (42). The convergence, of course, takes place only for those values of m for which $mD/r \ll 1$, and the period $2\pi b$ in the straight tube should be taken equal to $2\pi r_0$ while performing the comparison. The details of the latter are left to the reader.

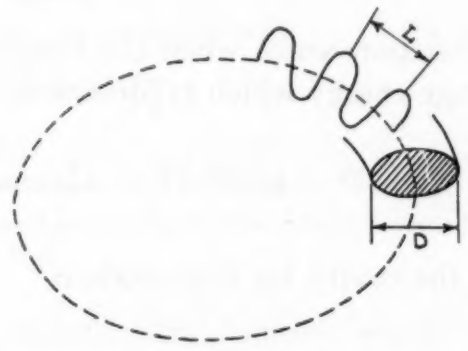

Fig. 4

We have reached the conclusion that the curvature effects, and the possibility of resonance, will appear when the charge density possesses ripples of such high frequency that mD is of the order of r, i.e., when the period L of a Fourier component is of the order of the cross-sectional dimensions of the tube.

5. Losses in the Walls

The traditional way to take the finite conductivity σ of the walls into account is to relate the tangential components of the electric and the magnetic fields at the wall by

$$\boldsymbol{E}_{\text{tang}} = (\boldsymbol{H}_{\text{tang}} \times \boldsymbol{u}_n)\,(1 + j)\sqrt{\frac{\omega\mu}{2\sigma}} \tag{46}$$

where $\boldsymbol{u}_n$ is the unit vector pointing into the metal. The formula is valid when the conductivity is sufficiently high to make the skin depth $\delta = \sqrt{2/\omega\mu_0\sigma}$ much smaller than the wavelength and the radius of curvature of the wall. By setting $\mu = \mu_0$ in the formulas, we have assumed the walls to be nonmagnetic. When $1/\sigma$ is small the value of $\boldsymbol{H}_{\text{tang}}$ can be taken, to first order, equal to the value at a perfectly conducting wall. The power going into the walls is given by

$$\tfrac{1}{2}\,\text{Re}\iint_S \boldsymbol{u}_n\cdot(\boldsymbol{E}\times\boldsymbol{H}^*)\,dS = \tfrac{1}{2}\sqrt{\frac{\omega\mu_0}{2\sigma}}\iint_S \left|\boldsymbol{H}_{\text{tang}}\right|^2 dS \tag{47}$$

where $|\boldsymbol{H}_{\text{tang}}|$ is the magnitude of the magnetic field at the wall. Formulas (46) and (47) are valid for single-frequency fields. The magnetic field at the surface, however, contains a mixture of harmonically related frequencies. An explicit formula can be obtained from (27). For a narrow beam:

$$\boldsymbol{h}_{\text{wall}} = \Lambda_{\max}\left\{\sum_m P_m \cos(m\varphi - m\Omega t + \phi_m)\,\boldsymbol{a}_m + \sum_m P_m \sin(m\varphi - m\Omega t + \phi_m)\,b_m\,\boldsymbol{u}_\varphi\right\}$$

where $\boldsymbol{a}_m$ and b_m stand for certain frequency-dependent double infinite sums. Vector $\boldsymbol{a}_m$ is tangent to the cross-sectional contour (c), and both $\boldsymbol{a}_m$ and b_m depend on the running coordinate c along that contour. Poynting's vector along the wall is $\boldsymbol{h}\cdot(\boldsymbol{u}_n \times \boldsymbol{e})$. Using (46), we find that

$$\boldsymbol{u}_n\times\boldsymbol{e} = \Lambda_{\max}\sqrt{\frac{\Omega\mu_0}{\sigma}}\left\{\sum_m \sqrt{m}\,P_m \cos\left(m\varphi - m\Omega t + \phi_m + \frac{\pi}{4}\right)\boldsymbol{a}_m + \sum_m \sqrt{m}\,P_m \sin\left(m\varphi - m\Omega t + \phi_m + \frac{\pi}{4}\right)b_m\boldsymbol{u}_\varphi\right\}.$$

The power loss then turns out to be

$$\Lambda_{\max}^2\pi\sqrt{\frac{R\beta}{2\sigma r_0}}\int_c\left[\sum_m \sqrt{m}\,P_m{}^2\,(|\,\boldsymbol{a}_m\,|^2 + b_m{}^2)\right]r\,dc$$

where $R = \sqrt{\mu_0/\varepsilon_0} = 377\ \Omega$ is the impedance of free space.

When one mode dominates all the others in magnitude, the power loss becomes (with M_{mnp} set equal to $\Lambda_{\max} K_{mnp}$ for convenience)

$$\Lambda_{\max}^2 \pi P_m \sqrt{\frac{R\beta m}{2\sigma r_0}} \frac{K_{mnp}^2}{(\omega_{mnp}^2 - m^2\Omega^2)^2} \int_c \left[(\boldsymbol{d}_{mnp})^2 + \frac{r^2}{m^2}(\operatorname{div} \boldsymbol{d}_{mnp})^2\right] r \, \mathrm{d}c \, .$$

Such a situation arises when the frequency is very close to the resonant frequency of the mode. The average energy which is present in the cavity is then, by classical methods

$$\iiint_V (\tfrac{1}{2}\varepsilon_0 E^2 + \tfrac{1}{2}\mu_0 H^2) \, \mathrm{d}V = \Lambda_{\max}^2 \pi \mu_0 P_m^2 \frac{K_{mnp}^2}{(\omega_{mnp}^2 - m^2\Omega^2)^2} \iint_S \left[(\boldsymbol{d}_{mnp})^2 + \frac{r^2}{m^2}(\operatorname{div} \boldsymbol{d}_{mnp})^2\right] r \, \mathrm{d}c \, .$$

The Q of the cavity for that mode is

$$\frac{2\pi \times \text{energy}}{T \times \text{power loss}} ,$$

where T is the period $2\pi/\omega_{mnp}$. It can be written as

$$Q = \frac{2}{\delta} \frac{\iint_S \left[(\boldsymbol{d}_{mnp})^2 + \frac{r^2}{m^2}(\operatorname{div} \boldsymbol{d}_{mnp})^2\right] r \, \mathrm{d}r \, \mathrm{d}z}{\int_c \left[(\boldsymbol{d}_{mnp})^2 + \frac{r^2}{m^2}(\operatorname{div} \boldsymbol{d}_{mnp})^2\right] r \, \mathrm{d}c}$$

where δ is the skin-depth at the resonant frequency. It is this value of Q which will limit the build-up of the mode. Coefficient D_{mnp} now satisfies the differential equation

$$\frac{\mathrm{d}^2 D_{mnp}}{\mathrm{d}t^2} + \frac{\omega_{mnp}}{Q}\frac{\mathrm{d}D_{mnp}}{\mathrm{d}t} + \omega_{mnp}^2 D_{mnp} = M_{mnp} P_m \begin{Bmatrix} \cos(m\Omega t - \phi_m) \\ -\sin(m\Omega t - \phi_m) \end{Bmatrix} .$$

The build-up of the amplitude after sudden injection of the beam at $t = 0$ is given by

$$D_{mnp} = \frac{P_m M_{mnp}}{\omega_{mnp}^2} Q \left[\sin(\omega_{mnp} t - \phi_m) + \sin\phi_m \, \mathrm{e}^{-\omega_{mnp} t/2Q} \cos\beta t + \frac{\omega_{mnp}}{\beta} \mathrm{e}^{-\omega_{mnp} t/2Q} \sin\beta t \left(\frac{\sin\phi_m}{2Q} - \cos\phi_m\right)\right]$$

where $\cos(m\Omega t - \phi_m)$ is used as a second member (the response to $-\sin(m\Omega t - \phi_m)$ follows without difficulty). The angular frequency β is equal to $\omega_{mnp}\sqrt{1 - 1/4Q^2}$. The transients die out after a time of the order QT, where $T = 2\pi/\omega_{mnp}$ is the period at resonance. For the first few cycles, an approximate value of the amplitude is given by

$$D_{mnp} \approx \frac{P_m M_{mnp}}{2\omega_{mnp}^2} [\omega_{mnp} t \sin(\omega_{mnp} t - \phi_m) + \sin\omega_{mnp} t \sin\phi_m] .$$

Conclusion and Acknowledgement

We have obtained general formulas for the fields excited by beams of particles in an accelerator. These formulas allow one, in principle at least, to analyze phenomena such as the interaction between two different beams which are simultaneously rotating in the accelerator. The effect of outside sources, gaps and cavities for example, has not been considered in this report, and will be the object of a future study. The use of the general formulas depends on a precise knowledge of the eigenvectors in the cavity. The latter can be written in closed analytical form for a vacuum chamber of rectangular cross section. The application of the analysis to that particularly interesting geometry will be taken up in another future report.

The author would like to acknowledge useful discussions with Drs. K. R. Symon, L. Jackson Laslett and V. K. Neil.

NUCLEAR INSTRUMENTS AND METHODS 8 (1960) 11–18; NORTH-HOLLAND PUBLISHING CO.

π^- STAR DETECTOR†

A. F. DUNAITZEV, YU. D. PROKOSHKIN and TANG SYAO-WEI

Joint Institute for Nuclear Research, Dubna, USSR

Received 25 February 1960

A scintillation detector possessing the selective sensitivity to π^- mesons is described. The detector records the stars due to π^- mesons coming to rest.

1. Introduction

Most of the π^- mesons stopping in matter give rise to stars—the nuclear disintegrations in which a considerable amount of energy is released, its magnitude being close to the pion mass (140 MeV). This feature makes π^- mesons distinct both from the light particles (μ mesons, electrons) which fail to produce high-energy stars, and from the positively charged nuclear-active particles (protons, π^+ mesons, etc.) producing stars only in flight and with a small probability. By using the scintillator of the scintillation counter as a substance in which the particles are brought to rest, and by recording only the pulses produced by stars, i.e., those corresponding to a large energy release in the scintillator, it is possible to accomplish a simple detector which possesses a selective sensitivity to π^- mesons. A principle possibility of constructing such a π^- star detector, which is not sensitive to other particles, is not doubtful since the recording efficiency for particles which do not produce high-energy stars may be obtained whatever low by increasing the threshold for the pulse amplitude discrimination at the output of the scintillation counter. However, with increasing the discrimination threshold the efficiency of the star recording also falls, although not so rapidly. Therefore, it is not clear *a priori*, whether it is possible to construct a practically usable star detector whose efficiency would be sufficiently high. To answer this question, it is necessary to investigate the amplitude spectra of pulses arising at the output of the scintillation counter when both π^- mesons and the particles which do not produce stars (e.g. π^+ mesons) come to rest in the scintillator. An effective star detector may be accomplished only if the major part of these spectra turn out to be not overlapped.

† This detector has been described briefly in ref. [1]).

2. Spectra of Pulses

To measure the spectra of pulses we made use of the arrangement shown in fig. 1. A collimated

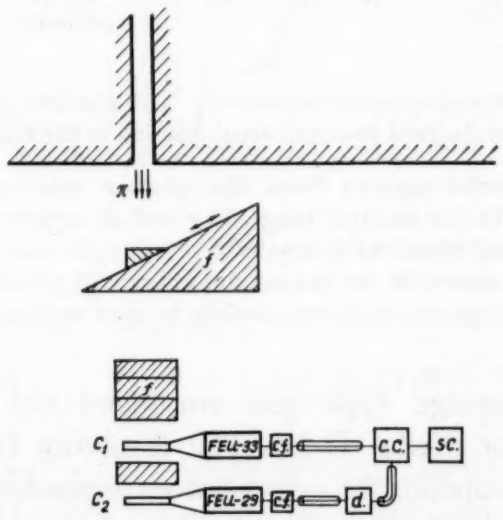

Fig. 1. Detector scheme. C_1 and C_2: scintillation counters; c.f.: cathode followers; c.c.: coincidence circuit; sc: scaler; d: variable delay (up to 5×10^{-8} sec) to compensate the time shift of counters C_1 and C_2 with variation of V_2; f: moderating absorbers.

beam of 170 MeV π^- mesons from the synchro-cyclotron of the Laboratory of Nuclear Problems of JINR passed through a graphite absorber. The π^- mesons slowing down were detected by a

[1]) A. F. Dunaitzev, Yu. D. Prokoshkin, Tang Syao-wei. Pribory i tekhnika eksperimenta (1960) (in press); Proceedings of the International Conference on high-energy accelerators and instrumentation (1959, CERN, Geneva) p. 592.

telescope consisting of two scintillation counters in coincidence. The plastic scintillators of both counters were $6 \times 6 \times 1.5$ cm³. The photomultiplier of the first counter FEU-33 worked in the regime of time resolution, the photomultiplier of the second counter FEU-29—as a spectrometric one. The coincidence circuit was

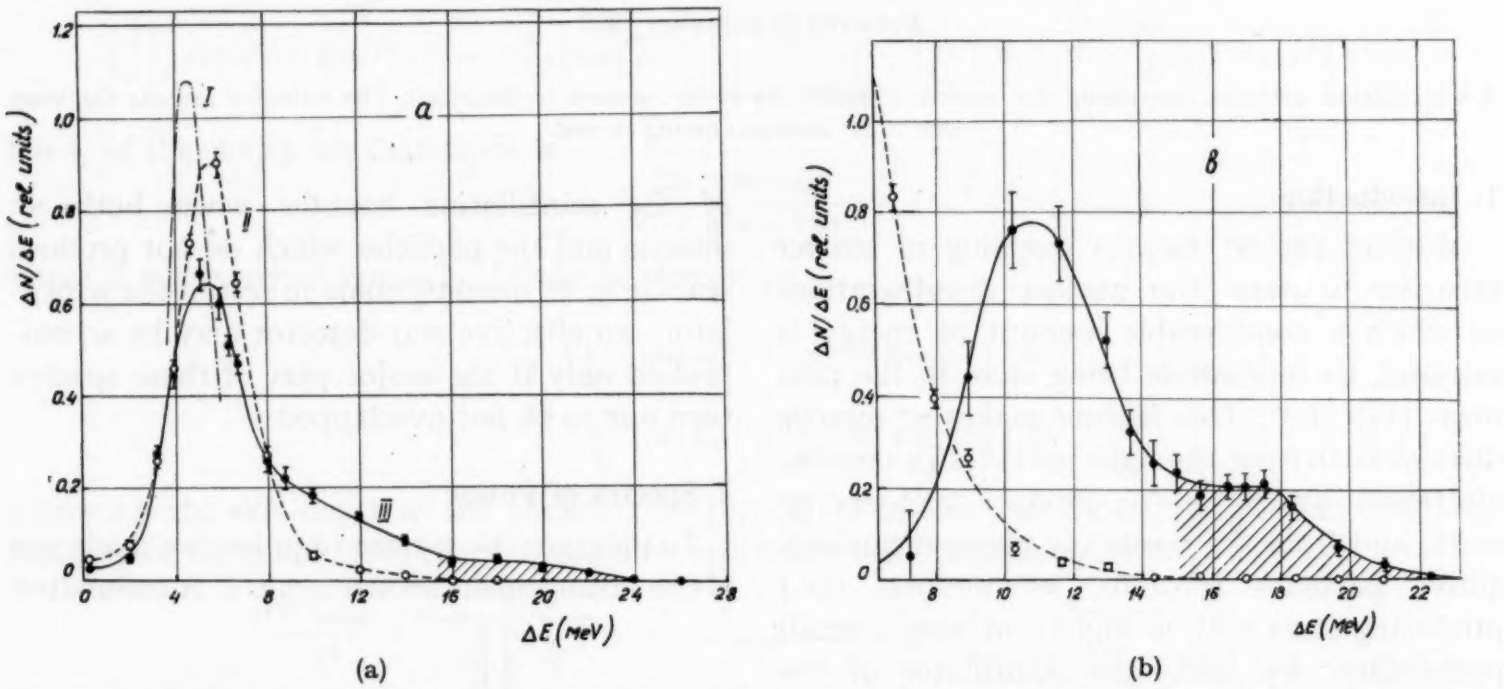

Fig. 2. Pulse spectra in counter C_2. The abscissa axis is the energy lost by π^- meson in the scintillator. The spectra are normalized to equal area. Shaded is the region of the spectrum not overlapped with the "stop spectrum".

(a) I: pulse spectra from the passing relativistic π^- mesons with the residual range 50 g/cm² of carbon and the range spread equal to $\pm$ 4 g/cm²;
II: the spectrum for the residual range 10 g/cm²;
III: the spectrum corresponding to zero residual range.

(b) $\frac{\text{III}}{\text{I}}$-pulse spectrum from π^- mesons stopping in the scintillator;
$\frac{\text{II}}{\text{I}}$-a part of spectrum II.

of the bridge type and employed the semiconductor diodes D-2A. The resolving time of the telescope for the coincidences depended upon the length of the pulse-forming short-circuited cables and was equal to 10^{-8} sec. From the output of the coincidence circuit the pulse was fed to start the pulse height analyzer AADO-1. Simultaneously, the pulse to be analyzed from the output of the counter C_2 was applied to the input of this analyzer.

The amplitude spectra of pulses were obtained with three different thicknesses of the absorber (fig. 2a). The first spectrum of those measured is a comparatively narrow line corresponding to the passage of the particles with relativistic ionization losses through the scintillator. The following spectrum was obtained when such absorber was chosen so as π^- mesons would lose almost all their energy in the detector, but they would not yet stop in C_2. At last, the third spectrum was measured with the thickness of the absorber corresponding to the maximum number of the stops of π^- mesons in the scintillator C_2. At such a position of the absorber 20% of all the π^- mesons incident on the scintillator stopped in it. The remaining ones passed the scintillator through. The spectrum of pulses corresponding to these passing π^- mesons must have a shape analogous to the second spectrum in fig. 2a. Therefore, by subtracting the second spectrum from the third one (after the corresponding normalization) it is possible to single out the pulse spectra corresponding to π^- mesons coming to rest only (fig. 2b).

When π^- mesons stop in the scintillator, the energy is released because of the two processes occurring in succession. Firstly, a π^- meson is slowed down losing rather large energy (≈ 10 MeV in our case) for the ionization of the medium. Then it produces a nuclear disintegration, and the outgoing particles of the star

leave a part of their energy in the scintillator. The spectrum presented in fig. 2b is, therefore, a result of the superposition of two distributions: the "stop spectrum" and the "star spectrum" corresponding to the two processes mentioned above. Only the latter of these distributions is characteristic of π^- mesons only. As to the "stop spectrum", it must be the same both for π^- mesons and for π^+ mesons; for μ mesons it is somewhat displaced to the region of small pulses.

An experimental comparison of the spectra of pulses produced when π^- and π^+ mesons come to rest in the scintillator has been made at the beams of π^- and π^+ mesons having the same average energy (70 MeV) and the same spread of ranges. The comparison has shown that an approximately one third part of the stopping π^- mesons yields the pulses exceeding the maximum pulse of the "stop spectrum". It is this part of the spectrum, shaded in fig. 2, that may be used for the work of the telescope in the regime of a star detector. It follows from what has been said that the expected recording efficiency of the stopped π^- mesons must be rather high ($\approx 30\%$).

3. Efficiency

In order the telescope shown in fig. 1 could detect only the stars due to π^- mesons it is sufficient to set at the output of the counter C_2 a discriminator which does not permit small pulses to reach the coincidence circuit. An analogous result may be obtained in a simpler manner by decreasing the voltage V_2 at the photomultiplier of this counter. Fig. 3 shows the change in the characteristics of the detector as the voltage V_2 decreases. (It should be, of course, borne in mind that all the values for V_2 given here and further have a relative character.) In this figure are plotted the results of measurements of π^- meson counting rate N as a function of the thickness of the matter R they traverse (absorber and scintillators). The mean range of π^- mesons was 62.5 g/cm² of carbon, that corresponds to an energy of 170 MeV; the range spread due to the beam being not monoenergetic and to straggling was found to be ± 4 g/cm². In the region of high voltages $V_2 > 1400$ V where the recording

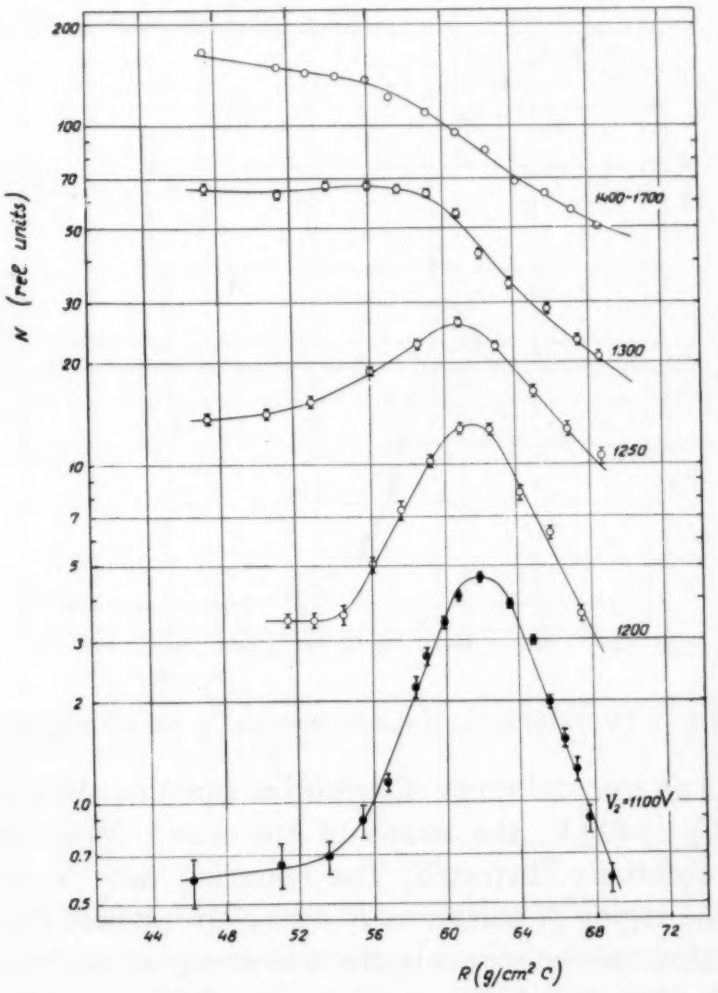

Fig. 3. The dependence of N upon R at various voltages V_2.

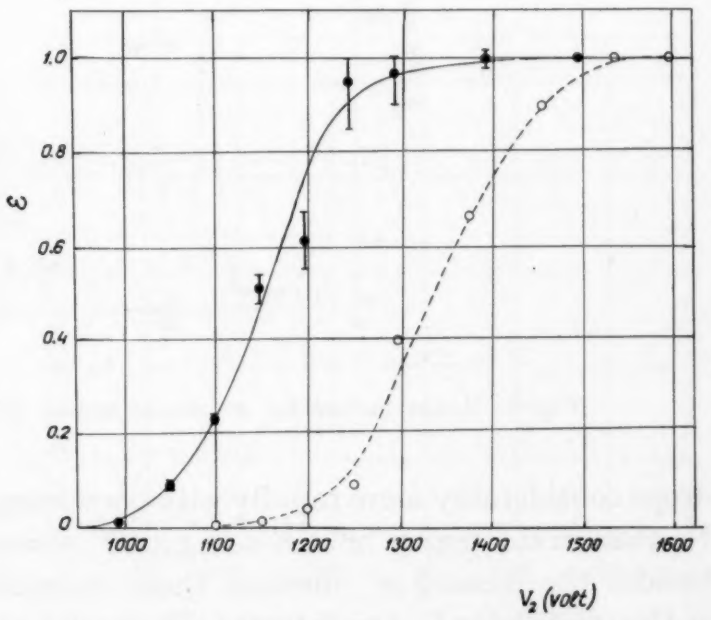

Fig. 4. Detector efficiency. $\overline{\mathrm{I}}$ — ε_{st}; O — ε_0. The efficiency ε_0 was measured for π^- mesons with residual range equal to 10 g/cm² C.

efficiencies for the passing and stopping π^- mesons are close to unity, and, therefore, do not change by varying V_2, the dependence $N(R)$

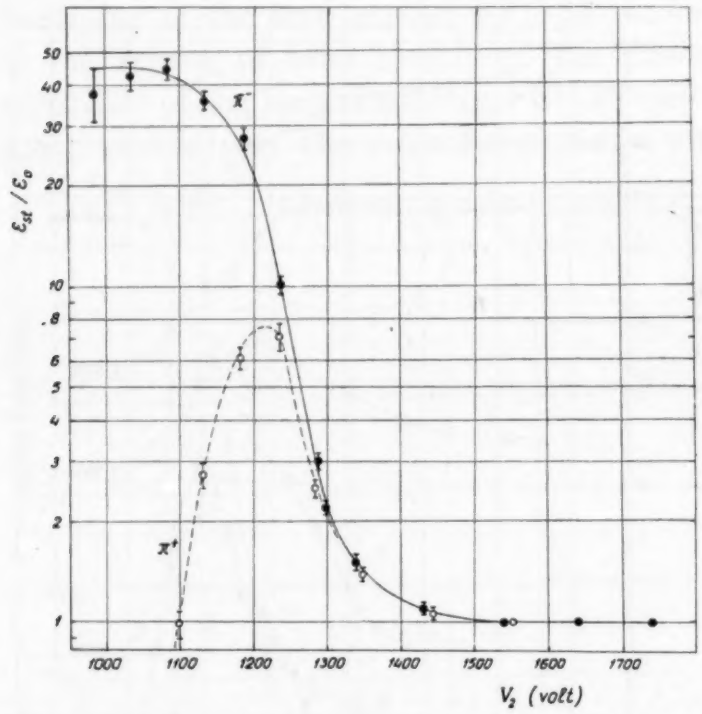

Fig. 5. The ratio $\varepsilon_{st}/\varepsilon_0$. $\overset{\top}{\underset{\perp}{\bullet}}$ -for π^- mesons; $\overset{\top}{\underset{\perp}{\circ}}$ -for π^+ mesons.

is an integral range distribution function. When $V_2 < 1400$ V, the shape of the curve $N(R)$ is essentially distorted. The counting rate N in the region of thickness $R \leqslant 50$ g/cm², where the telescope detects only the traversing π^- mesons drops considerably more rapidly with decreasing V_2 than in the region $58 \leqslant R \leqslant 66$ g/cm², where besides the passing π^- mesons, those stopped in the scintillator C_2 are detected. The variation of the shape of the curve $N(R)$ with the decrease of V_2 is going on up to $V_2 = 1100$ V. By a further diminishing of the voltage the shape of the "peak" alters no longer, and only an identical decrease in the magnitudes of N takes place for all the values of R. In this voltage region the curve practically coincides with the differential range distribution function.

Being aware of the range distribution function of π^- mesons it is not difficult to obtain from the dependences $N(R)$ the magnitudes of the recording efficiency of the passing (ε_0) and stopping (ε_{st}) π^- mesons. In calculating these efficiencies (fig. 4) use was made both of the curves from fig. 3 and of an analogous ones measured at the 67 MeV π^- meson beam. As is seen from fig. 4, at first the efficiency ε_0 drops with decreasing the voltage V_2 much quicker than ε_{st} in agreement with the spectra given in fig. 2. However, at low voltages the rise of the ratio $\varepsilon_{st}/\varepsilon_0$ becomes slower, and for $V_2 \leqslant 1100$ V, the magnitude of this ratio is no longer dependent upon V_2 (fig. 5). Such a behaviour of $\varepsilon_{st}/\varepsilon_0$ can be easily understood if we take into account that π^- mesons produce stars both when they are brought to rest in matter and in flight. The ratio of the probabilities for these two processes for our scintillator equals approximately 50, that is close to the value of $\varepsilon_{st}/\varepsilon_0$

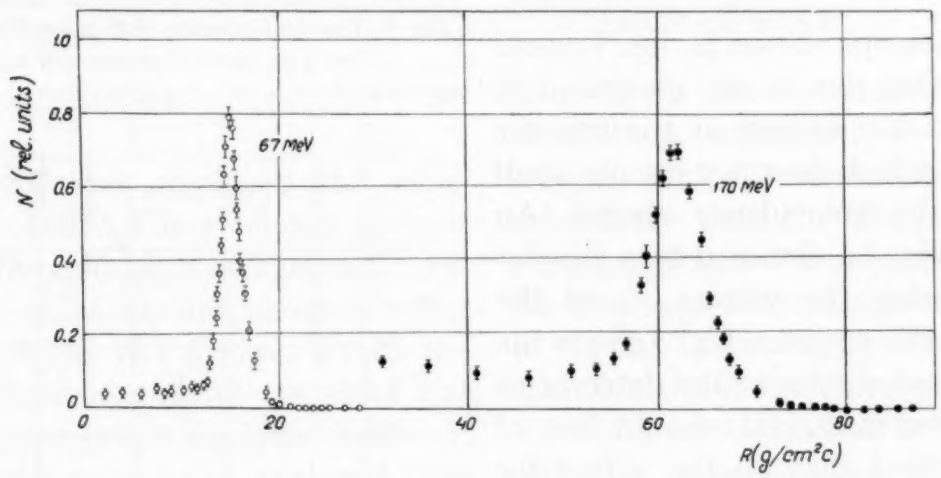

Fig. 6. Range curves for π^- meson beams at energies of 67 ($\overset{\top}{\underset{\perp}{\circ}}$) and 170 MeV ($\overset{\top}{\underset{\perp}{\bullet}}$); $V_2 = 1100$ V.

obtained for small voltages where the detector is sensitive only to stars.

The ratio $\varepsilon_{st}/\varepsilon_0$ changes with decreasing V_2 in another way when the detector records π^+ mesons (fig. 5). In contrast to π^- mesons, π^+ mesons give rise to stars only in flight. Therefore,

the magnitudes of $\varepsilon_{st}/\varepsilon_0$ for π^- and π^- mesons coincide only in the range of large values for V_2, where the detector effectively records the pulses belonging to the "stop spectrum". When one goes over to the region of voltages where the detector is sensitive only to stars, the efficiency ε_{st} for π^+ mesons falls, and the ratio $\varepsilon_{st}/\varepsilon_0$ decreases rapidly.

A comparison of the curves given in fig. 5 shows that the telescope begins to work in the regime of a star detector at the voltages $V_2 \approx 1100$ V. The efficiency ε_{st} corresponding to this voltage is equal approximately to 30%, what is close to the estimate obtained earlier from the analysis of the spectra. The recording efficiency for the π^- mesons coming to rest in the scintillator ε_{st} should not be confused with that for π^- mesons incident on the detector input w, which, in our case, is considerably lower than ε_{st} due to the disappearance of mesons when they are passing through the absorber of the detector, and due to a comparatively small thickness of the scintillator. If we use a thick scintillator, i.e., whose thickness is close to the spread of π^- meson ranges, then the latter factor from those mentioned above is removed. In this optimal case the ratio w/ε_{st} is found to be 70% at an energy of π^- mesons being 65 MeV, and 40%—at 170 MeV.

A star detector employing a thick scintillator may be used in experiments where a high efficiency of π^- meson recording is required. If the range curve of π^- mesons is necessary to be measured, the thickness of the scintillator should be taken small compared with the range spread. Typical range curves which are available when the telescope works as a star detector are presented in fig. 6. These curves have been measured at two different beams of π^- mesons with the mean energies of 67 and 170 MeV.

4. Selection Characteristics of the Detector

Since the star detector detects only high energy stars produced by stopping π^- mesons, it is little sensitive to other particles which do not create such stars. The selection ability of the star detector is convenient to be characterized by a selection coefficient K, which is the ratio of the recording efficiency for π^- meson stops to that of other particles both coming to rest in the scintillator (K_{st}) and those passing through the detector (K_0).

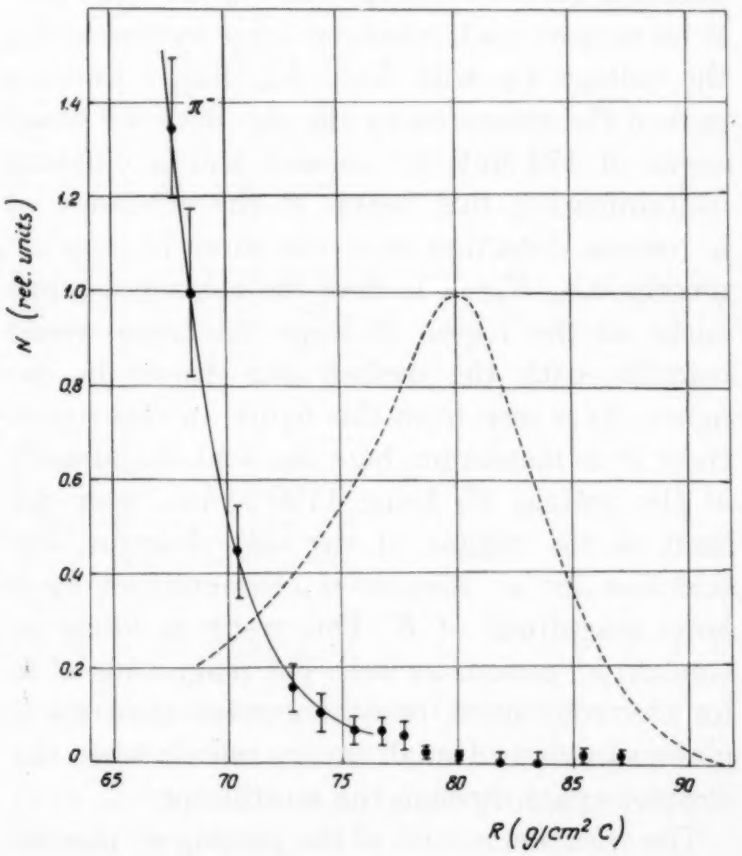

Fig. 7. Inefficiency of the star detector to μ^- mesons. $\frac{\cdot}{\cdot}$-the measured range curve. The real μ^- meson range curve is shown by the dashed line. $V_2 = 1100$ V.

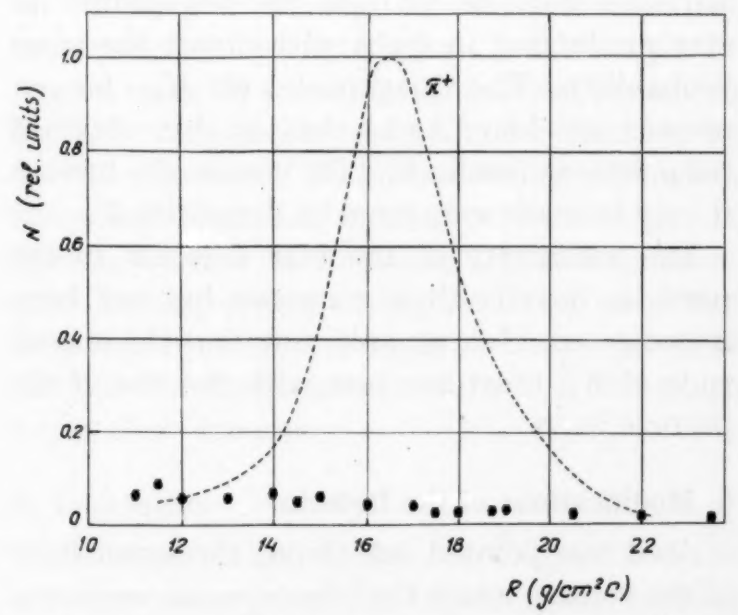

Fig. 8. The same as in fig. 7, but for π^+ mesons of 67 MeV mean energy.

μ mesons and electrons fail to produce high energy stars either in flight, or by the stopping. (When coming to rest in matter possessing large atomic weight μ^- mesons may give rise to stars, but with a small energy release.) Therefore, the selection coefficients K_{st} and K_0 for light particles may be made whatever large by decreasing the voltage V_2, with $K_0 \gg K_{st}$. Fig. 7 shows a part of the measured by the star detector range curve of 170 MeV π^- mesons and μ^- mesons contaminating this beam. If the efficiency of μ^- meson detection were the same like for π^- mesons, i.e., $K_{st} = 1$, then the measured range curve in the region of large thickness would coincide with the dashed line drawn in the figure. As is seen from this figure, in this region there is no maximum, here $K_{st} \geqslant 30$. So, already at the voltage V_2 being 1100 V, i.e., near the limit of the regime of the star detector, the selection for μ^- mesons is characterized by a large magnitude of K. This result is likely to concern μ^+ mesons as well. The magnitude of K for electrons must be still greater than for μ mesons in view of small energy release when the electrons pass through the scintillator.

The selection in case of the passing π^+ mesons is characterized, according to the measurements, by the same magnitude of $K_0 \approx 50$, as in case of π^- mesons. Note, that the magnitude of K_0 must be analogous for other nuclear-active particles since all of them are responsible for star production in flight with about the same probability. The magnitude of K_{st} for π^+ mesons was found to be close to that obtained for μ mesons (see fig. 8). Like in case of μ mesons it may be made very large by decreasing V_2.

The sensitivity of the star detector to the particles heavier than π mesons has not been investigated. Here we only note that the magnitude of K_{st} must decrease with the rise of the particle mass.

5. Modifications of the Detector

As it was pointed out above, the upper limit of the voltage where the telescope can work as a star detector turns out to be $V_2 = 1100$—1150 V. If we increase the voltage by 50—100 V, the detector starts to record the pulses due to the "stop spectrum". Here, as is seen from figs. 4 and 5, the recording efficiency for the stops ε_{st} may be found to be close to unity while the ratio $\varepsilon_{st}/\varepsilon_0$ remains still large. The telescope working in this regime (we shall call it a "stop detector"), unlike the star detector is equally sensitive to π^- mesons and to π^+, μ^- and μ^+ mesons (fig. 9).

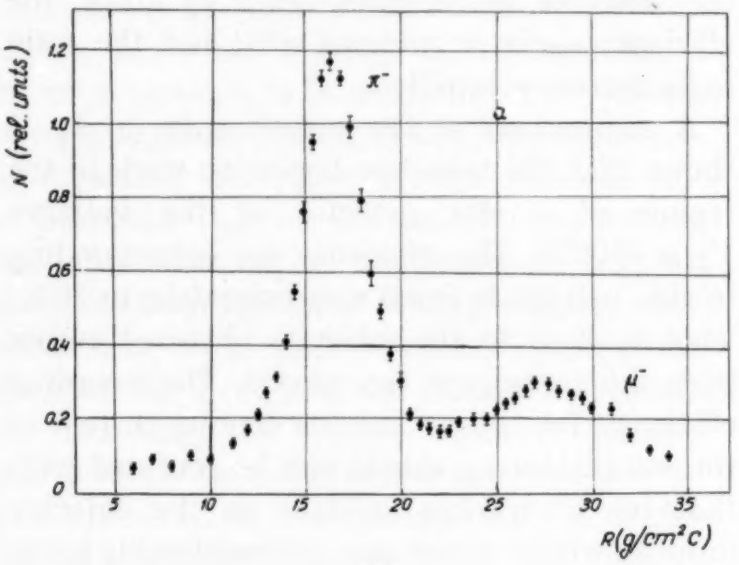

(a)

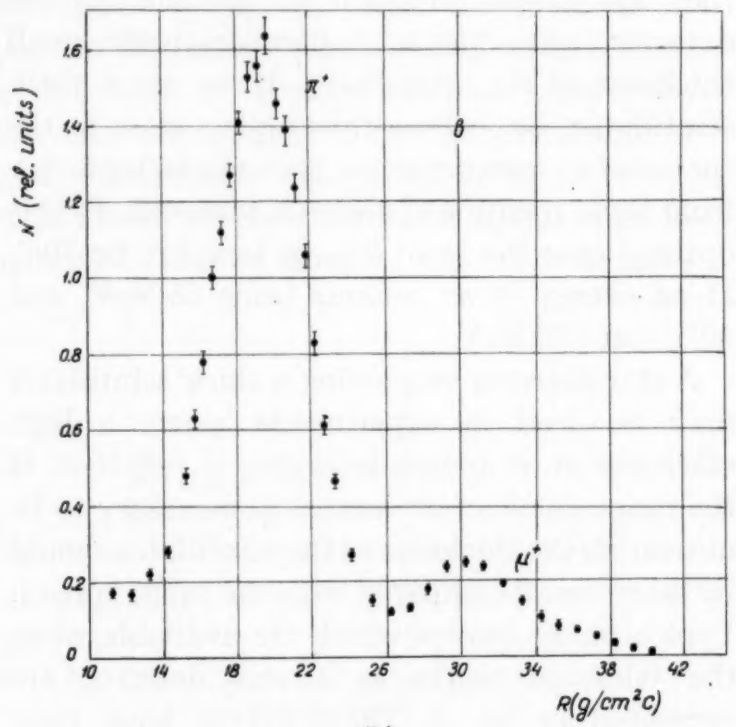

(b)

Fig. 9

Range curves measured by means of the stop detector.
(a): for the beam of π^- and μ^- mesons with the momentum 150 MeV/c. (π^- meson energy is 67 MeV).
(b): for the beam of π^+ and μ^+ mesons with the momentum 163 MeV/c. $V_2 = 1250$ V.

When the intensity of the π meson beam is $\approx 10^4\,\mathrm{sec}^{-1}$, the counting rate of the stop detector amounts to some hundred counts per second. Such large counting rate allows to make the measurements of the range curves $N(R)$ of only one counter, was found to be not very much different from the real range curve. However, the star detector consisting of only one counter could be hardly used for work under more difficult background conditions

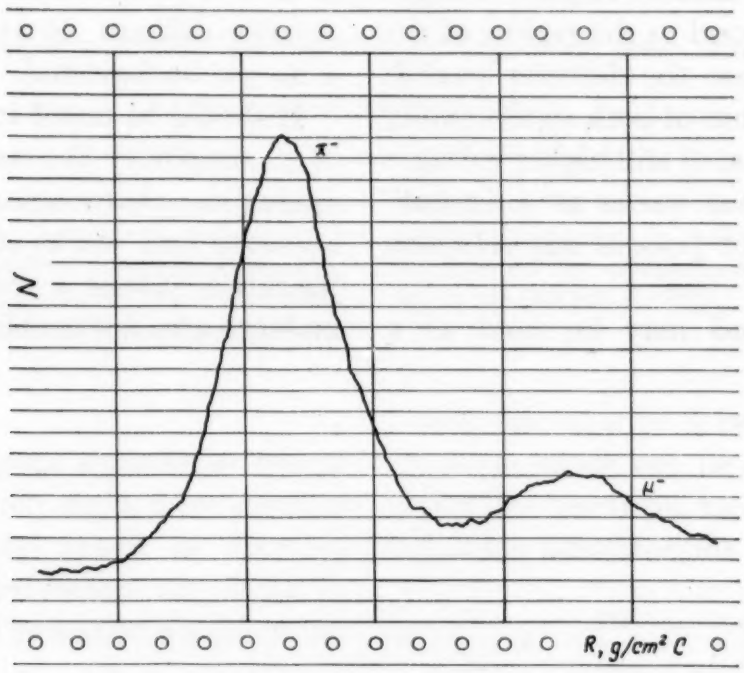

Fig. 10. Range curve registered on the record chart of the self-recording integrator. $V_2 = 1250$ V.

automatic. This presents considerable advantages in the case when in the course of an experiment it becomes necessary to control the magnitude of the beam energy frequently and quickly. For registering the range curve a self-recording integrator was connected to the output of the coincidence circuit. The motor of this integrator rotated synchronously with that moving the wedge-shaped absorber (fig. 1). A typical range curve thus measured is given in fig. 10. All the measurement procedure takes some minutes only.

The pulses in the counter C_2 detected in the regime of a star detector are so large that they essentially exceed all the outside pulses due to the background which is present in the experimental hall of the accelerator when working with the π^- meson beams. This allows to simplify the scheme of the star detector by excluding the counter C_1 and by connecting the input of the scaler directly with the output of the counter C_2. The range curve of 70 MeV π^- mesons measured by means of such a simplified detector consisting than in our case (e.g., in the proton or neutron beam).

Finally, let us point to one more modification of the star detector scheme. This modification consists in replacing the counter C_2 for the counter analogous to C_1, i.e., with a good time resolution but having a comparatively bad spectrometric characteristics. In this case so large a value for the ratio $\varepsilon_{st}/\varepsilon_0$ as that presented in fig. 5 is impossible to obtain; it is found to be 10—20. However, the star detector of such a simplified form has a practical advantage. It does not differ in anything from "standard" scintillation telescopes. So, the latter ones may be used as a star detector without essential changes for rough measurements of the range curve of π^- mesons.

6. Conclusion

An investigation of the characteristics of the detector shows that the region of its working voltages is separated into three essentially different parts. When the voltages are low, the

telescope works in the regime of a star detector, distinguishing π^- mesons coming to rest in the scintillator from other stopping and passing particles. The region of voltages corresponding to this regime is 150—200 V for the type of the photomultiplier we have chosen. Higher voltages of 1200—1270 V correspond to the regime of the stop detector. In this case the detector records the stops of π and μ mesons of both signs equally well. Finally, in the region of still higher voltages ($V_2 > 1400$ V) the detector works as a "usual" telescope which does not possess any selection properties.

The detector described may be used as a spectrometer which allows to measure the spectra of π^- mesons under the conditions of large outside background. It is most reasonable to apply this detector for investigating the spectra of π^- mesons in the low energy region (< 50 MeV) where the magnetic spectrometer is usually difficult to apply because of the large μ meson background.

It should be noted in conclusion that because of its simplicity the star detector possesses good operation characteristics. It can be easily adjusted and works stably; for the time of its operation (about a year) its parameters do not undergo any noticeable changes.

NUCLEAR INSTRUMENTS AND METHODS 8 (1960) 19–22; NORTH-HOLLAND PUBLISHING CO.

SPACE-CHARGE EFFECTS IN CYLINDRICAL BEAMS WITH UNIFORM ACCELERATION

C. D. MOAK†

Atomic Energy Research Establishment, Harwell, Didcot, Berks., England

Received 25 February 1960

The profiles of cylindrical beams of charged particles undergoing uniform acceleration have been derived for a large number of beam intensities, configurations and energies, for the case where the emergent beam is parallel. Derivations of the results are presented and their uses are illustrated. Use of the results for certain cases of non-parallel emergence is outlined. Tables of the integral required in the calculations are available as a Harwell report No. AERE-R. 3255.

1. Introduction

Profiles for mono-energetic cylindrical beams of charged particles in free flight were derived originally for use in the study of electron beams[1,2,3]), and these derivations are listed in a number of texts[4,5,6]). The initial assumptions are as follows:

1. The density of the beam is uniform and has an initial radius r_0 at $z = 0$.

2. The particles all have equal axial velocity and zero initial radial velocity.

3. The axial component of the field due to space charge is assumed to be negligible throughout.

The equation of motion of a particle on the edge of a beam of radius r (cm) is given by

$$MM_{\mathrm{p}}\frac{\mathrm{d}^2r}{\mathrm{d}t^2} = \frac{2QeI}{vr} \qquad (1)$$

where I is the current (e.s.u. per sec) of particles of axial velocity v (cm per sec) each having a mass of $M\,M_{\mathrm{p}}$ (grams) where M is the atomic weight number and having an effective charge of Qe (e.s.u.) where Q is the charge state of the particles. Substituting the values of e and M_{p}, and changing units, we have

$$5.8 \times 10^{-22}\left(\frac{M}{QI_{\mathrm{mA}}}\right) r\frac{\mathrm{d}^2r}{\mathrm{d}t^2} = \frac{1}{v} \qquad (2)$$

where I_{mA} is the current in milliamperes and v is in cm per sec.

† On leave from Oak Ridge National Laboratory, Oak Ridge, Tennessee, U.S.A.

For the case of a beam in free flight v is a constant which can be related to the voltage to which the particles have been accelerated. The following substitutions can be made:

$$R = \frac{r}{r_0};\; R' = \frac{\mathrm{d}R}{\mathrm{d}z};\; R'' = \frac{\mathrm{d}^2R}{\mathrm{d}z^2};\; v = \frac{\mathrm{d}z}{\mathrm{d}t} = \sqrt{\frac{2QeV}{M}}\,. \qquad (3)$$

With these substitutions eq. (2) reduces to

$$Kr_0^2(R')^2 = \ln R \qquad (4)$$

where

$$K = 24.33\left(\frac{Q}{M}\right)^{\frac{1}{2}} V_{\mathrm{kV}}^{\frac{3}{2}} I_{\mathrm{mA}}^{-1}$$

and V_{kV} is the potential in kilovolts to which the particles have been accelerated. Integration of eq. (4) gives

$$K^{-\frac{1}{2}}\frac{z}{r_0} = Z = \int_1^{R_f}\frac{\mathrm{d}R}{\sqrt{\ln R}}\,. \qquad (5)$$

Values of Z as a function of R have been given by Lash-Miller and Gordon[7]). From these values the beam radius (in units of initial beam

[1]) E. E. Watson, Phil. Mag. **3** (1927) 849.

[2]) B. v. Borries and J. Dosse, Arch. Electrotech. **32** (1938) 221.

[3]) A. V. Haeff, Proc. Inst. Radio Engrs. **27** (1939) 586.

[4]) O. Klemperer, Electron Optics (Cambridge Univ. Press, 1953) p. 202.

[5]) Zworykin, Morton, Ramberg, Hillier and Vance, Electron Optics and the Electron Microscope (John Wiley and Sons, New York, 1945) p. 591.

[6]) J. R. Pierce, Theory and Design of Electron Beams (D. van Nostrand Company, Inc., New York, 1954) Ch. IX.

[7]) W. Lash-Miller and A. R. Gordon, J. Phys. Chem. **37** (1931) 2785.

radius) can be plotted as a function of distance (in units of initial beam radius) with a scale factor, contained in $K^{-\frac{1}{2}}$, which depends upon beam current, voltage and particle charge to mass ratio. With the curves available, the requirement that the beam be parallel initially is no longer necessary. It remains necessary only that the initial radial velocity of each particle be proportional to its initial radius in cases where initial radial velocities are non-zero.

2. Discussion

For the case where the axial velocity is not constant, the derivations must differ beyond eq. (2). Certain special cases of this problem have been worked out. Moss has shown a small number of profiles for electron-beam focusing in a post-acceleration cathode-ray tube[8]). Special cases have been worked out by King, Hobbis and Harrison in design studies for a proton linear accelerator at Harwell[9]). In both these instances as well as in the present paper, uniform acceleration will be assumed. The calculations presented here will pertain to most cases of beams converging in the direction of positive acceleration. By starting with the same initial conditions as before and decelerating the particles uniformly towards rest, it turns out that a wide range of design conditions may be covered with a fairly complete set of beam profiles. This procedure is equivalent to assuming a final beam-condition in an accelerator, (viz. emergent beam parallel and final voltage V_{kV}) and deriving the profile of the beam back through the accelerator toward the source. In this case the velocity may be written as

$$v = \left(\frac{2QeV_{\mathrm{kV}}}{M}\right)^{\frac{1}{2}} \left(1 - \frac{z}{L}\right)^{\frac{1}{2}} \tag{6}$$

where V_{kV} is the final or maximum voltage to which the particles are accelerated; working backward through the accelerator. V_{kV} becomes the starting potential. The number L is the axial distance in which the particles come to rest. Making this substitution, eq. (2) becomes

$$DL^{-\frac{3}{2}} (L - z)\, r \frac{\mathrm{d}}{\mathrm{d}z}\left[(L - z)^{\frac{1}{2}} \frac{\mathrm{d}r}{\mathrm{d}z}\right] = 1 \tag{7}$$

where

$$D = 5.8 \times 10^{-22} \left(\frac{M}{QI_{\mathrm{mA}}}\right)\left(\frac{2QeV_{\mathrm{kV}}}{M}\right)^{\frac{3}{2}}.$$

If now we make the substitution that $x^2 \equiv (L - z)$ we have

$$r \frac{\mathrm{d}^2 r}{\mathrm{d}x^2} = \frac{4L^{\frac{3}{2}}}{Dx}. \tag{8}$$

If we make an additional substitution that $r \equiv 2L^{\frac{3}{4}} D^{-\frac{1}{2}} x^{\frac{1}{2}} q$, we have

$$q\left[x^2 \frac{\mathrm{d}^2 q}{\mathrm{d}x^2} + x \frac{\mathrm{d}q}{\mathrm{d}x} - \tfrac{1}{4} q\right] = 1\,. \tag{9}$$

A final substitution $u \equiv x\, \mathrm{d}q/\mathrm{d}x$ gives

$$u\, \mathrm{d}u = \frac{\mathrm{d}q}{q}\left[1 + \tfrac{1}{4} q^2\right]. \tag{10}$$

Eq. (10) integrates to

$$u = \pm \sqrt{2 \ln q + \tfrac{1}{4} q^2 - B}\,. \tag{11}$$

From the condition that initial radial velocity is zero (beam emerging parallel) we can evaluate B and eq. (11) reduces to

$$u = -\left(2 \ln \frac{2L}{r_0 D^{\frac{1}{2}}} q + \tfrac{1}{4} q^2\right)^{\frac{1}{2}}. \tag{12}$$

Returning to variables x and q we have

$$\left(2 \ln \frac{2L}{D^{\frac{1}{2}} r_0} q + \tfrac{1}{4} q^2\right)^{-\frac{1}{2}} \mathrm{d}q = \frac{\mathrm{d}x}{x} \tag{13}$$

and

$$\ln x + C = -\int_{\frac{r_0 D^{\frac{1}{2}}}{2L}}^{\frac{D^{\frac{1}{2}} r}{\sqrt{2L^{\frac{3}{2}}(L-z)^{\frac{1}{2}}}}} \left(2 \ln \frac{2L}{D^{\frac{1}{2}} r_0} q + \tfrac{1}{4} q^2\right)^{-\frac{1}{2}} \mathrm{d}q \tag{14}$$

$$C = -\ln x_0 = -\ln L^{\frac{1}{2}} \tag{15}$$

$$\ln \left(\frac{L - z}{L}\right)^{\frac{1}{2}} = -\int_{\frac{r_0 D^{\frac{1}{2}}}{2L}}^{\frac{D^{\frac{1}{2}} r}{\sqrt{2L^{\frac{3}{2}}(L-z)^{\frac{1}{2}}}}} \left(2 \ln \frac{2L}{D^{\frac{1}{2}} r_0} q + \tfrac{1}{4} q^2\right)^{-\frac{1}{2}} \mathrm{d}q\,. \tag{16}$$

If we set $w \equiv q/q_0$ and $L/(L - z) \equiv s$ we have

$$\ln (s^{\frac{1}{4}}) = \int_1^A (\omega^2 + a^{-2} \ln \omega^2)^{-\frac{1}{2}}\, \mathrm{d}\omega = y \tag{17}$$

where

$$A = \frac{r}{r_0} s^{\frac{1}{4}} \quad \text{and} \quad a = \frac{K^{\frac{1}{2}}}{2\sqrt{2}} \frac{r_0}{L}$$

where K is given in eq. (4).

[8]) H. Moss, Wireless Eng. **22** (1945) 316.

[9]) King, Hobbis and Harrison, Harwell report AERE GP/R. 1748 (1955).

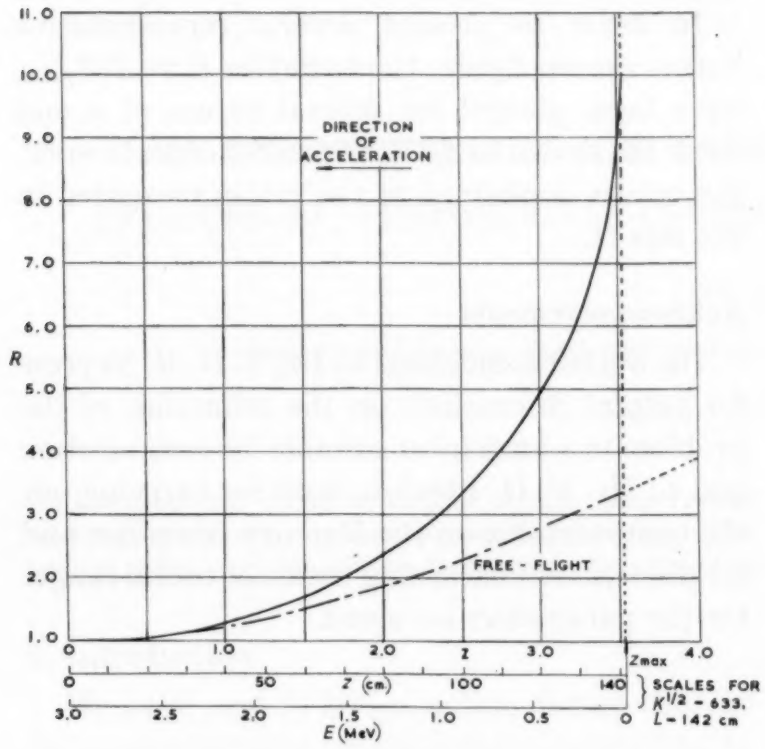

Fig. 1

For any specific problem the value of a will be a fixed parameter. If, for that value of a, the integral of eq. (17) is tabulated, then we will have values of s (and thus z) as a function of $(r/r_0)\, s^{\frac{1}{4}}$. From these values, r as a function of z may be derived and the profile of the beam will be mapped out. A particularly useful set of numbers derivable from the values of the integral of eq. (17) are the values of R as a function of Z where R and Z are defined exactly as in eq. (5) for the case of a beam in free flight.

A set of calculations has been carried out on the Mercury computer at Harwell. A wide range of values of a has been used; in the cases of small a (i.e. relatively gentle accelerations of rather intense beams) the profiles approach that of the free-flight case. For each value of a, the integral has been evaluated for enough values of A to give a particle energy variation of a factor of 10^4 except in cases of extreme radius variation. Only illustrative examples will be given here; a set of tables of y/a, R and Z as a function of A for various values of a is available as Harwell Report No. AERE R-3255.

3. Examples

An example which illustrates the use of the values of R and Z is the following accelerator situation:

Emergent beam: protons ($M = 1$, $Q = 1$); final beam energy 3 MeV ($V_{\mathrm{kV}} = 3000$); beam current 10 mA; final beam radius 0.063 cm.

Accelerator tube length, $L = 142$ cm.

$$K^{\frac{1}{2}} = 4.933 \left(\frac{Q}{M}\right)^{\frac{1}{4}} V_{\mathrm{kV}}^{\frac{3}{4}}\, I_{\mathrm{mA}}^{-\frac{1}{2}} = 633$$

$$a = \frac{K^{\frac{1}{2}}}{2\sqrt{2}} \frac{r_0}{L} = 0.1\ .$$

The curve for the case $a = 0.1$ is given in fig. 1. For comparison, a free-flight profile is shown for a beam of the same current and initial radius, but with no deceleration along the axial direction. The curve shown for $a = 0.1$ would clearly apply to the case where both the accelerator length and the initial radius were changed by any factor; in the new case, only the scale of z would have to be changed. If current and voltage were changed so as to maintain the same ratio of $I_{\mathrm{mA}}^{\frac{1}{2}}/V_{\mathrm{kV}}^{\frac{3}{4}}$ and if r_0 and L were kept

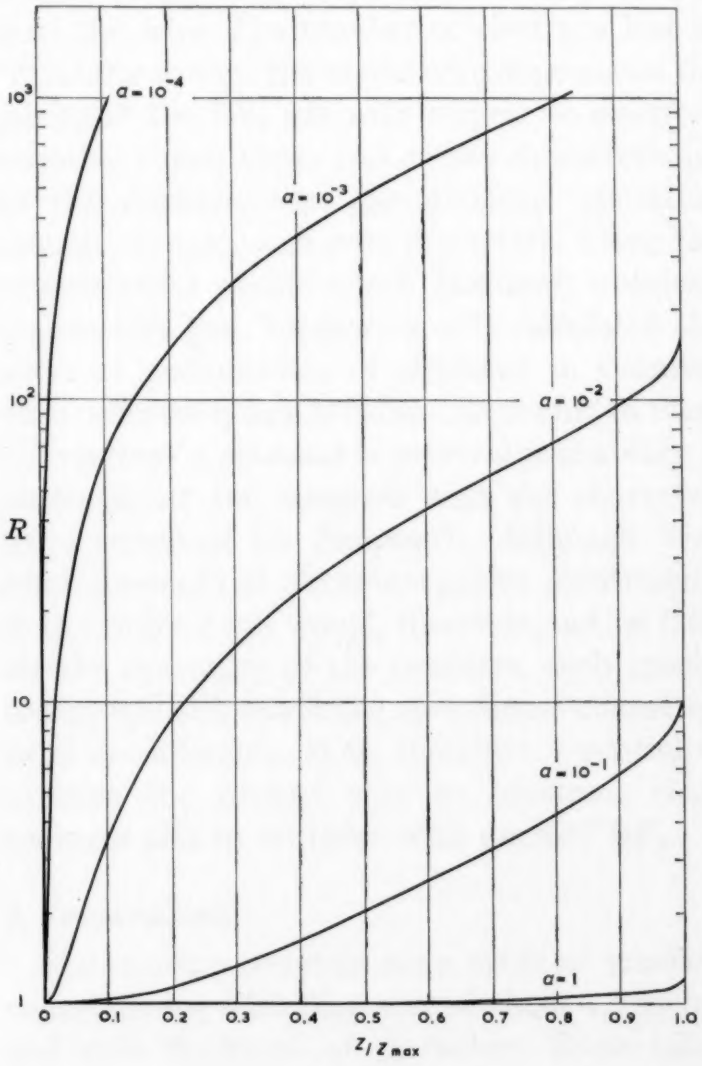

Fig. 2

fixed, then only the E scale would need to be changed. In general, any changes of I_{mA}, V_{kV}, r_0 and L which left $a = 0.1$ would be described by the solid curve of fig. 1, with appropriate scale changes in z and E.

The profiles, reading from right to left, may be terminated before reaching the origin and thus the beam will emerge in a converging condition. The terminated profile may then be joined to a free-flight profile appropriate to the energy at which the curve was terminated. In this way, beam radii at targets positioned away from the end of the accelerator may be derived. The calculations do not provide for cases where beams are diverging in the direction of positive acceleration.

In order to present several representative curves on one figure, the variables R vs Z/Z_{max}, have been plotted for several values of a and these are shown in fig. 2. For more accurate work, the reader is referred to the tables presented in the report.

Acknowledgements

The author is indebted to Dr. T. H. R. Skyrme for helpful discussions on the reduction of the problem to a form most suitable for computation and to Mr. P. D. Preston, both for carrying out the computations on the Mercury computer and for discussions concerning the most useful ranges for the parameters involved.

NUCLEAR INSTRUMENTS AND METHODS 8 (1960) 23–26; NORTH-HOLLAND PUBLISHING CO.

ON THE CONSTRUCTION AND LONG-TERM PERFORMANCE OF MEDIUM PRESSURE BF_3 PROPORTIONAL COUNTERS USED FOR COSMIC-RAY RECORDING

P. H. STOKER

Department of Physics, Potchefstroom University for C.H.E., Potchefstroom, South Africa

Received 10 February 1960

Construction and filling procedure of BF_3 proportional counters for a cosmic-ray neutron monitor is outlined. The method of improvement of the operational characteristics of the counters necessitated by deterioration over the first years of continuous operation is given.

1. Introduction

We have made[1]) BF_3 counters during 1955/56 for a neutron monitor constructed according to the standard design proposed by Simpson[2]) for the I.G.Y. These counters are in continuous operation, recording cosmic-radiation since early 1956. The essential features of the method of construction and of the performance of the counters since then will be reported.

Fowler and Tunnicliffe[3]) have observed a deterioration of their counters after the first filling, but stable performance was obtained by refilling the counters after three months. Other authors[4–6]) have reported on the deterioration of BF_3 counters caused by heavy neutron and gamma irradiation.

Properties of medium and high pressure BF_3 counters are strongly affected by electronnegative constituents in the filling gas[7,8]). In the presence of electronnegative constituents, electrons produced in the gas far from the central wire have less change in reaching the wire to initiate a gas discharge than those produced near the wire. The number of electrons lost in travelling toward the anode wire depends on the purity of the BF_3 gas with respect to electronnegative constituents and on the characteristics of the counter, viz. gas pressure, operating voltage, counter and wire diameters. Using the experimental results which Bistline[9]) obtained for his BF_3 gas, Tongiori *et al.*[7]) calculated the survival probabilities of electrons in counters with different characteristics. According to these calculations a reasonable survival probability is obtained for the counters with the characteristics proposed by Simpson[2]). Although very small amounts of electronnegative constituents in the counter gas would, therefore, not be fatal for the operation of the counters, such constituents will still affect the operational characteristics considerable. It is, therefore, essential to exercise the utmost care to construct clean counters and to fill them with purified BF_3.

2. Construction

The neutron counters were made of seamless copper tubing with diameter of about 1.5 inches and wall thickness of $\frac{5}{64}$ inches. These tubes were cleaned on a lathe by cotton soaked with

[1]) P. J. Kruger, M. Sc. Thesis (1955).

[2]) J. A. Simpson, Cosmic radiation neutron intensity monitor, (published by the Institute for Nuclear Studies, The University of Chicago, January, 1955).
J. A. Simpson, W. Fonger and S. B. Treiman, Phys. Rev. **90** (1953) 934.

[3]) I. L. Fowler and P. R. Tunnicliffe, Rev. Sci. Inst. **21** (1950) 734.

[4]) W. Abson, P. G. Salmon and S. Pyrah, Proc. Inst. Electrical Eng. **105**B (1958) 357.

[5]) O. F. Swift and R. T. Bayard, Nucleonics **17** (5) (1959) 122.

[6]) R. K. Soberman, S. A. Korff, S. S. Friedland and H. S. Katzenstein, Rev. Sci. Inst. **24** (1953) 1058.

[7]) V. Cocconi Tongiori, S. Hayakawa and M. Widgoff, Rev. Sci. Inst. **22** (1951) 899.

[8]) R. B. Mendell and S. A. Korff, Rev. Sci. Inst. **30** (1959) 442.

[9]) J. A. Bistline, Rev. Sci. Inst. **19** (1948) 842.

benzine and finally polished by dry cotton jammed in the tube. The 1 mil tungsten wire was silver-soldered into small brass rods with rounded edges, as illustrated in fig. 1. Before

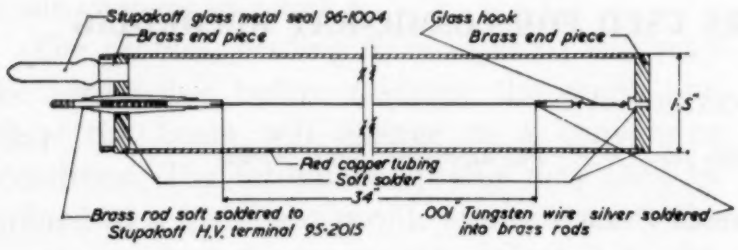

Fig. 1. The construction of the BF_3 proportional counters.

assembling the counter all the pieces were thoroughly cleaned in boiling water followed by washing with alcohol and benzine. After removal of cloth fibres and dust particles the pieces were assembled and the tinned end-pieces of brass soft-soldered to the tube. An assembled counter was immediately sealed to the vacuum and filling system, which was of glass tubing, Apiezon M grease being used for the stopcocks. All the counters had good vacuum properties. A batch of four counters was pumped for about four days while heated to 100° C. While the $BF_3 \cdot CaF_2$ complex† was outgassed at about 150° C, the counters were filled with argon to a few centimetres of Hg pressure to "soak" the walls of the counters. The generated BF_3 obtained by raising the temperature of the complex was purified by passing the gas through a trap at dry ice temperature and filled with sodium fluoride to remove hidrofluoric acid[4,7]) and condensible impurities. The BF_3 was frozen in a second trap immersed in liquid oxygen. The counters were then evacuated by pumping out the argon. Next they were filled for a few minutes with BF_3 by removing the liquid oxygen from the trap. The BF_3 was frozen again and then pumped together with the counters to a good vacuum. This temporary

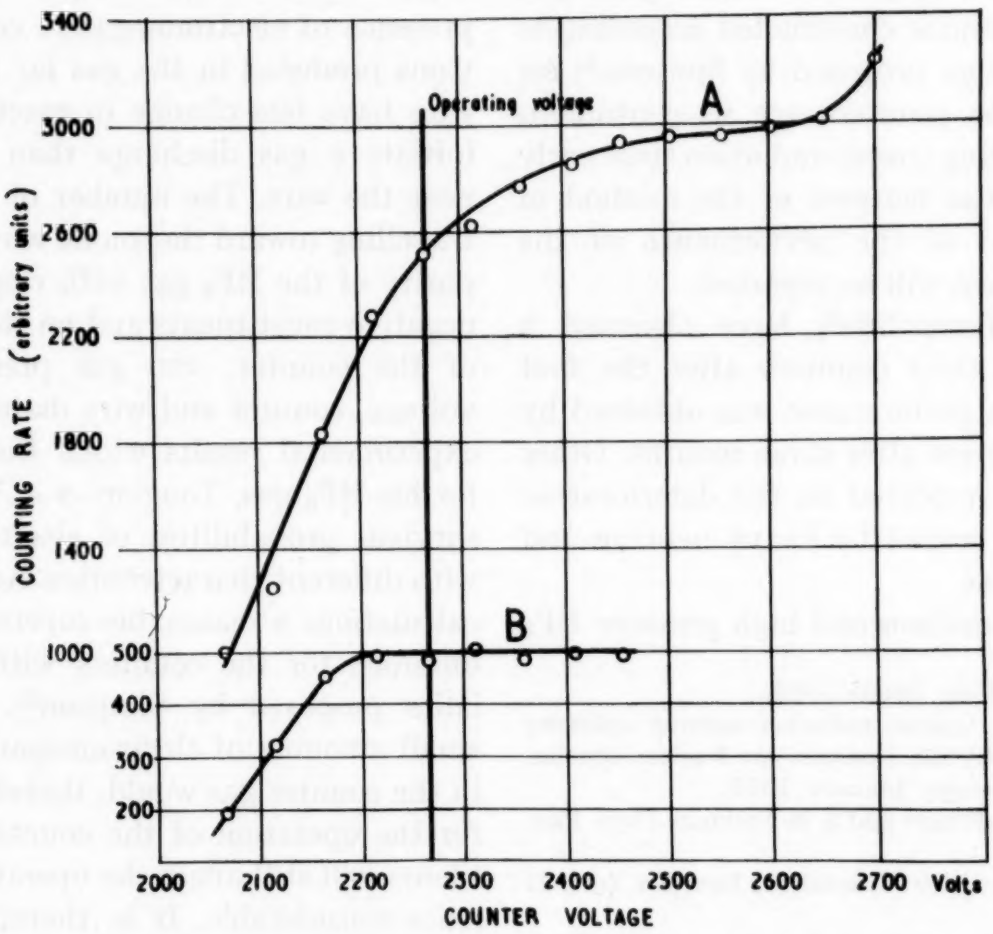

Fig. 2. Counter voltage characteristics after about a year of operation, curve A for a batch of six counters with anode wires connected together, curve B for a single counter.

† Enriched to 96% in the B^{10} isotope as obtained from Carbide and Carbon Chemical Division, Oak Ridge, Tennessee.

filling procedure was repeated once. With the final filling the pressure in the system was adjusted to 45 cm Hg, the counters sealed off and removed.

3. Performance of the Counters

With a narrow neutron beam from a radium-beryllium source (the gamma-rays were absorbed by lead) directed along the counter wire, deterioration caused a steady decrease in the calibration intensity by a 2 mg Ra–Be neutron source and registered cosmic ray neutron intensity with time. Some improvement was obtained by increasing the amplification of the amplifying unit, which had an amplification factor of about 1000 and a clipping time of several microseconds[2]). A steady performance and a return to the original intensity was only obtained by

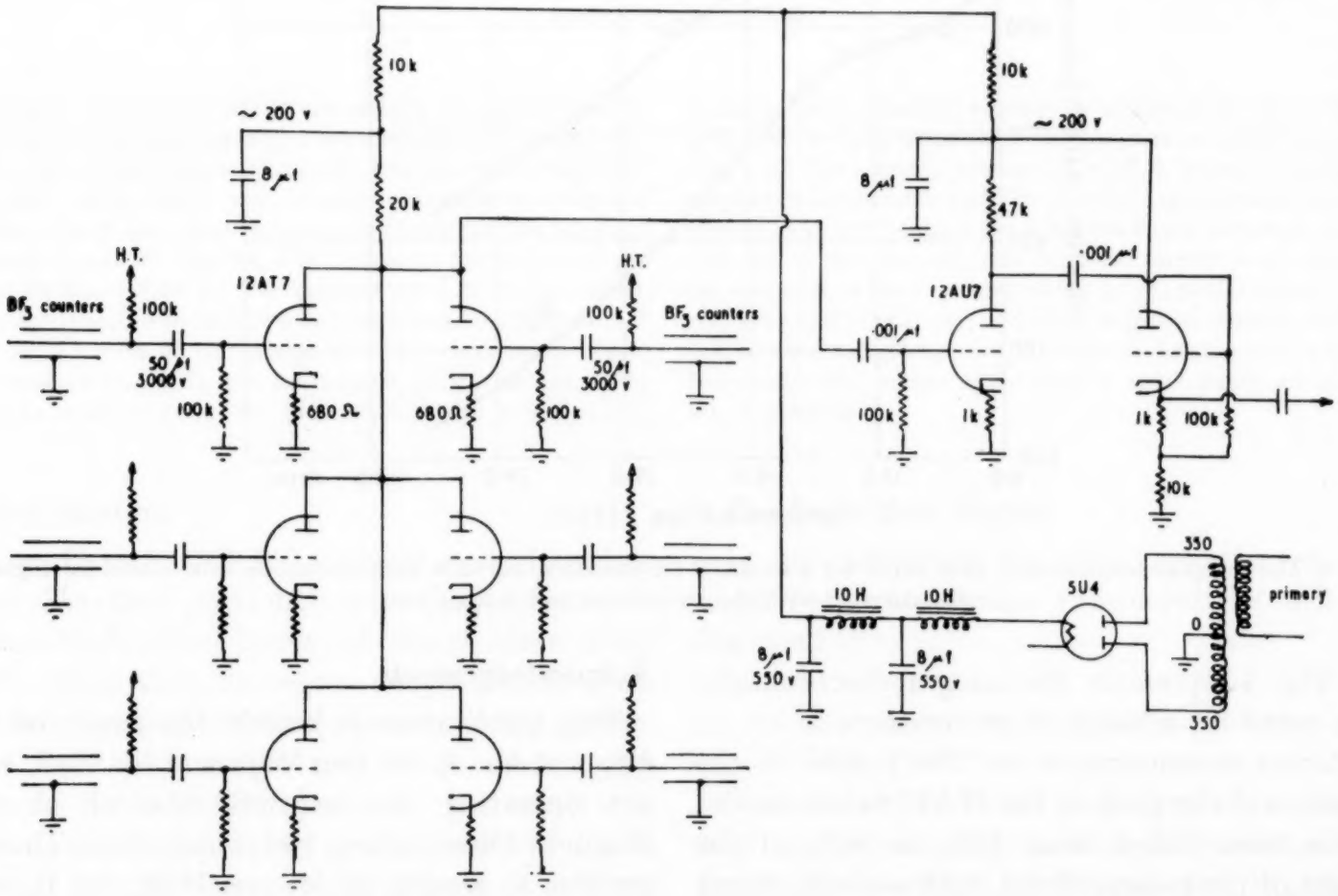

Fig. 3. The circuit for mixing and preamplifying the pulses of a batch of six BF_3 counters.

a double peaked pulse distribution similar to that reported by Fowler *et al.*[3]) and by Abson *et al.*[4]) for good counters, was obtained with no deterioration noticable after three months[1]). After about a year of continuous operation at the Magnetic Observatory at Hermanus, deterioration in the counting rate-voltage characteristics of a batch of six counters was observed. With the anode wires of the six counters connected together to the same head cathode follower, the plateau shifted to a higher voltage (see fig. 2). For single counters a plateau was still obtained at the operating voltage. This connecting the anode wire of each counter to an amplifying tube before mixing the pulses, thus decreasing the capacity on the wires of the single counters. The wiring diagram is shown in fig. 3. The mixing is done in the common plate circuit of the six halves of the 12AT7 tubes. The first halve of the 12AU7 reverses the pulse with some amplification and the second halve serves as cathode follower. The feed-back action of the cathode resistors is sufficient to ensure linearity and stability of this amplifying and mixing unit. The anode voltage can, therefore, be supplied by an unstabilized filtered rectifying unit.

A batch of six counters showed with this amplifying and mixing unit the same characteristic counting rate-operating voltage curve as obtained for the single counters (fig. 2, curve B). Fig. 4 represents the integral-discriminator bias curve for a batch of six counters.

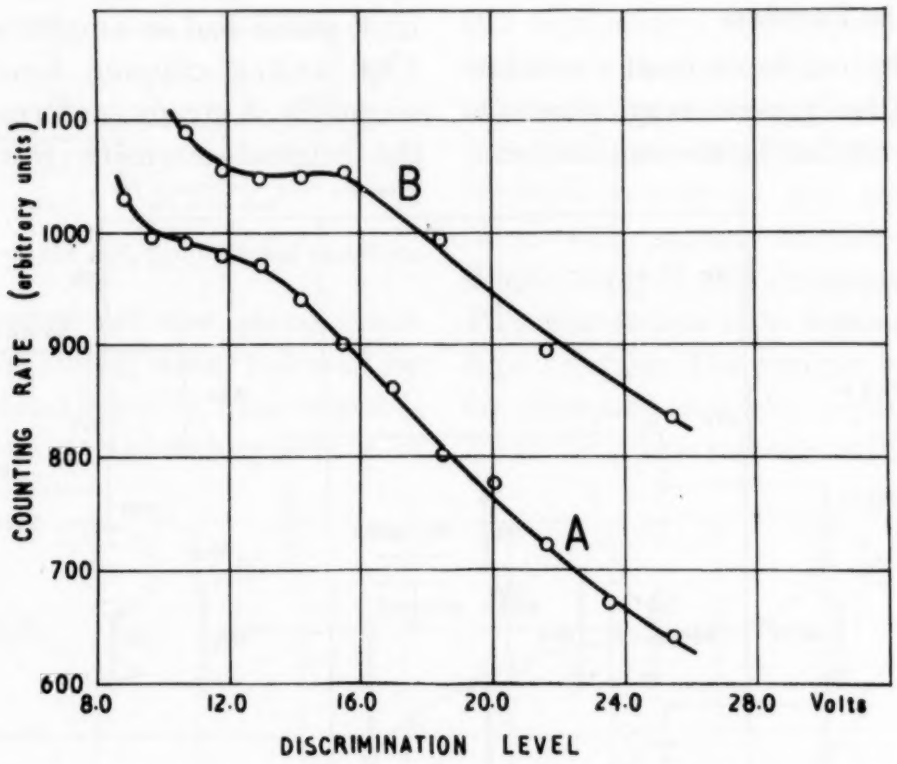

Fig. 4. The integral-discriminator bias curve for a batch of six counters, curve A with the anode wire connected together and curve B with the amplifying and mixing unit.

Recent measurements on the pulses of the counters at the grids of the 12AT7 tubes showed a rise time (taken from 10% to 90% of the height of the pulses) of 0.3 microseconds, decay times from 2 to 3 microseconds, and a pulse height distribution from 10 to 20 mV with a maximum at about 15 mV, as viewed on an oscillograph screen. The operation voltage of the counters was always 2260 volts.

A test of the temperature dependence of the neutron monitor set-up and registering units was made by varying the temperature of the room from 18° C to nearly 40° C, but no significant dependence was found under the neutron irradiation of a 2 mg Ra–Be source.

Acknowledgements

This publication is largely the result of the effort of Mr. A. M. van Wijk and his staff, who are operating the neutron monitor at the Magnetic Observatory, Hermanus, Cape. Thanks are due to Messrs. A. M. van Wijk and R. van der Walt for the information provided, and to Messrs. G. C. Snyman, P. I. Jongbloed and C. R. Smith for technical assistance.

The author wish to acknowledge the financial support provided by the South African C.S.I.R. for the construction of the monitor.

NUCLEAR INSTRUMENTS AND METHODS 8 (1960) 27–39; NORTH-HOLLAND PUBLISHING CO.

THE UTRECHT 850 kV CASCADE GENERATOR

I. BEAM DEFLECTION AND ENERGY CONTROL

C. M. BRAAMS and P. B. SMITH

Fysisch Laboratorium der Rijksuniversiteit te Utrecht, Nederland

Received 9 March 1960

The beam deflection magnet and energy control system of the Utrecht cascade generator are described. The uniform-field magnet has entrance and exit slits located outside the magnetic field. Since the cascade generator produces a vertical beam, the most convenient choice for the angle of deflection was 90 degrees. The radius of curvature of the beam in the region of the uniform field is 20 cm, which makes it possible to deflect a one-MeV beam of He^+ or D_2^+ ions with a field of 14.5 kilogauss. The whole assembly of the magnet and slits can be rotated about the incoming beam in order to direct the beam to different experimental arrangements. Energy control is achieved in two steps; first the exciting current of the magnet is stabilized, the magnetic field being measured with a proton magnetic resonance fluxmeter, and second the high tension is controlled so as to maintain the deflected beam centered on the exit slit of the magnet. The expected energy resolution of the system has been verified down to an energy spread (full width at half maximum) of 0.15% in proton energy. At this resolution a useful beam ($\approx 2\ \mu$A) is obtainable with a high-frequency ion source delivering a total beam of about 40 μA protons.

1. Introduction

The Utrecht 850 kV cascade generator has been described previously in several communications[1,2,3]). The latest of these dates from 1955. Since then numerous changes have been made in the associated equipment of the generator, and the generator itself has been converted from 50 Hz to 500 Hz operation. As a result it is now quite suitable for precision work. Since several of the improvements have not been adequately described in published form and since it is felt that such a publication may serve a useful purpose, this, and a companion publication have been prepared. In this article improvements in the beam deflecting and energy control systems will be described. In the second article[4]) will be found details on the beam current integration and measurement.

[1]) W. Maas, Thesis, Utrecht (1948).

[2]) Veenstra, Jongerius, Paris and Valckx, Physica **18** (1952) 378.

[3]) C. H. Paris, Thesis, Utrecht (1955).

[4]) P. J. M. Smulders and P. B. Smith, Nucl. Instr. & Meth. **8** (1960) 40.

[5]) K. T. Bainbridge, Part V, Experimental nuclear physics, editor E. Segrè (John Wiley and Sons, Inc., New York, 1953).

2. The Deflection Magnet

In the following the characteristics of the magnet and its design considerations will be discussed.

2.1. FOCUSSING OF TRAJECTORIES IN THE CENTRAL PLANE

The first-order focal properties of uniform-field sector magnets have been reviewed by Bainbridge[5]). The conditions for stigmatic focussing were first obtained by Cross[6]), and have been worked out in more detail by one of us[7]). We will here summarize some points which are relevant to the construction of the present beam analyzer. Our notation is illustrated in fig. 1. The plane which lies halfway between the parallel pole faces is called the central plane. One of the rays passing through the centers of the entrance- and the exit-slit is called the central ray, and we assume that all other rays make small angles with this central ray. Since the divergence of the incoming beam is small and its direction well determined, the

[6]) W. Cross, Rev. Sci. Instr. **22** (1951) 717.

[7]) C. M. Braams, Thesis, Utrecht (1956).

aperture, 2α, of the analyzer is made so small that we can neglect aberrations of second- and higher order in α and will treat only first-order focussing conditions. We also neglect effects of higher order in the quantities s'/r and s''/r, where s' and s'' are the entrance- and exit-slit openings.

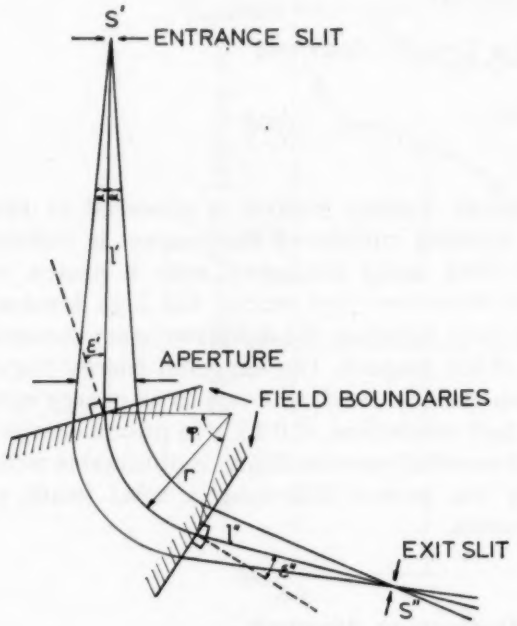

Fig. 1. Schematic representation of deflection magnet, illustrating notation used.

We further use the approximation that the field is uniform within sharp boundaries and zero outside. The entrance- and exit-slits are located at distances l' and l'' from the field boundaries; the normals to the field boundaries at the points of entrance and exit make angles ε' and ε'' with the central ray; in fig. 1 are indicated the directions in which ε' and ε'' are defined as positive. We call $\tan\varepsilon' = a'$ and $\tan\varepsilon'' = a''$. The radius of curvature of the central ray is r and the angle of deflection, φ.

If $\varepsilon' = \varepsilon'' = 0$, i.e., if the field boundaries are perpendicular to the central trajectory at the points of entrance and exit, the condition for the focussing of monoenergetic particles from the entrance slit on the exit slit is expressed by Barber's rule:

$$\tan\varphi = \frac{m' + m''}{r^2 - m'm''}, \tag{1}$$

or, with $\varphi = \frac{1}{2}\pi$:

$$m'm'' = r^2, \tag{1a}$$

where, for normal field boundaries, $m' = l'$ and $m'' = l''$. If ε' and $\varepsilon'' \neq 0$, i.e. for oblique field boundaries, eqs. (1) and (1a) are satisfied by virtual source and image distances, m' and m'', related to the true source and image distances, l' and l'', by the thin-lens formulae

$$\frac{1}{l'} - \frac{1}{m'} = -\frac{a'}{r} \quad \text{and} \quad \frac{1}{l''} - \frac{1}{m''} = -\frac{a''}{r}. \tag{2}$$

From (1) and (2) the condition for focussing follows:

$$\tan\varphi = \frac{l'(a''l'' + r) + l''(a'l' + r)}{(a'l' + r)(a''l'' + r) - l'l''} \tag{3}$$

which, for $\varphi = \frac{1}{2}\pi$, reduces to

$$\left(a' + \frac{r}{l'}\right)\left(a'' + \frac{r}{l''}\right) = 1. \tag{3a}$$

In what follows we will assume that eq. (3a) is satisfied, i.e., that the slits are located in such a way that monoenergetic particles from a point of the entrance slit are focussed in a point of the exit slit.

If we define the dispersion, D'', as the distance between the central ray with radius of curvature $r + \Delta r$ and the focus for rays with radius r, divided by Δr, this quantity is given by

$$D'' = (l''/r)(\sin\varphi + a'' - a''\cos\varphi) + 1 - \cos\varphi \tag{4}$$

or, if $\varphi = \frac{1}{2}\pi$,

$$D'' = (l''/r)(1 + a'') + 1. \tag{4a}$$

Similarly, we can define a quantity D', which we call the resolution factor, by changing double primes into primes in eqs. (4) and (4a). The total relative momentum spread of particles passing through entrance and exit slits of widths s' and s'' is then given by

$$\frac{\Delta r}{r} = \frac{s'}{D'r} + \frac{s''}{D''r}. \tag{5}$$

A beam analyzer often serves both to collimate the beam and to select the particle momentum. This implies that the entrance slit is fully illuminated by the incoming beam, and that the momentum spread in the unanalyzed beam is greater than that selected by the analyzer. Under these conditions, the intensity of the analyzed beam is proportional to $s's''/D''$,

which for a given analyzer and a given maximum energy spread, i.e., if only s' and s'' are variable, is at a maximum if $s'/D' = s''/D'' = \frac{1}{2}\Delta r$. At this maximum, $s's''/D'' = \frac{1}{4}D'r^2\,(\Delta r/r)^2$, which shows that under the conditions stated above, it is advantageous to choose a design in which D' and r are as large as possible. The design of an analyzer will generally be governed by many, perhaps conflicting, considerations, and no general rules can be given which are valid under all conditions and for all experimental requirements. We feel, however, that in most applications the value of the resolution factor, D', rather than that of the dispersion, D'', is decisive for the performance of our analyzer. The quantities D' and D'' are related to the image magnification, M, by the equation: $M = D''/D'$.

By changing double primes into primes in eq. (4a), one sees that D' increases with l'/r and with a'.

2.2. TWO-DIRECTIONAL FOCUSSING

In section 2.1, we have required without further justification that monoenergetic particles whose trajectories lie in the central plane must produce an image of the entrance slit on the exit slit. The reason is, of course, that this is the condition under which the momenta of the selected rays are independent of their directions. Since the analyzer has no dispersion in the perpendicular, or Z-direction, this does not imply that it should also bring particles whose trajectories make different angles with the central plane to a focus. We have considered three possible requirements with respect to focussing in the Z-direction: a parallel incoming beam may be required to produce either a parallel outgoing beam or a focus at the exit slit, or a source at the entrance slit may be required to be focussed on the exit slit. The first two alternatives may be chosen if the incoming beam is nearly parallel; the last one must be considered if the beam from the accelerator can be focussed on the entrance slit. The present analyzer was designed to produce a stigmatic image of the entrance slit on the exit slit.

Deflection in the Z-direction occurs in the fringing field unless the beam enters and leaves the magnetic field along lines prependicular to the field boundaries. The effect can again be described by thin-lens formulae, stating that Z-deflection occurs in lenses with focal lengths r/a' and r/a'', placed at the points of entrance and exit, respectively. We note that these lenses have the same absolute strengths, but opposite signs as those which, according to eq. (2), describe the effect of oblique field boundaries on the focussing in the central plane. Hence, oblique boundaries act very much like quadrupole lenses. An advantage of the latter is that one has more freedom in choosing their location and strength; a disadvantage, however, that special care is required to assure that their field strength varies proportionally with that in the main magnet, independent of hysteresis and saturation.

Applying the above-mentioned thin-lens formulae, one finds the following relation between the source distance l' and the distance L'', at

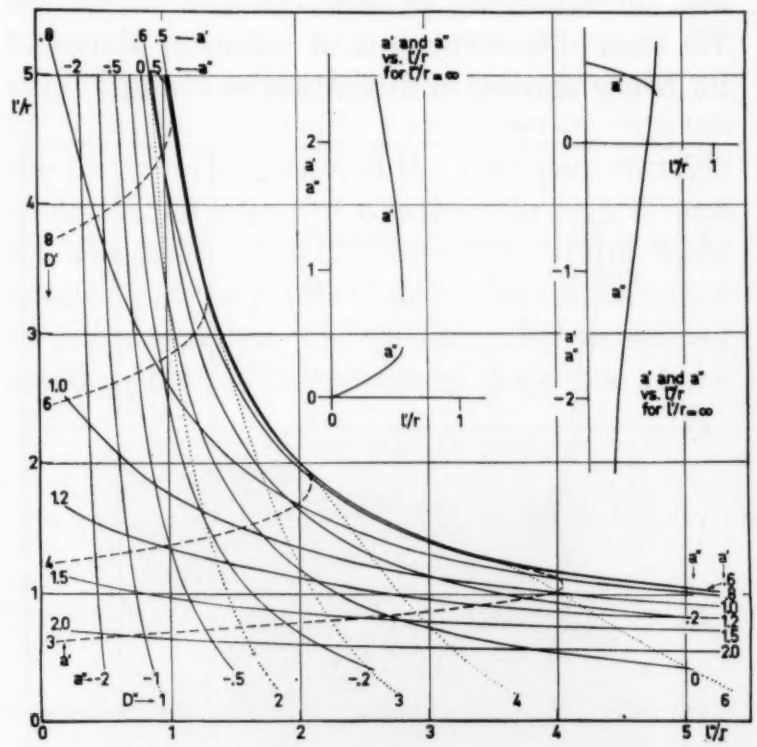

Fig. 2. The focussing condition presented as a family of curves of object distance (l'/r) against image distance (l''/r) for various values of the angles between the normals to the field boundaries and the beam (central ray). The radius of curvature of the central ray is given by r. For the entering beam this angle is given by $\varepsilon' = \tan^{-1}a'$, and for the beam at the exit the single primes are replaced by double primes.

which particles with different velocity components in the Z-direction come to a focus:

$$\frac{1}{a' - r/l'} + \frac{1}{a'' - r/L''} = \tag{6}$$

or, for 90-degree deflection:

$$\frac{1}{a' - r/l'} + \frac{1}{a'' - r/L''} = \tfrac{1}{2}\pi\,. \tag{6a}$$

The condition for stigmatic focussing with a 90-degree deflector is obtained by putting $L'' = l''$ in eq. (6a) and combining it with eq. (3a).

In fig. 2 are shown graphs of l'/r vs l''/r with a' and a'' as parameters. The asymptotic values are plotted in the inserts marked $l'/r = \infty$ and $l''/r = \infty$. This figure is not complete in that curves for $a' < 0.5$ and $a'' > 0.5$ are omitted, while the curves $a' = 0.5$ and $a'' = 0.5$ are only drawn to the left of the point $l'/r = l''/r = 2$, where they touch the envelope. The figure is completed by reflecting it in the line $l' = l''$ and interchanging primes and double primes. We then obtain two sets of values of a' and a'' for every allowed combination of l' and l''.

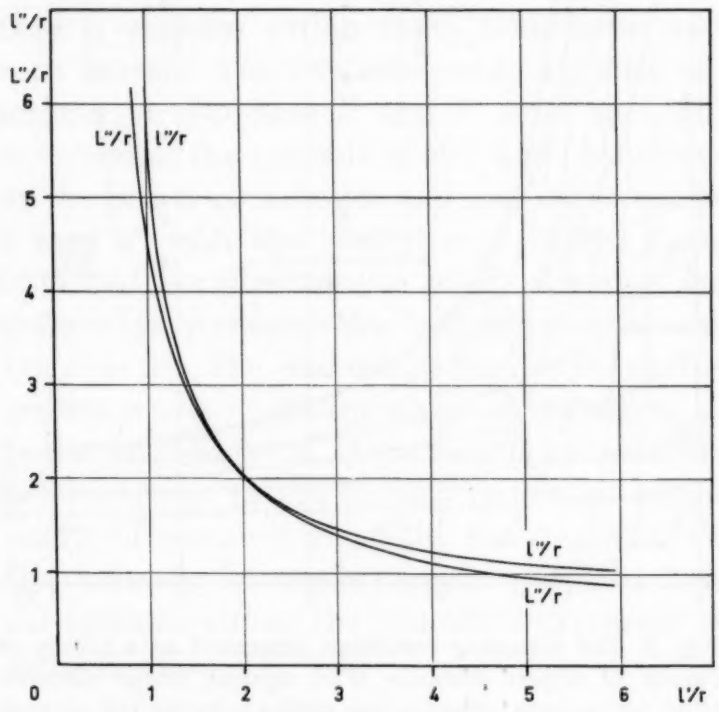

Fig. 3. The image distance in the central plane (l''/r) and in the Z-direction (L''/r) as a function of object distance (l'/r) for the choice of $a' = a'' = 0.5$ used in the design of our magnet. As can be seen the focussing is stigmatic over a relatively large range of values of the object distance.

Dashed and dotted lines in fig. 2 indicate values of D' and D'', respectively.

It is interesting to note that the curves for $a' = 0.5$ and $a'' = 0.5$ run very close together. This suggests that it is possible to obtain approximately stigmatic focussing over a wide range of values of l' and l'' by choosing $a' = a'' = 0.5$. This is borne out by a comparison between the astigmatic image distances l'' and L'' as functions of l', shown in fig. 3. Since moderate deviations from correct Z-focussing do not affect the performance of the analyzer, we have chosen oblique field boundaries with $a' = a'' = 0.5$ for our instrument. This leaves appreciable freedom in the choice of l' and l'' without necessitating the use of adjustable elements, such as a quadrupole lens or semicircular blocks, inserted in the pole faces at the points of entrance and exit.

2.3. DESIGN OF MAGNET AND SLIT SYSTEM

Because of space limitations and also for economy, the analyzer was made as compact as was compatible with the requirement that it should be able to bend a one-MeV beam of singly charged ions of mass number four, which has a momentum of 290 kilogauss-cm. The radius of curvature was, therefore, chosen to be 20 cm. The energy-defining slits were placed at $l' = l'' = 40$ cm; this is a compromise between the requirements that the exit slit and the target, on one hand, be placed as far as possible from the magnet to make room for measuring equipment around the target, and that the entrance slit, on the other hand, be placed at the largest possible value of l', in order to obtain the best possible energy resolution.

The shape of the magnet is shown in fig. 4. The yoke was machined from forged Armco iron and annealed in an inert atmosphere before the final grinding of precision surfaces. The two coils each consist of 1000 turns of 1.5 mm round copper wire, wound on 3 mm thick copper bobbins with 3 mm i.d. copper tubing soldered to the side plates for water cooling. Copper foil of 0.1 mm thickness was wound between successive layers of winding to improve heat conduction from the interior of the coil to the side

plates. The field in the 16 mm wide air gap is 1500 gauss per ampère up to about 10 A; the

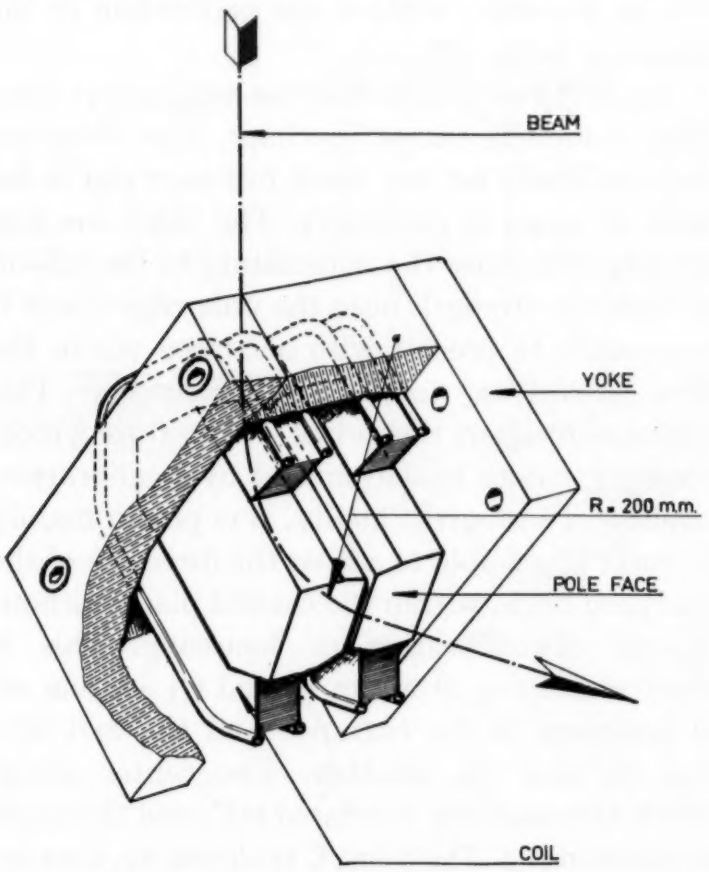

Fig. 4. Cutaway drawing of the magnet construction. See section 2.3 of the text.

coils have run continuously with a current of 12 A, which corresponds to a current density of 3.0 A/mm² averaged throughout the whole cross section of the coil, or 6.8 A/mm² in the windings.

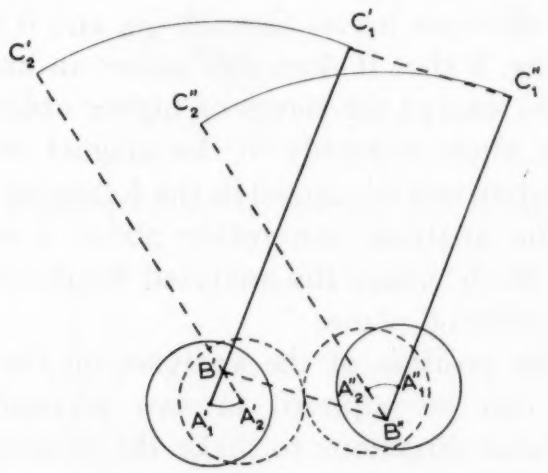

Fig. 5
Operation of the slit system. See section 2.3 of the text.

The design of the pole faces was based on the estimate that the deflection in the fringing field

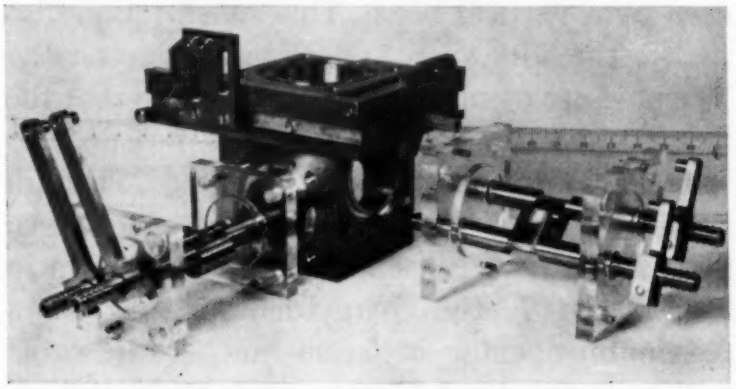

Fig. 6. Photograph of dismounted slit box.

can be accounted for by assuming the uniform field to drop sharply to zero at a boundary lying one gap width outside the pole-face edges. No detailed investigation of the validity of this procedure was made, but provisions have been made for adjusting the position of the slit system with respect to the magnet in case that the focussing should prove to be incorrect.

The slits consist of pairs of cylindrical jaws, which extend into hollow, liquid-cooled shafts, parallel to the cylindrical surfaces. Rotation of the shafts results in a displacement of the excentric jaws and, hence, opens or closes the slits. The operation is shown schematically in fig. 5, which represents a cross section through the slit jaws. The axes of the jaws pass through A′ and A″, the axes of rotation, through B′ and B″. The lever arms B′C′ and B″C″ are of equal lengths and the points C′ and C″ are constrained to move together, the distance C′C″ remaining equal to B′B″. The horizontal projection of the

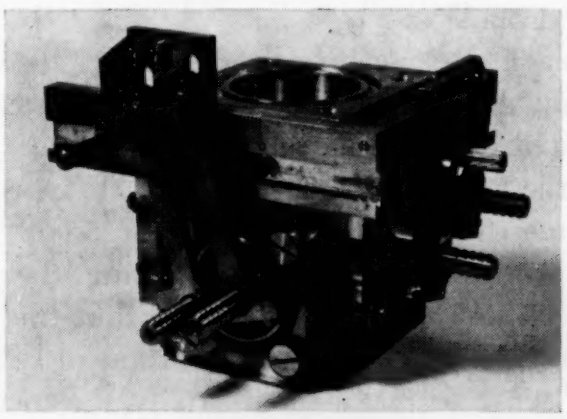

Fig. 7. Photograph of mounted slit box.

displacement of C′ and C″ is proportional to the corresponding variation in the slit opening, as

seen by a vertical beem. This construction also makes the slits open and close symmetrically. The jaws are mounted in lucite plates so that the beam current to each one can be measured or used to stabilize the accelerator voltage. Vacuum seals are made by rubber "o"-rings. An assembly of two perpendicular slits is shown in figs. 6 and 7; the energy-defining slit has a maximum opening of 5 mm and is adjustable with an accuracy of 0.1 mm, while the slit which opens in the Z-direction has a maximum opening of 10 mm, and is adjustable with an accuracy of 0.5 mm. It follows from eq. (5), that the relative energy spread (full width at half maximum), $\Delta E/E = 2\Delta r/r = (s' + s'')/800$, where s' and s'' are the entrance and exit slit openings, measured in mm. The slit jaws were originally made of stainless steel. This proved to be a mistake since the accelerator beam melted them very quickly. After the stainless steel was replaced by silver no further trouble has been found from this source even when sharply focussed 800 keV beams approaching one mA are used.

2.4. ADJUSTMENTS

The following adjustments of the positions of the slit systems with respect to the magnet are possible (fig. 8):

1. each one of the two blocks holding a slit assembly can be rotated slightly about the direction of the beam, so that the energy-defining slits can be placed perpendicular to the central plane;

2. each one can be moved in the Z-direction, so that the center of the slit system can be adjusted to lie in the central plane;

3. the whole frame holding the two slit systems can be moved in the direction of the line in the central plane bisecting the angle between the field boundaries, so that the ratios l'/r and l''/r can be varied simultaneously in the same sense to make them satisfy the focussing condition of eq. (3a);

4. the frame can be rotated about an axis, perpendicular to the central plane and going through the intersection of the lines perpendicular to the field boundaries at the points of entrance and exit, so that the angle of deflection can be adjusted, without the calibration or the focussing being affected.

The first two possibilities for adjustment need little comment except, perhaps, that they are only necessary for one block but were put in for both to preserve symmetry. The third one was necessary because the uncertainty in the fall-off of the field strength near the pole-edge made it impossible to predict with accuracy where the slits should be located for focussing. This adjustment alters the radius of curvature which, however, has to be determined by a calibration, anyhow. The fourth, finally, was put in mainly to make it possible to adjust the direction of the analyzed beam within the central plane without change of calibration or focussing. This is illustrated in fig. 9 where P_1 and Q_1 are one set of positions of the entrance and the exit slit, and P_2 and Q_2, another. The center about which the assembly is rotated is C, and the angle of rotation is β. The point C is chosen so, that by this rotation the ray r_1 transforms into the congruent ray r_2. Hence, if we consider r_1 and r_2 as the central rays for the two situations, the rotation leaves l', r, and l'' unchaged. The angles of entrance and exit, however, change by opposite amounts, but it is seen from eq. (3a) that this does not affect the focussing. The ray r_3, which enters through P_2 in a direction parallel to r_1, therefore leaves through Q_2, and it is seen from fig. 9 that it does this under an angle 2β with r_1, except for terms of higher order in β.

The whole assembly of the magnet with its slit system can be moved in the following ways:

5. the analyzer can rotate about a vertical axis, which makes the analyzed beam swing in the horizontal plane;

6. the position of the analyzer on the turntable can be adjusted in two perpendicular horizontal directions to make the entrance slit lie on the axis of rotation;

7. the position of the turntable can be adjusted in two perpendicular horizontal directions to make the beam from the accelerator pass through the entrance slit;

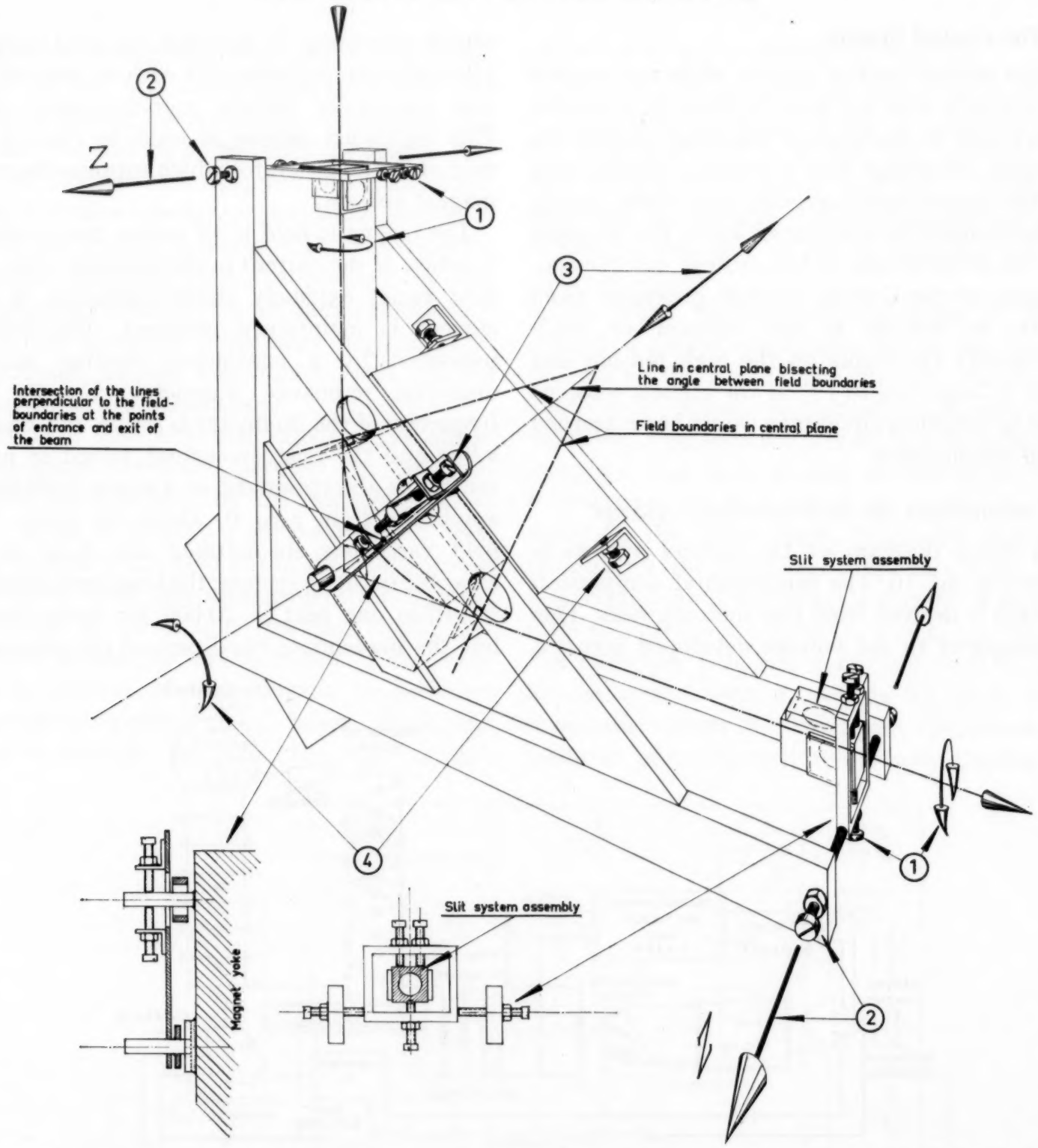

Fig. 8. Representation of the various adjustments possible of the slits with respect to the magnet. See section 2.4 of the text.

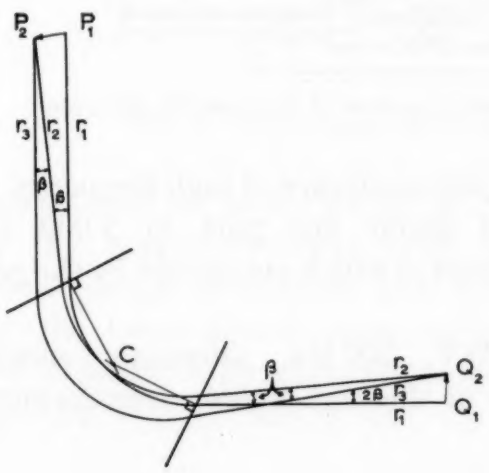

8. the turntable rests on four screws, by which the axis of rotation can be set vertical.

A very simple and compact design of the turntable with its horizontal adjustments was obtained by making use of a commercial ball race with ground flat end-surfaces on which the sliding motions (6 and 7) occur.

Fig. 9. Representation of the turning of rays in the central plane as a result of the fourth motion possibility discussed in section 2.4 of the text.

3. The Control System

The present control system, while not original in principle does not seem to have been applied previously to machines of this type, despite the obvious advantage that it presents of delivering to the target monoenergetic ions whose energy is determined by one control knob. The occasion for the development of this system was the conversion of the Utrecht cascade generator from 50 Hz to 500 Hz in the summer of 1957. Previously the ripple on the high tension had been so large (up to 1% at the highest tension) that no practical advantage would have accrued from stabilization.

3.1. PRINCIPLES OF THE CONTROL SYSTEM

A block diagram of the control system is shown in fig. 10. The fundamental comparison voltage is derived from two mercury cells. This is compared to the voltage developed across a mixed, providing, in principle, an ideal integral-plus-proportional controller with no zero setting and essentially infinite zero-frequency gain. This combined output is used to control the field of the dc generator which supplies the main magnet current.

The magnetic field is, of course, not a unique function of the current in the exciting coils. The field varies extemely slowly, however, if this current is maintained constant. The field is measured by a continuous reading nuclear magnetic resonance fluxmeter. Usually the frequency of the fluxmeter is set to the desired value and the magnet current varied so as to centre the absorption dip on a sweep variable in amplitude from zero to about 10 gauss. The field variations encountered are those to be expected in such a system; the long-term stability is within one part in 20 000 for many hours, but the inadequate band-pass of the generator

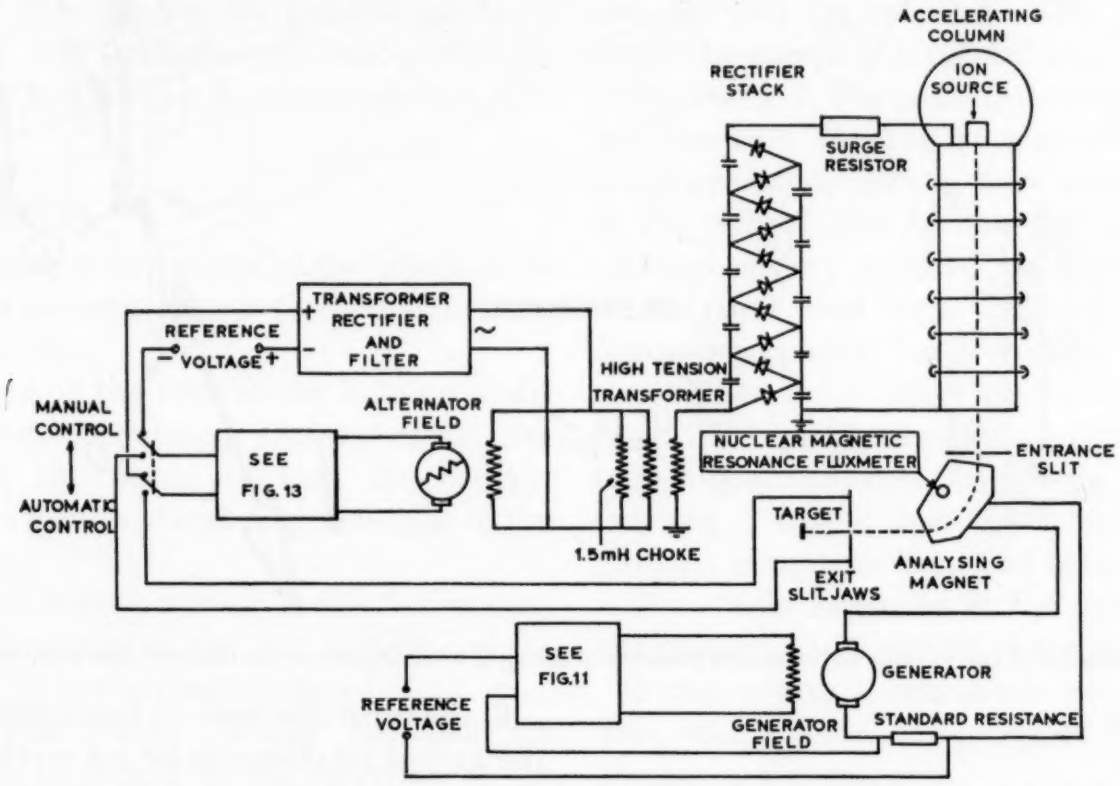

Fig. 10. Block diagram of the complete control and stabilization system of the cascade generator.

standard resistance by the magnet current. The error signal is impressed upon the inputs of two amplifiers in parallel, one an ordinary dc balanced amplifier, and the other a commercial "chopper" type amplifier driving a two-phase motor. The outputs of these two amplifiers are additively permits the occurence of high frequency fluctuations of about one part in 5 000 (average value) most of which are caused by the generator itself.

A 200 V, 500 Hz, alternator powers the primary of the high-tension transformer of the

cascade generator. The multiplier components, surge resistor, and accelerating tube were not modified during the frequency conversion. The transformer had to be replaced, of course. The new transformer was designed and constructed by N.V. Philips Gloeilampenfabrieken, constructors of the original machine. The large negative reactance reflected into the primary by the multiplying circuit load is partially cancelled by a 1.5 mH air-cored inductance designed and constructed by the Electronics Dept. of the Utrecht Physics Laboratory.

The high tension is controlled by the differential signal developed between the insulated magnet exit slit jaws by the impinging beam. This signal is heavily compensated and then used to control the field of the above mentioned alternator. With this arrangement the beam is controlled by the magnet current, making for extreme simplicity of operation. Alternative manual control of high tension is provided to permit "finding" the beam. Once the beam is through the slits, the high tension may be varied over its entire range by merely changing the magnet current. The system gain is high enough so that no zero setting is necessary, the beam always being at least as great as is obtainable by manual control, and usually greater.

3.2. THE MAGNET CURRENT STABILIZER

The stabilization principle used here is that of paralleling an integrator and an amplifier. In this section it will be shown that analysis of such systems is quite easy, and that a criterion may be found which permits rapid determination of the required gain of the dc amplifier before additive mixing.

The circuit diagram is shown in fig. 11. The analysis is carried out in the complex-frequency (s-) plane. In fig. 11 the transfer functions appropriate to each section of the system are indicated. The additive mixing is accomplished in such a way that, at least to first order, the transmission of each block is unaffected by signal in the other block. Thus the transfer function of the combined amplifiers from the error signal input to the grids marked A and B is given quite accurately by $(A_1 + p_B p_0/s(s+p_0))$. The open-loop pole-zero configuration is shown for the system with $A_1 = 0$, in fig. 12(a). For reasonable values of overall gain the system is unstable, as can be seen by the early crossing of the imaginary axis by the loci of the principal roots of the closed system response.

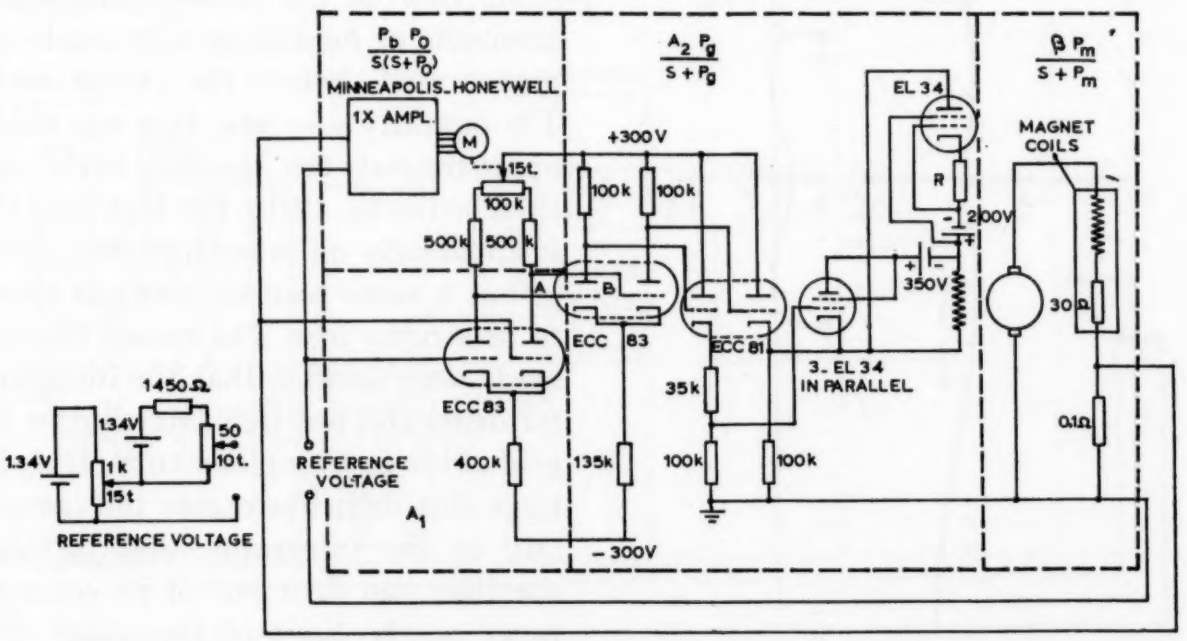

Fig. 11. Circuit diagram of the stabilization circuit of the deflection magnet.

In fig. 12(b) the pole-zero configuration and root loci are shown of the system with $A_1 \neq 0$. It can be seen that for high gain the system is stable due to the two complex zeros arising

from the parallel combination of the two types of amplifiers. Under these conditions the closed loop poles are given approximately by the triangles in fig. 12(b). It can be seen that the

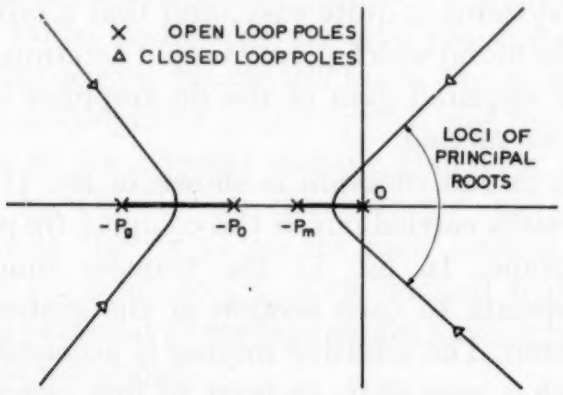

Fig. 12(a). Root loci of the stabilization circuit of the deflection magnet for the case of zero gain of the fast (direct-coupled) amplifier.

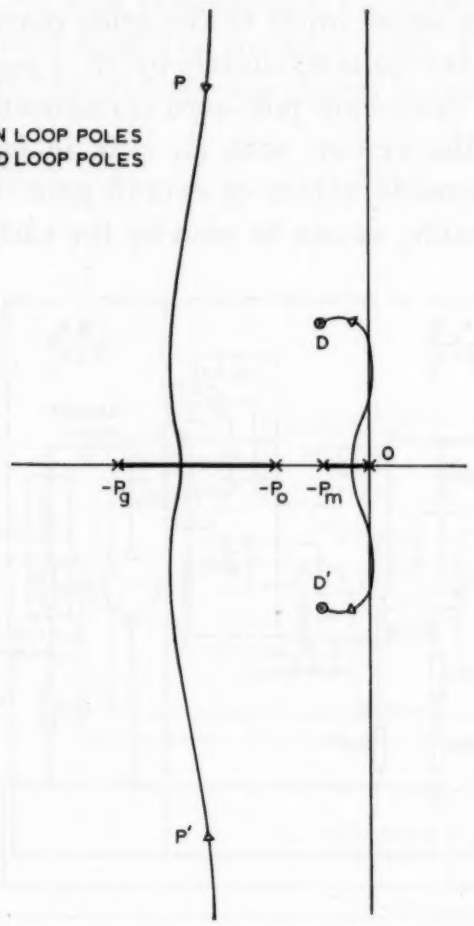

Fig. 12(b). The root loci of the system for $A_1 \neq 0$.

response is governed principally by the high frequency complex conjugate poles P and P′. The dipoles D and D′ are quite weak for very high gain, and, although of low frequency, contribute very little to the response of the system (they are, of course, responsible for the high precision). Caution must be exercised in the choice of values of A_1, p_0, and p_B, however. This can be seen by considering the position of the complex zeros as a function of these variables. They are found at $\frac{1}{2}p_0\,(-1 \pm j\sqrt{\gamma - 1})$ where $\gamma = 4p_B/A_1p_0$. It can be seen from the sketch in fig. 12(b) that for any values of the parameters the system is stable for very high gain. However, if the imaginary part of the coordinates of zeros is too large, the root loci will go very far into the right half-plane before returning to the zeros. This results in a conditionally stable system which may break into sustained oscillation if a temporary overload drives the system into a region where one or more elements become saturated, thus lowering the gain so that the right-hand poles move into the right half of the plane. It is probable that a similar system described by Havill and Rubins[8]) displays this type of behaviour. In their case, $A_1 = 1$ which will result in complex zeros located very far from the real axis for usual values of p_B and p_0.

In view of the above consideration, measurements of p_B and p_0 were made on the integrator used, before the circuit was designed. The quantity $\gamma = 4p_B/A_1p_0$ was made equal to approximately ten, resulting in the configuration sketched in fig. 12(b). For high gain the response is apparently quite independent of the value of γ, but a more realistic analysis shows this not to be strictly true. The reason that γ cannot be made very small is that the integrator corrects for drifts and low frequency flutter noise at the grid of the first amplifier tube. If A_1 is made too large this drift overcomes the correcting capacity of the integrator, and furthermore, the amplifier can drift out of its correct operating range or the limit of the range of correction afforded by the integrator.

Thus a correct compromise must be found for a given case. Fortunately γ can be arbitrarily varied over an enormous range by changing the amplification of the amplifier (A_1) or the gear reduction factor of the integrator (p_B). The

[8]) J. R. Havill and S. Rubin, Rev. Sci. Instr. **26** (1955) 515 (N).

behaviour of a correctly designed system is seen to depend principally on the location of the poles P and P′, and to a much lesser extent on the weak dipoles D and D′. In other words this system retains fully the advantages of speed and stability of a simple dc feedback amplifier, while possessing the precision of a chopper type integrating feedback system.

The weak point in the system is the generator. The ripple and noise introduced by this source could be corrected by static or dynamic filters applied to the output. Several such circuits have been described. In this case, however, it would have been better to use direct feed by vacuum tubes or transistors†, since the power consumption is not excessive (less than 5 kW). The generator was used in the present circuit because it already existed when the design was started. The magnetic field variations observed generator, and so cause no inconvenience. For that reason no filters (of the types mentioned above) were tried.

3.3. THE HIGH-TENSION STABILIZER

As can be seen from fig. 10, the high tension stabilizer can be operated in two completely diverse manners. The manual control requires no special discussion since the circuit is stable for practically any value of gain. The high tension itself is seen not to be stabilized by this mode of control. In practice it is therefore used only in putting the generator into operation. The automatic control mode would be unstable with any reasonable value of gain and so a discussion is given of the compensation used.

The circuit of the high-tension stabilizer is shown in fig. 13. Only the automatic control mode is shown. The various transfer functions

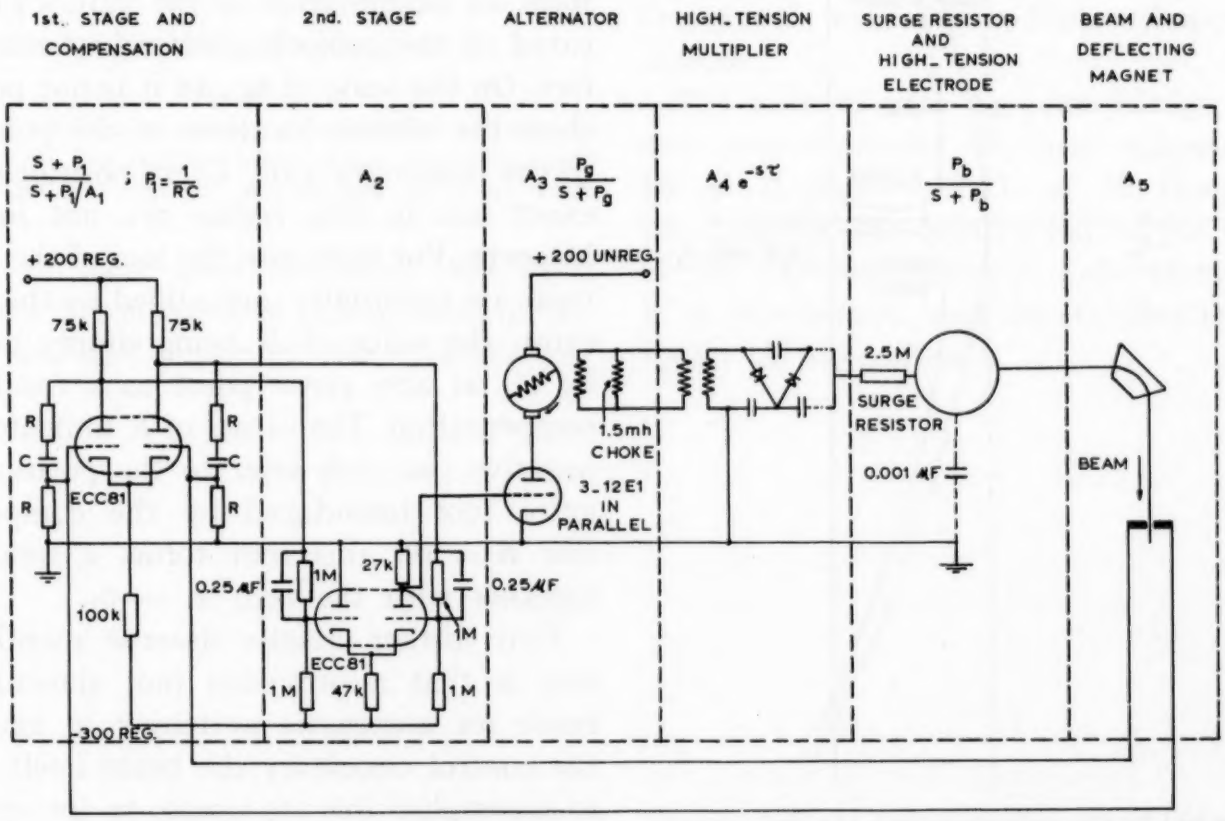

Fig. 13. Circuit of high-tension stabilizer.

are a factor of five less than the minimum instrumental width utilizable with the cascade

† Such a system has since been built at this laboratory for the deflection magnet of the 3 MeV Utrecht Van de Graaff generator. As expected, it shows neither long nor short term fluctuations greater than one part in 25 000.

are indicated. It is to be noted that the transfer function of the high-tension rectifier stack is treated as a pure time delay of $\frac{1}{2}$ of one cycle, that is 0.001 sec (τ). This approximation is valid for either increasing or decreasing voltage providing the load is adequate. For small load,

or large, rapid, changes it ceases to be valid for falling voltage. From the point of view of stability only small changes are usually of importance, however. The generator field time-constant ($1/p_g$) is about 1 sec, and there is also a $2\frac{1}{2}$ millisecond time constant ($1/p_B$) formed by the surge resistor and high-tension electrode capacity.

The various factors shown in fig. 13 are self-explanatory except for A_5, the effective amplification factor of the beam. This is the relationship between the change of the high tension and the voltage caused thereby on the slit jaws, through the deflecting action of the magnet. This factor may differ by several orders of magnitude under different circumstances and for this reason the effective resistance to ground of the slit jaws can be changed by the operator to suit conditions.

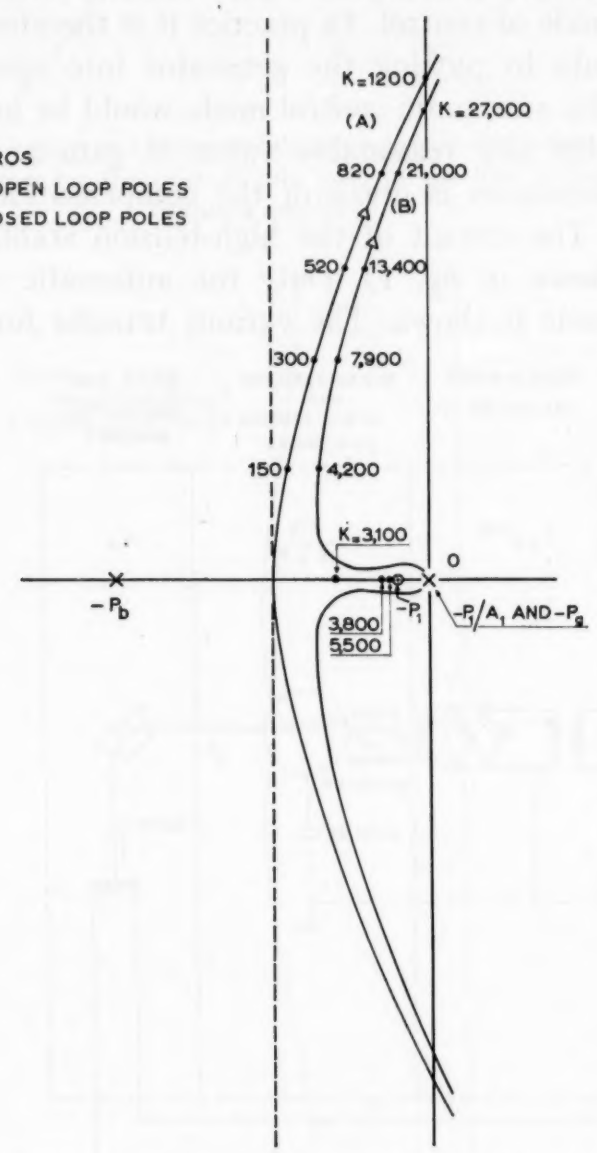

Fig. 14 Root loci for the uncompensated (A) and compensated (B) system.

In order to describe the theory of the circuit, a value of A_5 must be specified. In the discussion that follows a typical value will be assumed, which renders the zero-frequency loop gain equal to 10^4. This loop gain (K) is given by the product $A_1A_2A_3A_4A_5$. For a value of $K = 10^4$ the expected deviation of the beam from the center of the exit slit is negligible in comparison with the slit width and the machine ripple.

In fig. 14 the root loci are shown for the uncompensated system (A) (with the condensers, C, removed) and for the complete system (B). Without the time-lag factor $e^{-s\tau}$, the uncompensated root loci would be given by the dashed line. This factor contributes phase-shift which limits the usable gain.

The necessity for the compensation is obvious from an examination of the values of K indicated on the compensated and uncompensated loci. On the scale of fig. 14 it is not possible to show the relative locations of the poles closest to the imaginary axis. These positions and the exact loci in this region are not important, however. For high gain the loci of the principal roots are essentially unmodified by the compensator, the value of K being simply multiplied by A_1 at any given point as a result of the compensation. The values of K indicated on the negative real axis refer to the position of the extra root introduced by the compensation. For $K = 10^4$ this root forms a weak dipole together with the zero at $-p_1$.

Two further details deserve mention. The first is that a provision (not shown) is also made for automatic switching in and out of the control circuit by the beam itself. Circuits to accomplish this are simple to incorporate in the design but should be adapted to conditions likely to be met in the operation of a given machine. Secondly, two phase-lead condensers were incorporated in the coupling networks between the two stages of voltage amplification (fig. 13). These are not strictly necessary (nor very effective) but do produce a desirable effect of speed-up, at least in the manual control mode.

3.4. PERFORMANCE

The magnet, magnet current stabilizer, and high-tension stabilizer have been in operation of

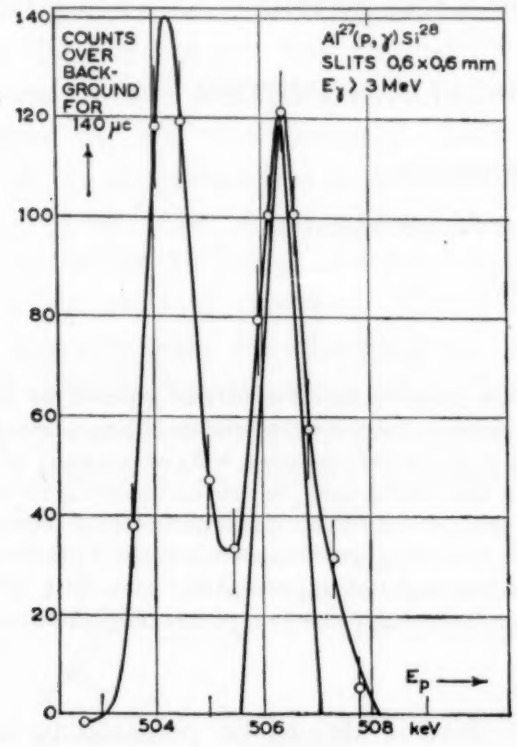

Fig. 15
Gamma-ray yield curve taken with the system described in this article. The reaction under study was $Al^{27}(p,\gamma)Si^{28}$ at the 504–506 keV doublet. See section 3.4 of the text.

a period of more than one year. The most difficult resolution problem encountered in this interval was the study of the 504–506 keV doublet in the Al^{27} (p,γ) reaction. In fig. 15 is shown the yield curve obtained at the time the upper of the two resonances was under study. The triangular resolution curve drawn underneath this resonance is the predicted shape of the yield curve for the slit opening used (0.75 mm) (see section 2.3). The extra width observed is accounted for by the target thickness of several hundred eV (the precise value was not determined). At this slit opening a beam of approximately 2 μA is available on the target located 40 cm beyond the exit slits of the magnet.

Acknowledgements

This investigation is part of the research program of the "Stichting voor Fundamenteel Onderzoek der Materie", and was made possible by financial support from the "Nederlandse Organisatie voor Zuiver Wetenschappelijk Onderzoek".

The authors wish to acknowledge the help and encouragement of their colleagues Prof. Dr. P. M. Endt and Dr. A. M. Hoogenboom. The magnet was constructed in the workshop of the Utrecht Physical Laboratory by Mr. F. A. Meeuwissen, and the stabilization circuits by Mr. A. Veenenbos.

NUCLEAR INSTRUMENTS AND METHODS **8** (1960) 40–45; NORTH-HOLLAND PUBLISHING CO.

THE UTRECHT 850 kV CASCADE GENERATOR

II. THE BEAM INTEGRATOR AND GALVANOMETER

P. J. M. SMULDERS and P. B. SMITH

Fysisch Laboratorium der Rijksuniversiteit te Utrecht, Nederland

Received 9 March 1960

A current integrator is described for the integration of currents from 0.01 to 500 μA with an accuracy of 0.1%. The principle used is essentially the same as that of the excellent circuit described earlier by Helmer and Hemmendinger. The modifications effected result in a considerable reduction in expense, as well as a lower input impedance. Due to increased high frequency gain much smaller condensers are necessary in order to maintain the input voltage within some hundredths of a volt of ground, at all times. The integrated current is measured as the number of output pulses, each pulse representing a fixed amount of charge. Except for the condensers, no special components are used. A low-impedance electronic galvanometer for operation in series with this integrator is also described. This circuit combines the advantages of imperceptible zero drift, fixed calibration, and essentially absolute protection against burn-out.

1. The Current Integrator

In section 1 follows a description of the new current integrator as well as a short discussion (section 1.1) of the motives underlying its development.

1.1. INTRODUCTION

In recent years great progress has been made in constructing current integrators, combining the qualities of accuracy (accurately quantized charge removal), low input impedance and high switching rate[1,2]). To date, the instrument which best satisfies these requirements is that of Helmer and Hemmendinger. These authors utilize a vibrating reed electrometer to detect input error. The removal of charge is accomplished in their circuit by a reversing condenser connected between the input and a precision voltage, the reversing rate being controlled by a variable frequency multivibrator. In addition the feedback connection of the vibrating reed electrometer is connected to the input through a condenser, thus lowering the input impedance. In the description of the circuit the suggestion is made that it should be possible to build a similar integrator without the use of such an expensive device as the vibrating reed electrometer. The present integrator is the direct result of this suggestion. It is felt that it is worth while to report upon the results obtained since an extremely accurate, wide-range instrument has been built at very low cost. Furthermore an improvement has been effected over the original circuit by feeding back with a low enough impedance and a high enough high-frequency gain, so that the input is maintained virtually at ground even during the switching pulses. Since the feedback condenser is effectively increased by the gain of the amplifier it is possible to use switching condensers one-fourth or one-fifth of the feedback condenser (in comparison with 1/600 in the circuit of Helmer and Hemmendinger). This has permitted an increase of the current range to fifteen times that of the original circuit, although using smaller condensers.

[1]) R. J. Helmer and A. Hemmendinger, Rev. Sci. Instr. **28** (1957) 649.

[2]) I. A. D. Lewis and B. Collinge, Rev. Sci. Instr. **24** (1953) 1113.

1.2. PRINCIPLE

The principle of operation may be seen from fig. 1. The beam current enters at the input of a two-stage direct-coupled balanced amplifier with

negative feedback condenser C_2. This feedback holds the input close to ground potential while the output voltage is $e_2 \approx -1/C_2 \int i\,dt$. When this voltage reaches the trigger level a pulse goes to the scale of two and the relay is closed or opened, which results in a reversal of the condenser C_1. By this action a charge $2BC_1$, where B is a precision reference voltage, is removed from the input. Thus the output raises by about $2BC_1/C_2$, and the trigger flips back to its original position. Meanwhile, the beam current goes on charging C_2 and the process described is repeated when the trigger level is reached again. The trigger pulses are also fed to a scaler. If the number of pulses is n, the integral of the current is $2nBC_1$.

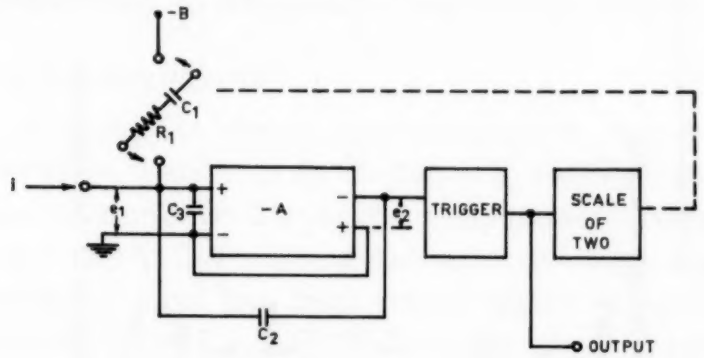

Fig. 1. Block diagram of the integrator.

The resistor R_1 in series with C_1 limits the current flow during the switching to a value low enough that the amplifier may cope with it. The condenser C_3 is necessary only in order to handle the surge of current before the amplifier has had time to act. Its value is not critical, and the charge flowing into it is very small compared to that flowing into C_2. The precision with which the output is given by the integral of the input, depends upon the gain, output impedance and frequency response of the amplifier. Under favorable conditions rather high precision is obtainable and a useful integrator can be made by determining the limits over which the output varies by a trigger tube[3]). The precision is normally limited by drifts of the trigger tube. Furthermore, to extend the range to more than one cycle (which is usually essential for general use) further errors are inevitably introduced by the time needed for the recycling procedure.

The present circuit uses the relationship between input and output only incidentally as a means of determining the rate at which charge should be removed from the input. Since at the moment of each trigger pulse the value of e_2 and so the charge on C_2 is the same, the charge which has flowed into the integrator must be equal to the charge removed per count and so the precision ultimately depends on the constancy of this charge "quantum". This is given by:

$$Q = 2BC_1\left(1 + \frac{V}{B}\right), \tag{1}$$

if V is the input voltage at the moment C_1 is reversed. The delay time τ of the relay and the output impedance R_0 cause this voltage to depend somwehat on current:

$$V = V_0 + \frac{i\tau}{AC_2} + \frac{iR_0}{A}, \tag{2}$$

if V_0 is the voltage that would obtain at the input when the output reaches the trigger level, under conditions of very small current. Differentiation of (1) (assuming that $B \gg V$) gives for the relative error in Q:

$$\frac{\Delta Q}{Q} = \frac{\Delta B}{B} + \frac{\Delta V_0}{B} + \left(\frac{\tau}{ABC_2} + \frac{R_0}{AB}\right)\Delta i\,. \tag{3}$$

The first term on the right hand represents instability of the constant voltage source, the second term drift at the amplifier input, and the last term is the current dependent error. The last two terms can be made negligible compared to $\Delta B/B$ by choosing suitable values of A, B, C_2 and R_0, so that the precision depends wholly on the stability of B. An interesting fact is, that for a given current the error is independent of the switching frequency, so one can go to the highest frequency where the relay will operate safely. In our apparatus $B = 85$ V, $A = 1200$, $R_0 \approx 2$ kΩ, $\tau = 6$ and 4 msec resp., for opening and closing the relay. The sum of the factors $i\tau/ABC_2$ and iR_0/AB is smaller than 3×10^{-4} for all currents to be measured.

[3]) W. A. Higinbotham and S. Rankowitz, Rev. Sci. Instr. **22** (1951) 688.

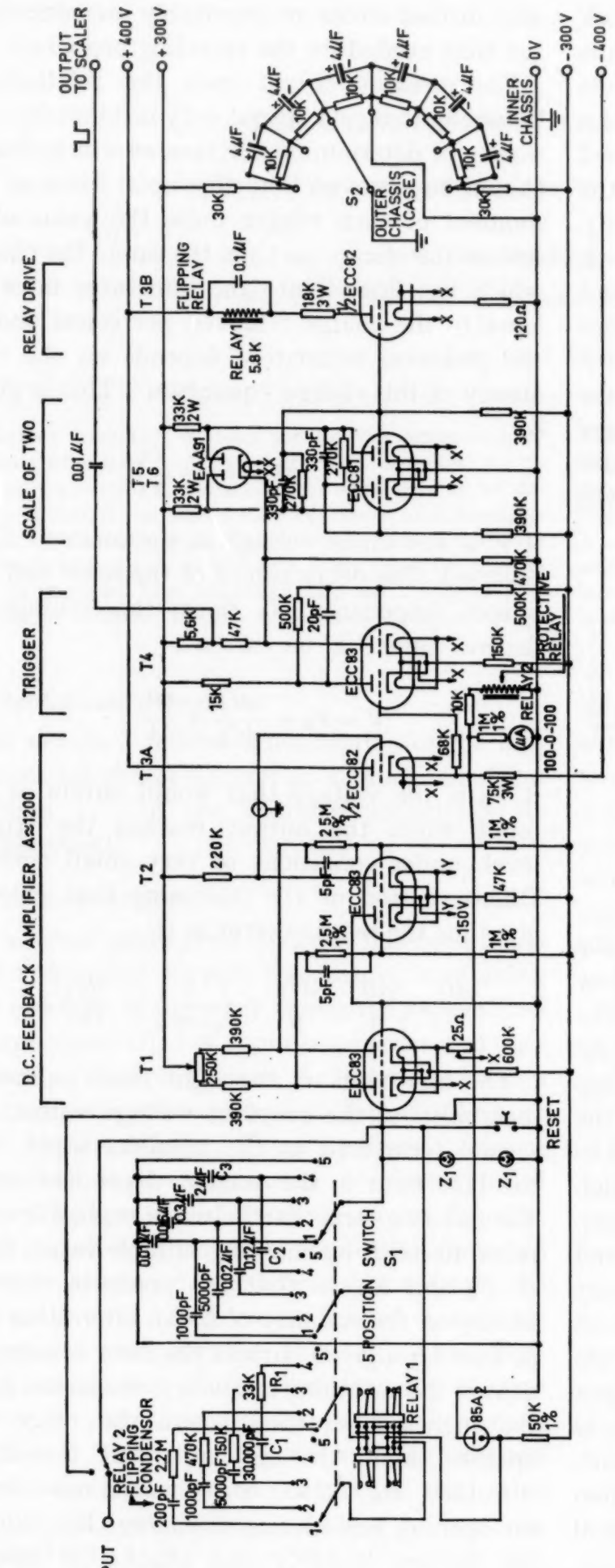

Fig. 2. Circuit diagram of the integrator.

The drift of the amplifier input is smaller than 0.01 V in several hours, resulting in a value of $\Delta V_0/B$ of the order of 10^{-4}. The ultimate stability thus depends on the 85 A2 voltage reference tube, which, according to the manufacturer, should give 0.1% stability under suitable conditions.

The peak to peak value of the input voltage is in our apparatus about 0.04 V. The mean input level however does not exceed a value of 0.02 V from ground for all currents to be measured. This value determines the leakage which may be permitted between target and ground. If, for instance, one wants to measure a current of 10 μA with 0.1% precision the leakage resistance must be higher than 2 MΩ, which is low enough to make use of watercooled targets.

1.3. CONSTRUCTION

A complete circuit, including plate voltage supplies, is given in fig. 2. Tubes T_1 and T_2 form the dc-amplifier. The heater voltage on the first tube is 4 V. By varying the cathode resistor a working point has been found where the grid current is $\approx 1.5 \times 10^{-11}$ A in the whole range used. This limits the practical use of the apparatus to currents higher than 10^{-9} A, which is low enough for practically all applications in nuclear physics. Tube T_3A is a cathode follower used to reduce the output impedance. This stage may be omitted when only the first three ranges of the apparatus are used. This fact is mentioned since currents above 85 μA (maximum permissible on scale 3) are not needed frequently and the elimination of the cathode follower results in a circuit which is absolutely stable. The phase-advance condensers in the grids of T_2 have been found, however, to produce complete stability when the cathode follower is included in the feedback loop. Admittedly a solution to the stability problem possessing a higher degree of safety could be found (the values of these condensers are quite critical), but further work was not deemed worthwhile since no trouble has been experienced with incipient or recurring oscillations. Through the four pole five position switch, S_1, one can choose four different sets of R_1, C_1, C_2 and C_3 while in the fifth position the input is short circuited. The time constant R_1C_1 is kept smaller than one eighth of the smallest time between two switchings, so that C_1 is always discharged to less than 0.03% of its original charge.

Tube T_4 is wired as a Schmitt trigger. The trigger level is about — 15 V and the hysteresis is 10 V. Tubes T_5 and T_6 form the scale of two, while T_3B is the relay driving tube. The reference voltage, B, is delivered by an 85 A 2 tube T_7 fed through precision resistors. The circuit is never turned off so as to guarantee the highest possible constancy of ambient conditions, and thus voltage, for this tube. The apparatus is protected in two ways: if the absolute value of the output of the amplifier becomes higher than 60 volts the relay 2 falls in and disconnects the input. If this relay does not work, for instance because the voltage supplies are out of order, two neon tubes connected between the input and ground protect the condensers against overvoltage.

All condensers connected to the input are Leclanché polystyrene condensers except the 2 μF condenser. Since the voltage across it is so small (maximum 0.04 V) soakage effects will not be important. Switch S1 is an E.B.E. switch with silicone deck. The relays are Siemens Trls 151/71e. The two halves of relay 1 are connected in parallel. Its insulation proved to be good enough, the leakage current being less than 10^{-11} A. The noise of this relay was reduced to an agreeable level by mounting it in a foam rubber house.

The integrator is mounted on a chassis which is insulated with perspex. The chassis level with respect to ground may be varied from + 150 to — 150 V by means of the seven position switch S2. This may be used as a check on the working of the suppressor used to retain secondary electrons on the target and also to measure the resistance between target and ground. The meter connected to the output of the amplifier is used to control the amplifier balance and may also be used to measure the grid current.

1.4. DISCUSSION

The performance of this integrator has been such as to warrant the construction of a duplicate for the Utrecht 3 MeV electrostatic accelerator. Both have been in daily use for many months and have shown themselves to be extremely flexible and reliable. Calibration checks have disclosed that the linearity is better than 0.1%.

2. The Galvanometer

In the following an electronic galvanometer suitable for use in combination with the integrator is described.

2.1. INTRODUCTION

The integrator just described makes it possible to perform high precision charge measurements even if the insulation of the target is not especially good. In order to take advantage of this property a low-impedance galvanometer must also be used since the galvanometer is usually in series with the integrator. Conventional moving-coil galvanometers of adequate sensitivity are generally of very low resistance, but possess several practical disadvantages. They are seldom robust, usually cumbersome, and of course, quite expensive, while subject to easy burnout. In addition the limited frequency response of such instruments sometimes deprives the accelerator operator of essential information on fast beam fluctuations.

For these reasons an electronic galvanometer has been constructed, combining in a simple circuit the following advantages:

(a) An input impedance given by 20 kΩ divided by the number of microamperes for full-scale deflection;

(b) A non-adjustable deflection sensitivity which is at least as precise and constant as a high-quality commercial galvanometer;

(c) No zero-set adjustment; the zero does not drift nor change perceptibly for scale changes from 0.1 μA to 1 mA full-scale deflection; and

(d) Essentially complete safety from burnout even if quite high positive or negative voltages are accidentally connected to the input.

2.2. DESCRIPTION

The circuit makes use of unity voltage feedback around a two-stage balanced amplifier. The operation may be understood by reference to fig. 3. The amplifier is adequately represented by a real voltage gain, A, an infinite input impedance, and an output impedance, R_0. The input impedance is given by R_f/A (within an error of $1:A$, i.e., 1:1000 in our circuit). The meter current is iR_f/R_m†, where i is the input current. Thus the deflection sensitivity depends only upon precision resistors and a robust meter whose calibration can be expected to be extremely constant since it can never be subjected to serious overload (see below for further discussion of this point).

The lack of zero-drift is perhaps the most important innovation involved in this circuit. Because of the unity feedback the drift at the

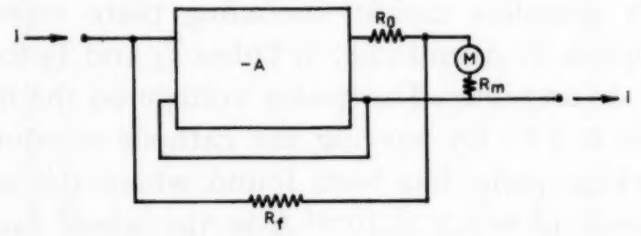

Fig. 3. Block diagram of the electronic galvanometer

output is just equal to the drift at the input. Since the input is a balanced stage operating under essentially ideal conditions, we can expect this drift never to exceed 50 mV. Full-scale deflection of the meter corresponds to an output voltage of 20 volts, hence the zero drift should never exceed 1/400 of full scale, an undetectable deflection. It should be noted that in designing such a circuit there is considerable latitude in the parameters, but that vanishingly small zero-shift must be purchased for the price of increasing the input impedance. This could be circumvented by increasing the circuit gain, however in order to hold the circuit to two

† The correct expression is actually

$$i\frac{R_f}{R_m}\frac{\left(1+\frac{R_0}{AR_f}\right)}{\left(1-\frac{1}{A}-\frac{R_0}{AR_m}\right)}.$$

The correction terms can at most amount to 0.2%, or less than a detectable deflection.

double triodes this expedient was not resorted to in this case.

The circuit is outstanding as to capacity to withstand overload. This can be of importance in accelerator use where short circuits (or gas discharges) between target and secondary-

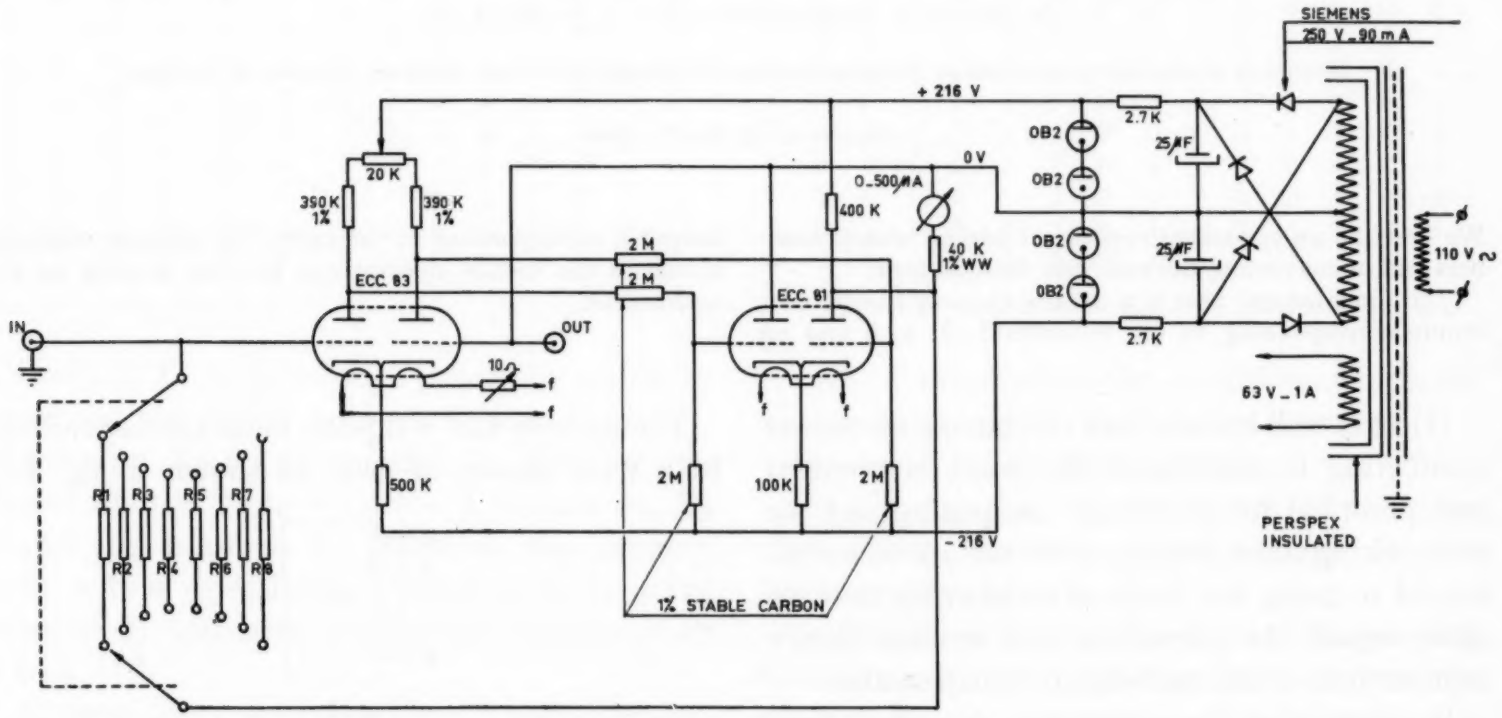

R_1 = 100 M	1%	STABLE	CARBON
R_2 = 20 M	1%	"	"
R_3 = 10 M	1%	"	"
R_4 = 2 M	1%	WIRE	WOUND
R_5 = 1 M	1%	"	"
R_6 = 200 K	1%	"	"
R_7 = 100 K	1%	"	"
R_8 = 20 K	1%	"	"

Fig. 4. Circuit diagram of the electronic galvanometer.

electron suppressor are a possibility. Under overload conditions (that is, with the voltage measured at the input more than a few tenths of a volt) the amplifier itself can deliver no more than 1 mA to the meter, this amounting to only a factor of two overload. Increasing the applied input voltage up to 40 volts on the 1 mA scale and up to more than 200 volts on all other scales decreases the overload since the input current flows through the meter in the opposite direction to that of the amplifier output current. The input tube itself, since the cathode resistor is very high, can easily follow positive input voltages of as much as 200 volts without destructive grid current, and in most cases can tolerate a negative grid voltage of 200 volts for a short time without breaking down.

2.3. CIRCUIT DIAGRAM

The complete circuit diagram is shown in fig. 4. The power is provided by a transformer insulated with perspex, so that the insulation to ground is quite as good as that required for the input of the integrator. The entire circuit, including power supply, is built onto the back of the meter itself, thus making for an extremely compact unit.

2.4. CONCLUSION

As in the case of the integrator, identical circuits have been built for both the Van de Graaff accelerator and the cascade generator. The operation of both has been completely trouble free for several months.

Acknowledgements

This investigation is part of the research program of the "Stichting voor Fundamenteel Onderzoek der Materie", and was made possible by financial support from the "Nederlandse Organisatie voor Zuiver Wetenschappelijk Onderzoek".

NUCLEAR INSTRUMENTS AND METHODS 8 (1960) 46–54; NORTH-HOLLAND PUBLISHING CO.

TRANSISTORIZED APPARATUS FOR ACCUMULATION AND BINARY-DECIMAL CONVERSION

D. BRINI, A. GANDOLFI and G. L. TABELLINI

Istituto di Fisica dell'Università di Bologna. Istituto Nazionale di Fisica Nucleare. Sezione di Bologna

Received 28 March 1960

We describe an apparatus capable of adding binary numbers and of converting the sum into decimal form.

The fundamental unit is a decade element having four inputs corresponding to the numbers 1, 2, 4, 8 and an output Z corresponding to the carry. The number which is stored in the decade element can be read directly on an instrument.

(I) It is well known that the binary system of numbering is considered the most convenient and practical for electronic computing and for memorizing data. Furthermore we are so accustomed to using the decimal numbering that we often regard the conversion of a written binary number into a decimal form as indispensable.

In particular the apparatus described here will be utilized in conjunction with the memorisation and registration system for various counting channels, in the Cosmic Rays station at the Institute of Physics of the Bologna University. Each of the counting channels corresponds to a fixed time-interval.

This apparatus, besides being capable to convert a memorised number in a binary form into a decimal form, gives the possibility to accumulate an *a priori* fixed number of data of each channel.

Obviously the first requirement of such an apparatus corresponds to the most common case, the conversion of the counting of a binary scaler into a decimal form.

This problem has already been dealt with by various authors[1–6]). Since in our case we require also the addition operation, we thought, for reasons of economy, of an apparatus capable of making simultanously both accumulation and conversion of data.

† The numbers from 2^0 at 2^n are sent as pulses following in the corresponding inputs.

The system has n inputs, each corresponding to a fixed power of two, as shown in fig. 1†.

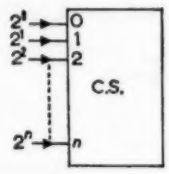

Fig. 1

For instance, if 1011 is the number to be converted (and to be summed to the numbers previously sent into the system) we shall have, successively in time, a pulse on 0 input, a second pulse on input 1 none on 2 and a last pulse on input 3.

In our case, we have 17 inputs, the 17th corresponding to $2^{16} = 65536$ units.

(II). The fundamental unit of the apparatus is a particular decade element with 10 stable states capable, therefore, to store a decimal number. It has four inputs X_1, X_2, X_3, X_4, and

1) R. K. Richards, Arithmetic Operations in Digital Computers (D. Van Nostrand Company, 1955).

2) J. F. Couleur, BIDEC, A Binary-to-Decimal or decimal-to-Binary Converter (I.R.E. Trans. Elect. Comp. Vol. EC7 N.4, Dec. 1958).

3) L. Dadda, Le conversioni automatiche nella calcolatrici Elettroniche binarie, Energia Elettrica 1 (1959).

4) S. H. Caldwell, Switching Circuits and Logical Design (J. Wiley and Sons, 1958).

5) J. Millman and H. Taub, Pulse and Digital Circuits (McGraw-Hill Book Company, 1956).

6) A. W. Lo *et al.*, Transistor Electronics (Prentice-Hall, Inc., 1955.)

TABLE 1

(a)	(b)				(c)					(d)					(e)					(f)				
					$X_1(+1)$					$X_2(+2)$					$X_3(+4)$					$X_4(+8)$				
	Y_4	Y_3	Y_2	Y_1	τ_4	τ_3	τ_2	τ_1	Z	τ_4	τ_3	τ_2	τ_1	Z	τ_4	τ_3	τ_2	τ_1	Z	τ_4	τ_3	τ_2	τ_1	Z
0	0	0	0	0	0	0	0	1	0	0	0	1	0	0	0	1	0	0	0	1	0	0	0	0
1	0	0	0	1	0	0	1	1	0	0	0	1	0	0	0	1	0	0	0	1	0	0	0	0
2	0	0	1	0	0	0	0	1	0	0	1	1	0	0	0	1	0	0	0	0	0	1	0	1
3	0	0	1	1	0	1	1	1	0	0	1	1	0	0	0	1	0	0	0	0	0	1	0	1
4	0	1	0	0	0	0	0	1	0	0	0	1	0	0	1	1	0	0	0	0	1	1	0	1
5	0	1	0	1	0	0	1	1	0	0	0	1	0	0	1	1	0	0	0	0	1	1	0	1
6	0	1	1	0	0	0	0	1	0	1	1	1	0	0	0	1	1	0	1	0	0	1	0	1
7	0	1	1	1	1	1	1	1	0	1	1	1	0	0	0	1	1	0	1	0	0	1	0	1
8	1	0	0	0	0	0	0	1	0	1	0	0	0	1	1	0	1	0	1	1	1	1	0	1
9	1	0	0	1	1	0	0	1	1	1	0	0	0	1	1	0	1	0	1	1	1	1	0	1

an output Z. A pulse on X_1 (equal number 1) increases the stored number from n to $n + 1$, a pulse on X_2 (equal number 2) increases the stored number from n to $n + 2$, a pulse on X_3 (equal to number 4) increases the number from n to $n + 4$, lastly a pulse on X_4 (equal to number 8) increases the stored number from n to $n + 8$.

If these operation give a carry, a pulse appears on output Z and the number of lowest order is stored in the decade element.

The choice of the 4 inputs corresponding to the four numbers 1, 2, 4, 8 has been determined by making a compromise as discussed in Appendix A.

The whole apparatus is made by 6 decade elements, capable therefore to sum and convert numbers up to 10^6. The 6^{th} decade element is used only to store the carries; it will have therefore only input X_1.

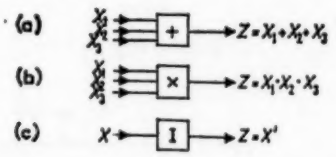

Fig. 2

(III). The scheme of the decade element is based on 4 bistable symmetric multivibrators (flip-flop), used as a memorising element, and on the principle that two pulses cannot exist simultanously on different inputs.

Table 1 summarises the conditions which the decade must satisfy. The columns show:

(a) the stored decimal numbers;

(b) Y_1, Y_2, Y_3, Y_4 the states of the four memorising elements corresponding to the stored number of (a);

(c) which of the four flip-flops corresponding to column (b) should change its state after the pulse on X_1 (= 1) in order to obtain the number $n + 1$ and also whether there is Z carry†;

(d), (e), (f) which of the four flip-flops should change its state after a pulse on X_2 (= 2), on X_3 (= 4) and on X_4 (= 8) respectively.

By using table 1 and the Boole algebra

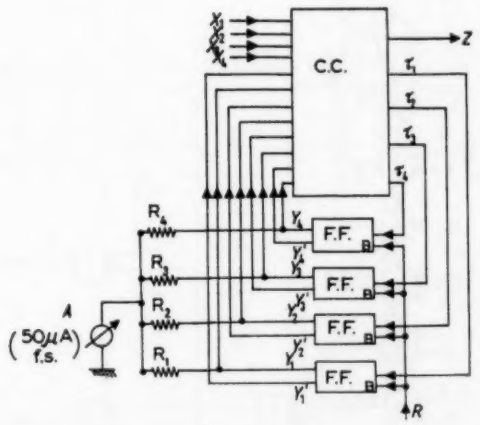

Fig. 3

(see appendix B) the following equations describing the behaviour of the decade element are obtained:

† The change of state of the i-th flip-flop takes place when $\tau_i = 1$.

$$\tau_1 = X_1$$

$$\tau_2 = X_1 Y_1 Y_4' + X_2 Y_4' + X_3(Y_2 Y_3 + Y_4) + \\ + X_4 (Y_2 + Y_3 + Y_4)$$

$$\tau_3 = X_1 Y_1 Y_2 + X_2 Y_2 + X_3 Y_4' + X_4 (Y_2' Y_3 + Y_4)$$

$$\tau_4 = X_1 Y_1 (Y_2 Y_3 + Y_4) + X_2 (Y_2 Y_3 + Y_4) + \\ + X_3 (Y_2' Y_3 + Y_4) + X_4 Y_2' Y_3'$$

$$Z = X_1 Y_1 Y_4 + X_2 Y_4 + X_3 (Y_2 Y_3 + Y_4) + \\ + X_4 (Y_2 + Y_3 + Y_4) \qquad (1)$$

where the Y_i' represent the complementary outputs of Y_i (es. $Y_1 = 1$, $Y_1' = 0$). The (1) indicate therefore the logic operations necessary to satisfy the conditions required by the apparatus.

Precisely three types of elementary circuits are necessary. They are sketched in fig. 2:

(a) logic circuit for addition;
(b) logic circuit for multiplication;
(c) inverter circuit.

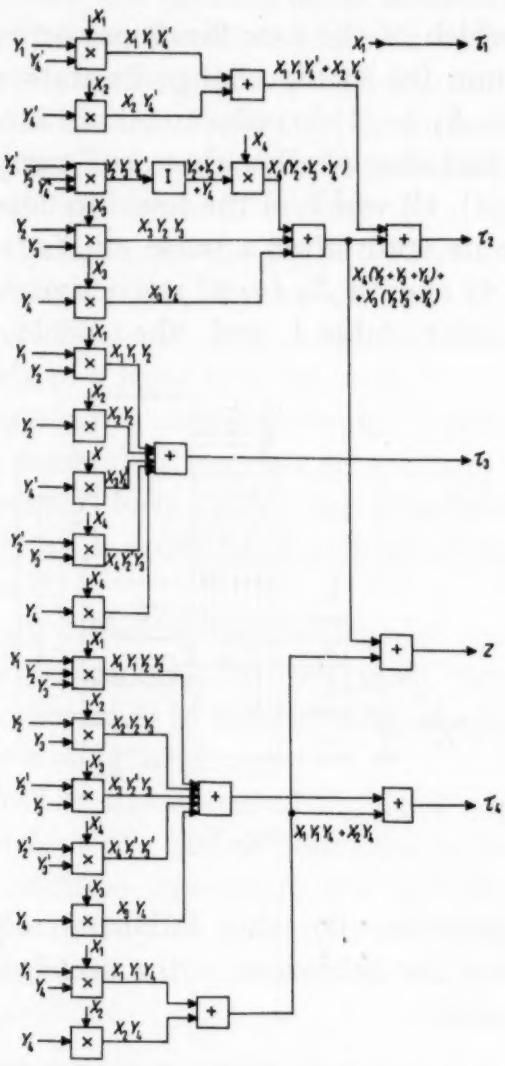

Fig. 4

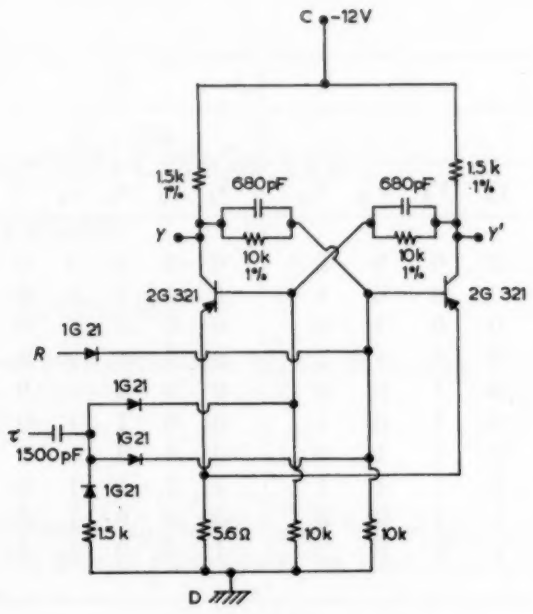

Fig. 5 (a)

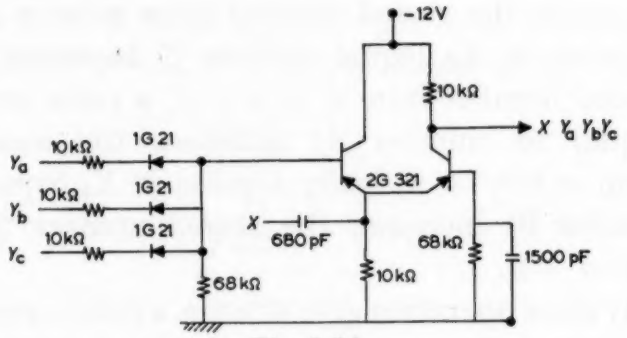

Fig. 5 (b)

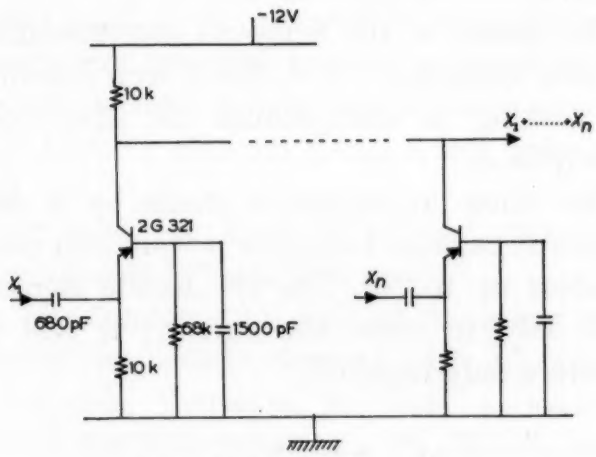

Fig. 5 (c)

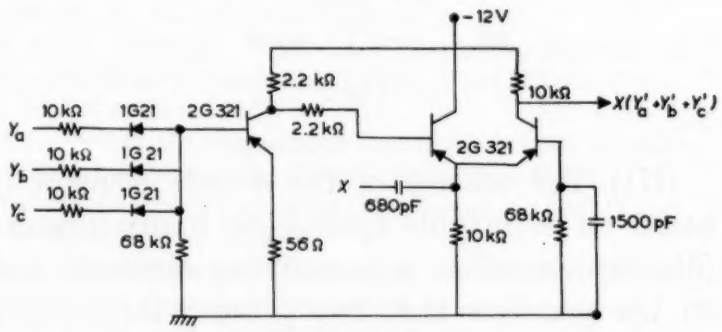

Fig. 5 (d)

The whole scheme of the decade element could be of the type shown in fig. 3, where C.C. indicates the block of combinational circuit made essentially of the three elementary circuits of fig. 2.

The stored decimal counting of the decade element can be read with the instrument A, by taking the voltage levels of the four flip-flops through R_1, R_2, R_3, R_4.

The block diagram of fig. 4 shows how the combinational circuit was made.

Fig. 5 shows the detailed schemes of the elementary circuits used. Their mounting was made on printed circuits. The elementary circuits are:

(a) Flip-flop, where R represents the positive input pulse for reset, τ is the triggering positive input pulse, Y and Y' give the complementary states of the circuits;

(b) the circuit for multiplication, where Y_a, Y_b, Y_c and X correspond to the 4 inputs to be multiplied and $(Y_a \cdot Y_b \cdot Y_c \cdot X)$ is the output;

(c) the circuit for addition, where the X_i are the pulses to be summed and $\sum X_i$ is the output;

(d) the combinational circuit of multiplication, inversion and successive multiplication. The first transistor makes the inversion of the input $Y_a \cdot Y_b \cdot Y_c$ giving $Y_a' + Y_b' + Y_c'$. The output will be given by $(Y_a' + Y_b' + Y_c') \cdot X$.

We point out that the inputs X_i are pulses, while Y_i or Y_i' are voltage levels corresponding to two states.

(IV) The checks of the decade element have been made by sending separately pulses into the four inputs X_1, X_2, X_3, X_4, and by observing in a synchroscope the distribution of the outputs with respect to the inputs. If the apparatus works correctly the distribution corresponding to the waveform chart shown in fig. 6 must appear. In this figure:

(a) represents the sequency of the input pulses;

(b) gives the distribution of Z outputs if the input (a) is sent into X_1;

(c), (d), (e) give the distribution of the Z outputs if the triggering pulses are sent respectively into X_2, X_3, X_4.

A further check could be carried out by observing the waveforms on the instrument A of fig. 3 when the pulses are sent to the four inputs separately. Then one should observe the waveforms as shown in fig. 7, represented by (a), (b), (c), (d) and corresponding to the four inputs X_1, X_2, X_3 and X_4.

TABLE 2

n	0	1	2	3	4	5	6	7	8	9	10	11	12	13	14	15	16
2^n	1	2	4	8	16	32	64	128	256	512	1.024	2.048	4.096	8.192	16.384	32.768	65.536
10	X_1	X_2	X_3	X_4	X_2 X_3	X_2	X_3	X_4	X_2 X_3	X_2	X_3	X_4	X_2 X_3	X_2	X_3	X_4	X_2 X_3
10^2	—	—	—	—	X_1	X_1 X_2	X_2 X_3	X_2	X_1 X_3	X_1	X_2	X_3	X_1 X_4	X_1 X_4	X_4	X_2 X_3	X_1 X_2
10^3	—	—	—	—	—	—	—	X_1	X_2	X_1 X_3	—	—	—	X_1	X_1 X_2	X_1 X_2 X_3	X_1 X_3
10^4	—	—	—	—	—	—	—	—	—	—	X_1	X_2	X_3	X_4	X_2 X_3	X_2	X_1 X_3
10^5	—	—	—	—	—	—	—	—	—	—	—	—	—	—	X_1	X_1 X_2	X_2 X_3
	0	R	R	R	R	$3R$	$3R$	$3R$	$3R$	$5R$	$4R$	$3R$	$3R$	$5R$	$5R$	$7R$	$9R$

Total = $57R$.

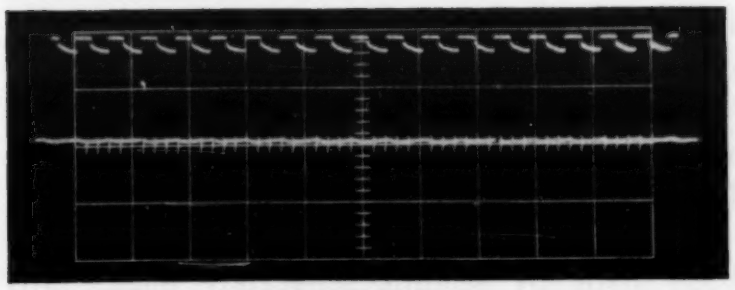

Fig. 6 (a)–(b)

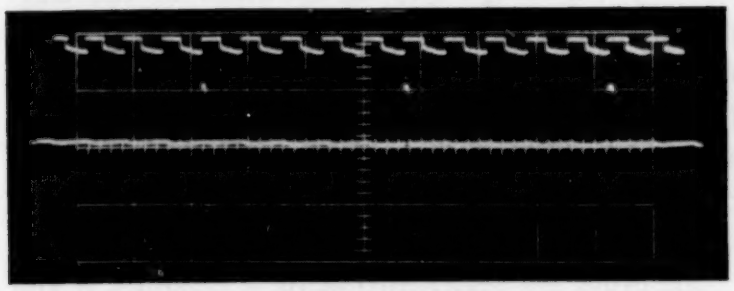

Fig. 6 (a)–(c)

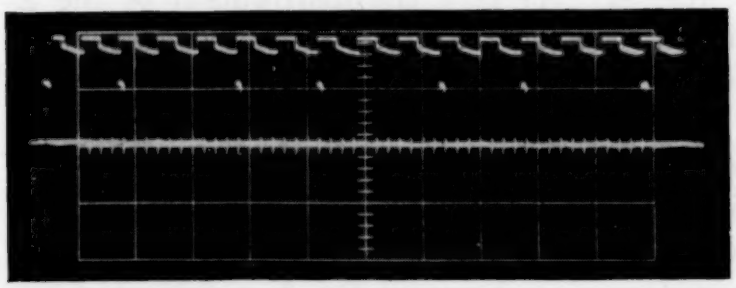

Fig. 6 (a)–(d)

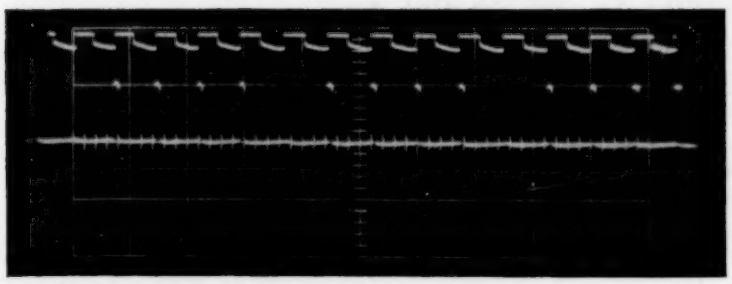

Fig. 6 (a)–(e)

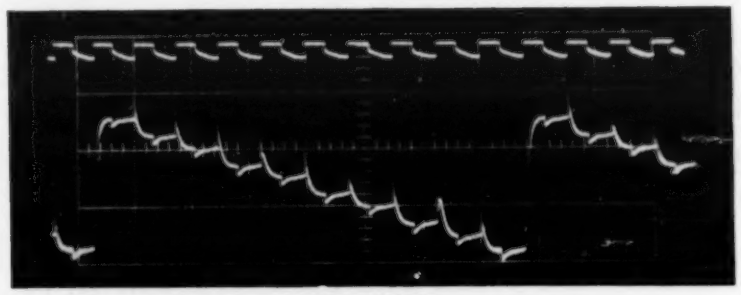

Fig. 7 (a)

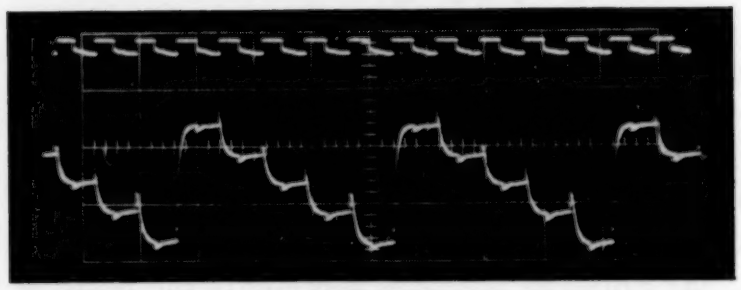

Fig. 7 (b)

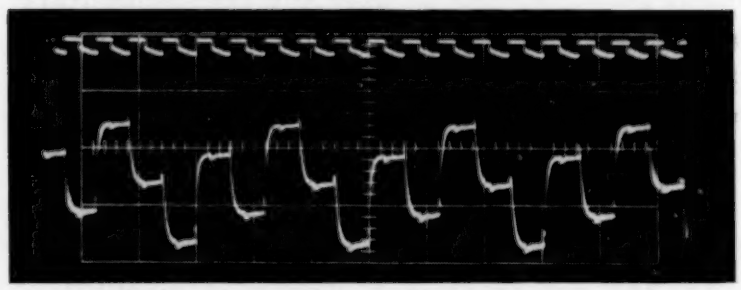

Fig. 7 (c)

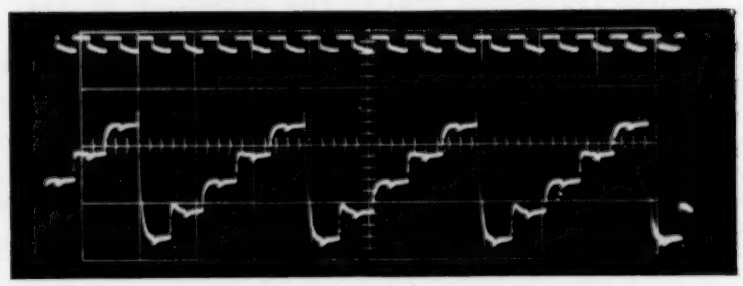

Fig. 7 (d)

The average resolution obtained is about 10 μs, using positive pulses of few volts coming from a convenient former.

The power required for a decade element is about 170 mA $\times$ 12 volts.

(V) The whole apparatus consists of 6 decades, as pointed out above. The distribution of the pulses on the various inputs of the 6 decades is shown in table 2.

As no input of any decade element can be simultaneous to another input, it is necessary to delay conveniently each trigger with an R delay which should not be lower than the resolution of the apparatus.

The last line of table 2 shows the delays to be fixed between each input. As one can see, the complete elaboration of a number of 17 binary figures can be made in a time of $57R$, which, considering the resolution of the apparatus, correspond to about 0.5 ms.

The block diagram of the triggers distribution is shown in fig. 8, where R or nR delays are obtained by monostable multivibrators made as indicated in fig. 9.

The test of the whole apparatus can be carried out simply by sending N pulses into any

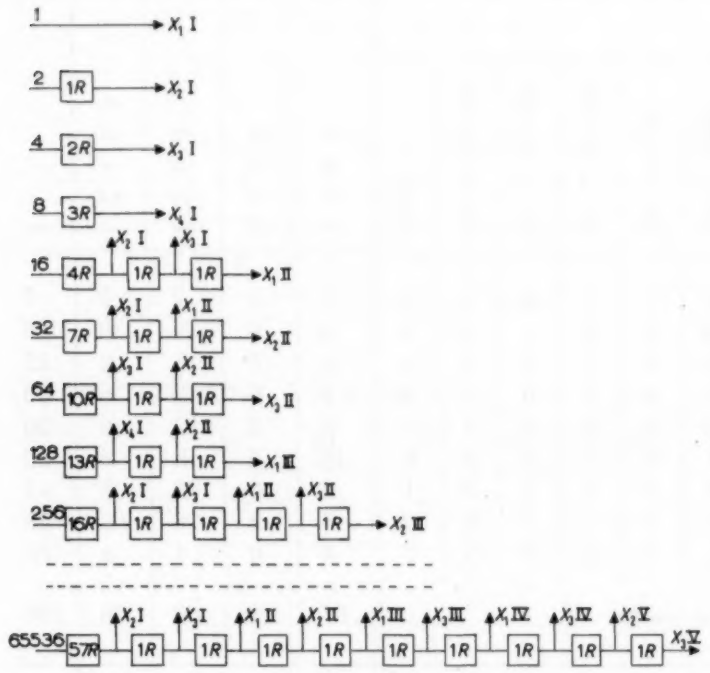

Fig. 8

of the inputs corresponding to a given power of two (2^i). The counting stored by the apparatus (measured by A instruments) should be $N2^i$.

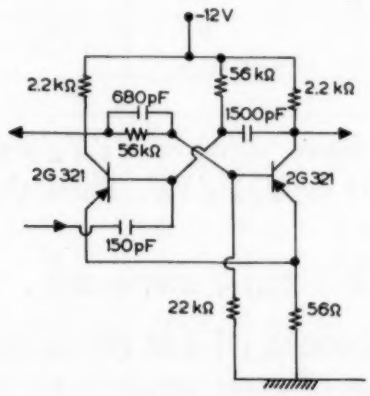

Fig. 9

We wish to thank, Mr. Merli for his help in mounting our apparatus.

Appendix A

The choice of the four inputs $X_1\,X_2\,X_3\,X_4$ was suggested by a compromise. In fact only one input X_1 could have been taken into account. In this way we would have simplified the circuit of the decade element but we would have complicated the distribution of the pulses for each decimal number to be elaborated, and it would have increased very much the time of elaboration. On the other hand, in order to obtain a shorter operation time, we could have taken nine inputs each corresponding to nine numbers 1.....9, but in this case we would have to increase considerably the number of the components in each decade element.

The choice of the four inputs X_1, X_2, X_3, X_4 allows therefore a reasonable compromise between good operation-time and economy in the apparatus. The choice of the numbers corresponding to the four inputs was suggested by the idea to obtain a minimum operation time. The latter is proportional to the number of the pulses, following in the time, to be sent into the apparatus.

Table 3 shows in columns (a), (b) the frequencies of the decimal numbers corresponding to a given power of two, up to the maximum power 2^{16}. As it appears, the most frequent numbers are 2, 1, 6, 4 and 8. Therefore it is evident that it is more convenient to choose the four inputs within these five numbers. Column (c) shows the pulses necessary to elaborate all the 17 powers of 2, considering the groups 1–2–4–8, 1–2–4–6, 1–2–6–8. As can be seen, the number of pulses needed and consequently the operating time does not depend on the choice of the group of the four numbers. Columns (d) and (e) show, for a comparison, the cases corresponding to the five most convenient inputs, and to a single input corresponding, of course, to number 1. In the first case, the operating time is 15% shorter, in the second one it increases by about 300%.

Appendix B

The logic algebra (or Boole algebra) takes into account only the variables which two different values (or states) corresponding to 0 or to 1 can assume. It is therefore useful to study the circuits which elaborate codified data in a binary form.

The fundamental logic operations (to which, in practice, real circuits must correspond) are the following:

(a) addition:

$$0 + 0 = 0;\quad 1 + 0 = 0 + 1 = 1;\quad 1 + 1 = 1;$$

TABLE 3

(a)	(b)																		(c)			(d)	(e)
decimal numbers	binary numbers to elaborate																						
	$2^0 = 1$	$2^1 = 2$	$2^2 = 4$	$2^3 = 9$	$2^4 = 16$	$2^5 = 32$	$2^6 = 64$	$2^7 = 128$	$2^8 = 256$	$2^9 = 512$	$2^{10} = 1024$	$2^{11} = 2048$	$2^{12} = 4096$	$2^{13} = 8192$	$2^{14} = 16.384$	$2^{15} = 32.768$	$2^{16} = 65.536$	Total	1, 2, 4, 8	1, 2, 4, 6	1, 2, 6, 8	1, 2, 4, 6, 8	1
1	1	0	0	0	1	0	0	1	0	1	1	0	0	1	1	0	0	7	7	7	7	7	7
2	0	1	0	0	0	1	0	1	1	1	1	1	0	1	0	1	0	9	9	9	9	9	18
3	0	0	0	0	0	1	0	0	0	0	0	0	0	0	1	1	1	4	8	8	8	8	12
4	0	0	1	0	0	0	1	0	0	0	1	1	1	0	1	0	0	6	6	6	12	6	18
5	0	0	0	0	0	0	0	0	1	1	0	0	0	0	0	0	2	4	8	8	12	8	20
6	0	0	0	0	1	0	1	0	1	0	0	0	1	0	1	1	2	8	16	8	8	8	48
7	0	0	0	0	0	0	0	0	0	0	0	0	0	0	0	1	0	1	3	2	2	2	7
8	0	0	0	1	0	0	0	1	0	0	0	1	0	1	1	1	0	6	6	12	6	6	48
9	0	0	0	0	0	0	0	0	0	0	0	0	1	1	0	0	0	2	4	6	4	4	18
													No. pulses						67	66	68	58	196

(b) multiplication:

$$0\times1 = 1\times0 = 0; \quad 1\times1 = 1; \quad 0\times0 = 0;$$

(c) inversion:

$$0' = 1; \quad 1' = 0\,. \tag{1}$$

From these we get the important rules:

$$X + X' = 1 \quad \text{and} \quad (X_1 \cdot X_2 \cdots X_4)' = X_1' + X_2' + \cdots + X_n'\,. \tag{2}$$

It is clear therefore that if we want to assembly an apparatus with one or more variable inputs, capable to satisfy a whole combination of inputs and to give an output 1, it will be enough to sum up the outputs of various circuits, each satisfying separately and univocally one single required combination.

Actually these circuits carry out only the inversion and logic multiplication operations. In fact, for instance, the combination $Y_1 = 0$, $Y_2 = 0$ and $Y_3 = 1$, can be represented by $Z = Y_1'\, Y_2'\, Y_3'$.

To make a synthesis of a combinational circuit means then to obtain the whole of the required combinations.

Let us assume, for instance, that these are given by table 4

TABLE 4

	Y_1	Y_2	Y_3	Z
a	0	0	1	1
b	0	1	1	1
c	1	0	0	1

We shall have $Z(a) = Y_1'Y_2'Y_3'$; $Z(b) = Y_1'Y_2Y_3$; $Z(c) = Y_1Y_2'Y_3'$. Then the required equation is:

$$Z = Z(a) + Z(b) + Z(c)\,. \tag{3}$$

Taking into account (1) and (2) we can simplify eq. (3). This is of great importance in practice, because it reduce the number of circuits and consequently of the utilised components. We shall have:

$$Z = Y_1'Y_3(Y_2 + Y_2') + Y_1Y_2'Y_3' = = Y_1'Y_3 + Y_1Y_2'Y_3\,.$$

If there are no more than 4 variables, it is useful to use the so called Karnaugh map, which consists of a square divided into 16 cells, each representing one of the 16 possible combinations of the variables of input ($2^4 = 16$). With this method, the simplifications appear immediate, considering the following most common cases:

(a) Two adjacent cell case.

(Y_1Y_2) \ (Y_3Y_4)	00	01	11	10
00	0	0	0	0
01	0	1	1	0
11	0	0	0	0
10	0	0	0	0

(b) four adjacent cell case.

(Y_1Y_2) \ $(Y_3Y)_4$	00	01	11	10
00	0	0	0	0
01	1	1	0	0
11	1	1	0	0
10	0	0	0	0

(c) Eight adjacent cell case.

(Y_1Y_2) \ (Y_3Y_4)	00	01	11	10
00	0	0	0	0
01	1	1	1	1
11	1	1	1	1
10	0	0	0	0

(a)
We have: $Z = Y_1'Y_2(Y_3'Y_4 + Y_3Y_4) = Y_1'Y_2Y_4$.
The variable for which the two cells differ, disappears.

(b)
We have: $Z = Y_1'Y_2Y_3' + Y_1Y_2Y_3' = Y_2Y_3'$
The two variables for which the four cells differ, disappear.

(c)
We have $Z = Y_2Y_3' + Y_2Y_3 = Y_2$.
The three variables which differ going from one cell to another disappear.

TABLE 5

		X_1	X_2	X_3	X_4
Y_2Y_1	Y_4Y_3	00—01—11—10	00—01—11—10	00—01—11—10	00—01—11—10
τ_1	00	1 1 0 or 1 1	0 0 0 or 1 0	0 0 0 or 1 0	0 0 0 or 1 0
	01	1 1 0 or 1 1	0 0 0 or 1 0	0 0 0 or 1 0	0 0 0 or 1 0
	11	1 1 0 or 1 0 or 1	0 0 0 or 1 0 or 1	0 0 0 or 1 0 or 1	0 0 0 or 1 0 or 1
	10	1 1 0 or 1 0 or 1	0 0 0 or 1 0 or 1	0 0 0 or 1 0 or 1	0 0 0 or 1 0 or 1
τ_2	00	0 0 0 or 1 0	1 1 0 or 1 0	0 0 0 or 1 1	0 1 0 or 1 1
	01	1 1 0 or 1 0	1 1 0 or 1 0	0 0 0 or 1 1	0 1 0 or 1 1
	11	1 1 0 or 1 0 or 1	1 1 0 or 1 0 or 1	0 1 0 or 1 0 or 1	1 1 0 or 1 0 or 1
	10	0 0 0 or 1 0 or 1	1 1 0 or 1 0 or 1	0 1 0 or 1 0 or 1	1 1 0 or 1 0 or 1
τ_3	00	0 0 0 or 1 0	0 0 0 or 1 0	1 1 0 or 1 0	0 1 0 or 1 1
	01	0 0 0 or 1 0	0 0 0 or 1 0	1 1 0 or 1 0	0 1 0 or 1 1
	11	1 1 0 or 1 0 or 1	1 1 0 or 1 0 or 1	1 1 0 or 1 0 or 1	0 0 0 or 1 0 or 1
	10	0 0 0 or 1 0 or 1	1 1 0 or 1 0 or 1	1 1 0 or 1 0 or 1	0 0 0 or 1 0 or 1
τ_4	00	0 0 0 or 1 0	0 0 0 or 1 1	0 1 0 or 1 1	1 0 0 or 1 1
	01	0 0 0 or 1 1	0 0 0 or 1 1	0 1 0 or 1 1	1 0 0 or 1 1
	11	0 1 0 or 1 0 or 1	0 1 0 or 1 0 or 1	0 0 0 or 1 0 or 1	0 0 0 or 1 0 or 1
	10	0 0 0 or 1 0 or 1	0 1 0 or 1 0 or 1	0 0 0 or 1 0 or 1	0 0 0 or 1 0 or 1
Z	00	0 0 0 or 1 0	0 0 0 or 1 1	0 0 0 or 1 1	0 1 0 or 1 1
	01	0 0 0 or 1 1	0 0 0 or 1 1	0 0 0 or 1 1	0 1 0 or 1 1
	11	0 0 0 or 1 0 or 1	0 0 0 or 1 0 or 1	0 1 0 or 1 0 or 1	1 1 0 or 1 0 or 1
	10	0 0 0 or 1 0 or 1	0 0 0 or 1 0 or 1	0 1 0 or 1 0 or 1	1 1 0 or 1 0 or 1

By using the requirements of the decade element given in table 1, it is possible to build the 20 maps of table 5 relative to the five outputs τ_1, τ_2, τ_3, τ_4 and Z, and the four inputs X_1, X_2, X_3, X_4. 0 or 1 indicates the flip-flop states which in a normal working condition are not possible (corresponding as they do to the decimal numbers from 10 to 15).

Taking into account the above mentioned rules and choosing 1 or 0 for the not allowed states, according to the best obtainable simplification, we can write the equation describing the behaviour of the decade element. We shall have:

	Not allowed states chosen as 1
$\tau_1 = X_1$	X_1 map
$\tau_2 = X_1Y_2Y_4' +$ $+ X_2Y_4' +$ $+ X_3Y_2Y_3 + X_3Y_4 +$ $+ X_4(Y_2 + Y_3 + Y_4) =$ $= X_1Y_1Y_4' + X_2Y_4' + X_3(Y_2Y_3 + Y_4) +$ $+ X_4(Y_2'Y_3'Y_4')$	1100, 1101, 1111, 1110, 1011 1010 1100, 1100, 1111, 1110, 1011 1010
$\tau_3 = X_1Y_1Y_2 +$ $+ X_2Y_2 +$ $+ X_3Y_4' +$ $+ X_4(Y_2Y_3 + Y_4) =$ $= X_1Y_1Y_2 + X_2Y_2 + X_3Y_4' + X_4(Y_2'Y_3 + Y_4)$	1111, 1011 1111, 1110, 1010 1100, 1101, 1111, 1011, 1010
$\tau_4 = X_1Y_1(Y_2Y_3 + Y_4) +$ $+ X_2(Y_2Y_3 + Y_4) +$ $+ X_3(Y_2'Y_3 + Y_4) +$ $+ X_4Y_2'Y_3' =$ $= X_1Y_1(Y_2Y_3 + Y_4) + X_2(Y_2Y_3 + Y_4) +$ $+ X_3(Y_2'Y_3 + Y_4) + X_4Y_2'Y_3'$	1101, 1111, 1011 1100, 1101, 1111, 1110, 1011, 1010 1100, 1101, 1111, 1110, 1010
$Z = X_1Y_1Y_2 +$ $+ X_2Y_4 +$ $+ X_3(Y_2Y_3 + Y_4) +$ $+ X_4(Y_2 + Y_3 + Y_4) =$ $= X_1Y_1Y_2 + X_2Y_4 + X_3(Y_2Y_3 + Y_4) +$ $+ X_4Y_2'Y_3'Y_4'$	1101, 1111, 1011 1100, 1101, 1111, 1110, 1011, 1010 1100, 1101, 1111, 1110, 1011, 1010 1100, 1101, 1111, 1110, 1011, 1010

NUCLEAR INSTRUMENTS AND METHODS 8 (1960) 55–60; NORTH-HOLLAND PUBLISHING CO.

APPARATUS AND LABORATORY FOR PROCESSING NUCLEAR EMULSION STACKS

H. ENGELHARDT, I. HAUSER and U. KRECKER

Deutsche Akademie der Wissenschaften zu Berlin, Kernphysikalisches Institut Zeuthen

Received 9 January 1960

In the following an apparatus is described for processing nuclear emulsion stacks with an area up to 35 × 45 cm². The apparatus is so constructed that 3.5 l of emulsion, thickness 400 μ, can be processed during 5 days. The procedure for developing nuclear emulsions of type NIKFI R is represented.

1. Introduction

When the construction of the Synchrophasotron at the Joint Institute of Nuclear Research, Dubna U.S.S.R., was completed, there arose the need to have enough capacity for the development of nuclear emulsion stacks. To meet this requirement in the Kernphysikalisches Institut der Deutschen Akademie der Wissenschaften, Zeuthen, a laboratory was built which works for all the member states of the Joint Institute of Nuclear Research. The new apparatus used in this laboratory makes it possible to treat emulsion pellicles up to 35 × 45 cm². This apparatus and the procedure are described in this paper.

2. Development Procedure

The method of development used in this apparatus is based on the temperature cycling method by Dilworth *et al.*[1]) with dry hot stage. The procedure and the composition of the solutions are adapted to the development of emulsions type NIKFI R, 400 μ thick[2–4]). All emulsions are mounted before processing. The development procedure consists of the following steps:

[1]) C. C. Dilworth, G. P. S. Occhialini and L. Vermaesen, Bulletin du Centre de Physique Nucléaire de Bruxelles No. 13a, (Febr. 1950).

[2]) D. M. Samoilowitsch and I. S. Pissanko, J. Techn. Phys. No. 2 (1956) 45.

[3]) J. Beljakow, L. G. Koslowa, L. N. Iwanowa and K. D. Tolstow, J. Sci. Appl. Photogr. Cinema **2** (1957) 325.

[4]) S. J. Ljubomilow, private communication.

2.1. PREPARATION OF THE GLASS

The cleaned glass plates, 1.2—1.3 mm thick, are immersed three times in a solution of the following composition:

4	g	Gelatine
10	g	Sodium silicate
0.75	g	Alum chronium
0.5	g	Thymol
60	ml	Ethyl alcohol
to 1000	ml	Distilled water

Henceforth it is possible to get special glass for mounting NIKFI R emulsions.

2.2. MOUNTING

Before mounting, that surface of the pellicle which is to be mounted must be rubbed down with an alcohol-water solution of 25% or 30% according to the time elapsed between the manufacture of the emulsion and its use. Otherwise a black sediment will be formed during the processing upon the surface of the emulsion. In this way 3—4 μ has to be removed. Then the pellicles are mounted on glass in the same solution as described before. In this solution the pellicle must be laid down on the glass plate and moved back and forth, until it sticks to the glass. This procedure lasts about 3—5 sec. Then the emulsion must immediately be taken out of the solution, cleaned, and then rolled with a machine-roller. After mounting, the pellicles are air dried for about 2 h and simultaneously cooled down from room temperature to 3° C.

2.3. PRESOAKING

The emulsions are soaked in distilled water of 3° C for 2.5 h.

2.4. SOAKING WITH COLD DEVELOPER

The emulsions are taken out of the presoaking bath and put for 2.5 h in the cold developer solution (3° C), having the following composition:

2.5 g Amidol
12 g Sodium sulphite (anhydrous)
ca. 2 g Citric acid, in order to have a *p*H-value of 6.6 to 1000 ml distilled water.

2.8. FIXING

The fixing bath consists of a 30% hypo solution to which potassium metabisulphite is added in order to have a *p*H of 6.9. The flow of hypo over the emulsions amounts to nearly 6 cm/min i.e. 1.5 l/min through one tray containing 0.176 l emulsion and 20 l hypo. The fixing time is 50% longer than that of the clearing time. This corresponds to a time of about 40 h. The temperature is approximately 5° C. At the beginning the fixing solution contains no silver but at the end the concentration amounts to

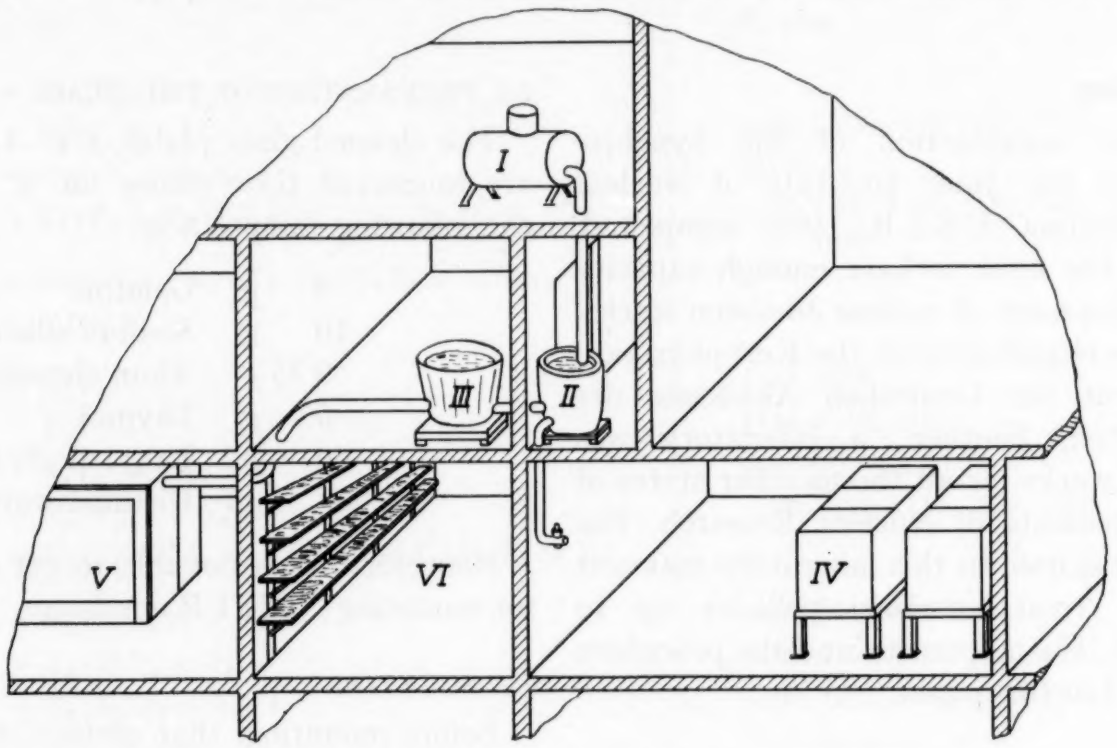

Fig. 1. Scheme of location of the rooms for processing.
I. water destillator, II. containers for distilled water, III. preparation of fixing solution, IV. development, V. fixing room, VI. drying room.

2.5. DRY HOT STAGE

After the plates have been taken out of the developer the surfaces of the emulsions are gently wiped off with filterpaper and then the plates are put immediately into a thermostat of 24° C for a period of 40 min.

2.6. STOP BATH

The development is interrupted by immersing the emulsions into a solution of 0.5% acetic acid of 3° C for 2.5 h.

2.7. INTERMEDIATE WASHING

The stop bath is let off and replaced by distilled water of 3° C for 2.5 h.

8 g/l. This is the greatest concentration attainable in our fixing unit with emulsions of 400 μ thickness. Corrosion is not found.

2.9. DILUTION AND WASHING

At the end of fixing the hypo is diluted with tap water over a period of 12 h, so that the concentration decreases proportionally to time until it reaches less than 1%. Simultaneously the temperature increases to the temperature of the tap water of approximately 13—15° C. Then the washing is started and is continued over a period of 24 h with running tap water by the same flow as during fixing.

2.10. DRYING

The emulsions are soaked for a time of 2 h in each of the five alcohol-water solutions with increasing concentrations of the successive baths by steps of 20%, beginning with 10%. To each solution 5% glycerin is added. Afterwards the emulsions are dried in air of room temperature and about 60—70% atmospheric humidity.

3. Apparatus

The laboratory for processing nuclear emulsion stacks consists of six rooms with an area of 162 m² for mounting, processing, fixing and for the preparation and storage of distilled water and fixing solution (fig. 1).

For mounting the pellicles on the glass a double wall tank of stainless steel is used through which temperature conditioning water can circulate (fig. 2). The dimensions of the inside tank are 65 × 55 cm². During mounting the glass plates are placed on a lattice (a) of PVC. When the dimensions of pellicles are smaller another smaller tank is used. After mounting the plates are passed through a machine-roller (fig. 3). It consists of a roller (a) coated with soft rubber of 0.4 cm thickness. The roller is driven slowly forward and backward by means of a small motor. The pressure between the roller and the tabletop can be adjusted with four springs (b). The roller can be moved up and down with a lever (c).

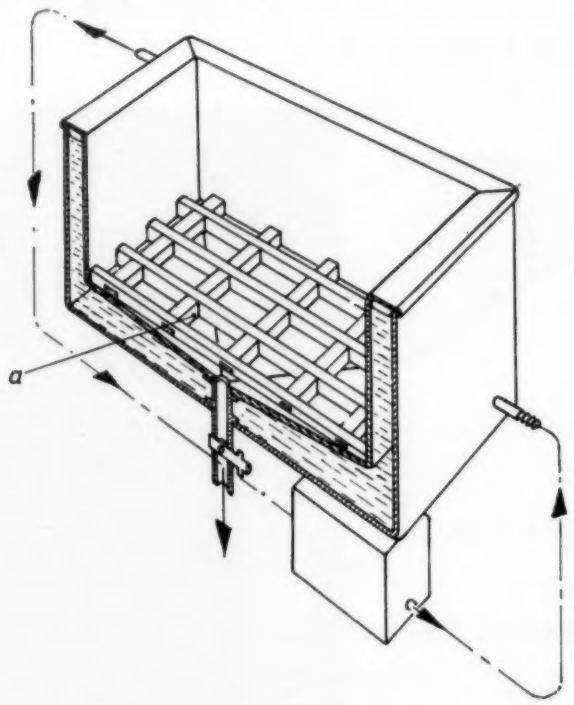

Fig. 2. Double wall tank for mounting.

After the plates have been passed through the roller they are immediately placed on trays of PVC (thickness 8 mm) and fixed there with springs in order to avoid that they swimm about while they are soaked in the diverse solutions. The area of a tray is 54 × 41 cm². Little disks are fixed on the surfaces of the trays in order to avoid that the plates will stick to the trays. The trays

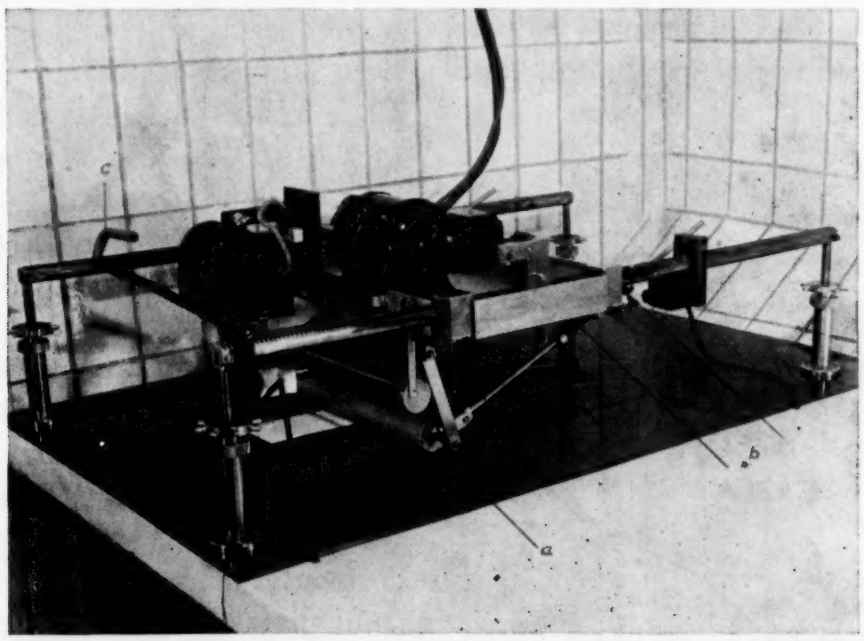

Fig. 3. Machine-roller for mounting pellicles.

(maximal 14) are placed in a rack of stainless steel one upon another and are fixed with pins. Two successive trays are separated by a distance of 1 cm (fig. 4).

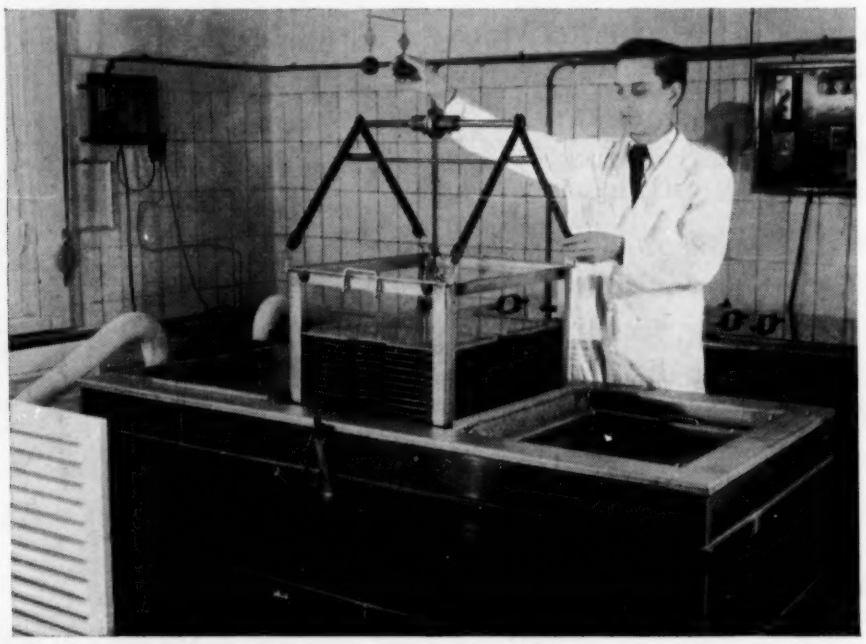

Fig. 4. Double wall tank for the processing steps of low temperature with rack withdrawn.

During the processing steps at low temperature, cooling down of the pellicles, presoaking, cold development, stopbath, and intermediate washing the emulsions are in these racks. For these steps two identical double wall tanks of stainless steel are used (figs 4 and 5). Each tank includes 3 containers. A cooling liquid circulates through the jackets of the tanks; a contact thermometer controls the function of the pumps and thus the temperature is regulated within the containers with an accuracy of $\pm$ 0.2 °C. An electrically driven pulley is used to transport the racks from one container to the next one.

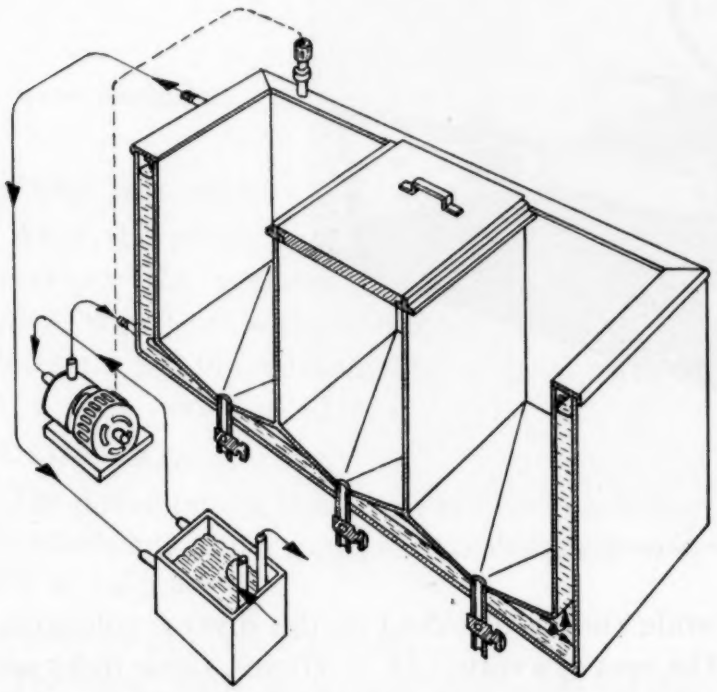

Fig. 5. Cut-away drawing of the tank of fig. 4 with cooling system (schematically).

The warm stage of development takes place in a temperature controlled cupboard (fig. 6) with ten sections (each of them has an area of 59×52 cm^2). Every section consists of a metal-tub (fig. 7) over which a soft rubber membrane is stretched, so that the glass plates with the pellicles remain in close contact with the rubber kept at a controlled temperature over the whole surface. Each tub is revolving around a tubular axis allowing the water for temperature conditioning to run in and out. In order to put the emulsions in and out the cupboard every section can be opened successively by moving the tubs up or down. When closed the tubs are horizontal and the sections are protected by front plates against the surroundings. The temperature of the rubber membrane and inside the cupboard differs no more than $\pm$ 0.1° C from the fixed value. After the intermediate washing the racks are transported to the fixing room in a lighttight car. For fixing two identical apparatus are used. Each consists of a big rack with ten

trays (fig. 8), made of plastic (Haveg) which is resistant to corrosion. Every tray has an area of $150 \times 48\ cm^2$. In fig. 9 the arrangement and function of the trays are shown. The fixing solution is pumped from a tank with a cooling coil into the back channel (a), runs through the holes (b) over the pellicles and flows back into the tank. The current velocity of the hypo can be regulated with cocks in front of the channels. The pipe system is similar to that shown in fig. 6. The dilution of hypo and the washing is also done in this apparatus. For the preparation of the fixing solution there exist two vessels. In the first vessel water and sodium thiosulphate are mixed by stirring. Then the solution is pumped through a filter into the second vessel and cooled down to a temperature of $-8°$ C in order to reach afterwards a temperature of about $+5°$ C in the fixing apparatus. For soaking the emulsions in the alcohol-water solutions they are put in two vessels. Each of them has a volume of 70 l and is able to take up all the emulsions fixed in one of the two fixing apparatus.

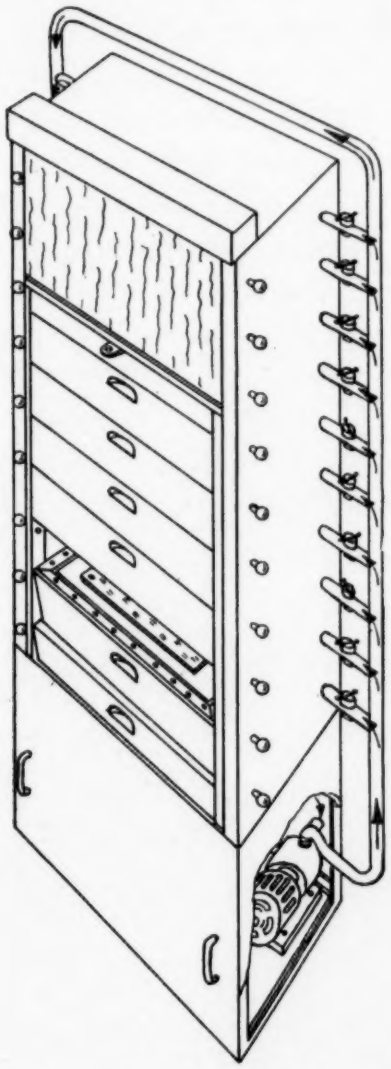

Fig. 6. Cupboard for the warm stage of development.

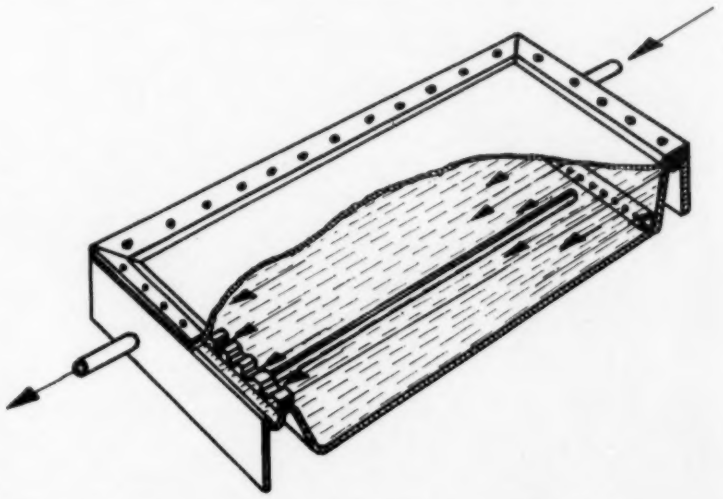

Fig. 7a. Cut-away drawing of the metal-tub of the cupboard shown in fig. 6.

3.5 l of emulsion of 400 μ thickness can be processed simultaneously in the fixing apparatus. The capacity of the cupboard for the warm stage of development is about 0.7 l emulsion; this means that 5 developments are necessary to fill the fixing apparatus. The time difference between the first and the last development is about 15 h and the whole processing from the beginning to its last stage takes five days.

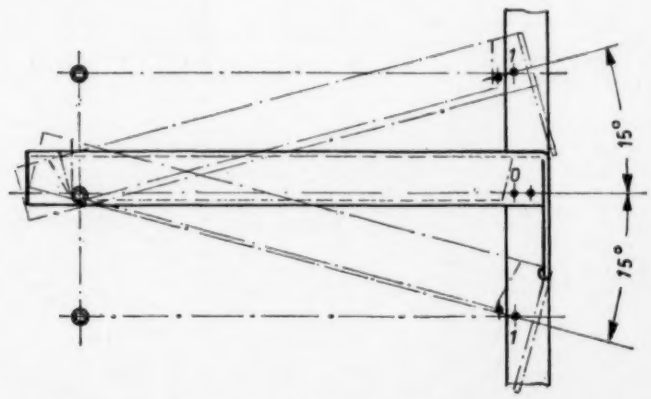

Fig. 7b. Metal-tub in the various positions.

4. Results

Until now a number of emulsion stacks have been developed in our laboratory and from this it is evident that the process supplies reproducible results.

After having taken out a representative stack NIKFI R, 400 μ, $10 \times 20\ cm^2$ we found the following values:

Fig. 8. Fixing apparatus (opened), below the trays the tank with the cooling coil.

The average blob density of tracks with plateau ionisation amounts to 22.7 blobs/100 μ and the fog is 1.15 grains/1000 μ^3.

The gradient of development is about 5%. This value is calculated as the ratio between the difference of the blob density in the upper and the lower layers (each 30 μ thick) to the density of the upper layer.

The distortions measured by the method of Cosyns and Vanderhaeghe[5]) amount to about 20μ.

The area of bubbles related to the total area of emulsion is 0.038%.

Acknowledgement

The authors wish to thank the autorities of the Amt für Kernforschung und Kerntechnik, der DDR, the Joint Institut for Nuclear Research, Dubna, and the Deutsche Akademie der Wissenschaften zu Berlin, especially the Direction of the Kernphysikalisches Institut for the generous help to accomplish the whole work. Thanks are also due to the Laboratoire de Physique Nucléaire, Université Libre de Bruxelles and to Dr. K. Lanius for stimulating discussions and to Dr. H. Heitler, Bristol, for his valuable correspondence. The authors express their gratitude to G. Nowatzki for the construction of the apparatus and to all those who participated in this work.

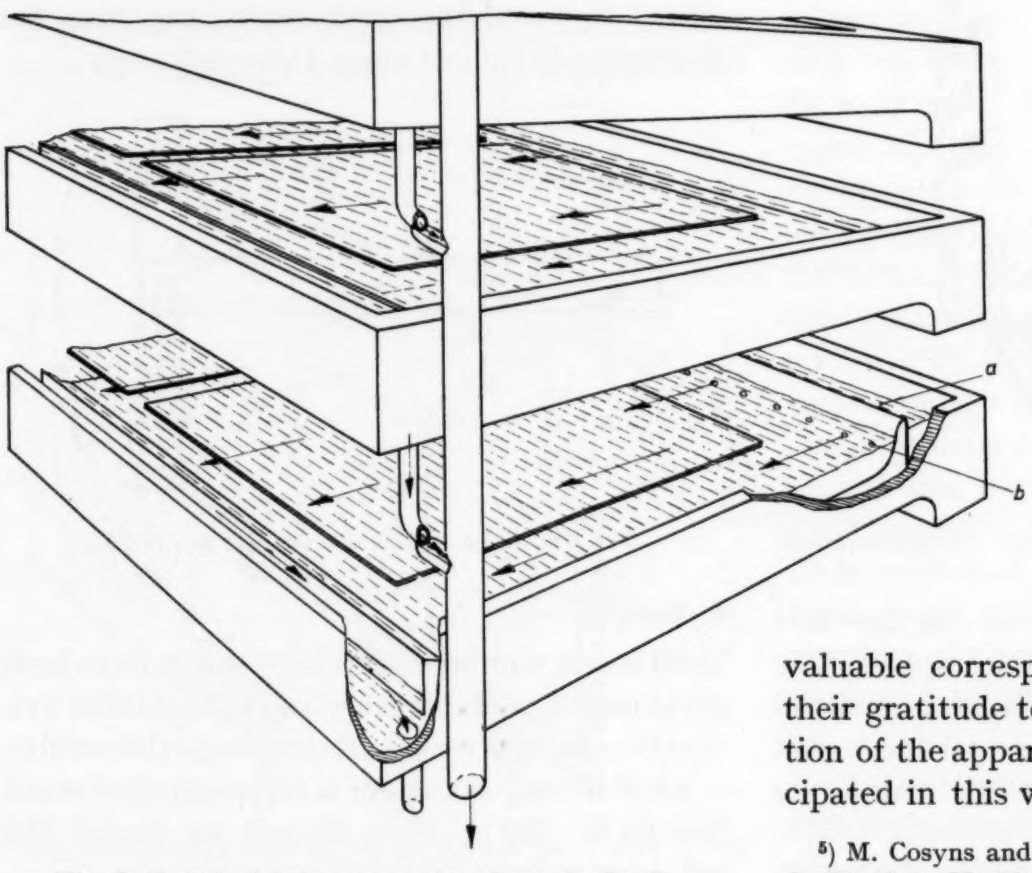

Fig. 9. Detail of fixing apparatus shown in fig. 8.

[5]) M. Cosyns and G. Vanderhaeghe, Bulletin du Centre de Physique Nucléaire de Bruxelles No. 15, (Febr. 1950).

NUCLEAR INSTRUMENTS AND METHODS 8 (1960) 61–69; NORTH-HOLLAND PUBLISHING CO.

OPTIMUM CONDITIONS FOR DOUBLE FOCUSING BETA RAY SPECTROMETERS

MITSUO SAKAI

Institute for Nuclear Study, University of Tokyo, Japan

Received 1 March 1960

Formulas for theoptimum dimensions of the source and the solid angle for the double focusing spectrometer, including the sector type spectrometer, were given in function of the given resolution. The maximum luminosity derived these formulas was compared with each other. It was found that the sector type double focusing spectrometer, of which the field parameters α and β are equal to $\frac{1}{2}$ and $\frac{1}{4}$, respectively, has a configuration with very good focusing properties. It has, in sense of the generalized Barber's law, such a configuration that the deflection angle is $\frac{8}{3}\pi$ and the distance between the image and the exit boundary of magnetic field is equal to the reference radius.

The results were also compared with the ordinary semicircular spectrometer, the Konopinski type semicircular spectrometer and the solenoid lens type spectrometer. These kinds of spectrometer have a nearly equal maximum luminosity, about ten times smaller than that of any type of double focusing spectrometer.

1. Introduction

The optimum conditions for a beta ray spectrometer have been discussed by several authors. Geoffrion[1]) discussed the optimum conditions for the uniform field semicircular spectrometer and DuMond[2]) for the solenoid lens type spectrometer, taking into account not only the solid angle but also the source dimensions. By using the same treatment, we discussed in the early article[3]) the optimum conditions for the spiral orbit spectrometer[4]) and the characteristics of three types of spectrometer, namely, semicircular, lens type and spiral orbit spectrometer were compared with each other. Verster[5]) discussed the electron optical properties of magnetic beta ray spectrometer and described transmission and luminosity versus line width for the different spectrometers.

In the present article, the theory of optimum conditions was developed and was applied to various types of double focusing beta ray spectrometer[6]), including the sector type double focusing spectrometer[7,8]). Especially the latter type was examined in details, in connection with the INS beta ray spectrometer[9]), in which, for the first time, the sector type double focusing principle was adopted. From this study, it was revealed that there existed a new geometrical setting which had as much good focusing properties as those of the ordinary $\pi\sqrt{2}$ focusing spectrometer. For comparison, the focusing properties of the ordinary semicircular spectrometer, the Konopinski type semicircular spectrometer and the solenoid lens type spectrometer were also discussed. The final results were expressed by the formulas for the optimum dimensions of the source and the solid angle in function of the given resolution. Finally, the usefulness of a spectrometer was discussed from the point of view of the maximum luminosity.

In the next section, the general treatment of the theory of optimum conditions was presented. In section 3, the aberration formula and the resolution formula of the sector type double focusing spectrometer was discussed and new setting was proposed. The aberration formula

[1]) C. Geoffrion, Rev. Sci Instr. **20** (1949) 638.

[2]) J. W. M. DuMond, Rev. Sci. Instr. **20** (1949) 160.

[3]) M. Sakai, Jour. Phys. et Radium **14** (1953) 570.

[4]) G. Miyamoto, Proc. Phys., Math. Soc. Japan, (in Japanse) **17** (1943) 587;
M. Sakai, Jour. Phys. Soc. Japan **5** (1950) 178; **5** (1950) 184.

[5]) N. F. Verster, Progress in Nucl. Phys. **2** (1952) 1.

[6]) K. Siegbahn and N. Svaltholm, Nature, Lond. **157** (1946) 872;
N. Svartholm and K. Siegbahn, Arkiv f. Mat. astro. o. fysik **33A**, No. 21 (1946).

[7]) David L. Judd, Rev. Sci. Instr. **21** (1950) 213.

[8]) E. S. Rosenblum, Rev. Sci. Instr. **21** (1950) 586;
H. Ikegami, Rev. Sci. Instr. **29** (1958) 943.

[9]) M. Sakai and H. Ikegami, Jour. Phys. Soc. Japan **13** (1958) 1076.
T. Yamazaki, H. Ikegami and M. Sakai, Jour. Phys. Soc. Japan **13** (1958) 1080.

and the resolution formula for various $\pi\sqrt{2}$ type double focusing spectrometers were treated in section 4 and those for the semicircular and lens type spectrometer were summarized in section 5. In section 6, according to the general discription presented in section 2, the mathematical formulation was derived and the optimum conditions of the different spectrometers were presented. The dependency of the slit width of the detector on the optimum condition was examined briefly in section 7. The comparison of different spectrometers was made in the last section, and their usefulness was discussed.

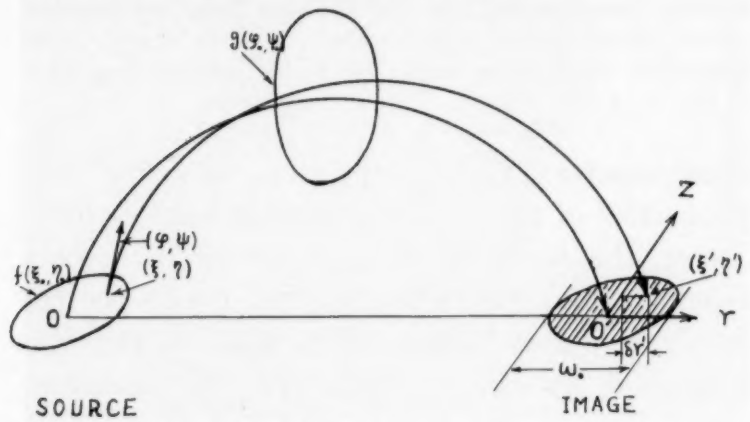

Fig. 1. Electron trajectories in a spectrometer. The coordinates used in the description are shown.

2. Presentation of the Problem on Optimum Conditions

For the general presentation of the problem, let us consider the schematical set-up of a spectrometer, shown in fig. 1. The source is assumed to emanate monoenergetic electrons with momentum p uniformly in all directions, to have an area A defined in general by $f(\xi_0, \eta_0) = 0$ and to be viewed by the solid angle Ω, defined by a defining baffle which is expressed approximately by $g(\varphi_0, \psi_0) = 0$, being independent of ξ_0 and η_0. The defining baffle is usually placed at the middle of the electron trajectories. Then the total number of electrons coming from this source through this defining baffle reaching at the detector plane can be expressed as $A\Omega$, which is defined as the luminosity L, where the number of monoenergetic electrons emitted by the source in all directions per unit area per unit time is normalized to the unit intensity. In the following discussions all lengths are measured in units of the reference radius, namely, the radius of curvature of electron with momentum p in the magnetic field H_0.

After passing though the defining baffle each electron, lavelled by $(\xi, \eta, \varphi, \psi)$, as shown in fig. 1, hits on a point (ξ', η') in the detector plane. The assembly of this image point forms the image of the source and its density corresponds to the blackening of photographic plate in a beta ray spectrograph. These circumstances were schematically demonstrated in fig. 1 by a hatched area. In this case the r coordinate is chosen along the right edge of two images of electrons differing in momentum by Δp, both of which are lavelled by (0, 0, 0, 0) and the z coordinate rectangular to the r coordinate. The origin of this coordinate system is chosen as the image point of the electron of momentum p and the initial condition (0, 0, 0, 0). In general, the height of the detector slit is set along the z coordinate.

Then, the r coordinate of the image point of electron $(\xi, \eta, \varphi, \psi)$ is expressed by

$$\begin{aligned}\delta r' = {} & a_1\xi + a_2\xi^2 + b_1\eta + b_2\eta^2 + \\ & + \alpha_1\varphi + \alpha_2\varphi^2 + \beta_1\psi + \beta_2\psi^2 \\ & + \text{second order cross terms of } \xi\eta,\ \varphi\psi \text{ and } \eta\psi \text{ etc.} \\ & + \text{heigher order terms.} \end{aligned} \tag{1}$$

This is the ordinary aberration formula. And the formula for the z coordinate can be also written in the same manner. The focusing study in the spectrometer is just to search for the conditions which make the coefficients of terms in eq. (1) as small as possible. Then the maximum value w_0 of coordinate of an image (see fig. 1) can be considered as the line width of a monoenergetic electron bundle with momentum p coming from the source through the defining baffle.

Using eq. (1) and introducing the dispersion D, the resolution can be defined by

$$\frac{\Delta p}{p} = \frac{w_0}{D} = W_0 \tag{2}$$

where Δp is the difference between the momenta of two groups of monoenergetic electrons, of which the spectrometer gives two images separated just by w_0. The resolving power is

defined by the inverse of the resolution. Then, the problem of obtaining the optimum conditions can be reduced to achieving the greatest possible luminosity for a given resolving power. The mathematical treatment will be developed in section 6.

Strictly speaking, this problem setting is not exact, because the effect of the detector slit width should be considered. This effect is treated in section 7. It will be seen in that section that the optimum condition taking into account the effect of slit width is nearly equal to the condition without consideration of that effect. Therefore, the present problem setting might be justified.

In the following three sections, we shall deduce the formulae for W_0 and L of the different spectrometers.

3. Resolution and Luminosity of Sector Type Double Focusing Spectrometer

The magnetic field in this case is assumed to exist only in a sectorial region between the planes $\vartheta = 0$ and $\vartheta = \Phi$ of a cylindrical polar coordinate system r, ϑ and z. In this region the field is assumed to be symmetric about the plane $z = 0$ and to be independent of ϑ. Following Shull and Dennison's equations[10]), the axial and radial components of the field can be expressed by

$$H_z = H_0 \left[1 - (r-1)\,\alpha + (r-1)^2\,\beta + z^2\left(\tfrac{1}{2}\alpha - \beta\right)\right], \quad (3)$$

$$H_r = zH_0 \left[-\alpha + 2\beta\,(r-1)\right], \quad (4)$$

where α and β are the field parameters and H_0 is the field at the reference radius. It is a well known fact that we get the double focusing spectrometer for $\alpha = \frac{1}{2}$. In the case of $\Phi = \pi\sqrt{2}$, the spectrometer becomes an ordinary double focusing spectrometer which will be discussed in the next section.

The second order aberration formula for this type of spectrometer was for the first time derived by Rosenblum[8]). Introducing the magnification M into this formula, we get the following second order formula for the case of $\beta = \frac{1}{4}$:

[10]) F. Sull and D. Dennison, Phys. Rev. **71** (1947) 681; Phys. Rev. **72** (1947) 256.

$$\delta r' = +M\delta r + \tfrac{1}{8}(\cos\varphi - 1)\,(1 + \cos\varphi - 2M)\,\delta z^2 + \frac{1}{3}\frac{(2\cos\varphi + 1)}{\sin^2\varphi}\frac{M-1}{M^2}$$
$$[3M - (2\cos\varphi - 1)\,(M^2 + M + 1)]\,\delta\varphi^2 - \frac{1}{3}\frac{1 - M^3}{M^2}\delta\psi^2 - \frac{\sqrt{2}\,(\cos\varphi - 1)}{\sin\varphi}$$
$$[1 + \cos\varphi - M - M^2]\,\delta z\delta\psi\,, \quad (5)$$

where M is defined as

$$M = \cos\varphi - \tan\varphi''\sin\varphi\,, \quad (6)$$

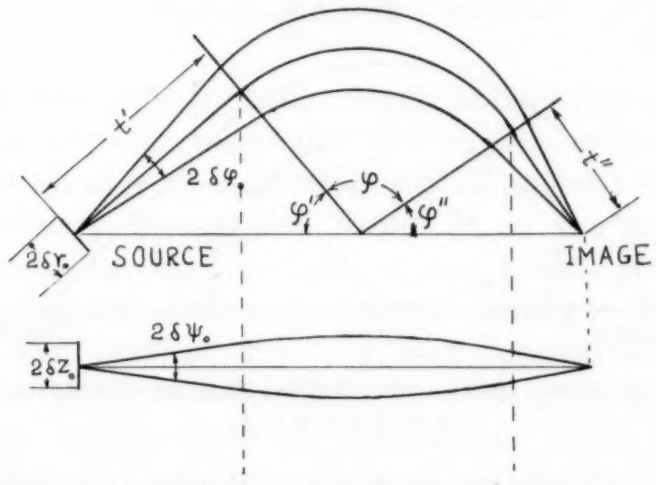

Fig. 2. Geometric relations in the generalized Barber's law. The radial and vertical focusings are presented.

and φ and φ'' are the angles which satisfied the generalized Barber's law, i.e., $\varphi = \Phi/\sqrt{2}$ and $\tan\varphi'' = t'' = T''/\sqrt{2}$ where Φ and T'' are the deflection angle and the distance between the exit pole boundary and the image, respectively (see fig. 2). In this case the initial condition for the electron is denoted by (δr, δz, $\delta\varphi$ and $\delta\psi$) instead of by (ξ, η, φ and ψ) used in section 2. For deriving this equation, δr is assumed as the second order small quantity and the terms containing δr except that of the first order are neglected. This neglection can be justified since the coefficient of δr cannot vanish, and since, as we can see in section 6, in case of the optimum condition, all the terms involved in W_0 should be the same order of quantity and since δz, $\delta\varphi$ and $\delta\psi$ can be regarded as the first order of small quantity.

Now, let us look for the focusing conditions. The third term of eq. (5) can be vanished, no

matter how φ'' may be, if φ satisfied the condition

$$2\cos\varphi + 1 = 0\,, \tag{7}$$

which means that $\varphi = \frac{2}{3}\pi$. Introducing this value into the coefficient of the last term, we get the following condition for vanishing this coefficient:

$$M^2 + M - \tfrac{1}{2} = 0\,. \tag{8}$$

From eq. (6), we get

$$\tan\varphi'' = 1 \tag{9}$$

that is,

$$\varphi'' = \tfrac{1}{4}\pi\,.$$

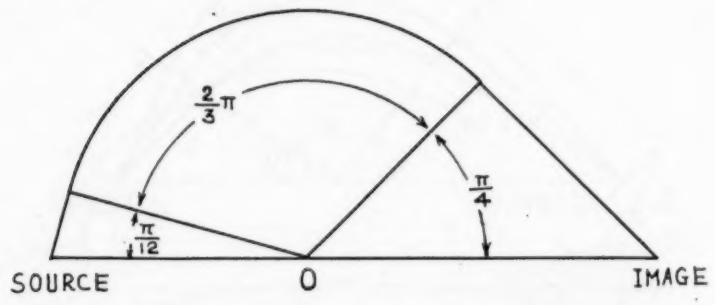

Fig. 3. New sector type double focusing setting with $\alpha = \frac{1}{2}$ and $\beta = \frac{1}{4}$.

Therefore the configuration of the generalized Barber's law becomes a very simple form as presented in fig. 3. And in this case, eq. (5) is given by

$$\delta r' = -\frac{1+\sqrt{3}}{2}\delta r - \frac{2\sqrt{3}+3}{8}\delta z^2 - \frac{3+\sqrt{3}}{2(2+\sqrt{3})}\delta\psi^2\,. \tag{10}$$

Then, the line width w_0 becomes

$$w_0 = (1+\sqrt{3})\delta r_0 + \frac{2\sqrt{3}+3}{8}\delta z_0^2 + \frac{3+\sqrt{3}}{2(2+\sqrt{3})}\delta\psi_0^2\,. \tag{11}$$

Since the dispersion D is given by the formula[7])

$$D = 2(1 - M) \tag{12}$$

we get following resolution formula corresponding to eq. (2):

$$W_0 = \frac{1}{\sqrt{3}}\delta r_0 + \frac{2+\sqrt{3}}{8(\sqrt{3}+1)}\delta z_0^2 + \varepsilon\delta\varphi_0^2 + \frac{1}{2(2+\sqrt{3})}\delta\psi^2{}_0 \tag{13}$$

where ε is the measure of error of focusing adjustment, either of the magnetic field or of the geometrical setting, and this value should be in general one order smaller than the coefficient of the other terms.

The aberration formulas for $\beta = \frac{3}{8}$ and $\beta = \frac{1}{8}$ are also derived and carefully examined. However, no interesting configuration could be obtained, except for $\beta = \frac{3}{8}$, where the aberration formula can be written as follows;

$$W_0 = \left|\frac{\cos\varphi}{(1-\cos\varphi)}\right|\delta r_0 + \left|\frac{\cos\varphi}{8}\right|\delta Z_0^2 + \left|\frac{7\cos^2\varphi + 7\cos\varphi + 4}{12\cos^2\varphi}\right|\delta\varphi_0^2 + \left|\frac{1+\cos\varphi}{4\cos\varphi}\right|\delta\psi_0^2 \tag{14}$$

if the condition

$$\varphi'' = 0$$

is satisfied.

For the INS sector type double focusing spectrometer which has the spectrometer configuration of $\alpha = \frac{1}{2}$, $\beta = \frac{1}{4}$,

$$\varphi = \pi/\sqrt{2} \qquad (\text{i.e., } \Phi = \pi) \quad \text{and} \quad \varphi'' = 0\,,$$

the resolution formula becomes:

$$W_0 = 0.38\,\delta r_0 + 0.133\,\delta z_0^2 + 0.021\,\delta\varphi_0^2 + 0.35\,\delta\psi_0^2 + 1.12\,\delta z_0\delta\psi_0\,. \tag{15}$$

The resolution formula for the same configuration but $\beta = \frac{3}{8}$ can be calculated from eq. (14) and given by

$$W_0 = 0.38\,\delta r_0 + 0.076\,\delta z_0^2 + 0.79\,\delta\varphi_0^2 + 0.192\,\delta\psi_0^2\,. \tag{16}$$

In all cases treated in this section, the luminosity is expressed by the following equation;

$$L = \frac{4}{\pi}\delta r_0\delta z_0\delta\varphi_0\delta\psi_0\,. \tag{17}$$

4. Resolution and Luminosity of $\pi\sqrt{2}$ Double Focusing Spectrometer

According to the ref.[6]), the general resolution formula in this case can be written as follows;

$$W_0 = \tfrac{1}{2}\delta r_0 + \left|\frac{4\beta-3}{12}\right|\delta z_0^2 + \left|\frac{1-8\beta}{6}\right|\delta\varphi_0^2 + \left|\frac{8\beta-3}{6}\right|\delta\psi_0^2\,. \tag{18}$$

Therefore the resolution of the following 4 cases is given by:

for $\beta = \frac{1}{8}$,

$$W_0 = \tfrac{1}{2}\delta r_0 + \tfrac{5}{24}\delta z_0^2 + \varepsilon\delta\varphi_0^2 + \tfrac{1}{3}\delta\psi_0^2 , \tag{19}$$

for $\beta = \frac{3}{8}$,

$$W_0 = \tfrac{1}{2}\delta r_0 + \tfrac{1}{8}\delta z_0^2 + \tfrac{1}{3}\delta\varphi_0^2 + \varepsilon\delta\psi_0^2 , \tag{20}$$

for $\beta = \frac{3}{4}$,

$$W_0 = \tfrac{1}{2}\delta r_0 + \varepsilon\delta z_0^2 + \tfrac{5}{6}\delta\varphi_0^2 + \tfrac{1}{2}\delta\psi_0^2 , \tag{21}$$

for $\beta = \frac{1}{4}$,

$$W_0 = \tfrac{1}{2}\delta r_0 + \tfrac{1}{8}\delta z_0^2 + \tfrac{1}{8}\delta\varphi_0^2 + \tfrac{1}{8}\delta\psi_0^2 . \tag{22}$$

In the last case, all the electrons, of which the direction $(\delta\varphi, \delta\psi)$ satisfies the condition of

$$\delta\varphi^2 + \delta\psi^2 = \delta\chi^2 \tag{23}$$

have the same aberration. Therefore, if we set a defining baffle which satisfies the condition of $\delta\varphi_0^2 + \delta\psi_0^2 = \delta\chi_0^2$, eq. (22) can be rewritten by:

$$W_0 = \tfrac{1}{2}\delta r_0 + \tfrac{1}{8}\delta z_0^2 + \tfrac{1}{8}\delta\chi_0^2 . \tag{24}$$

The meaning of this baffle is to choose a conical electron bundle. We call this special baffle as circular defining baffle. As we shall see in section 6, the use of the circular defining baffle can improve the spectrometer properties largely. Of course, this argument can be applied also to the case of eq. (21) where we have to use an elliptical defining baffle.

The luminosity in the cases of eqs. (19), (20), (21) and (22) has the same formula:

$$L = \frac{4}{\pi}\delta r_0\delta z_0\delta\varphi_0\delta\psi_0 \tag{25}$$

and in the case of eq. (23), it becomes

$$L = \delta r_0\delta z_0\delta\varphi_0\delta\psi_0 . \tag{26}$$

5. Semicircular Spectrometer and Lens Type Spectrometer

5.1. SEMICIRCULAR SPECTROMETER

In this spectrometer the magnetic field is characterized by $\alpha = 0$, corresponding to radial focusing after π and no axial focusing.

The resolution formula is given[5]) by

$$W_0 = \delta r_0 + |\beta|\,\delta z_0^2 + \left|\frac{3+4\beta}{6}\right|\delta\varphi_0^2 + \left|\frac{1+(\pi^2-4)\beta}{2}\right|\delta\psi_0^2 + |2\pi\beta|\,\delta z_0\delta\psi_0 . \tag{27}$$

Putting β equal to zero, we have the ordinary homogeneous spectrometer and find the formula for W_0;

$$W_0 = \delta r_0 + \tfrac{1}{2}\delta\varphi_0^2 + \tfrac{1}{2}\delta\psi_0^2 . \tag{28}$$

In this case the effect of δz can be automatically included in the ψ term in connection of the following condition

$$2\,\delta z_0 = \pi\delta\psi_0 . \tag{29}$$

Since the solid angle Ω is $(1/2\pi)\,\delta\varphi_0\,\delta\psi_0$, the luminosity can be given by

$$L = 4\,\delta r_0\delta z_0\frac{1}{2\pi}\delta\varphi_0\delta\psi_0 = \delta r_0\delta\varphi_0\delta\psi_0^2 . \tag{30}$$

In this case it seems worth noting that the spectrometer properties can be improved by means of a circular defining baffle instead of a ordinary rectangular baffle. It is the same reason as that in case of $\alpha = \frac{1}{2}$ and $\beta = \frac{1}{4}$ mentioned at the end of the preceeding section.

The case of $\beta = -\frac{3}{4}$ was considered by Beiduk and Konopinski[11]) in order to eliminate the radial spherical aberration. Since the dispersion remains unchanged, we obtain

$$W_0 = \delta r_0 + 0.75\,\delta z_0^2 + \varepsilon\delta\varphi_0^2 + 2.70\,\delta\psi_0^2 + 4.7\,\delta z_0\delta\psi_0 . \tag{31}$$

The luminosity in this case can be expressed by the same formula as eq. (25).

5.2. LENS TYPE SPECTROMETER

In general the aberration formula is complicated. In the present article only the simple solenoid spectrometer in which the electrons start in the direction of 45 degree to the symmetrical axis was treated. According to ref. [2]), we have

$$W_0 = 1.12\,\delta r_0 + 2.5\,\delta\varphi_0^2 \tag{32}$$

and

$$L = \frac{\pi}{\sqrt{2}}\delta r_0^2\delta\varphi_0 . \tag{33}$$

The results on W_0 and L obtained in section 3, 4 and 5 are summerized in table 1.

[11]) F. M. Beiduk and F. J. Konopinski, Rev. Sci. Instr. **19** (1948) 594.

TABLE 1
Dependence of initial conditions on the resolution and the luminosity.

Setting	W_0					L
α β Φ	δr_0	δz_0	$\delta\varphi_0$	$\delta\psi_0$	$\delta z_0\,\delta\psi_0$	$\delta r_0\,\delta z_0\,\delta\varphi_0\,\delta\psi_0$
	$a(n_1)$	$b(n_2)$	$\alpha(n_3)$	$\beta(n_4)$	$\gamma(1,1)$	$l(m_1m_2m_3m_4)$
$\frac{1}{2}$ $\frac{1}{4}$ $\frac{2}{3}\sqrt{2}\pi$	$\frac{1}{\sqrt{3}}$ (1)	$\frac{2+\sqrt{3}}{8(1+\sqrt{3})}$ (2)	ε (2)	$\frac{1}{2(2+\sqrt{3})}$ (2)		$\frac{4}{\pi}$ (1, 1, 1, 1)
$\frac{1}{2}$ $\frac{1}{4}$ π	0.38 (1)	0.133 (2)	0.021 (2)	0.35 (2)	1.12 (1,1)	$\frac{4}{\pi}$ (1, 1, 1, 1)
$\frac{1}{2}$ $\frac{3}{8}$ π	0.38 (1)	0.076 (2)	0.53 (2)	0.16 (2)		$\frac{4}{\pi}$ (1, 1, 1, 1)
$\frac{1}{2}$ $\frac{1}{8}$ $\pi\sqrt{2}$	$\frac{1}{2}$ (1)	$\frac{5}{24}$ (2)	ε (2)	$\frac{1}{3}$ (2)		$\frac{4}{\pi}$ (1, 1, 1, 1)
$\frac{1}{2}$ $\frac{3}{8}$ $\pi\sqrt{2}$	$\frac{1}{2}$ (1)	$\frac{1}{8}$ (2)	$\frac{1}{3}$ (2)	ε (2)		$\frac{4}{\pi}$ (1, 1, 1, 1)
$\frac{1}{2}$ $\frac{3}{4}$ $\pi\sqrt{2}$	$\frac{1}{2}$ (1)	ε (2)	$\frac{5}{6}$ (2)	$\frac{1}{2}$ (2)		$\frac{4}{\pi}$ (1, 1, 1, 1)
$\frac{1}{2}$ $\frac{1}{4}$ $\pi\sqrt{2}$	$\frac{1}{2}$ (1)	$\frac{1}{6}$ (2)	$\frac{1}{6}$ (2)	$\frac{1}{6}$ (2)		$\frac{4}{\pi}$ (1, 1, 1, 1)
$\frac{1}{2}$ $\frac{1}{4}$ $\pi\sqrt{2}$ circular baffle	$\frac{1}{2}$ (1)	$\frac{1}{6}$ (2)	$\frac{1}{6}$ (2)			1 (1, 1, 1, 1)
0 0 π	1 (1)		$\frac{1}{2}$ (2)	$\frac{1}{2}$ (2)		1 (1, 0, 1, 2)
$0-\frac{3}{4}$ π	1 (1)	0.75 (2)	ε (2)	2.70 (2)	4.7 (1,1)	$\frac{4}{\pi}$ (1, 1, 1, 1)
lens type	1.12 (1)		2.5 (2)			$\frac{\pi}{\sqrt{2}}$ (2, 0, 1, 0)

6. Theoretical Formulation for the Optimum Conditions

The out-line of the problem setting was already described in section 2. Since the optimum conditions are those for achieving the greatest possible luminosity L for a given resolution W_0, these conditions can be expressed mathematically, by using Lagrange's method of undetermined coefficient, as follows:

$$\frac{\partial U}{\partial \delta r_0}=0\,,\quad \frac{\partial U}{\partial \delta z_0}=0\,,\quad \frac{\partial U}{\partial \delta\varphi_0}=0\,,\quad \frac{\partial U}{\partial \delta\psi_0}=0 \tag{34}$$

where a new function

$$U=W_0+\lambda L \tag{35}$$

is introduced. As seen in table 1, W and L can be written in general as follows:

$$W_0=a\delta r_0{}^{n_1}+b\delta z_0{}^{n_2}+\alpha\delta\varphi_0{}^{n_3}+\beta\delta\psi_0{}^{n_4}+\gamma\delta z_0\delta\psi_0\,. \tag{36}$$

and

$$L=l\delta r_0{}^{m_1}\delta z_0{}^{m_2}\delta\varphi_0{}^{m_3}\delta\psi_0{}^{m_4}\,. \tag{37}$$

Then, the conditions of eq. (34) yield the optimum values of δr_0, δz_0, $\delta\varphi_0$ and $\delta\psi_0$ in case of $\gamma=0$. They are:

TABLE 2

Optimum dimensions and maximum luminosity

Setting α	β	Φ	δr_0	δz_0	$\delta\varphi_0$	$\delta\psi_0$	L
$\frac{1}{2}$	$\frac{1}{4}$	$\frac{2\sqrt{2}}{3}\pi$	$3.46\left(\frac{W_0}{5}\right)$	$2.42\left(\frac{W_0}{5}\right)^{\frac{1}{2}}$	$\left(\frac{1}{\varepsilon}\right)^{\frac{1}{2}}\left(\frac{W_0}{5}\right)^{\frac{1}{2}}$	$2.74\left(\frac{W_0}{5}\right)^{\frac{1}{2}}$	$29.2\left(\frac{1}{\varepsilon}\right)^{\frac{1}{2}}\left(\frac{W_0}{5}\right)^{\frac{5}{2}}$
$\frac{1}{2}$	$\frac{1}{4}$	π	$5.26\left(\frac{W_0}{5}\right)$	$1.44\left(\frac{W_0}{5}\right)^{\frac{1}{2}}$	$6.99\left(\frac{W_0}{5}\right)^{\frac{1}{2}}$	$0.89\left(\frac{W_0}{5}\right)^{\frac{1}{2}}$	$59.9\left(\frac{W_0}{5}\right)^{\frac{5}{2}}$
$\frac{1}{2}$	$\frac{3}{8}$	π	$5.26\left(\frac{W_0}{5}\right)$	$3.62\left(\frac{W_0}{5}\right)^{\frac{1}{2}}$	$1.41\left(\frac{W_0}{5}\right)^{\frac{1}{2}}$	$2.50\left(\frac{W_0}{5}\right)^{\frac{1}{2}}$	$85.4\left(\frac{W_0}{5}\right)^{\frac{5}{2}}$
$\frac{1}{2}$	$\frac{1}{8}$	$\pi\sqrt{2}$	$4\left(\frac{W_0}{5}\right)$	$2.19\left(\frac{W_0}{5}\right)^{\frac{1}{2}}$	$\left(\frac{1}{\varepsilon}\right)^{\frac{1}{2}}\left(\frac{W_0}{5}\right)^{\frac{1}{2}}$	$1.73\left(\frac{W_0}{5}\right)^{\frac{1}{2}}$	$19.3\left(\frac{1}{\varepsilon}\right)^{\frac{1}{2}}\left(\frac{W_0}{5}\right)^{\frac{5}{2}}$
$\frac{1}{2}$	$\frac{3}{8}$	$\pi\sqrt{2}$	$4\left(\frac{W_0}{5}\right)$	$2.83\left(\frac{W_0}{5}\right)^{\frac{1}{2}}$	$1.73\left(\frac{W_0}{5}\right)^{\frac{1}{2}}$	$\left(\frac{1}{\varepsilon}\right)^{\frac{1}{2}}\left(\frac{W_0}{5}\right)^{\frac{1}{2}}$	$25.0\left(\frac{1}{\varepsilon}\right)^{\frac{1}{2}}\left(\frac{W_0}{5}\right)^{\frac{5}{2}}$
$\frac{1}{2}$	$\frac{3}{4}$	$\pi\sqrt{2}$	$4\left(\frac{W_0}{5}\right)$	$\left(\frac{1}{\varepsilon}\right)^{\frac{1}{2}}\left(\frac{W_0}{5}\right)^{\frac{1}{2}}$	$1.10\left(\frac{W_0}{5}\right)^{\frac{1}{2}}$	$1.41\left(\frac{W_0}{5}\right)^{\frac{1}{2}}$	$10.6\left(\frac{1}{\varepsilon}\right)^{\frac{1}{2}}\left(\frac{W_0}{5}\right)^{\frac{5}{2}}$
$\frac{1}{2}$	$\frac{1}{4}$	$\pi\sqrt{2}$	$4\left(\frac{W_0}{5}\right)$	$2.45\left(\frac{W_0}{5}\right)^{\frac{1}{2}}$	$2.45\left(\frac{W_0}{5}\right)^{\frac{1}{2}}$	$2.45\left(\frac{W_0}{5}\right)^{\frac{1}{2}}$	$74.6\left(\frac{W_0}{5}\right)^{\frac{5}{2}}$
$\frac{1}{2}$	$\frac{1}{4}$	$\pi\sqrt{2}$ circular baffle	$4\left(\frac{W_0}{5}\right)$	$2.45\left(\frac{W_0}{5}\right)^{\frac{1}{2}}$	$3.46\left(\frac{W_0}{5}\right)^{\frac{1}{2}}$		$117.3\left(\frac{W_0}{5}\right)^{\frac{5}{2}}$
0	0	π	$2\left(\frac{W_0}{5}\right)$	$3.14\left(\frac{W_0}{5}\right)^{\frac{1}{2}}$	$1.41\left(\frac{W_0}{5}\right)^{\frac{1}{2}}$	$2\left(\frac{W_0}{5}\right)^{\frac{1}{2}}$	$11.3\left(\frac{W_0}{5}\right)^{\frac{5}{2}}$
0	$-\frac{3}{4}$	π	$2\left(\frac{W_0}{5}\right)$	$0.71\left(\frac{W_0}{5}\right)^{\frac{1}{2}}$	$\left(\frac{1}{\varepsilon}\right)^{\frac{1}{2}}\left(\frac{W_0}{5}\right)^{\frac{1}{2}}$	$0.37\left(\frac{W_0}{5}\right)^{\frac{1}{2}}$	$0.675\left(\frac{1}{\varepsilon}\right)^{\frac{1}{2}}\left(\frac{W_0}{5}\right)^{\frac{5}{2}}$
Lens type			$3.57\left(\frac{W_0}{5}\right)$		$0.63\left(\frac{W_0}{5}\right)^{\frac{1}{2}}$		$17.9\left(\frac{W_0}{5}\right)^{\frac{5}{2}}$

$$\delta r_0 = \left\{\frac{1}{a}\frac{m_1}{n_1}\frac{W_0}{N}\right\}^{1/n_1}, \tag{38}$$

$$\delta z_0 = \left\{\frac{1}{b}\frac{m_2}{n_2}\frac{W_0}{N}\right\}^{1/n_2}, \tag{39}$$

$$\delta\varphi_0 = \left\{\frac{1}{\alpha}\frac{m_3}{n_3}\frac{W_0}{N}\right\}^{1/n_3}, \tag{40}$$

$$\delta\varphi_0 = \left\{\frac{1}{\beta}\frac{m_4}{n_4}\frac{W_0}{N}\right\}^{1/n_4}, \tag{41}$$

where

$$N = \frac{m_1}{n_1} + \frac{m_2}{n_2} + \frac{m_3}{n_3} + \frac{m_4}{n_4}.$$

The luminosity for this case can be expressed by:

$$L = \left(\frac{1}{a}\frac{m_1}{n_1}\right)^{m_1/n_1}\left(\frac{1}{b}\frac{m_2}{n_2}\right)^{m_2/n_2}\left(\frac{1}{\alpha}\frac{m_3}{n_3}\right)^{m_3/n_3}\times \times\left(\frac{1}{\beta}\frac{m_4}{n_4}\right)^{m_4/n_4}\left(\frac{W_0}{N}\right)^{N}. \tag{42}$$

In case of $\gamma \neq 0$, the derivation of the optimum values is rather complicated. However, in the cases appeared in table 1, namely, in the case of $m_2 = m_4 = 1$ and $n_2 = n_4 = 2$, we have the following simple formulas for the optimum conditions:

$$\delta r_0 = \frac{2}{a}\frac{W_0}{5} \ , \tag{38'}$$

$$\delta z_0 = \left(\frac{\beta}{b}\right)^{\frac{1}{2}} \frac{1}{\{(b\beta)^{\frac{1}{2}} + \frac{1}{2}\gamma\}^{\frac{1}{2}}} \left(\frac{W_0}{5}\right)^{\frac{1}{2}} , \tag{39'}$$

$$\delta\varphi_0 = \left(\frac{1}{\alpha}\right)^{\frac{1}{2}} \left(\frac{W_0}{5}\right)^{\frac{1}{2}} , \tag{40'}$$

$$\delta\psi_0 = \left(\frac{b}{\beta}\right)^{\frac{1}{2}} \frac{1}{\{(b\beta)^{\frac{1}{2}} + \frac{1}{2}\gamma\}^{\frac{1}{2}}} \left(\frac{W_0}{5}\right)^{\frac{1}{2}} , \tag{41'}$$

and the luminosity is

$$L = l\frac{2}{a}\left(\frac{1}{\alpha}\right)^{\frac{1}{2}} \frac{1}{\{(b\beta)^{\frac{1}{2}} + \frac{1}{2}\gamma\}} \left(\frac{W_0}{5}\right)^{\frac{5}{2}} . \tag{42'}$$

This formula demonstrates clearly the effect of γ-term on the maximum luminosity.

Introducing the values a, b, α, β and l into eqs. (38), (39), (40), (41), (42), (38'), (39'), (40'), (41') and (42'), the optimum dimensions for the source and the solid angle and the maximum luminosity can be expressed as a function of W_0. The results are tabulated in table 2.

7. Optimum Condition for the Detector Slit Width

In the preceding sections we assumed the detector to have a slit of a very narrow width df and of very long height along Z coordinate.

The intensity distribution curve taken by this detector corresponds to the electron density curve along the image width. This curve can be calculated easily[3]), and the area under it is equal to L. As, in reality, we use a detector with finite slit width f in a spectrometer, the effective image width will be enlarged to be $w_0 + f$ and the intensity distribution curve taken by this detector can be obtained by integrating the density distribution curve in the domain f along the image width. Therefore, the problem should be presented as follows; the peak value $\mathscr{W}$ of the intensity distribution curve is as large as possible at the given effective resolution $\mathscr{W}_0$. Since $\mathscr{W}_0$ and $\mathscr{L}$ can be expressed by the following formulas:

$$\mathscr{W}_0 = W_0 + \tfrac{1}{2}af = W_0' + a\delta r_0 + \frac{1}{2}\frac{a}{|M|}f \tag{43}$$

and

$$\mathscr{L} = \varkappa L = \varkappa \delta r_0{}^{m_1} L' , \tag{44}$$

the optimum condition for the slit width can be derived from the following formulas:

$$\frac{\partial U'}{\partial f} = \frac{1}{2}\frac{a}{|M|} + \lambda\frac{\partial \varkappa}{\partial f}\delta r_0{}^{m_1} L' = 0 , \tag{45}$$

$$\frac{\partial U'}{\partial \delta r_0} = a + \lambda m_1 \varkappa \delta r_0{}^{m_1-1} L' = 0 , \tag{46}$$

where

$$U' = \mathscr{W}_0 + \lambda\mathscr{L} . \tag{47}$$

Hence, we get

$$2|M|\delta r_0 \frac{\partial \varkappa}{\partial f} = m_1 \varkappa . \tag{48}$$

Since $\varkappa$ is a function of f, depending upon the density distribution curve, and since $\varkappa$ is equal to zero in case of $f = 0$, $\varkappa$ can be expressed, as the second order approximation, by

$$\varkappa = C_1 f + C_2 f^2 . \tag{49}$$

Introducing eq. (49) into eq. (48), we have

$$f = \frac{2|M|\delta r_0}{m_1}\left(1 + \frac{C_2}{C_1}\frac{2|M|\delta r_0}{m_1}\right) . \tag{50}$$

In practical purpose, it is sufficient to consider the f value up to the first order, that is,

$$f \approx \frac{2|M|\delta r_0}{m_1} . \tag{51}$$

Since m_1 is equal to 1 for all spectrometers except the lens type spectrometer and since $\varkappa$ is about same order of figure in every case, we might discuss the usefulness of the spectrometer by the luminosity L instead of $\mathscr{L}$.

8. Discussion

Although it is not exactly the case, the value L numerically derived in section 6 in function of W_0 can be considered as a measure of the usefulness of the spectrometers, as it has been proved in the preceding section. Since we can reduce the value of ε to the order of 10^{-2}, let us substitute this value for ε in the formula of L.

Now, it is revealed that the new setting of the sector type double focusing spectrometer has a large L value and it is even larger than that in the standard $\pi\sqrt{2}$ spectrometer. Since the field distribution with $\beta = \frac{1}{4}$ can be achieved easily by using a cone type pole face[12]), and since the

[12]) E. Arbman and N. Svartholm, Arkiv. f. Fysik **10** (1956) 1.

source and the detector could be put outside the magnetic field in this type of spectrometer, this setting should be one of the powerful tool not only for the nuclear spectroscopy but also for the charged particle detector in the nuclear reaction experiment.

The INS setting has also been found to have a rather good luminosity which is comparable with that in the $\pi\sqrt{2}$ spectrometer with $\beta = \frac{1}{4}$. Since, for this setting, we can use a long arm between the source and the magnetic boundary, a spectrometer, using the INS setting, should be also one of the important spectrometers in near future, especially for the purpose of electron angular correlation measurement.

So far as the $\pi\sqrt{2}$ spectrometer is concerned, both of the spectrometers with $\beta = \frac{3}{8}$ and $\beta = \frac{1}{8}$ have about the same L value which is nearly three times larger than that of the spectrometers with $\beta = \frac{3}{4}$ and $\beta = \frac{1}{4}$. In the last spectrometer ($\beta = \frac{1}{4}$), it is worth noting that we can improve the L value by $\frac{1}{2}\pi$ times by means of a circular defining baffle.

In the present treatment, the lens type spectrometer has a luminosity 1.5 times larger than that of semicircular spectrometer. The reason of this lies upon the fact that the density distribution curve for the lens type has a trapezoid form while that for the semicircular spectrometer has a triangular form[3]). If the slit width of the detector is taken into consideration, L of semicircular spectrometer can be about twice larger than that of the lens type spectrometer, because, according to eq. (51), the slit width for the former spectrometer can be taken twice wider than that in the latter one. Therefore, we have about the same $\mathscr{L}$ value in both of the spectrometers. This conclusion is consistent with the result obtained in ref. [3]).

It is rather suprising that the Konopinski type spectrometer has a rather small L value which is comparable to that of the ordinary semicircular spectrometer. This is partly due to the large γ value which appears in the resolution formula (eq. (31)).

The author wishes to thank Messrs. H. Ikegami and T. Yamazaki for the helpful discussions.

NUCLEAR INSTRUMENTS AND METHODS **8** (1960) 70–72; NORTH-HOLLAND PUBLISHING CO.

CIRCUIT ALLONGEUR D'IMPULSIONS RAPIDES

A. SARAZIN, J. SAMUELI, G. DUCROS et P. RAIMBAULT

Institut d'Etudes Nucléaires, Alger

Reçu le 25 Mars 1960

A pulse lengthener is described meant to be used together with a multichannel analyzer, in order to study the amplitude of pulses in the nanosecond range. The circuit is linear from 0.8 to 14 volts and its recovery time is 0.5 μs.

Les discriminateurs et les analyseurs d'amplitude sont des appareils très employés dans les expériences de physique nucléaire. Or la détermination de l'amplitude maximum des impulsions électriques fournies par les détecteurs actuels (détecteurs à scintillateurs plastiques, compteurs Čerenkov) est relativement difficile, à cause de la rapidité de ces impulsions.

On demande en effet aux circuits de mesure d'amplitudes de donner une indication de l'amplitude réelle, c'est-à-dire non intégrée, de l'impulsion et ceci indépendamment, si possible, de sa durée et de son temps de montée. Les circuits discriminateurs rapides existant actuellement ne répondent qu'imparfaitement à ce problème, cependant que les analyseurs multicanaux ne peuvent que donner une indication de l'amplitude intégrée de signaux rapides.

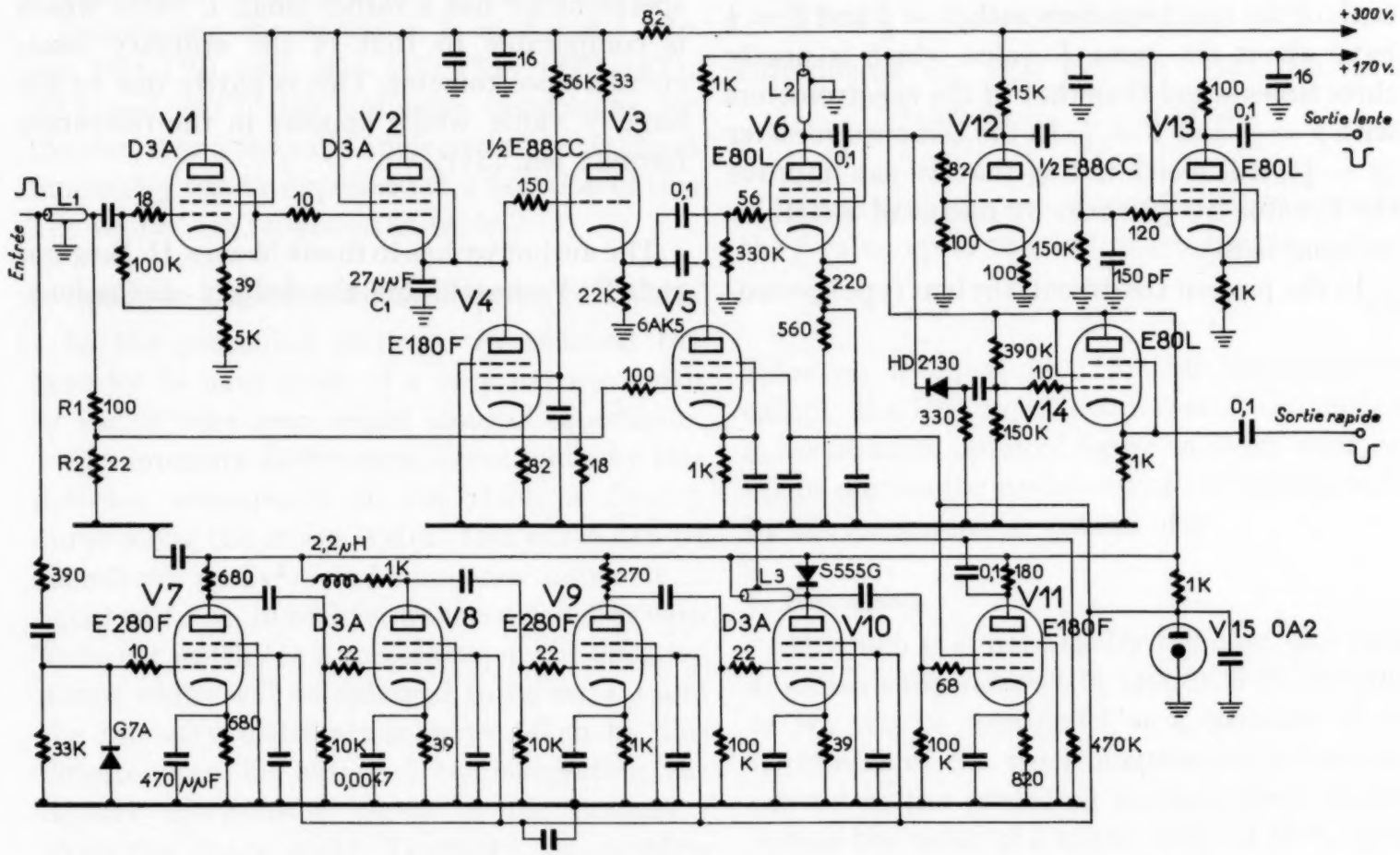

Fig. 1. Schéma général du circuit élargisseur. Toutes les capacités sont des 0.01 microfarad sauf indications contraires; L_1: RG 63 U, 4 m. L_2: RG 114 U, 12 m. L_3: RG 114 U, 12 m.

Une solution à ce problème consiste à réaliser un allongeur d'impulsions, c'est-à-dire un circuit convertissant des signaux rapides en impulsions longues, d'amplitude proportionnelle à l'amplitude cherchée. L'impulsion ainsi obtenue peut être alors envoyée sur un discriminateur classique ou un analyseur multicanaux.

Le circuit que nous décrivons ici est conçu pour recevoir des impulsions de largeur supérieure à 2×10^{-9} seconde, d'amplitude comprise entre 0.8 et 14 volts et de temps de montée inférieur à 1.5×10^{-8} seconde.

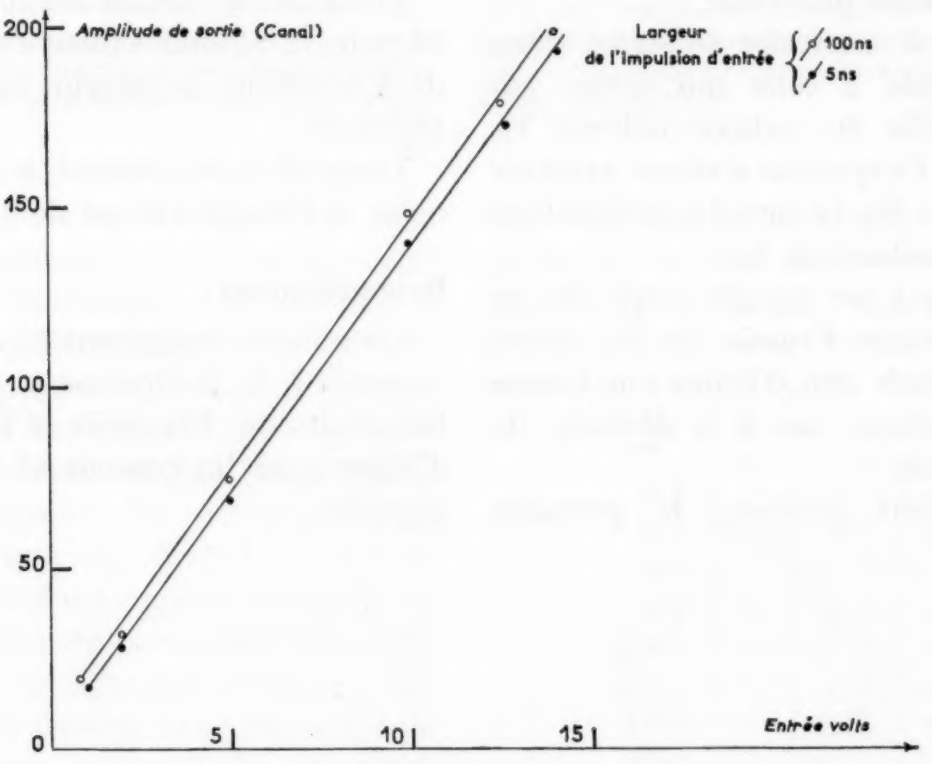

Fig. 2. Réponse du circuit.

PRINCIPE

Le principe des allongeurs d'impulsions est le suivant: on charge un condensateur à l'amplitude maximum de l'impulsion. Après le passage de l'impulsion le condensateur reste chargé à la même valeur jusqu'à ce qu'on le décharge. De nombreux circuits destinés à des impulsions d'entrée dont la durée est de l'ordre de la microseconde ont été réalisés ces dernières années[1,2]).

[1]) M. A. Meyer, Nuclear Instruments **1** (1957) 62.
[2]) R. W. Schumann, J. P. MacMahon, Rev. Sci. Inst. **27** (1956) 675.

Détail des circuits. Le schéma général est donné figure 1. L'élargisseur proprement dit, constitué par les tubes V_1, V_2, V_3 et V_4, est prévu pour des impulsions positives. L'impédance d'entrée est de 125 ohms.

Les tubes V_1 et V_2 chargent le condensateur C_1 à l'amplitude maximum du signal d'entrée. Le tube V_4 qui contrôle la charge de C_1 et qui est normalement débloqué, est à cet effet amené au cut-off par une impulsion provenant d'un circuit de mise en forme déclenché par le signal d'entrée.

L'emploi, pour V_2, du tube D3A Siemens de pente 35 mA/V permet d'obtenir une faible constante de temps de charge de C_1.

La ligne à retard L_1 permet de bloquer V_4 quelques millimicrosecondes avant l'arrivée de l'impulsion sur la grille de V_2.

Le circuit de mise en forme fournissant le signal envoyé sur la grille de V_4 utilise les tubes V_7, V_8, V_9, V_{10} et V_{11}. Les trois premiers tubes servent à amplifier et élargir les impulsions d'entrée très courtes. Dans le cas de signaux relativement larges, les faibles valeurs des capacités de découplage de cathode des divers tubes introduisent une contre-réaction sélective qui

limite la largeur des signaux dès le second tube.

L'ensemble V_7, V_8 et V_9, dont V_8 est monté en limiteur, permet donc une première standardisation des signaux avant d'attaquer V_{10} dont la charge anodique est une ligne à retard d'impédance 185 ohms. La longueur de cette ligne définit la durée de l'impulsion élargie, soit 120 ns environ. L'impulsion délivrée par la mise en forme est indépendante de la forme du signal d'entrée lorsque ses caractéristiques répondent aux conditions définies plus haut.

Le tube V_5 sert à soustraire du signal élargi une impulsion égale à celle qui arrive par capacité sur la grille du cathode follower V_3. Pour cela V_5 reçoit l'impulsion d'entrée atténuée par le diviseur R_1 — R_2. Le signal négatif obtenu est envoyé sur la cathode de V_3.

Le signal résultant est ensuite coupé par un cable, à 100 ns, dans l'anode de V_6. Cette opération est effectuée afin d'éviter une longue descente de l'impulsion, due à la décharge de C_1 qui est indésirable.

Deux sorties sont prévues: la première fournit des impulsions négatives rectangulaires allongées à 100 ns. La sortie s'effectue par le cathode follower V_{14}.

La seconde donne des impulsions lentes, intégrées par V_{12}. Le tube V_{13} sert d'adapteur d'impédance. Cette sortie donne des impulsions négatives utilisables avec des sélecteurs multicanaux à mémoire magnétique.

Les caractéristiques essentielles du circuit sont les suivantes:

Linéarité: le circuit est linéaire entre 0.8 et 14 volts. L'affaiblissement entre des impulsions de 5 et 100 ns de largeur, est inférieur à 1 dB (figure 2).

Temps de recouvrement: le temps de recouvrement de l'élargisseur est de 0.5 μs.

Remerciements

Les auteurs souhaitent exprimer leurs remerciements à M. le Professeur A. Blanc-Lapierre, Directeur de l'Institut d'Etudes Nucléaires d'Alger pour les conseils et l'aide qu'il leur a apportés.

NUCLEAR INSTRUMENTS AND METHODS 8 (1960) 73–75; NORTH-HOLLAND PUBLISHING CO.

THE EFFECT OF GAMMA-BACKGROUND ON THE BF_3 PROPORTIONAL COUNTER

J. CSIKAI and M. BUCZKÓ

ATOMKI *Debrecen, Hungary*

Received 1 March 1960

The integral amplitude distribution of the BF_3 proportional counter was found to be changing by the effect of a strong gamma background. In the function of electronic amplification, the distortion of amplitude distribution was investigated with counters of different cathodes. The distortion of amplitude distribution due to the effect of gamma radiation may be explained by the positive space charge developing around the anode.

For the detection of slow neutrons, the BF_3 proportional counter is very widely used on account of the favourable cross-section of $B^{10}(n,\alpha)Li^7$ reaction. The neutrons often have to be detected in the presence of intensive gamma radiation, wherefore the effect of gamma background on the operation of BF_3 proportional counter was investigated. The investigation is very important from the point of view of determining the absolute neutron intensity as well as of such relative measurements where the intensity of gamma background varies (e.g. the measurement for the slowing down and diffusion lengths of neutrons with Ra–Be or (γ,n) sources).

The investigations were carried out by two types of counters ("a", "b"). The walls of the counters were made from soda glass of 0.5 mm thickness. The sensitive volume of the "a" type counter was a 160 mm long cylinder 17 mm in diameter; the anode was tungsten 0.1 mm in diameter; a thin layer of graphite upon the inside surface of the glass wall served the purpose of cathode; the pressure of BF_3 gas was 260 mm Hg. The sensitive volume of "b" type counter was a 30 mm long cylinder 9 mm in diameter; the anode was tungsten of 0.1 mm in diameter; a layer of graphite upon the outer surface of the glass wall served as cathode; the pressure of BF_3 gas was 200 mm Hg. The BF_3 gas was produced by the thermal decomposition of $CaF_2(BF_3)_2$[1]). The electronegative

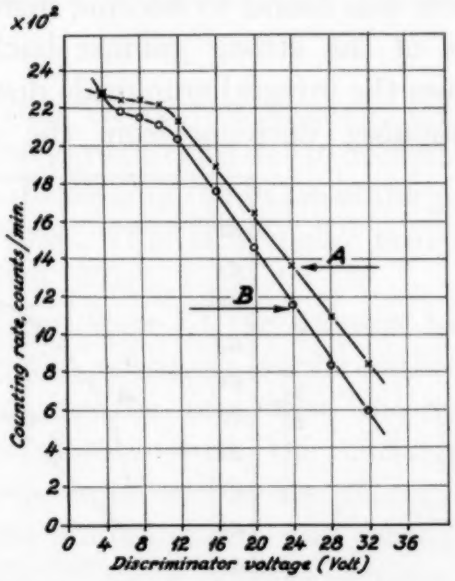

Fig. 1. Integral amplitude distribution of impulses derived from the neutrons: (A) without gamma background, (B) with gamma background.

contamination of the gas—estimated by the length and slope of the plateaux[2])—was not more than that of gas obtained from commercial BF_3 gas by two fractional distillations and thermodiffusion. During the investigations, the BF_3 counter was placed on the surface of a paraffin cylinder of 30 cm height and 25 cm in diameter, inside of which at 3 cm from the surface, there was a 3 curie Po–Be neutron

[1]) A. C. Graves and D. K. Froman, National Nuclear Energy Series, div. V. 3, 47 (McGraw-Hill Book Company, Inc. New-York, 1952).

[2]) A. Milojević, M. Kurepa and S. Ribnikar, Proceedings of the Second International Conference Geneva, 1958. Vol. 14, p. 325. P/493.

source. Co^{60} isotope was made available for gamma source.

When placing a Co^{60} isotope of 4 mc close by an "a" type counter, the integral amplitude

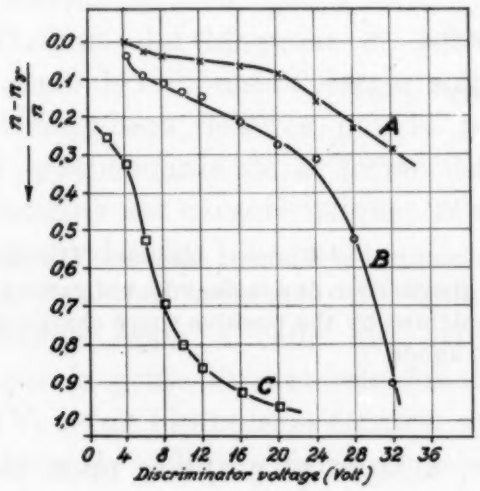

Fig. 2. The effect of gamma background on the operation of counters with different cathodes: (A) internal graphite, (B) internal brass and (C) external graphite.

distribution was found to become distorted by the effect of the strong gamma background. Fig. 1 shows the integral amplitude distribution of the impulses deriving from the neutrons without gamma background (A), and with gamma background (B). The voltage of the counter was 50 V lower than the voltage corresponding to the electron-threshold (V_e) and so the impulses produced by the electrons could not be detected. In case of high gamma intensity, the plateau of integral amplitude distribution disappears completely, in consequence of which the impulses produced by the neutrons and gamma rays cannot be seperated.

Under the same conditions, the distortion of amplitude distribution was examined by using counters of different cathodes. Fig. 2 shows the $(n - n_\gamma)/n$ quantity in the function of the discriminator voltage (where n and n_γ represent the number of impulses from the neutrons without or with gamma background) when internal graphite (A), internal brass (B) and external graphite (C) cathodes were used. As it can be seen in fig. 2, the effect of gamma background is the smallest in the case of an internal graphite cathode.

The distortion of amplitude distribution was investigated also in the function of electronic amplification. At $V_e - 50$ V counter voltage in each single electronic amplification, the n and n_γ values were measured at 10 and 20 V discriminator voltage. In fig. 3, the dependence from electronic amplification of $(n - n_\gamma)/n$ quantities obtained by a "b" type counter is shown when using two gamma sources of different intensities. At 10 (A, C) and 20 (B, D) V discriminator voltage, the A and B curves, were obtained by placing the Co^{60} isotope of 3 mc close by the counter, while C and D curves were produced by placing the Co^{60} isotope of 45 mc at a distance of 1 cm from the counter. As fig. 3 shows, at low electronic amplification, that is, at high gas amplification, the effect of gamma background is quite

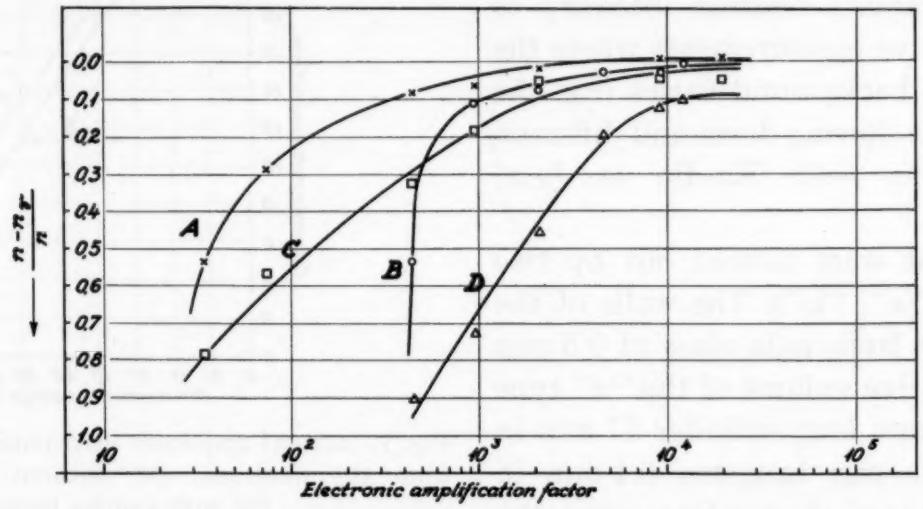

Fig. 3. The effect of gamma background on the amplitude distribution of a "b" type counter, in the case of different electronic amplifications.

significant and decreases to a considerable degree when electronic amplification is increased. For the sake of comparison, in the case of an "a" type counter, too, the $(n - n_\gamma)/n$ quantities were determined as the function of electronic amplification at 10 (C) and 20 (D) V discriminator voltage so that the Co^{60} preparation of 45 mc was placed at a distance of 1 cm from the counter (fig. 4). As it can be seen in figs. 3 and 4, the investigation was made possible by the resolving time of the electronic apparatus.

Around the anode, a positive space charge develops because of electron multiplication. In the case of a given gamma intensity, the greater the value of the gas amplification factor, the greater are the positive space charges. An account of the positive space charges the multiplication of the electrons produced by the alpha particle and recoil nucleus deriving from $B^{10}(n,\alpha)Li^7$ reaction develops in a weaker electric field and thus gas amplification and through it the height of impulses will be

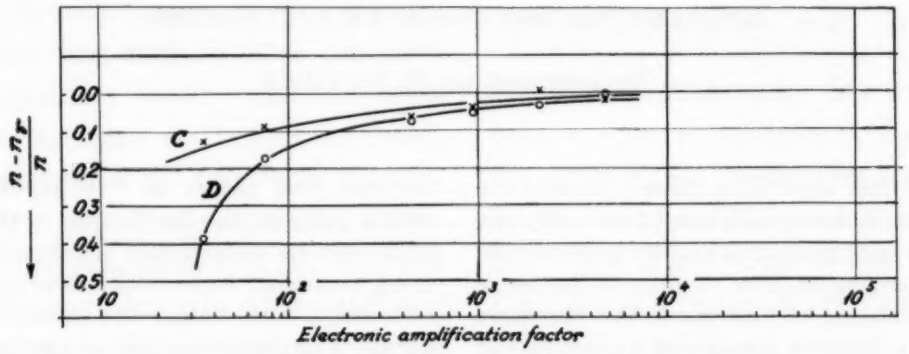

Fig. 4. The effect of gamma background on the amplitude distribution of an "a" type counter, in the case of different electronic amplifications.

The investigation reveals that the effect of gamma background upon the BF_3 counter is not negligible and depends on the cathode, the value of the gas amplification factor, the initial order of magnitude of ionization as well as on the intensity of gamma background. Presumably, these are responsible for the discrepancy of the results of measurements obtained[3,4,5]) in a strong gamma background by a BF_3 proportional counter and by a method insensitive to the gamma background.

The effect of gamma background upon the BF_3 proportional counter may be explained as follows: the great number of electrons produced by intensive gamma radiation multiplies because of gas amplification near the anode. Around the anode, a positive space charge develops because of electron multiplication. In the case of a given gamma intensity, the greater the value of the gas amplification factor, the greater are the positive space charges. An account of the positive space charges the multiplication of the electrons produced by the alpha particle and recoil nucleus deriving from $B^{10}(n,\alpha)Li^7$ reaction develops in a weaker electric field and thus gas amplification and through it the height of impulses will be smaller (fig. 1). In this manner, the effect of gamma background also has to decrease together with the decrease in the value of the gas amplification factor. This is actually proved by the data shown in figs. 3 and 4.

The dependence of the gamma background effect on the substance of the cathode can be explained by the fact that the number of electrons ejected from the cathode by the external radiation and by the photons produced during gas amplification—and through this the magnitude of space charges—change with the substance of the cathode. The greater effect on the counter with external cathode can be explained by its greater resolving time.

We are indebted to Prof. A. Szalay, director of this Institute for making these investigations possible. Thanks are due to Mr. B. Schlenk for having planned and constructed the necessary electronic apparatuses.

[3]) L. Nagy and O. Orient, KFKI Közlemények (Comm. Centr. Res. Inst. Phys., Budapest) **2** (1957) 253.

[4]) K. E. Larsson, Ark. f. Fys. **9** (1955) 293.

[5]) R. Montalbetti, L. Katz and J. Goldemberg, Phys. Rev. **91** (1953) 659.

NUCLEAR INSTRUMENTS AND METHODS 8 (1960) 76–78; NORTH-HOLLAND PUBLISHING CO.

ÜBER DIE BESTIMMUNG DER ZUFÄLLIGEN KOINZIDENZEN IN SCHNELL-LANGSAM-KOINZIDENZ-ANORDNUNGEN

T. MAYER-KUCKUK

Max Planck Institut für Kernphysik, Heidelberg

und

R. NIERHAUS

Kernreaktor Bau- und Betriebs-G.m.b.H., Karlsruhe

Eingegangen am 28. März 1960

In some applications of fast slow coincidence circuits the random coincidence rate is not small compared with the true coincidence rate. In such cases it is usually necessery to correct for random coincidences. The random coincidence rate is considered as consisting of four parts, the first part corresponding to three randomly coincident pulses at the inputs of the slow triple coincidence circuit, the other parts corresponding to the three possibilities of true coincidences between two pulses at two inputs randomly coincident with a pulse on the third input of the slow circuit. The four parts can be determined separately either by calculation using measured coincidence resolving times,or by counting with delay lines before the inputs of the slow coincidence circuit. The determination of random coincidences only by using a delaying cable before one input of the fast coincidence circuit does not appear appropriate.

Um bei einer Zweifach-Koinzidenzstufe die Zählrate der zufälligen Koinzidenzen zu bestimmen, kann man entweder die Impulse des einen Koinzidenz-Eingangs verzögern, sodass alle systematischen Koinzidenzen ausgeschlossen sind, oder man bestimmt die Zählraten in beiden Koinzidenz-Eingängen und berechnet die Zahl der zufälligen Koinzidenzen hieraus und aus der gemessenen Koinzidenz-Auflösezeit τ. Wenn N_1 und N_2 die Zählraten an den Koinzidenz-Eingängen bezeichnen, und wenn die Zählrate der systematischen Koinzidenzen N_s genannt wird, dann ist die Zählrate der zufälligen Koinzidenzen $N_z = 2\tau\ (N_1 - N_s)\ (N_2 - N_s)$. Solange N_1 und N_2 gross gegen N_s sind, ist näherungsweise $N_z = 2\tau N_1 N_2$.

Beide Methoden lassen sich auf Schnell-Langsam-Koinzidenz-Anordnungen übertragen. Abb. 1 zeigt das Blockschaltbild einer solchen Anordnung. Die Eingänge der "langsamen" Koinzidenzstufe sind mit E_1, E_2, E_3 bezeichnet. Auf E_3 kommen die Impulse aus der "schnellen" Koinzidenzstufe. Die Zählraten an den Eingängen E_1, E_2, E_3 seien N_1, N_2, N_3. Die Zählrate der zufälligen Koinzidenzen setzt sich aus vier Anteilen zusammen:

(1) zufällige Koinzidenzen zwischen E_1, E_2 und E_3, Zählrate N_z^{123};

(2) zufällige Koinzidenzen zwischen E_1 und systematischen Koinzidenzen zwischen E_2 und E_3, Zählrate $N_z^{1(23)}$;

(3) zufällige Koinzidenzen zwischen E_2 und systematischen Koinzidenzen zwischen E_1 und E_3, Zählrate $N_z^{2(13)}$;

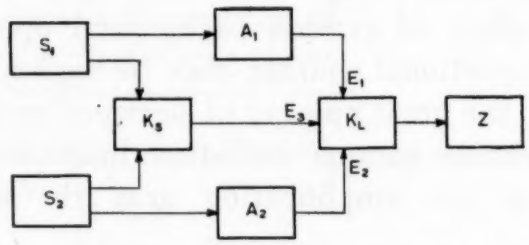

Abb. 1. Prinzipschaltbild einer Schnell-Langsam-Koinzidenz-Anordnung. S_1 und S_2 sind zwei Szintillationszähler. Rasch ansteigende Impulse daraus werden der schnellen Koinzidenzstufe K_s zugeführt. Energieproportionale Impulse gehen auf die Analysatoren A_1 und A_2. A_1 und A_2 bestehen im allgemeinen aus Linearverstärkern mit Einkanal- oder Integral-Diskriminatoren. Auf die langsame Dreifach-Koinzidenzstufe K_L kommen Impulse aus den Analysatoren und aus der schnellen Koinzidenzstufe. Z ist ein Zählgerät.

(4) zufällige Koinzidenzen zwischen E_3 und systematischen Koinzidenzen zwischen E_1 und E_2, Zählrate $N_z^{3(12)}$.

Wenn der Koinzidenzwirkungsgrad der Schnell-Langsam-Koinzidenz-Anordnung 1 ist, dann kann es nicht vorkommen, dass eine systematische Koinzidenz zwischen E_1 und E_2 vorliegt, die nicht auch systematisch mit E_3 koinzidiert. Es verschwindet dann der vierte Anteil.

Die vier Anteile lassen sich mit Verzögerungskabeln einzeln bestimmen. Zur Bestimmung des ersten Anteils braucht man zwei Verzögerungskabel, die man vor irgend zwei der drei Eingänge der langsamen Stufe schaltet, und deren verschiedene Längen so bemessen sind, dass nicht nur systematische Dreifach-Koinzidenzen, sondern auch alle systematischen Zweifach-Koinzidenzen ausgeschlossen sind. Bei der Bestimmung des zweiten Anteils wird man nur die Impulse des Eingangs E_1 verzögern. Von der gemessenen Zählrate muss man noch die Zählrate des ersten Anteils abziehen, um die Zählrate des zweiten Anteils zu erhalten. Das liegt daran, dass beim zweiten Anteil die systematischen Koinzidenzen zwischen E_2 und E_3 Koinzidenzpartner von E_1 sind, dass aber bei der Messung alle Koinzidenzen zwischen E_2 und E_3, d.h. auch die zufälligen Koinzidenzen, als Koinzidenzpartner von E_1 auftreten. Zur Bestimmung des dritten Anteils wird man die Impulse des Eingangs E_2 verzögern, zur Bestimmung des vierten Anteils die Impulse des Eingangs E_3. Die Zählrate des ersten Anteils muss immer subtrahiert werden. In praktischen Fällen werden häufig nur der zweite oder der dritte Anteil oder der zweite und der dritte Anteil eine Rolle spielen.

Es ist nicht möglich, die Zählrate der zufälligen Koinzidenzen dadurch zu bestimmen, dass man vor den einen Eingang der schnellen Koinzidenzstufe ein Verzögerungskabel schaltet. Durch ein solches Kabel würden alle systematischen Koinzidenzen in der schnellen Koinzidenzstufe ausgeschlossen. Ein grosser Beitrag von zufälligen Koinzidenzen rührt aber von Ereignissen her, die zu einer systematischen Koinzidenz in der schnellen Stufe führen.

Die Übertragung der zweiten Methode erfordert die Messung der Zählraten von Zweifach-Koinzidenzen in der langsamen Dreifach-Koinzidenzstufe und die Bestimmung der Koinzidenzauflösezeiten für zufällige Koinzidenzen. Wenn man die Eingangsimpulse an den Eingängen E_1, E_2, E_3 in ausreichender Näherung als Rechteckimpulse der Längen t_1, t_2, t_3 betrachten kann, die im Falle einer Überlappung eine Koinzidenz ergeben, dann ist der erste Anteil der zufälligen Koinzidenzen

$$N_z^{123} = 3\tau^2 N_1 N_2 N_3 \quad \text{mit} \quad 3\tau^2 = t_1t_2 + t_1t_3 + t_2t_3\dagger .$$

Bei der Bestimmung des zweiten Anteils kann man wieder so vorgehen, dass man die Zählrate der zufälligen Koinzidenzen zwischen E_1 und allen Koinzidenzen zwischen E_2 und E_3 ermittelt und dann den ersten Anteil subtrahiert. Um die Zählrate N_k^{23} der Koinzidenzen zwischen E_2 und E_3 zu messen, wird der Eingang E_1 unwirksam gemacht. Die Zählrate der zufälligen Koinzidenzen zwischen E_1 und den Koinzidenzen zwischen E_2 und E_3 ist

$$N_z^{1(23)} + N_z^{123} = 2\tau_{1(23)}(N_k^{23} - N_s)\, N_1 .$$

N_s bezeichnet die Zählrate der systematischen langsamen Dreifach-Koinzidenzen. Gegen N_1 ist N_s vernachlässigt. Um die Koinzidenzauflösezeit $\tau_{1(23)}$ für zufällige Koinzidenzen zwischen E_1 und Koinzidenzen zwischen E_2 und E_3 zu messen, gibt man auf den Eingang E_1 Impulse aus einem Impulsgeber oder aus einem Szintillationszähler mit einem unabhängigen Präparat. Wenn dann N_g^1 die Zählrate an E_1 ist und N_g^k die Koinzidenzzählrate, dann ist

$$\tau_{1(23)} = N_g^k/(2N_g^1 N_k^{23}) .$$

Da im allgemeinen die Impulslängen der Eingangsimpulse bekannt sind, läuft die Messung

† Die Zählrate der zufälligen Koinzidenzen zwischen E_1 und E_2 ist $N_z^{12} = (t_1 + t_2)\, N_1 N_2$. Wenn z.B. $t_1 < t_2$ ist, hat die Gesamtheit der Koinzidenzimpulse der Länge $< t_1$ die relative Wahrscheinlichkeit $2t_1$, alle Impulslängen $< t_1$ sind gleich wahrscheinlich; Koinzidenzimpulse der Länge t_1 haben die relative Wahrscheinlichkeit $t_2 - t_1$. Die mittlere Länge des Koinzidenzimpulses ist daher $t_1t_2/(t_1 + t_2)$. Die Zählrate des ersten Anteils der zufälligen Koinzidenzen wird

$$N_z^{123} = (t_1t_2/(t_1 + t_2) + t_3)\, N_z^{12} N_3 = 3\tau^2 N_1 N_2 N_3 .$$

darauf hinaus, dass man den mittleren Überlappungsgrad der koinzidierenden Impulse zwischen E_2 und E_3 bestimmt. Entsprechendes gilt für den dritten Anteil: Mit einem Impulsgeber oder einem unabhängigen Präparat wird die Koinzidenzauflösezeit $\tau_{2(13)}$ für zufällige Koinzidenzen zwischen E_2 und allen Koinzidenzen zwischen E_1 und E_3 ermittelt. Zur Bestimmung der Zählrate N_k^{13} der Koinzidenzen zwischen E_1 und E_3 wird E_2 unwirksam gemacht. Es wird

$$N_z^{2(13)} = 2\tau_{2(13)} (N_k^{13} - N_s) N_2 - N_z^{123} .$$

Genauso findet man für den vierten Anteil

$$N_z^{3(12)} = 2\tau_{3(12)} (N_k^{12} - N_s) (N_3 - N_s) - N_z^{123} .$$

Die Zählrate aller zufälligen Koinzidenzen ist

$$\begin{aligned} N_z &= N_z^{123} + N_z^{1(23)} + N_z^{2(13)} + N_z^{3(12)} \\ &= 2\tau_{1(23)} (N_k^{23} - N_s) N_1 + 2\tau_{2(13)} (N_k^{13} - N_s) N_2 \\ &\quad + 2\tau_{3(12)} (N_k^{12} - N_s) (N_3 - N_s) - 6\tau^2 N_1 N_2 N_3 . \end{aligned}$$

In vielen Fällen werden N_k^{23}, N_k^{13}, N_k^{12} und N_3 soviel grösser als N_s sein, dass man auf die Subtraktion von N_s verzichten kann. In anderen Fällen kann man für N_s die Zählrate der gemessenen Dreifach-Koinzidenzen N_k einsetzen, insbesondere wenn der Anteil der zufälligen Koinzidenzen nicht sehr gross ist. Der Aufwand einer Iterationsrechnung dürfte im allgemeinen nicht gerechtfertigt sein. Meistens werden nur höchstens zwei der vier Summanden Berücksichtigung verdienen.

NUCLEAR INSTRUMENTS AND METHODS 8 (1960) 79–91; NORTH-HOLLAND PUBLISHING CO.

NONLINEAR OPERATIONS ON PULSES BY MEANS OF p–n JUNCTIONS

G. GIANNELLI and L. STANCHI

Centro Studi Nucleari, Ispra, Italy

Received 15 February 1960

Some researches on the voltage-current characteristics of *p–n* junctions are described. It has been found that by means of a suitable method of using a transistor, its emitter-base junction shows a characteristic that approximates the theoretical one much better than diodes do. In particular some types of transistors have been found whose i_E, v_{EB} characteristic is strictly logarithmic over more than five decades of current while selected samples attain six decades. The use of such junctions for multiplying or dividing between them two or more pulses is described and the various problems arising in such application and in more general ones, like exponentials are analyzed.

1. Introduction

The method of mass identification of particles, described by Stokes *et al.*[1]) requires to carry out the product of two simultaneous pulses, coming from two detectors traversed by the same particle. The electronic apparatus used to obtain the product, developed by Briscoe[2]), is based on the formula:

$$AB = \tfrac{1}{4}[(A + B)^2 - (A - B)^2] \qquad (1.1)$$

and the squares have been obtained by means of special electronic tubes.

A similar method has been employed by L. Colli *et al.*[3]), see fig. 1. A beam composed of protons, deutons and tritons passes through a proportional counter in which the particles lose a very small part of their energy and then impinge a scintillation counter. The pulse A of the proportional counter is approximately:

$$A \propto \frac{\mathrm{d}E}{\mathrm{d}x} \propto \frac{m}{E} \qquad (1.2)$$

the pulse B of the scintillation counter is:

$$B \propto E \qquad (1.3)$$

where E is the energy of the particle, m is its mass and $\mathrm{d}E/\mathrm{d}x$ is the specific energy loss.

The computer executes the product $A \times B$, which is approximately independent of the mass. In this way the single-channel discriminator allows to obtain on the 100-channel

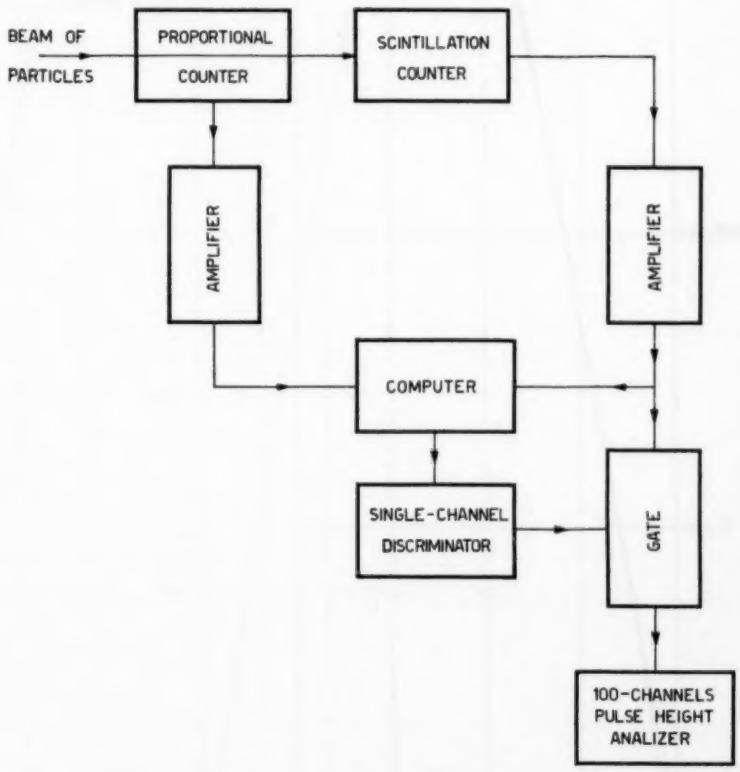

Fig. 1. Block diagram of the electronic set-up for the experiments of L. Colli *et al.*

[1]) R. H. Stokes, J. A. Northrop and K. Boyer, Apparatus for Measuring Energy Spectra of Mass-selected Particles in Coincidence with Fission, Rev. of Sc. Instr. **29** (1958).

[2]) William L. Briscoe, Electronic Computer for Mass Identification of Particles, Rev. of Sc. Instr. **29** (1958).

[3]) L. Colli, F. Cvelbar, S. Micheletti and M. Pignanelli, (n,d) Reactions with 14 MeV Neutron Energy, Il Nuovo Cimento Serie X, Vol. **13** (1959);

L. Colli, F. Cvelbar, S. Micheletti and M. Pignanelli, Structures in the Proton Spectra from (n,p) Reactions, Il Nuovo Cimento Serie X, Vol. **14** (1959);

L. Colli, F. Cvelbar, S. Micheletti and M. Pignanelli, (n,d) Reactions with 14 MeV Neutrons on ^{27}Al, ^{40}Ca, ^{55}Mn, ^{63}Cu, ^{103}Rh., Il Nuovo Cimento Serie X, Vol. **14** (1960).

analyzer energy spectra of particles of a single type. A better discrimination in regard to the mass may be obtained with more elaborated operations. The problem is widely discussed by Stokes *et al.*[1]).

In this paper we describe a method for obtaining the product of pulses that we have developed for the experiments of L. Colli *et al.* The method is based on the formula:

$$\ln AB = \ln A + \ln B\,. \tag{1.4}$$

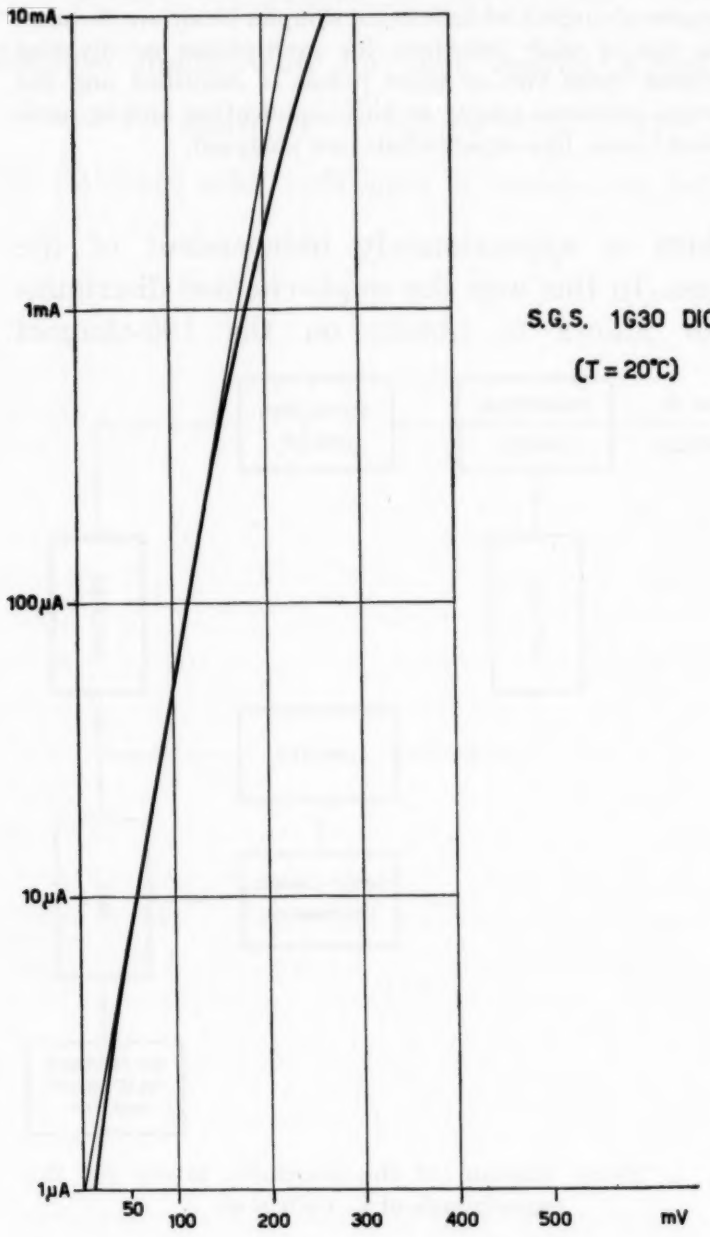

Fig. 2. Characteristic of a Ge junction diode.

This has been possible because we have found a new method to use semiconductor junctions in order to obtain logarithms with precision over a wide range. The method is versatile, it is possible to do in a simple way various mathematical operations and it can possibly find other applications in nuclear physics.

2. Method Used to Obtain the Logarithm

As well known the range of validity of the equation of the junction diode deduced by the linear theory[4]):

$$i = I_0 e^{\vartheta v} - I_0 \tag{2.1}$$

with $\vartheta = q/kT$ and I_0 constant at a given temperature, is limited. In the germanium it does not extend to the high injection levels, while in the silicon it does not nearly exist at room temperature. The studies on the divergences of the actual characteristics from (2.1) have been reviewed by J. L. Moll[5]). In the silicon, at low currents, the current produced by generation of charges in the depletion layer becomes appreciable in respect to the values given by (2.1). This phenomenon would appear also in the germanium at low temperature. At high currents, both in germanium and in silicon, the actual characteristics may be interpreted by a law of the type (2.1) but with a value $\vartheta = q/2kT$, and is explained by the phenomenon of the conductivity modulation in the less doped material. In addition, the effect of the ohmic resistance of the junction materials becomes appreciable at high currents. Finally for a logarithmic conversion it is necessary to restrict the range to values of current sufficiently greater than I_0.

In fig. 2 we give the measured characteristic of a germanium junction diode that is typical of a class of examined diodes. This characteristic in the semilogarithmic diagram is never truly rectilinear.

We thought that we would obtain better results with the use of the emitter-base junction of a germanium transistor, with the collector

[4]) W. Shockley, The Theory of p—n Junctions in Semiconductors and p—n Junction Transistors, The Bell Syst. Techn. J. **28** (1949).

[5]) J. L. Moll, The Evolution of the Theory for the Voltage-Current Characteristic of p–n Junctions, Proc. I.R.E. **46** (1958);

See also E. Baldinger, W. Czaja and M. Nicolet, Der Einfluss nichtidealer Emitterübergänge auf das Verhalten von Flächentransistoren, Helvetica Physica Acta **29** (1956) 428.

inversely biased at constant voltage (fig. 3). The chief reasons were: (a) in the low current region we should have a decrease of importance of the second term of the right-hand side of the (2.1).

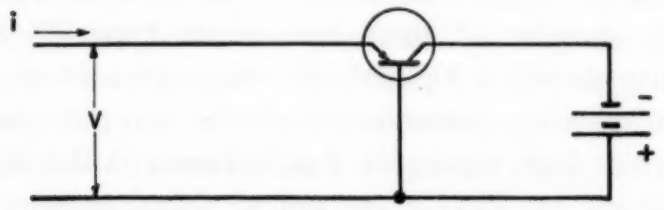

Fig. 3. Connection of transistors which for the emitter-base junction gives a characteristic that is logarithmic over a wide range.

The equation for such a junction, that is calculated in the Appendix A, is:

$$i_E = I_{ES}\, e^{qv_{EB}/kT} - \rho I_{ES} \qquad (2.2)$$

where $\rho = 1 - \alpha = \alpha/\beta$ and α and β are respectively the common-base and common-emitter current gains of the transistor.

(b) at high currents should be less the influence of the series resistance which in this case is the base spreading resistance divided per β. Besides in the base of transistors the conductivity modulation, which strongly influences the current gain[6]), should not appreciably affect the relation between the concentration at the emitter junction and the current. This relation is determined by the width of the base while in diodes is function of the diffusion length which is affected by conductivity modulation.

We have measured the characteristics i_E, v_{EB} of six types of p–n–p and n–p–n alloy-junction transistors. The best results have been obtained with transistors 2N404, whose characteristics have been measured on 14 samples. The characteristics of the best sample, of the worst and of a typical one are shown in fig. 4. The characteristics are accurately logarithmic in a range that in the worst sample is of two decades and in the best one is of four. Moreover we have noted that in all the samples the logarithmic range includes the two decades from 10 μA to 1 mA. The semilogarithmic slope of the characteristics is exactly equal to the theoretical value.

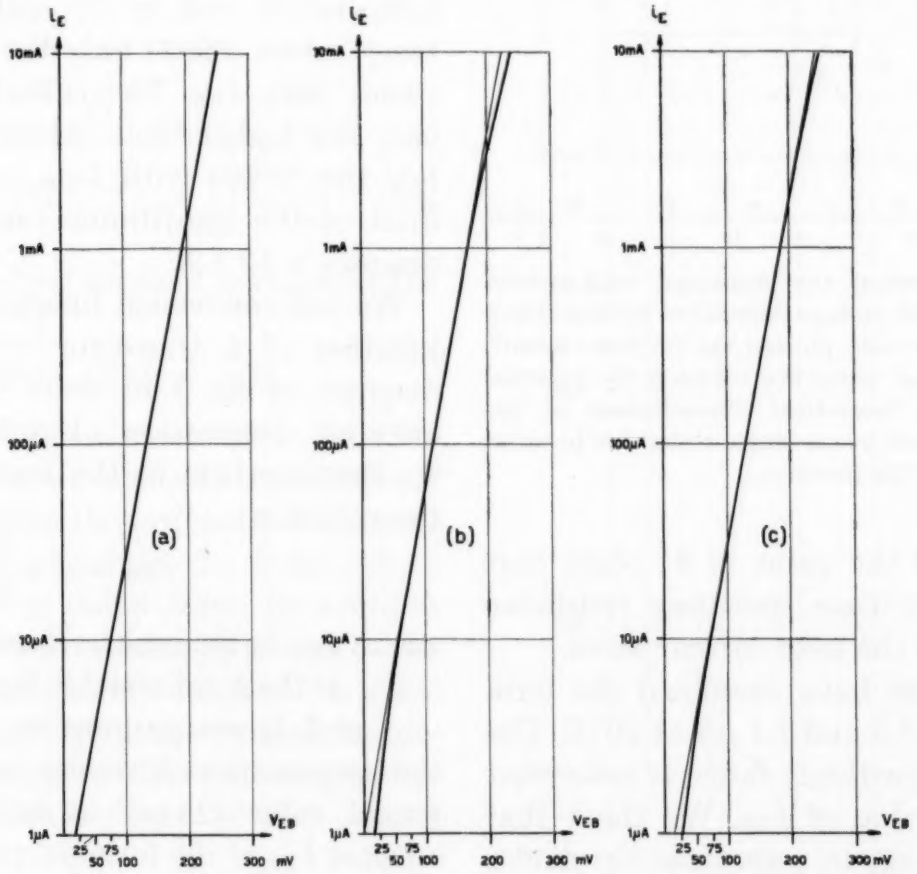

Fig. 4. Voltage-current characteristics of R.C.A. alloy-junction transistors type 2N404 at $V_{CB} = -2$ V and $T = 20$ °C. (a) best sample which shows a logarithmic range of four decades, (b) worst sample: two decades, (c) typical sample.

The characteristic at high currents has been studied on a sample. The voltage difference between the characteristic and the extrapolated logarithmic line is shown in fig. 5 as a function of the base current and it is seen that the difference from the characteristic as given by eq. (2.2) is fully explained by a simple

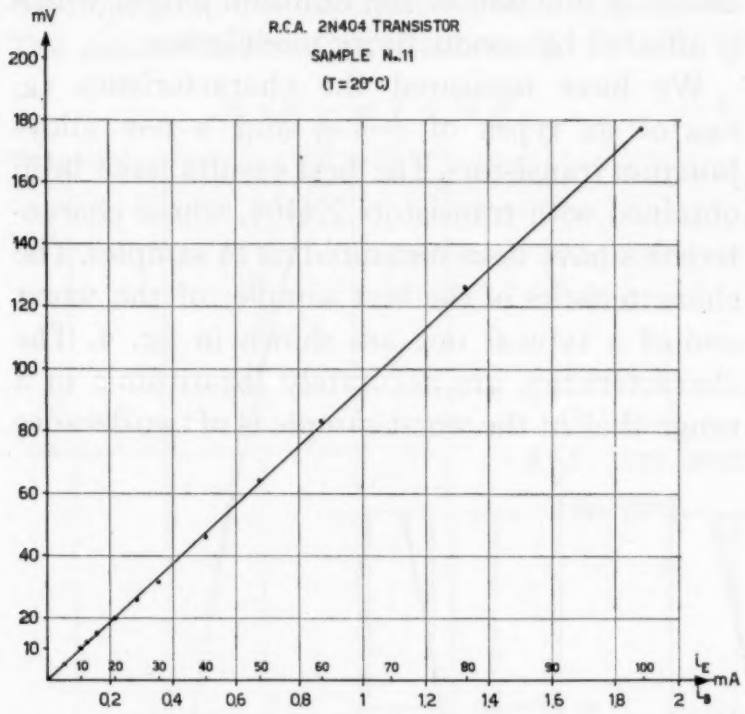

Fig. 5. Difference between the measured emitter-base voltage and the junction voltage calculated extrapolating the low-current characteristic, plotted against base current. This diagram shows that difference between the external characteristic and the theoretical characteristic of the junction is fully explained by an ohmic resistance in series to the junction.

ohmic resistance of the value of 94 ohms that we interpret as the base spreading resistance $r_{BB'}$ through which the base current flows.

In the samples we have examined the term I_{ES} varies between 0.5 and 1.1 μA at 20° C. The low limit of the logarithmic range is somewhat greater than the value of I_{ES}. We think that this limited advantage in respect to the diodes is due to the fact that at low current β decreases[6]) so that the advantage due to the coefficient ρ in eq. (2.2) is reduced.

The drift transistors give markedly superior results. The logarithmic range at the low current side extends down to values practically equal to I_{ES} and at the high current side up to values somewhat higher to those found on alloy-junction transistors; in addition they have much smaller values of I_{ES}. Measurements on five samples of drift transistors type 2N274 have shown a logarithmic range of four decades: from 10^{-6} to 10^{-2} A (at 20° C). Measurements on five samples of drift transistors type 2N384 have shown a logarithmic range greater than five decades, common to all the samples examined, and values of I_{ES} between 0.015 and 0.05 μA (at 20° C). A typical characteristic is shown in fig. 6. All the measurements have been made with transistors immersed in oil and thermostated with the precision of $\pm$ 0.1° C. Moreover at high currents the measurements have been carried out in such a way that errors due to self-heating of the junction did not affect the precision of the measures.

The logarithmic range is influenced by the temperature and by the collector voltage. The temperature affects only the lower limit, which varies with I_{ES}. The collector voltage affects only the higher limit, which increases with it. For the 2N384 with $V_{CB} = -2$V, the higher limit of the logarithmic range common to all samples is 10^{-2} A.

We call conversion junction the emitter-base junction of a transistor employed as in the diagram of fig. 3 in order to obtain the logarithmic conversion of pulses. We represent its characteristic in the logarithmic region by the equation:

$$v_{EB} = A \ln \frac{i}{I_0} \tag{2.3}$$

where v_{EB} is the emitter-base voltage

i is the total emitter input current

A and I_0 are parameters which depend on the temperature. A results equal to the theoretical value (25 mV at 20° C); I_0 which substitutes I_{ES} of the formula (2.2), varies from a sample to another.

3. Polarization of the Conversion Junctions

The term I_0 of eq. (2.3) varies strongly with temperature and is different from a sample to

[6]) W. M. Webster, On the Variation of Junction-Transistor Current-Amplification Factor with Emitter Current, Proc. I.R.E. **42** (1954).

another. It is possible to obtain a logarithmic characteristic with a fixed value of I_0 by the use of a particular method of polarization. This method consists in polarizing the conversion junction with a constant current I_P that is set to zero each time a pulse arrives and for the whole duration of the pulse. In this way the amplitude v_S of the output voltage pulse is the difference between the voltage v_{tot} produced by the input pulse of current i_S and the voltage V_P existing across the junction before and after the pulse that is the voltage due to the current I_P:

$$v_S = v_{tot} - V_P \tag{3.1}$$

$$i_S = I_0 \left(e^{v_{tot}/A} - \rho\right) = I_0 \left[e^{(v_S + V_P)/A} - \rho\right] \tag{3.2}$$

$$I_P = I_0 \left(e^{V_P/A} - \rho\right) . \tag{3.3}$$

From these we obtain:

$$i_S = I_0 \left[\frac{I_P + \rho I_0}{I_0} e^{v_S/A} - \rho\right] =$$

$$= (I_P + \rho I_0) \left[e^{v_S/A} - \frac{\rho I_0}{I_P + \rho I_0}\right] . \tag{3.4}$$

With the normal values for drift transistors the order of magnitude of

$$10^{-9} \text{ A} \quad \text{and} \quad \rho I_0/(I_P + \rho I_0)$$

for $I_P \geqslant 1\ \mu$A is absolutely negligible, so that the relation v_S, i_S is practically independent from I_0. This simplifies the problems of temperature compensation, because the temperature effect appears only in the A term. In addition the substitution of the constant I_0 proper of the junction with an arbitrary constant I_P gives more freedom for satisfying the various requirements and in particular allows to choose the most suitable dynamic range of the output signal v_S.

4. Problems of the Application of the Method

In the case of pulses applied to a conversion junction, eq. (2.3) is valid for the istantaneous values only if the rise time of the pulses is sufficiently larger than the rise time of the conversion junction that is determined by the α cut-off frequency of the transistor. The parameter of the pulse which is of interest is always the amplitude and therefore all the operations must result as operations on the amplitudes.

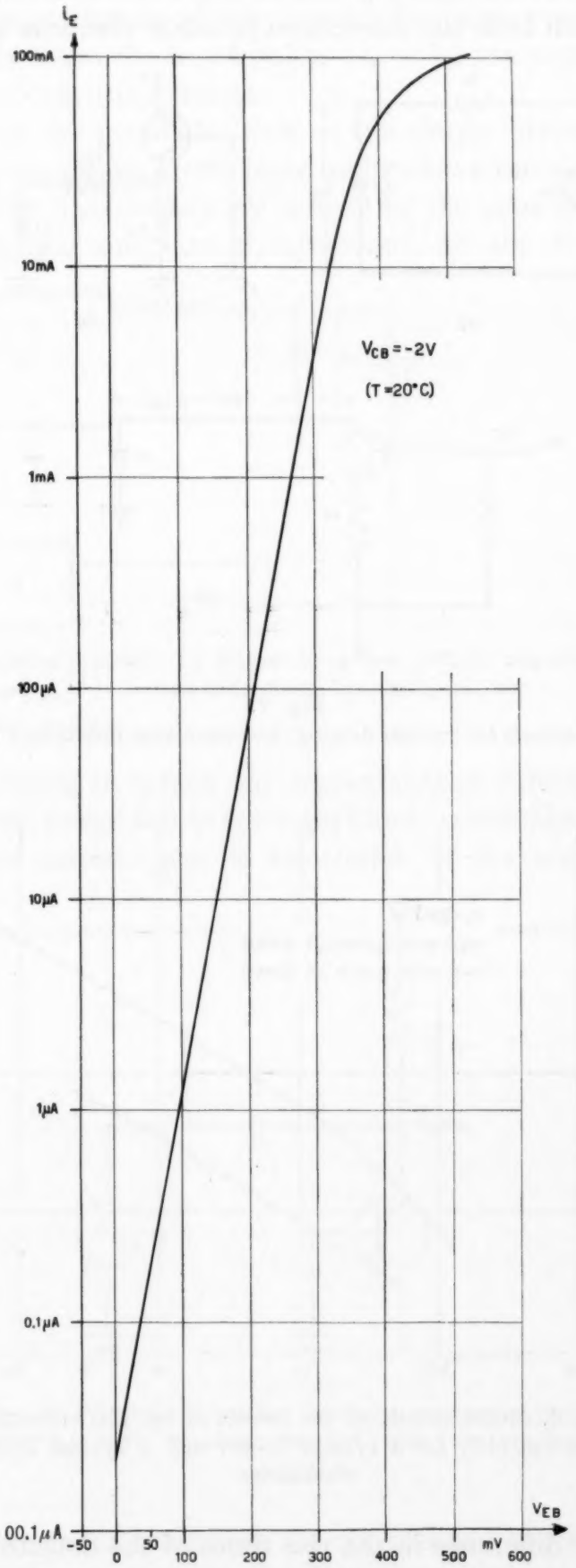

Fig. 6. Typical voltage-current characteristic of R.C.A. drift transistor 2N384.

To do so the maxima of the pulses must be simultaneous. The best way (but not the only one) to satisfy these two requirements is to work with rectangular pulses having a duration larger than both the conversion junction rise time and

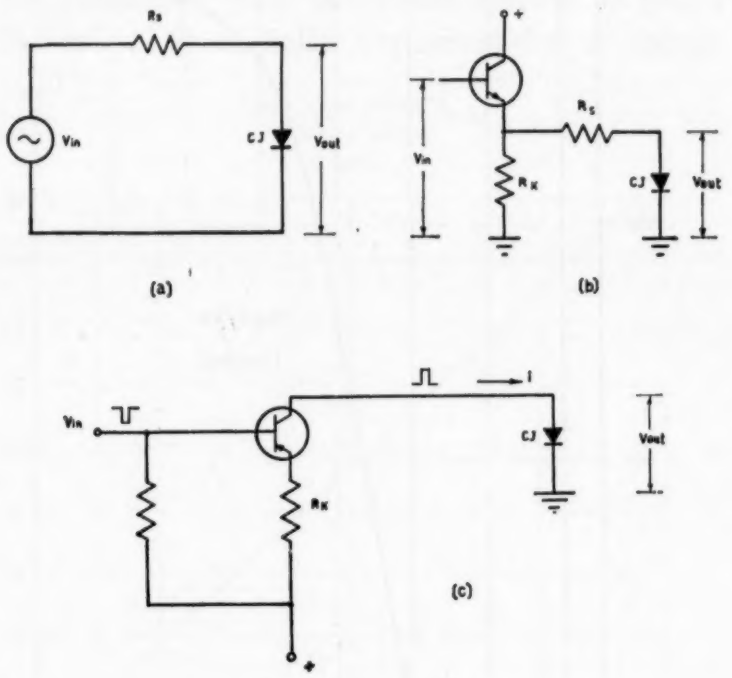

Fig. 7.
Methods for current driving the conversion junctions CJ.

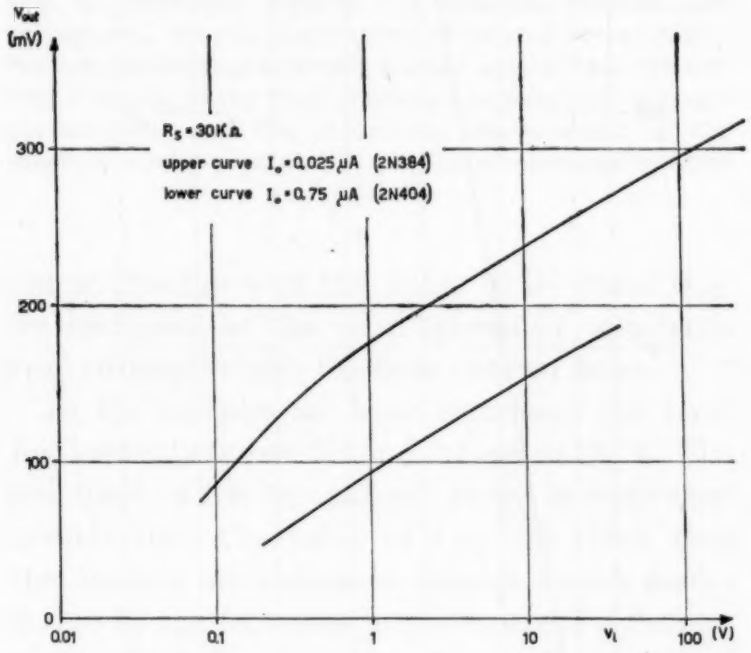

Fig. 8. Characteristic of the circuit of fig. 7(a) calculated from eqs. (4.1) for a typical 2N404 and a typical 2N384 transistors.

the difference in the rise times of the detectors, or generally than the coincidence time of the pulses as defined for each experiment.

For obtaining the logarithm the conversion junction must be driven by a current generator that must have particular requirements. Essentially it must: (a) supply pulses of a single sign because the negative signals produce high negative voltages (theoretically infinite) across the junction; (b) have an internal resistance much higher than the maximum junction resistance in the working range; (c) have an output current equal to zero when signals are not present. We examined many solutions. The simplest (fig. 7a) is a voltage generator v_{in} transformed in a current generator by means of a high series resistance R_s. There is an error due to the voltage drop on the conversion junction, which is subtracted from v_{in}. The relation between the input voltage v_{in} and the output voltage v_{out} is given by the system:

$$\begin{cases} v_{out} = A \ln \dfrac{i}{I_0} \\ v_{in} = R_s i + v_{out} . \end{cases} \tag{4.1}$$

The resulting characteristics, similar to the type shown in fig. 8, are analyzed in the Appendix B.

In order to minimize the error, v_{in} must be much greater than v_{out}, thus this method can be used only with limited dynamic ranges. In this case it appears more convenient to use the 2N404 transistors than the 2N384 ones, because the 2N404 may be used at higher currents with lower impedance levels.

The voltage generator may be an emitter follower (fig. 7b) with base-emitter voltage equal to zero in the quiescent state. In this case there is another error due to the base-emitter voltage drop in the emitter-follower. It is not possible to use an electronic tube cathode follower.

High precisions may be obtained by more elaborated systems. One could think of amplifiers with current feed-back, or of amplifiers with voltage feed-back where in the latter the voltage across the conversion junction is added to the input as in the diagram of fig. 9, but it is easy to see that these two methods are actually simply different ways of viewing the same

diagram. We point out that the more simple current feed-back amplifier, that is a transistor with emitter feed-back resistance and output taken from the collector, see fig. 7c, drives to errors of the same type of those of the circuit of fig. 7a because of the drop in the base-emitter junction of the transistor itself. Here R_s is substituted by the emitter feed-back resistance R_k.

Finally another cause of error to take into account is the load applied to the conversion junction by the utilizer circuit.

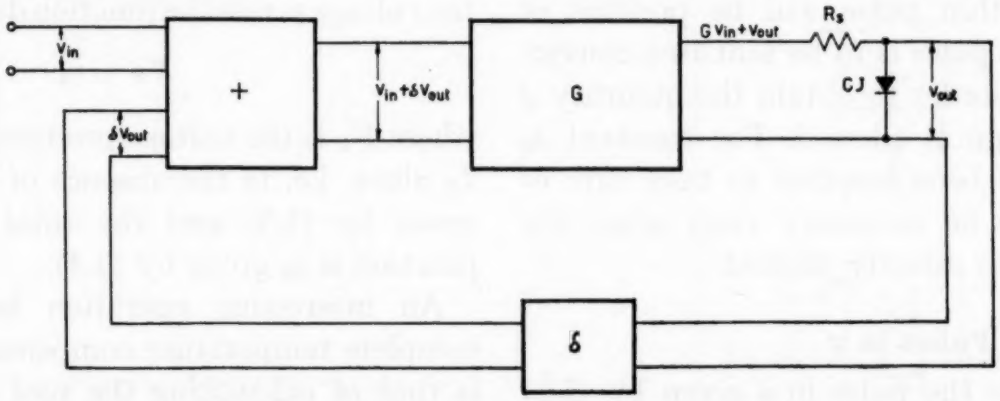

Fig. 9. System for compensating the voltage drop on the conversion junction CJ driven by a low output impedance amplifier through the resistance R_s. It is required that $\delta = 1/G$, then the voltage across R_s will be:

$$G\,(v_{in} + \delta v_{out}) - v_{out} = G v_{in}\,.$$

5. Arithmetical Operations with the Conversion Junctions

On the logarithm pulses (that is the pulses proportional to the logarithm of the amplitude of the input pulses) all linear operations can be performed in a quite conventional way. In a general way, by means of an adder, a pulse will be obtained whose amplitude v_u is proportional to ln u, and u is given by the formula:

$$u = k_0 \prod_1^n (a_i + k_i)^{h_i} \qquad (5.1)$$

here the a_i are numbers proportional to the amplitudes i_i of the input pulses and k_0, k_i, h_i are constants. The constants k_i are obtained by adding to the pulses a_i pulses of constant amplitude and simultaneous to them.

In the quite general case when at least one of the k_i is equal to zero it is necessary to provide a system that maintains the output at the zero value whenever one of the pulses a_j whose corresponding k_j is zero, is absent. That because the physical system cannot represent logarithms of zeroes. This requirement is satisfied by a coincidence among the input pulses that controls a gate on the output pulse. Since the logarithmic characteristic holds only in a finite range the system must in addition supply the output pulse only when the input pulses $(a_i + k_i)$ are within the logarithmic range.

In the particular case of the simple division of two pulses, if the input pulses have the same shape, that is they are defined by the same time function and are simultaneous, in the time interval in which the instantaneous values of both pulses fall in the logarithmic characteristic the output pulse is horizontal. If the above-

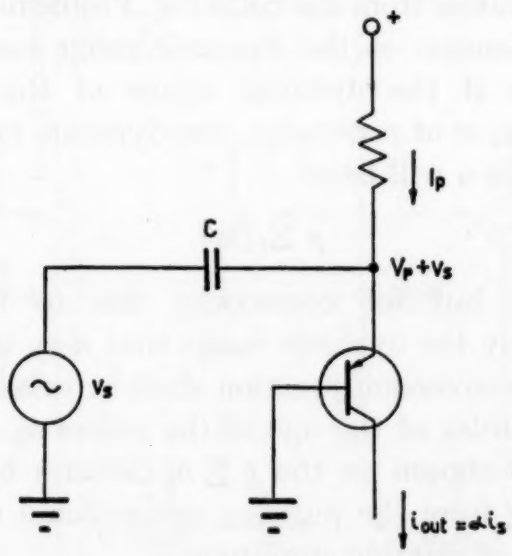

Fig. 10. Principle of voltage driving a conversion junction polarized with constant current with the method of section 3.

mentioned conditions are not satisfied and even if the maxima are simultaneous, spikes higher than the horizontal portion can be produced in

correspondence to the rise and decay of the pulses and it is necessary to operate with rectangular pulses and to isolate the horizontal portion by suitable linear gate systems[7]). Similar phenomena can occur in correspondence of the interval of time where one or both the pulses are out of the logarithmic region. Also operations of type (5.1) can give the same type of phenomena when some h_i are smaller than zero.

The product of the pulses $(a_i + k_i)^{h_i}$ may be greater or smaller than unity and the corresponding logarithm pulse will be positive or negative. If this pulse is to be sent to a conversion junction in order to obtain the quantity u no change of sign is allowed. The constant k_0 of eq. (5.1) has been inserted to take care of that. This may be necessary even when the logarithm pulse is directly utilized.

6. Operations on Pulses ln u

In many cases the pulse ln u given by (5.1) may be directly used; it can be analyzed by a pulse-height analyzer in order to obtain a spectrum having constant resolution in u. If it is necessary to obtain the pulse u a conversion junction voltage driven by the pulse ln u can be used and the pulse of current proportional to u is taken from the collector. Problems about the extension of the dynamic range can arise because if the dynamic range of the input pulses a_i is of p decades, the dynamic range of the pulse u will be of:

$$p \sum_1^n{}_i |\, h_i \,|$$

decades but for corrections due to the k_i. Generally the dynamic range that may be used with a conversion junction shall be smaller, i.e. of the order of the one of the pulses a_i, and it may be chosen on the $p \sum h_i$ decades by subtracting from the pulse v_u proportional to ln u a pulse of suitable amplitude.

Between the conversion junction which supplies the output pulse of amplitude u and those which operate on the input pulses there is some temperature compensation and precisely are eliminated only the variations due to the parameter A of eqs. (4.1) not those due to I_0. If all the conversion junctions are polarized following the method described in section 3 a complete temperature compensation is obtained.

In order to apply this type of polarization to junctions used for conversion from logarithms to numbers it is necessary to use the circuit of fig. 10. The polarization current I_P is supplied continuously, that is also during the pulses. Then if the capacitance C is sufficiently large, the voltage across the junction during the pulse is:

$$V_P + v_S$$

where V_P is the voltage produced by the current I_P alone, i.e. in the absence of the pulse and is given by (3.3) and the total current in the junction is i_S given by (3.4).

An interesting operation because by it a complete temperature compensation is attained is that of calculating the root of order $\sum h_i$ of the pulse u†. The demonstration is given in Appendix C. If the root of order $\sum h_i$ is calculated the dynamic range of the output pulse

$$\frac{1}{\sum_1^n{}_i h_i}$$
$$(u)$$

is equal to the dynamic range of the input pulses. If all the h_i are positive, both the reduction of the dynamic range and the temperature compensation is attained.

7. Apparatus Constructed

For L. Colli *et al.*'s experiments, see fig. 1, we have constructed a computer which makes the operation $a \times (b + b_0)^h$, where a is the pulse from the proportional counter, b is the pulse from the scintillation counter and b_0 is a constant. b_0 and the exponent h have been added in order to investigate the possibility of obtaining a better discrimination in respect to the mass.

The schematic of the computer is given in fig. 11.

[7]) G. Giannelli, Transistorized Linear Gate, To be published.

† It is impossible to effect this operation in the case of the simple division and generally when $\sum h_i = 0$.

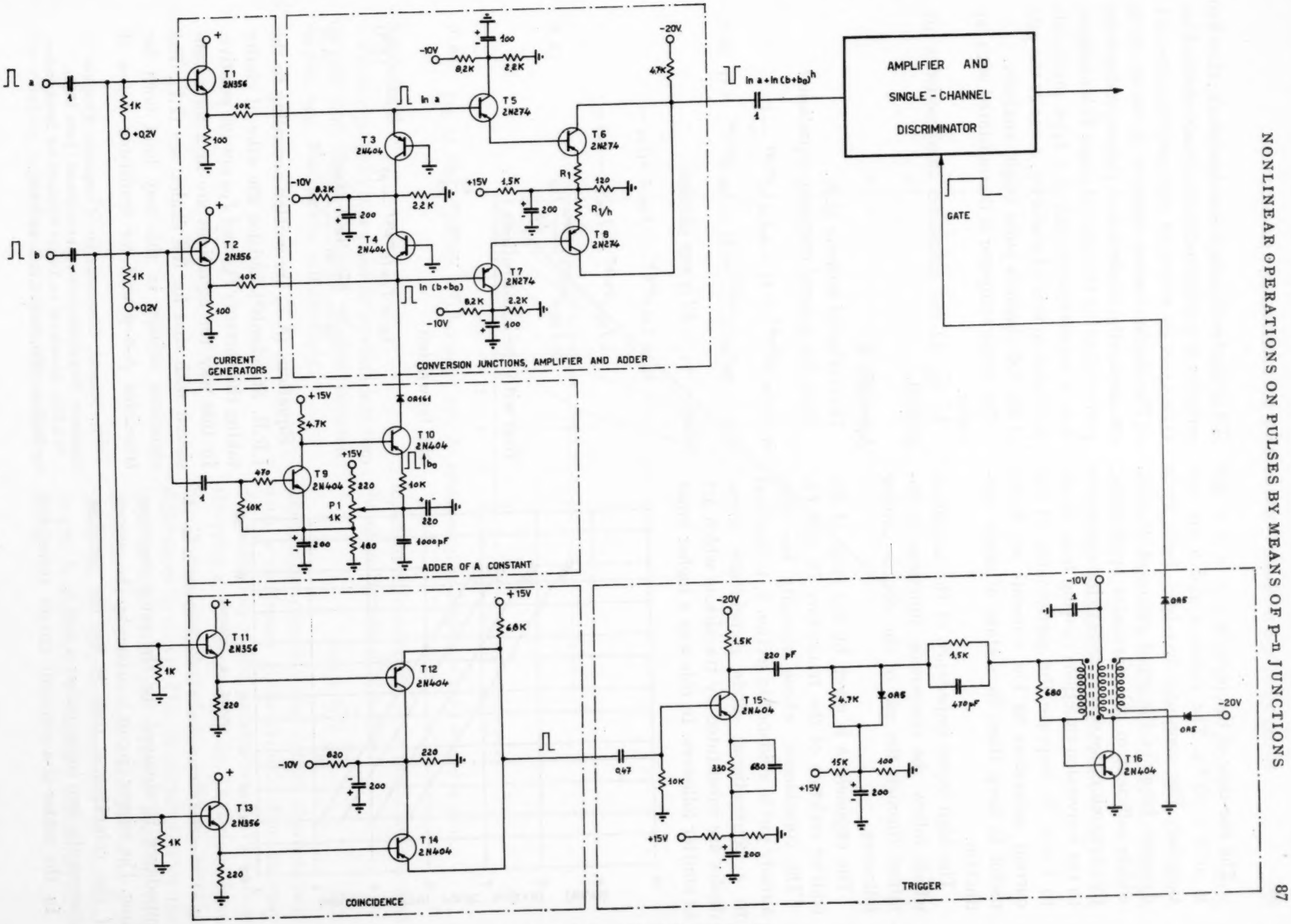

Fig. 11. Schematic of the computer.

The rise-time of the pulse $\ln a + \ln (b + b_0)^h$ is of 2×10^{-7} s. The pulses a and b are rectangular. The computer has been built for a dynamic range of the input pulses of 20 to 1, widely sufficient in this particular application; this dynamic range corresponds to input currents to the conversion junctions ranging from 50 μA to 1 mA. To improve the performance of the current generators at low currents we found useful to keep them in a state of slight conduction.

The high input impedance of the amplifiers which follow the conversion junctions is obtained through the use of the double emitter followers.

The exponent h is given by the ratio of the emitter resistors of the transistors T6 and T8.

The coincidence, whose necessity has been already put in evidence in section 5, is identical to a conventional diode coincidence where diodes are substituted by transistors which act as emitter followers. In this way a higher input impedance is obtained for the same response time. The trigger circuit is driven by the output of the coincidence, that is by the smallest between the two input pulses a and b.

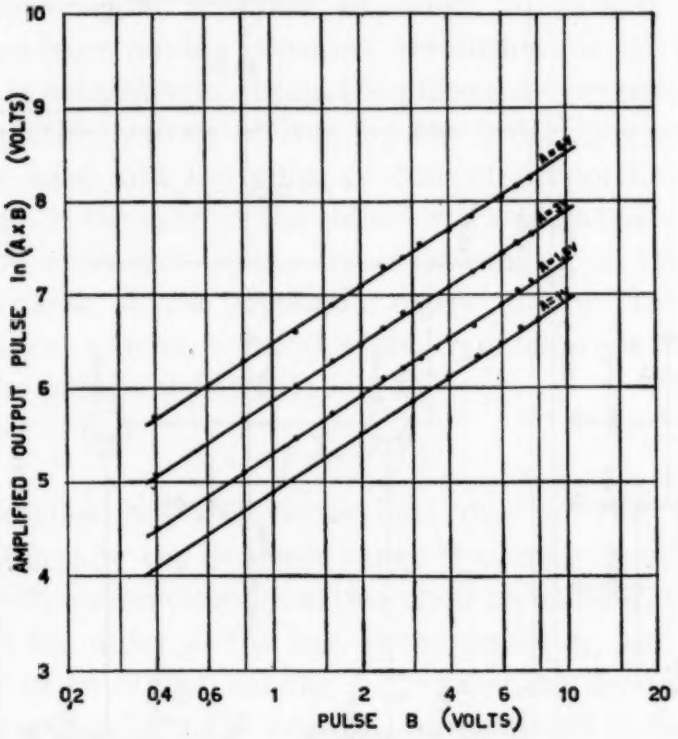

Fig. 12. Measured characteristics of the computer of fig. 11.

In the adder-of-a-constant circuit transistor T9 saturates if pulse b exceeds 50 mV; then T10 supplies a current pulse that is adjustable from 0 to 1 mA by means of the potentiometer P1.

The single-channel analyzer is set so as to encompass the whole line of pulses produced by particles having the selected mass. This analyzer, that is transistorized and of a type previously developed in this laboratory[8]), controls the gate of the 100-channels pulse height analyzer.

The whole computer is thermostated with tap water.

In fig. 12 the measured characteristics are plotted.

Appendix A

Derivation of formula (2.2).

From the general transistor equations:

$$i_E = I_{ES}\,(e^{qv_E/kT} - 1) - \alpha_I I_{CS}\,(e^{qv_C/kT} - 1)$$

$$i_C = -\alpha_N I_{ES}\,(e^{qv_E/kT} - 1) + I_{CS}\,(e^{qv_C/kT} - 1) \quad \text{(A.1)}$$

when $-v_C >> kT/q$ one obtains:

$$i_E = I_{ES}\,e^{qv_E/kT} - I_{ES} + \alpha_I I_{CS} =$$

$$= I_{ES}\,e^{qv_E/kT} - I_{ES}\,(1 - \alpha_N) =$$

$$= I_{ES}\,e^{qv_E/kT} - \frac{\alpha_N}{\beta_N} I_{ES} \quad \text{(A.2)}$$

that with the substitution:

$$\rho = 1 - \alpha_N = \frac{\alpha_N}{\beta_N}, \quad \text{(A.3)}$$

can be written:

$$i_E = I_{ES}\,(e^{qv_E/kT} - \rho) \quad \text{(A.4)}$$

or:

$$v_E = \frac{kT}{q} \ln \frac{i_E + \rho I_{ES}}{I_{ES}}. \quad \text{(A.5)}$$

Equations (A.1) are written according to the I.R.E. Standards[9]) and for the sake of clarity taking the currents I_{ES} and I_{CS} always positive. In this way the equations are in a form consistent with that for the diodes, see (2.1). The equations written in this way hold both for transistor p–n–p and for transistor n–p–n if

[8]) L. Stanchi, Discriminatore d'ampiezza d'impulso a transistor, Strumentazione e Automazione (June 1959).

[9]) I.R.E. Standards on Letter Symbols for Semiconductor Devices, 1956, Proc. I.R.E. **44** (1956).

currents i_E, i_C and voltages v_E, v_C are taken as the direct currents and voltages of the emitter and collector junctions, that is i_E (i_C) is positive when entering in the emitter (collector) for transistors *p–n–p* and when coming out for transistors *n–p–n*.

$$y = x + \ln (1 - ay\, e^{-x}) . \qquad (B.2)$$

Eq. (B.2) has been calculated for different values of the parameter a and is plotted in the diagram of fig. 13.

For the utilization of the circuit of fig. 7a for

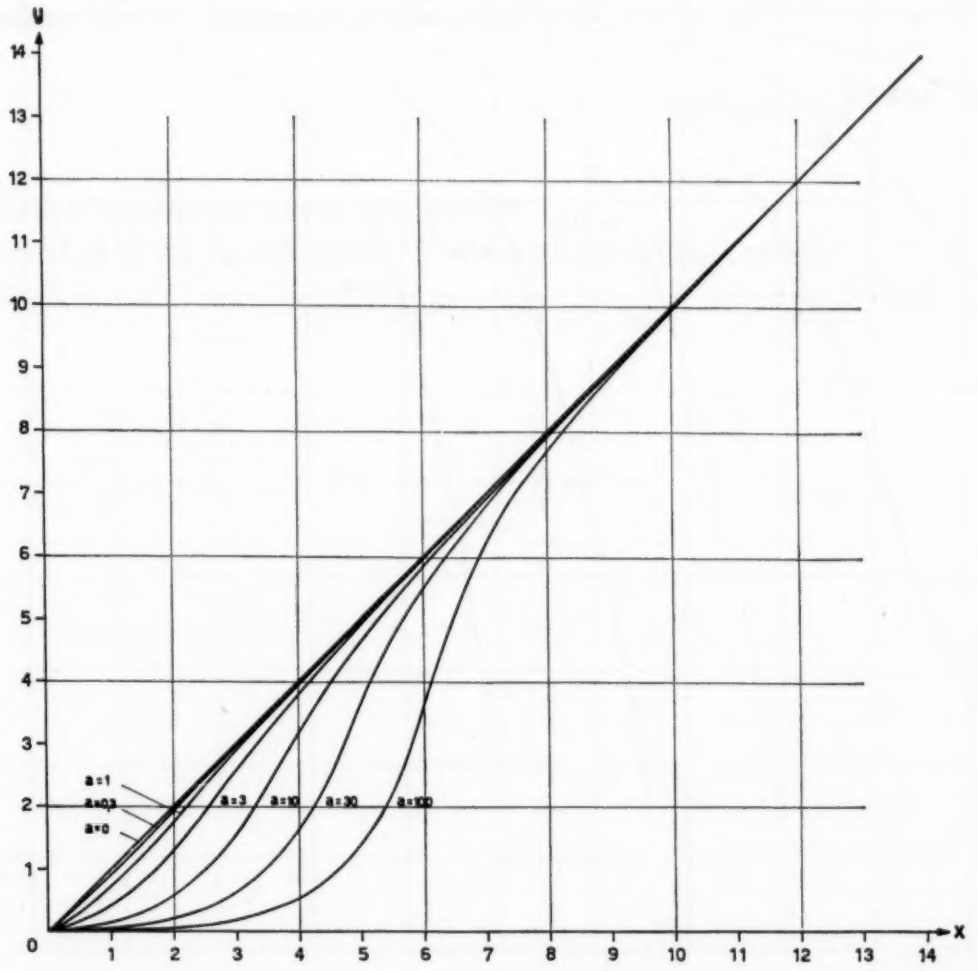

Fig. 13. Plot of the eqs. (4.1) calculated with the adimensional quantities x, y and a defined in (B.1).

Appendix B

From eqs. (4.1) it is possible to eliminate the current and obtain a direct relation between v_{in} and v_{out}. Making the substitutions:

$$x = \ln \frac{v_{in}}{R_s I_0}$$

$$y = \frac{v_{out}}{A}$$

$$a = \frac{A}{R_s I_0}, \qquad (B.1)$$

this relation is written in adimensional form:

logarithmic conversion it is important to find the characteristic of the type:

$$v_{out} = B \ln \frac{v_{in}}{V_0} \qquad (B.3)$$

which approximates the actual characteristic with a minimum given error ε. For an easy determination of the parameters B, V_0 and of the error ε, the diagram of fig. 14 derived from fig. 13 has been plotted; its ordinates are the differences $(y - x)$. The characteristics of the type of eq. (B.3) are straight lines in this diagram. It will be noted when the error ε is taken as an horizontal segment of constant length, it represents a constant percentile error in v_{in}.

Appendix C

In the text it has been stated that if one derives the root of order $\sum_1^n {}_i h_i$ of the quantity u, a complete compensation of temperature variation is achieved. This requires that for all the conversion junctions the parameter A be the same and the parameters I_0 vary with temperature in the same ratio. The compensation of the variations of these parameters takes place between the junctions that calculate the logarithm from one side and the junction that calculate the inverse from the other side.

Let i_i and l_i $(i = 1,2 \cdots n)$ be the currents injected to those conversion junctions which calculate the logarithm, related to the quantities a_i and k_i of eq. (5.1) by a proportionality factor having the dimensions of a current:

$$i_i = I_c a_i$$
$$l_i = I_c k_i \ . \qquad \text{(C.1)}$$

From (C.1), (2.3), (5.1) the pulse v_u (proportional to $\ln u$) is:

$$v_u = \sum_1^n {}_i h_i A \ln \frac{i_i + l_i}{I_i f(T)} + A \ln k_0 \qquad \text{(C.2)}$$

where I_0 of the (2.3) is given by:

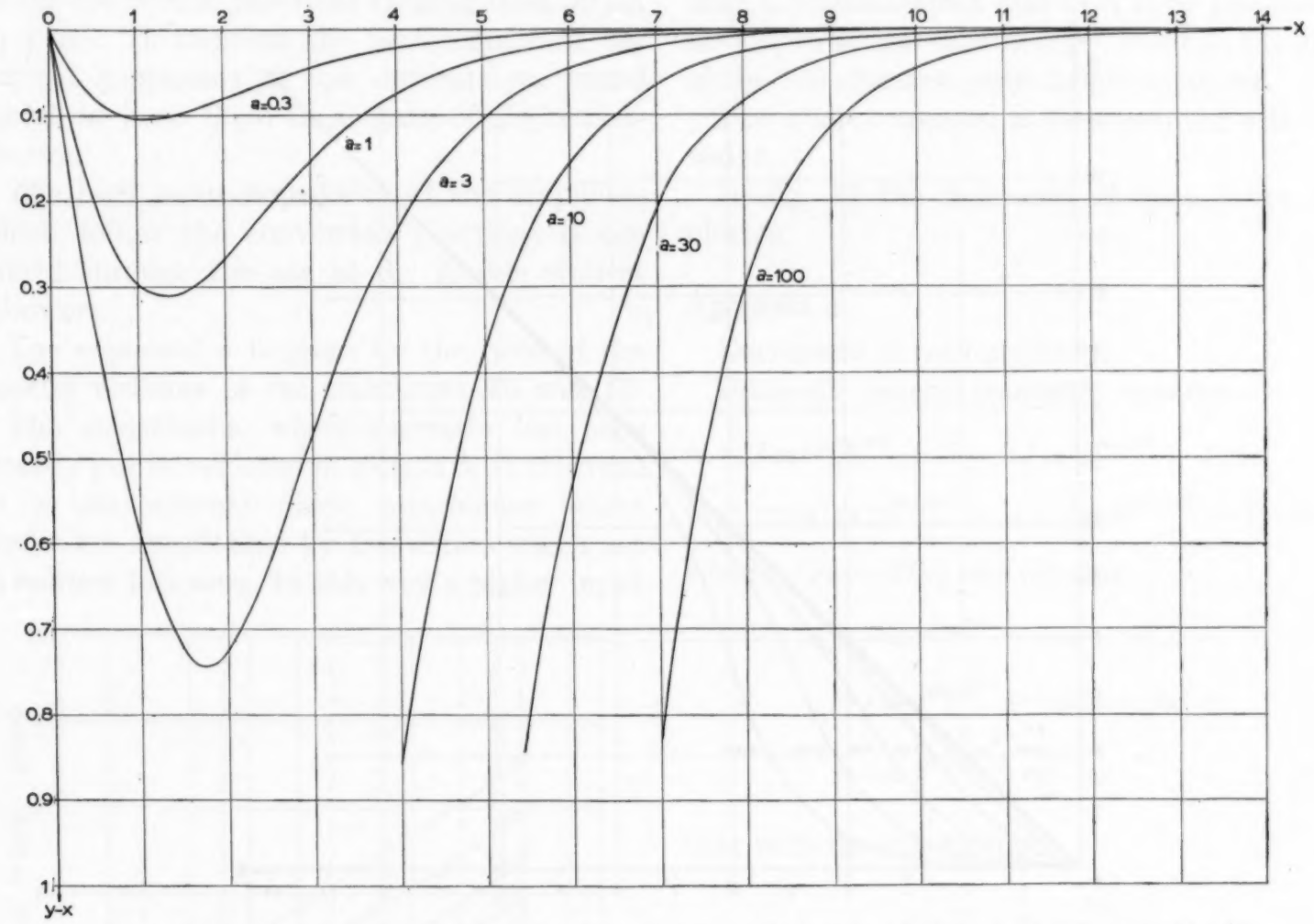

Fig. 14. Diagram obtained from fig. 13 plotting $(y—x)$ on the axis of ordinates with an expanded scale.

$$I_{0i} = I_i f(T) \qquad \text{(C.3)}$$

where I_i is a constant and is different for each junction and $f(T)$ is a function of temperature and is the same for all the junctions. We divide (C.2) by $\sum_1^n {}_j h_j$:

$$\frac{v_u}{\sum_1^n {}_j h_j} = \frac{A}{\sum_1^n {}_j h_j} \ln \left\{ k_0 \left[\prod_1^n {}_i \left(\frac{i_i + l_i}{I_i} \right)^{h_i} \right] \left[\frac{1}{f(T)} \right]^{\sum_1^n {}_i h_i} \right\} =$$

$$= A \ln \left\{ \frac{1}{f(T)} \left[k_0 \prod_1^n {}_i \left(\frac{i_i + l_i}{I_i} \right)^{h_i} \right]^{\frac{1}{\sum_1^n {}_j h_j}} \right\} . \qquad \text{(C.4)}$$

If we apply this voltage pulse to the terminals of a conversion junction having the characteristic:

$$i = I_{n+1} f(T)\, e^{v/A}, \qquad \text{(C.5)}$$

the current pulse in the junction will have an amplitude i_u given by:

$$i_u = I_{n+1} f(T)\, e^{v_u/(A \sum_1^n j^{h_j})} = I_{n+1} \left[k_0 \prod_1^n{}_i \left(\frac{i_i + l_i}{I_i} \right)^{h_i} \right]^{\frac{1}{\sum_1^n j^{h_j}}} = \frac{I_{n+1} I_c}{\left[\prod_1^n{}_i (I_i)^{h_i} \right]^{\frac{1}{\sum_1^n j^{h_j}}}} (u)^{\frac{1}{\sum_1^n j^{h_j}}} \qquad \text{(C.6)}$$

where all temperature dependent terms are absent.

It is to be noted that if all I_0 are equal between themselves, that is:

$$I_1 = I_2 = \cdots = I_n = I_{n+1} \qquad \text{(C.7)}$$

one simply has:

$$i_u = I_c (u)^{\frac{1}{\sum_1^n i^{h_i}}}. \qquad \text{(C.8)}$$

NUCLEAR INSTRUMENTS AND METHODS 8 (1960) 92–105; NORTH-HOLLAND PUBLISHING CO.

DETECTEUR DE PARTICULES LOURDES A JONCTION n–p AU SILICIUM

G. AMSEL, P. BARUCH et O. SMULKOWSKI

Laboratoire de Physique Nucléaire de l'Ecole Normale Supérieure, Paris

Reçu le 28 mars 1960

Silicon n–p junctions were used to detect heavy charged particles produced by nuclear reactions inside the accelerator vacuum chamber, at room temperature, The response to particle energy dissipated in the barrier, is linear. The width of resolved peaks at half maximum is independent of incident particle energy and is equivalent to 40 keV for α particles and 30 keV for protons and deuterons. The rise time of the signal due to particles stopped in the barrier is of the order of 1 millimicrosecond while that due to particles traversing it has a slow component; this allows their distinction electronically. The detectors are insensitive to γ rays and neutrons.

1. Introduction

Les réactions nucléaires provoquées par des ions lourds ont fait l'objet d'un grand nombre de travaux au cours des dernières années. Ces réactions s'accompagnent de l'émission de particules chargées de diverses natures dont l'identification pose un problème délicat. De plus, la détection doit s'opérer souvent en présence d'un flux intense de neutrons et de rayons γ, qui produisent un important bruit de fond.

L'analyse de spectres aussi complexes pose des problèmes difficiles, qui n'ont été que partiellement résolus par les détecteurs de particules lourdes utilisés jusqu'à présent. Il semble qu'un pas en avant peut être accompli par les détecteurs à jonction, dont l'étude date d'une époque récente. McKenzie et Bromley[1]) ont réalisé parmi les premiers un détecteur de ce type à l'aide de jonctions or-germanium. Cependant, le bruit élevé dû au germanium ne permet l'emploi de ce type de détecteur qu'à la température de l'azote liquide.

Pour éviter cet inconvénient, nous avons entrepris l'étude d'un détecteur à jonction au silicium, qui peut fonctionner à la température ambiante[2]).

Nous exposons ici les résultats obtenus ainsi qu'un essai d'interprétation des phénomènes observés.

2. Principe du Détecteur à Jonction

Une particule chargée crée dans un semiconducteur des paires d'électron-trou de la même façon qu'elle crée des paires d'ions dans un gaz. McKay[3]) a mesuré l'énergie nécessaire

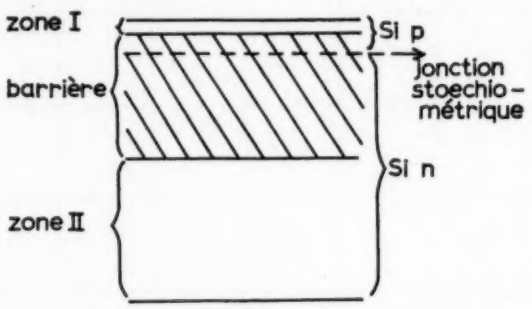

Fig. 1. Représentation schématique d'une jonction réalisée par diffusion de gallium dans du silicium de type n.

pour la création d'une paire de porteurs libres: elle est de 2.9 eV dans le germanium, soit environ 10 fois plus faible que dans un gaz. Dans le silicium elle est de 3.25 eV. Les paires électron-trou ont une durée de vie finie dont la valeur dépend de la concentration des impuretés. La collection des charges est totale lorsque le temps de collection est négligeable devant la durée de vie. Pour recueillir les charges, il faut que les porteurs se déplacent avec une grande

[1]) J. M. McKenzie and D. A. Bromley, Phys. Rev. Letters (April 1, 1959) 303.

[2]) G. Amsel, P. Baruch et O. Smulkowski, Comptes rendus des Séances de l'Académie des Sciences (22 Février 1960) p. 1468.

[3]) K. G. Mc Kay, Phys. Rev. **84** (1951) 829.

vitesse: pour cela un champ électrique intense est nécessaire.

Lorsqu'on polarise une jonction (fig. 1) en non conduction, il s'établit de part et d'autre de la jonction stoéchiométrique une zone B où le champ électrique est très intense. Cette zone où le champ est de l'ordre de 10^4 V/cm, est appelée zone de charge d'espace ou "barrière". Les porteurs s'y déplacent à des vitesses de l'ordre de 10^7 cm/s, donc le temps nécessaire pour parcourir une distance de 100 μ est de 10^{-9} s. Ce temps est négligeable devant la durée de vie, bien supérieure à la μs dans la région non dopée. Une collection totale de la charge créée dans la barrière est donc réalisée. Cette charge produit une impulsion de tension inversement proportionnelle à la capacité du détecteur.

En dehors de la barrière, il existe deux zones dans lesquelles le champ électrique est nul ou très faible et où les porteurs se déplacent par diffusion.

Dans la zone I fortement dopée comprise entre la barrière et la surface d'entrée, la durée de vie est très faible; la collection y est nulle. Cette zone se comporte comme la fenêtre d'un compteur proportionnel. Dans la zone II, où la durée de vie est élevée, une fraction des porteurs créés peut atteindre la barrière et contribuer au signal.

L'épaisseur (ε) de la barrière varie sensiblement comme $V^{\frac{1}{2}}\rho^{\frac{1}{2}}$, où V est la tension de polarisation et ρ la résistivité du matériau de base. Pour une jonction donnée, l'épaisseur maximum n'est limitée que par la tension de claquage. La capacité varie approximativement comme ε^{-1}.

3. Réalisation

Les jonctions sont obtenues par diffusion d'éléments III ou V dans du silicium. Par exemple par diffusion de gallium dans du silicium de type n ou de phosphore dans du silicium de type p.

Des jonctions du premier type utilisant du silicium du type n de résistivité voisine de 35 Ωcm, ont été réalisées sur notre proposition[4]). La concentration en surface du gallium est de l'ordre de 3×10^{17} par cm^3. La jonction stoéchiométrique se situe à 5 μ de la surface. La tension de claquage varie légèrement d'une jonction à l'autre; elle est généralement comprise entre 60 et 80 V. La surface des jonctions est de l'ordre de 4 mm^2. Nous donnons en exemple la variation du courant inverse en fonction de la polarisation (fig. 2) pour une des jonctions utilisées.

Ce type de détecteur a été l'objet d'une étude approfondie pendant que d'autres jonctions ayant des caractéristiques différentes étaient en cours de réalisation. Nous avons cherché à améliorer plus particulièrement deux caractéristiques du détecteur, en réalisant:

(1) une zone insensible à l'entrée plus mince par une diffusion moins profonde et un dopage en surface moins élevé;

(2) une zone de collection totale plus étendue,

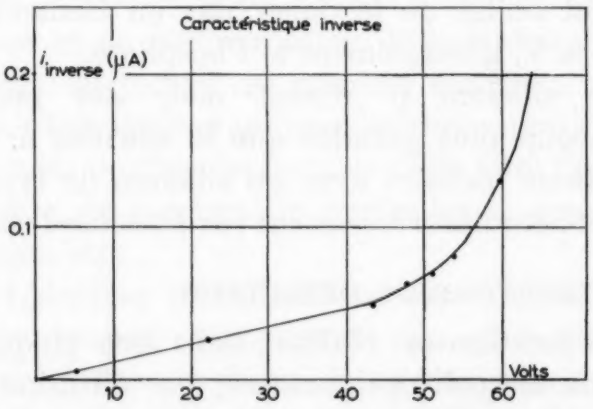

Fig. 2. Caractéristique inverse d'une jonction, placée dans son vide et dans la pénombre. La tension de claquage est définie par le coude de la caractéristique.

en repoussant la limite de la tension de claquage et en utilisant du silicium plus pur. Ceci nous a conduit à choisir du silicium de type p, la jonction s'obtenant alors par diffusion de phosphore.

Cette variété de silicium peut atteindre des résistivités allant jusqu'à plusieurs milliers d'ohms·cm. La résistivité d'un monocristal ne détermine la concentration des impuretés que dans le seul cas où ces impuretés sont constituées par des éléments d'un même groupe, autrement dit que le cristal n'est pas compensé. Généralement le silicium de type n de haute résistivité

[4]) Les jonctions ont été réalisées par la Cie LTT, Conflans Ste Honorine, France.

est compensé. Ceci est dû au fait qu'il est pratiquement impossible d'éliminer totalement le bore dont la présence dans le silicium lui confère le caractère p.

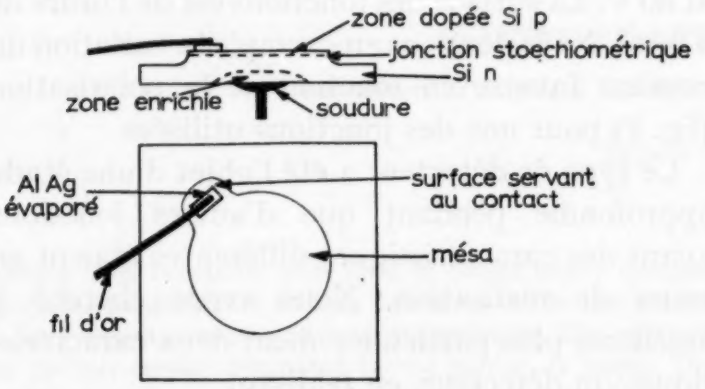

Fig. 3. Forme schématique de la jonction. Le contact sur la face diffusée ne doit pas empiéter sur la surface utile circulaire.

Pour obtenir du silicium n de haute résistivité, on est obligé de le doper par un élément du groupe V, généralement le Phosphore.

Le silicium p atteint donc des puretés beaucoup plus grandes que le silicium n. Des jonctions réalisées avec du silicium de type p, ont été étudiées récemment par Friedland *et al.*[5]).

3.1. STRUCTURE DU DETECTEUR

La jonction est réalisée, dans une plaquette de silicum poli optiquement, par diffusion sur

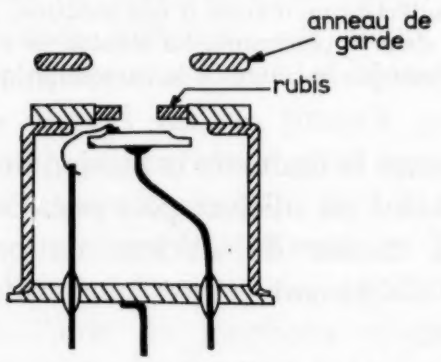

Fig. 4
Aspect d'un détecteur avec diaphragme et anneau de garde.

l'une des faces. La surface utile appelée "mésa", de forme circulaire, à laquelle est attenante une petite plage servant à la connexion électrique, est dégagée par attaque à l'acide. On obtient la forme indiquée figure 3. Le contact sur la face dopée est réalisé au moyen d'un fil d'or soudé par thermocompression sur une plage de métal évaporé et allié. Le contact avec la plaquette s'obtient par soudure après enrichissement local du silicium.

La jonction est montée sur une embase de transistor de façon que la surface dopée puisse être exposée au faisceau des particules (fig. 4). La surface de la "mésa" est légèrement en retrait du plan supérieur du capuchon sur lequel est fixé un diaphragme. Ce diaphragme sert à délimiter la partie utile de la surface de la jonction; il est réalisé par un rubis de montre enchassé dans un disque métallique. Le rubis a été choisi pour des raisons qui sont exposées dans le chapître traitant des résolutions. Un anneau de garde isolé et polarisé négativement par rapport à la masse est placé devant le diaphragme. Son rôle est de repousser les électrons secondaires émis par la cible, cf. section 8.

3.2. MONTAGE ET UTILISATION

Le détecteur peut être monté dans la chambre à diffusion de l'accélérateur. Son faible encombrement permet d'observer les produits de réactions à des angles très faibles par rapport au faisceau des particules incidentes. Le montage dans le vide évite toute fenêtre entre la cible et la face d'entrée du détecteur.

Pour réduire au minimum les capacités de connexions, une cathodyne est montée sous vide

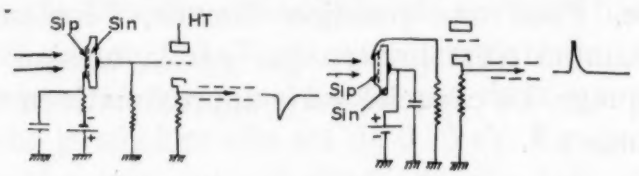

Fig. 5. Schémas de montages électriques permettant d'obtenir des impulsions de signe voulu. On remarque que la face d'entrée n'est jamais portée à un potentiel positif.

près du détecteur. Ce tube peut être remplacé par un transistor connecté "base à la masse". Dans notre expérience, nous avons utilisé un tube subminiature 6AK5.

Pour ne pas annihiler l'effet de l'anneau de garde, il faut choisir un montage électronique tel que la face d'entrée du détecteur ne soit pas

[5]) Stephen S. Friedland, James W. Mayer and John S. Wiggins, Nucleonics (February 1960).

portée au potentiel positif. La figure 5 montre deux schémas possibles, fournissant des impulsions, soit négatives, soit positives.

4. Méthode d'Etude du Détecteur

La réponse du détecteur a été étudiée sous trois aspects:

L'évolution de l'amplitude et du temps de montée des impulsions en fonction de l'énergie pour diverses particules et pour diverses tensions de polarisation;

La valeur absolue de ces amplitudes;

La dispersion en amplitude des impulsions dues à des particules mono-cinétiques.

Trois types de particules ont été utilisées: protons, deutons et rayons α. Ces particules étaient produites par des réactions nucléaires: des cibles minces sans support ont été soumises au bombardement du faisceau de protons ou de deutons de l'accélérateur Van de Graaff de 2 millions de volts de l'Ecole Normale Supérieure.

Les réactions utilisées pour obtenir les diverses particules étaient les suivantes:

deutons: diffusion élastique par

$$Ag,\ Al^{27},\ O^{16},\ C^{12}\ .$$

Domaine d'énergie: 0.2 à 2 MeV.

protons: diffusion élastique par Al^{27}, ainsi que les réactions

$$O^{16}\ (d,p)\ O^{17};\qquad Q = 1.92\ \text{MeV}\ .$$

$$C^{12}\ (d,p)\ C^{13};\qquad Q = 2.72\ \text{MeV}\ .$$

Domaine d'énergie: 0.3 à 4.5 MeV.

particules α:

$$O^{16}\ (d,\alpha)\ N^{14}\ ;\qquad Q = 3.12\ \text{MeV}\ .$$

$$Al^{27}\ (d,\alpha)\ Mg^{25}\ ;\qquad Q = 6.70\ \text{MeV}\ .$$

Une source de polonium fournissait des particules α de 5.3 MeV.

Domaine d'énergie: 2.7 à 7 MeV.

Les cibles utilisées étaient des films minces de:

Al_2O_3 de 40 et 20 $\mu g/cm^2$

Al de 20 et 7 $\mu g/cm^2$

Ag de 50 $\mu g/cm^2$.

Le carbone était présent sur toutes ces cibles, à l'état de contamination.

Les impulsions du détecteur étaient amplifiées par un amplificateur Ecko et envoyées, après passage à travers un amplificateur loupe, dans un analyseur d'impulsions à 100 canaux, du type RIDL.

5. Evolution de l'Amplitude et du Temps de Montée des Signaux

5.1.

1. Pour déterminer les conditions d'utilisation du détecteur, il est nécessaire de relever les courbes amplitude-énergie. Le réseau de ces courbes tracées pour diverses tensions de polarisation et pour diverses particules décrit le comportement du détecteur. De même il est important de connaître l'évolution du temps de montée des impulsions; en effet l'amplitude elle-même, après amplification, dépend du temps de montée, selon le choix du temps d'intégration et de différentiation de l'amplificateur. L'étude de toutes ces courbes montrera qu'il est possible d'effectuer une discrimination entre particules de diverses natures et de faire l'étude sélective de spectres de particules α, protons, deutons, etc.

2. L'analyse mathématique des courbes obtenues permet d'interpréter les phénomènes observés. Elle explique le mécanisme de la collection des charges et permet l'investigation des propriétés du semiconducteur dans la masse en fonction de la profondeur. Ces calculs, ainsi que les propriétés de la jonction qu'on en déduit, sont présentés en appendice.

5.2. DESCRIPTION DU MECANISME DE COLLECTION

1. *Dans la barrière*

La collection est totale; la relation amplitude-énergie dissipée est linéaire. Le temps de montée des impulsions est de l'ordre de 10^{-9} s.

2. *Au dela de la barrière*

Dans cette zone les porteurs se déplacent par diffusion. Les particules qui pénètrent dans cette zone donnent naissance à une impulsion qui a deux composantes. Une composante rapide correspondant à l'énergie dissipée dans la barrière. Une composante lente correspondant

à la collection par diffusion; cette collection est incomplète, car les porteurs ont une durée de vie finie dans le silicium, de l'ordre de quelques μs.

5.3.

Ainsi la courbe amplitude-énergie s'écarte de la linéarité lorsque la particule pénètre dans la zone de diffusion. Sa forme dépend des constantes de temps de l'amplificateur utilisé, qui peut transmettre plus ou moins fidèlement la composante lente de l'impulsion. La courbe passe par un maximum d'autant plus aigu que la constante de temps de différentiation est plus faible.

pour des tensions de polarisation comprises entre 9 et 45 V. L'épaisseur de la zone insensible est de 1.5 μ à 10% près. On voit que la barrière s'avance largement dans la zone dopée, puisque la jonction stoechiométrique est à 5μ de la surface. En réalité, l'épaisseur de la zone insensible varie avec la tension, mais si lentement qu'il n'est pas possible de le mettre en évidence.

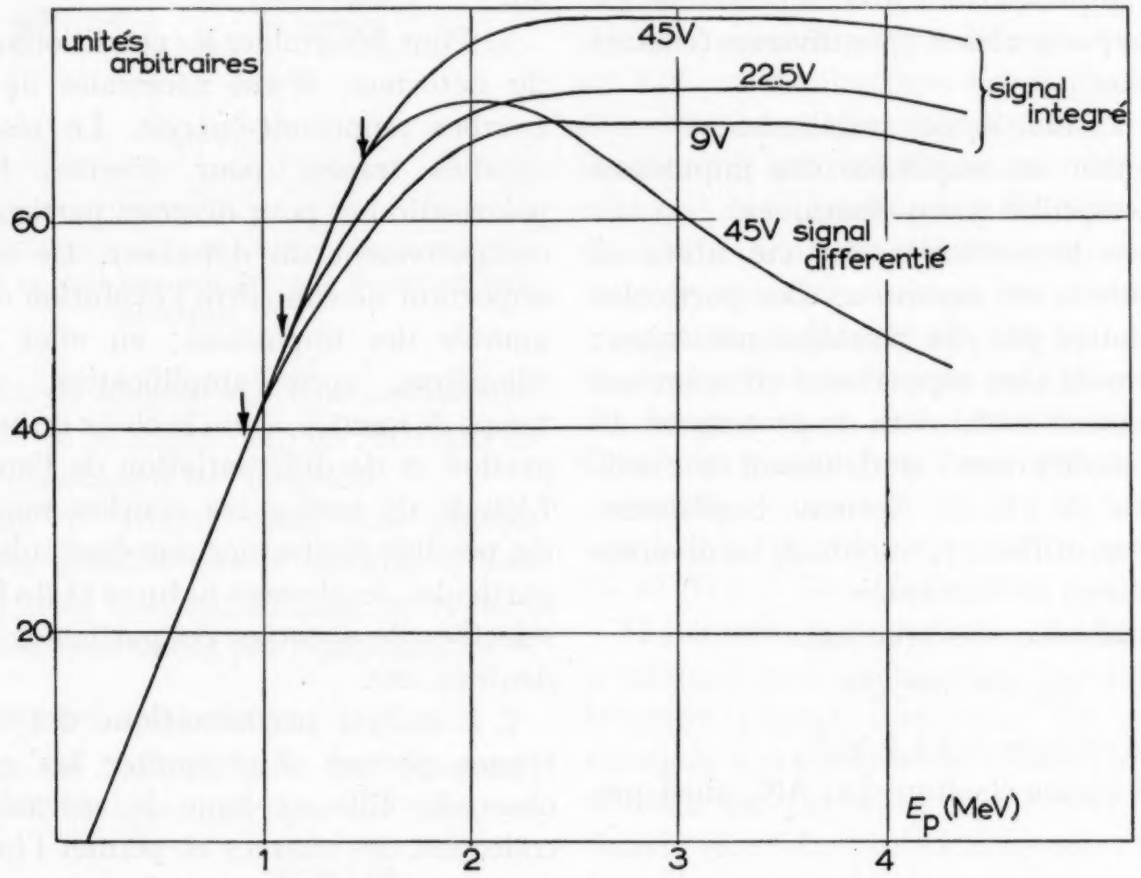

Fig. 6. Courbes d'amplitude du signal en fonction de l'énergie des protons incidents pour diverses tensions de polarisation. Les flèches indiquent les énergies pour lesquelles la réponse s'écarte de la linéarité.

5.4. RESULTATS

Pour illustrer les considérations qui précèdent, nous présentons les résultats de l'étude de l'un des détecteurs que nous avons utilisés.

La figure 6 montre les courbes d'amplitude mesurées avec des protons pour diverses tensions de polarisation. Les courbes ont été normalisées au même gain. Toutes ces courbes coupent l'axe des énergies au point d'abscisse 140 keV

L'épaisseur de la barrière est à 2μ près:

à 9 V: 17 μ

à 22 V: 21 μ

à 45 V: 27 μ .

La variation semble suivre une loi en $V^{0.4}$ plutôt que $V^{\frac{1}{2}}$.

La figure 7 montre les 2 familles d'impulsions dues à des particules arrêtées dans la barrière et à des particules plus pénétrantes.

La partie rapide des impulsions a été obervée avec un oscilloscope Tektronix et des amplificateurs Hewlett Packard d'une bande passante de 200 Mc/s. Le temps de montée des impulsions

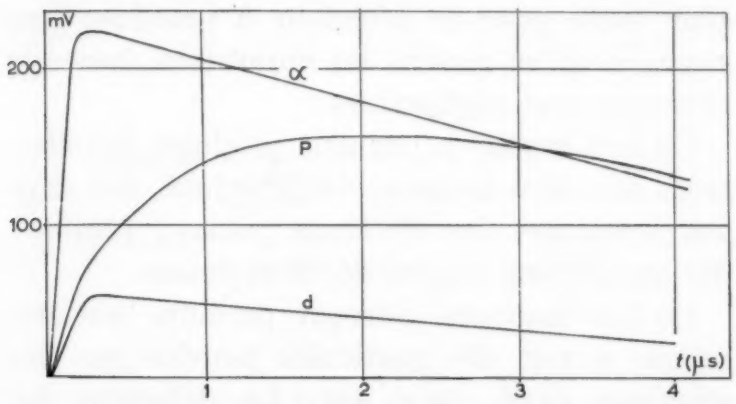

Fig. 7. Formes des impulsions suivant le parcours de la particule, les particules α et les deutons sont arrêtés dans la barrière, les protons ont par contre une notable partie de leur parcours dans la zone de diffusion.

était le temps de montée propre de l'électronique, soit 10^{-8} s. Notons que Friedland *et al.*[5]) ont également observé un temps de montée égal à celui de leur électronique, soit 3×10^{-9} s. Ceci est en accord avec le temps de montée théorique de 10^{-9} s.

La composante lente des impulsions a été observée avec un préamplificateur Ecko de gain 40 et de bande passante 4 Mc/s, dont la constante de temps de différentiation était supérieure à 10 μs. La constante de temps d'intégration était de 12 μs.

La figure 8 montre l'évolution du temps de montée de la composante lente en fonction du parcours. On voit que la variation est d'abord sensiblement linéaire, avec une pente de l'ordre de 0.3 μs/10μ. La pente est légèrement plus faible avec des tensions plus fortes ce qui prouve qu'un faible champ électrique résiduel subsiste dans la zone de diffusion et contribue au mouvement des porteurs. De plus, la relation cesse d'être linéaire pour les temps supérieurs à 3 μs environ, c'est-à-dire comparables à la durée de vie.

Cette évolution du temps de montée peut s'expliquer par la théorie de la diffusion.

5.5. DISCRIMINATION ENTRE PARTICULES

Constatons que les résultats ci-dessus s'expriment tous en fonction du parcours. Les courbes d'amplitude pour diverses particules se déduisent les unes des autres par affinité, si on prend le parcours comme variable. C'est ce qui a été vérifié pour les deutons. Ainsi la barrière maximum que nous avons obtenue avec cette jonction étant de 27μ, la limite de linéarité est de 1.5 MeV pour les protons, 2 MeV pour les deutons, 5.5 MeV pour les particules α.

Deux méthodes permettent de distinguer des particules de diverses natures:

(a) La zone de diffusion peut jouer le rôle de détecteur d'anticoïncidence. Un dispositif électronique simple permet d'éliminer la famille d'impulsions ayant une composante lente. Ainsi les particules pénétrantes sont identifiées. Cette méthode est d'autant plus souple qu'on peut contrôler électriquement l'épaisseur de la barrière, donc le domaine d'énergie exploré, pour diverses particules. Signalons qu'on peut opérer sans polarisation, le potentiel de contact, qui est de 1.1 V, étant suffisant pour créer une mince barrière.

(b) Si on ne dispose pas d'un montage d'anticoïncidences pour éliminer complètement les impulsions gênantes dues à des particules pénétrantes, on peut néanmoins "déplacer" un pic dû à un groupe de particules pénétrantes par rapport aux autres pics, en modifiant les constantes de temps d'intégration et de différentiation de l'amplificateur. Ainsi les réactions O^{16} (d,d) O^{16} et O^{16} (d,α) N^{14} ont été étudiées simultanément en présence des réactions

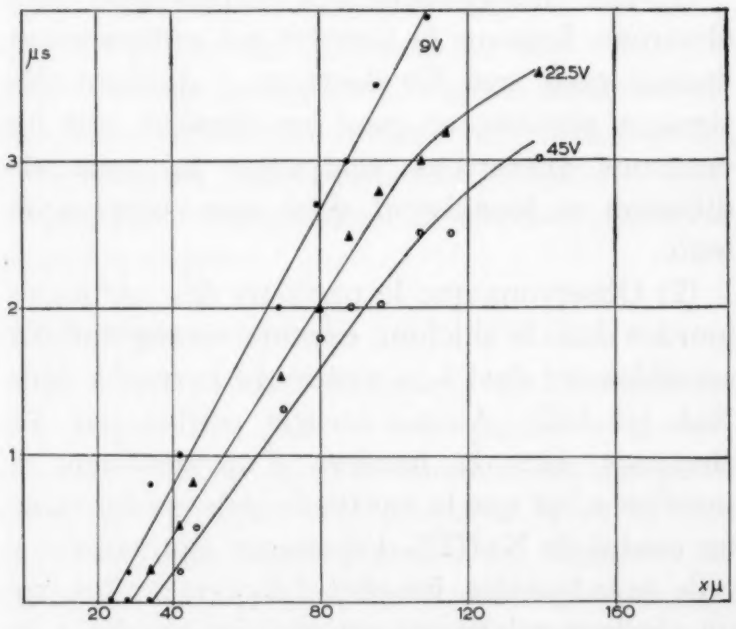

Fig. 8. Courbes représentant le temps de montée de la composante lente des impulsions dues à des particules très pénétrantes, pour diverses tensions de polarisation.

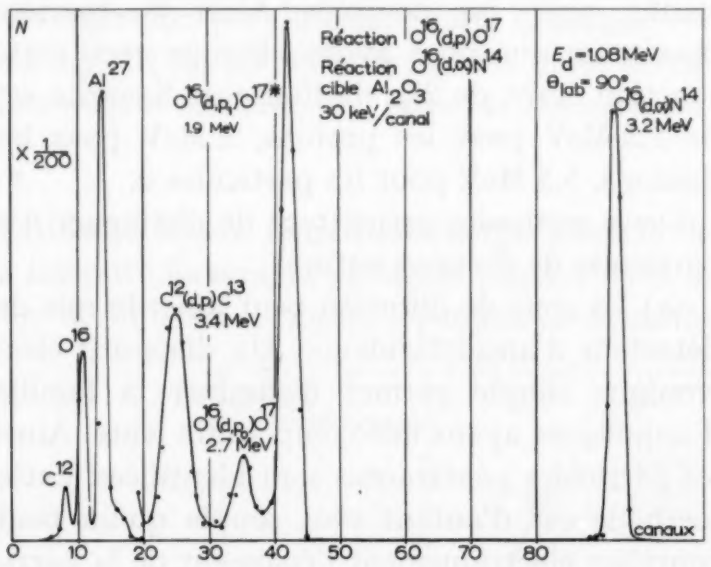

Fig. 9. Spectre complet obtenu par bombardement d'une cible de Al_2O_3 par des deutons.

O^{16} (d,p) O^{17} et C^{12} (d,p) C^{13}. Les pics dus aux protons pouvaient être groupés de manière à ne pas gêner la lecture des spectres dans leur partie utile, en mettant à profit la forme de la courbe amplitude-énergie (figure 6).

Le spectre représenté fig. 9 illustre cette méthode. On constate l'ordre inversé et la place des trois pics de protons qui sont groupés de manière à ne pas empiéter sur les spectres des deutons et des particules α.

REMARQUES

(1) Les mêmes principes s'appliquent aux électrons. Lorsque la barrière est suffisamment épaisse pour que les électrons y donnent des signaux gênants, on peut les éliminer, car les électrons traversent également la zone de diffusion et fournissent donc une composante lente.

(2) Observons que le parcours des particules lourdes dans le silicium, exprimé en mg/cm² est sensiblement égal à la moitié du parcours dans NaI (et CsI). Ainsi l'énergie perdue par les électrons dans la barrière d'un détecteur à jonction n'est que la moitié de celle perdue dans un cristal de NaI(Tl) d'épaisseur équivalente à celle de la barrière. En effet, l'énergie perdue par un électron relativiste est proportionnelle à la masse traversée. L'amplitude relative des impulsions dues aux électrons est donc deux fois plus faible pour le détecteur à jonction. Ceci explique qu'en général les impulsions dues aux électrons sont négligeables.

(3) Les rayons γ peuvent produire des électrons soit dans la masse du détecteur, soit dans son voisinage. Ces électrons peuvent produire des impulsions, comme décrit ci-dessus.

(4) Les neutrons peuvent produire soit des rayons γ soit des particules lourdes par des réactions (n,p), (n,α) etc. Le détecteur est inévitablement très sensible à ces dernières, en général fort peu nombreuses.

(5) Dans certaines applications où le flux de particules pénétrantes (électrons haute énergie par exemple) est très important, il est utile de réduire la durée de vie dans la zone de diffusion pour éviter l'empilement des impulsions. Ceci est possible sans réduction de la profondeur de la barrière.

6. Valeurs Absolues des Amplitudes et Rapport Signal-Bruit

(a) L'amplitude de l'impulsion de tension produite par une particule d'énergie E_{MeV}, C étant la capacité totale, est:

$$V = \frac{q}{C} = \frac{E \times 10^6}{3.25}\,\frac{e}{C}$$

$$V_{\text{mV}} = 50\,\frac{E_{\text{MeV}}}{C_{\text{pF}}}$$

quel que soit le détecteur utilisé. Le gain varie donc comme C^{-1}. La mesure de C^{-1} peut se faire en observant l'amplitude due à un groupe de particules d'énergie fixe, pour diverses tensions de polarisation. La courbe obtenue est normalisée par évaluation de la constante de temps de décharge de la capacité dans une résistance connue. L'avantage de cette méthode est qu'elle permet de faire la mesure dans les conditions mêmes de l'expérience, le détecteur étant en place dans la chambre à diffusion. Pour éviter la distorsion de la courbe due à la variation de l'épaisseur de la barrière, il faut opérer avec des particules de faible parcours. Il est facile de contrôler si une telle distorsion est apparue: deux groupes de deutons d'énergie voisine

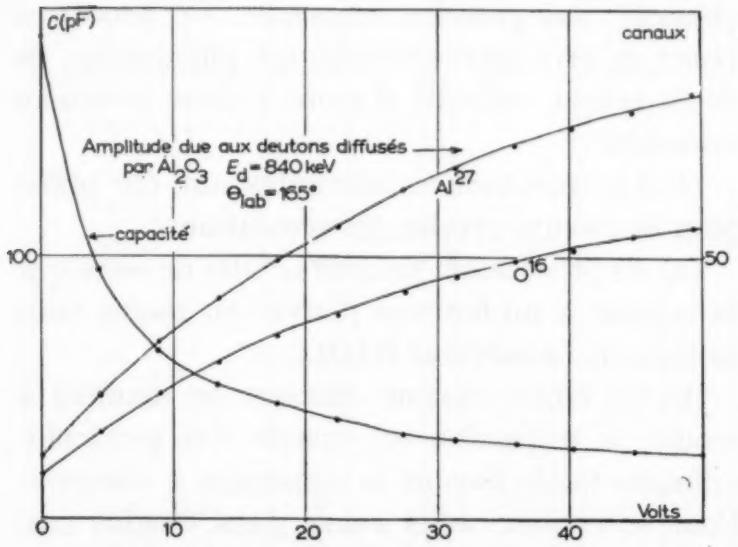

Fig. 10. Variation de la capacité du détecteur en fonction de la tension de polarisation.

(diffusés par O^{16} et Al^{27}) sont utilisés; tant que le quotient de deux amplitudes reste constant, les courbes reproduisent fidèlement les variations de C^{-1}. La figure 10 montre la courbe des amplitudes et la fonction $C(V)$ corrigée pour les capacités parasites; cette courbe peut se mettre sous la forme:

$$C_{pF} = 25\left(\frac{V}{45}\right)^{-0.6}.$$

Remarquons que C ne varie pas tout à fait comme l'inverse de l'épaisseur de la barrière. L'amplitude absolue est de 1.5 mV/MeV pour une polarisation de 45 V. La stabilité en amplitude à long terme n'est limitée que par l'amplificateur.

(b) Le rapport signal/bruit est élevé pour deux raisons:

le temps de montée est très court; le nombre moyen d'impulsions fortuites dues au bruit pendant la durée de l'impulsion est d'autant plus faible que celle-ci est plus courte.

La valeur de l'énergie de création des paires d'électron-trou est faible (10 fois plus petite que dans un compteur à gaz). L'erreur absolue sur la mesure de la charge recueillie étant limitée dans tous les cas à quelques centaines de charges électroniques, le rapport signal/bruit est 10 fois meilleur que pour un compteur à gaz.

Le bruit dû à la jonction elle-même n'intervient pas à condition que le courant inverse soit de l'ordre de quelques dixièmes de microampère (voir section 8). L'énergie minimum détectable était limitée dans notre cas par le bruit d'entrée du préamplificateur Ecko. Aucune précaution spéciale n'avait été prise pour rendre le bruit minimum, la détection de signaux équivalent à une énergie dissipée de 100 keV était cependant possible.

La dispersion en amplitude à mi-hauteur du pic, due au bruit de l'amplificateur équivaut à moins de 10 keV si on opère avec une polarisation suffisante, pour rendre la capacité du détecteur assez faible. Le bruit ne limite donc pas la surface utile du détecteur à 4 mm². L'augmentation de cette surface est un problème de technologie de semi-conducteurs.

(c) Si l'on connecte plusieurs détecteurs en parallèle, une particule d'énergie E pénétrant dans un quelconque des détecteurs, et arrêtée dans la barrière, provoque une impulsion d'amplitude proportionnelle à:

$$\frac{E}{\sum C_i}.$$

On peut ainsi utiliser plusieurs détecteurs avec une seule chaîne d'amplification et une polarisation commune. Ce montage peut être très utile pour l'étude de réactions fournissant un spectre simple.

Par exemple, la réaction O^{16} (d,α) N^{14}, fournit un seul groupe de particules α, dont l'énergie varie très rapidement avec l'angle d'observation. Des détecteurs décalés d'une trentaine de degrés, permettraient l'enregistrement simultané, par un analyseur d'impulsions, de spectres relatifs à plusieurs angles.

7. Résolution

(1) La dispersion statistique de l'amplitude des impulsions dues à une particule monocinétique arrêtée dans la barrière, est indépendante de l'énergie de la particule. C'est là une des propriétés fondamentales du détecteur à jonction. La largeur à mi-hauteur du pic exprimée en unités d'énergie est en moyenne de 30 keV pour les protons et les deutons, 40 keV pour les particules α.

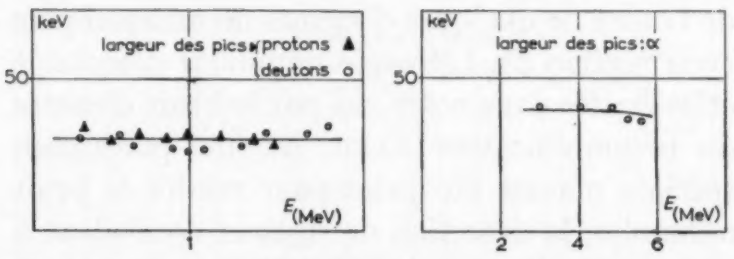

Fig. 11. Dispersion, évaluée en énergie, des impulsions dues à différentes particules.

La figure 11 montre les résultats pour les trois types de particules.

(2) Examinons les facteurs qui influent sur la dispersion en amplitude.

(a) La dispersion statistique sur le nombre de paires électron-trou créées est négligeable étant donné leur très grand nombre.

(b) Des irrégularités d'épaisseur de la zone insensible ne conduiraient pas à une largeur constante en fonction de l'énergie. Le phénomène observé, prouve au contraire que cette zone a une épaisseur bien constante.

(c) Le phénomène de dispersion statistique de l'énergie perdue dans la zone insensible ne conduit qu'à une dispersion de 9 keV pour les protons, faible devant les 30 keV observés.

(d) Le bruit électronique est inférieur à 10 keV, comme on l'a vu au chapître précédent.

(3) Nous avons ainsi conclu que les largeurs observées représentent une propriété intrinsèque du cristal. Ceci est confirmé par une mesure de Friedland *et al.*[5]) qui ont trouvé la même largeur que nous pour les particules α du polonium, avec des jonctions de type différent dont la zone insensible était bien plus faible.

Il est difficile d'expliquer pourquoi la dispersion est indépendante de l'énergie pour une particule de type donné. On peut néanmoins admettre que le phénomène qui provoque cette dispersion ne se manifeste que vers la fin du parcours de la particule. Il semblerait qu'au dessous d'une certaine vitesse, la particule peut céder de l'énergie au cristal par un processus autre que la création de paires d'électron-trou (ou créer des paires avec une énergie qui diffère localement de 3.25 eV). Quel que soit ce processus, il ne peut pas se répéter de nombreuses fois, sinon une forte dispersion ne pourrait pas prendre naissance. Ce processus pourrait être par exemple un phénomène de déplacement collectif d'atomes dans le réseau cristallin.

(4) Les précautions suivantes ont été prises pour la mesure précise des résolutions:

(a) les pics étaient toujours étalés de sorte que la largeur à mi-hauteur couvre au moins trois canaux de l'analyseur RIDL.

(b) les cibles étaient choisies de manière à rendre la dispersion en énergie des particules diffusées faible devant la dispersion à observer. Pour le vérifier, nous avons dans chaque cas, utilisé deux cibles, l'une ayant une épaisseur double de celle de l'autre. On constatait que les résultats fournis par les deux cibles étaient identiques.

Les diffusions élastiques ont été étudiées sur des cibles de Al^{27} de 7 $\mu g/cm^2$. Pour cette cible, la dispersion en énergie des deutons et des protons diffusés à l'arrière était inférieure à 6 keV.

Pour les réactions nucléaires, nous avons utilisé des cibles de Al_2O_3 de 17 $\mu g/cm^2$: la dispersion de l'énergie des particules α était également inférieure à 6 keV.

Notons que des cibles de Al de 30 μg déforment déjà notablement les spectres dus aux protons et deutons diffusés. En effet, le spectre d'énergie des particules diffusées est rectangulaire; sa largeur s'ajoute directement à la largeur observée, la loi de composition par le carré des largeurs n'étant pas appliquable dans ce cas.

(c) Toutes les réactions utilisées fournissent des particules dont l'énergie varie très rapidement en fonction de l'angle d'observation. L'ouverture angulaire du détecteur a été maintenue inférieure à 1.5°.

(d) Nous avons enfin constaté que la résolution baisse si les constantes d'intégration et de différentiation de l'amplificateur Ecko sont trop grandes. Nous avons choisi les deux constantes égales à 0.32 μs.

Ces précautions sont indispensables dans tout travail où l'on veut profiter au maximum des possibilités offertes par le détecteur.

Signalons que le taux de comptage peut

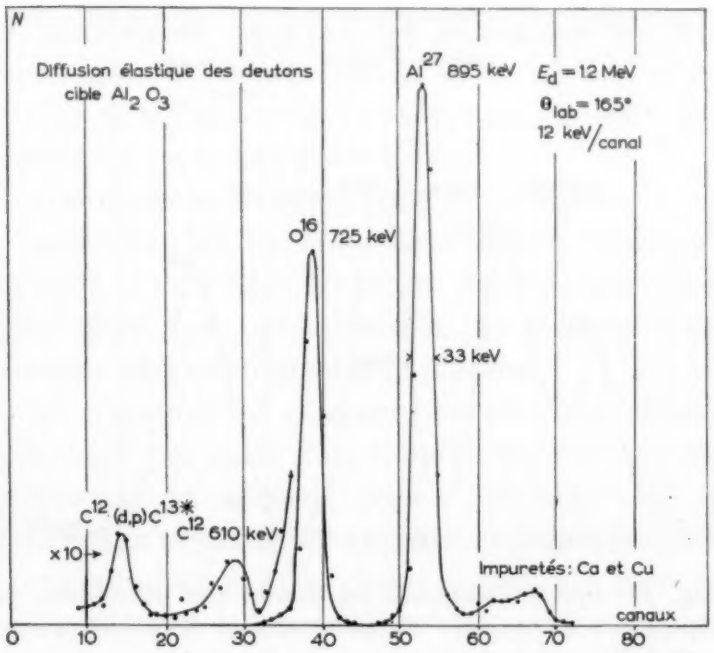

Fig. 12. Spectre des deutons diffusés élastiquement par une cible de Al_2O_3. Il faut remarquer que le carbone est inévitablement présent sur la cible, à l'état de contamination.

atteindre 10^4 c/s sans que la résolution soit diminuée.

(5) La forme des pics est sensiblement gaussienne. Pour réduire le nombre de coups en dehors des pics, nous avons utilisé un diaphragme en rubis d'horlogerie. Celui-ci présente plusieurs avantages:

les bords du trou sont parfaitement polis;

le diamètre du trou est connu au micron près ce qui facilite les mesures de section efficace absolue;

la diffusion coulombienne par les bords est faible, le rubis étant formé des noyaux légers Al^{27} et O^{16}.

Avec ce dispositif, le nombre de coups en dehors du pic était inférieur à 1% du total pour les particules α du polonium.

(6) Les figures 9, 12, 13, 14, 15 présentent quelques spectres caractéristiques. Tous ces spectres ont été enregistrés avec une cible de Al_2O_3 d'une épaisseur de 35 $\mu g/cm^2$.

La figure 12 montre un spectre de deutons diffusés élastiquement. Le petit pic double, au dessus du pic de Al, est attribué à des impuretés de masse voisine de celle de Ca et de Cu, présentes dans l'aluminium à raison de quelques $^0/_{00}$. Les protons de la réaction C^{12} (d,p_1) C^{13*}, d'une énergie de 440 keV sont également détectés.

La largeur des pics est un peu supérieure à 30 keV à cause de l'épaisseur de la cible.

La figure 13 montre un spectre de protons diffusés; l'écartement des groupes est ici bien plus faible. En pratique, on peut distinguer facilement deux groupes de protons séparés par 50 à 60 keV.

Le spectre complet dû à l'effet des deutons sur Al_2O_3 a été présenté figure 9. Pour enregistrer correctement un tel spectre en entier, il faudrait disposer de 300 ou 400 canaux. On voit que la résolution sur les protons est mauvaise: les particules qui pénètrent dans la zone de diffusion fournissent en effet un spectre mal résolu.

La figure 14 représente les nombreux pics dus à la réaction Al^{27} (d,α) Mg^{25}. On distingue les pics correspondant à 9 niveaux de Mg^{25}. Les pics apparaissaient plus larges qu'ils ne sont en réalité, le nombre des canaux étant insuffisant pour étudier en détail un spectre aussi étendu. Ainsi le doublet correspondant au niveaux excités 6 et 7 de Mg^{25} et les pics dus à la réaction O^{18} (d,α) N^{16} ne sont pas séparés (la section efficace de cette dernière réaction est si élevée qu'elle s'observe en dépit de la faible proportion de O^{18}, 0.2%, présent dans l'oxygène naturel). Observons que le pic dû à l'état fondamental de Mg^{25} est élargi à la base, en effet la particule α de 6.4 MeV, pénétrait légèrement dans la zone de diffusion.

La figure 15 illustre la limite des possibilités de séparation de groupes de particules α. Le détecteur a été placé à divers angles et les

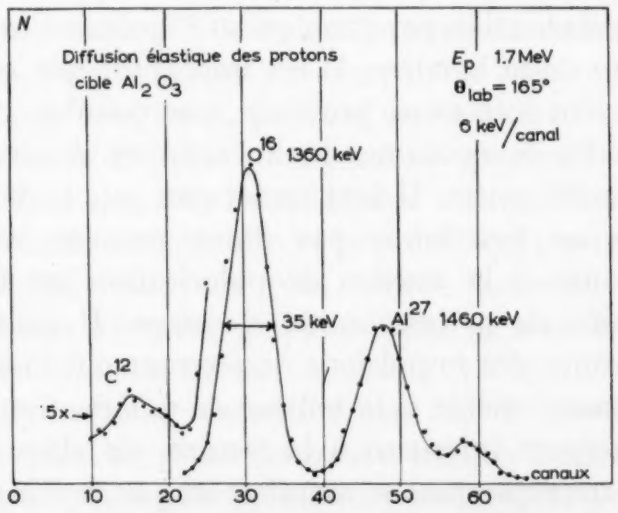

Fig. 13. Spectre des protons diffusés par une cible de Al_2O_3.

spectres enregistrés successivement, l'énergie de bombardement restant fixe. La séparation en énergie due au déplacement angulaire est portée

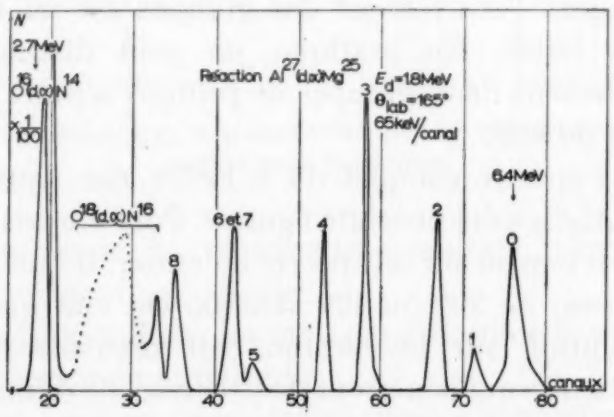

Fig. 14. Spectre complet de la réaction Al^{27} (d,α) Mg^{25}. Le pic dû à O^{16} est à une échelle 100 fois plus petite.

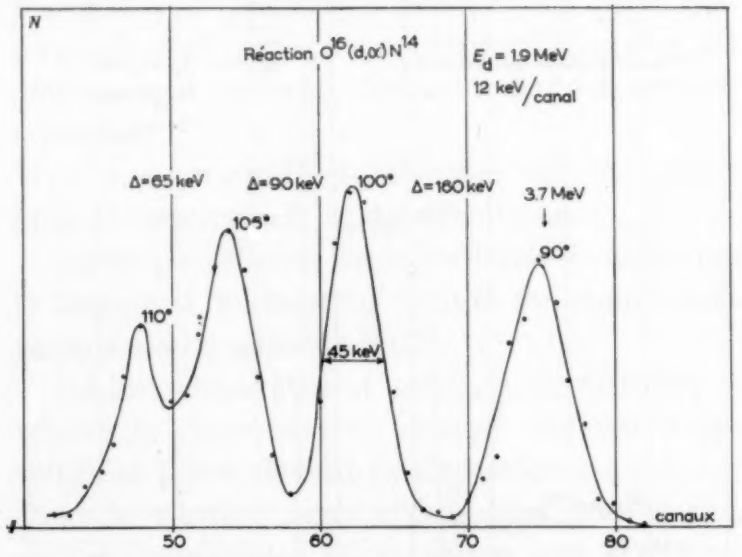

Fig. 15. Spectre illustrant les limites des possibilités de séparation de groupes de particules α. Il a été obtenu artificiellement à partir du groupe des particules α dues à la réaction O^{16}(d,α)N^{14}, en déplaçant angulairement le détecteur: les pics ont été enregistrés successivement sans effacer la mémoire de l'analyseur RIDL.

sur la figure. On voit que deux groupes dont les énergies diffèrent de 90 keV peuvent être complètement séparés. Deux groupes distants de 60 keV donnent deux pics qui sont encore aisément décomposables. Le spectre montre que l'ouverture angulaire doit être maintenue très faible pour cette réaction, si on veut éviter l'élargissement des raies.

8. Stabilité des Caractéristiques

Le détecteur est essentiellement constitué par une diode, polarisée en non conduction, dont deux caractéristiques électriques sont particulièrement importantes:

tension de claquage,
courant de saturation, ou courant inverse.

(a) La tension de claquage limite la tension de polarisation par conséquent l'épaisseur maximum de la barrière. Il est important que cette barrière soit aussi profonde que possible pour étendre le domaine de linéarité et rendre la capacité petite. Il faut remarquer que le détecteur ne fonctionne pas d'une manière satisfaisante si la tension de polarisation est trop voisine de la tension de claquage. Il peut se produire des impulsions de courant ou "microplasmas" même si la tension de polarisation est nettement inférieure à la tension de claquage. Ces microplasmas se manifestent par des impulsions qui augmentent en nombre et en amplitude lorsque la tension de polarisation croit. Un de nos détecteurs présentait ce phénomène pour une tension de l'ordre de 45 V alors que le coude de la caractéristique inverse se situait vers 70 V. Les microplasmas sont la conséquence de défauts accidentels dans la jonction: dislocations dans le cristal, non uniformité de la diffusion, etc. pouvant créer des petites zones où le champ électrique est plus élevé. Le phénomène des microplasmas a été étudié par D. G. Rose[6]). La tension de claquage varie selon les échantillons d'un même lot de fabrication. Par contre, pour une même jonction, elle apparaît stable au cours du bombardement.

(b) Le courant inverse détermine le bruit de la jonction. Ce bruit peut avoir différentes sources:

bruit thermique: faible dans le silicium;
bruit de surface: la jonction étant dans le vide, ce bruit est supprimé;
bruit de recombinaison-génération, analogue au bruit de grenaille, il croît très rapidement avec le courant inverse. Celui-ci doit être inférieur au microampère pour que le bruit de la jonction soit négligeable devant celui de l'amplificateur.

[6]) D. J. Rose, Phys. Rev. **105** (1957) 413.

Nous avons constaté que le courant inverse peut augmenter rapidement au cours de l'utilisation si les précautions suivantes ne sont pas prises; et pour lesquelles il faut:

maintenir la jonction dans la pénombre;

empêcher les électrons secondaires, émis par la cible, d'atteindre la surface du détecteur. Ceci peut être fait, par exemple au moyen d'un anneau de garde fortement polarisé.

Si toutefois le courant atteint une valeur excessive par suite d'un bombardement électronique de la surface, une "guérison" de la jonction s'obtient par exposition pendant quelques minutes à l'air. Nous avons attribué ce phénomène à la chimi-désorbtion de l'oxygène, accélérée sous vide par la lumière et le bombardement électronique.

Le bombardement par des particules lourdes pénétrantes provoque une lente augmentation du courant inverse; cependant la jonction est régénérée en quelques heures de repos. Cet effet est dû à l'introduction de défauts dans la masse. Néanmoins, un flux intégré de l'ordre de 10^{11} particules par cm^3 en 10 heures, ne provoque pas une augmentation gênante du courant inverse. Ceci permet de travailler avec des taux de comptage usuels en spectroscopie. Un de nos détecteurs a été soumis au bombardement pendant plus de 200 heures au cours de nos expériences, sans subir de dommages.

9. Applications

(1) Nous avons étudié la diffusion élastique des deutons par O^{16} et Al^{27} dans le domaine d'énergie de bombardement de 0.6 à 2 MeV. Cette expérience avait été primitivement abandonnée; aucun instrument pour la détection des deutons de faible énergie ne convenait pour la réaliser.

La figure 16 montre la courbe d'excitation de la diffusion élastique des deutons par O^{16} et de la réaction O^{16} (d,α) N^{14} tracées simultanément au cours d'une même expérience. Une telle courbe comporte 120 points et a pu être réalisée en une seule journée.

Une étude de distribution angulaire sur la réaction O^{16} (d,α) N^{14} est en cours avec un

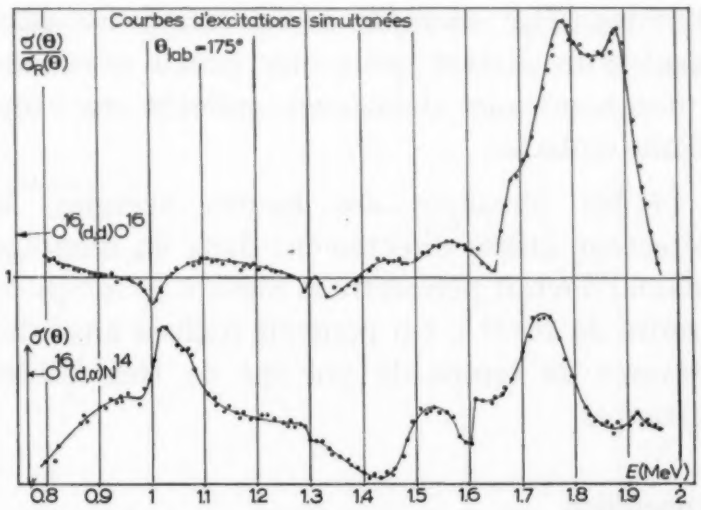

Fig. 16. Courbes d'excitations des deux réactions O^{16}(d,α)N^{14} et O^{16}(d,d)O^{16} tracées simultanément, au cours d'une seule journée de travail (chaque courbe comporte 120 points).

système de trois détecteurs utilisés en parallèle. Cette expérience continue un travail commencé avec des compteurs proportionnels, utilisés aux prix de grandes difficultés, vu la faible énergie des particules α (2.7 à 3.5 MeV).

L'étude de la réaction O^{18} (d,α) N^{16} est en préparation. Cette réaction produit 4 groupes de particules α séparés en moyenne de 90 keV. L'expérience apparaît possible à réaliser avec le nouveau détecteur.

(2) Envisageons quelques possibilités nouvelles du détecteur en physique nucléaire classique.

La diffusion élastique des deutons et des protons par les noyaux légers devient aisée à étudier. Des spectres de protons de faible énergie, provenant par exemple de réactions (d,p) de Q faible ou même négatif, peuvent être explorés en présence de protons énergiques, sans que le bruit de fond dû aux neutrons ou aux rayons γ ne masque le spectre. Des niveaux très serrés peuvent être explorés.

Des corrélations angulaires peuvent être étudiées avec des coïncidences très rapides, des durées de vie très brèves peuvent être mesurées.

Enfin, des ions plus lourds peuvent être détectés avec des jonctions dont la zone insensible est assez faible.

(3) Le faible encombrement du détecteur et son prix bas (pas de haute tension stabilisée, pas de photo-multiplicateur) permettent l'utilisation simultanée d'un très grand nombre

d'unités. Par exemple l'exploration du plan focal d'un aimant peut être prévu avec une "mosaïque" de détecteurs montés sur une même embase.

(4) En physique des hautes énergies, le détecteur utilisé directement dans un montage coaxial devrait permettre la mesure de temps de l'ordre de 10^{-10} s. On pourrait réaliser ainsi des mesures de temps de vol sur de très faibles distances.

Appendice

CALCUL DE L'EFFICACITE DE COLLECTION; LONGUEUR DE DIFFUSION

(1) Rappelons que la diffusion des porteurs libres dans une zone où le champ électrique est nul obéit à l'équation

$$D\Delta q = \frac{q}{\tau} + \frac{\partial q}{\partial t} \qquad (1)$$

où q est la densité de charge, D la constante de diffusion qui vaut 10 cm²/s pour le silicium et τ la durée de vie des porteurs. L'équation (1) n'est valable que si τ est constante dans la masse. Il résulte de (1) qu'en régime permanent, la densité de charge varie comme $e^{-x/L}$, x étant la distance à une source de charge ponctuelle. L est appelé longueur de diffusion et vaut: $L = \sqrt{D\tau}$.

(2) L'analyse de la courbe représentative de la charge totale recueillie, en fonction du parcours de la particule, permet le calcul de la longueur de diffusion. Le tracé de ces courbes a été effectué à l'aide d'un oscilloscope Tektronix 545 A; la jonction débitant sur une résistance de 400 kΩ, ce qui conduisait à une constante de temps de 12 μs. On était ainsi assuré de ne pas déformer les impulsions en amplitude, de sorte que celles-ci étaient proportionnelles à la charge totale recueillie.

(3) *Calcul de l'efficacité de collection*

(a) Pour établir une correspondance entre l'énergie et la profondeur de pénétration des particules dans la jonction, il faut connaître la relation parcours-énergie dans le silicium. Ces données ont été extraites de l'ouvrage de Wahling[7]) par interpolation entre les valeurs données pour Al et A. Indiquons qu'une expression analytique simple exprime le pouvoir d'arrêt du silicium pour des protons d'énergie comprise entre 0.25 et 5 MeV.

$$-\frac{dE}{dx}\, 10^{-15}\ \mathrm{eV/cm^2\ atome} = 8\, E_{\mathrm{MeV}}^{-0.63} = 23\, R^{-0.39}\,\mu .$$

Cette expression a servi aux calculs qui vont suivre.

(b) La fraction $f(x)$ de la charge $q(x)$ créée entre les profondeurs x et $x + dx$, qui est effectivement recueillie aux bornes de la jonction est appelée efficacité de collection. On suppose que $f(x)$ est indépendante de la densité de charges. Le but des mesures est la détermination de $f(x)$. Exprimons les amplitudes en unités de charge électrique et prenons comme variable non pas l'énergie E mais le parcours R de la particule incidente. Alors la charge totale recueillie $A(R)$ pour une particule de parcours R est:

$$A(R) = \int_0^R f(x)\cdot q(x,R)\, dx ,$$

$q(x,R)$ étant la charge produite par une particule de parcours R à la profondeur x. Or, $q(x,R)$ est de la forme $q\,(R - x)$, $R - x$ étant le parcours résiduel de la particule au point x. $q(x)$ est proportionnel à dE/dx. Donc

$$A(R) = \int_0^R f(x)\cdot q\,(R - x)\, dx = f * q\,. \qquad (2)$$

Ainsi A(R) est le produit de convolution de f et de q et se calcule aisément par transformation de Laplace. $A(R)$ étant obtenu par l'expérience et $q(x)$ étant une fonction connue, le calcul de $f(x)$ s'opère par inversion de l'équation intégrale (2). Dans notre cas (x) est de la forme x^{-p} et

$$A(R) \sim \int_0^R \frac{f(x)\, dx}{(R - x)^p}\,.$$

Cette équation est du "type d'Abel" et sa solution fournie par sa transformée de Laplace est

$$f(x) = \frac{\sin p\pi}{\pi} \int_0^x \frac{A'(t)\, dt}{(x - t)^{1-p}}\,. \qquad (3)$$

Cette expression simple a servi aux calculs numériques.

[7]) Ward Wahling, Handbuch der Physik, Vol. **34**, p. 202.

(c) Le calcul numérique de l'efficacité de collection a été effectué uniquement dans la zone de diffusion. On a admis que l'efficacité vaut 1 dans la barrière, dont les limites ont été déterminées comme indiqué section 5. Pour une tension de 45 V. nous avons trouvé que l'efficacité de collection peut se mettre sous la forme

$$f(r) = e^{-r/L} \quad \text{avec} \quad L = 60 \pm 5\mu\,,$$

r étant l'abscisse dans la zone de diffusion.

Ceci prouve que le silicium est bien homogène dans sa masse. En admettant que la constante de diffusion est 10 cm²/s, on trouve pour la durée de vie

$$\tau = \frac{L^2}{D} = 3.6 \pm 0.6\,\mu\text{s}\,.$$

La longueur de diffusion L calculée pour d'autres tensions de polarisation est sensiblement la même, comme il fallait s'y attendre.

La figure 17 représente l'efficacité de collection pour une polarisation de 45 V:

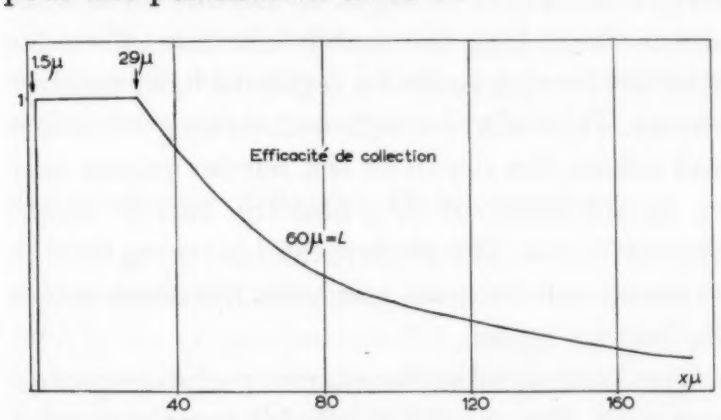

Fig. 17. Courbe représentative de l'efficacité de collection en fonction de la distance de la face d'entrée.

La figure 18 montre la courbe d'amplitude mesurée à 45 V et la courbe calculée avec l'efficacité de collection déterminée ci-dessus.

(d) Cette méthode est générale: elle permet l'étude directe des semiconducteurs, même non homogènes, en profondeur. L'équation (3) permet le calcul de la longueur de diffusion même quand elle varie dans la masse.

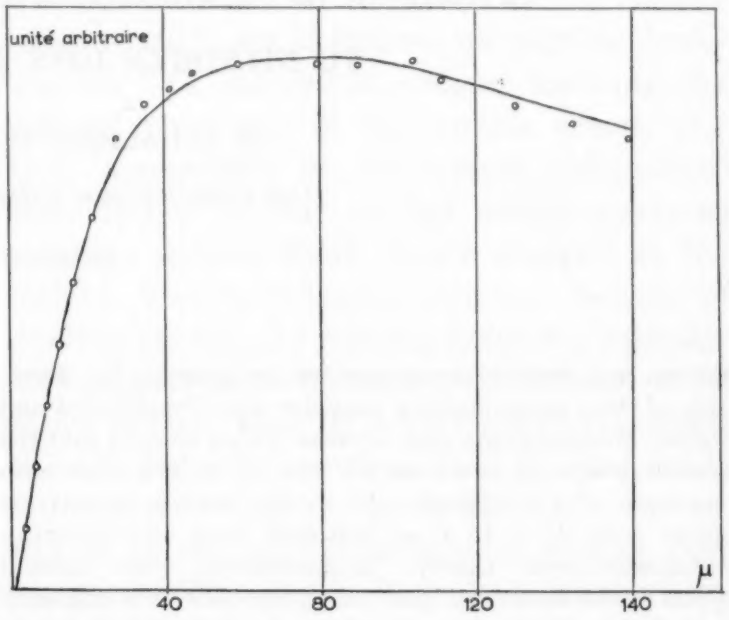

Fig. 18. Courbe théorique de l'amplitude calculée à partir de l'efficacité de collection représentée figure 17, et points expérimentaux. Nous avons porté en abscisse le parcours des particules, c'est la raison pour laquelle cette courbe ne présente pas de partie linéaire.

Remerciements

Nous remercions Monsieur le Professeur Y. Rocard qui a mis à notre disposition les facilités du Laboratoire de Physique de l'Ecole Normale Supérieure et Monsieur le Professeur H. Halban pour ses encouragements et ses conseils.

Nous remercions Monsieur G. Bishop pour ses conseils dans le domaine de la Physique Nucléaire.

Nous remercions Monsieur le Professeur P. Aigrain dont les conseils en matière de Physique du Solide nous ont apporté une aide importante pour la réussite de nos expériences.

Nous remercions la Compagnie LTT pour la réalisation des détecteurs ainsi que le Commissariat à l'Energie Atomique pour l'aide matérielle qu'il a bien voulu nous accorder.

NUCLEAR INSTRUMENTS AND METHODS **8** (1960) 106–116; NORTH-HOLLAND PUBLISHING CO.

RESPONSE OF SEMICONDUCTOR SURFACE-BARRIER COUNTERS TO NITROGEN IONS AND ALPHA PARTICLES

M. L. HALBERT and J. L. BLANKENSHIP

Oak Ridge National Laboratory†, Oak Ridge, Tennessee

Received 8 April 1960

Silicon and germanium surface-barrier counters for detection of short range ionizing particles were constructed and tested. Measurements with artificial pulses showed that the barrier height V_0 is about 0.6 volt in Si, and that with variation of the applied bias V, the barrier capacity is linear with $(V_0 + V)^{-\frac{1}{2}}$ as expected from the Schottky exhaustion-layer theory. Measurements with natural alpha particles showed that the charge-collection efficiency is probably 100%, the energy loss per electron-hole pair is 3.50 ± 0.05 eV in Si and 2.83 ± 0.03 eV in Ge, and the pulse-height resolution is outstandingly good. Two independent measurements with cyclotron-produced N^{14} ions up to 25 MeV showed that the pulse-height response is linear with energy. The ratio of N^{14} to alpha pulse height is equal to the energy ratio within 1%. The response to a continuous energy distribution of alpha particles indicates that the sensitive depth is on the order of 20 μ greater than the barrier depth calculated from the Schottky theory. The excess sensitive depth probably represents diffusion into the exhaustion layer of holes produced below it.

1. Introduction

In heavy-ion nuclear physics there has long existed a need for a detector with linear pulse-height response and good resolution. The development of surface-barrier counters by Mayer and Gossick[1]) and the extensive measurements on them by Walter *et al.*[2,3]) showed that these devices would probably be ideal detectors for short-range particles. These counters in many respects behave as thin solid-state ionization chambers. Aside from linearity and good resolution, the absence of windows, their compact size and short rise time, and their insensitivity to gamma rays, neutrons, and fast charged particles indicated that a program to make such counters for heavy-ion detectors would be well worthwhile. Additional advantages anticipated for these counters were their relative insensitivity to magnetic fields and the possibility of changing the depth of the sensitive region simply by varying an external bias.

The existence of an asymmetric potential barrier at the surface of a semiconductor is a well known phenomenon in semiconductor physics[4]). The barrier on the surface of an n-type crystal is thought to be due to surface states which trap the mobile electrons from the interior, leaving behind a region of fixed positive charge. Typically, for high-resistivity germanium and silicon the depth of the barrier region may be on the order of 10 μ and the barrier height about 0.6 volt. The electric field is strong enough to sweep out electrons and holes liberated within the barrier region.

The successful surface-barrier alpha spectrometer of Mayer and Gossick[1]) consisted of a

† Operated for the USAEC by Union Carbide Nuclear Company.

[1]) J. Mayer and B. Gossick, Rev. Sci. Instr. **27** (1956) 407; James W. Mayer, J. Appl. Phys. **30** (1959) 1937.

[2]) Walter, Dabbs, Roberts and Wright, Oak Ridge National Laboratory Report CF 58-11-99 (1958);
Walter, Dabbs and Roberts, Oak Ridge National Laboratory Report ORNL-2877 (1960).

[3]) Walter, Dabbs and Roberts, Bull. Am. Phys. Soc., Series II, **3** (1958) 181;
Walter, Roberts and Dabbs, Bull. Am. Phys. Soc., Series II, **3** (1958) 304;
Walter, Dabbs and Roberts, Bull Am. Phys. Soc., Series II, **5** (1960) 38.

[4]) J. Bardeen, Flow of Electrons and Holes in Semiconductors, Part 8, Chapter 4 of Handbook of Physics, edited by E. U. Condon and Hugh Odishaw (McGraw-Hill Book Company, Inc., New York, 1958), especially the section beginning on p. 8–60.

thin gold film deposited on n-type Ge. Large-area (up to one square inch) Au-Ge surface-barrier counters have been used by Walter *et al.* for detection of alpha particles and fission fragments[2,5]). Similar counters of smaller area were made by McKenzie and Bromley[6]) and used successfully for detection of protons and alphas.

Silicon counters have a great advantage over germanium in that they perform well at room temperature. For good resolution, Ge counters must be chilled to dry ice or liquid nitrogen temperatures. Considerable work on Si surface-barrier counters has been reported recently[7–10a]).

Successful high-resolution counters have also been made of p-type silicon[11–13]). These are analogous to the surface-barrier counters described here, except that hole-trapping sites are established at the surface by applying a hole-trapping material, usually phosphorus.

Other semiconductor devices have been used for detection of ionizing particles: point-contact germanium diodes[14]), p–n junctions in germanium[15,16]) and silicon[17]), and p–n–p transistors[18]). All of these devices have, however, very small sensitive area and are not well suited for energy measurements.

2. Calculation of Barrier Characteristics

In this section several approximate formulas are given for estimating barrier characteristics which are important in the design of particle detectors. They are based on the exhaustion-layer theory of Schottky[4]).

The origin of the trapping sites normally present on the semi-conductor surface and the factors controlling their density are not fully understood[19]). Fortunately, the barrier characteristics which are of interest for particle detection may be calculated without knowing the detailed properties of the surface states. The basic assumption of the simple exhaustion-layer theory is that all the mobile electrons within a certain depth D are trapped at the surface, leaving behind a uniform density of positive charge. By solving Poisson's equation with appropriate boundary conditions, it is easily shown that $D = (KV_0/2\pi eN)^{\frac{1}{2}}$, where K is the dielectric constant, V_0 is the magnitude of the barrier height, e is the electronic charge, and N is the excess density of donors over acceptors. The depth may be increased by applying a negative bias to the surface. If the magnitude of the bias is V, the depth D is then given by $[K\,(V_0 + V)/2\pi eN]^{\frac{1}{2}}$ or

$$D = 1051\sqrt{\frac{K\,(V_0 + V)}{N}}\ \text{cm} \qquad (1)$$

if potentials are in volts and N is in cm^{-3}.

For Ge and Si, $K = 16$ and 11.8, respectively[20]). The net impurity concentration N for n-type material may be estimated from the room temperature resistivity ρ and the relation $N = 1/\rho\mu_n e$; the electron mobility μ_n is 3900 cm^2/sec-volt for Ge and 1200 for Si[21]). In the counters that were made at this laboratory, N was in the range of 10^{12} to 10^{14} cm^{-3}.

[5]) Dabbs, Walter, Roberts and Parker, Bull. Am Phys. Soc., Series II, **5** (1960) 22.

[6]) J. M. McKenzie and D. A. Bromley, Phys. Rev. Letters **2** (1959) 303.

[7]) J. M. McKenzie and D. A. Bromley, Bull. Am. Phys. Soc., Series II, **4** (1959) 457.

[8]) E. Nordberg, Bull.Am. Phys. Soc., Series II, **4**(1959) 457.

[9]) Halbert, Blankenship and Goldman, Bull. Am. Phys. Soc., Series II, **5** (1960) 38.

[10]) J. L. Blankenship and C. J. Borkowski, Bull. Am. Phys. Soc., Series II, **5** (1960) 38; Proceedings of the Seventh Scintillation Counter Symposium, I. R. E. Transactions on Nuclear Science (to be published).

[10a]) G. Dearnaley and A. B. Whitehead, Harwell Report AERE-R-3278.

[11]) Friedland, Mayer and Wiggins, Nucleonics **18**, No. 2 (Feb. 1960) 54.

[12]) Miller, Brown, Donovan and Mackintosh, Proc. Seventh Scintillation Counter Symposium, I.R.E. Transactions on Nuclear Science (to be published).

[13]) R. W. Jackson, RCA Victor Research Laboratories, Montreal (private communication).

[14]) K. G. McKay, Phys. Rev. **76** (1949) 1537.

[15]) Orman, Fan, Goldsmith and Lark-Horowitz, Phys. Rev. **78** (1950) 646.

[16]) K. G. McKay, Phys. Rev. **84** (1951) 829.

[17]) K. G. McKay and K. B. McAfee, Phys. Rev. **91** (1953) 1079.

[18]) D. C. Brown and B. P. Faraday, Nuclear Instruments **1** (1957) 133.

[19]) Semiconductor Surface Physics, edited by R. H. Kingston (University of Pennsylvania Press, Philadelphia, 1957).

[20]) American Institute of Physics Handbook (McGraw Hill Book Company, Inc., New York, 1957), p. 5–132.

[21]) Reference 20, page 5–159.

The value of V_0 depends on the properties of the material and the temperature. For a Ge counter at 77° K, $V_0 \approx 0.6$ volt[2]). Measurements described below on a Si counter at room temperature gave $V_0 \approx 0.5$ volt. Other Si counters have shown $V_0 \approx 0.7$ to 0.8 volt.

The external bias V that may be applied varies considerably from one counter to another. An objectionable amount of noise is generated by some counters without any bias. However, the counters used in these measurements will tolerate an external bias of about 5 volts for Ge and 70 volts for Si without becoming excessively noisy.

The Si counter to be described has been operated with a barrier depth of about 30 μ (7.2 mg/cm^2) with no difficulty. It is possible to achieve much deeper barriers in higher-purity material.

The signal voltage appearing across the counter for a charge q collected by the barrier is $q/(C_b + C_s)$, where C_b is the capacity of the barrier and C_s is the stray capacity. For a surface barrier of area A, $C_b = KA/4\pi D$, or

$$C_b = 8.41 \times 10^{-5} A \sqrt{\frac{KN}{V_0 + V}} \text{ pF} \qquad (2)$$

if potentials are in volts, N in cm^{-3}, and A in cm^2. In this work C_b/A was typically on the order of several hundred picofarads/cm^2. The charge q collected for energy E dissipated in the sensitive region is given by

$$q = e \frac{E}{\varepsilon} \eta \qquad (3)$$

where ε is the average energy per electron-hole pair and η is the charge collection efficiency.

The published values of ε are about 3.0 eV in Ge[16]), and 3.6 eV in Si[17]). If we compare these figures with the typical value of $\varepsilon = 30$ eV for gases, it is clear that for the same capacity the surface barrier counter is capable of better resolution than a gas counter. In practice, because of the larger capacity of barriers of reasonable area, it has been difficult to surpass the best resolution that can be achieved with a carefully designed Frisch grid ionization chamber. Recently, however, this has been accomplished. Spectra of natural alpha particles have been obtained which show less than 0.3% full width at half maximum[10]).

3. Manufacture of Counters

Making surface-barrier counters is basically simple. Our procedure may be outlined as follows. Single-crystal material is cut into 1 mm-thick wafers of the desired area. The wafers are carefully lapped and a copper wire or foil is soldered to one face to make an ohmic contact with the body of the crystal. One can solder directly to Ge; for Si the surface is first nickel plated. The crystal is then cast in epoxy resin so that the other face is exposed. After further preparation of the surface, including etching in modified CP-4 (5 parts nitric acid, 3 parts hydrofluoric, and 3 parts glacial acetic acid), a semi-transparent layer of gold is evaporated onto the crystal and the surrounding resin to form an electrical connection with the surface barrier. A photograph of the various steps in the manufacture of a counter is shown in fig. 1. More detailed instructions on the manufacture of these counters are given by Blankenship and Borkowski[10]).

Extreme care must be taken in all steps to

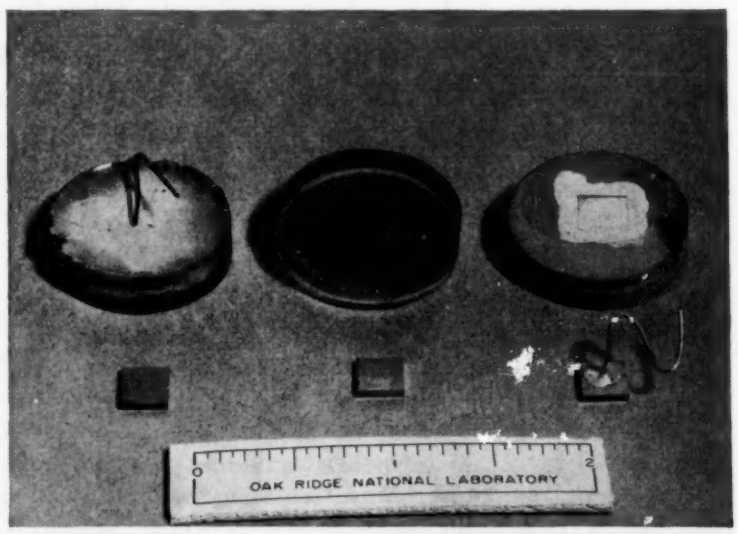

Fig. 1. Manufacture of silicon counters. From left to right in the foreground are 5 × 5 mm silicon wafers, first after being cut to shape and lapped; next, after nickel plating; and then after soldering a wire to the rear. In the background are shown the rear of a counter after casting in epoxy resin; the front of a counter after the final lapping; and a completed counter after etching, masking with polystyrene, and evaporation of the gold film.

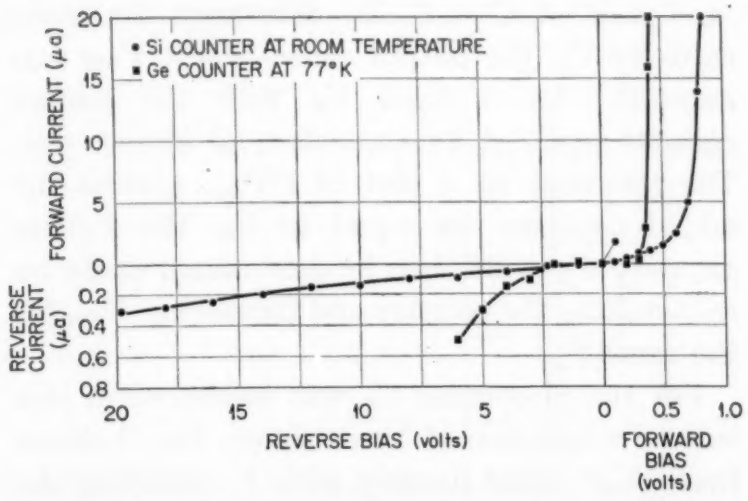

Fig. 2. Current-voltage characteristics of the counters used in this work.

achieve a high proportion of successful counters. Assuming that the surface has been carefully prepared so that it is free of irregularities which would degrade the resolution, the major problem is to keep the noise level as low as possible. It appears that selection of highly perfect crystals, meticulous cleanliness, and thorough, rinsing after etching are important.

The measurements to be described here were made with two of the first successful counters. The Ge counter was made of 40 ohm-cm material and the Si counter of 50 ohm-cm material. The exposed surface of each was a 5 × 5 mm square. The effective area was actually smaller, probably $\frac{1}{6}$ cm², because a layer of polystyrene, intended to minimize leakage, was applied around the edge of the embedded wafer before evaporation of the gold. The polystyrene is evident in the photograph. The thickness of gold on the Si counter was sufficient to cut transmission of white light approximately 50%. By neutron activation analysis, the gold film was found to be about 150 μg/cm². The gold on the Ge was of similar thickness but its thickness was not measured.

4. Testing of Barriers

A rapid qualitative test of a counter may be made by measuring its current-voltage characteristic. Fig. 2 shows a portion of the characteristic for the two counters used in this work. It was generally found that the counters with the smallest reverse current have the lowest noise levels. However, no quantitative relationship between reverse current and noise level could be established. For example, the Si counter at 0.6 μA reverse current showed no increase in noise above that generated by the electronics, but for the same current the Ge counter was so noisy that the pulse-height resolution was markedly degraded.

A low-noise preamplifier with gain 1000 was designed especially for this type of counter. It has a cascode input with a 5842/417 A high-performance triode and uses the large capacity at the input to keep the grid-current noise low. The equivalent noise at the input is about 5 μV rms.

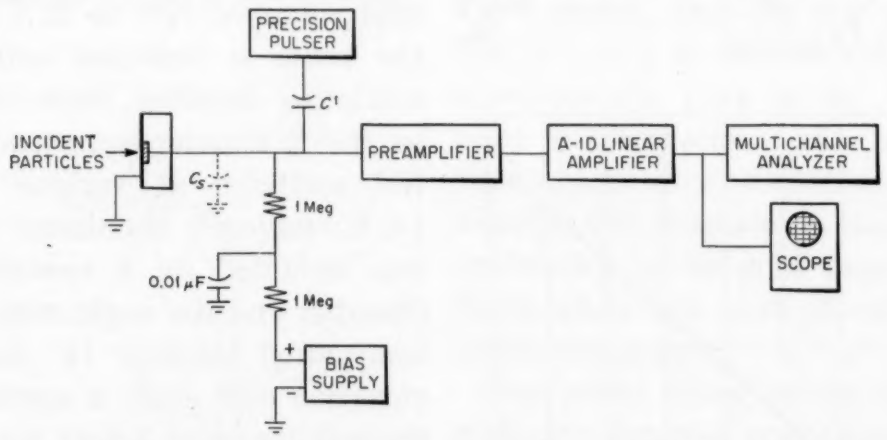

Fig. 3. Schematic diagram of electronics, showing connections to the preamplifier, bias supply, and test pulser. The capacitor C' was approximately one picofarad.

(In normal operation the signal from the Si counter is about 400 μV/MeV.) The preamplifier was connected by about 200 feet of coaxial cable to an A-1D linear amplifier with delay-line clipping. The clipping time was normally 1.0 μsec, ample to collect all the charge carriers

liberated within the barrier region. Since the preamplifier gain was so high the amplifier was modified to provide increased inverse feedback in both loops. The amplifier output went to a 256-channel pulse height analyzer.

Fig. 3 shows how the counters were connected. The gold surface was grounded and positive bias applied to the back. This gave negative signal pulses. One can equally well ground the back and put a negative bias on the front, giving positive pulses. There may be a slight disadvantage in the latter arrangement since dust might be attracted to the front surface.

The bias voltage was supplied by a battery through an RC filter network. The upper one-megohm resistor served also to determine the decay time of the pulses since the back resistance of the barrier is usually much greater.

Test pulses were put on the counter through the capacitor C' (≈ 1 pF in the present work). The linearity of the entire system was checked by using a highly stable mercury-relay pulse generator having an output attenuator linear to 0.1%. The pulser was very useful for measuring barrier characteristics as well. If the pulse amplitude is V_p and C is the total capacity to ground, the signal V_s at the preamplifier input is given by

$$V_s = V_p \frac{C'}{C + C'} \tag{4}$$

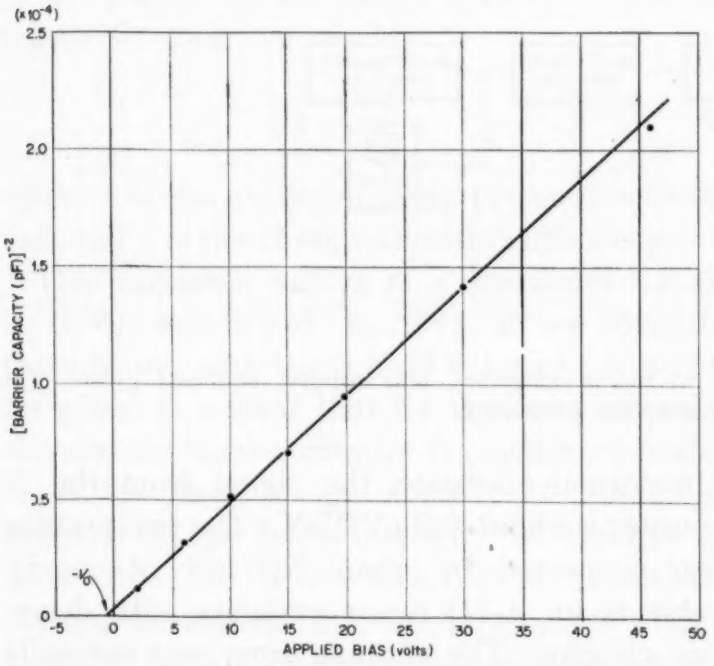

Fig. 4. Experimental check of eq. (2) for the Si counter.

or V_pC'/C if $C' \ll C$. To determine the stray capacity C_s, the output pulse height V_{out} was measured for a fixed V_p with the barrier counter replaced by capacitors of known size. The intercept on a plot of $1/V_{out}$ against the added capacity wa equal to C_s. The barrier capacity C_b could then be determined easily by re-installing the counter and measuring V_{out} for the same V_p.

For the Si counter C_b was measured in this way as a function of bias voltage. Fig. 4 shows that $1/C_b^2$ varies linearly with V, verifying the prediction of the Schottky theory (eq. (2)). The intercept gives $V_0 = 0.5 \pm 0.1$ volt. The slope of the line, assuming $K = 11.8$ and $A = \frac{1}{6}$ cm^2, gives $N = 0.90 \times 10^{14}$ cm^{-3}. This agrees, within the expected errors, with $N = 1.04 \times 10^{14}$ cm^{-3}, as calculated from the manufacturer's specification of the resistivity. The capacity of the Ge counter was measured at one bias voltage, giving $N = 0.36 \times 10^{14}$ cm^{-3}. This is also in satisfactory agreement with the value 0.41×10^{14} from the nominal value of the resistivity.

5. Measurements with N^{14} Ions and Alpha Particles

5.1. EXPERIMENTAL DETAILS

The Oak Ridge 63-Inch Cyclotron accelerates triply-charged N^{14} to 27.7 MeV. A portion of the beam is deflected and passes through a scattering chamber. Some of the measurements on the Si counter were made by detecting the N^{14} scattered at various angles by a thin (≈ 0.2 mg/cm^2) aluminum target. The counter was mounted on a movable arm inside the chamber and the angle with the incident beam was varied between 13° and 58°. The energy variation with angle is appreciable; in this way the relative pulse height for N^{14} from about 15 to 25 MeV was determined quite accurately.

Data were also obtained for both the Ge and Si counters over a wider range of energies by degrading the beam energy with nickel absorbers of known thickness. For these measurements the Al target was removed so that the beam passed undisturbed through the scattering chamber. A foil changer was placed at the exit port and

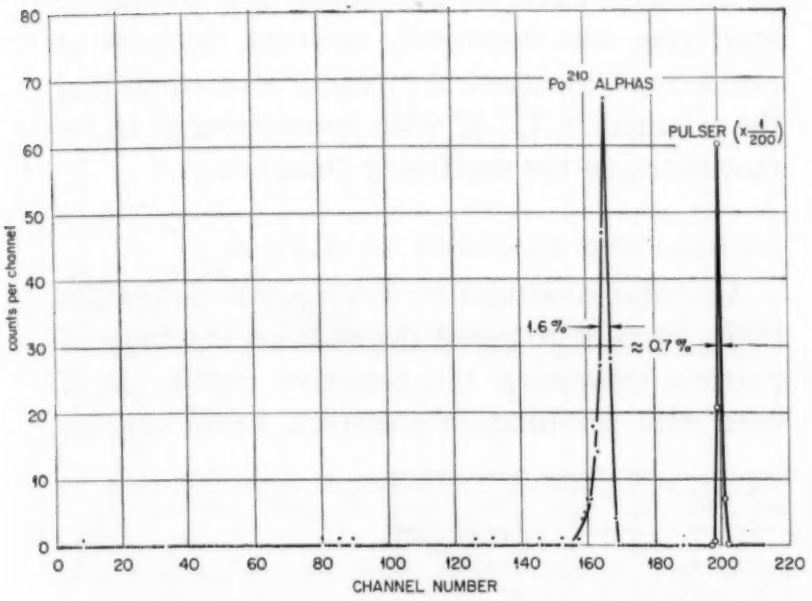

Fig. 5. Pulse-height spectrum of Po^{210} alphas. Si counter, 19 volts bias.

beyond it a 0.2 mg/cm² target of gold leaf oriented at 45° to the beam direction. Nitrogen ions from the cyclotron traversed the Ni absorber, were scattered through 90°, and passed through the target to the counter under test. The counter was mounted on re-entrant cylinder which was filled with liquid nitrogen when the Ge counter was being tested. Near the counter was a weak polonium-210 source. The angular spread of the incident particles was limited by a $\frac{3}{32}$-inch diameter collimator placed on the counter.

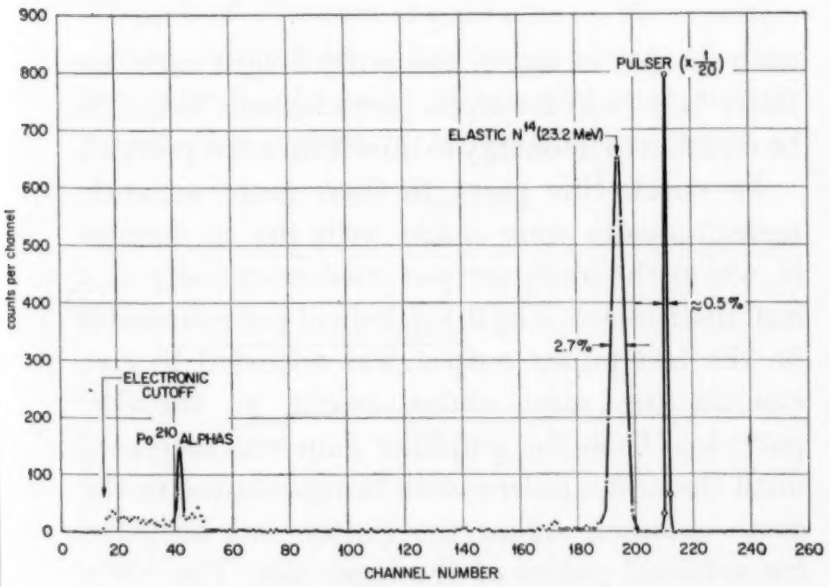

Fig. 6. Pulse-height spectrum of N^{14} ions scattered from gold. Si counter, 19 volts bias.

[22]) Reynolds, Scott and Zucker, Phys. Rev **95** (1954) 671.

Fig. 5 shows a spectrum of alpha particles from the Po^{210} source taken with the Si counter at 19 volts bias. The pulser was operating simultaneously; the cyclotron was off. The full width at half maximum, 1.6%, is actually quite poor compared with what has been obtained (0.3%) with more recently manufactured counters and a lower-noise preamplifier[10]). Nevertheless, it is interesting that even for this counter the resolution approaches the limit set by the signal-to-noise ratio, as indicated by the width of the pulser peak. The noise generated by the counter itself was always negligible compared with the electronic noise.

Unlike the Si counter, the Ge counter often exhibited changes in pulse height and noise level from day to day, though for any one set of data the results were consistent. This may have been due to disturbances caused by the frequent cycling between room temperature and liquid nitrogen temperature. Operated at 77° K and 5 volts bias, the Ge counter gave 2.0% resolution on several occasions. This counter did generate appreciable noise; at best, the noise level at 5 volts was about 20% higher than at 0 volts.

A typical beam-on spectrum for the Si counter at 19 volts bias with no absorber in the beam is shown in fig. 6. The peaks for the elastic N^{14}, Po^{210} alphas, and the test pulser are evident. The N^{14} peak is considerably broader than the alpha-particle peak of fig. 5. From signal-to-noise considerations the opposite would be expected. It may be concluded that most of the width is due to spread in the beam energy, non-uniformity in the gold target, straggling, etc. When absorbers were placed in the beam, the width was greater.

The initial beam energy was determined by replacing the gold scattering apparatus with a hydrogen gas target. Protons recoiling in the forward direction were stopped in nuclear emulsions and their track length was measured. This method has been used previously[22]). The energy after the beam passed through the various Ni absorbers could be determined to an accuracy of about $\pm$ 1 MeV from the experimental range curve by Reynolds, Scott and Zucker[22]).

The fringing field of the cyclotron was about 80 gauss where the counters were located. No magnetic shielding was provided for them. The preamplifier, placed in a region of much stronger field, was shielded. The pulse height dropped about 2.5% when the magnetic field was turned on. Since the same shift was observed for both alphas and test pulses, it is probable that imperfect shielding of the preamplifier was responsible, and the counter itself is insensitive to a magnetic field of this strength.

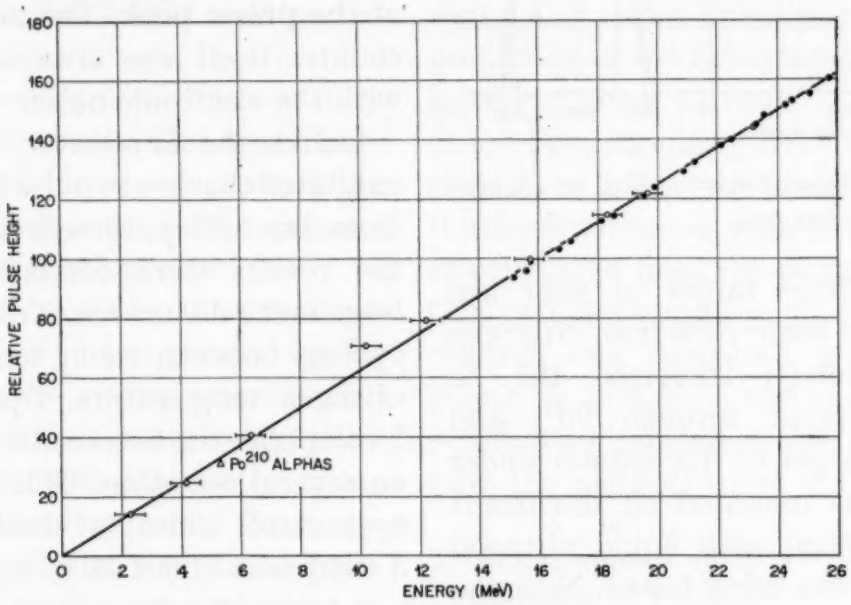

Fig. 7. Relative pulse-height response of the Si counter to N^{14} ions and to Po^{210} alpha particles. For the solid dots, the N^{14} was scattered by a thin Al foil; the energy variation was accomplished by changing the angle of scattering, and the bias was 45 volts. For the open circles, the N^{14} was scattered at 90° by a gold foil; the energy was varied by degrading the incident beam energy with nickel absorbers, and the bias was 19 volts. The error bars are estimates of the uncertainty in the range-energy relation used to convert absorber thickness to energy loss.

5.2. RESPONSE TO N^{14} IONS

Fig. 7 shows all the data on the response of the Si counter for N^{14}. For the open circles the energy variation was accomplished by degradation in Ni absorbers; the bias was 19 volts. The solid dots are based on the scattering of N^{14} by Al at various angles; for these points the counter was operated at 45 volts. The response to N^{14} appears to be linear. As a check of the linearity, the ratio of pulse height to energy was calculated for all the solid dots; the rms deviation from the mean ratio is only 0.5%, which is comparable with the errors in locating the peak positions and the uncertainty in energy loss as the N^{14} passes through the target.

A similar curve, obtained for the Ge counter at 1.6 volts bias, is also linear. No aluminum scattering was measured, however, because of the difficult mechanical problem of maintaining the counter at 77° K while permitting it to be moved inside the scattering chamber.

5.3. RELATIVE RESPONSE TO ALPHAS

A careful investigation was made to determine if the counter response depends on the type of particle traversing the sensitive region, as it does with scintillation counters. From spectra such as that of fig. 6, the pulse-height ratio for the N^{14} ions and the alpha particles was found to be equal to their energy ratio within a few percent.

To check this point further, more accurate measurements were made with the Si counter in which the analyzer was used essentially as a null instrument. The 0.1% helical potentiometer on the test pulser output was adjusted to give exactly the same pulse height as the N^{14} particles. Then the amplifier gain was increased until the alpha pulses were being counted in the same channel. Again the pulser was adjusted for artificial pulses of the same size. The N^{14}/α pulse-height ratio was thus equal to the attenuation ratio. The results with this method are probably accurate to about $\frac{1}{2}$%.

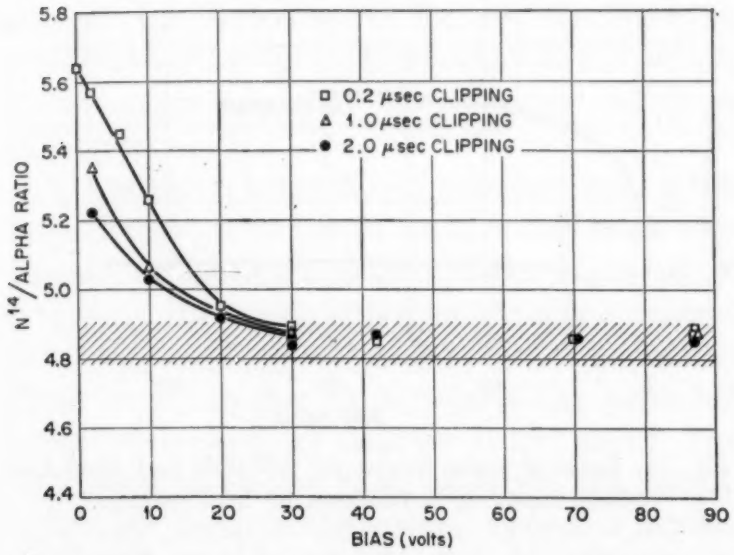

Fig. 8. Ratio of pulse height for N^{14} ions and Po^{210} alpha particles as a function of bias voltage and amplifier clipping time. The diagonal lines represent the measured energy ratio and its limits of error.

Two independent sets of measurements were carried out, one with N^{14} scattered through 90° by Au and the other with N^{14} scattered through 20° by an Al foil. The length of the delay line used for clipping was also varied in the latter runs to see how the ion collection time affected the N^{14}/α ratio. The Al data are shown in fig. 8. For comparison, the energy ratio with its estimated uncertainty (4.83 ± 0.06) is given as a row of diagonal lines. This energy ratio includes a correction for energy loss of the N^{14} in the scattering foil and for both particles in the 150 $\mu g/cm^2$ evaporated gold film on the counter.

It is evident from fig. 8 that above 40 volts the pulse-height ratio equals the energy ratio within the accuracy to which the latter is known. The same result was found for the data obtained by scattering from the Au target. The behavior of the pulse-height ratio at low bias may be explained qualitatively. The alphas have a longer range than the N^{14} ions. As the barrier depth is reduced the N^{14}/α pulse-height ratio should therefore increase. The curves for different clipping times indicate that with longer collection time more of the holes produced below the exhaustion region can contribute to the pulse height.

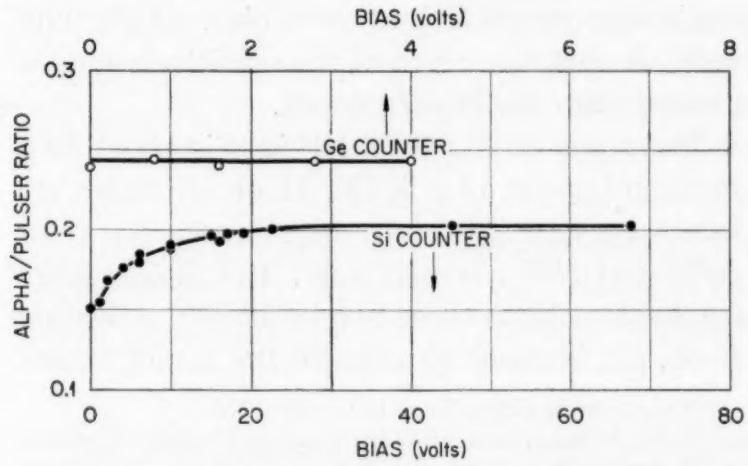

Fig. 9. Ratio of pulse height for Po^{210} alpha particles and fixed test pulser input as a function of bias voltage.

5.4. DETERMINATION OF ε

The pulse height for particles of a given energy increases as the bias is raised. Several effects are reasponsible. First of all, C_b decreases according to eq. (2). Second, if $\eta < 1$, then raising the bias would tend to increase η and also the pulse height. Third, there will be an increase in the pulse height if the depth of the sensitive region at the initial bias is not great enough to stop the particles.

It is of interest to study the latter two effects because of their importance for precise energy measurements. This necessitates eliminating the effect of the variation in C_b, which may be easily done by taking the ratio of pulse height for the particles and for a fixed pulser signal. The ratio for the alpha particle data (from spectra such as that in fig. 5), is given for both counters in fig. 9 as a function of bias voltage. The ratio does not increase in the Ge counter as the bias is raised. This indicates that $\eta = 1$. The same behavior is seen at high bias with the Si counter. The variation at low bias is understandable if the range of the alphas exceeds the sensitive depth at low bias.

Taking $\eta = 1$ in the level portion of each curve, it is possible from eqs. (3) and (4) to calculate the magnitude of ε for each counter. The numbers obtained from these curves are $\varepsilon_{Si} = 3.3 \pm 0.3$ eV and $\varepsilon_{Ge} = 2.8 \pm 0.3$ eV, in agreement with McKay's values of 3.6 ± 0.3 and 3.0 ± 0.3, respectively. The error is due principally to uncertainty in the capacity C'. The ratio $\varepsilon_{Si}/\varepsilon_{Ge}$ from these data is more accurate since it does not depend on C'. It

equals 1.20 ± 0.05, in excellent agreement with the ratio of McKay's values. From more precise work with other counters, the values of ε obtained were 3.50 ± 0.05 eV for Si and 2.83 ± 0.03 eV for Ge.

Fig. 10 shows the ratio of pulse height for the N^{14} ions (23.2 MeV in counter) to the pulse height for the same pulser input as in fig. 9. The Si counter shows a long plateau beginning at 19 volts. It appears, however, that collection is incomplete for the Ge counter, at least below 4 volts bias. The higher ionization density and lower electric field in the Ge barrier may account for the difference in behavior between the Ge and Si. The data above 19 volts for the Si counter and at 4 volts for the Ge counter give $\varepsilon_{Si}/\varepsilon_{Ge} = 1.23$. This is in agreement with the ratio obtained with the Po^{210} alphas, indicating that $\eta \approx 1$ for the Ge counter at 4 volts.

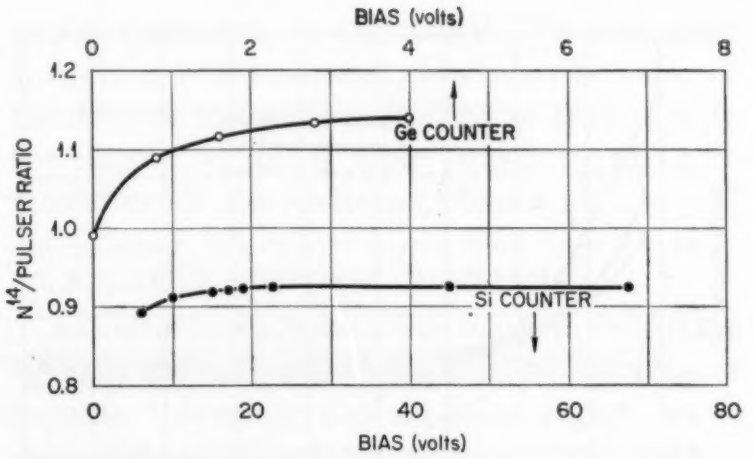

Fig. 10. Ratio of pulse height for N^{14} ions and fixed test pulser input as a function of bias voltage.

for the Si and ≈ 7 volts for the Ge. The ratio plotted in fig. 9 should be expected to increase at first and then become level. This behavior was observed for the Si counter, but the plateau begins at a considerably lower bias than the predicted 70 volts. The Ge points form a plateau

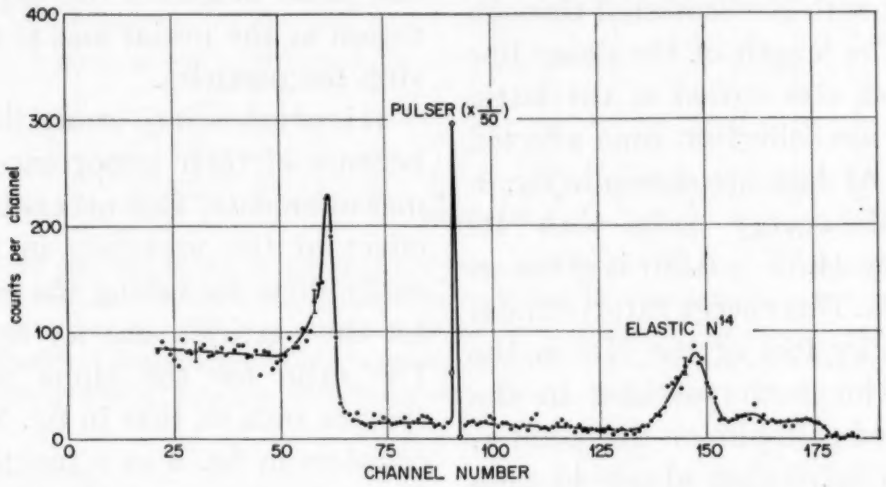

Fig. 11. Pulse-height spectrum of particles from N^{14} bombardment of carbon. Si counter, 45 volts bias.

5.5. SENSITIVE DEPTH

The data of figs 9 and 10 may also be used to estimate the sensitive depth of the counters. The range of 5.3-MeV alphas is about 31 μ in Si and 19 μ in Ge. These numbers were obtained as follows. For silicon, the ratio of alpha range in Si to that in Al was calculated from the data of Gobeli[23]) and multiplied by the range in Al interpolated from Whaling's tabulation[24]). For germanium, Gobeli's ratio of Ge to Cu range was multiplied by Whaling's value for the Cu range.

The barrier depth D according to eq. (1) is equal to the alpha range if $V_0 + V \approx 70$ volts beginning practically at zero bias. These data indicate that the depth of the sensitive region is greater than the barrier depth.

The range of 23.2-MeV N^{14} ions is about 19 μ in Si and about 12 μ in Ge. These estimates are based on experimental range-energy data for Al^{25}) and Ni^{22}), respectively. The bias voltage needed to achieve these barrier depths, according to eq. (1), is about 30 volts for the Si and 2 volts

[23]) G. Gobeli, Phys. Rev. **103** (1956) 275.

[24]) W. Whaling, The Energy Loss of Charged Particles in Matter, in Handbuch der Physik, edited by S. Flügge Vol. **34** (Springer-Verlag, Berlin, 1958) p. 193.

[25]) Webb, Reynolds and Zucker, Phys. Rev. **102** (1956) 749.

for the Ge. Referring to fig. 10, the Si curve levels off well before the predicted bias is reached, again suggesting that the sensitive depth is greater than D.

A somewhat more direct measurement of the sensitive depth in the Si counter was made as a byproduct of another experiment intended to study the scattering of N^{14} by C^{12}. Fig. 11 shows a typical spectrum at 45 volts bias. The peak in channel 147 is due to N^{14} elastically scattered from C^{12} (energy in counter = 15.7 MeV). The resolution is poorer than with the Au target, probably because the carbon target is thicker and less uniform, and the energy in the counter is smaller. In the low channels a continuum may be seen which rises and then drops sharply. This continuum is probably due to the continuous distribution of alpha particles produced by nuclear reactions in the target. The peak corresponds to the maximum alpha particle energy that can be lost in the counter, and is due to alphas of range equal to the depth of the sensitive region. A series of similar spectra was obtained as a function of bias voltage for three choices of amplifier clipping time. Alphas from the Po^{210} source established the energy scale. The cutoff energies were calculated and then the corresponding alpha ranges estimated from the range in Al as previously described.

As shown in fig. 12, the sensitive depth determined in this way is greater than the calculated depth and increases with increasing clipping time. This result may be a consequence of the diffusion of holes produced below the exhaustion layer. If a pulse of charge carriers is introduced into a field-free region, the pulse quickly assumes a Gaussian shape which spreads with the passage of time[26]). The characteristic width is given by $\sqrt{D_p t}$. Here t is the time after injection and D_p is the diffusion constant. The latter may be calculated from the relation $D_p = \mu_p kT/e$ where μ_p is the hole mobility,

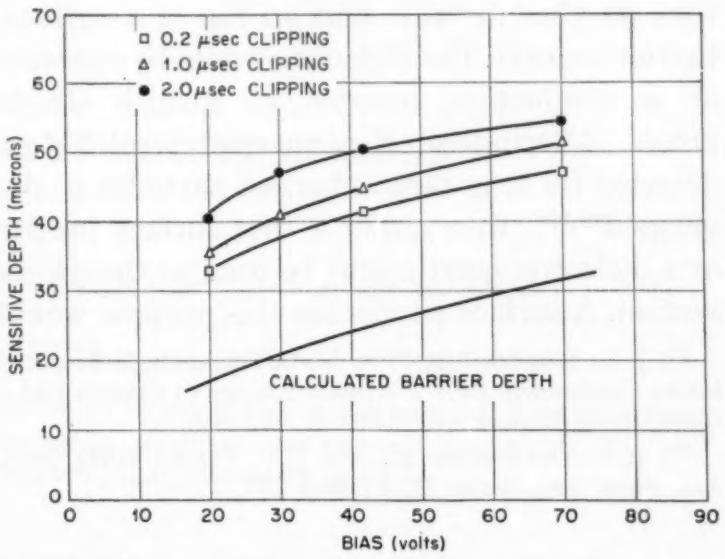

Fig. 12. Sensitive depth as a function of bias and amplifier clipping time.

k = Boltzmann's constant, and T = absolute temperature[27]). In the present problem, concerning holes diffusing through silicon at room temperature, $D_p \approx 10$ cm²/sec. For the clipping times used in these measurements, $\sqrt{D_p t}$ varies between 15 and 45 μ. Although no quantitative estimate of the excess sensitive depth has been made, it ought to be of the same order of magnitude. The measured values of the excess depth are approximately 15, 20, and 25 μ for amplifier clipping times of 0.2, 1.0 and 2.0 μsec, respectively. It is therefore concluded that the data show qualitatively the effect of diffusion into the exhaustion region of holes produced below it.

6. Further Remarks

Surface-barrier counters probably will be of great value in detection of high energy heavy ions. For example, 160-MeV O^{16} ions have a range of approximately 46 mg/cm² Al[28]), corresponding to about 200 μ of silicon. A counter with this great a barrier depth was recently made of 3600 ohm-cm n-type silicon. The pulse-height resolution with such energetic particles should of course be extremely good.

A solid-state particle-selective spectrometer would be a very useful device. Several schemes are possible using the well-known dE/dx, E method. For short-range particles, it may be possible to deposit a thin dielectric layer and

[26]) W. Shockley, Electrons and Holes in Semiconductors (D. Van Nostrand Company, Inc., New York, 1950) p. 350.

[27]) Transistor Teachers Summer School, Phys. Rev. 88 (1952) 1368.

[28]) L. C. Northcliffe (private communication).

then another metallic film on top of a surface-barrier counter. The dielectric would be operated as a conduction counter to furnish dE/dx pulses. Alternately, if a successful solid-state detector for long-range charged particles is developed[29,30]), then either a thin surface barrier or a dielectric layer might be used as the dE/dx section. A surface barrier for this purpose would have a great advantage: its thickness could be easily adjusted to suit experimental requirements.

[29]) J. L. Blankenship, Proc. Sixth Tripartite Instrumentation Conference, Part 5, Atomic Energy of Canada Ltd.,, Chalk River Report AECL-805, p. 75 (1959).

[30]) J. D. Van Putten, Jr., and J. C. Vander Velde, Bull. Am. Phys. Soc., Series II, 5 (1960) 197.

Acknowledgements

We wish to thank C. E. Ryan and M. V. Goldman for the manufacture of the counters, E. E. Fairstein for the design of the special preamplifier, G. W. Leddicotte for the activation analysis of the evaporated gold film, G. A. Palmer for assistance in taking data, and W. L. Brown, F. J. Walter, and A. Zucker for helpful discussions.

NUCLEAR INSTRUMENTS AND METHODS 8 (1960) 117–120; NORTH-HOLLAND PUBLISHING CO.

A STABILIZING SYSTEM FOR A 700 kV CASCADE GENERATOR

J. C. TIEMEYER

Scientific Equipment Division of N.V. Philips' Gloeilampenfabrieken Eindhoven, The Netherlands

Received 22 April 1960

A 700 kV 4-stage cascade generator in open air driving an ion accelerating tube with a beam current of 1.2 mA, was stabilized by a double-loop feedback system. A stability of the high voltage of 0.03% per hour with a maximum deviation of 0.1% was noted on the measuring potentiometer. The energy resolution was found to be approx. 100 eV by measuring (p,γ) resonances in Al^{27}.

1. Introduction

In some forms of nuclear research and measurements, accelerated ions of accurately defined energy are frequently used. These ions are often produced in a H.T. accelerator in which the ions traverse a potential difference in an evacuated tube.

In the installation in question the potential difference is produced by a 4-stage cascade generator with selenium rectifiers. The generator is supplied with 500 c/s, by a 10 kVA converter via a H.T. transformer.

Without special precautions the output voltage of a cascade generator shows some minor variations. The slow components up to a frequency of approx. 0.1 c/s may run up to 5% of the output voltage and originate from:

(a) mains-voltage variations,

(b) warming-up of the generator,

(c) slow load variations.

The fast components amount to 1% of the output voltage and originate from:

(d) the load ripple, i.e. 500 c/s and 1500 c/s (3rd harmonic),

(e) fast load fluctuations, e.g. corona effects.

Owing to these H.T. variations the accelerated particles have a certain energy dispersion. Measurement of and research on nuclear reactions occurring at a critical energy level, (nuclear resonances) is greatly hampered or even prevented by this dispersion.

For this reason, limitation of the energy dispersion in the accelerated particles by means of the best possible stabilization is desirable and increases the useful scope of the accelerator.

2. Stabilization with a Double-Loop Feedback System

The H.T. can be stabilized by feedback of the H.T. variations via the exciting winding of the converter at the 500 c/s supply voltage of the cascade generator.

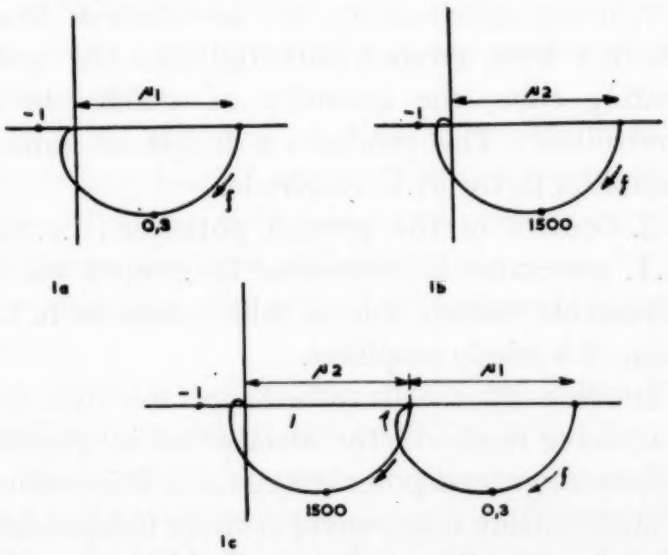

Fig. 1. Nyquist diagram of 1a: Slow feedback loop. 1b: Fast feedback loop. 1c: Fast and slow feedback loop parallel.

Owing to the time-constants of converter and cascade generator, the closed-loop gain already starts to decrease at frequencies as low as 0.3 c/s at a rate of 40 db/decade; consequently this loop is only suitable for correcting slow variations. The Nyquist diagram of this slow feedback loop is shown in fig. 1a.

Fast variations can only be stabilized in a circuit with time constants smaller than 10^{-4} sec, corresponding with a cut-off frequency of at least 1500 c/s, so that the 3rd harmonic of the load ripple is also stabilized.

For fast stabilization of the H.T. the following methods of affecting the H.T. are suited:

1. Control with a stabilizing tube between H.T. generator and load. This is used for stabilizing low-tension supply apparatus, but presents difficulties with positive H.T. in the control of the stabilizing tube which operates under full H.T.[1]).

2. Controlling the internal resistance of the H.T. generator with the aid of an additional adjustable load current.

This control current can be obtained:

a. by a stabilizing tube in parallel with the load, as used in shortcircuit protected L.T. supply apparatus and small H.T. supply apparatus.

b. by an adjustable corona discharge[2]).

This method increases the risk of breakdown of the H.T. generator, and furthermore it is acting too slowly owing to the transit time of the electrons.

c. in ion accelerators, by an electron beam emitted from ground potential into the accelerating tube, the intensity of which can be controlled[3]). This produces a dangerous gamma radiation in the H.T. electrode.

3. Control of the ground potential; i.e. the H.T. generator is connected to ground via an adjustable voltage source, which may be in the form of a triode amplifier.

In view of the drawbacks of the first two stabilizing methods, the installation in question employed ground-potential control. This method of stabilization is moreover entirely independent of the cascade generator and the accelerating tube, and can therefore be readily added to existing installations.

The Nyquist diagram of a fast feedback loop obtained with earth potential control is shown in fig. 1b.

To limit the necessary control range and accordingly the size of the fast stabilizer, the fast feedback loop was arranged in parallel with a slow feedback loop stabilizing the H.T. via the 500 c/s converter. The fast stabilizer is then kept in its operating point by the slow feedback loop and has to stabilize only the fast variations, which amount to 7 kV in this case.

The Nyquist diagram for the combined slow and fast stabilization is then formed by the vector sum of both diagrams (1a and 1b). Owing to the large difference in cut-off frequency (0.3 and 1500 c/s respectively) the locus of the slow feedback loop is affected in such a way that the origin is displaced to the beginning of the locus of the fast feedback loop. For the slow feedback loop locus the point $-1, +j0$, which determines the stability, is therefore moved to the left by a factor of μ_2. The closed-loop gain in the slow loop can now be increased by a factor μ_2 without risk of oscillating.

In this way a feedback factor of 10^4 and more can be realized for slow variations. In practice this means that the long-term stability will be limited only by the quality of the error detection.

3. Error Detection

The H.T. is measured with an oil-cooled measuring resistor, made up of 4 sections, each for 175 kV. Each section consists of 600 wirewound 150 kΩ resistors, shunted with a 400 pF paper capacitor (C_m) for improving the frequency response. The temperature coefficient of the resistors used is below $25 \times 10^{-6}/°$ C; the permanent resistance deviation is within 0.1%. The reference voltage is variable between 0 and — 150 V with a 10-turn helical potentiometer, has a stability of better than 0.01% per hour, and is taken up from a high-quality stabilized supply unit.

4. The Control Circuit

A block diagram of the circuit is shown in fig. 2.

The error signal is primarily amplified by a Landsberg-type[4]) D.C. amplifier stabilized against drift, with a bandwidth of 100 kc/s and a gain of 20 000.

The amplifier output controls both the slow and the fast control systems. The fast feedback loop comprises a triode amplifier with 2 series-connected transmitting tubes TB 4/1250. The

[1]) G. Dome and H. D. Hoop, Electronics (June 20, 1958).

[2]) J. L. Mc. Kibben, D. H. Frisch and J. M. Hush, Phys. Rev. **70** (1946) 117.

[3]) S. J. Bame and L. M. Baggett, Rev. Sci. Instr. **20** (1949) 839.

[4]) S. Landsberg, Philips Res. Rep. 11.161–171 (1956).

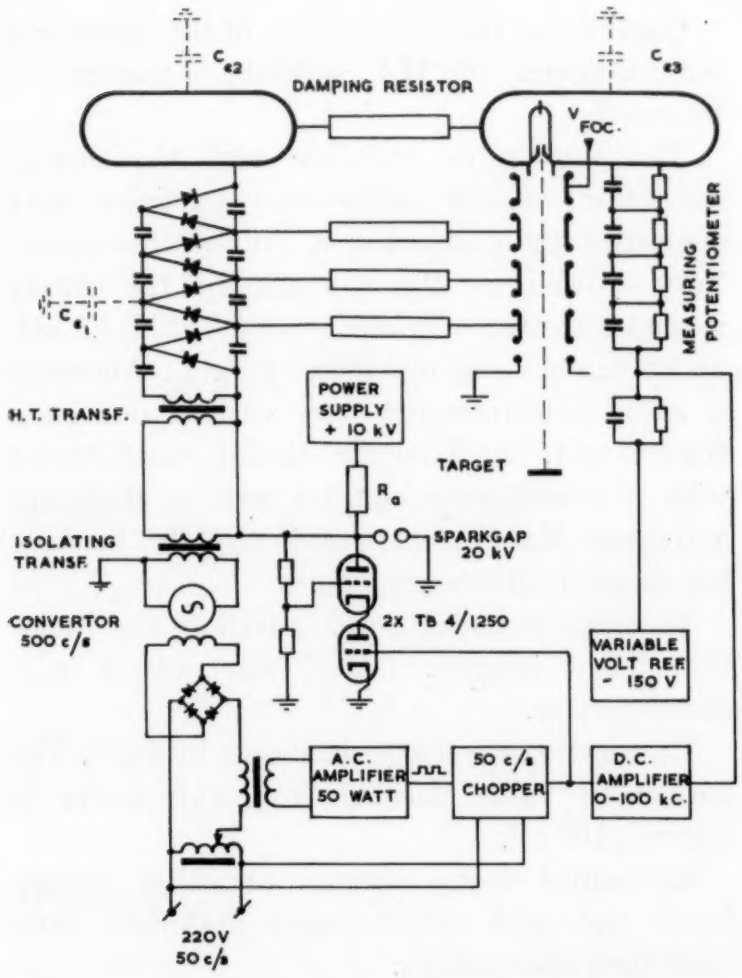

Fig. 2. Block diagram of stabilized 700 kV cascade generator.

effective control range is 7 kV at an anode supply voltage of 10 kV. The plate-current at the operating point is approx. 80 mA.

The design of this amplifier, aside from the desired control range is primarily determined by 500 c/s currents which flow from the a.c. side of the cascade generator, via stray capacitances such as C_{e_1}, to earth. Owing to the voltage feedback from the output of the fast stabilizer via the cascade generator and measuring resistor, to the input, the triode amplifier will be controlled in such a way that these earth currents are only passed via the triodes.

The plate-current at the operating point must therefore be greater than the amplitude of these earth currents and the internal resistance of the circuit must be low to prevent accessive modulation of the triodes. In the fast feedback loop a closed-loop gain of approx. 200 is possible. The following time constants determine the frequency response and stability:

1. upper damping resistance (800 kΩ) with load capacitance $(C_{e_3} + C_m) = 10^{-4}$ sec; cut-off frequency approx. 1500 c/s.

2. internal resistance of the fast stabilizer with earth capacitances C_{e_1} and $C_{e_2} = 16 \times 10^{-6}$ sec; cut-off frequency approx. 10 kc/s.

3. cut-off frequency D.C. amplifier = 100 kc/s.

In the slow feedback loop the amplified error signal is converted by a vibrator into an alternating-voltage signal of the mains frequency and then amplified up to about 50 W at full modulation.

This output is in series with the supply of the rectifier producing the exciting current of the converter. Depending upon the polarity of the error signal, the output voltage of the A.C. amplifier is either in phase or on anti-phase with the mains voltage and increases or reduces the generator output. The control range is $\pm 10\%$. A variable transformer with servomotor keeps the control automatically in the centre of the control range.

If only the slow feedback loop is used a closed-loop gain of approx. 100 $\times$ is permissible. The following time constants determine the frequency response and stability:

1. converter: 0.5 sec; cut-off frequency approx. 0.3 c/s.

2. cascade generator: dependent upon the load; was averaged at 0.5 sec.

The db-log f diagram of the combined slow and fast stabilization is the sum of the separate diagrams and is shown in fig. 3. The curve directly indicates the feedback factor for each frequency.

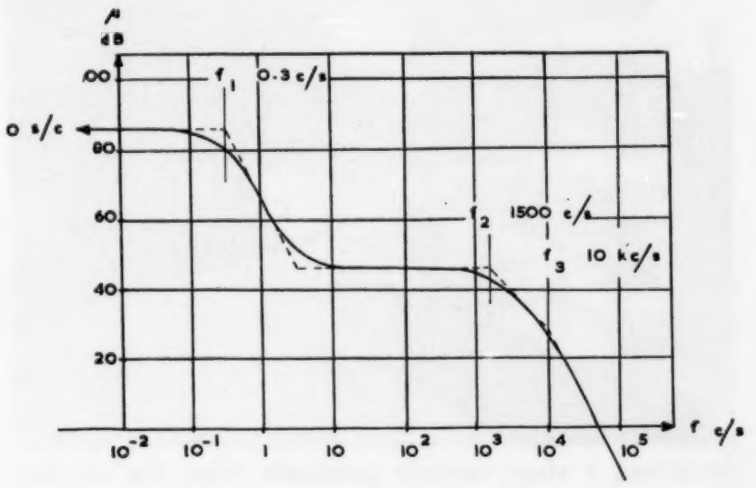

Fig. 3. Db-log f curve of double loop feedback system.

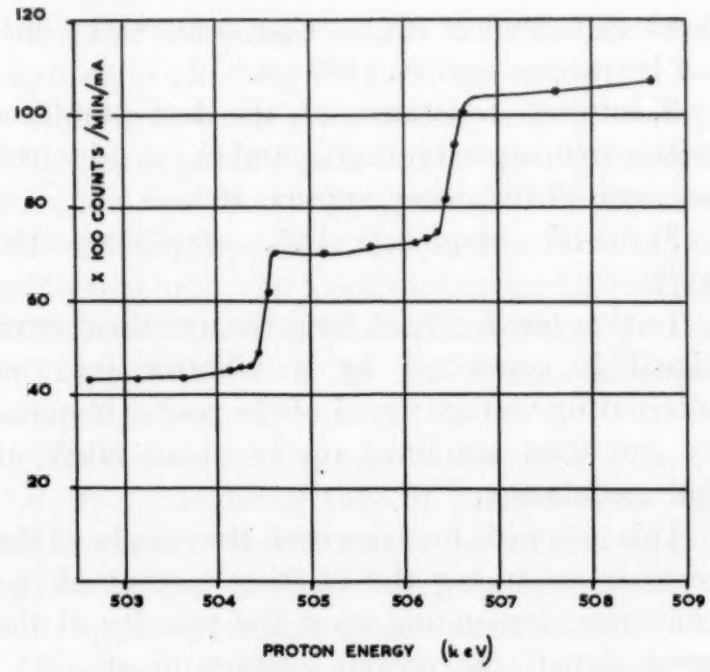

Fig. 4 Gamma ray curve of $Al^{27}(p,\gamma)$ Si^{28}.

5. Results

The long-term stability was examined by measuring the current in the measuring potentiometer with the aid of a compensation circuit. The stability of the measuring current was found to be better than 0.03% per hour with a maximum drift of 0.1% throughout the measuring periode (10 hours).

Considering the high quality of the measuring potentiometer, the H.T. stability is assumed to be equal.

The short-term stability and the energy resolution of the accelerated particles were examined by measuring a nuclear resonance. Very suitable for this purpose are the closely spaced resonances in $Al^{27}(p,\gamma)Si^{28}$ at 504.5 keV and 506.5 keV, as reported by S. L. Andersen *et al.*[5]). Measurements were carried out on a thick target. The gamma radiation was detected with a scintillation counter with a thallium-activated NaI-crystal fitted directly beneath the target in the beam axis.

To suppress background radiation, the radiation below approx. 2 MeV was cut-off in a discriminator.

The gamma-ray curve is shown in fig. 4. The half-width value derived from this curve is approx. 100 eV.

Resonance measurements at other energy levels and with other target materials have confirmed this result[6]).

[5]) S. L. Andersen, T. Holtebekk, C. Lönsjö and R. Tangen, Nucl. Phys. **4** (1957) 39–43.

[6]) S. Wagner and M. Heitzmann, Zeitschr. f. Naturfors. (1960) To be published.

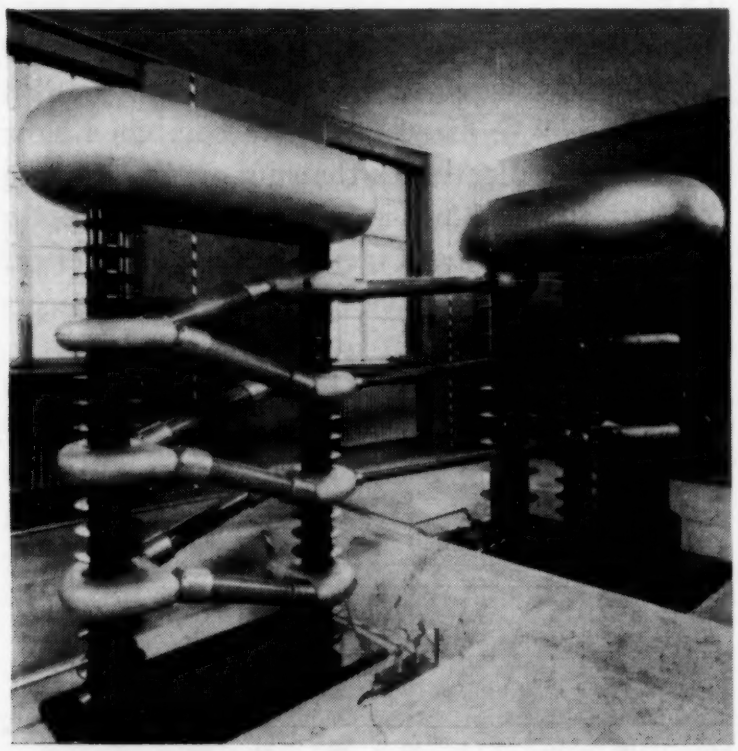

Stabilized 3 stage cascade generator with ion accelerator, installed at Staatliche Ingenieursschule, Essen, Germany.

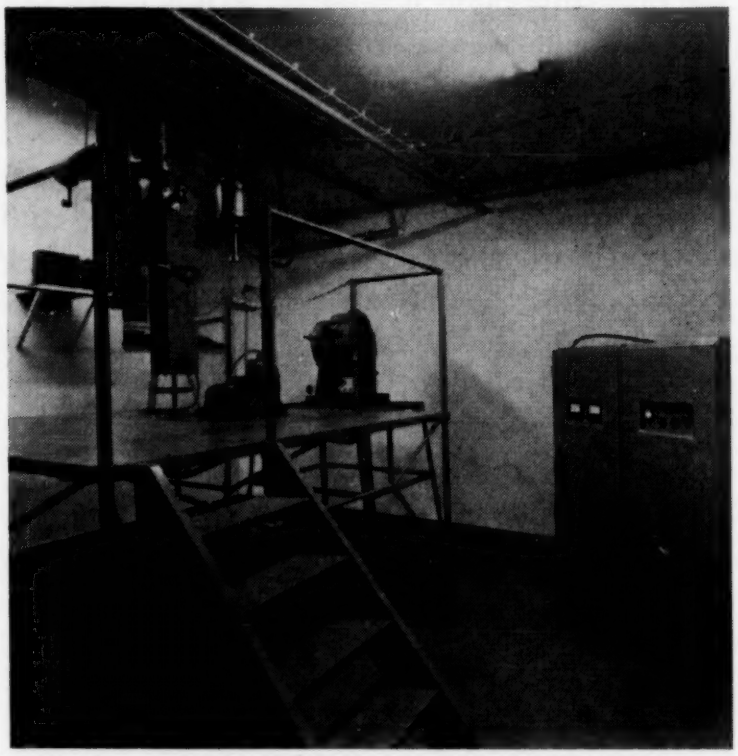

Target room of ion accelerator. Note the fast stabilizer in the right of the figure. The slow stabilizer is built in the control desk situated in the control room.

NUCLEAR INSTRUMENTS AND METHODS 8 (1960) 121–145; NORTH-HOLLAND PUBLISHING CO.

A SIEGBAHN-EDVARSON TYPE IRONFREE DOUBLE FOCUSING BETA-RAY SPECTROMETER

C. DE VRIES and A. H. WAPSTRA

Institute of Nuclear Research, Amsterdam

Received 10 May 1960

An ironfree double focusing beta ray spectrometer with 30 cm radius for precision energy and intensity measurements has been constructed. It can be used for the focusing of electrons with an energy up to 2.6 MeV. The cooling system limits errors due to temperature effects to about one part in 10^5 in the relative $B\rho$-values of the electrons throughout the whole energy region. The long and short term stability of the coil current, delivered by a d.c. generator, is in the order of $1:10^5$. External magnetic fields are compensated; fluctuations on the most important component of these fields are automatically suppressed to less than 10^{-8} Wb/m^2. The field shape satisfies the conditions for first order focusing in the radial direction and second order focusing in the axial direction to a high degree: $\alpha = -0.500 \pm 0.003$ and $\beta = 0.39 \pm 0.02$. The maximum transmission is about 1%; the smallest linewidth obtained so far has been 0.013%.

1. Introduction

During the past few years the interest in instruments with the double focusing field shape has rapidly increased, as this field shape meets to a high extent the beta-spectroscopic requirement of a large ratio of transmission and resolution (both expressed in percentages). The additional requirement of high precision has proven to be best satisfied when this particular field shape is realized with ironfree constructions.

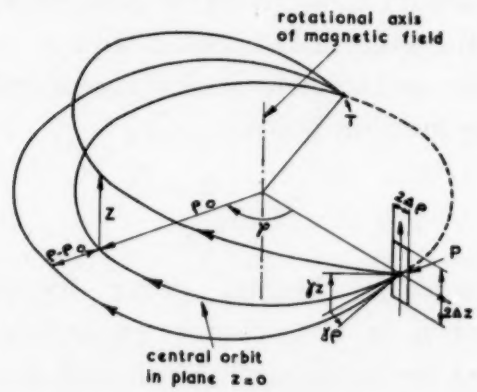

Fig. 1. Explanation of the symbols in the text.

Before discussing some existing air cored instruments we shall briefly present the focusing properties of axially symmetric magnetic fields.

Consider the trajectories of electrons of momentum p in an axially symmetric magnetic field with a plane of symmetry. A possible orbit in the symmetry plane is a circle, concentric with the axis of the field; this is called the central orbit. Cylindrical coordinates ρ, z and φ will be used (see fig. 1). The Taylor expansion of the magnetic field around the central orbit $\rho = \rho_0$ in the median plane $z = 0$ is:

$$B(\rho) = B(\rho_0)\{1 + \alpha\delta + \beta\delta^2 + \cdots\}$$

where

$$\delta = \frac{\rho - \rho_0}{\rho_0}, \quad \alpha = \frac{\rho_0}{B(\rho_0)}\left(\frac{\mathrm{d}B}{\mathrm{d}\rho}\right)_{\rho_0}$$

and

$$\beta = \frac{\rho_0^2}{2B(\rho_0)}\left(\frac{\mathrm{d}^2B}{\mathrm{d}\rho^2}\right)_{\rho_0}.$$

This series expansion and the Maxwell equations determine the entire field distribution around the central path. If only paths are considered at small angles γ_ρ and γ_z with the central path (see fig. 1), the influence of all terms of higher order than δ can be neglected.

For such first order calculation Svartholm and Siegbahn[1]) showed the equations of motion of the particles to be:

$$\begin{aligned} \delta'' &= -(1 + \alpha)\,\delta \\ z'' &= \alpha z\,. \end{aligned} \tag{1}$$

[1]) N. Svartholm and K. Siegbahn, Ark. Mat. Astr. Fys. A **33**, No. 21 (1946).

Using the boundary condition $\delta = 0$ and $z = 0$ for $\varphi = 0$, (point P in fig. 1) one finds the solution:

$$\delta = \frac{a}{\rho_0} \sin (\alpha + 1)^{\frac{1}{2}} \varphi$$
$$z = \frac{b}{\rho_0} \sin (-\alpha)^{\frac{1}{2}} \varphi \,. \tag{2}$$

For periodicity in ρ and z, α must lie between the values -1 and 0. If Ψ_ρ and Ψ_z are defined as the angles at which for the first time first order focusing takes place in the radial and axial direction respectively, then

$$\Psi_z = \pi (-\alpha)^{-\frac{1}{2}}$$
$$\Psi_\rho = \pi (1 + \alpha)^{-\frac{1}{2}} \,. \tag{3}$$

Evidently, $\alpha = -\frac{1}{2}$ gives double focusing after $\pi\sqrt{2}$ radians. Other suitable choices of α have been discussed by Lee Whiting[2]) and Mladjenović[3]). Here we will restrict ourselves to $\alpha = -\frac{1}{2}$. Then the solution for the orbit equations (2) is given by:

$$\delta = \frac{a}{\rho_0} \sin \frac{\varphi}{\sqrt{2}}$$
$$z = \frac{b}{\rho_0} \sin \frac{\varphi}{\sqrt{2}} \,. \tag{4}$$

This solution can also be written:

$$\rho - \rho_0 = \gamma_\rho \rho_0 \sqrt{2} \sin \frac{\varphi}{\sqrt{2}}$$
$$z = \gamma_z \rho_0 \sqrt{2} \sin \frac{\varphi}{\sqrt{2}} \tag{5}$$

which expresses the distances $(\rho - \rho_0)$ and z from the central orbit as a function of γ_ρ, γ_z and φ.

Double focusing occurs at the point φ $(\rho_0, 0, \pi\sqrt{2})$ only for electrons having a momentum $p_0 = eB(\rho_0)\rho_0$. Electrons having a slightly different $B\rho$-value focus at the point φ' $(\rho_0 \pm d, 0, \pi\sqrt{2})$ with

$$d = 4\rho_0 \left(\frac{\Delta B\rho}{B\rho} \right)_{\rho_0} \,.$$

Monoenergetic electrons will be measured as lines with a finite width in consequence of the spherical aberration of the focusing system and the finite dimensions of the source and the counter slit. The shape of this line will be called the spectrometer window curve. The resolution R can be defined now as the relative width at half height of the line, plotted in the $B\rho$-scale:

$$R = \frac{\Delta B\rho}{B\rho} \,.$$

The resolution is mostly expressed in percentages. Related quantities are the resolving power, which is the inverse of the resolution and the base line width R_0 which is the relative width at the base of the line. The ratio between R and R_0 depends on the intensity distribution within the line. In turn this intensity distribution depends on the special conditions under which the line is measured. Under simplifying assumptions the connection between R and R_0 can be given exactly[4]). In practice the following formula is a rather good approximation:

$$R \approx \tfrac{1}{2} R_0 \,.$$

The "energy resolution" is related with the "momentum resolution" through the relation:

$$\frac{\mathrm{d}E}{E} = \frac{E + 2}{E + 1} \frac{\mathrm{d}p}{p} \tag{6}$$

which formula is obtained by differentiating the relativistic relation between E and p.

For the special field under consideration the following relation holds:

$$R_0 = \frac{d}{4\rho_0} \,. \tag{7}$$

In discussing second order focusing the coefficient β in the Taylor expansion of the field must be considered. Shull and Dennison[5]) have shown that the image coordinates ρ^* and z^* for an electron emitted from the point $(\rho + \Delta\rho, \Delta z)$ at $\varphi = 0$, with a momentum

[2]) G. E. Lee-Whiting, Can. J. of Phys. **35** (1957) 570.
[3]) M. Mladjenović, Nucl. Instr. **7** (1960) 11.
[4]) H. Wild and O. Huber, Helv. Phys. Acta **30** (1957) 3.
[5]) F. Shull and D. Dennison, Phys. Rev. **71** (1947) 681; **72** (1947) 256.

$eB(\rho_0)\rho_0$ at the angles γ_ρ and γ_z to the tangent on the central orbit are:

$$\rho^* = \rho_0 - \Delta\rho + \frac{1}{\rho_0}\left(\tfrac{4}{3}\beta - 1\right)\Delta z^2 + \tfrac{2}{3}(1 - 8\beta)\,\rho_0\gamma_\rho^2 + 2\left(\tfrac{8}{3}\beta - 1\right)\rho_0\gamma_z^2$$

$$z^* = -\Delta z + \frac{8\beta}{\rho_0}\Delta\rho\Delta z + 4\left(\tfrac{8}{3}\beta - 1\right)\rho_0\gamma_\rho\gamma_z\,. \qquad (8)$$

From these image coordinates and eq. (7) an expression for the base resolution R_0 can be obtained as function of source dimensions ($2\Delta\rho \times 2\Delta z$), counterslit width t, the opening angles γ_ρ and γ_z and the field coefficient β:

$$R_0 = \frac{\Delta B\rho}{B\rho} = \frac{2\Delta\rho + t}{4\rho_0} + \frac{1}{{\rho_0}^2}\,|\,\tfrac{4}{3}\beta - 1\,|\,(2\Delta z)^2 + \tfrac{1}{6}\,|\,1 - 8\beta\,|\,\gamma_\rho^2 - \tfrac{1}{2}\,|\,\tfrac{8}{3}\beta - 1\,|\,\gamma_z^2\,. \qquad (9)$$

Eq.(9) shows that the resolution R_0 is independent of the axial opening angle for $\beta = \frac{3}{8}$; then the influence of γ_ρ on the resolution goes as $\frac{1}{3}\gamma_\rho^2$. For $\beta = \frac{1}{8}$ there is no limit to γ_ρ to second order and the resolution is proportional to $\frac{1}{3}\gamma_z^2$. In this respect there is no preference for $\frac{1}{8}$ or $\frac{3}{8}$. However, there are some arguments in favour of the choice $\frac{3}{8}$. The term in eq. (9), containing the source height will be smaller for $\frac{3}{8}$ then for $\frac{1}{8}$. Due to this fact about 30% higher luminosity (defined as transmission × source area) can be obtained, if one uses the field shape with second order axial focusing instead of second order radial focusing. With the choice $\beta = \frac{3}{8}$ double focusing is obtained not only on the central orbit $\rho = \rho_0$, but also for other values of ρ, which makes possible photographic detection for an extended energy region. For the construction described below the choice $\beta = \frac{3}{8}$ is the natural one, since the radial opening angle is limited more severely then the axial one.

2. Existing Ironfree Instruments with $\alpha = -\frac{1}{2}$ and $\beta = \frac{3}{8}$

The realization of the required field shape with air coils has been obtained so far in two essentially different ways: (1) with pairs of thin coils placed symmetrically to the plane of symmetry as indicated in figs. 2a and 2b and (2) with long coaxial cylindrical coils (figure 2c). The principle shown in fig. 2a is due to Moussa and Bellicard. Fig. 2b shows a design for sixth order axial focusing as computed by Lee-Whiting and Taylor which has been realized by Graham, Ewans and coworkers in Chalk River. The construction indicated in figure 2c has been designed and built by Siegbahn and Edvarson. The relative dimensions of the above mentioned instruments can be seen from the radii of the different central orbits.

We will give now some features of these instruments.

The apparatus of Moussa and Bellicard[6]) ($\rho_0 = 210$ mm, $\beta = \frac{3}{8}$) consists of four pairs of coils placed in series for the current delivered by a high voltage supply (8 kV). The short range stability of the current is about $1:10^4$. At the maximum attainable energy of 1.3 MeV the current is about 0.5 A. The instrument is not provided with a cooling system; the temperature of the largest coils increases to about 100° C when measuring at the highest current. Therefore the instrument is mainly used at low currents. The earth magnetic field is compensated only in the direction perpendicular to the electron orbit. The instrument is provided with a G.M. counter. The maximum attainable transmission is about 1%; at this transmission a resolution of 0.9% has been reached for the ThB F-line. The highest resolution reported so far is in the order of 0.2%. Another spectrometer built along the same lines as the Moussa spectrometer is present in Nashville, [Baird[7]) and Nall[8])]. The radius of the central orbit is 300 mm, $\beta = \frac{3}{8}$, the maximum attainable energy is 1.3 MeV.

A complete description of the Chalk River machine has not yet been published. Some preliminary results have been reported by Ewan

[6]) A. Moussa and J. B. Bellicard, J. Phys. Radium **15** (1954) 85A;
J. B. Bellicard and A. Moussa, J. Phys. Radium **17** (1956) 532.
[7]) Q. L. Baird, Thesis, Nashville (1958).
[8]) J. C. Nall, Thesis, Nashville (1958).

et al.[9]). The radius of the central orbit is 1 meter and the maximum energy is 4 MeV. The transmission can be varied from 0.1 to 1% of 4π cooled with constant temperature water from a closed circuit circulating system. The coil current is measured by the voltage drop across

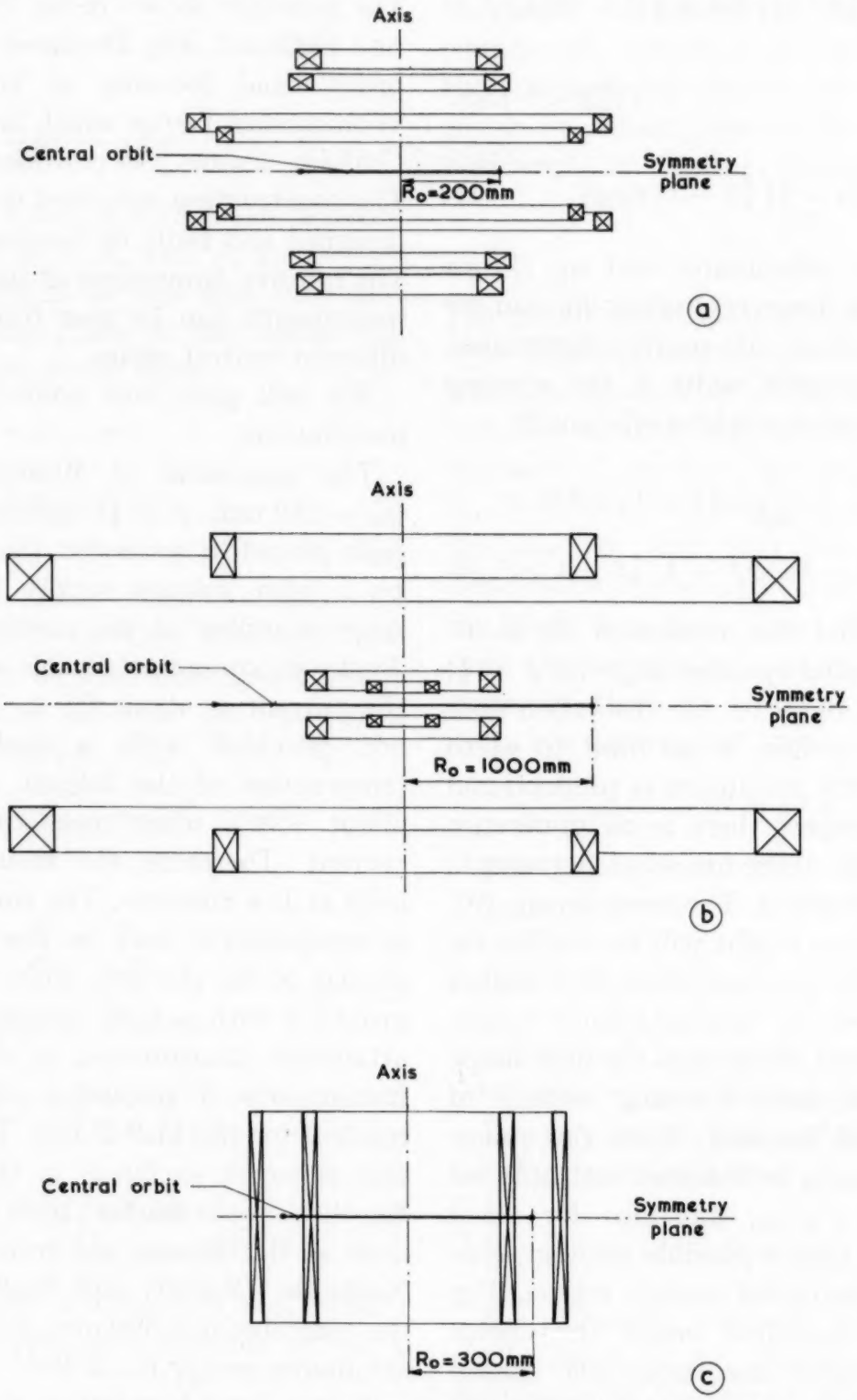

Fig. 2. Different ironfree arrangements yielding the double focusing field shape, due to (a) Moussa; (b) Lee-Whiting and Taylor; (c) Siegbahn and Edvarson.

with corresponding momentum resolution of 0.01% to 1%. The spectrometer coils are powered from a generator (600 V–50 A) and a precision standard resistor; this voltage drop is stabilized within one part in 10^5 from the reference voltage. Observed drifts in the positions of the lines of one part in 10^4 due to the temperature and external field fluctuations will

[9]) G. T. Ewan, J. S. Geiger, R. L. Graham and D. R. Mackenzie, Can. J. Phys. **37** (1959) 174.

be reduced in the future with the aid of stabilization equipment. The best momentum resolution obtained so far has been 0.013% at a transmission of 0.07%.

The instrument of Siegbahn and Edvarson[10]) ($\rho_0 = 300$ mm, $\beta = \frac{3}{8}$) consists of two coaxial counter coupled solenoids with radii of 240 mm and 360 mm and heights 500 mm. A vacuum chamber is located between the two coils in the median plane of the construction; its position can be adjusted with respect to the coils. A temperature change of 1° C in one of the coils or in the vacuum chamber is computed to cause an error in the $B\rho$-determinations of about one part in 10^5. The coils are therefore water cooled with the help of copper tubing, soldered to the inside of the copper frames; they can thus be kept constant in temperature within 1° C. The copper coils are connected in series and fed by a series of high capacity storage batteries, which guarantees the stability of the current within one part in 10^5. With small changes in the cooling system, the authors think it possible to measure beta energies up to 1 MeV while retaining the accuracy of a few parts in 10^5. This accuracy has been reached for beta energies up to 360 keV. External fields are compensated with a set of three pairs of Helmholtz coils, the currents of which are also supplied by batteries. The dimensions of the vacuum chamber allow a maximum transmission of 0.2%. The highest resolution reported so far is 0.019% at a radial opening angle of 0.01 radians.

Except for the instrument described in this thesis, the only other spectrometer of the Siegbahn type has been built by Mladjenović[3]) with a radius of the central orbit of 500 mm. The author reports a smallest linewidth of 0.018%.

From the ironfree instruments discussed, the Moussa type has in principle the advantage of a better accessibility of both the source and the counter position. The scale of the design of Moussa himself makes this advantage somewhat doubtful; it is, however, fully realized in the Chalk River instrument. The dimensions of the last instrument allow all sorts of experimental arrangements close to the source and the counter. The enormous radius of the central orbit $\rho_0 = 1000$ mm, on the other hand, requires very involved precautions against external field disturbances. As shown in section 5 these precautions are already rather involved with $\rho_0 = 300$ mm if the highest precision in the $B\rho$-determinations is desired. A definite disadvantage of the use of many coils in order to realize the desired field shape is that the degree of symmetry of the field, required for high resolution work, is only reached for a very high accuracy in the geometrical setting of these coils. In this respect the design used by Siegbahn and Edvarson is relatively simple because only two coils are involved here. These considerations and also the very good results reported by Siegbahn and Edvarson induced us to construct an instrument along the same general lines. We wished, however, to be able to measure much higher beta-energies (up to 3 MeV) with the same accuracy; the cooling of the coils had therefore to be improved considerably. Secondly, as large a transmission as possible was desired. Therefore, the instrument was designed such that the whole space between the coil tanks could be used as a vacuum chamber; the choice $\beta = \frac{3}{8}$ makes that the whole space can indeed be used since now the axial opening angle can be chosen relatively large, as is made clear in section 1. The design, made on the basis of these considerations, is described below (section 3.1).

The use of a vacuum chamber occupying the total height of the apparatus complicates the positioning of the G.M. counter and the source somewhat. The heavy constructions, needed to ensure a reproducible geometrical setting of source and counter, will be described in section 3.2, where also the special features of the counter system and the adjustable diaphragms are given.

A description of the automatically regulated cooling system, ensuring constant temperature of the coils at (25 ± 1)° C, even at the maximum power input, is given in section 3.3. The outline

[10]) K. Siegbahn and K. Edvardson, Nucl. Phys. **1** (1956) 137.

of the vacuum system is given in section 3.4.

The use of storage batteries for a current of 170 A (corresponding to 2.6 MeV electrons) is rather unpleasant; it was therefore planned to obtain the magnet current from a motor-generator set. The regulation of the current is then easy but a rather involved stabilization equipment is required in order to suppress the ripple on the d.c. voltage. The electronic device used for this purpose will be described in section 4.

A set of three pairs of Helmholtz coils is used for compensating external fields. These fields vary continuously due to various reasons: railroad traffic at 100 metre distance, automobile traffic even nearer and the influence of a cyclotron magnet at a distance of 75 meter. The most important component is therefore automatically compensated; the equipment for this will be described in section 5.

A general impression of the instrument can be obtained from the picture.

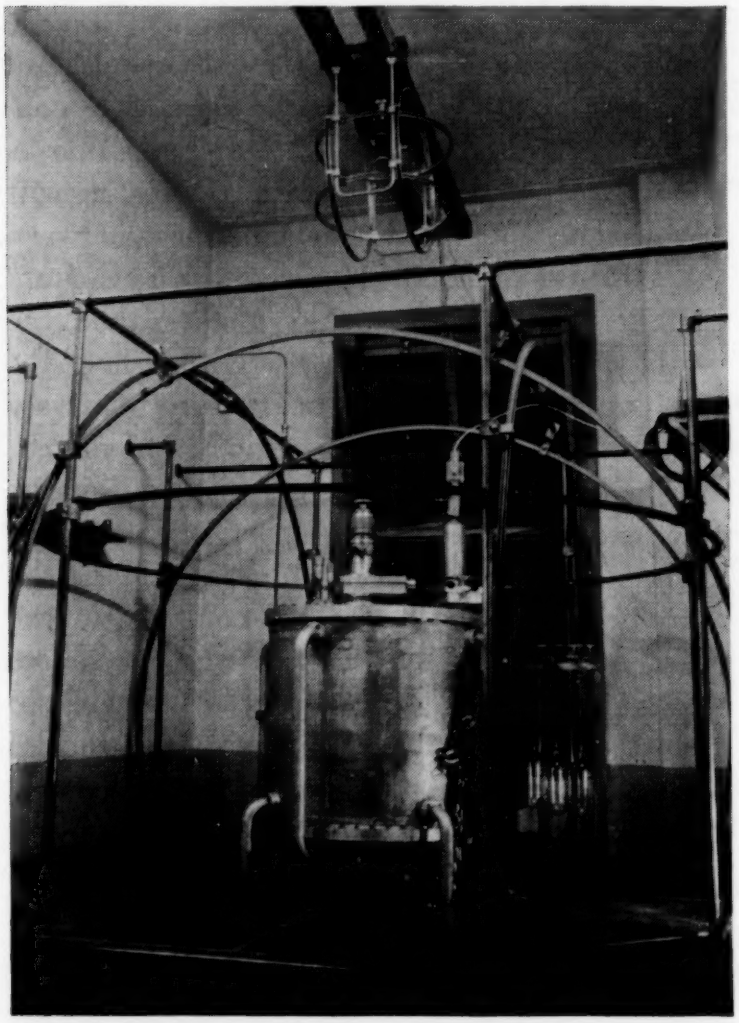

View of the ironfree double focussing spectrometer.

3. Construction of the Spectrometer

3.1. CONSTRUCTION OF COIL TANKS AND WINDING PROCEDURE

The spectrometer has been located in an old building constructed mainly out of brick walls

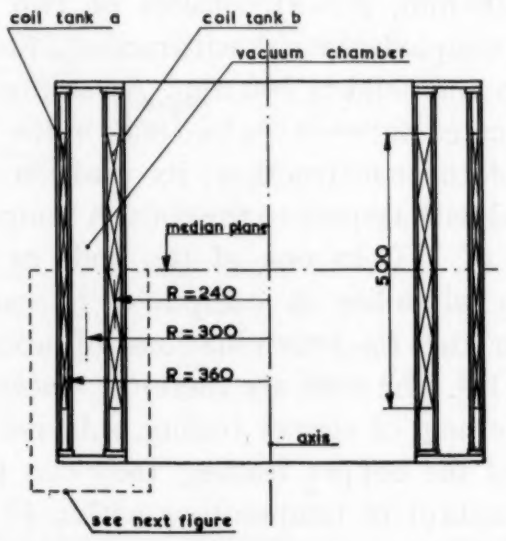

Fig. 3. Geometry of the spectrometer. The inner and outer coil are each enclosed between two cylinders. This construction allows for a cooling system, whereby each winding of the coils is brought in contact with the fluid. The coil units serve at the same time as vacuum chamber walls.

and wooden beams which is therefore suitable for housing an ironfree instrument. In addition, care has been taken to remove all obvious pieces of ferromagnetic materials from the spectrometer room and its immediate neighbourhood. The result of these precautions was found to be satisfactory.

The floor construction under the spectrometer was renewed such that the same foundation could be used for the spectrometer and for the large Helmholtz coils. A wooden platform facilitates the manipulation of the different parts of the instrument which is placed on a wooden base with three adjustable supports. These supports, made of brass, enable a final adjustment with respect to the Helmholtz coils; all the copper vacuum and cooling tubes are connected to the instrument by flexible joints.

The severe requirements on temperature stability of the coils have mainly determined the construction. Effective cooling under any working condition can best be obtained by allowing each winding to be in direct contact with the cooling medium. The use of tubes with inside cooling was not advisable; due to the fact

that the coils had to be kept thin in order to keep the space between inner and outer coils as large as possible the necessary flow of cooling liquid could then not be delivered without a very

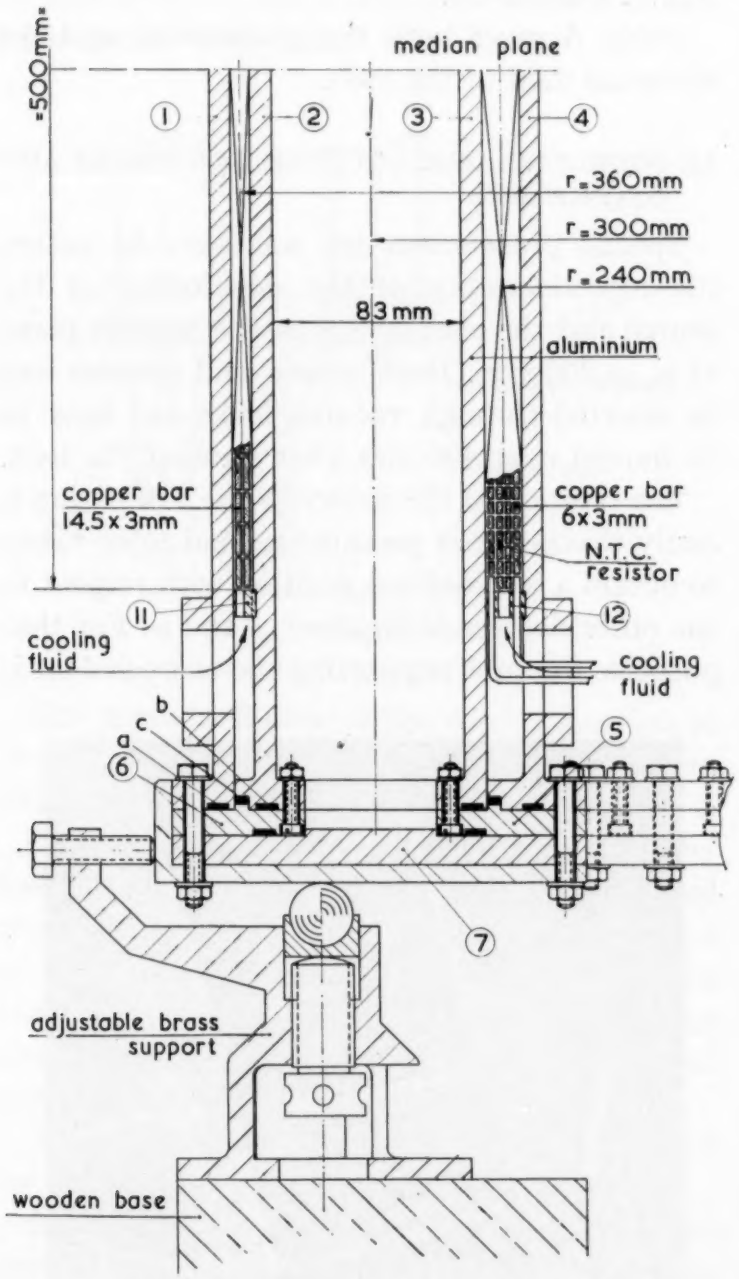

Fig. 4. Construction of the spectrometer.

high pumping pressure. Therefore, it was decided to cool the windings from the outside. Thus, the construction shown in figures 3 and 4 was chosen. Both coils are enclosed in cylindrical coil tanks which also serve as vacuum chamber walls. Each tank consists of two cylinders, made of pure aluminium (iron impurities less than 0.1 %). These cylinders made of rolled sheets were welded by the argon arc process and machined to an accuracy of 0.1 mm†.

After the winding procedure, described below, the cylinders 1 and 3 are placed over the coils. The coil tanks are completed by bolting the flanges 5 and 6 on both sides to the cylinders. These flanges are sealed with polyvinilchlorid (p.v.c.) gaskets, a, b and c, in such a way that the space between the seals a and b can be evacuated if necessary. The two coil tanks are placed concentric to each other by bolting them to the flange 7 and a similar flange on the top side of the coil tanks (not shown). These flanges are machined with an accuracy of 0.1 mm to assure concentricity of the two coils. Although this construction does not allow a final adjustment of the two coils, it assures their mutual position not being disturbed. Moreover this construction gives the opportunity of using the coil tanks as vacuum chamber walls.

The dimensions of the vacuum chamber are such that a radial opening angle can be obtained of 0.09 radians; the maximum axial opening angle is fixed at 0.35 radians. The maximum solid angle is therefore 1%. Both angles can be adjusted from outside by means of movable shutters at a position schematically shown in figure 5, which is a horizontal cross section in the median plane. The figure also shows the geometrical configuration of coils, source, counter, baffles and lead shielding.

The spectrometer coils are made of electrolytical pure copper bar, the dimensions of which are indicated in fig. 4. The distances between successive windings of one layer are 1 mm for the inner coil and 2.7 mm for the outer coil (see also section 6.1). These distances are fixed by using spacers of pertinax, 20×1 mm and 20×2.7 mm, placed at distances of 50 mm. Pertinax strips, $500 \times 5 \times 1$ mm, at distances of 20 mm, keep the layers 1 mm apart from each other and from the walls of the coil tank. These strips and the spacers are machined to an accuracy of 0.1 mm. The copper coils are thus wound with a precision of 0.1 mm with respect to cylindrical symmetry and homogeneity over the height of the coils. The coils are mounted

† We are very much indebted to N.V. Philips for carrying out perfectly this difficult work.

between two pairs of rings to fix the coil position in the vertical direction. One ring of each pair is shown in fig. 4 (11 and 12). These rings contain holes for admitting the coolant which will then

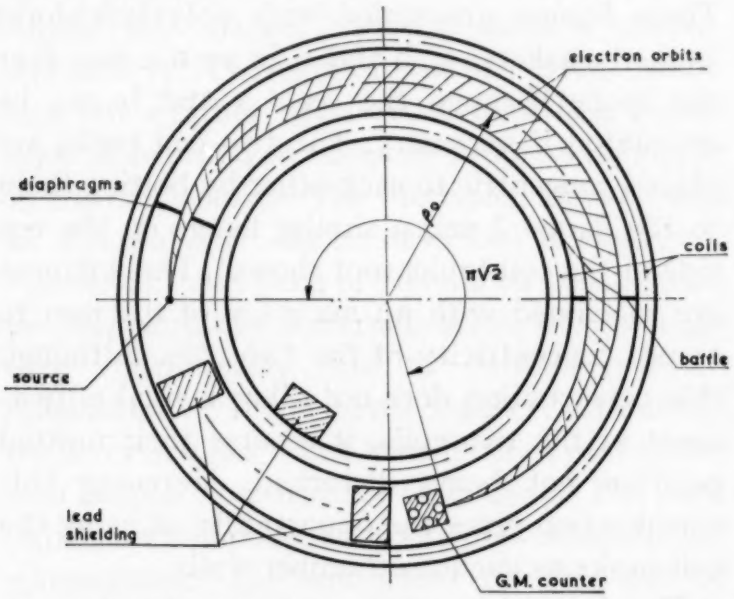

Fig. 5. Position of source, counter, diaphragms and lead shielding in the median plane of the spectrometer.

flow predominantly in the axial direction between the layers. The holes are distributed in such a way that they offer a minimum resistance to the liquid flow.

Fig. 6 gives a close up of the outer coil during the winding procedure; the figure shows also the positioning of a N.T.C. resistor between the windings. These resistors (Philips, B8 32007) with a negative temperature coefficient of the resistance of 75 Ω/° C are used to measure the temperature of the coils.

The inner coil contains 6 of these elements,

TABLE A
Geometrical and electrical data of the coils

	Outer coil	Inner coil
Number of turns	56	280
Mean radius	360 mm	240 mm
Height	500 mm	500 mm
Dimension of copper windings	3 × 14.5 mm 2 layers	3 × 6 mm 4 layers
Resistance	0.051 Ω	0.41 Ω
Maximum dissipated power	1500 W	12 000 W
Calibration constant	59×10^{-6} Wb·m^{-1}·A^{-1}	

placed in such a way that it is possible to get information about the temperature distribution in this coil. The outer coil in which the heat production is much lower, is provided with 2 N.T.C. resistances.

Table A gives both the geometrical and the electrical data of the coils.

3.2. SOURCEHOLDER, COUNTER EQUIPMENT AND DIAPHRAGMS

Special precautions are necessary to ensure the reproducibility of the positioning of the source and the counter slit in the median plane at $\rho_0 = 300$ mm. Both source and counter can be inserted through vacuum locks and have to be moved over 400 mm after passing the lock.

The position of the source in the z-direction is easily checked, but precautions had to be taken to obtain a well defined position with respect to the other degrees of freedom, ρ and φ. For that purpose, the tube supporting the sourceholder is

Fig. 6. Close-up of the outer coil during the winding procedure, showing the two layers of the coil which are separated by pertinax strips. A small N.T.C. resistor is inserted between two windings of the second layer to measure the temperature of the coil.

made of a thick, chromiumplated copper tube (ø 25 mm), which is guided by a 100 mm long akulon seal. A copper frame supporting the sourceholder can be fitted onto this tube, as may be seen in fig. 7; the sourceholder is fixed to this frame with small clamps (not shown).

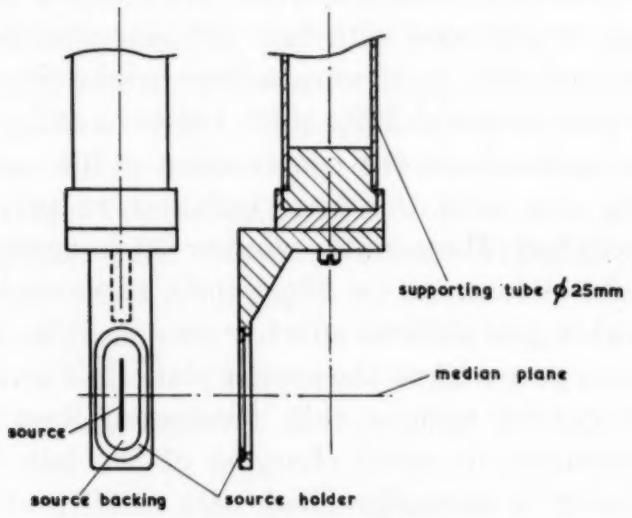

Fig. 7. Source holder.

The reproducibility of the source position in the radial direction is of the order of 0.02 mm which means better than one part in 10^4.

Instead of the frame, supporting the sourceholder, another construction can be attached which allows displacing the source in the radial as well as in the tangential direction. This construction was used for testing the focusing properties of the spectrometer by means of calibration lines (see section 6.2).

The following arguments have been considered for the counter construction:

1. According to formula (9), the resolution is dependent on the slit width; it is therefore necessary to provide for the use of different entrance slit widths to the counter. It is even possible that, during one run, different widths would be desirable: e.g. large widths for measurements of a continuous beta spectrum and narrow ones for conversion lines.

2. The counter slit and the source have to be perpendicular to the median plane of the magnetic field. This requires good reproducibility of the slit geometry.

3. It is necessary to use an extremely hin counter window to allow intensity determinations of electrons at very low energies. Use is reported of foils made of formvar as thin as 10 μg/cm^2. Such foils are rarely free from having pinholes and are easily damaged. A simple replacement procedure is required.

In connection with these considerations the

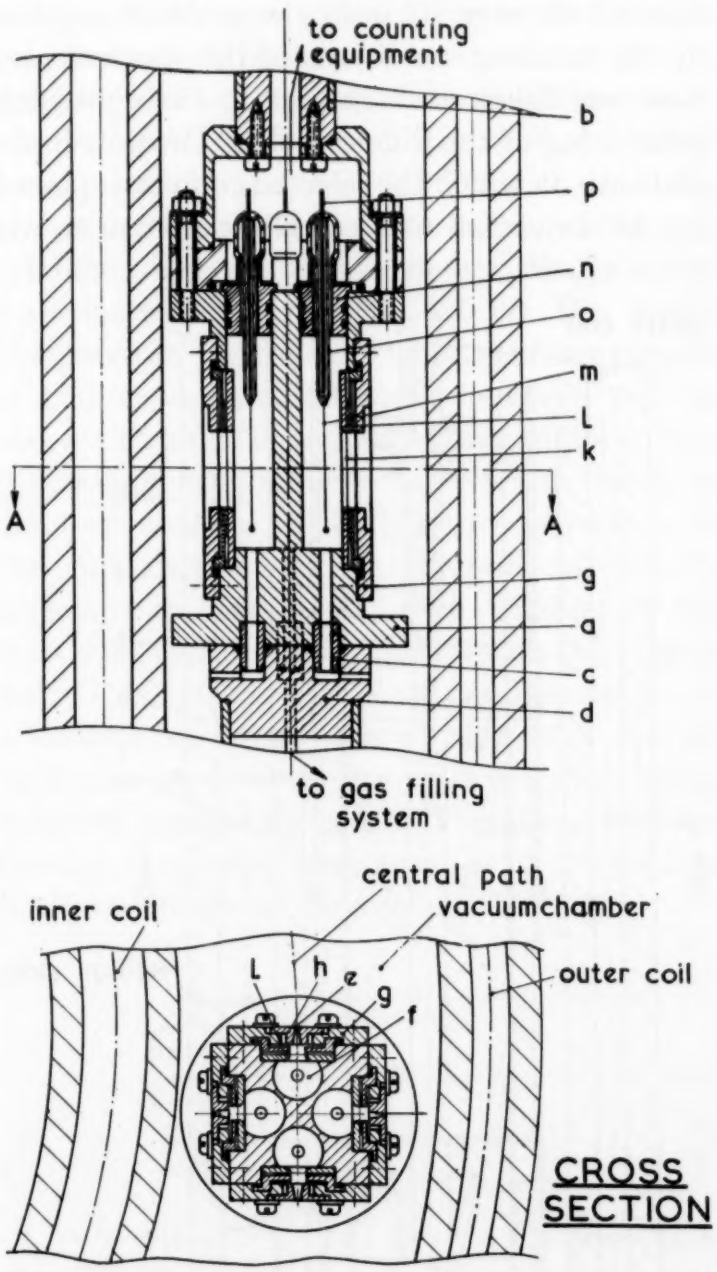

Fig. 8. Side-window Geiger-Müller counter system. For detailed explanation see text.

construction of fig. 8 was developed. This figure presents a vertical and a horizontal cross section.

A heavy copper block (a), supported by a chromium plated copper tube (b) (ø 32 mm), can be placed on a platform (d) such that its position is accurately defined by means of four studs (c). The copper block contains four similar counters; each of the counters can be

chosen as detector of the focused electrons with a simple action from outside the vacuum. Changing from one counter to another takes about half a minute.

The platform is fitted to the bottom of the vacuum chamber such that the slit (e) of the selected counter (f) is in the position required by the focusing conditions of the spectrometer. Care was taken with respect to the equivalent positioning of the different slits. The hole in the platform, in which the selected counter is placed, can be connected to a gas filling system as well as with the high vacuum side of the vacuum system. The counters not used during the measurements are kept evacuated.

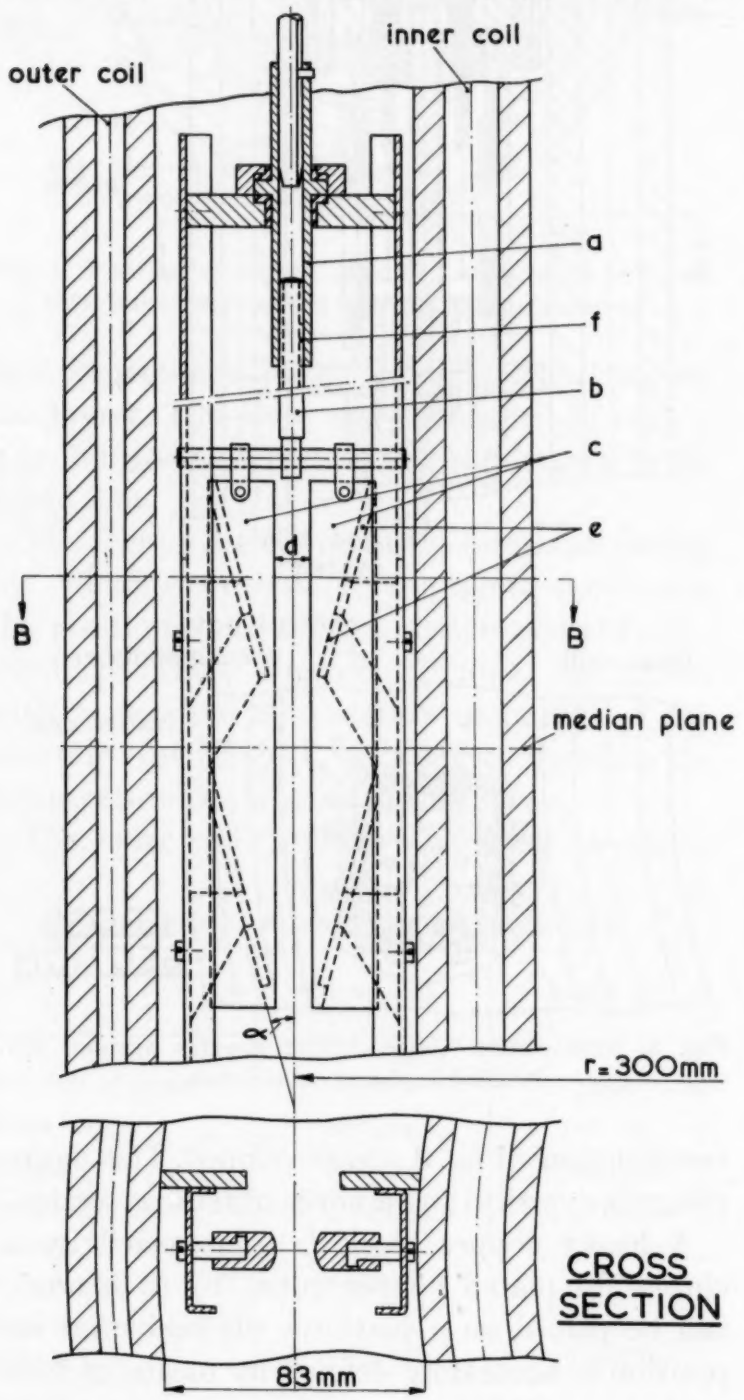

Fig. 9. Diaphragm for the radial opening angle of the electron beam.

The counter slit is defined with the aid of movable copper strips (h) fixed in a copper plate (g). They can be adjusted from 3 mm down to, say, 0.05 mm. Thus, the counter block may be provided with four different slitwidths. The counters (⌀ 15 mm, active height 50 mm) are provided with 200 μ thick tungsten cathodes. The figure shows the construction of the copper plug (n), with the glass isolation to prevent discharges. The counter window (k) is normally made of formvar ($\approx 50\ \mu g/cm^2$), supported by a nylon grid with an effective area of 95%. This grid is prepared on the copper plate (l). The foils are coated with a thin conducting layer of aluminium to avoid charging of the foil. The counter is normally filled with a 90%—10% mixture of argon-alcohol at a pressure of 6 cm Hg. The platinum thread holder (p) of the selected counter can be connected with a plug to the quenching circuit which circuit is of the type described by Den Hartog and Muller[11]; it has a fixed dead time of 0.38 milliseconds and is placed as near as possible to the Geiger counter in order to diminish the chance of external perturbations. The high voltage for the counter is provided by a Philips power supply (P.W. 4022); the counts are registered by a five decades scaler unit and a preset count/time unit (Philips P.W. 4032 and P.W. 4052). These units are placed in the control panel at about 7 meter from the spectrometer.

The system has shown to work satisfactorily. Under the conditions mentioned above, the counters have a plateau with a length of about 100 V and a slope of about three percent. The natural background is about 10 c/min. The shielding from the source allows working with rather strong activities without raising the background too much. With the formvar foils used ($\approx 50\ \mu g/cm^2$) the cut off of the counter is about 4 keV. These foils are practically free from leakages; when buffering with a one liter vessel

[11]) H. de Hartog, Thesis, Amsterdam (1948);
H. de Hartog and F. A. Muller, Physica **16** (1950) 17.

the counter pressure remains constant during long periods.

Some test measurements proved that for counting rates below 15 000 c/min the efficiency is not significiently dependent on the counting rate and the results are reproducible even if intensities are determined with a time interval of several days. Above 15 000 c/min the slope of the plateau increases, thus causing comparison of line intensities to be unreliable when dealing with widely different peak counting rates. For the majority of measurements the counting rate remains below 15 000 c/min, but in order to be able to work with higher counting rates the system will be made to work as a continuous flow proportional counter; this can be done without changing the construction severely.

The diaphragms are designed such that the opening angles in both directions can be achieved without disturbing the vacuum. The problem of adjusting the radial opening angle in the median plane, at a distance of 400 mm above this plane, was solved as shown in fig. 9.

Two shutters (c) are mounted on oblique guide rails (e), so that they close the opening angle when moving downwards. This movement is controlled by turning a shaft (a) around a screw (f) on a long support (b). The radial distance (d) of the shutters depends on the pitch of the screw (f) and the angle α. Therefore, the angular displacement of the shaft (a) can be calibrated in units of radial solid angle γ_ρ, using the relation between γ_ρ and $d[= 2\ (\rho - \rho_0)]$ as given by formula (5). The angular displacement of this shaft can be read off from the outside by means of a micrometer scale. The same can be done for the axial opening angle setting. The adjustment of this opening angle is much easier to achieve and need not to be discussed. The edges of the copper shutters were machined as indicated in fig. 9. Special care was taken to assure symmetry of the slit dimensions with respect to the median plane and to the cylindrical plane $\rho = 300$ mm. As already discussed in section 3.1, the diaphragms allow a maximum solid angle of 1%.

3.3. COOLING SYSTEM

3.3.1 *Construction*

Siegbahn and Edvarson[10]) computed that a temperature rise of 1° C in one of the spectrometer coils relative to the other one, introduces an error in the $B\rho$-determination of about one part in 10^5. A temperature change in the vacuum chamber, which in their apparatus is a separate element, also effects the accuracy. They therefore maintain the temperature of their instrument constant at (18 ± 0.2)° C with the help of water cooled tubes on the inside of the coil cylinders. The maximum power dissipated in their instrument is about 350 W. The power dissipated in the coils of the present instrument at beta-energies of 2.6 MeV, however, will be about 13.5 kVA. This makes it mandatory, that the cooling system has to be very effective if, at different energies, a temperature constancy of the coils within 1° C is desired. As already discussed in section 3.1, each winding of the coils is brought in direct contact with the cooling fluid. This method of cooling requires the use of a cooling medium with a very high specific resistance in order to keep the electric leakage currents sufficiently small. Therefore, kerosine having a specific resistance of $2 \times 10^{14}\ \Omega$/m has been chosen as the coolant.

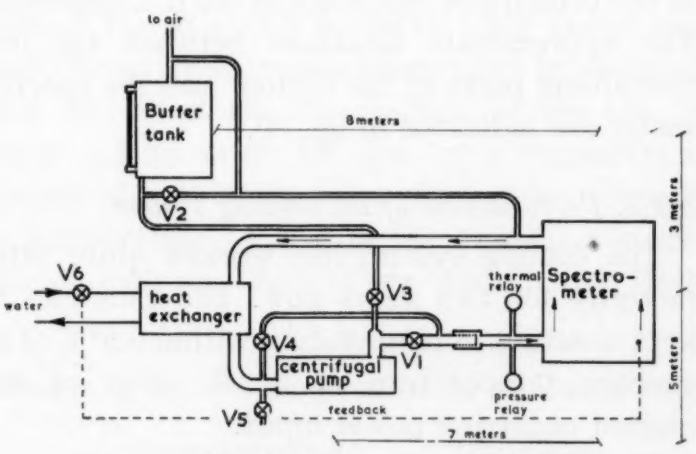

Fig. 10. Cooling system.

The rate of flow of the coolant was determined by the allowed temperature rise of the kerosine during its, mainly axial, passage through the coils. This temperature rise must be kept as small as possible to avoid large temperature gradients in the coils. The two coils are placed

in series for the coolant, which first flows through the outer coil and then through the inner one. The coolant enters both coil tanks at the bottom and leaves at the top. Homogeneity of the flow over the coils is enhanced by having four separate entry and exit ports, spaced 90° apart on the circumference of the coil tanks.

The cooling arrangement is shown schematically in fig. 10. The flow of the kerosine (400 liter per minute) is caused by a centrifugal pump (Sihi Z 8520 K/KK) working at a pressure of 1.3 atmospheres. The capacity of the heat exchanger is 10 kVA at a temperature difference of 10° C. Several filters in the main circuit prevent the entrance of electrically conducting particles which could shortcircuit the bare windings. Under working conditions, only the valves V_1, V_2 and V_6 are open. The other valves are only used if the kerosine has to be removed from the coil tanks to the buffer tank; this can be done with the help of the Sihi pump. The temperature of the coils can be kept constant at (25 ± 0.5)° C by automatically adjusting the position of the motor-driven valve V_6 in response to the signal obtained from one of the N.T.C. resistances built in the inner coil.

As safeguards, a thermo-relay and a pressure-relay are built in which are inserted electrically in the primary of the motor of the d.c. generator. The approximate distances between the iron containing parts of the system and the spectrometer are indicated in fig. 10.

3.3.2. *Performance of the cooling system*

The cooling system has worked quite satisfactorily for two years now. The coils can be kept constant in temperature within 0.5° C at an average temperature of 25° C, even at the highest occurring power input.

The N.T.C. resistor used for the stabilization system is situated in the median plane and between two layers of the inner coil. Thus, in fact the temperature of this resistor is stabilized, which means that for a discussion of the influence of the temperature distribution within the coils on the $B\rho$-determinations, one should consider the temperature difference between the coils and the N.T.C. resistor. At low currents this difference will be negligible; at high currents, however, one may expect the existence of (a) a temperature gradient in the direction of the kerosine flow and thus a difference between the average temperatures of both coils which are cooled in series and (b) a temperature jump between the inner coil and the coolant; the temperature of the resistor will lie somewhere between that of the inner coil and of the kerosine.

By means of the N.T.C. resistors inserted within the coils, we were able to investigate the temperature gradients in both coils at the maximum power input. When measuring at an energy of 2.6 MeV the power input in the inner coil is about 12 kVA, while the power input in the outer coil is then 1.5 kVA. The measurements showed that the axial gradient in the inner coil is about 1° C over the height of the coil, while the gradient in the outer coil can be neglected. These measurements also indicated that gradients in the φ-direction are not larger than 0.5° C per 180 degrees. Here we have assumed that the gradients as measured with the N.T.C. resistors are representative for those of the coils themselves. The absolute temperature of the coils at high coil current deviates from the temperature of the resistors. Therefore we decided to perform an independent measurement from which we could obtain information about the average coil temperature relative to that of the N.T.C. resistor used for the stabilization system. For this purpose we measured the resistances of the two copper coils at low as well as at high currents; during these measurements the temperature of the resistor in the median plane of the inner coil was kept constant within 0.2° C. From these measurements the difference in the average temperature of both coils at 170 A coil current was found to be about 0.9° C, whereas the average temperature of the inner coil was about 0.4° C higher than that of the resistor.

The above results are presented in fig. 11. A stream line of the kerosine is taken as the horizontal axis, while the temperature is plotted along the vertical axis. The temperatures given

are relative to that of the resistor in the median plane of the inner coil, which temperature is approximately 25° C. The dotted lines indicate the temperature of the kerosine at 170 A coil current as can be deduced from the combined knowledge of the ratio of the power inputs in both coils and of the ratio of the surfaces of the

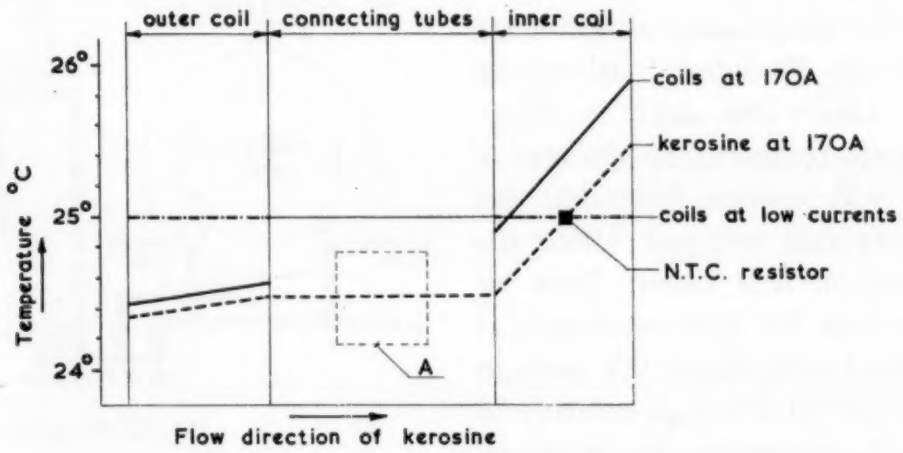

Fig. 11. Temperature distribution within the coils: – · – · – at low currents, ———— at the maximum coil current.

The figure shows that the temperature of the N.T.C. resistor, positioned in the median plane of the inner coil, follows that of the kerosine. For a discussion of the error in the $B\rho$-determination due to the temperature distribution of the coils at high currents, see text. The position of the box containing the resistors R_m (see figure 13), which box is inserted in one of the tubes connecting the inner and the outer coil for the kerosine, is indicated by the square A; thus these resistors are kept at kerosine temperature.

coils being in contact with the kerosine. Fig. 11 shows also that the manganin resistances R_m used for the bridge circuit of the magnet current device and inserted in box A, are kept constant in temperature within 1° C at any coil current.

Now we will discuss the effect on the positions of lines in consequence of (a) an overall temperature change of 1° C and (b) the temperature distribution at the maximum coil current as given in fig. 11.

Siegbahn and Edvarson[10]) have calculated the influence on the $B\rho$-determinations of a temperature change of 1° C in one of the coils or in the vacuum chamber. In our case, however, a straightforward calculation can not be given, because each copper coil is situated between two aluminium cylinders while these coil units are bolted together by aluminium flanges, the temperature distribution of which determine the position of the source- and counter construction. Therefore we preferred to determine experimentally (a) the effect of a temperature change of one of the coils relative to the other one and (b) the effect of an overall temperature change.

Table B presents the potentiometer reading at the top of a conversion line (ThB F-line) measured under different conditions with respect to coil temperatures. The temperature difference between the coils during run B could be obtained by switching off the cooling pump at the end of run A; maintaining the same coil current run B could be taken after about one hour. From these measurements can be deduced that the effect on the position of the line is about 2.2 parts in 10^5 due to a temperature change of 1° C in the inner coil, while a change in temperature of 1° C in the outer coil corresponds with an effect of one part in 10^5. Both

TABLE B

Influence of the coil temperatures on the line position

	Potentiometer reading at the top of the F-line (halfwidth 0.04 %)	Temperature	
		inner coil	outer coil
Run A	69 390	18.2° C	18.2° C
Run B	69 412†	30.2° C	21.2° C
Run C	69 417†	30.2° C	30.2° C

† Corrected for shift in the compensation level of the external magnetic field (see section 5.3).

line shifts are in the same direction. Thus an overall temperature change of 1° C will cause an error in the $B\rho$-determinations of 3.2 parts in 10^5. The same shift is found also (a) when measuring the same line with the use of another manganin resistance R_m (see fig. 13) and (b) when measuring a line different in $B\rho$-value by a factor of 2 (ThB L-line).

The influence of the temperature distribution at high currents on the $B\rho$-determinations can be found using the above line shifts in consequence of the separate temperature changes of the two coils. We will assume here that the gradient in the inner coil will not affect the positions of the lines in first order. Then we arrive at the result that the lines measured at 2.6 MeV will be shifted with about 0.5 parts in 10^5 towards higher current readings relative to low energetic lines. If necessary, the measurements can be corrected for this error because of its systematic character.

As will be discussed in section 5.3 a temperature change of 1° C of the inner coil will also cause a deviation from the true line position due to the fact that part of the external field compensation system is dependent on this coil temperature. This line shift is about one part in 10^5 per 1° C with the same sign as the line shift discussed above.

Thus we arrive finally at the following errors in the $B\rho$-determinations due to the cooling system:

a. The error due to an overall temperature change of 1° C is 4.2 parts in 10^5.

b. The error due to the difference in temperature of both coils at higher currents is at most one part in 10^5.

3.4. VACUUM SYSTEM (Fig. 12)

The vacuum tank of the spectrometer, which has a volume of 100 liter, is exhausted by an oil diffusion pump made of brass and copper (Philips O 4), backed by a rotating pump (Edwards 1S150). The latter pump is placed at a distance of 8 meter from the spectrometer. The connecting tubes are made of copper and are 60 mm in diameter. Aluminium air locks for admission of the source and the counter can be connected to the fore vacuum or the oil diffusion pump by valves V_5, V_6, V_7 and V_8; the gas filling system of the Geiger counter can be connected to the oil diffusion pump. The pressure in the

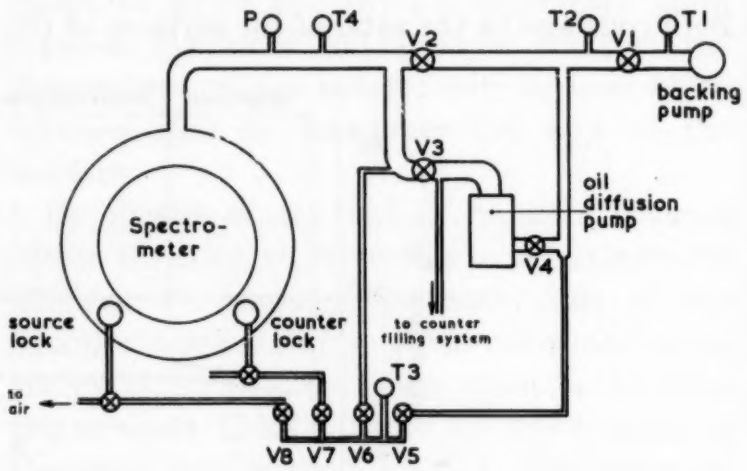

Fig. 12. Vacuum system.

different parts of the system can be read on four thermocouple manometers (T_1—T_4) (Philips Th 2), whereas in the vicinity of the tank the high vacuum can be measured with an ionization gauge (P). Most of the valves, indicated in the figure are Dikkers-Jenkins globe valves with slight modifications as described by Zilverschoon[12]) to make them useful for high vacuum work.

With this vacuum system it takes about 20 minutes to evacuate the vacuum chamber from atmospheric pressure down to about 10^{-4} mm Hg.

4. Generation, Stabilization and Regulation of the Magnet Current

4.1. INTRODUCTION

The magnet current supply of the spectrometer has been designed under the following considerations:

a. The maximum coil current must be about 170 A in order to obtain a magnetic field intensity, that will bend a beam of electrons of 2.6 MeV along a circle with a radius of 300 mm (see table A). For low energy work stabilized currents as low as a few A (5 keV $\triangleq$ 4 A) should be attainable.

[12]) C. J. Zilverschoon, Thesis, Amsterdam (1954).

b. The determination of the line position with a precision of a few parts in 10^5, as is feasible when dealing with a resolution of, say 0.02%, demands a long range stability of the field intensity of one part in 10^5 or better in the whole current range.

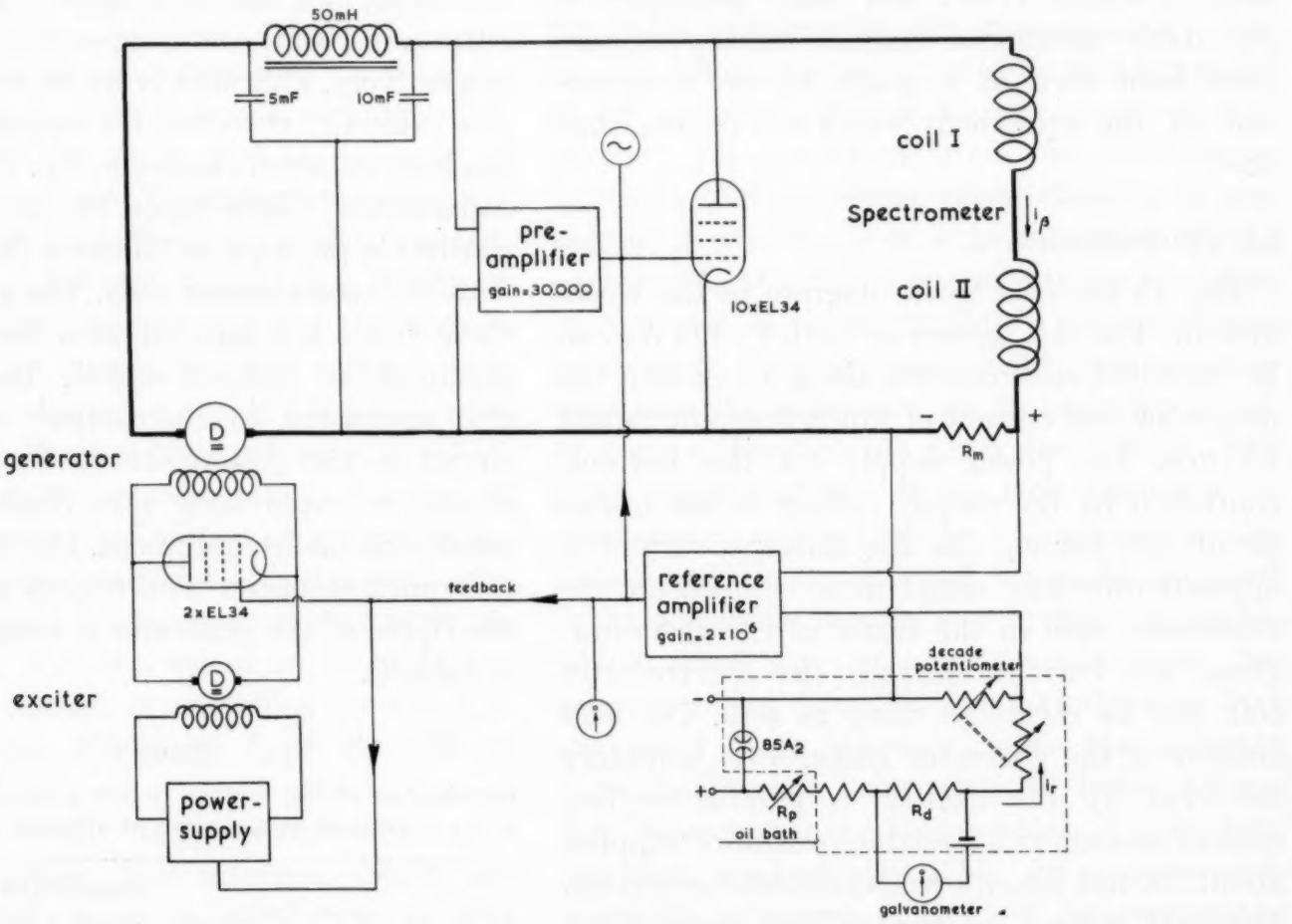

Fig. 13. Block diagram of the magnet current supply.

c. The stability of the current must be such that the line broadening due to current fluctuations is relatively small. This can be called short range stability. If we demand, that this line broadening be not more than one tenth of the intended resolution of a few parts in 10^4, the short range stability must be a few parts in 10^5 or better.

As already mentioned in section 2, the use of storage batteries for currents up to 170 A is rather unpleasant although it would be the most natural choice with respect to the stability requirements. Therefore we decided to use a motor-d.c. generator. Such a current source is very suitable for a beta-ray spectrometer where the current settings must be quickly and often changed; it offers the opportunity of regulating the main current through the coils electronically with the help of an exciter for the field current of the generator. On the other hand, the ripple of any d.c. generator is orders of magnitudes larger than permitted by the above considerations. Thus, a rather involved stabilization equipment had to be designed.

A convenient system has been described by Verster[13]) for the regulation of an ironfree short lens beta-ray spectrometer (long range stability better than 1:10^3). The current through the spectrometer causes a voltage drop across a standard resistor; this voltage drop is compared with an adjustable reference voltage. The voltage difference is used as a signal for a device which adjusts the current in the main circuit. This arrangement not only keeps the spectrometer current constant, but it also allows a determination of the absolute value of this current, because the reference voltage is determined by a constant

[13]) N. F. Verster, Appl. Sci. Res. B1 (1949) 358.

current flowing through a four decade resistor.

An improved version has been developed by Schutten[14]) for the stabilization of the magnetic field of the Amsterdam isotope separator (Zilverschoon[12])). The short range stability of the magnetic field of this iron containing instrument is about $1:10^4$. The main principles of the above mentioned magnet current supplies have been used as a guide for the construction of the equipment which will be described now.

4.2. EQUIPMENT

Fig. 13 shows a block diagram of the whole system. The d.c. generator (110 V, 170 A) can be regulated electronically using an exciter, the maximum coil current of which does not exceed 170 mA. The power supply for this current, controlled by the output voltage of the bridge circuit (see below), can also deliver a current in opposite direction, sufficient to compensate the remanence field in the stator of the generator. Thus, the current through the spectrometer coils can be regulated down to zero. The field current of the generator (max. 3 A) is mainly delivered by the exciter; a parallel feeding system serving as a variable resistance supplies about 200 mA into the field coils of the generator. The grid voltage of the parallel tubes ($2 \times$ EL 34) is also controlled by the output of the bridge circuit. This parallel feeding system reduces the time delay of the exciter (≈ 1 second), because now voltage variations on the output of the bridge circuit will supply current in the generator field coils rather than voltage as would be the case if these variations were fed back via the power supply of the exciter. The parallel system is effective only for variations with a frequency lower than a few cycles per second. Higher frequencies due to (a) the instability of the position of the rotor of the generator, (b) the revolution of the rotor and (c) the collector, could not be suppressed in an effective way by this feedback system, because of the time delay in the generator itself ($\frac{1}{10}$ second). Thus, these frequencies had to be suppressed directly in the main circuit. This demands a rather elaborate set up in view of the desired stability and of the very low impedance of the air coils (600 μH, 0.5 Ω) and has been carried out as follows:

First a π-filter was placed in the main circuit, consisting of a self inductance (50 mH at a d.c. current of 100 A) and 2 capacitors, 5 and 10 mF respectively. This filter is by no means sufficient (see table C); therefore the output capacitance has been enlarged electronically. The "electronic capacitance" (impedance for 25 Hz $\approx$ 2 mΩ) consists in principle of 10 tubes (EL 34) parallel with the spectrometer coils. The grid voltage of these tubes is regulated with the output of a pre-amplifier (gain 3×10^4). These grids are also connected to the output of the bridge circuit as this has shown to be effective with respect to suppressing slow oscillations of the whole stabilizing equipment. The effectiveness of this quick stabilizer with respect to suppressing the ripple of the generator is roughly indicated in table C.

TABLE C

Instabilities of the voltage in the generator-spectrometer circuit as measured at different points

	Instabilities due to		
	Jumping of the rotor	Revolution of the rotor	Collector
Without stabilization	$\approx 0.1\%$	$\approx 1\%$	$\approx 1\%$
With π-filter	$\approx 0.1\%$	0.1%	$< 0.01\%$
With π-filter and quick stabilizer	0.003%	0.001%	—

The bridge circuit indicated in the block diagram will be discussed in more detail, because it partly determines the precision of the measurements. The circuit consists of a resistor R_m through which the main current i_β is flowing, a five decade potentiometer and a reference current i_r. The resistor R_m is a combination of four manganin resistors for different ranges of i_β. They are inserted in the cooling system of

[14]) J. Schutten, Appl. Sci. Res. B2 (1952) 249.

the spectrometer (see fig. 11); thus, they are kept constant at a temperature of 25 ± 1° C. Their values are chosen such, that the voltage drop across them due to i_β can be read off with an accuracy of better than two parts in 10^5 by means of a five decade potentiometer,

$$10 \times (1000 + 100 + 10 + 1 + 0.1)\ \Omega\ ,$$

through which a reference current i_r(= 0.1 mA) is flowing. The potentiometer is manufactured by the N.V. Bleeker, Zeist, with an accuracy of about one part in 10^5. The reference current is kept constant at 0.1 mA with an accuracy better than one part in 10^5 with the aid of a stabilized neon tube (Philips 85A2) and can be checked continuously by comparing the voltage drop across a high resistance R_s (10.1874 kΩ) with the voltage of a Weston standard cell (1.01874 V) and adjusted to the correct value by means of the potentiometer R_p. The five decade potentiometer, the Weston standard cell, the neon tube and R_d are kept at a constant temperature, 25.0 ± 0.1° C, with the aid of an oil bath, the temperature of which is controlled by a N.T.C. resistor (Philips, Miniature Type B8 320 05 P/330).

The output of the bridge circuit is fed to a reference amplifier. This amplifier (input impedance 100 kΩ) is of the same type as that described by Schutten[14]). The d.c. signal is first converted into an a.c. voltage by means of a modified Brown converter (400 c/sec), amplified in four stages of push pull and finally synchronously rectified by a four triode circuit. The d.c. gain of this amplifier is about 2×10^6. The output of this amplifier controls different parts of the stabilizing system as described above.

4.3. PERFORMANCE

The magnet current system has been in use for 18 months. Up till now it has worked quite satisfactorily. How far the requirements for this device have been met will be discussed now.

Any stabilized coil current can be obtained just by choosing a certain setting of the potentiometer of the bridge circuit. The time delay for steps of 0.1 A or less is negligible, whereas it takes about 1 minute to increase or decrease the coil current by 15 A.

The stability of the main current can be checked on the control desk by means of a d.c. meter, which is connected to the output of the reference amplifier and an oscilloscope, which is connected to the output of the pre-amplifier of the quick stabilizer in the primary circuit (see fig. 13). Fluctuations, in the order of a few parts in 10^6 are observable on the d.c. meter at any current. The spectrum from the oscilloscope indicates that the short range stability of the voltage across the coils is in the order of one part in 10^5. At rather low currents say less than 15 A, the short range stability is somewhat less good, up to about one part in 10^4, because some very slow fluctuations seem to be independent of the d.c. level of the generator voltage. The short range stability of the field intensity in consequence of that of the voltage across the coils is not known, although it may be expected to be somewhat better due to the coil tanks, which form short-circuited windings in the generated field. An experimental indication that the short range stability meets the ultimate requirements has been obtained from calibration measurements, during which a resolution has been reached of 0.013% for a conversion line with an energy of 222 keV (corresponding to a coil current of about 30 A).

The long range stability of the average d.c. level of the current could be checked during measurements stretched out over several days; shifts in the positions of the different lines did not exceed a few parts in 10^5.

As the reading of the potentiometer of the bridge system is used for the determination of the coil current we will discuss now possible sources of error in the current determinations:

a. Leakage currents from the coils through the cooling fluid to the coil tanks, causing the coil current to be different from the current through R_m (see fig. 13). From section 3.3.1 we may conclude that leakage currents are orders of magnitudes lower than one part in 10^5 of the coil current.

b. Temperature changes in the different parts

of the bridge circuit. As described in section 4.2 all essential parts are kept at a constant temperature such that no temperature changes can occur which will affect the precision of one part in 10^5.

d. Other sources of error, e.g. contact potentials and leakage currents in the bridge circuit. Special attention has been paid to these sources of errors. Although nothing could be found

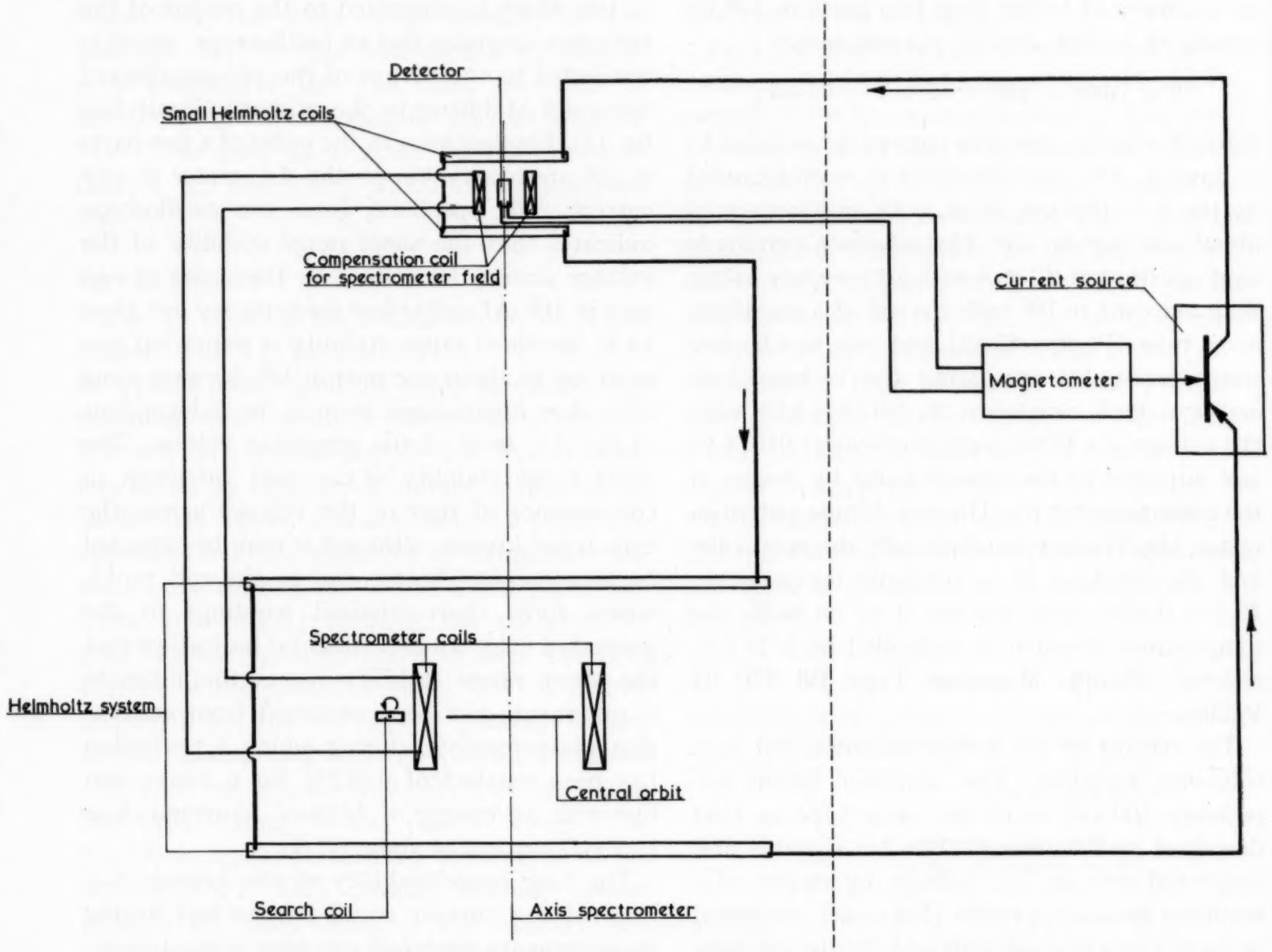

Fig. 14. Block diagram of the automatic compensation of the external magnetic field.

c. Deviation of the potentiometer reading from the true value. Each current reading is corrected for the zero resistance of this potentiometer. In addition, the true resistance can deviate from that indicated by the reading due to errors in the calibration of this element. The calibration has been carried out with an accuracy of one part in 10^5 by N.V. Bleeker at Zeist, Holland. This calibration procedure has been repeated after a time interval of about one year; no deviations have been found larger than two parts in 10^5.

which could affect the precision of one part in 10^5, it is felt that this measuring device need to be checked with precision compensating bridges if the highest possible accuracy is desired. The combined uncertainty due to the last two sources of error is assumed to be two parts in 10^5 for any current reading.

5. External Field Compensation

5.1. INTRODUCTION

The magnetic field intensity in an ironfree instrument is linearly proportional to the

current through the coils if no external fields are present. This fact makes it possible to use coil current readings as a measure for the momentum of the focused electrons. A known constant external field can be corrected for in computing electron momenta from current readings. The field gradient

$$\alpha = \frac{\rho_0}{B_0}\left(\frac{dB}{d\rho}\right)_{\rho_0},$$

however, is then dependent on the coil current. An external field of 0.45×10^{-4} Wb/m^2 (vertical component of the earth magnetic field at Amsterdam) would give a difference of 2% in the value of α at magnetic field intensities of 1 and 2×10^{-3} Wb/m^2, which means that the focusing properties would be seriously dependent on the field intensity. It is therefore necessary to compensate the external field. In addition, fluctuations of magnitudes up to 5×10^{-7} Wb/m^2 occur due to earth currents from railroad traffic at 100 meter from the instrument, while the 72″ synchrocyclotron magnet at this Institute as well as cars parking near the spectrometer building may cause field intensities of about 10^{-6} Wb/m^2; this means that the compensating system should be checked continually. The above considerations apply mainly to the vertical component of the external field; the horizontal component is less important since the electron orbits are mainly horizontal.

In order to be able to use the instrument with the intended precision of a few parts in 10^5 in the lowest previsaged energy region corresponding to a field intensity of about 10^{-3} Wb/m^2, external fields should be compensated with a precision of a few parts in 10^{-8} Wb/m^2.

5.2. COMPENSATION SYSTEM

In connection with the situation of the spectrometer room relative to the horizontal direction of the earth magnetic field, the horizontal component is compensated by means of two pairs of Helmholtz coils with their axis perpendicular to each other and with radii of 1.25 meter and 1.30 meter. The currents through these coils are delivered by power supplies which are stabilized within one part in 10^3. The values of these currents are such that the corresponding residual field at the centre of the spectrometer is less than 10^{-7} Wb/m^2. The d.c. levels of these currents can be checked by comparing the voltage drop across a precision resistance with the voltage of a standard cell. Fluctuations of the horizontal component of the external field are not compensated; an investigation of the influence of these fluctuations has shown that it is not necessary to compensate for them.

The z-component of the external field at the central orbit ($\rho_0 = 300$ mm) is compensated by means of a third pair of Helmholtz coils (radius = 1.20 meter). About 65 ampere-turns are necessary for compensating a magnetic field of 0.45×10^{-4} Wb/m^2; 340 turns are used in order to keep the necessary current conveniently low with a view towards automatic compensation of this vertical component. The compensation circuit will be described now (see fig. 14).

On the axis and 2.2 meter above the median plane of the spectrometer a magnetometer is placed within a small pair of Helmholtz coils (radius = 0.25 meter). This pair of Helmholtz coils, connected in series with the main Helmholtz coils, is designed such that it eliminates the external magnetic field at the position of the detector if the external field at the central orbit is compensated by the main Helmholtz coils. The detector is a magnetometer from the "Institut Dr. Förster", Reutlingen, Germany (type 1.103). The maximum sensitivity of this instrument is about 10^{-9} Wb/m^2. The output voltage of this instrument controls a transistorized current source for both pairs of Helmholtz coils. The overall gain of this feedback system is 4000. The detector is mounted 2.2 meter above the median plane to allow for an accurate compensation of the fringing field of the spectrometer. This compensation is performed by means of an extra coil around the detector, which coil is connected parallel to the spectrometer coils and the standard resistor R_m, as shown in fig. 16.

5.3. PERFORMANCE

The zero method system reduces the fluctuations described above to less than 10^{-8} Wb/m² at the position of the field detector. Thus, external field fluctuations equally strong at the positions of detector and central orbit, e.g. due to

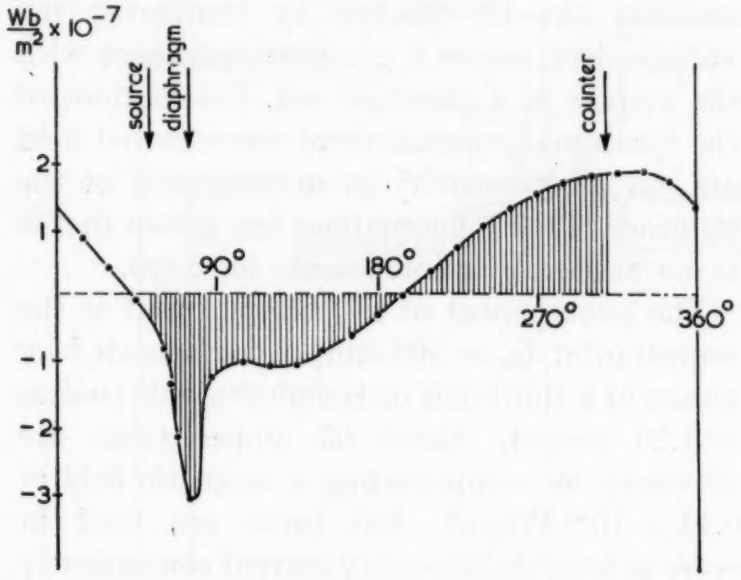

Fig. 15. Residual magnetic field along the central orbit.

changes in the intensity of the earth magnetic field, railroad traffic and the fringing field of the synchrocyclotron, will contribute less than one part in 10^5 to the spectrometer field even when measuring electron lines at an energy as low as 8 keV. Disturbances from nearby parking cars, however, still can cause a shift of 10^{-7} Wb/m² in the field intensity at the electron orbits due to the distance between the field detector and the median plane of the spectrometer. During high precision work, therefore, automobiles are not allowed to park within a radius of 20 meter. In addition, precautions have to be taken also for preventing disturbances, which might be caused by displacing iron containing equipment in the building.

The residual external field along the central orbit has been measured with a second magnetometer of the same sensitivity as the one used for the feedback system. As shown in fig. 15 the result follows a sinusoidal curve with a maximum amplitude of 1.5×10^{-7} Wb/m². The zero level, which has been adjusted by shifting the position of the detector of the feedback system in the axial direction, has been chosen such, that the integral of the intensity of the residual field over the central orbit between source and counter is nearly zero. Thus, this residual field which is probably due to imperfections of the Helmholtz system, can be neglected in most cases. Only for the very low energy region a correction to the $B\rho$-determinations has to be applied. The figure also shows that a peak near to the diaphragms is superimposed on the periodic field. This is due to iron impurities in a brass rod used for the construction of the diaphragms. Here again the influence of this disturbance can be neglected in all the usual work.

Long term drift of the adjusted compensation level may be caused by displacements of the field detector relative to the Helmholtz coils and to the spectrometer and also by a shift in the zero voltage level of the electronic equipment. The cause of a shift in the zero voltage level can be twofold (a) the d.c. level of the balanced amplifier may be out of balance, which can easily be checked and (b) the response of the field detector may become asymmetric about zero (Sokolowski[15])). To check the long term drift we attached a search coil to the spectrometer tank in the median plane and 250 mm outside the central orbit (see fig. 14). The sensitivity of this search coil is such, that a shift of 2×10^{-8} Wb/m² can be detected by means of a galvanometer equipment. During several months a long term drift of the compensation level of more than 5×10^{-8} Wb/m² has not been observed. Mainly due to the uncertainty in the difference in the field intensities at the positions of search coil and central orbit, we cannot exclude an external field contribution of 5×10^{-8} Wb/m² to the magnetic field generated by the spectrometer coils. This possible contribution means that a systematic uncertainty of 0.015×10^{-6} Wb/m in the determinations of the $B\rho$-values of electron lines should be taken into account.

Finally we will discuss the influence of the circuit used in order to compensate for the fringing field of the spectrometer at the position of the detector (fig. 16). In principle such a

[15]) E. Sokolowski, Ark. f. Fysik **15** (1959) 1.

compensation is not necessary; without it, the automatic external field compensating system will add to the spectrometer field, due to the feedback system, a homogeneous field approximately 0.2% of the spectrometer field which does not even disturb seriously the field shape in the spectrometer.

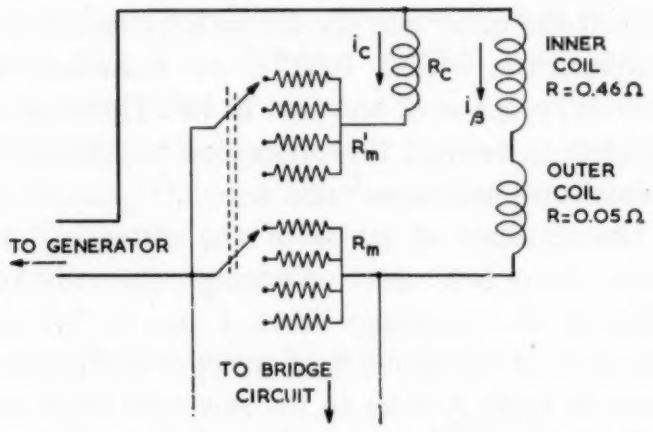

Fig. 16. The circuit to compensate the stray field of the spectrometer at the position of the field detector by means of the coil R_c.

At higher spectrometer currents, however, the intensity of the fringing field becomes larger than the earth field intensity; since it has the opposite sign, this introduces a complication in the feedback system. Therefore we decided to connect a compensation coil R_c to the spectrometer coils as indicated in fig. 16. The current ratio i_c/i_β is constant at any spectrometer current provided that (a) at each choice of R_m the corresponding resistance R'_m is chosen and (b) the resistances of R_c, the inner coil and of R'_m remain constant. The resistance of the outer coil and of R_m can be neglected in this consideration. Due to the fact that R'_m and R_c are made of constantan and manganin respectively, only temperature fluctuations of the copper inner coil can affect the constancy of the ratio i_c/i_β. The average temperature of this coil is kept constant within 1° C at all currents (see section 3.3). The temperature coefficient of the resistance of copper is 0.45% and the ratio between the spectrometer magnetic field at the central orbit and at the position of the compensating coil R_c is about 600. The influence on the $B\rho$-determinations in consequence of temperature fluctuations of the coils of 1° C is therefore about one part in 10^5. Only when measuring with the highest precision, the magnitude of this error becomes comparable with other errors; in that case it is possible to keep the temperature of the coils constant within a few tenths of one degree. We conclude therefore that the errors due to the fact that the compensating coil has been connected in parallel to the spectrometer coils can be neglected in all cases.

6. Determination of the Field Coefficients

6.1. DIRECT FIELD MEASUREMENTS

The values of the field coefficients α and β are obtained from the magnetic field distribution, which was measured using the Hall effect. The effective area of the hall plate used (Siemens and Halske, hall generator type FA 21) is 1×2 mm^2, which is sufficiently small to avoid the necessity to correct for the extension of the field measuring element. The hall voltage at 0.02 Wb/m^2 is about 1 mV when the current i_h through the plate is 75 mA; this voltage can be measured with an accuracy better than 0.1%. This precision enables one to determine α and β with sufficient accuracy. The temperature coefficient of the hall constant, which is defined as the ratio between the output voltage and the product of the field intensity and the current through the plate, is about 0.05% per °C. Since the measurements were carried out between the two spectrometer coils, which were kept at a temperature constant within 0.5° C, this temperature coefficient did not introduce serious uncertainties. The hall voltage has been measured with a null method using the bridge circuit shown in fig. 17.

The reading of the high precision decade resistor R_d at zero bridge current is taken as a measure of the hall voltage.

Since the method is relatively new, we tested its reliability. The ironfree spectrometer offers an ideal opportunity to test the linearity of the detector response; by changing the magnetic field intensity B in well defined steps (with an accuracy better than one part in 10^4) the hall voltage is measured as a function of B. The

region from (0—250) $\times 10^{-4}$ Wb/m² has been investigated in this way. The result, analyzed with the aid of a least square method, gave no

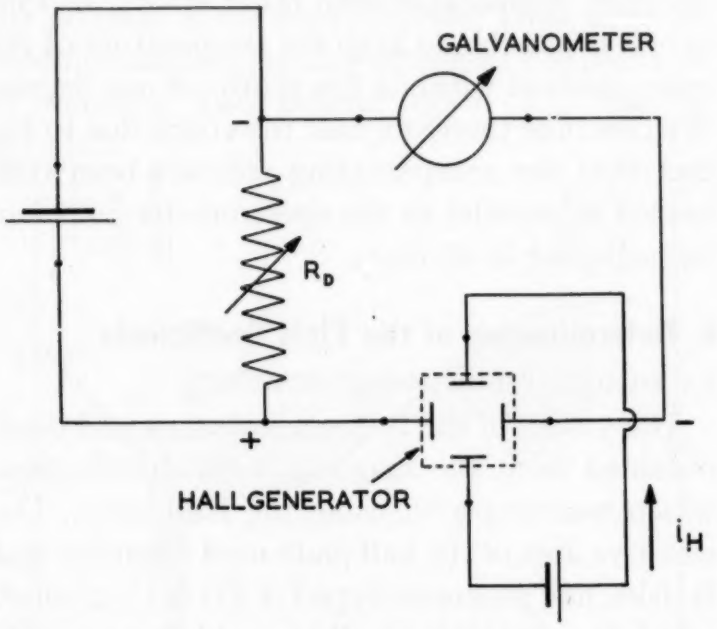

Fig. 17. The bridge circuit used to measure the output voltage of the hall generator.

departures from a straight line greater than 0.1 %. In the region from (190–210) $\times 10^{-4}$ Wb/m², which region is of special interest because the field distribution has been measured at an average field intensity of 200 $\times 10^{-4}$ Wb/m², the departures from linearity were even smaller than 0.05 %. The reproducibility of the measurements has been found to be about one part in 10^4.

A measurement of the axial symmetry of the spectrometer field was undertaken in the median plane at different radii: $r_1 = 300$ mm and $r_2 = 330$ mm. No aberrations larger than three parts in 10^4 could be detected over the whole circle. The field distribution was measured by shifting the detector in the radial direction over well defined distances. The result showed that the first order coefficient was about 8% lower than the desired value $\alpha = -\frac{1}{2}$. According to formula (3) this deviation will seriously spoil the transmission because the two foci will diverge then over an angle of about 0.35 radians.

The first order field coefficient α is dependent on the ampere-turns ratio of the two coils λ. A different value for α, therefore, can be obtained by shunting one of the coils or by changing the number of windings of one of the coils. We used the first method to obtain the better value of λ. Fig. 18 shows that λ had to be changed from 4.5 to 5.0 in order to obtain the correct α. This rather large change in λ means that the shunt in parallel with the outer coil should take about 10% of the coil current; rather small fluctuations in the resistance of the coil and the shunt would therefore be able to spoil precision measurements. Indeed the outer coil should be kept constant in temperature within 0.03° C to maintain the desired precision of one part in 10^5. Therefore we decided to rewind the outer coil to obtain the correct ampere-turns ratio $\lambda = 5$.

The number of turns of the outer coil has been decreased by enlarging the distance between the windings from 1 mm to 2.7 mm. The data of the number of turns of both coils as given in table A refer to the rewound outer coil.

The measurement of the field distribution of the coils at $\lambda = 5$ yielded the value -0.500 ± 0.003 for the first order coefficient α, whereas the second order coefficient β was 0.43 ± 0.04.

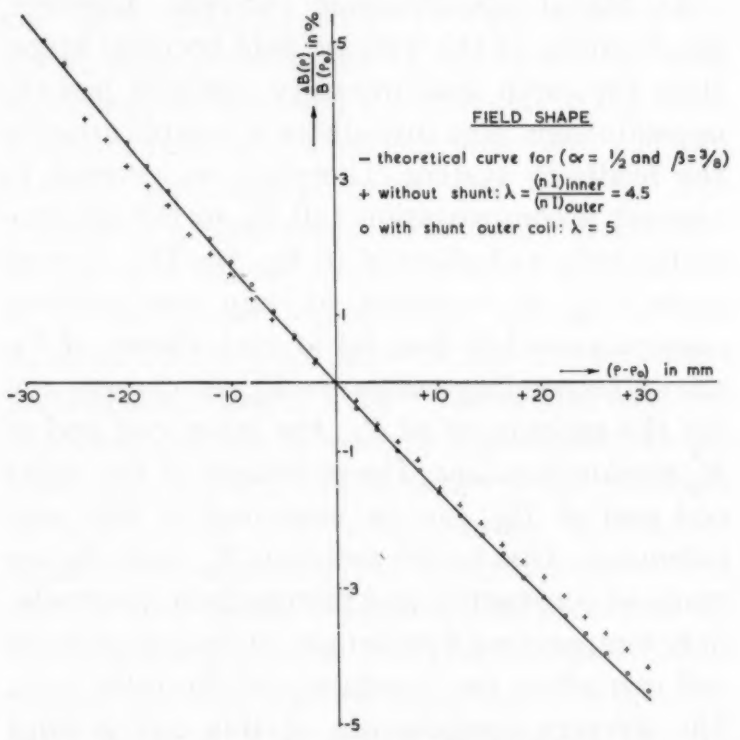

Fig. 18. Comparison between the theoretical field shape and the field shape as measured with a hall generator at two values of the ampere-turns ratio of inner and outer coil: $\lambda = 4.5$ and $\lambda = 5$.

In the next section these results will be compared with the results of the indirect test of the field coefficients by means of conversion lines.

6.2. FIELD COEFFICIENTS FROM CONVERSION LINE MEASUREMENTS

Maximum deviations of the coefficients α and β from the theoretical values $-\frac{1}{2}$ and $\frac{3}{8}$ respectively, can be found by comparing the experimentally obtained line width with that given by formula (9) which gives the base resolving power for a spectrometer with α exactly equal to $-\frac{1}{2}$ and an arbitrary value of β. For a field shape with $\alpha = -\frac{1}{2}(1+\varepsilon)$ the beam width δ_{ast} in the plane $\Psi = \pi\sqrt{2}$ will be, according to formula (3) and (5): $\delta_{ast} = \rho_0 \pi\sqrt{2}\, \gamma_\rho\, \varepsilon$.

Assuming that the base resolution R_0 is twice as large as the line width at half maximum R the following expression holds:

$$R = \frac{s+t}{8\rho_0} + \frac{|1-8\beta|}{12}\gamma_\rho^2 + \frac{|8\beta-3|}{12}\gamma_z^2 + \frac{\pi\sqrt{2}}{8}\varepsilon\gamma_\rho + \frac{|4\beta-3|}{96\rho_0^2}h^2 . \quad (10)$$

During measurements with conversion lines for calibration purposes the 222 keV L_1-line in ^{212}Bi (ThB I-line) has been measured under the following conditions:

Source width	s	= 0.07 mm
Source height	h	= 10 mm
Counter slit width	t	= 0.1 mm
Radial opening angle	γ_ρ	= 0.013 radians
Axial opening angle	γ_z	= 0.05 radians
Resolution	R	= 0.018% .

The resolution R has to be corrected for contributions to the line width, which might be caused by:

a. inaccurate mutual aligning of the source and the counter slit;

b. inaccurate position of the counter slit with respect to the focusing angle $\Psi_\rho = \pi\sqrt{2}$;

c. source effects;

d. fluctuations on the magnetic field;

e. natural line width of the transition.

The method of aligning the source relative to the counter slit will be discussed elsewhere[16]). Here we will neglect a possible contribution from an inaccurate alignment of the source.

Fomula (2), which gives the relation between the radial focusing angle Ψ_ρ and the first order field coefficient α, shows that a positioning of the counter slit outside the theoretical focusing plane $\Psi = \pi\sqrt{2}$ introduces a contribution to the line width which must be either added or subtracted from the contribution due to a possible deviation in α. This fact may be even used to minimize the contribution to the line width arising when the experimental field shape deviates from that given by theory. In our case the accuracy in the geometrical setting of Ψ is about 0.003 radians. From formula (2) it follows that this possible error is equivalent with an error in α of about 0.1%. In connection with the result of the present investigation we will neglect a possible contribution to the line width due to an error in the exact position of the counter slit.

Source effects can seriously contribute to the line width. The source used for the present investigation, however, may be regarded as ideal and therefore we will not take into account a possible line broadening due to source effects.

Fluctuations on the magnetic field can be caused by (a) fluctuations on the magnet current (b) external field fluctuations and (c) temperature fluctuations of the coils which are limited to 0.2° C for this measurement. Once again for the present investigation of the maximum errors in the field coefficients we assume no line broadening due to this effect present.

The natural line width of the transition under consideration is about 10 eV. Using formula (6) we find that the momentum resolution due to the finite level width is 0.0025%. As will be justified in a forthcoming article[16]) this contribution may be added linearly to the theoretical line width as given by formula (9).

From the above considerations it follows that the corrected resolution will be 0.0145%. Inserting this value together with the above given numerical values of s, h and t into formula (10) yields:

$$\frac{|1-8\beta|}{12}\gamma_\rho^2 + \frac{|8\beta-3|}{12}\gamma_z^2 + \frac{\pi\sqrt{2}}{8}\varepsilon\gamma_\rho = 7\times 10^{-5} . \quad (11)$$

[16]) C. de Vries, Nucl. Phys. **18** (1960) 428.

First it will be assumed that β equals the theoretical value $\frac{3}{8}$ which eliminates the influence of the axial opening angle to the second order. Then we find for ε:

$$\varepsilon = \pm 0.0058$$

from which follows

$$\alpha = -0.500 \pm 0.003 .$$

If we assume on the other hand that α has exactly the value $-\frac{1}{2}$, then equation (11) yields

$$\beta = 0.375 \pm 0.025 .$$

These results agree with those of the direct measurements, as shown in table D.

TABLE D

	Field coefficients	
	α	β
Theoretical	$-\frac{1}{2}$	$\frac{3}{8}$
Hall generator measurements	-0.500 ± 0.003	0.43 ± 0.04
Conversion line measurements	-0.500 ± 0.003	0.375 ± 0.025
Combined results	-0.500 ± 0.002	0.39 ± 0.02

Averaging the results of this and the preceding section yields the result also indicated in table D.

It is to be noted that the method of testing the focusing properties of the magnetic field as carried out in this section delivers only a result for the field coefficients which is an average over an extended region of the field. For the L_1-transition used above the maximum deviation of the electron paths from the central orbit is:

$$\Delta\rho = 5.5 \text{ mm}$$
$$\Delta z = 21 \text{ mm} .$$

A more extended region ($\Delta\rho = 36$ mm and $\Delta z = 150$ mm) has been used during measurements of conversion line intensity ratios. A typical set of data for the K-line of the 412 keV transition in ^{198}Hg is:

$$s = 3 \text{ mm}$$
$$h = 20 \text{ mm}$$
$$t = 3.2 \text{ mm}$$
$$\gamma_\rho = 0.085 \text{ radians}$$
$$\gamma_z = 0.35 \text{ radians}$$
$$R = 0.38\% .$$

Still under the assumption that $R = \frac{1}{2} R_0$, the calculation using these conditions yields the result that the field shape follows exactly that predicted by theory.

Summarizing we may conclude that the field shape of the present instrument agrees very well with that required by theory for first order focusing in both directions and for second order axial focusing. In practice the opening angles γ_ρ and γ_z are adjusted in such a way that $\gamma_z/\gamma_\rho = 4$; for this ratio of the opening angles the contributions of γ_ρ and γ_z to the line width resulting from spherical aberration are about the same, if the second order field coefficient equals the value 0.39 (see formula (9)).

7. Final Remarks

With the instrument presented in the preceding sections several kinds of measurements have been carried out, which will be published elsewhere[16,17,18]). Typical data with regard to resolution and luminosity used during these measurements are summarized in table E. From this table it can be concluded that the

TABLE E

Source area (mm^2)	Transmission (%)	Line width (%)
0.7	0.013	0.013
6	0.11	0.057
60	1.0	0.35
140	1.0	0.50

[17]) C. de Vries and J. H. Dijkstra, Nucl. Phys. **18** (1960) 446.

[18]) C. de Vries, E. J. Bleeker and Mrs. N. Salomons-Grobben, Nucl. Phys. **18** (1960) 454.

spectrometer is suitable for precision measurements requiring high resolution as well as for investigations on source material with a low specific activity, where a large source area has to be used. Calibration measurements[16]) with the aid of conversion lines ranging in energy from 150 keV–2.5 MeV show the linearity of the instrument to be better than one part in 10^4.

The authors wish to thank Professor P. C. Gugelot for his interest in this work. It constitutes part of the research program of the Institute for Nuclear Research, made possible by financial support from the Foundation for Fundamental Research of Matter (F.O.M.) and the Netherlands' Organization for Pure Scientific Research (Z.W.O.).

NUCLEAR INSTRUMENTS AND METHODS 8 (1960) 146–150; NORTH-HOLLAND PUBLISHING CO.

IMPROVEMENTS IN THE FAST NEUTRON TIME OF FLIGHT TECHNIQUE USING PULSE SHAPE DISCRIMINATION IN AN ORGANIC PHOSPHOR

R. BATCHELOR, W. B. GILBOY, A. D. PURNELL and J. H. TOWLE

Atomic Weapons Research Establishment, Aldermaston, Berkshire, England

Received 8 May 1960

A very simple pulse shape discriminator based upon the method suggested by Owen[1]) has been developed for the scintillation detector of a neutron time of flight apparatus. Almost complete cancellation of γ-ray pulses is obtained with the circuit adjusted to pass neutrons of energies greater than 0.4 MeV. By discriminating against γ-rays with the detector placed inside a large water shield, the random background has been reduced by a large factor. The improvement obtained is illustrated with an inelastic neutron spectrum taken with iron at 4 MeV incident neutron energy. In this case the background reduction factor is between 5 and 10.

1. Introduction

One of the principal difficulties in fast neutron spectroscopy with the time of flight technique is to obtain a sufficiently high ratio of true events to background counts. This problem is particularly acute for systems which employ post acceleration pulsing of a Van de Graaff beam, as developed by Cranberg[2]). At high beam energies considerable background is generated by the unwanted beam being swept by the deflection system, either into the deflector plates or into metal parts further down the beam pipe assembly. For some applications, particularly inelastic neutron scattering experiments, this background can become prohibitively high.

One possible method of reducing the background is, of course, to use top terminal pulsing of the generator[3,4]). However, as far as is known, this technique has not yet been used for high energy inelastic scattering, although it is likely to be actively pursued in the future.

This paper describes a second and very simple method of reducing the background. The technique is based on the recent development by Brooks[5]) and Owen[1]) of discrimination between neutron and gamma ray pulses in certain organic scintillators by their difference in shape. In a time of flight spectrometer the background radiation incident on the well-shielded neutron detector consists of neutrons and γ-rays and cosmic rays, the latter being mainly lightly ionising μ-mesons. In the shield itself, which typically consists of a mixture of paraffin wax and lithium carbonate, or perhaps water alone, many of the background neutrons are likely to be converted into γ-rays by capture and inelastic scattering events. The radiation incident on the detector is therefore likely to be composed of a large proportion of γ-rays. Normally the detector is surrounded with an inch or two of lead to attenuate these γ-rays. By applying pulse shape discrimination to the detector, it is possible to reduce considerably the effect of the remaining γ-radiation without substantially reducing the neutron detection efficiency.

A method of reducing background, based on this technique, has previously been described by

[1]) R. B. Owen, A.E.R.E., Harwell, Report No. EL/R 2712 (1958) and I.R.E. Transactions on Nuclear Science, NS — 5 No. 3 (1958) 198.

[2]) L. Cranberg, Proceedings of the International Conference on the Peaceful Uses of Atomic Energy **4** (1955) paper 577.

[3]) V. E. Parker and R. F. King, Bull. Am. Phys. Soc. (1956) 70.

[4]) C. M. Turner and S. D. Bloom, Rev. Sci. Instr. **29** (1958) 480.

[5]) F. D. Brooks, Nuclear Instruments and Methods **4** (1959) 151.

Neilson *et al.*[6]). The method we describe was conceived independently and is believed to be rather more simple than that described previously. The performance is illustrated with an inelastic neutron spectrum taken for iron at 4.06 MeV incident neutron energy.

2. Description of Apparatus

The system to be described here has been incorporated into the time of flight spectrometer used on the Aldermaston 6 MV Van de Graaff generator. Details of the spectrometer have been described previously[7]). More recently the paraffin and lithium carbonate shield originally used has been replaced by a larger water shield. The detector, surrounded with 2″ of lead, sits in the centre of a cylindrical water tank, 4 ft in diameter and of height 4 ft. A suitable collimator, 2″ in diameter, is inset into the tank to provide an absorption-free path for the "true" neutrons incident on the detector. If further attenuation

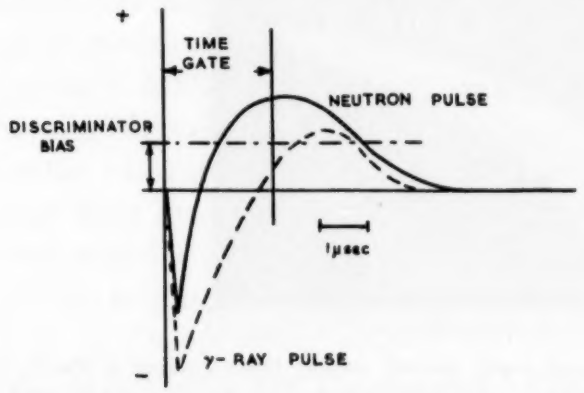

Fig. 1. Dynode pulses from the "Owen type" circuit for a 6 MeV neutron and a 2 MeV γ-ray. The positive swing of the γ-ray pulse, in this case, rises above the discriminator bias level but does not cross this level within the time gate.

of the neutrons emitted directly from the source (these of course should be eliminated in a scattering experiment) is desired, one or two smaller water shields in the form of truncated cones can be added. In order to take full advantage of the pulse shape discrimination technique, the detector used is an organic liquid scintillator type NE213†, contained in a glass cylinder 2″ diameter, $2\frac{1}{2}$″ long, with flat ends. This scintillator is viewed by two photomultipliers, type RCA 6810A, connected in coincidence, and each biased well into noise. The neutron detection efficiency rises with increasing neutron energy to

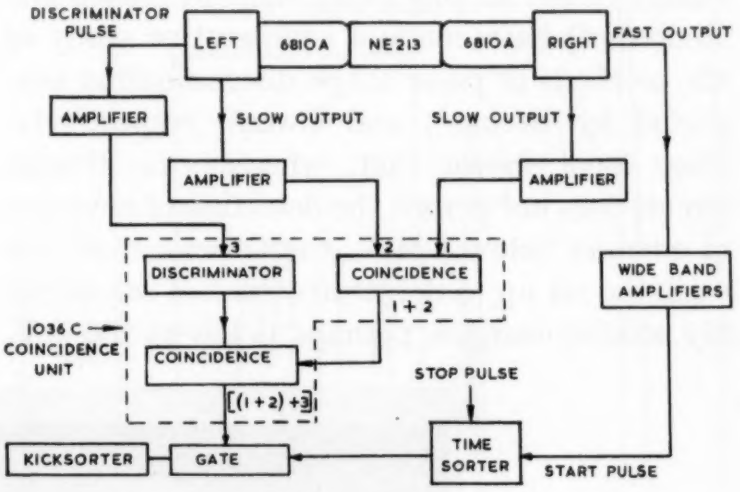

Fig. 2. Simplified block diagram of the time of flight electronic apparatus using pulse shape discrimination.

a value of about 30% at 0.8 MeV and then remains approximately constant. The value at 0.4 MeV is about 15%.

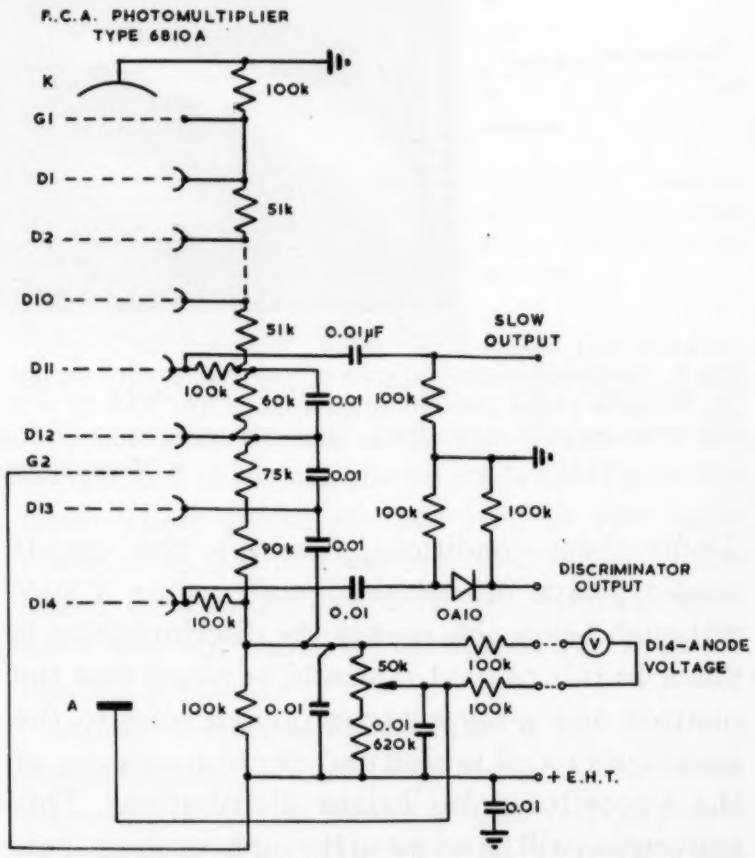

Fig. 3. Photomultiplier circuit for pulse shape discrimination.

† Supplied by Nuclear Enterprises, (G.B.) Ltd. Edinburgh.

[6]) G. C. Neilson, W. K. Dawson and F. A. Johnson, Rev. Sci. Instr. **30** (1959) 963.

[7]) R. Batchelor and J. H. Towle, A.W.R.E. (Aldermaston) Report No. NR/P-12/58 (1958); and Proc. Phys. Soc. **73** (1959) 193.

An important requirement of the n–γ discriminator is that it should not greatly impair the neutron detection efficiency over the entire energy range. At this Establishment, Souch and Redfearn[8]) have made a comparative study of the methods of pulse shape discrimination suggested by Brooks[5]) and Owen[1]) respectively. They have shown that, whereas the Brooks circuit does not permit the detection of neutrons of energies below 1 MeV, the Owen circuit can easily be set up to detect neutrons of considerably smaller energies, perhaps as low as 200 keV. against high energy γ-rays. Fig. 1 shows diagrammatically, pulses for a 6 MeV neutron and a 2 MeV γ-ray, these having approximately the same integral pulse height. As can be seen the γ-ray will, in this case be detected since the positive swing rises above the discriminator bias voltage. Note, however, that the dynode returns to positive voltage earlier in the case of the neutron pulse. The time difference is approximately 1 μsec (the value depends on the integrating time constant of the following amplifier which in this case was 0.2 μsec). Therefore, by accepting

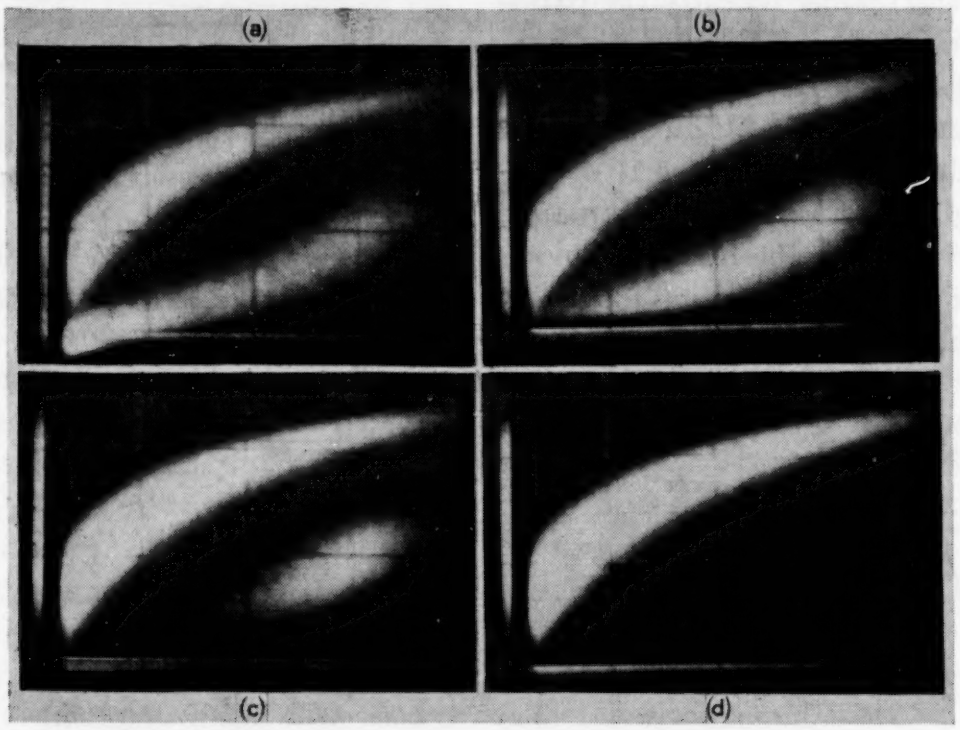

Fig 4. Oscilloscope photographs of neutron events (upper trace), and γ-ray events (lower trace), using a Po-Be source. (a) No pulse shape discrimination applied. (b) [1 + 2) + 3]. Coincidence resolving time 4 μsec, bias level adjusted to cut out low energy γ-rays and to pass 0.4 MeV neutrons. (c) [(1 + 2) + 3]. Resolving time = 2 μsec. (d) [(1 + 2) + 3]. Resolving time = 1 μsec.

Under these conditions, however, this circuit passes γ-rays of energies greater than 2 MeV although below this energy the discrimination is good. In this context it should be noted that the neutron and γ-ray energies quoted refer to the maximum recoil proton and electron energies of the respective pulse height distributions. This convention will be adopted throughout this paper.

An examination of the pulses obtained from the last dynode of a photomultiplier wired in the manner discussed by Owen[1]) suggested to us a simple method of improving the discrimination only those pulses which exceed the bias level within a time interval of one or two μsec after the start of the pulse, additional discrimination against high energy γ-rays can be obtained.

Fig. 2 shows how a scheme employing this idea is incorporated into the electronic arrangement used in the time of flight spectrometer. The left hand photomultiplier is wired, as shown in fig. 3, to give slow linear and "Owen" outputs. A crystal diode, type OA 10, is included to limit the negative swing of the last dynode pulse so that blocking effects in the following amplifier can be reduced. Otherwise the circuit

[8]) A. E. Souch and J. Redfearn, private communication.

is very similar to that originally proposed by Owen. The "Owen pulse" is amplified by a non-blocking amplifier and is then fed into the third channel of a triple coincidence unit Harwell type 1036C. Here amplitude discrimination first takes place and the resultant pulse, if any, is put into coincidence with the coincidence pulse from channels 1 and 2. Without pulse shape discrimination this (1 + 2) pulse is the one which gates the output of the time sorter through to the pulse height analyser. With pulse shape discrimination the final coincidence pulse [(1 + 2) + 3] fulfils this function, the time restriction, discussed in the previous paragraph, being obtained by reducing the resolving time of this circuit. In the 1036C unit this resolving time can be varied from 0.1 μsec to 4 μsec.

The oscilloscope photographs in fig. 4 illustrate the effect of varying this [(1 + 2) + 3] resolving time with pulses produced by a Po-Be source. The amplified "Owen pulses" and the amplified slow linear pulses were applied to the Y and X plates of the C.R.O. respectively. In fig. 4(a) the C.R.O. brightness control is switched by the coincidence (1 + 2) output to produce a spot at the extremity of the trace. The spots fall into two clear lines, the upper one representing neutrons and the lower one γ-rays. In 4(b), (c) and (d) the brightness control is switched by the [(1 + 2) + 3] coincidence output. The resolving time in (b) is 4 μsec, and the channel 3 discriminator is adjusted to cut out low energy γ-rays while still passing approximately 0.4 MeV neutrons. In (c) the resolving time is 2 μsec and in (d) 1 μsec, at which value no γ-ray events are seen.

3. Performance

Fig. 5 shows the improvement obtained with pulse shape discrimination for a typical inelastic neutron scattering experiment. Neutrons of energy 4.06 MeV, produced by bombarding a tritium gas cell with 4.95 MeV protons, are scattered by a 160 g iron sample in the form of a hollow cylinder. A long counter was used to monitor the neutron output and normalise the various runs shown in fig. 5. The lower solid

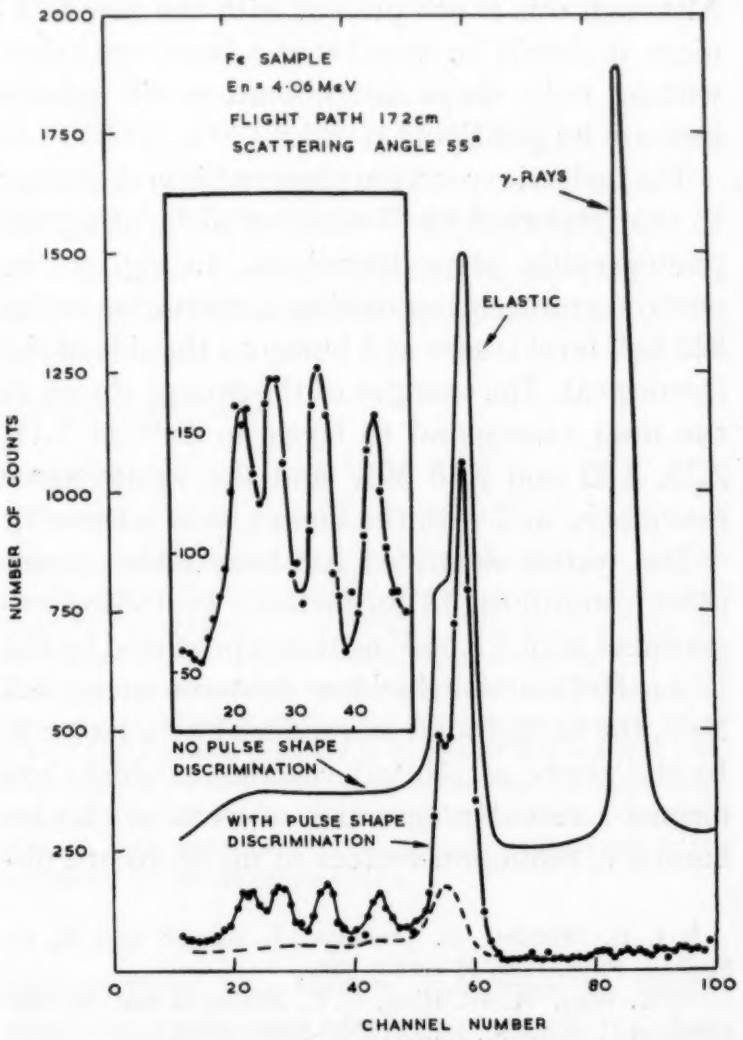

Fig. 5. Time spectra of neutrons, at 4.06 MeV incident neutron energy, scattered by iron illustrating the reduction in background obtained with pulse shape discrimination and with the scatterer removed.

curve was obtained with pulse shape discrimination applied. Each channel corresponds to 2.06 nanosec. Several inelastic peaks are observed and these are shown more clearly in the inset. These peaks are not seen in the upper curve of fig. 5 which was recorded without pulse shape discrimination, since the running time used was not sufficient to obtain the required statistical accuracy.

Another interesting feature of fig. 5 is the disappearance of the γ-ray peak in the lower curve. From the statistical accuracy of the points in this region we infer that the detection efficiency for the γ-rays observed in this experiment, which probably have a mean energy of about 1 MeV, has been reduced by a factor of at least 300. Very often the γ-ray peak is used as a calibration peak in a time of flight spectrum.

Although this is not present with the new technique it should be noted that a short run taken without pulse shape discrimination will quickly indicate its position.

The inelastic spectrum observed is very similar to that reported by Weddell *et al.*[9]), using the photographic plate technique. In fig. 5 the neutron group corresponding to scattering to the 845 keV level is seen as a bump on the side of the elastic peak. The energies of the groups shown in the inset correspond to levels in Fe^{56} at 2.16, 2.73, 3.03 and 3.18 MeV and the values agree reasonably well with the known level scheme[10]).

The system described has been tested under other conditions. In an inelastic scattering experiment with 7.5 MeV neutrons produced by the D(d,n)He^3 reaction, incident deuteron energy 4.3 MeV, the background was reduced by a factor 4. In the study of (He^3,n) reactions, which has formed a recent programme of work at this laboratory, reduction factors of up to 20 are observed. Using a source of ^{7}Li(p,n)^{7}Be neutrons, the neutron detection efficiency at 500 keV neutron energy is found to be about 90% of its former value. Above 1 MeV there is no significant decrease in the efficiency.

The application of pulse shape discrimination reduces the natural background rate from the shielded detector, (no external sources present and no accelerated beam) from 120/min to 6/min. The latter is well below that expected from cosmic rays, which would be about 20/min for this detector. The discriminator must therefore reject a large fraction of the cosmic ray pulses. This effect may be of more general interest in low level counting rate experiments.

In conclusion, this work shows that a very significant improvement in the neutron time of flight technique can be obtained by the application of pulse shape discrimination. A further improvement can be made with top terminal pulsing. This should be particularly significant for proton beams in excess of 5 MeV and deuteron beams, since in the present arrangement these beams produce very intense neutron backgrounds in the region of the deflector plates.

[9]) J. B. Weddell, B. Jennings, I. Alexoff and R. L. Mellens, Phys. Rev. **98** (1955) 582.

[10]) K. Way, R. W. King, C. L. McGinnis and R. van Lieshout, U.S.A.E.C. Report TID-5300 (1955).

NUCLEAR INSTRUMENTS AND METHODS **8** (1960) 151–172; NORTH-HOLLAND PUBLISHING CO.

THE OSCILLOSCOPE METHOD OF MEASURING NUCLEAR HALF-LIVES

I. BERGSTRÖM[a,b,c,d], E. C. O. BONACALZA[a], A. JECH[b], M. PEREZ[b] and P. THIEBERGER[a,b,c,e]

[a]*Instituto de Física, Facultad de Ciencias, Universidad de Cuyo, San Carlos de Bariloche, Argentine*

[b]*Departamento de Física, Facultad de Ciencias Exactas y Naturales, Universidad de Buenos Aires, Buenos Aires, Argentine*

[c]*Nobel Institute of Physics, Stockholm 50, Sweden*

Received 14 April 1960

It is shown that the modern fast oscilloscopes now available commercially, are very simple and powerful tools for measuring nuclear half-lives. The advantages and the limitations of the method are discussed. In order to illustrate the problems which are associated with measurements in different half-life regions, seven half-lives associated with metastable states in the following nuclei were measured: Pb^{205} (4.1ms), Pb^{206} (125 μs), Ta^{181} (17.5 μs), Rb^{85} (1.0 μs), Pb^{204} (302 mμs), Pb^{203} (55 mμs) and Ta^{181} (11.0 mμs). The half-lives measured thus cover a half-life ratio of almost 10^6:1, but it is shown that in favourable cases this ratio might be as large as 10^8:1. Thus the oscilloscope method can be used in the whole region where conventional delayed coincidence technique is applicable. It is significant for the usefulness of the method that when studying half-lives which were reasonably well known and only chosen for the purpose of investigating the oscilloscope method itself, a new half-life was discovered in one of the samples used (Pb^{203} (55 mμs)). A very great advantage of the oscilloscope is the fact that it can be very easily used as a multichannel time analyzer, by continuously photographing the events on the oscilloscope screen.

1. Introduction

The measurements of nuclear half-lives contribute in an important way to our systematic knowledge of nuclei, because in many cases they give information about the matrix elements of electromagnetic and other modes of transitions between nuclear states. In addition, the presence of delayed gamma transitions may often simplify the establishment of complicated level-schemes.

During the past ten years a considerable amount of information has been obtained about electromagnetic transitions of nuclear metastable states[1,2]). Transitions having half-lives larger than about 1 s are thus relatively well known by now. Therefore it is to be expected that many of the most interesting cases of nuclear isomerism, which will be discovered in the future will have half-lives considerably shorter than 1 s. Also in the field of alpha-spectroscopy[3]) and for the search of new elements the techniques of measuring short half-lives have become very essential. In this region delayed coincidence technique may be used and recently a considerable amount of work has been performed in order to extend the lower limit of this method. A somewhat different type of experiments used in connection with accelerators are the ones performed with pulsed beams[4]). A lot of interest has also recently been focussed onto the possibilities of developing new methods for half-lives shorter than 10^{-11} s[5,6,7]). Restricting ourselves to the region where half-lives can be relatively easily measured by delayed coincidence technique (10^{-9}–10^{-1} s),

[d] On leave of absence on a UNESCO-contract from the Royal Institute of Technology and the Nobel Institute of Physics, Stockholm, Sweden.

[e] During the later phase of this investigation working at the Nobel Institute of Physics on a scholarship from the Consejo Nacional de Investigaciones Científicas y Técnicas (Argentine).

[1]) M. Goldhaber and A. W. Sunyar, Beta and Gamma-ray Spectroscopy (North-Holland Publishing Company, 1955).

[2]) I. Bergström and G. Andersson, Arkiv för Fysik **12** (1957) 415.

[3]) P. A. Tove, Arkiv för Fysik **13** (1958) 579.

[4]) R. B. Duffield and S. H. Vegors, Phys. Rev. **112** (1958) 1958.

[5]) T. R. Gerholm, Arkiv för Fysik **11** (1956) 75.

[6]) B. Johansson and T. Alväger, Nucl. Instr. **3** (1958) 49.

[7]) A. E. Blaugrund, Phys. Rev. Letters (Sept. 1, 1959).

there are surprisingly few systematic investigations reported. Very probably one of the reasons for this is that the equipment used was often limited only to a small part of this half-life region. Obviously an instrument which covers the whole time region mentioned above would be very useful. The accuracy and flexibility of fast modern oscilloscopes, are so outstanding that we considered it worthwhile to investigate systematically, whether the oscilloscope would be such a universal instrument. The use of a cathode ray tube oscilloscope for measuring half-lives was reported for the first time already in 1947[8]) (see below), and is thus not a new method. Since then it has not been used very frequently, and as far as we know there are no systematic investigations published about the applicability and the limitations of the method.

Fast oscilloscopes and pulse height analyzers are now standard tools in most nuclear laboratories, even the smaller ones, which is usually not the case with equipment for measuring nuclear half-lives in a wide time region. One of the main advantages with this combination of equipment, is of course, that it can be rapidly put together for measuring a half-life and that the same components are immediately available for other purposes when the measurements have been finished.

2. Previous Work and the Origin of this Work

It is interesting to note that the very first delayed coincidence measurement reported already in 1934 by J. C. Jacobsen[9]) was performed in a way rather similar to the oscilloscope method. A light beam was deflected by two crossed "moving iron oscillographs" to which the pulses from two G.M. counters were fed. The deflected beam was focussed onto a moving photographic film and the delayed events could be distinguished from the prompt ones by the special shape of the picture on the film. The first successful measurement (1947) of a nuclear half-life with a cathode ray oscilloscope is due to S. Rowlands[8]). He measured the 140 μs state of RaC′, which is fed by β-particles and decays by α-particle emission. A schematic drawing (fig. 1) indicates the experiment by Rowlands. Pulses originating from the detection of the β-particles released the sweep and the delayed pulses from the alpha decay were fed to the y-plates of an Ultrascope Mark 6. The delayed pulses appearing on the screen were counted visually and though the half-life obtained was considerably longer than previously reported values, Rowlands clearly showed that the method worked.

In his thesis[10]), P. Axel discusses a measurement of a half-life in Cd obtained by using the oscilloscope method. In 1948 a group at the University of Illinois tried to measure the half-life of a 70 keV state in Gd, reached in a slow neutron capture reaction[11]). In order to check the possibility of using the oscilloscope method in a case like this one, they first successfully remeasured the 0.5 μs half-life in Ge^{72}. No half-life was, however, observed in Gd. In these experiments the sweep was triggered by the capture gamma-rays and pulses due to conversion electrons of the 70 keV gamma ray were used for intensity modulation of the electron beam and also after a certain constant delay fed to the y-plates. In this way the delayed

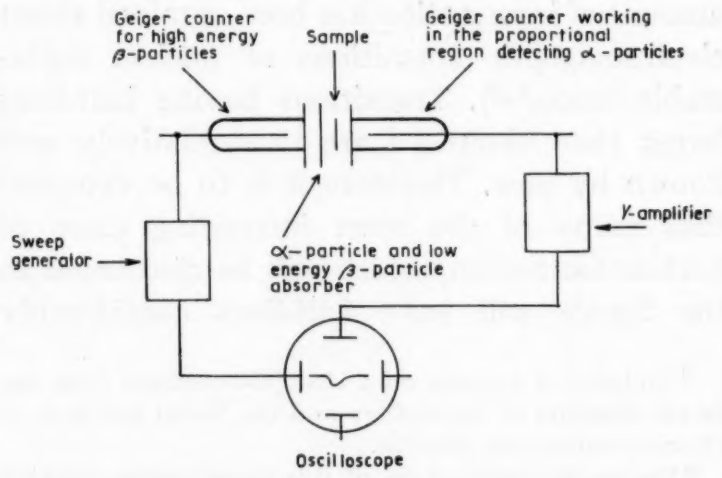

Fig. 1. Schematic drawing of the set-up used in the first measurement of a nuclear half-life (the 140 μs state of RaC′) with the oscilloscope method by S. Rowlands[8]).

[8]) S. Rowlands, Nature **160** (1947) 191; Journal of Scient. Instr. **25** (1948) 218.

[9]) J. C. Jacobsen, Nature **133** (1934) 565.

[10]) P. Axel, Physics Department, University of Illinois, Thesis (1948) (unpublished).

[11]) O. Sala, P. Axel and M. Goldhaber, Phys. Rev. **74** (1948) 1249.

events appeared as "sharp knees" on the screen, which was continuously photographed. This group was thus evidently the first one which used the oscilloscope as a multichannel time analyzer.

Not until 1953 were the next measurements with this method reported. D. Alburger[12]) discovered the metastable state in Pb^{206} by letting X-rays, detected by a NaI crystal, trigger a Tektronix 511 AD and observing the delayed γ-pulses fed to the γ-plates, through a movable 1.5 cm slit in front of the screen. The light from the delayed events seen through this slit was optically focussed onto a photomultiplier and by changing the slit position and counting the light pulses a half-life of 145 ± 15 μs was obtained. This half-life was remeasured by B. Åström[13]) in 1957 with a rather different method. The cathode ray tube of a Tektronix 535 was used only for inspection purposes and the oscilloscope worked essentially as a delayed-pulse generator. Åström obtained a value of 128 ± 5 μs.

For the sake of completeness it should also be mentioned that R. Ballini[14]) in 1953 suggested a method in which not a commercial oscilloscope but rather a cathode ray tube and especially designed electronics were used. With this equipment Ballini searched for half-lives in the region 1 ms–1 μs, but only the case of Ta^{181} ($T_{\frac{1}{2}} = 17.2$ μs) was measurable.

The oscilloscope is nowadays also frequently used in high energy physics for the determination of small time differences. An example of a life-time determination of the π^- meson is presented in a recent paper by J. Ashkin *et al.*[15]). The application of the oscilloscope in this kind of measurements is, however, somewhat different from that one used for the determination of nuclear half-lives.

[12]) D. Alburger and M. H. L. Pryce, Phys. Rev. **92** (1953) 514.

[13]) B. Åström, Arkiv för Fysik **12** (1957) 237.

[14]) R. Ballini, Annales de Physique **8** (1953) 441.

[15]) J. Ashkin, T. Fazzini, G. Fidecaro, Y. Goldschmidt-Clermont, N. H. Lipman, A. W. Merrison and H. Paul, CERN, Geneva, circulated preprint.

[16]) S. H. Vegors and R. L. Heath, Phys. Rev. (to be published) (see also Phys. Rev. Letters (Dec. 15, 1959) p. 590).

It is clear from the above that the work performed so far with the oscilloscope method concerns only a few measurements of nuclear half-lives in the region 0.5–140 μs. During a summer course in nuclear physics at the Instituto de Fisica in Bariloche, Argentine (Jan. 7–March 7, 1959), in which the authors took part, some preliminary measurements with this method were made. The outcome of this experiments was so unexpectedly successful that we felt that this method very probably was useful in a much wider half-life region than had been believed until then. Already during the summer-school in Bariloche, we confirmed the extraordinarily interesting suggestion by Vegors and Heath[16]) of a 4 ms isomeric state in Pb^{205}. This case gave us experience regarding the possible upper limit of the method. After the end of the summer-school the measurements were continued at the Physics Department of the Buenos Aires University and three half-lives of 125, 17.5 and 1.0 μs in the decay of Pb^{206}, Ta^{181} and Rb^{85}, respectively, were studied. Finally two of us (I.B. and P. T.), after coming to Sweden, continued studying the lower limit of the oscilloscope method essentially by measuring the half-lives of the first 4^+ state in Pb^{204} (302 mμs), a 55 mμs-state in Pb^{203} (discovered when measuring the half-life of Pb^{204}) and the 11.0 mμs state in Ta^{181}. The ratio between the longest and shortest half-life studied in this work is thus almost 10^6:1 but we believe that the method with favourable cases should be able to cover a ratio of about 10^8:1, which certainly is a considerable half-life region for a single instrument, the parts of which are available in most nuclear laboratories.

3. Different Ways of Applying the Oscilloscope Method

In fig. 2 an extremely simple case of nuclear isomerism is indicated. Let us assume that the half-life $T_{\frac{1}{2}}$ to be measured is due to a state B. "a" symbolizes signals telling us that nuclei in the state B have been created, and "b" are signals giving information that the same state has decayed. "a" may not only be due to

pulses from the detection of alpha- and beta-particles, conversion electrons, gamma-rays or X-rays, but in a nuclear reaction these signals may also be due to inelastically scattered

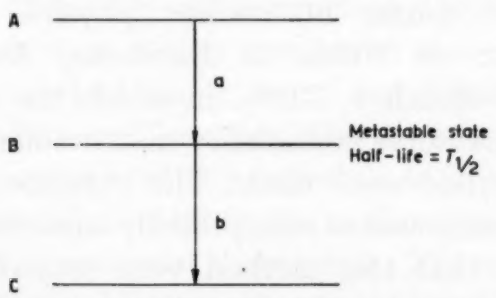

Fig. 2. Simplified schematic drawing of the level scheme corresponding to the feeding and decay of the metastable states studied. In the following the detectors accepting the photons or particles corresponding to transitions a and b and the pulses produced in them will be denoted by the same letters.

particles or pulses associated with the beam of a pulsed accelerator. However, we are not going to include these last two cases in the following discussion. "b" usually originates from pulses due to detected beta-, gamma- and X-rays and conversion electrons.

The detectors used in the experiments, when adjusted to accept the a- and b-pulses, will also detect "unwanted" pulses. The pulses may be due to cosmic ray background or to the fact that the decay scheme is much more complicated than indicated in fig. 2. The samples may also contain "impurities" of unwanted radioactive nuclei. All the pulses detected when the detectors are set to accept the a- and b-pulses will be denoted a′ and b′, respectively, in the following.

It is obvious that in cases where the half-lives studied are long compared to the time fluctuations in the detecting devices and in the oscilloscope itself, the distribution of events (corrected for random events) along the sweep direction, gives directly the decay of the metastable state studied and that thus the logarithm of the number of true, delayed events plotted as a function of the sweep time should give a straight line.

Figs. 3, 4 and 5 show some of the possibible ways of using an oscilloscope for half-life measurements. For detailed explanations the reader is referred to the figures and the figure texts. We shall return to these figures when discussing special features of the oscilloscope method. In

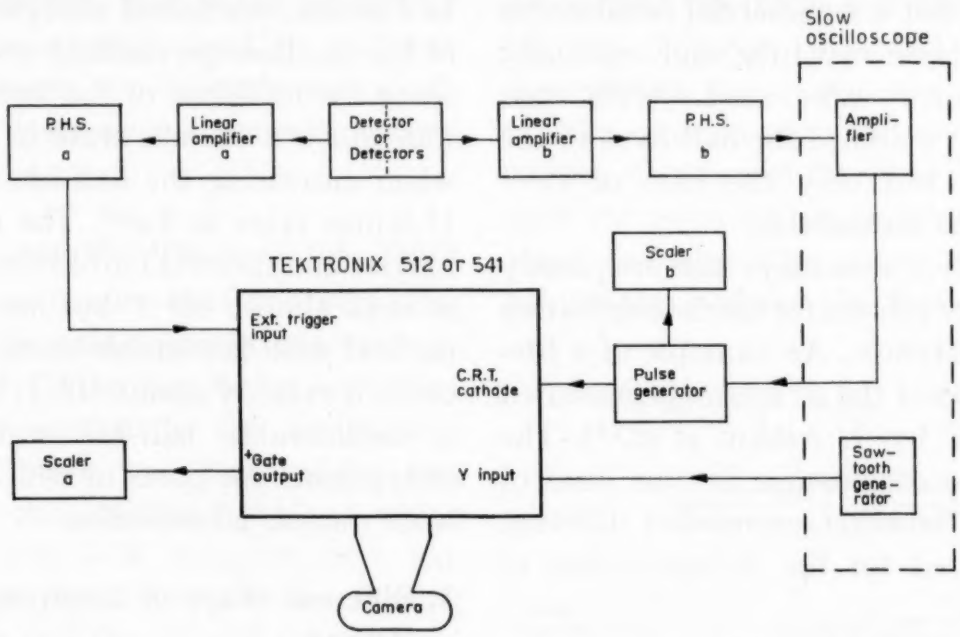

Fig. 3. Block diagram of one of the instrument combinations used for photographic recording of delayed events corresponding to half-lives between 10 μs and 5 ms. In these experiments the b′-pulses triggered a pulse generator, the output pulses of which intensity modulated the electron beam and were also counted by the scaler b. The light spots on the oscilloscope screen corresponding to the delayed events were uniformly distributed in the vertical direction of the screen by feeding the pulses from a saw-tooth generator to the y-plates of the oscilloscope and were recorded by having the camera shutter open and the film being stationary. Because of the sweep dead-time, it is advisable to count the number of released sweeps rather than the number of triggering signals from the pulse height selector. This is achieved by connecting the scaler a to the gate output of the oscilloscope.

For the measurements on Pb^{206} and Pb^{205} a single well crystal detector was used. For half-lives shorter than about 10 μs two detectors should always be used in order to avoid pile-up problems in the linear amplifiers.

most cases the a′-signals were used to trigger the oscilloscope. (There may of course exist cases where it is more favourable to trigger the oscilloscope with the b′-signal and delay the arrival of the a′-signal.) There are essentially two ways of using the b′-signals:

A. The signals may be fed to the y-plates of the oscilloscope, which, for example, was the case for the three last measurements listed in table 1.

B. In other cases the b′-signals may modulate the electron beam intensity in such a way that the delayed events may appear as a point on the oscilloscope screen (cf. figs. 6 and 9). The four longest half-lives measured in this work were obtained by using this method.

The b′-events appearing on the oscilloscope screen may be detected in the following ways:

a. Visual detection. This method is associated with the same difficulties as the first scintillation measurements of the Rutherford school. The measurements are slow and are associated with personal systematic errors of the observer, and should only be used in exceptional cases. Nevertheless if the equipment needed for the methods 3.b and 3.c discussed below is not available, it is certainly also possible to measure the half-life in this way, as fig. 15 shows, even if the measurements are very time-consuming because of the slowness of the human response.

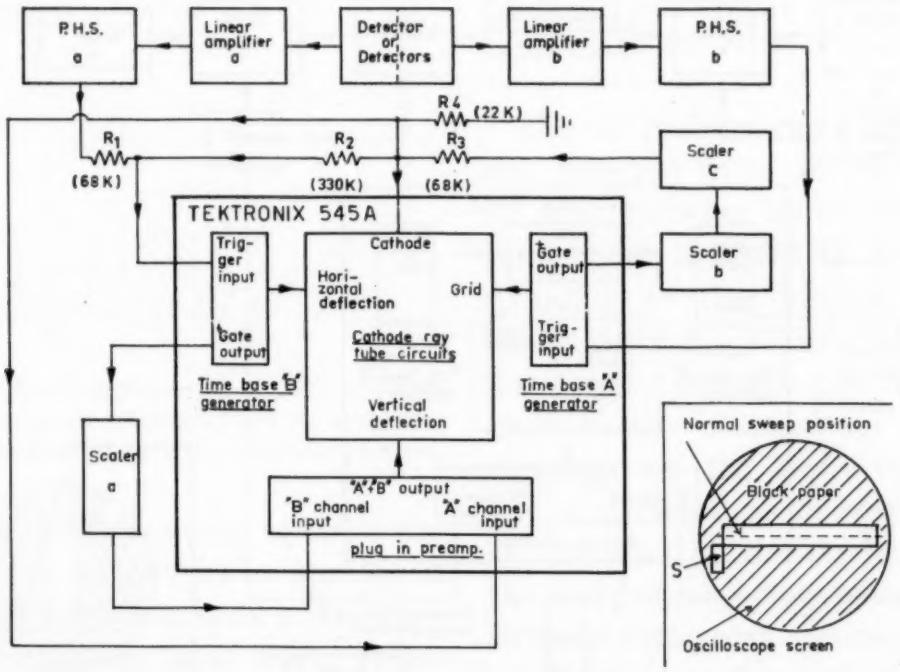

Fig. 4. Simplified block diagram showing the way in which a Tektronix 545 A was used for determining half-lives larger than about 1 μs.

Here the light spots corresponding to delayed events are produced by means of the time base "A" generator, while the time base "B" generator produces the sweeps (horizontal display switch in position "B" intensified by "A") It was found convenient to disable one of the sections of the lockout multivibrator in the time base "A" generator in order to make allowance for the possibility of more than one sweep "A" to occur for each sweep "B". In cases where the number of random events is small, the probability of having more than one b′-event per sweep is negligible and thus this precaution is not necessary.

The measurements were completely automatized by using a camera with a motor driven film. Thus, the normal sweep position was stationary and vertical deflections produced from the scalers a and c could be used in order to produce information about the counting rates in both the channels, which is needed in order to calculate the number of random events. For the a-pulse this is simply done by shifting the sweep from its normal position upwards in such a way that the light spots are hidden for a certain number of counts as explained in the text. The counting rate corresponding to the b-signals was controlled by recording light spots appearing in the slit S each 6400 b-events. In order to achieve this the number of b-events was scaled down by a suitable factor by means of scalers b and c. In order to obtain the wanted light spot in S, pulses from the scaler c have to be fed simultaneously to the cathode for intensity modulation of the electron beam, to the sweep B trigger input in order to release sweep b and thus unblank the beam and finally to the y-plates in order to deflect the sweep position downwards. This was done by means of R_1, R_2, R_3, R_4 which were chosen so as to give the right pulse heights and to decouple to a certain extent the output of the pulse height selector a from the cathode.

b. Photographic recording. For half-lives longer than about 1 μs the sensitivity of the fastest commercial films now available allowed photographic recording of the delayed events on the screen with the equipment used in this work. The great advantage of this method is, of course, that the oscilloscope can be used as a multichannel time analyzer. The films used in this work were 25 DIN Kodak 3 X and 29 DIN AGFA Isopan Record. The points on the film obtained by letting the b′-pulses intensity modulate the electron beam were counted by projecting the film on a piece of white paper with a magnification of about 30 (see fig. 6). A centimeter scale of the oscilloscope was also photographed and projected onto the same paper, thus providing a suitable time scale. Since the points representing the delayed events on the screen had a diameter of about 0.5 mm, it was not considered worth-while to divide the sweep interval into more than 10 "channels". The photographic method is especially useful in the ms-region, where the long measuring-times involved in the use of one-channel methods make the measurements almost impossible. There are simple ways of continuously obtaining the information necessary for the calculation of the random events on the same film used for the delayed events and this will be discussed further in 4.1. Figs. 12, 13 and 14 show the half-lives of metastable states in Pb^{205}, Pb^{206} and Ta^{181} obtained by using photographic recording.

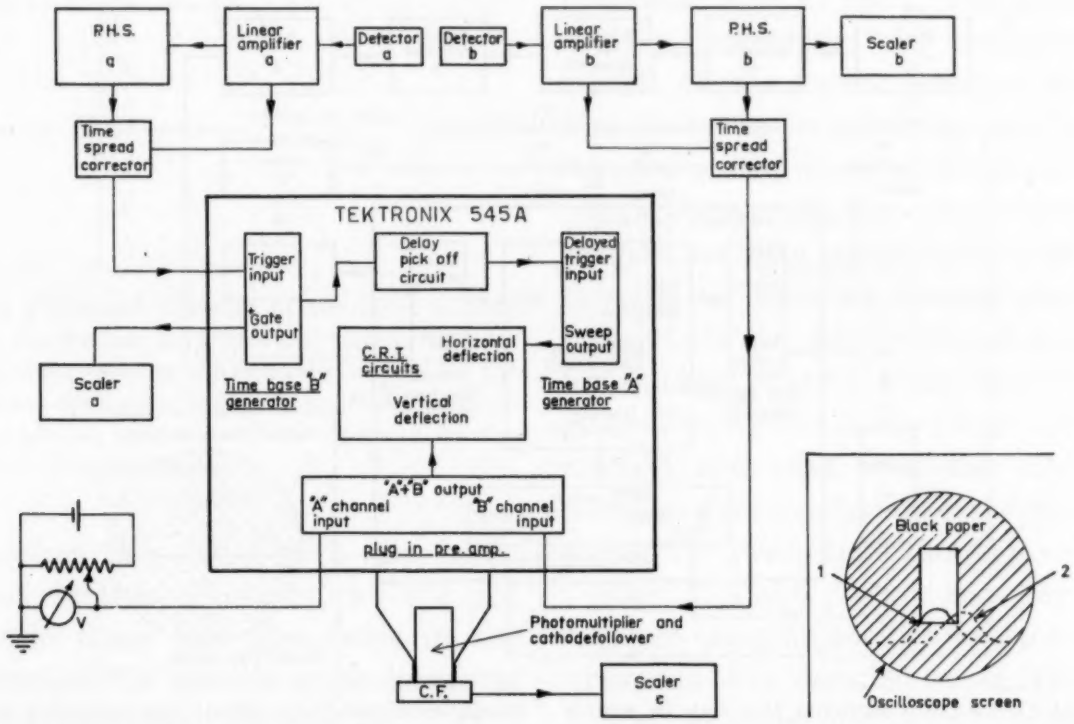

Fig. 5. Simplified block diagram of the set-up used for measuring half-lives from 10 mμs to about 1 μs and also for obtaining the resolution curves of fig. 10.

The horizontal display switch was in this case set at the position "A" delayed by "B". In this way the release of sweep "A" can be delayed by a well known, and continuously variable amount and the various points of the coincidence curve obtained without changing the position of the slit in front of the oscilloscope screen. However, for the shortest half-life (10 mμs), the steps between successive delay values needed were so small that it was necessary to set the delay control to a constant position and to change instead the horizontal position of the sweep, the corresponding potentiometer having been calibrated accurately in centimeters beforehand. To obtain the electronic resolution curve" of fig. 10 I, a third method had to be used because of the much smaller delay changes needed. The potentiometer and the voltmeter shown in this figure were used for this purpose. The reader is referred to fig. 10 I and to the text for the description of this way of operation.

The short pulses from the time-spread corrector of channel b were fed to the vertical deflection system of the oscilloscope and viewed through a slit (see inset) by a photomultiplier connected to a scaler. It is quite evident that the effective time channel width depends not only on the slit width but also on the discrimination level of the scaler C, on the intensity control setting of the oscilloscope and on the amplification in the photomultiplier. Thus, on event, giving a pulse like "I" would be counted while one producing a pulse like "2" might be rejected because the amount of light reaching the photomultiplier is smaller.

c. Photomultiplier detection. There are many ways of using a photomultiplier for the detection of the b′-events, where the visual detection and photographic recording is less convenient and

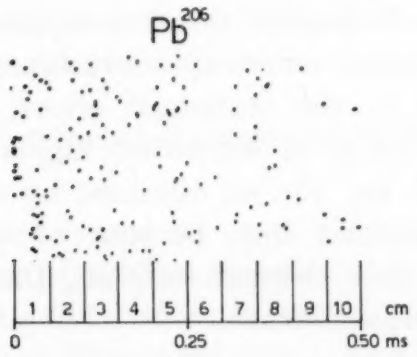

Fig. 6. The delayed events from the decay of the 7^- state in Pb^{206} on the oscilloscope screen photographed by a camera having the film continuously moving in the vertical direction.

below we are going to discuss only some of the most obvious ones. The screen may be uncovered or partly covered by a mask in such a way that the photomultiplier detects only those pulses which are visible through a slit in this mask.

3.1. UNCOVERED SCREEN AND VARIATION OF THE SWEEP VELOCITY

In this case the number ΔN of true delayed events on the screen detected by the photomultiplier is

$$\Delta N = \int_0^{t=\mu x} \lambda N_0 \, e^{-\lambda t} \, dt = N_0(1 - e^{-\lambda \mu x}) \qquad (1)$$

x = sweep interval
t = sweep time
μ = sweep velocity.

Thus, a straight line is obtained if the logarithm of $(N_0 - \Delta N)$ is plotted as a function of the total sweep time t. N_0 may be obtained by using extraordinarily long sweep times if this is allowed by the number of random events. In a measurement of the half-life of the 7^- state in Pb^{206}, the ratio between true and random coincidences was about 1.5, even at time $t = 12$ half-lives. ΔN is at this time to a very good approximation equal to N_0. Since this method thus very conveniently gives the number N_0, there are no reasons to make half-life plots in the conventional way, because for each point measured the half-life can be calculated according to (1). Fig. 7 shows as an illustration the preliminary result of a determination of the half-life of the 7^- state in Pb^{206} made in this way.

3.2. CONSTANT SWEEP VELOCITY AND VARIATION OF SLIT POSITION RELATIVE TO THE SWEEP ORIGIN

The slit position can obviously be changed in two different ways one of which was used by D. Alburger when he discovered the half-life of the 7^- state in Pb^{206} [12]). The light pulses corresponding to the delayed events were made visible through a slit in a piece of paper covering the screen and the position of this slit was mechanically changed for each "point" to be measured on the decay curve. An equivalent but simpler way is to keep the position of the slit constant on the screen and instead change the sweep origin, which in some oscilloscopes can be done with great accuracy.

3.3. CONSTANT SLIT POSITION AND VARIATION OF THE SWEEP VELOCITY

This method was used by one of us several years ago[17]) but was not considered to be reliable, because the observed and calculated numbers of random events did not agree. We now know that this must have been due to the presence of the 4 ms half-life in Pb^{205}, which at

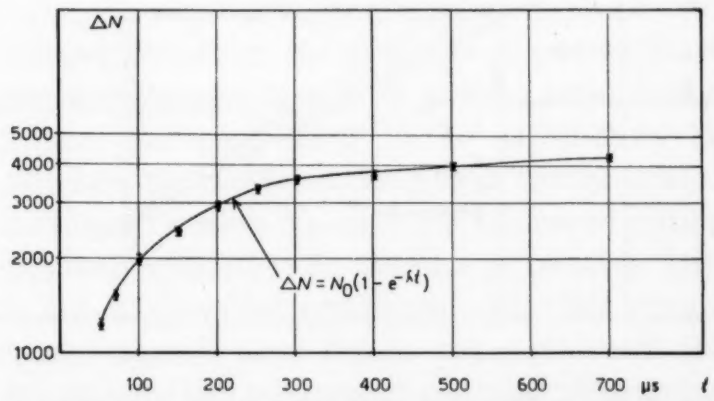

Fig. 7. The number of delayed coincidences as a function of the timegate width (from time zero to time $t = x\mu$, where x is the visible part of the sweep beginning at its origin and μ the sweep velocity) using Bi^{206}-sample and the arrangement of fig. 4, but with a photomultiplier instead of a camera. For large values of t, N approaches N_0, which makes it possible to calculate the half-life for each measured point.

[17]) I. Bergström, Nobel Institute of Physics, Stockholm (unpublished measurements).

that time was not known. In this case the number ΔN of delayed events appearing in the slit and counted by the photomultiplier is

$$\Delta N = \int_{t_1}^{t_2} \lambda N_0 \, e^{-\lambda t} \, dt = N_0 \, e^{-\lambda t_1} \quad (1 - e^{-\lambda (t_2 - t_1)})$$

where

$$t_2 - t_1 = \mu (x_2 - x_1) = \mu \Delta x \quad (\Delta x = \text{slit width}) .$$

In this case $\log N/(1 - e^{-\lambda \mu \Delta x})$ plotted as a function of t_1, should give a straight line from which the half-life can be obtained. This has to be done by a procedure of successive approximations, since the ordinate in such a plot contains the unknown decay constant. The influence of this becomes less and less important for lower sweep velocities. Fig. 8 shows a measurement of the half-life of the metastable state in Pb^{206} obtained in this way. The last part of the curve ΔN plotted as a function of t_1 gives the half-life in what we may call the zero order approximation. This half-life is 189 μs and thus too large (cf. table 1). If the value of the corresponding decay constant is used in the expression above we obviously overcorrect the number of delayed events and the half-life 117 μs is obtained. This procedure was repeated and the following approximations gave the half-lives 137, 127 and 129 μs respectively. We thus see that the half-lives obtained in this way rapidly converge towards values where the deviations are small compared to the statistical errors. The final value of 128 μs is somewhat higher than the values (cf. fig. 13) we obtained by the photographic method but, because of the poorer statistics, (one channel method), the deviation is not at all significant.

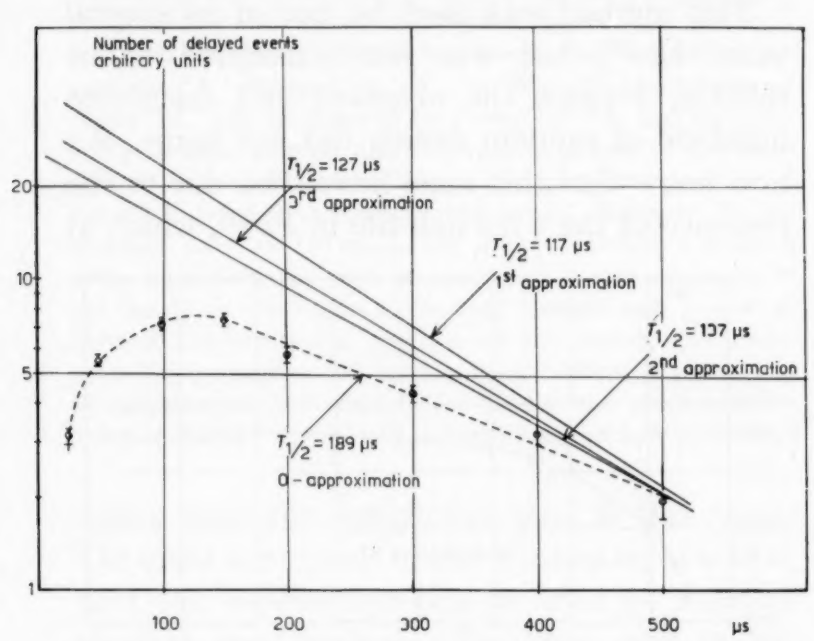

Fig. 8. The number of delayed coincidences (obtained with a constant slit width and a variable sweep velocity) as a function of the delay time which in this case was equal to the gate time. The lower curve shows the experimentally obtained result (Pb^{206}). For large values of the delay time, the slope of this curve should give a rough value of the half-life (see the text). Using a procedure of successive approximations described in the text, the upper curves are obtained and, as can be seen, the half-lives so obtained converge rather quickly towards the final value of 128 μs.

3.4. CONSTANT SLIT WIDTH AND DELAY OF THE RELEASE OF THE MAIN SWEEP

Some of the fast modern oscilloscopes, for example the Tektronix 545, are equipped in such a way that it is possible to delay the release of the main sweep by a certain time which is variable and which is well known. Letting the photomultiplier view a part of screen and varying the delay of the main sweep is a method reminding of the conventional way of measuring a half-life with a stop watch and counting during constant time intervals. This method is one of the most attractive ones. The absolute value of the slit width and the position of the sweep origin is not relevant, which indeed is important because in certain time regions the pulse width is comparable to the slit width and the effective value of the slit is dependent on the discriminator level of the scaler used to count the b′ events (cf. fig. 5). Note, for example, that in both methods described in 3.1 and 3.2 the uncertainty in the knowledge of the origin of the sweep as well as of the absolute value of the slit width contribute considerably to the final errors of the result obtained. The half-lives of the metastable states of Pb^{204}, Pb^{203} and Ta^{181} (11 mμs) were measured in this way. From the statistical point of view it is also important to use as wide time channels as possible. In the case of Pb^{204}, an 8 cm channel corresponding to approximately 160 mμs was used. When the half-life becomes comparable to the coincidence resolution curve, the slit width must, of course,

be decreased and, in the case of the measurement of Pb^{203}, it was about 40 mμs. The problems which arise when still shorter time differences are measured are discussed in 4.2.2. where we describe the special arrangement used in order to measure time differences which are only a fraction of a mμs.

4. Sources of Errors and Limitations of the Method

The measurement of a nuclear half-life with an oscilloscope is thus essentially a question of determining the number of true, delayed events as a function of the time interval corresponding to a certain part of the sweep on the oscilloscope screen. We may therefore expect that some of the limitations of the method are to be found in the oscilloscope itself and that other limitations are the same as are involved in any delayed coincidence method. Some of the most apparent quantities relevant for the discussion of errors and limitations of the oscilloscope method are thus:

1. *The number of random events.* The knowledge of the number of true, delayed events is not only limited by statistics, but also by the imperfect knowledge of the time channel Δt used. In both these respects the random events play an important role. Below we shall discuss a way of continuously controlling the number of random events which is useful for the oscilloscope method and which is especially suitable for determinations of long half-lives.

2. *Sweep properties* like the accuracy of the sweep time, the sweep linearity and the sweep stability.

3. *The background* from cosmic rays and unwanted radiation from the nuclide studied or from other nuclides present in the sample used. These problems, which are especially important in measurements of long half-lives, will be discussed in detail below in section 4.4.

4.1. DETERMINATION OF THE NUMBER OF RANDOM EVENTS

The number of true, delayed events are, of course, obtained by subtracting the random events from the total number of detected events. The number of random events N_r is

$$N_r = \frac{N_{a'} N_{b'} \Delta t}{T} \quad \text{where} \quad t = \Delta x \mu$$

T = total measuring time.
$N_{a'}$ = the total number of sweeps counted by a separate scaler (see figs. 3, 4 and 5).
$N_{b'}$ = the total number of b′-signals.
μ = sweep velocity
Δx = efficient sweep interval used, in some cases depending on the discrimination level of the scaler registering the photomultiplier pulses (cf. section 3.4).

In all half-life regions in which we have worked, there was a very satisfactory agreement between the number of measured and calculated random events. It is, of course, very important that the measured random events in the case of a constant time channel be independent of the delay time, otherwise unknown systematic errors might give rise to a distribution of events which could be incorrectly interpreted as a half-life. Especially in the ms-region, where the number of true events may be considerably smaller than the number of random events, it is advisable to check that a "horizontal line" is obtained if the a′- and b′-signals are coming from independent sources (cf. fig. 11).

As has already been pointed out, in the ms-region we photographically recorded the delayed events on the oscilloscope screen. Since many exposures lasted 18 hours continuously, it was not considered to be satisfactory to calculate the random events from the integrated number of events $N_{a'}$ and $N_{b'}$ measured during this long time-interval, because of possible drift in the electronical equipment. For this reason special signals were fed to the y-plates of the oscilloscope from the scalers counting the number $N_{a'}$ and $N_{b'}$ of the a′- and b′-signals, respectively. These signals were regularly registered by the photographic film in the following way. For each 9000th a′ event a signal was fed from the fourth Decatron tube of the scaler used, to the y-plates and the sweep postion was hereby changed in such a way that the points on the

oscilloscope screen representing the delayed events were hidden behind a strip of black paper (cf. fig. 4). The sweep returned to its normal position when the Decatron reached

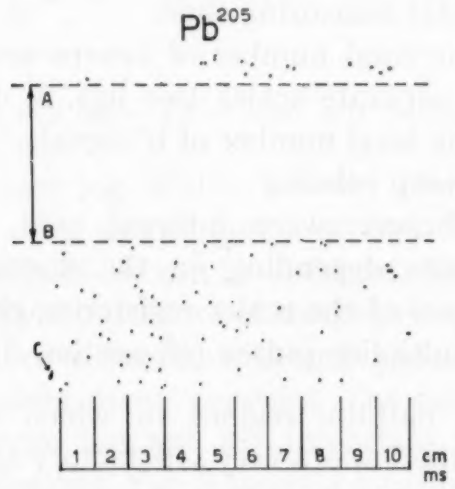

Fig. 9. The delayed events from a Bi^{205}-sample obtained in the same way as was the case for the Bi^{206}-sample (cf. fig. 6). The region A–B and the point C are related to the number of sweeps and events detected by counter b in a way discussed in 4.1, thus providing the necessary information for calculating the number of random events.

$N_{a'} = 10\,000$ and had this position for the next 9000 $N_{a'}$-events. The distance A–B on fig. 9 corresponds to the time interval in which no delayed events were seen by the film. Thus, the events on the film will be distributed into groups, each group corresponding to $N_{a'} = 9000$. In a similar way, a pulse is fed from another scaler to the y-plates each time $N_{b'} = 6400$. The sweep origin was in this case shifted about 1 cm and was made visible for the film through a narrow vertical slit in the black paper in front of the screen. Such a pulse registered by the film is seen at C in fig. 9. The distance between two such points in the film thus corresponds to $N_{b'} = 6400$.

4.2. SWEEP PROPERTIES

4.2.1. *Accuracy and linearity*

In order to obtain information of the absolute accuracy of the sweep velocity and the sweep linearity, calibrations were performed for the sweep velocities used in the measurements, by displaying on the oscilloscope screen periodical signals of known frequencies. For the Tektronix 545 used the deviations in the linearity and the sweep velocities given by the factory, were in all cases less than 0.7%. This high accuracy of modern oscilloscopes makes them very convenient for half-life-measurements.

4.2.2. *Jitter in triggering time and sweep stability*

These properties were checked by replacing the pulses from the detectors by pulses from a pulse generator, which were fed in parallel to both channels. In this way we obtain what may be called an electronic coincidence resolution curve, which does not include the time spread of the detecting devices but only that due to the oscilloscope itself and the electronics used. The electronic resolution curve presented in fig. 10 I was obtained by using the delayed sweep operation and having the photomultiplier viewing the screen through a slit of the size 1×10 mm^2 in the black paper covering the screen (cf. fig. 5). The pulse was amplified so much that within the field of view of the screen it was linear and the slit was placed parallel to the linearly rising part of the pulse. It was not possible with the oscilloscope used (Tektronix 545) to change the delay of the main sweep by sufficiently small time intervals and for this reason we had to use another method. By means of a potentiometer connected to the "A"-input of the preamplifier of the oscilloscope, a small variable D.C.-voltage was superimposed on the pulse fed in through the "A"-input and thus the vertical position of the pulse on the screen could be slightly varied (cf. fig. 5). This produces an effect equivalent to a horizontal shift of the pulse. The amount of this shift can be calculated from the knowledge of the D.C.-voltage, the amplification for the "A"-input and the slope of the pulse on the screen.

The very steep edges of the resolution curve as well as the 100% efficiency, are remarkable. According to this result, it seems in principle possible, and not at all difficult, to measure time differences as small as one or a few tenths of a mμs, even with an oscilloscope like the Tektronix 545 used in most of our experiments, which is not the fastest one commercially available.

4.3. LIMITATIONS FOR SHORT HALF-LIVES

Going back to fig. 10 I it is now justified to state that the oscilloscope itself will not set a lower limit for half-life measurements. The b-signals have still lower energies (75 and 279 keV respectively). If the latter channel is set to accept gamma-rays of the energy 126 keV, there is a broadening and a shift in the resolution

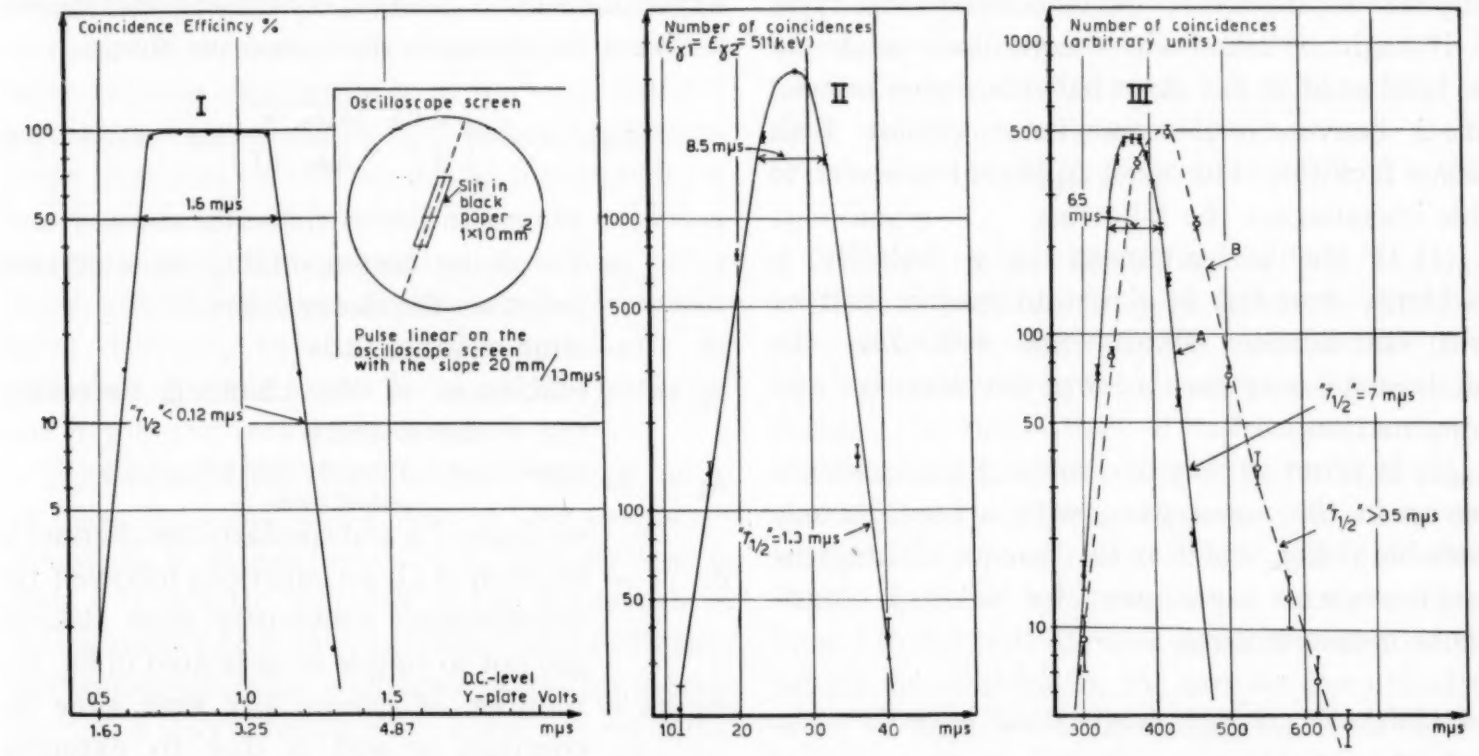

Fig. 10. Electronic coincidence resolution curve obtained by using the arrangement of fig. 5, but replacing the signals from the detectors by signals from a pulse generator. The way in which the short delay in this case was changed is described in section 4.2. II. Prompt coincidence resolution curve using the 511 keV gamma rays from the annihilation process (Na^{22}-sample). Both discriminators were set on the photopeaks. III. Prompt coincidence resolution curve when the gamma ray energies are 70 and 279 keV, respectively, and the delayed coincidence curve, obtained when the 279 keV channel is shifted to a positon corresponding to 126 keV.

This indicates the presence of a metastable state in the Pb^{203}-sample used.

widths and the slopes of the measured prompt coincidence curves will thus almost entirely be due to the time spread in the detecting devices used.

In our measurement we diminished the time spread due to pulse height spread by using a time correction circuit included in the coincidence circuit constructed by B. Johansson[18]) (used only for the shortest half-lives). Fig. 10 II shows the prompt coincidence resolution curve when the a- and b-detectors accepted the 511 keV gamma rays from the annihilation process. For a and b signals of these energies it would thus be possible to measure a half-life of a few mμs with the set-up we used. Fig. 10 III shows how the width and the slope of the resolution curve are changed when the a- and curve, which are typical for b-signals from a metastable state. The sample used in this case was Bi^{203} and fig. 18 shows a more carefully performed measurement which confirms the suggestion of a metastable state in Pb^{203}.

In fig. 19 the half-life measurement of the 615 keV-level in Ta^{181} is presented. It can be concluded from these measurements that in cases where the a- and b-signals originate from gamma rays of energies of about 150 and 500 keV detected by NaI-crystals it would be possible to estimate a half-life as short as 2 mμs by comparing the shift of the center of gravity of the delayed and prompt coincidence curves.

Thus, using NaI-crystals, under normal conditions the shortest resolution time available from the point of view of the oscilloscope could

[18]) B. Johansson, Nucl. Instr. 1 (1957) 274.

hardly be used in our measurements, and one can conclude that the difficulties and the limitations in the short half-life region for a set-up such as the one we used, are the same as for any fast arrangements of the conventional type.

It might be asked why the oscilloscope should be used at all in the short half-life region instead of a conventional coincidence circuit with delay facilities. The most apparent answers to this question are the following:

(1) If the measurement of a half-life is suddenly essential in a certain project and no fast coincidence circuits are available, the oscilloscope may save a lot of development and construction work.

(2) It is not so easy to construct a coincidence set-up in the mμs-region, with a continuously variable delay, which is the feature making the oscilloscope so convenient for delayed coincidence measurements.

4.4. LIMITATIONS FOR LONG HALF-LIVES

In this region even more than in the region of short half-lives, the sweep facilities of most oscilloscopes go far beyond those which can be used in delayed coincidence measurements. There is thus no limitation regarding the sweep possibilities.

A discussion of the limitations for long half-lives will almost be the same for any delayed coincidence method as for the oscilloscope method. Since we have not been able to find sufficiently far-reaching discussions in the literature, we have made some calculations, the main results of which will be presented here.

The statistical relative error E of a certain point on the decay curve can be written

$$E = \sqrt{\frac{N_r + N_c}{TN_c^2}} \qquad (2)$$

N_r = number of random coincidences per unit time
N_c = number of real coincidences per unit time
T = total measuring time.

Remembering that the number N_c proportional to the number of disintegrations in the source and that the number N_r is a quadratic function of the same number, one sees that E approaches a constant value E_{min} for infinitely strong sources. The statistical error can thus never be smaller than E_{min}. Substituting in (2) expressions for N_r and N_c containing parameters relevant for the error discussion we obtain:

$$E_{min} = e^{t/\tau}\left(\frac{\tau}{\Delta}\right)^{\frac{1}{2}}\sqrt{\frac{h_a h_b}{\varepsilon_a \varepsilon_b}\frac{\tau}{\delta T}} \quad \text{for} \quad \Delta \ll \tau \,. \qquad (3)$$

τ = the mean life of the state studied
t = the delay corresponding to a certain point on the decay curve
Δ = time channel ($\mu\Delta x$)
ε_a, ε_b = efficiences of the channels detecting the events a and b
$h_a = \frac{\text{wanted events + unwanted events from the source}}{\text{wanted events}}$ in channel a and similarly for channel b
δ = fraction of all a-transitions followed by b-transitions (obviously most decays are not so simple as indicated in fig. 2).
n_a, n_b = number of counts per unit time in counters a and b due to external background.

It can be shown that in many actual cases when reasonable source strengths are used, the value of E may differ from E_{min} by only a small amount. For instance, if the source strength is adjusted to give a ratio $N_r/N_c = 1$, and if n_a and n_b both can be neglected compared to N_a and N_b, (counts from the source), one obtains $E = \sqrt{2}\,E_{min}$.

In all cases one could, in principle, obtain a statistical error E close to E_{min} by choosing a sufficiently strong sample. As discussed in more detail below, this is in practice only possible to a certain extent due to systematic errors which become more important the higher the ratio N_r/N_c is.

From (2) we can immediately attain some conclusions which are of decisive importance when discussing the upper limit of the delayed coincidence method.

(a) For analogous conditions and for equivalent points on the decay curve, (t/τ and Δ/τ the same) the total measuring time must be proportional to the half-lives if the same value of E_{min}

is to be obtained. Thus it is evident that the half-life measurements can become too time consuming for long half-lives. The mother activity feeding the metastable state may also decay before it is possible to collect sufficient statistics. Multichannel time analyzers therefore often become indispensable in the long half-life region. As we have pointed out before, the oscilloscope itself can be used as such an instrument for half-lives larger than about 1 μs. In addition electromagnetically separated activities offer the possibility of replacing mother nuclei which have decayed, because of the small risk of introducing other longer lived nuclei increasing the number of unwanted events.

(b) For a certain case and for a wanted value of $E_{\min}$, the total time T required for the measurements is proportional to h_a and h_b and is thus a quadratic function of the impurities in the sample. From this the convenience of using electromagnetically separated activities is evident in a very striking way. There are certainly many cases where the use of electromagnetically separated radioactive samples will make possible measurements which otherwise cannot be performed. So, for example, we have frequently used sources produced in the 190 MeV Uppsala proton synchrotron. It is clear that all the activities, which are produced in nuclear reactions in which as many as 12 nucleons may be boiled off, would in many cases produce a prohibitively large number of unwanted events. The electromagnetic separation of some of the samples used in this work was performed with the 160 cm electromagnetic separator of the Nobel Institute. Figs. 12 and 13 illustrate how the efficiency of the measurements is increased when separated radioactive samples are used.

(c) The well known importance of using high efficiency of the detectors is also seen from (2).

(d) From (2) it is also clear that the branching ratio δ in many cases may set a limit to the possibility of measuring a half-life in general and that this will be especially critical for long half-lives.

Regarding the use of (2) a few comments should be made:

(1) In the short half-life region, the fulfilment of the condition $N_r/N_c = 1$ may result in such high counting rates that they cannot be used because of limitations in the detectors and pulse height analysers. On the other hand, the time T, which in such cases would result from (2), is generally so small that one can easily afford to work with much lower activities and much better ratios of N_r/N_c and to increase T correspondingly.

(2) For long half-lives, the condition $N_r/N_c = 1$ (if it is possible to fulfil it at all) leads to extremely low counting rates and the condition of negligible background might no longer be fulfilled. In these cases, if one wants to obtain a statistical error not much bigger than $E_{\min}$, one is forced to increase the source intensity and work with a poorer ratio N_r/N_c. On the other hand, since the total measuring time is proportional to the half-life measured, we see that the longer the half-life is, the less we can afford to work far from the ideal conditions. How far one can go in increasing the ratio N_r/N_c and how this depends on the coincidence set-up used, is illustrated below. First let us, in order to get an idea of the limit we are speaking about, introduce some typical values in (2) and see for this hypothetical case, which the longest measurable half-life would be. For $E_{\min} = 5\%$ and when

$$t/\tau = 2 \quad \varepsilon_a = \varepsilon_b = 0.2$$

$$t/\Delta = 5 \quad b = 1$$

$$h_a = h_b = 2 \quad T = 24\ \text{h}\,,$$

we obtain

$$\tau_{\max} \approx 0.11\ \text{sec.}$$

The reason for the impossibility of using arbitrarily high ratios of N_r/N_c can be found in the fact that the accuracy, and mainly the stability of the time channel Δt is never perfect. Obviously an error of 1% in this resolving time will produce a change of only 1% in the number of real delayed coincidences provided the number of random coincidences is negligible. This uncertainty, however, will be 10% if $N_r/N_c = 9$. Thus, the more accurate our set-up is, the higher the ratio N_r/N_c which can be tolerated and thus

TABLE 1

Summarized information of th

Nucleus studied	Half-life of mother activity	Triggering signal a	a detected in	Delayed signal b
Pb^{205}	15.3 d	73 keV EC X-rays	$1\frac{3}{4}'' \times 2''$ hole NaI-crystal	mainly 987.8 keV
Pb^{206}	6.4 d	73 keV EC X-rays	$1\frac{3}{4}'' \times 2''$ hole NaI-crystal	γ-rays of energy > 100 keV
Ta^{181}	45 d	100–300 keV β-particles	3 mm anthracen crystal	133 keV γ-ray
Rb^{85}	64 d	13 keV EC X-rays	3 mm anthracen crystal	513 keV γ-ray
Pb^{204}	11.22 h	73 keV EC X-rays	$1\frac{3}{4}'' \times 2''$ NaI(Tl)-crystal	899.2 keV and 375 keV γ-rays
Pb^{203}	11.76 h	73 keV EC X-rays	$1\frac{3}{4}'' \times 2''$ NaI(Tl)-crystal	126.3 keV γ-ray
Ta^{181}	45 d	137 keV γ-ray	$1\frac{3}{4}'' \times 2''$ NaI(Tl)-crystal	482 keV, 346 keV and 136 keV γ-rays

correspondingly longer half-lives may be measured without putting impossible restrictions on the background.

The oscilloscope is by no means outstanding in this respect. The possible errors and fluctuations of the time channels, including the errors arising in the visual counting of the points, might safely be estimated as < 1%, but not very much smaller, and the ratios N_r/N_c can thus not be too high; the highest value depending, of course, on the precision wanted.

Let us mention finally that in the above mentioned case if the external background $n_a = n_b = 1$ count per second and $E = \sqrt{2}\, E_{min} = 7\%$ the ratio N_r/N_c would be:

$$N_r/N_c = 11.4\,.$$

For $n_a = n_b = 0.1$ count per second and the same value of the error we would have:

$$N_r/N_c = 1.64\,.$$

The conclusions we can draw from this are:

(1) For a given set-up the longest measurable life time is to a great extent dependent on the counting rate due to the external background and it is not necessary to emphasize the importance of keeping this contribution as low as possible.

(2) Using high precision instruments (which should not be too difficult to construct in the 10^{-3} sec–1 sec region) one could, at least in favourable cases, cover this region of half-lives, which is often regarded as a difficult one.

5. Comments on the Measurements

In table 1 are collected the most relevant data of the measurements on the different nuclides used. In general, the main purpose was not to obtain the highest possible accuracy in each case but rather to study the method itself. For example, the half-life of the metastable state in Rb^{85} can be measured much more accurately than we did. The half-lives were chosen in such a way that they should give us experience in a wide half-life region. In some cases, however,

l
half-life measurements performed

b detected in	Oscilloscope used	Type of oscilloscope detection	Total measuring time	Half-life this work (approximately least square fit)	Previous measurements
Same crystal as for a signal	Tektr. 512, 541, 545A	Photographic	110 h	4.15 ± 0.15 ms	4.8 ± 1.5 ms[16])
Same crystal as for a signal	Tektr. 512, 541, 545A	Photographic	79 min	123 ± 3 μs	123 ± 3 μs[21]) 128 ± 5 μs[13])
1½″ × 2″NaI(Tl) crystal	Tektr. 541	Photographic	99 min	17.5 ± 0.8 μs	17.2 μs [14]) 18.8 μs 18.1 μs 22 μs 20 μs } [22])
1½″ × 2″ NaI(Tl)-crystal	Tektr. 541	Visual	170 min	1.0 ± 0.1 μs	0.90 ± 0.04 μs[23])
1¾″ × 2″ NaI(Tl)-crystal	Tektr. 545A	Photo multiplier	280 min	316 ± 6 mμs	260 mμs 300 mμs } [22])
1¾″ × 2″ NaI(Tl)-crystal	Tektr. 545A	Photo multiplier	9 h	55 ± 5 mμs	previously not know
1¾″ × 1″ NaI(Tl)-crystal	Tektr. 545A	Photo multiplier	70 min	11.0 ± 0.4 mμs	10.6 mμs 10.4 mμs 11.0 mμs } [22])

there were special reasons to be more careful. A critical analysis of "irregularities" in the half-life curve of the known metastable state in Pb^{204} led to the discovery of a hitherto unknown case of nuclear isomerism in Pb^{203} (55 mμs).

Pb^{205}:

The first Bi^{205}-samples used in Bariloche were obtained by irradiating natural lead in the Buenos Aires synchro-cyclotron with 29 MeV deuterons. The measurements were started about 2 months after the end of the irradiation. The source used was thus the Bi-activity trapped in the metallic lead. In addition to Bi^{205}, there was also Bi^{206} and Bi^{207} present. Because of these impurities and the relatively high cosmic ray background (altitude about 800 meters) the true, delayed events were only 20% of the total number of events counted during the first ms. Under such circumstances, we would never have been able to observe the 4 ms half-life reported by Vegors and Heath[16]) if the oscilloscope method could not be used in this case as a multichannel time analyzer. The experimental set-up used in these first measurements is shown in fig. 3. The b′-signals (Pb K X-rays) were used for intensity modulation of the electron beam in the way described previously. In addition, a saw-tooth voltage was fed to the y-plates which distributed the delayed events (points) in the vertical direction (4 cm) of the oscilloscope screen (cf. fig. 3). After having obtained a suitable point density in the first time channel (1 ms corresponding to the first 1 cm on the screen) the film was manually moved before the next exposure. The random coincidence rate was obtained by simultaneously counting the number of released sweeps (a′-signals) and the number of b′-signals. Even if the statistics in these first measurements were poor, they unambiguously confirm the conclusions drawn by Vegors and Heath of the existence of a 4 ms metastable state in Pb^{205}. Note, for example, that the number of delayed events decays with

the same half-life as Bi^{205}, which supports the assumption that the 4 ms half-life is due to a metastable state in Pb^{205} (see fig. 11). This was and the detector arrangements do not give rise to a distribution of events, which may be wrongly interpreted as a half-life. In order to

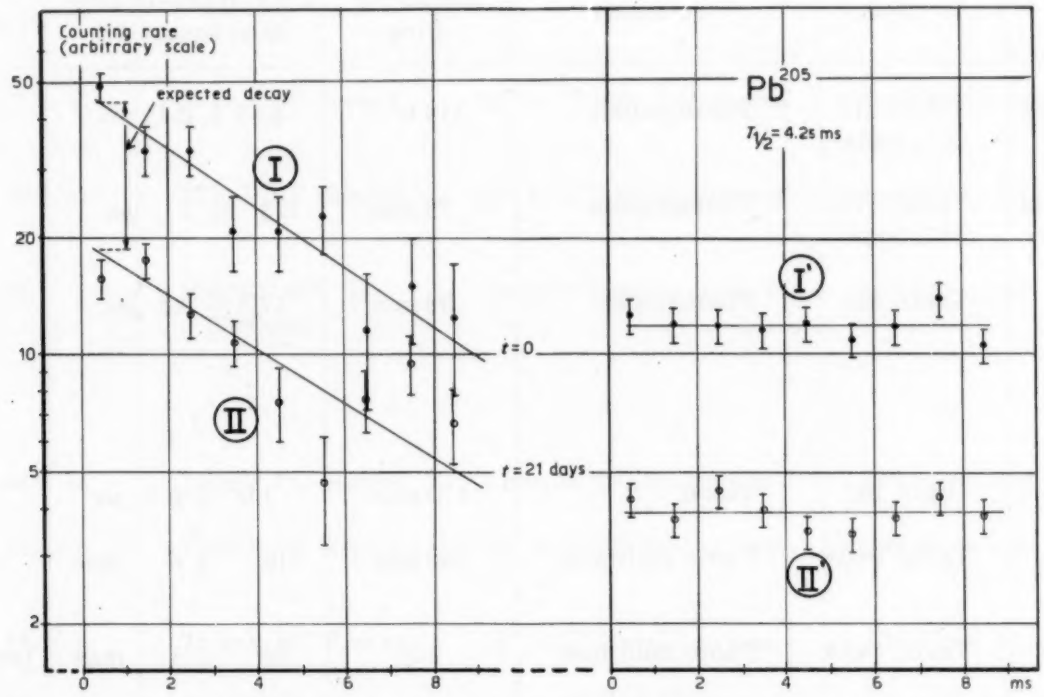

Fig. 11. First measurements of the 4 ms half-life of the $i_{13/2}$-state in Pb^{205} using the arrangement of fig. 3. Curves I and II show that the mother activity decays with the same half-life as Bi^{205}. Curves I′ and II′ were obtained by using two independent sources and detectors, thus showing that curves I and II are due to a nuclear decay.

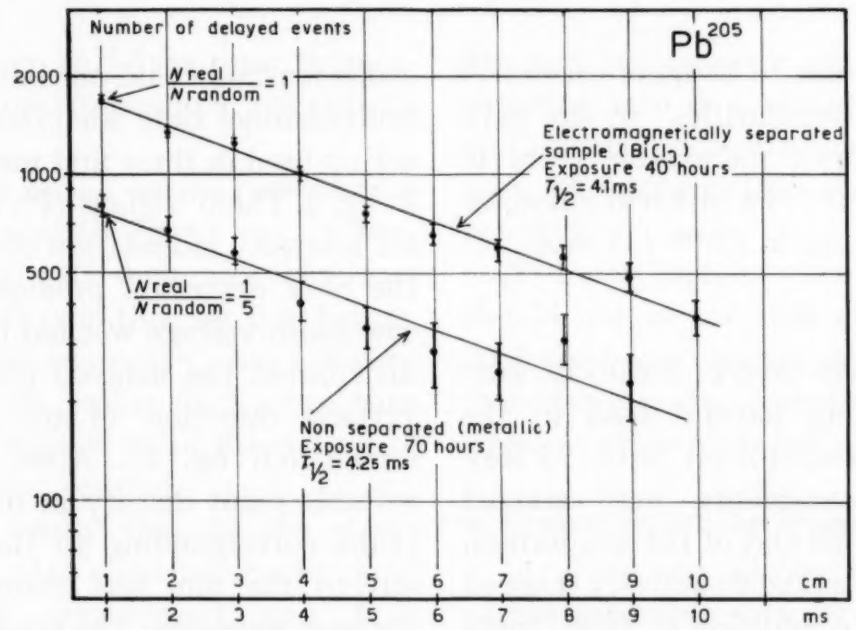

Fig. 12. Decay curves of the $i_{13/2}$ state in Pb^{205} showing the advantage of using electromagnetically separated radio-active samples in delayed coincidence measurements. The upper curve was obtained with the arrangement shown in fig. 4 and the lower curve with that shown in fig. 3.

definitely proved in later experiments in which we used electromagnetically separated Bi^{205}.

When the ratio of real to random coincidences is as poor as it was in these experiments, it is necessary to be sure that the oscilloscope itself prove that we really observed a nuclear decay we used in separate experiments independent sources for the a′- and b′-signals. As can be seen at the right of fig. 11, we obtained in this case horizontal lines within the experimental

errors. The sum of the two Bariloche measurements is presented in fig. 12. Since the value of the half-life obtained was shorter than that reported by Vegors and Heath two of us (I. B. and P. T.) repeated these experiments in Stockholm. The experimental conditions were

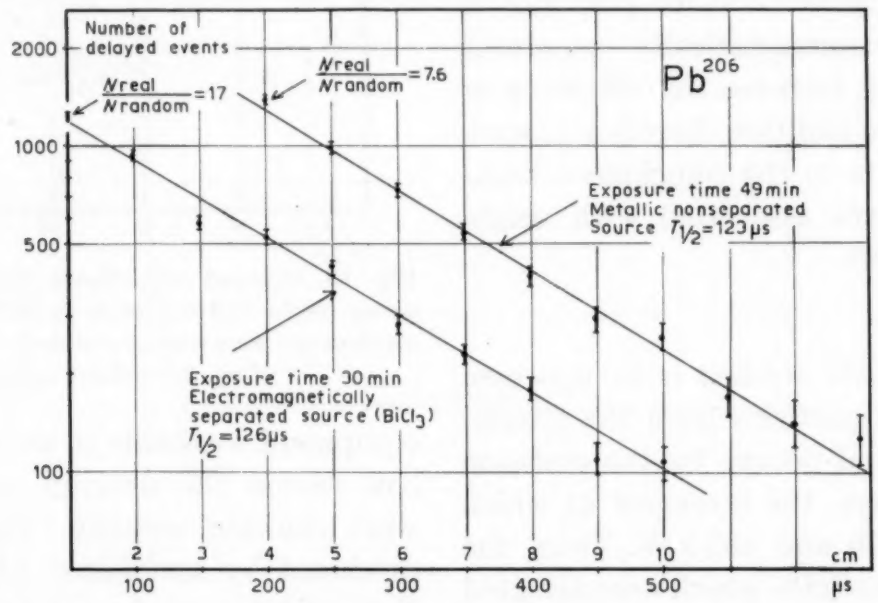

Fig. 13. Half-life curves of the decay of the 7^- state in Pb^{206}. The upper curve was obtained by using the arrangement of fig. 3 and the lower curve with that shown in fig. 4. Notice the advantage of using electromagnetically separated samples.

now better. For example the use of electromagnetically separated Bi^{205} greatly increased the efficiency of the measurements (cf. formula (2), section 4.4). In addition, the measurements were simplified by using a motor driven film in the camera continuously registering the events on the oscilloscope screen. In section 4.1 we have also described how the random events were continuously controlled. Thus, the complete automatization of the measurements also contributed to the better statistics obtained in the Stockholm measurements. The sum of the first three Stockholm measurements is also shown in fig. 12. In later experiments with better statistics a "tail" appeared at the end of the half-life curve which may be the explanation of the longer half-life reported by Vegors and Heath. We checked carefully that the tail was not due to an instrumental effect. It is not clear at the moment whether this tail ("half-life" about 10 ms) is due to another metastable state in Pb^{205} or whether it is due to some unknown systematic error.

Recent measurements by R. Stockendal[19]) and by D. Alburger[20]) have in a very beautiful way solved the problem of the "missing" $i_{13/2}$-state in Pb^{205}. Combining the experiments by Stockendal, Alburger those performed by Vegors and Heath and our results one concludes that the 4 ms half-life should be due to the $i_{13/2}$-state which decays by the following transitions: 26.22 keV (M2), 310.5 keV (E3) and 1014.0 keV (M4). This is certainly one of the most interesting cases of nuclear isomerism that has been reported.

Pb^{206}:

The half-life of the famous 7^- state in Pb^{206} has been measured by several workers and was especially suitable for checking the properties of our method in the 100-μs region. The first measurement was performed with a fresh metallic non separated sample obtained after irradiating natural lead with 29 MeV deuterons for 30 minutes in the Buenos Aires synchrocyclotron. Later we repeated this experiment in Stockholm with an electromagnetically separated sample, because the 4 ms half-life in Pb^{205},

[19]) R. Stockendal, Nobel Institute of Physics, Stockholm, Phys. Rev. **118** (1960) 1074, and Arkiv för Fysik **17** (1960) 553.

[20]) D. Alburger, Brookhaven National Laboratory, Phys. Rev. **118** (1960) 1076.

which was not well established when the previous measurements were performed, may have contributed to uncertainties in the coincidence background. The results are shown in fig. 13 and as can be seen, the half-life values are in good agreement with those obtained by Tove[21]) and Åström[13]) (cf. table 1). Note that also in this case the electromagnetically separated samples considerably increase the efficiency of the measurements. In addition there is a guarantee of no contribution to the coincidence background from half-lives associated with neighbouring mass numbers.

Ta^{181}:

The metastable state studied is in this case fed by 450 keV beta-particles from the ground state of 45 d Hf^{181} and decays by the emission of several gamma-rays, the strongest of which have the energies 136 and 133 keV. Thus, the a-signals were beta-particles, which were detected by a 3 mm anthracene crystal and the discriminator setting chosen was such that the ratio of the beta-particles and the gamma-rays detected by this crystal was an optimum. The result of this measurements, which was performed in Buenos Aires with a sample obtained from the Swedish R1-reactor, is shown in fig. 14 and the half-life obtained is in good agreement with one of the previously reported values[14,22]) (cf. table 1).

Rb^{85}:

The half-life was in this case too short to be measured by the photographic method with the

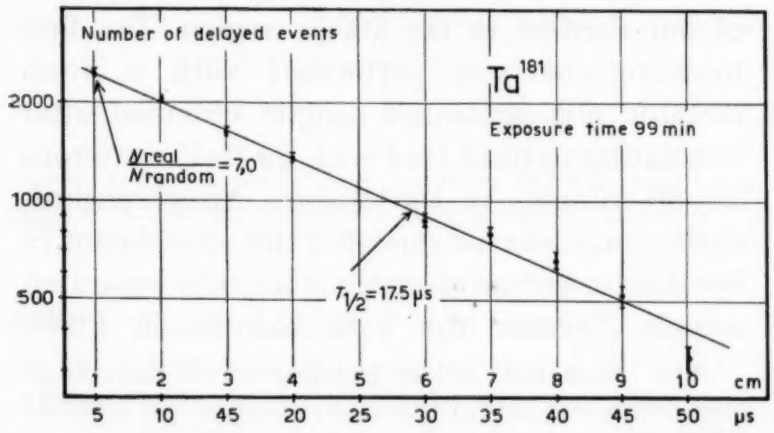
Number of delayed events
Ta181
Exposure time 99 min
Nreal / Nrandom = 7,0
T1/2 = 17.5 μs
2000
1000
500
1 2 3 4 5 6 7 8 9 10 cm
5 10 45 20 25 30 35 40 45 50 μs

Fig. 14. Half-life curve of the 615 keV level in Ta^{181} obtained with the arrangement of fig. 3.

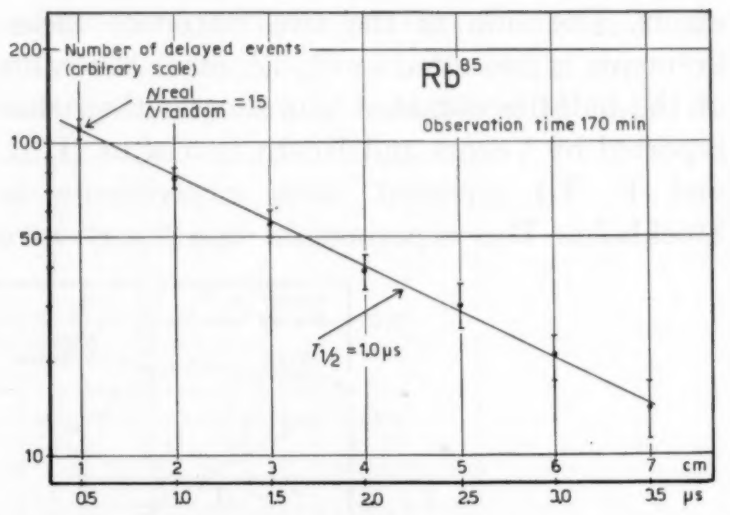

Fig. 15. Delayed coincidence curve corresponding to the decay of the 513 keV state in Rb^{85}. The light spots on the oscilloscope screen were counted visually. The arrangement of fig. 3 (without camera) was used.

equipment available to us in Buenos Aires. For this reason the delayed events on the screen were counted visually. The sample used was produced by irradiation of natural Rb in the Buenos Aires synchro-cyclotron and was neither chemically nor magnetically separated. (Note that in this case the a-signals were the 13 keV capture X-rays from Rb.) In spite of these difficulties, a half-life is obtained (see fig. 15) which, though the statistics admittedly are poor, agrees reasonably well with previous measurements[23]). By using an isotopically pure sample and by detecting the delayed events by a photomultiplier, a much more accurate value would easily be obtained.

Pb^{204}:

Bi^{204} was produced by irradiating natural lead with 50 MeV protons in the Uppsala 190 MeV synchro-cyclotron. The first source was obtained by simply dissolving part of the lead in hydrochloric acid and using part of this solution. Thus the source contained many activities, the main ones being 11.8 h Bi^{203}, its daughter 52 h Pb^{203} and 11.2 h Bi^{204}.

Fig. 16 shows the result of a measurement with such a source. In this case a 2 cm slit in

[21]) P. A. Tove, Nucl. Instr. **1** (1956) 95.

[22]) D. Strominger, I. M. Hollander and G. T. Seaborg, Rev. of Mod. Phys. **30** (1958) 585.

[23]) J. G. Siekman, Nuclear Physics **2** (1956) 254.

front of the oscilloscope screen selected the upper part of the delayed pulses in a channel of about 40 mμs. Fig. 16 shows clearly the half-life of the well known 4^+ state in Pb^{204}. However, if the contribution of the decay of this 300 mμs state is subtracted, a symmetric coincidence resolution curve is not obtained for small

Fig. 17 shows the results of two independent measurements of the activity deposited on mass number 204 (activity half-width about 1.5 mm, line distance between mass numbers 203 and 204 about 8 mm). Note the favourable ratio of random to real coincidences again due to the electromagnetically separated samples. The half-

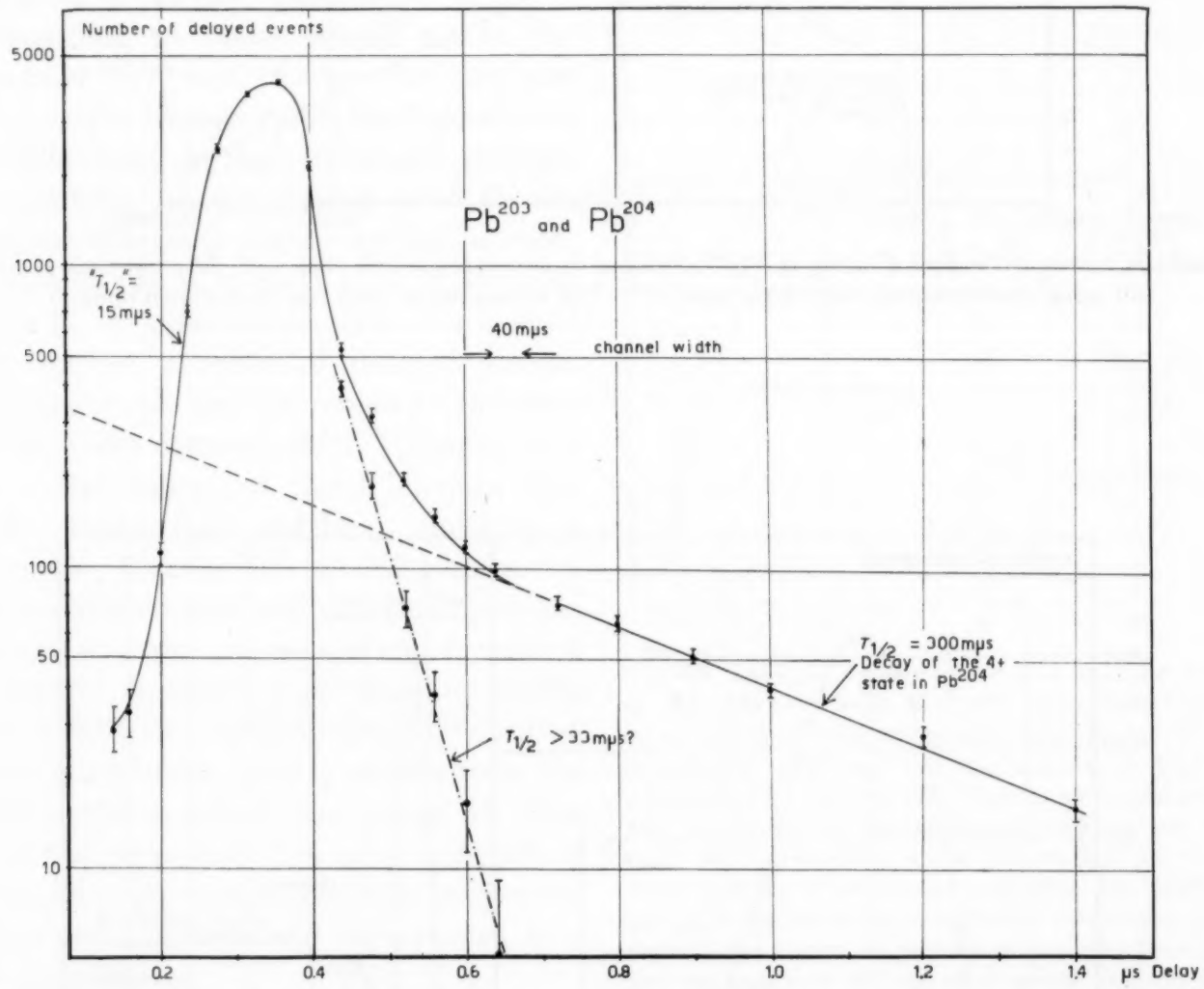

Fig. 16. Coincidence curve obtained by studying not separated Bi-activities (the main ones being Bi^{203} and Bi^{204}) and using the arrangement shown in fig. 5. As can be seen, two half-lives and a considerable number of prompt coincidences are present (see also figs. 17 and 18).

sweep times. The asymmetry indicates a half-life which would be considerably shorter than 300 mμs and probably longer than 33 mμs. The only way of getting a satisfactory answer was to use electromagnetically separated samples. In order to give the reader an idea of the efficiency of the separation and the weak samples required in experiments of this type, it can be mentioned that the irradiation lasted for only half an hour and that less than 0.1 % of the separated sample was used in the experiments to be discussed below.

life obtained is in good agreement with one of the previously reported values (cf. table 1).

Pb^{203}:

The results obtained when using the activity deposited on mass number 203 are shown in fig. 10 III and in fig. 18. Fig. 10 III shows a quick run which indicates that the asymmetry observed in the coincidence resolution curve of the first measurements mentioned above is indeed due to a half-life in Pb^{203}. Curve A and B were obtained when the b′-signals were selected

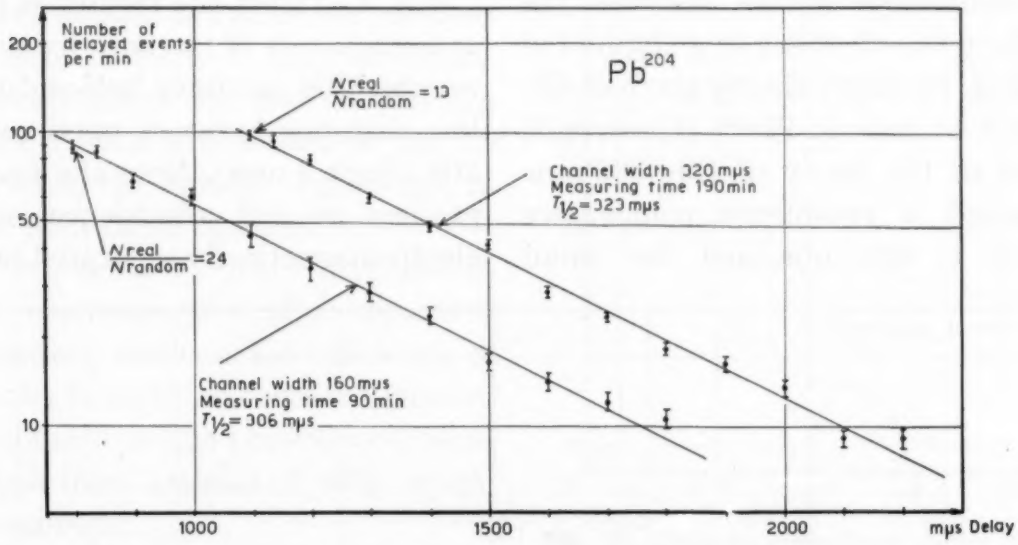

Fig. 17. Half-life curves of the first 4^+ state in Pb^{204} obtained in two independent runs with different time channel widths and using electromagnetically separated Bi^{204}. The arrangement used was that shown in fig. 5.

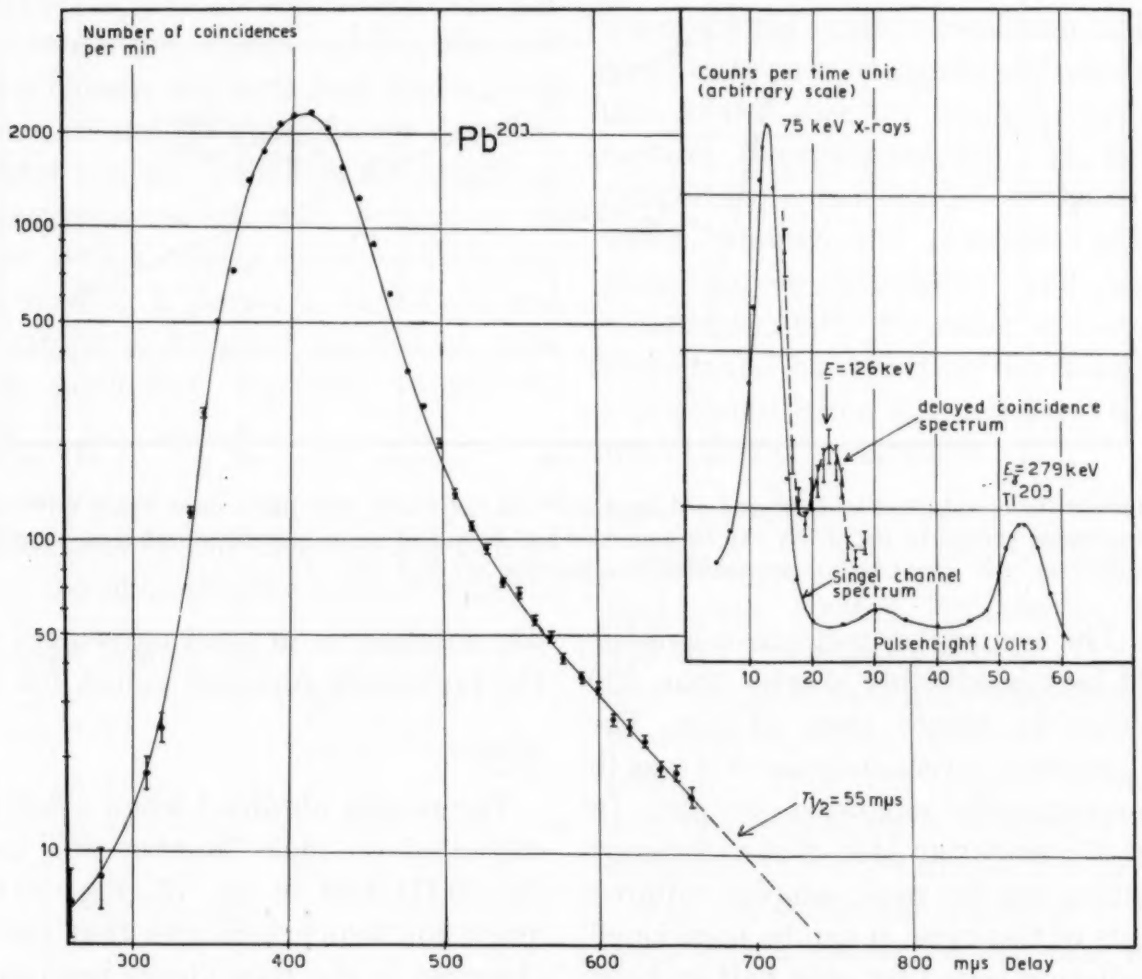

Fig. 18. Prompt and delayed coincidences obtained by using an electromagnetically separated Bi^{203}-sample and the arrangement given in fig. 5. The inset shows the one-channel spectrum of the sample used and the delayed coincidence spectrum obtained with a delay of 520 mμs and a time gate of 160 mμs. As can be seen from the figure, there is a gamma ray with an energy of 126 keV associated with the 55 mμs half-life in Pb^{203}.

with a discriminator setting corresponding to 279 and 126 keV, respectively, and the other channel selecting the K X-rays. The shift and the increase of the width of the resolution curve is typical for what is to be expected from the presence of a half-life. The discriminator setting (126 keV) was chosen because Stockendal *et al.*[24]) have reported a 126 keV gamma-ray in Pb^{203} which, according to them, should go to the groundstate of Pb^{203} and we suspected that this gamma-ray might be responsible for the observed half-life. The inset in fig. 18 shows the one channel spectrum of the sample used in the energy region discussed above. As can be seen, the 126 gamma ray is so weak that it does not show up in the one channel spectrum. The dashed curve shows the number of delayed events observed on the oscilloscope screen at the time 520 mμs with the channel width 160 mμs, as a function of the energy of the b′-signals. The coincidence curve thus obtained shows in a convincing way that the 126 keV E2 gamma ray is indeed associated with the observed half-life. The half-life was also more carefully measured (cf. fig. 18) but, as can be seen from the results obtained, there was a considerable contribution of prompt coincidences, mainly coming from the 52 h Pb^{203}-activity, which had grown in after the end of the separation. The measurements of other features of the metastable state discovered are being continued and will be reported in a separate paper[25]).

The prompt coincidence curve, which can be seen in fig. 19, was obtained by using the annihilation radiation of the positrons from a Na^{22}-sample. The energy settings of the discriminators were not changed when measuring prompt and delayed coincidences, and the low

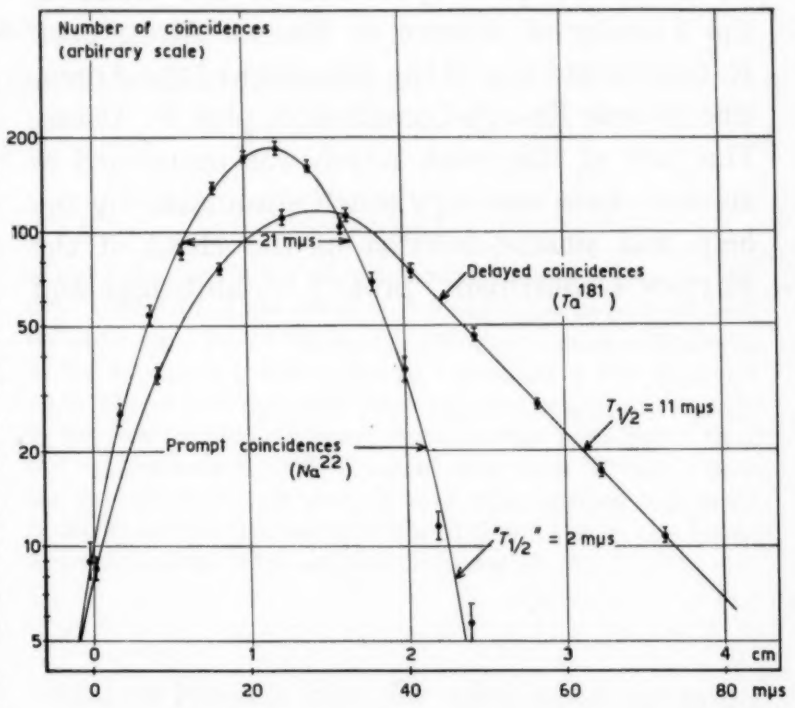

Fig. 19. Delayed coincidence curve showing the half-life of the 482 keV level in Ta^{181} and prompt coincidence curve obtained with the annihilation quanta from a Na^{22}-sample. In both cases the discriminator settings were the same and 2″ × 1¾″ NaI(Tl) crystals were used as detectors. The slit width on the oscilloscope screen was 5 mm (10 mμs) but the effective width was smaller due to the sensitivity setting of the scaler counting the delayed events (cf. fig. 5). In order not to introduce systematic errors in the shift of the center of gravity of the coincidence curves it was necessary to use the same sweep rates in both cases.

Ta^{181} (THE 482 keV-LEVEL):

The sample used was obtained in the same way as that used in the measurements of the 615-keV level. In this case, however, the strong gamma rays with energies 147 and 482 keV (feeding and de-exciting the 482 keV level) corresponding to the a- and b-events were detected by two NaI-crystals. energy channel could thus accept only part of the Compton scattered 511 keV quanta while the other channel was wide enough to accept the 511 keV photo peak completely. According to theoretical calculations (see for example ref.[26])), the slope and the width of the prompt coincidence curve is about the best one which can be expected when using NaI-crystals for detecting gamma rays of the above mentioned energies.

The value of the half-life of the 482 keV level is in reasonably good agreement with the previous measurements[27]) (cf. table 1).

[24]) R. Stockendal, T. Novakov, B. Johansson and M. Schmorak, Arkiv för Fysik **14** (1958) 85.

[25]) I. Bergström, P. Thieberger and J. Uhler (to be published).

[26]) J. J. Peyre, Internal publication **17** (1958), Comisión Nacional de Energía Atómica, Buenos Aires, Argentina.

[27]) H. de Waard, Nucl. Instr. **2** (1958) 73.

Acknowledgements

It is a great pleasure to acknowledge the contribution of all those who helped to realize the summer school in nuclear physics in Bariloche from which this work originates. Our thanks are especially due to the head of Instituto de Física in Bariloche, prof. J. Balseiro, the Dean of the Faculty of Science in Buenos Aires, prof. R. Garcia and one of the Directors of the Argentine Atomic Energy Commission, prof. F. Alsina. The part of this work which was performed in Buenos Aires was very much stimulated by the help and sincere interest of the Head of the Physics Department, prof. J. Giambiaggi and by the equipment which was put at our disposal by Dr. J. Peyre and Dr. M. Sametband from the Argentine Atomic Energy Commission. It is also a great pleasure for us to acknowledge the importance of the equipment which was obtained from the field equipment department of UNESCO in Paris.

One of us (P. T.) also gratefully acknowledges a scholarship from the Argentine Research Council (CNICT) which made it possible for him to take part in the completion of this work in Sweden. He also wants to thank the Head of the Nobel Institute prof. Manne Siegbahn and his Swedish colleagues for their hospitality.

NUCLEAR INSTRUMENTS AND METHODS 8 (1960) 173–184; NORTH-HOLLAND PUBLISHING CO.

ON THE EFFICIENCY OF THE REACTION $H^3(d,n)He^4$ IN TITANIUM TRITIDE BOMBARDED WITH DEUTERONS

E. M. GUNNERSEN and G. JAMES

Atomic Weapons Research Establishment, Aldermaston, Berkshire

Received 10 April 1960

The lack of accurate energy loss data in metals (and particularly in titanium tritide) of deuterons of less than 100 keV has been shown to cause large uncertainties in calculations of the neutron yield produced by the $H^3(d,n)He^4$ reaction when a titanium tritide target is bombarded with low energy deuterons. Direct measurements of the energy loss in titanium hydride foils of 40–150 keV deuterons have been made, and have been used in combination with data in the literature for other metals and higher ion energies to recalculate the neutron yield from this $H^3(d,n)He^4$ reaction in titanium tritide for the deuteron energy range 9–150 keV. Using this yield curve, a technique has been described for estimating how tritium concentration varies with depth in the titanium tritide material by examing the observed variation of neutron yield with incident angle and energy of the bombarding deuteron beam. It has been found that the concentration peak is never less than 3000 Å below the surface, and that there is very little tritium contained in an upper surface layer of about 500 Å, or in the lower one-third of the titanium tritide material.

Introduction

Observed neutron yields from the $H^3(d,n)He^4$ reaction in thin titanium tritide targets bombarded with 40–150 keV deuterons are usually considerably less than the expected yields calculated from the known reaction cross-sections and from the known average tritium concentration in the target materials. This divergence may be due to inaccurate calculation of the neutron yield expected from a hypothetical thin titanium tritide target possessing constant tritium concentration throughout its thickness, or to the error introduced by assuming that the tritium concentration in the actual target examined is constant throughout its thickness.

In Part A the former cause of divergence has been investigated by examining how the available experimental data on the $H^3(d,n)He^4$ reaction cross-sections, and on the energy loss of deuterons in titanium tritide, can best be used in the calculation of neutron yield. Also in this section is described an experiment which was designed to check the validity of the available energy loss data by measuring directly the rate of energy loss of very low energy deuterons in titanium hydride foils. By using these optimum experimental data, the calculation of the neutron yield curve (i.e. neutrons/μcoulomb of deuterons, over the energy range 9–150 keV) has then been carried out for a hypothetical target ($\approx$ 15 000 Å) having a constant tritium atomic ratio of 1.5 tritium atoms per titanium atom throughout its thickness.

In Part B the actual variation with depth of the tritium concentration in the target material has been investigated experimentally by bombarding various targets with deuterons from a Cockroft-Walton accelerator over a range of incident angles and energies. This has not only yielded estimates of the contamination layer thicknesses (e.g. of titanium oxide on the titanium tritide surface), but has also yielded considerable information about the actual distribution of tritium in the lower layers of the evaporated titanium tritide material (i.e. just above the supporting nickel backing).

Some miscellaneous information on the secondary electron coefficients of titanium hydride due to H_2^+, D_1^+ and D_2^+ bombardment is presented in an appendix.

A. EXPECTED NEUTRON YIELD FROM A THIN TITANIUM TRITIDE TARGET OF UNIFORM TRITIUM ATOMIC RATIO 1.5

1. Method of Calculation

It is assumed that the tritium atomic ratio (i.e. concentration) of 1.5 tritium atoms per titanium atom is constant throughout the whole thickness of the target material ($\approx$ 15 000 Å), and that any surface contamination layer is of negligible thickness.

Since the angular dependence of the differential cross section for the reaction $H^3(d,n)He^4$ is isotopic up to at least 200 keV (Allen and Poole[1], Argo *et al.*[2]), the total yield of neutrons per incident deuteron of energy E is given by

$$Y = \int_0^E \frac{4\pi n_t \, d\sigma/d\omega}{d\varepsilon/dx} \, d\varepsilon \qquad (1)$$

where n_t is the number of tritium atoms/cm^3 (a constant), $d\sigma/d\omega$ is the differential cross-section for the $H^3(d,n)He^4$ reaction, and $d\varepsilon/dx$ is the rate of energy loss of deuterons of energy ε in the titanium tritide target.

The value of the constant n_t is obtained as follows. If the target material TiT_N contains $N = 1.5$ tritium atoms/titanium atom, then the density ρ_{TiT_N} of the target material is

$$\rho_{TiT_N} = \frac{48 + 3N}{48} \times \rho_{Ti} \times 0.85 = 4.22$$

where

$$\rho_{Ti} = 4.54 \, .$$

The factor 0.85 arises from the 15% expansion which the titanium lattice undergoes during tritiation. The number n_t of tritium atoms/cm^3 is then

$$n_t = \frac{1.5 \times \rho_{TiT_N} \times 6.02 \times 10^{23}}{A_{TiT_N}} = 7.26 \times 10^{22} \, .$$

The differential cross-sections $d\sigma/d\omega$ for the reaction $H^3(d,n)He^4$ has been measured by Conner, Bonner and Smith[3] for 10–1752 keV deuterons, and by Arnold *et al.*[4] for 7.5–120 keV deuterons. The agreement in the overlapping region is excellent. The resultant data used for $d\sigma/d\omega$ for the overall energy range 7.5–150 keV has therefore not been reproduced here, but can be obtained from the above references.

Provided the numerical evaluation of the integral in eq. (1) is accurate, the chief source of error in calculating Y over an extended energy range is the lack of reliable experimental data on the rate of energy loss $d\varepsilon/dx$ of deuterons in titanium tritide. Since the integration covers all energies of the deuterons from the incident energy E down to the point where all their energy is absorbed, the value of Y is quite as dependent on $d\varepsilon/dx$ as it is on the reaction cross-sections. There are no available experimental figures on the rate of energy loss of deuterons in either titanium tritide, titanium alone, or tritium alone for the required energy range. Moreover, most available data on the rate of energy loss of deuterons in other metals usually does not extend down to energies less than 100 keV (Allison and Warshaw[5]). Warshaw[6], however, has made some measurements on the rate of energy loss of protons in aluminium, copper, silver and gold for the proton energy range 50–350 keV, and Reynolds *et al.*[7] have published some results on the energy losses of deuterons in tritium gas for the deuteron energy range 60–700 keV. These latter agree reasonably well with some energy loss measurements made by Phillips[8] for 20–160 keV deuterons in tritium. The best approximation to use for the value of $d\varepsilon/dx$ for deuterons in TiT_N is that value obtained by assuming that Bragg's law holds (i.e. that the energy loss in a compound is the sum of the energy losses in its separate constituents).

[1]) Allen and Poole, Proc. Roy. Soc. A **204** (1951) 500.
[2]) Argo, Taschak, Agnew, Hemmendinger and Leland, Phys. Rev. **87** (1952) 612.
[3]) Conner, Bonner and Smith, Phys. Rev. **88** (1952) 468.
[4]) Arnold, Phillips, Sawyer, Stovell and Tuck, Phys. Rev. **93** (1954) 483.
[5]) Allison and Warshaw, Revs. Mod. Phys. **25** (1953) 779.
[6]) Warshaw, Phys. Rev. **76** (1945) 1759.
[7]) Reynolds, Dunbar, Wenzel and Whaling, Phys. Rev. **92** (1953) 742.
[8]) Phillips, Phys. Rev. **90** (1953) 532.

$$\frac{d\varepsilon}{dx} = \frac{48}{48+3N}\left(\frac{dE}{dx}\right)_{Ti} + \frac{3N}{48+3N}\left(\frac{dE}{dx}\right)_{T_2},$$

$$= 0.914\left(\frac{dE}{dx}\right)_{Ti} + 0.086\left(\frac{dE}{dx}\right)_{T_2} \text{ for } N = 1.5\,. \quad (2)$$

There is evidence that this law holds sufficiently accurately for those compounds in which it has been investigated provided the incident energy is not too low (Segrè[9], Phillips[8], Reynolds *et al.*[7], Dalgarno and Griffing[10]). Just how low in deuteron energy it is possible to go before the law deviates for titanium tritide is uncertain.

The values used in eq. (2) of $(dE/dx)_{Ti}$ for deuterons are obtained by interpolating with respect to $A^{-\frac{1}{3}}$ between Warshaw's two experimental curves for protons in aluminium and in copper. This curve has then been extrapolated back to the origin to obtain the lower energy, energy loss values.

Since

$$(dE/dx)_{\text{protons}}(\varepsilon) = (dE/dx)_{\text{deuterons}}(2\varepsilon)\,,$$

the values for deuterons are simply obtained by doubling the energy scale. Table 1 contains this data for $(dE/dx)_{Ti}$. The values used in eq. (2) of $(dE/dx)_{T_2}$ for deuterons are obtained by combining the results of Reynolds *et al.*, with those of Phillips, and extrapolating down to lower energies. The final figures of $(dE/dx)_{T_2}$ for deuterons, and the values of $(d\varepsilon/dx)_{TiT_{1.5}}$ for deuterons calculated from eq. (2), are given in table 1.

The numerical evaluation of the integral (1) for incident deuteron energies 9–150 keV has been carried out by plotting the integrand graphically, and carrying out the numerical integrations by square counting up to each incident deuteron energy E. The resultant yield curve of neutrons/μcoulomb of deuterons, is shown in fig. 1.

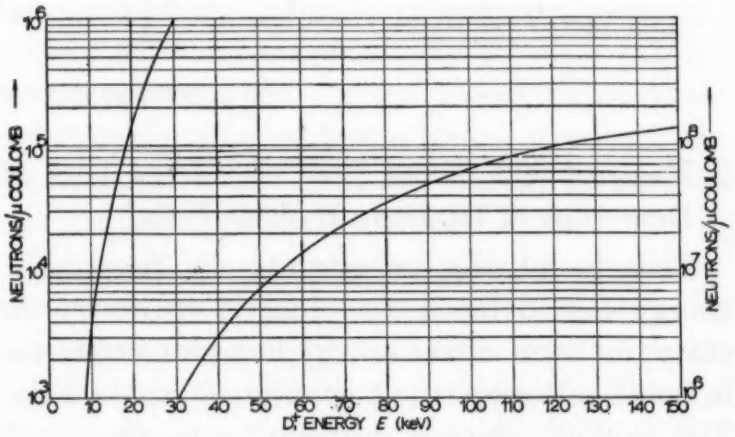

Fig. 1. Yield curve for $TiT_{1.5}$

Saker and Wood[11] of S.E.R.L. Baldock, using the same method and similar cross-section and energy loss data, later repeated the above calculation for the atomic ratio 1.5, and extended it to cover other atomic ratios ranging between 0.2 and 2.3. Their yield curve for the atomic ratio 1.5 fits the curve in fig. 1. within the thickness of the line over the whole energy range. Most of the inaccuracy in these calculations arises from uncertainty in the energy loss figures for deuterons in titanium tritide. Because of the extrapolation involved at low energies, it would be unjustifiable to claim an accuracy

TABLE 1

Energy loss value for deuterons in Ti, T_2 and $TiT_{1.5}$ (values are in keV/mg/cm²)

E (keV)	$(dE/dx)_{Ti}$	$(dE/dx)_{T_2}$	Estimated $(d\varepsilon/dx)_{TiT_{1.5}}$	Measured $d\varepsilon/dx$ in TiH foils
10	59	≈ 490	96.0	—
15	88	≈ 600	132.0	—
20	108	≈ 704	159.4	—
25	132	802	189.6	—
30	149	890	212.6	—
35	163	960	231.6	—
40	177	1023	249.8	278
45	187	1081	263.8	289
50	193	1128	273.3	298
60	210	1183	294.0	315
70	223	1238	309.9	327
80	233	1268	321.7	336
90	242	1281	331.4	343
100	252	1290	341.9	346
110	260	1294	348.9	348
120	265	1295	353.5	350
130	269	1288	356.7	—
140	273	1281	359.0	—
150	276	1270	361.2	—
160	278	1251	361.3	—
170	280	1231	362.0	—

[9]) Segrè, Experimental Nuclear Physics, Vol. 1 (Wiley & Sons, 1953), p. 205.

[10]) Dalgarno and Griffing, Proc. Roy. Soc. A **232** (1955) 423.

[11]) Saker and Wood, S.E.R.L., Baldock. Tech. Memo. No. 413 (1958).

greater than 10%, and it may be very much worse than this for $E < 20$ keV. It is important to note, however, that above 20 keV, the general shape of the yield curve is far more likely to be correct than the absolute position of the curve on the ordinate scale.

The results were consistent with the assumption that the D_1^+ beam contained not more than $\frac{1}{2}$% of H_2^+.

After analysis, the beam was collimated by stops E_1, E_2 (fig. 2). The annular stop E_2 was held at a negative potential of — 900 V, while

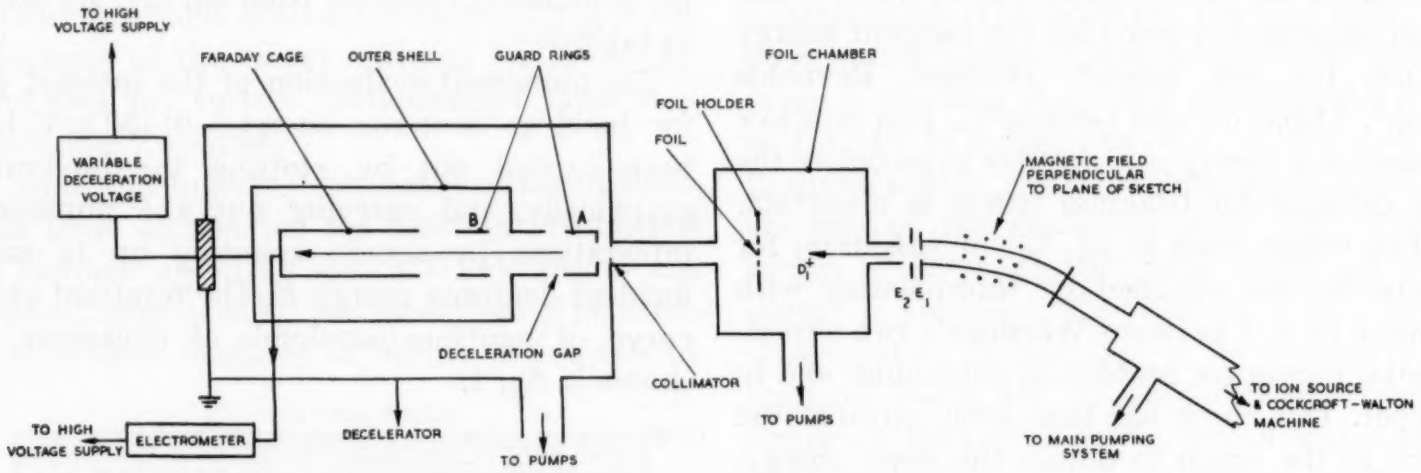

Fig. 2. Schematic layout of energy loss apparatus.

2. Measurement of the Rate of Energy Loss of Deuterons in Titanium Hydride Foils

Because of the uncertainty in the above energy loss data, it was judged necessary to carry out some direct energy loss measurements in some self-supporting titanium hydride foils. The method adopted was similar to that used by Phillips in his measurements on the energy loss of protons in gases[8]. A conventional Cockcroft-Walton machine fitted with an r.f. ion source was used to provide deuterons in the energy range of 40–150 keV. The ion beam from the accelerator tube was deflected by means of an electromagnet (fig. 2) in order to separate beams of different "e/m". A plot of the square of the magnet current at each peak of the spectrum against the appropriate "e/m" yields the straight line shown in fig. 3. The magnet current was calibrated against "e/m" by the usual flip-coil method, and this was checked accurately at a few points by proton resonance. The contamination of the D_1^+ beam with H_2^+ was roughly estimated by two methods:

(a) By chemical analysis of the deuterium gas;

(b) By measuring the relative intensities of the three beams H_1^+; D_1^+, H_2^+; and D_2^+.

the stop E_1 was left at earth potential. The ion energy was determined by measuring the voltage of the set with a calibrated micro-ammeter and a calibrated oil immersed resistance column of 2.28×10^9 ohms. The probable error in the mean energy was ≈ 3%. The pressure in the main accelerator tube was usually about 5×10^{-6} mm Hg, and at the detector end, $1\text{–}5 \times 10^{-5}$ mm Hg.

To measure the energy lost in a foil of titanium hydride, due to excitation, ionisation and charge exchange (but excluding that due to nuclear scattering), a decelerator similar to that used by Phillips[8] was placed beyond stops

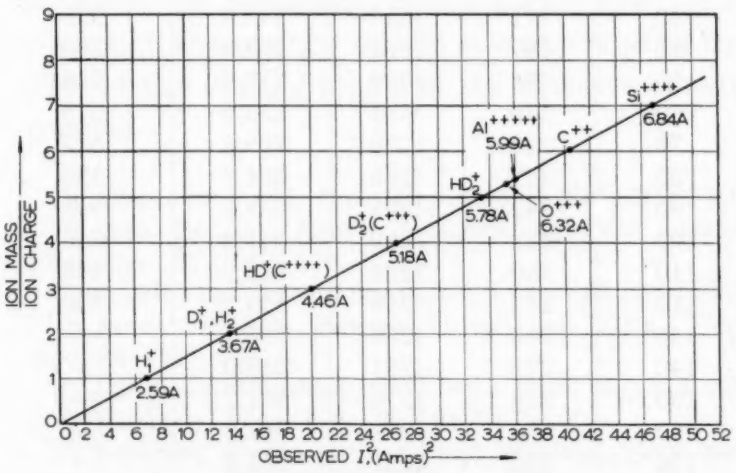

Fig. 3. Magnet calibration at 89 keV.

E_1, E_2 (fig. 2). This measured the deceleration voltage required to just bring the ions to rest. A guard ring A at — 300 V prevented secondary electrons from entering the deceleration gap (acceleration for electrons). The beam current (10^{-9}–10^{-10} A) was collected by a Faraday cage

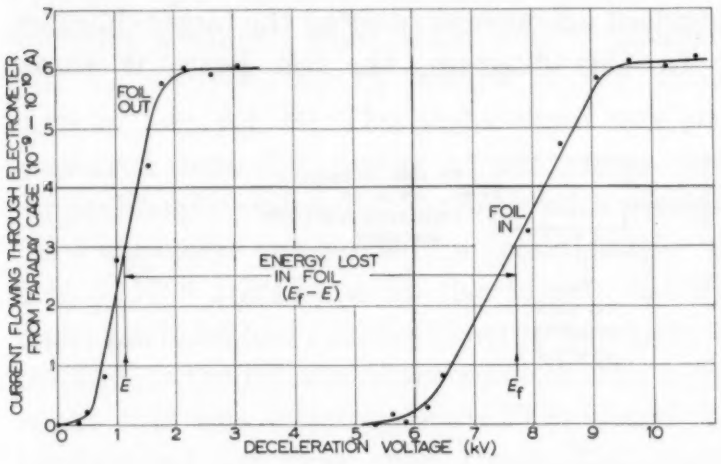

Fig. 4. Typical deceleration curves.

inside the high voltage terminal, and was measured by an electrometer. Another guard ring B, at — 300 V with respect to the Faraday cage, prevented secondaries from escaping from the Faraday cage. The outer shell was kept at about + 2000 V with respect to the Faraday cage so that any ions getting past the deceleration gap were all drawn into the Faraday cage and measured. A remotely controlled power supply at high voltage potential could vary the voltage applied across the deceleration gap. The type of plot obtained for collected beam current versus deceleration voltage is shown in fig. 4.

The energy loss in a foil of thickness x mg/cm² for each energy value $(E + E_f)/2$ is given by $E_f - E$. The inherent energy spread in the incident beam, obtained by plotting the "foil-out" deceleration curve, was usually about 2 keV. It was found to be impossible to extend the measurements below 40 keV, since (a) the energy loss (5–10 keV) in the foils became too large in proportion to the incident energy E (i.e. self-supporting foils could not be made thin enough), and (b) at less than 40 keV energy, increased scattering made it necessary to use much larger beam currents than were needed at high energies, and these larger beams tended to destroy the foils.

Self-supporting titanium hydride foils ranging in thickness from 15 to 50 μg/cm² were used. The foil thickness was estimated by weight and area determination, but even though the titanium film was always first exposed to an atmosphere of pure hydrogen after evaporation, it was very likely that a large fraction of the resultant foil material was titanium oxide. During each energy loss measurement, it was found essential to surround the foils with a surface cooled with liquid nitrogen, and also to use a subsidiary pumping system in the region of the foils. If these precautions were not taken, the energy loss $E_f - E$ was found to increase significantly after a few minutes exposure to the beam: this was probably caused by carbon deposition on the foil.

To check the accuracy of these energy loss measurements, gold and aluminium foils were examined for comparison with other figures available in the literature at about 100 keV. Within the accuracy of the experiment ($\approx 10\%$) the energy loss values obtained for 100 keV deuterons in aluminium and gold agreed with those published in Allison and Warshaw's review[5].

The measured figures for $d\varepsilon/dx$ in titanium hydride are quoted in table 1. These figures have been obtained by averaging the results for several foils of differing thicknesses. A comparison with the estimated figures for $TiT_{1.5}$ shows that the method of extrapolation and interpolation used in obtaining these $TiT_{1.5}$ figures was not greatly in error. Because of the uncertainty in the composition of the titanium hydride foils, it was decided that to seek an improvement in the accuracy of the measurements would not be worthwhile.

B. ASSESSMENT OF TITANIUM TRITIDE TARGETS

1. Apparatus and Method

A comparison with expected neutron yield can best be carried out by bombarding each target with a steady, collimated beam of magnetically analysed D_1^+ or D_2^+ ions of well defined energy (such as from a Cockcroft-Walton machine). If the incident angle which the ion beam makes with the target surface is varied, then the path length of the ions through any surface contamination layer will vary accordingly. This alters the effective incident ion energy by virtue of the energy lost in the contamination. Since the yield curve in fig. 1 is a very steep function of energy at low energies, it follows that varying the angle of incidence of the ion beam should provide a sensitive means of estimating surface contamination thickness. Actually this technique proved to be sufficiently sensitive to estimate variations in the tritium concentration in the bulk of the titanium tritide underneath the surface contamination layer.

The apparatus consisted of a Cockroft-Walton assembly similar to that described in Section A. Similar stops E_1, E_2 were used: the opening in E_2 being larger than that in E_1, so that none of the direct ion beam could strike the edges of E_2. In this way, electrons coming down the accelerator tube (e.g. secondaries from the unfocused beams striking the magnet tube), and secondary electrons produced in the target chamber beyond E_1, E_2 (see fig. 5) were not able to affect the measurements of the incident ion current entering the target chamber.

In this diagram, the ion beam is shown

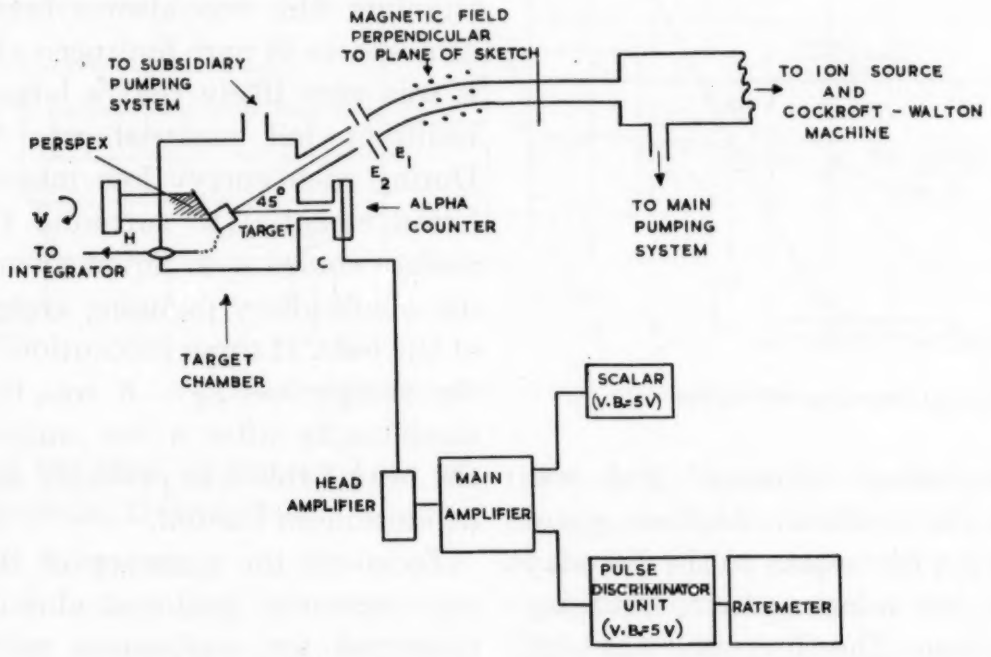

Fig. 5. Schematic layout of apparatus for target assessment.

striking the target at normal incidence. The target can, however, be rotated by turning handle H through angle ψ, and the angle θ which the beam makes with the normal to the target surface is then given by

$$2\cos\theta = 1 + \cos\psi .$$

The angle θ could be measured and reproduced to an accuracy of about $\frac{1}{2}°$. As the target is turned, the current distribution on the target surface will change as a result of the ion beam spot changing from circular to elliptical. However, provided none of the beam ever misses the titanium tritide surface on the target, and provided carbon deposition on the target surface is negligible, the shape of the ion beam spot is unimportant, since:

(a) The total current collected remains constant;

(b) The alpha counter window at C sees all of the target at all θ;

(c) The angle between the alpha counter axis and the ion beam direction remains constant at 45° for all θ.

The most reliable method of measuring the number of neutrons/sec produced in a titanium tritide target by the $H^3(d,n)He^4$ reaction, is to measure the number of alpha particles/sec entering a known solid angle and to convert this to neutrons/sec by means of the usual method (see ref. [12]). This alpha count rate was measured here by means of an argon flow proportional counter (fig. 5) whose mica window (≈ 1 mg/cm^2) sub-tended a solid angle of 2.44×10^{-4} steradians at the target. All the alpha particles had sufficient energy to penetrate through to the far side of the counter. The alpha count rate was usually about 200/sec and the background not more than 1/min. The charge collected by the target during a counting interval was measured by a current integrator, so that ion beam fluctuations during an alpha count were unimportant.

To prevent carbon deposition on the target surface from the ion beam, it was found necessary to connect a subsidiary pumping system direct to the target chamber, to cool the target chamber walls with liquid nitrogen, and to use a palladium leak for the ion source gas input. Heating the target to just below the dissociation temperature 230° C of titanium tritide was also tried, but was found to be unnecessary, since the preferential deposition of the carbon in the beam on to the cooled target chamber walls prevented any carbon becoming detectable on the unheated target surface until more than about 3000 μcoulombs of D_1^+ had been collected. This figure could, however, be as low as 500 μcoulombs if the beam strength were allowed to rise above about 5 μA; hence, when examining a target, the precaution was always taken of keeping the beam strength at about 2 μA and of exposing the target to this 2 μA for the minimum time necessary to get sufficient alpha count accuracy.

If we assume that the tritium distribution inside the titanium tritide is a step function (i.e. is zero concentration up to a depth d, and thereafter is finite and constant, such that the average number of tritium atoms/titanium atom over both the surface layer and the titanium tritide is 1.5), then there are two methods we may use for calculating d from the values of the neutrons/μcoulomb of deuterons, n_0, n_{ψ_1}, n_{ψ_2}, n_{ψ_3}, measured at different angles 0°, ψ_1, ψ_2, ψ_3.

Let $\rho_1 = 5$ g/cm^3 be the density of the titanium oxide contamination layer, and ρ_2 the density of titanium tritide.

Let E be the deuteron energy at the target surface, E_0 be the deuteron energy for normal incidence at the bottom of the surface layer (i.e. just before entering the titanium tritide), E_1 the same for an angle of incidence θ_1, etc.

(a) Evaluation of d by direct comparison of neutron yields at normal incidence, yielding d_N:

The observed neutrons/μcoulomb at $\psi = 0°$ will be less than it would be if $d = 0$. The difference between E and the energy E_0 (read from fig. 1) which would give the observed neutron yield, therefore is the energy lost in the contamination layer. If we assume that the figures in table 1 for $(d\varepsilon/dx)_{TiT_{1.5}}$ will suffice for this contamination layer too, we can then estimate d_N.

(b) Evaluation of d by variation of incident angle, yielding d_θ:

As ψ is increased from 0° to ψ_1, the deuterons have to go through an additional path length Δd in the surface layer, where

$$\Delta d = (\sec\theta_1 - 1)\, d\,, \quad 2\cos\theta_1 = 1 + \cos\psi_1\,.$$

By again using the calculated yield curve in fig. 1. for $TiT_{1.5}$, the value of the energy E_1 corresponding to the observed neutron yield n_{ψ_1} is obtained. The additional energy lost by the deuterons in the surface layer due to increasing the angle ψ from 0° to ψ_1 is therefore $E_0 - E_1$. We can then estimate d_θ from

$$\int_{E_0}^{E_1} \rho_2 \frac{dx}{d\varepsilon}\, d\varepsilon = \rho_1 (\sec\theta_1 - 1)\, d_\theta\,.$$

This can be repeated for other angles ψ_2, ψ_3 and the values obtained for d_θ should all be identical.

It should be emphasised that, whereas the

[12]) Benveniste and Zenger, UCRL 4266 (1954).

value of d_N is based on a single reading (viz. at $\psi = 0°$) of the neutron/μcoulomb, and depends sensitively on the absolute energy E, the value of d_θ, in contrast, is evaluated from the slope of the curve of observed neutrons/μcoulomb against ψ. The value of d_θ is therefore more reliable, and should be affected to a lesser extent by any error in the absolute value of E or by any uncertainty in the calculated yield curve for $TiT_{1.5}$.

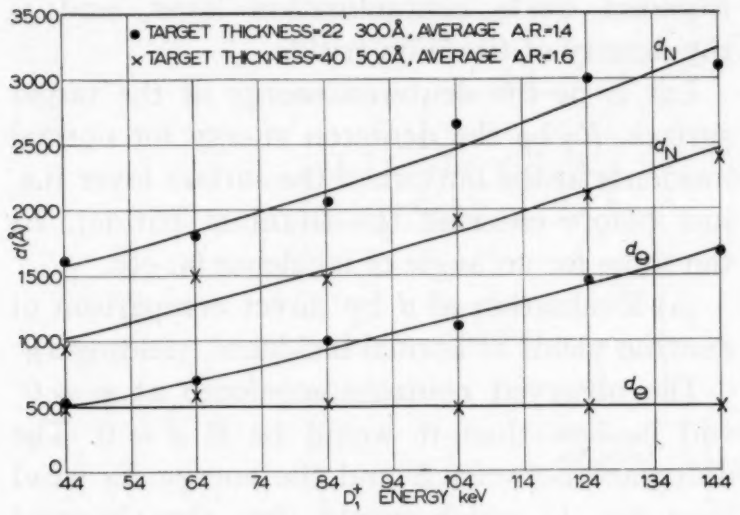

Fig. 6.
Dependence of contamination thickness on D_1^+ energy.

2. Interpretation of Results

Values of d_N and d_θ against E for a typical target are plotted in fig. 6. About one dozen titanium tritide targets, of thicknesses ranging between 10 000 Å and 25 000 Å, but manufactured under differing conditions, were examined by this technique. All the experimental data cannot be included here, but table 2 gives one typical set of readings. Also examined was a target of much greater thickness, 40 500 Å. The values obtained for d_N, d_θ for this target are also given in fig. 6.

From fig. 6, we see that for a thin target, $d_N \gg d_\theta$, and both d_N and d_θ increase with E. On a much thicker target, the dependence of d_θ on E disappears. Ideally, we should expect d_θ and d_N to be equal and both independent of E. The above effects can, however, be explained qualitatively by the inadequacy of the assumption that the concentration of tritium is constant within the titanium tritide underneath the surface contamination layer.

Let us suppose that the actual tritium concentration follows a curve such as that shown in fig. 7.

When the beam is made to strike the target oblique, the neutron yield will become greater due to failure of the deuterons to reach the lower region of the target where the tritium concentration is small, and hence the difference between neutron yield at 0^0 and at θ is less than it would be if the tritium concentration were uniform below the surface layer. At a given energy this leads to a value of d_θ which should be less than the value of d_N, which is what has been observed.

Moreover, at normal incidence, the further the deuterons penetrate into the lower regions of the target where the tritium concentration is small, the smaller is the neutron yield. Thus the estimated d_N should rise with energy, and this should hold for d_θ too, but to a lesser extent. Such a dependence on energy should disappear if the target is made so thick that the deuterons cannot reach this lower concentration region. Again, this is what has been observed.

To obtain an exact measurement of the distribution of tritium inside the target material, one should ideally first guess a plausible tritium distribution curve (such as in fig. 7), divide it up into a large number of regions of effectively constant tritium concentration, and, by using the yield curves of Saker and Wood[11] for targets of tritium atomic ratio between 0.2 and 2.3, calculate the expected variation of neutron yield with E and θ. Comparison with experiment should then tell one whether the chosen distribution is correct.

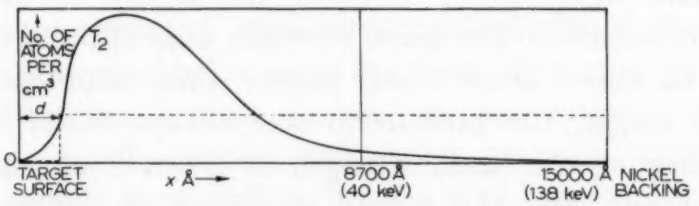

Fig. 7. Distribution of tritium inside target.

This was too tedious to carry out precisely, but one target was studied roughly by this procedure, and the tritium distribution curve in

TABLE 2

Neutron yield readings for a typical TiT target
(target thickness = 22 300 Å, Average A.R. = 1.4)

E (keV)	ψ°	μcoulombs of D_1^+	α's/μcoulombs	Average neutrons/μcoulomb	Expected neutrons/ μcoulomb if $\bar{d}=0$
44	0	184.6	7.62	4.61×10^5	4.51×10^6
	45	217.8	6.54	4.03×10^5	4.51×10^6
	−45	194.7	6.97		
	−60	195.1	6.24	3.70×10^5	4.51×10^6
	60	178.0	6.16		
	75	224.0	5.93	$3.60_5 \times 10^5$	4.51×10^6
	−75	246.8	6.16		
	0	181.7	7.84		
64	0	184.4	44.8	2.71×10^6	1.71×10^7
	45	160.6	40.1	$2.39_5 \times 10^6$	1.71×10^7
	−45	163.7	39.0		
	−60	167.9	34.2	$2.10_5 \times 10^6$	1.71×10^7
	60	165.6	35.5		
	75	166.8	30.3	$1.79_5 \times 10^6$	1.71×10^7
	−75	147.4	28.9		
	0	165.1	44.75		
84	0	76.4	143.8	8.73×10^6	4.00×10^7
	45	79.9	114.0	7.06×10^6	4.00×10^7
	−45	78.6	114.3		
	−60	70.5	107.0	6.56×10^6	4.00×10^7
	60	72.9	105.2		
	75	71.6	94.7	5.86×10^6	4.00×10^7
	−75	78.1	94.8		
	0	73.4	138.5		
104	0	80.2	276.2	1.74×10^7	7.01×10^7
	45	61.7	246.0	1.54×10^7	7.01×10^7
	−45	63.4	248.1		
	−60	60.4	233.2	1.41×10^7	7.01×10^7
	60	61.7	218.5		
	75	61.6	188.0	1.20×10^7	7.01×10^7
	−75	62.4	197.0		
	0	56.3	281.0		
124	0	31.65	537.0	$3.41_5 \times 10^7$	1.01×10^8
	45	31.45	487.0		
	−45	31.15	478.0		
	−60	31.65	450.0	$2.91_5 \times 10^7$	1.01×10^8
	60	31.75	473.0		
	75	31.75	364.0	$2.33_5 \times 10^7$	1.01×10^8
	−75	30.60	376.1		
	0	31.20	546.0		
144	0	19.85	876.0	5.73×10^7	1.27×10^8
	45	19.80	794.0	5.08×10^7	1.27×10^8
	−45	20.06	805.0		
	−60	20.60	735.0	$4.61_5 \times 10^7$	1.27×10^8
	60	20.06	717.0		
	75	19.85	616.0	$3.96_5 \times 10^7$	1.27×10^8
	−75	20.91	630.0		
	0	20.13	925.0		

fig. 7 was the result. Such a curve gave approximately the observed dependence of yield on E and θ, but the observed absolute yields were all a little lower than those calculated. The shape of the distribution is, however, substantially correct.

compound $TiT_{2.0}$. It was usual in a 15 000 Å target to observe a contamination surface layer 500–1000 Å thick, and it was found that the cleanliness and vacuum in the tritation apparatus, and the time that the target was subsequently exposed to air, greatly affected this

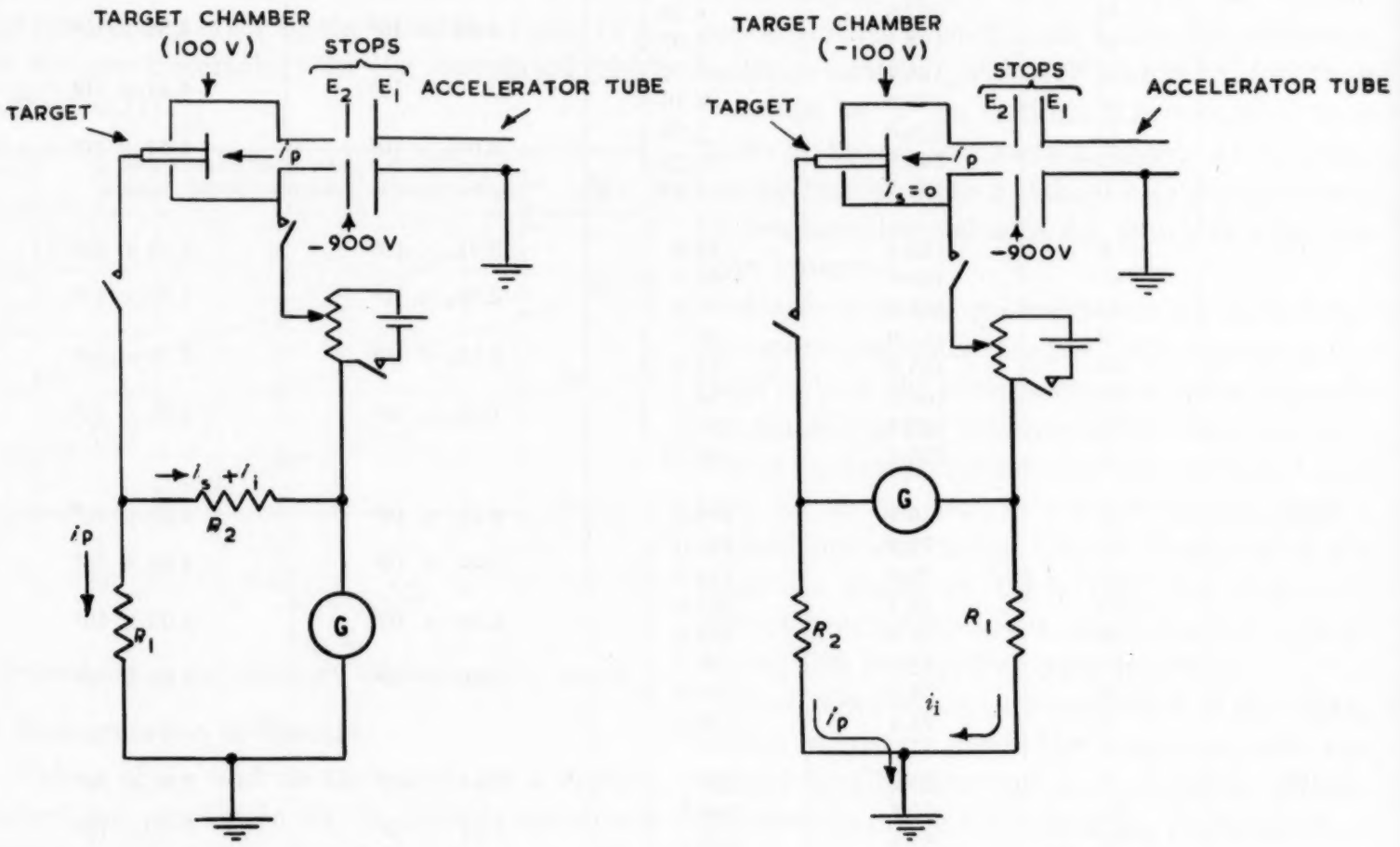

Fig. 8. (a) Bridge circuit for measuring secondary electron ratio (δ). (b) Bridge circuit for measuring i_i/i_p.

The main results of this assessment are that, in a 15 000 Å target, about the last 6 000 Å next to the backing of nickel contains very little tritium. This is supported by the method of manufacture, since the first layers of titanium vapour condensed on the nickel backing during the evaporation process are probably relatively full of gaseous "poisons" from clean-up of the evaporation vessel. Another observation is that the peak of the curve does lie a little above the atomic ratio 2.0. This means that some tritium must be in interstitial lattice positions. Again, this result is supported by the fact that in the manufacture of some targets, the titanium takes up more tritium than could go into the layer thickness. A detailed account of the method of manufacture of the targets used in this investigation has been published by Cole[13].

A subsidiary, but important result of this investigation is that if higher DT neutron yields are desired (e.g. for radiation damage work), it is far better to concentrate first on maintaining a clean target surface with as much tritium as possible in the surface layers, before trying to increase the yield by increasing the incident deuteron beam. Very often, high currents give very little increase in neutron output because the target surface becomes contaminated, and the high wattage drives off a good

[13]) Cole, S.E.R.L., Baldock. Tech. Memo. No. 355 (1957).

deal of the surface tritium. If the above precautions in maintaining clean targets are observed (and this should not be difficult with a large area, cooled, rotating drum target of atomic ratio 1.6 and thickness 50 000 Å), then it should be possible to construct a relatively small and inexpensive mono-energetic fast neutron facility —small compared to a reactor. For example, under the above conditions, a beam consisting of 1 mA of D_1^+ and 1 mA of D_2^+ at 125 keV should yield a steady output slightly in excess of 10^{11} DT neutrons/sec. The wattage dissipated on the type of rotating target described above would not exceed 4 watts/cm², and this should not produce any appreciable target deterioration. The Arkansas neutron facility[14] uses a stationary target with a wattage dissipation of some hundreds of watts/cm², and yet is able to maintain a steady yield of 4×10^{10} DT neutrons/sec for long periods.

If ion currents of about 10 mA are available, and provided the clean target surface is preserved by the above recommendations with a large area rotating target, then by using a high current 125 kV power pack, it seems feasible that a facility capable of producing a steady yield of 10^{12} DT neutrons/sec could be built. It should be emphasised, however, that a Cockroft-Walton machine (which is a complex and precise instrument designed for nuclear and atomic measurements) is not suitable if such yields are required for long periods. As can be observed in fig. 1, using energies above 125 keV gives very little increase in neutron output, and merely increases the wattage dissipated in the target.

Acknowledgements

We should like to thank the techniques group in S.S.N.R. at A.W.R.E. for producing the foils used in the energy loss meaurements, and S.E.R.L., Baldock for supplying the titanium tritide targets. In particular, we should like to acknowledge the assistance of Dr. E. W. Saker and Mr. J. D. L. H. Wood, S.E.R.L., Baldock, for making available the results of their yield calculations, and also the helpful discussions with Mr. P. O. Hawkins, S.E.R.L., Baldock, who initiated the work in the first place. We are grateful to the Director of A.W.R.E. for permission to publish.

14) Bronner, Ehlers, Eukel, Gordon, Marker, Voelker and Fink, Nucleonics **17** (1959) 94.

Appendix

SECONDARY ELECTRON EMISSION FROM TITANIUM HYDRIDE

The apparatus used for the assessment of the tritium targets was modified and used to determine the secondary electron emission coefficients δ of some titanium hydride targets. The target chamber was used as the secondary electron collector by insulating it from the accelerator tube and by making it 100 V positive with respect to the target. This 100 V was found to be adequate to collect all secondary electrons emitted from the target. By means of the bridge circuit in fig. 8(a), it was possible to measure the incident ion current i_p and the resultant secondary electron current i_s separately. If R_1 and R_2 in this bridge are adjusted to give a null deflection on galvanometer G, then

$$\delta = i_s/i_p = R_1/R_2 - i_1/i_p ,$$

where i_1 is the current arising from ionisation of the residual gas in the target chamber. An advantage of this bridge method is that the balance point remains steady during any fluctuations in the beam. In fact, testing to see

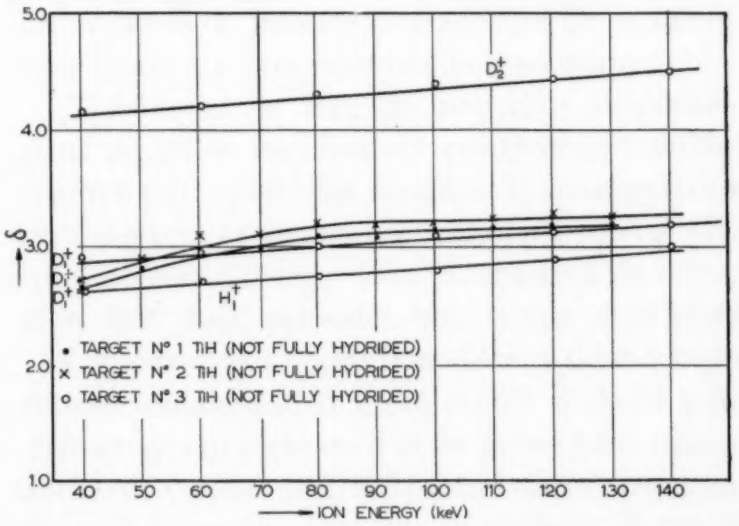

Fig. 9. Equilibrium values of δ at 5×10^{-5} mm Hg.

that this balance does not alter with i_p provides a check on whether any spurious currents are being included in the measurements (e.g. leakage currents across insulators, or secondaries getting past E_2, etc.).

In order to determine the value of i_1/i_p, another bridge circuit was arranged (fig. 8(b)) in which the target chamber was made 100 V negative with respect to the target. In this way, secondary electrons from the target were repelled by the target chamber walls, so that $i_s = 0$. At balance,

$$(i_p - i_1) R_2 = i_1 R_1 .$$

Actually, i_1/i_p turned out to be negligibly small (< 0.02) when the target chamber vacuum was better than about 1×10^{-4} mm Hg. However, at higher pressures, anomalously large values of δ will be obtained unless this correction for i_1 is made.

As expected, the state of cleanliness of the titanium tritide surface was found to affect δ. If the target had previously been exposed to the atmosphere for several days, the δ measured immediately after pumping down below 5×10^{-5} mm Hg was appreciably higher than the true value. Only after hours of pumping did the measured δ settle down to a steady equilibrium value. Where the target had been stored under vacuum, the equilibrium value of δ was obtained almost immediately after pumping down in the target chamber. The values of δ presented in fig. 9 are the lowest equilibrium values obtained after hours of pumping.

NUCLEAR INSTRUMENTS AND METHODS **8** (1960) 185–194; NORTH-HOLLAND PUBLISHING CO.

APPAREIL AUTOMATIQUE POUR LA MESURE DES GRADIENTS LOCAUX DU FLUX DE NEUTRONS DANS UN REACTEUR

P. MULOT, R. POUSSOT, A. P. SCHMITT et C. P. ZALESKI

Groupe d'Etude de Piles Rapides, Département de Recherche Physique, Commissariat à l'Energie Atomique, C.E.N., Saclay, Gif-sur-Yvette (S & O)

Reçu le 9 janvier 1960

An apparatus designed to measure strong gradients of neutron fluxes as may occur in nuclear reactors is described. Strips of material to be activated are exposed to the neutron flux and the induced beta activity is measured as function of position.

Sections 2 and 3 describe the electronic and mechanical parts of the apparatus. Performance data are presented in section 4; sample data are shown in section 5.

1. Principes Généraux

La mesure de la distribution spatiale du flux des neutrons dans une pile est directement liée à la détermination de certains de ses paramètres physiques et aux études relevant de son exploitation.

En particulier, l'étude de cette distribution au niveau de certaines solutions de continuité s'est révélée intéressante pour évaluer par exemple:

les contraintes thermiques dans les éléments combustibles,

le facteur d'utilisation thermique d'un réseau hétérogène,

la déformation de la distribution du flux créé par la présence dans le réseau de corps étrangers (canal d'eau, barres de contrôle, etc.).

La mesure de telles répartitions spatiales de flux doit tenir compte des trois remarques suivantes:

(1) La présence du détecteur de neutrons ne doit pas perturber la distribution à mesurer. La méthode de détection basée sur le principe de l'activation de détecteurs métalliques semble assez bien s'adapter à cette exigence.

(2) Les distributions à mesurer peuvent présenter un gradient assez élevé. Pour les mesurer convenablement, il est nécessaire que la position relative des détecteurs soit aussi précise que possible au moment de l'irradiation. La solution consistant à utiliser un détecteur continu semble séduisante. Il faut alors posséder un appareil de mesure de l'activité de ce détecteur ayant un bon pouvoir de résolution.

(3) Souvent le flux de neutrons disponible pour de telles mesures est relativement faible; d'autre part, pour des facilités de manipulation du détecteur et de son support, il est souhaitable qu'il ne soit pas trop actif. L'appareil de détection doit donc posséder une bonne sensibilité.

L'appareil que nous allons décrire tient compte de ces remarques. Il a été étudié d'abord pour utiliser des détecteurs d'or se présentant sous la forme de bandes de 2/100 ème de mm d'épaisseur, de 6 à 7 mm de largeur et jusqu'à 30 cm de longueur†.

Après irradiation du détecteur dans un flux de neutrons de valeur moyenne convenable, on détermine l'activité relative induite le long de la bande en mesurant point par point le rayonnement β qu'elle émet. L'activité en un point correspond à l'activité moyenne d'une partie de la bande (tranche) définie par un diaphragme rectangulaire lié au système de détection du rayonnement.

Pour réaliser la mesure, la bande et son support sont placés entre deux ensembles scintillateur-photomultiplicateur, dont l'un reçoit le

† Les premières mesures décrites ici à titre d'exemple ont été effectuées avec des bandes d'or. Moyennant certaines modifications possibles du montage actuel, d'autres métaux se laminant correctement peuvent être utilisés comme détecteurs.

rayonnement total $(\beta + \gamma)$ émis par la tranche et le rayonnement du reste de la bande, l'autre ne recevant que le rayonnement γ émis par l'ensemble de la bande, le rayonnement β étant absorbé par un écran convenable.

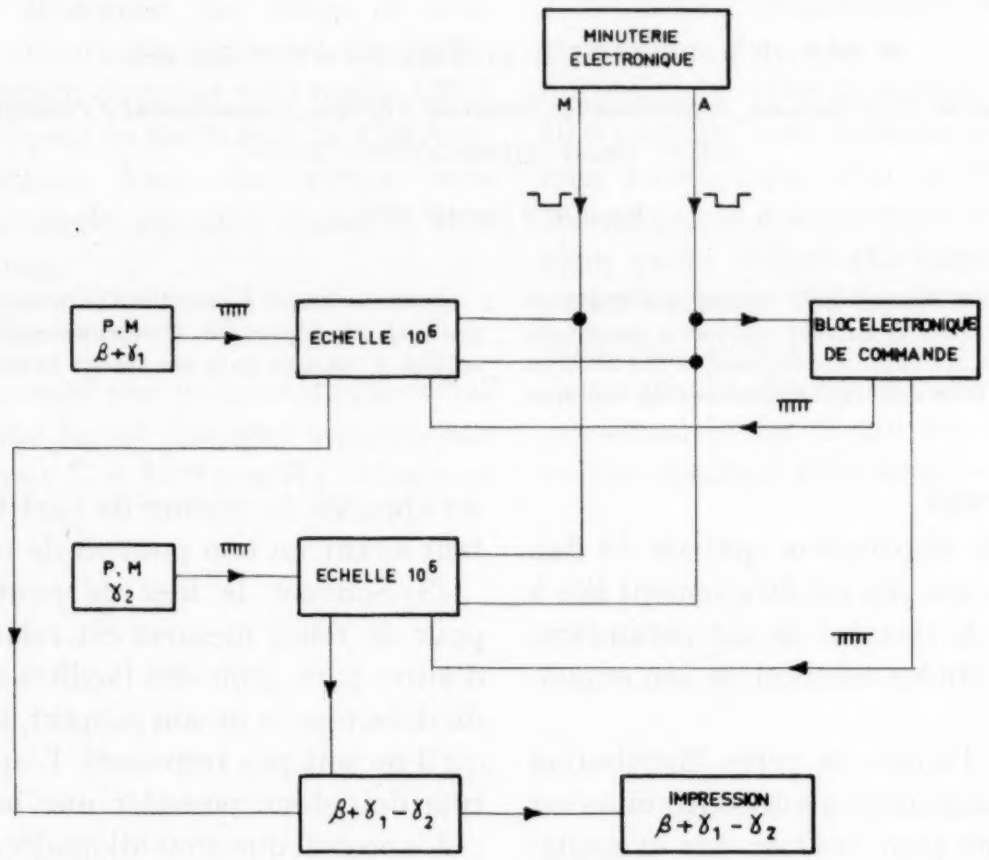

Fig. 1. Bloc diagramme sommaire.

Par soustraction des deux réponses moyennant certains ajustements préalables, nous obtenons le seul rayonnement β émis. Suivant la collimation adoptée, définissant la tranche explorée, le pouvoir de résolution est différent. La collimation réalisée par des diaphragmes interchangeables est rendue nécessaire par le compromis qui se présente entre la quantité de flux de neutrons disponible pour l'irradiation et la sensibilité liée à la résolution de l'appareil de mesure.

L'avancement de la bande irradiée devant les ensembles de détection est réalisée à l'aide d'un système mécanique de pas à pas.

Le critère de précision sur la mesure de l'activité de chaque tranche de la bande explorée conduit, compte tenu de l'irradiation maximum utilisable, à une durée de comptage par tranche souvent assez grande. Pour éviter l'immobilisation de personnel et les erreurs humaines dans les relevés, cet appareil est conçu de telle sorte que tous réglages préalables étant effectués, la valeur relative de l'activité β d'une tranche à une autre tranche de largeur définie, qui sont séparées par un pas déterminé, s'enregistre automatiquement sur une machine à écrire.

2. Description de la Partie Electronique

2.1. L'ENSEMBLE COMPREND

2 photo-multiplicateurs (PM) DARIO-53AVP, leurs alimentations et leurs préamplificateurs. Ils sont équipés de petits scintillateurs "plastiques" minces pour rayonnement β †.

2 échelles de comptage à grande capacité (10^6) vitesse de comptage 200—250 kHz.

1 groupe électronique de commande.

1 minuterie électronique donnant deux temps préréglés, l'un dit "temps de comptage", l'autre "temps d'arrêt".

1 décodeur électromécanique et une machine à écrire destinée à frapper les résultats.

† L'épaisseur de ces scintillateurs est ajustée sur l'énergie du rayonnement β émis par le détecteur utilisé.

2.2. FONCTIONNEMENT (fig. 1)

Cette partie électronique doit assurer l'automatisme et enregistrer le résultat du comptage $(\beta + \gamma - \gamma)$ correspondant à chaque tranche de la bande irradiée se présentant devant les PM.

Le déroulement des opérations, entièrement automatique, est contrôlée par une minuterie électronique. Sur cette minuterie, deux comptes prédéterminés sont disponibles. Le premier réglant le temps de comptage, le second le temps d'arrêt.

Un oscillateur piloté par quartz sert de base de temps et, convenablement démultiplié, alimente les deux comptes de la minuterie.

Le départ de celle-ci délivre une impulsion dite de synchronisme qui commande le démarrage des échelles de comptage et du compte prédéterminé du "temps de comptage".

Les informations en provenance des deux PM vont s'accumuler sur leur échelle correspondante pendant tout ce temps. La fin du compte prédéterminé du temps de comptage est commandée par une impulsion de synchronisme délivrée par la minuterie; cette même impulsion déclenche le compte du "temps d'arrêt" et démarre le bloc électronique de commande.

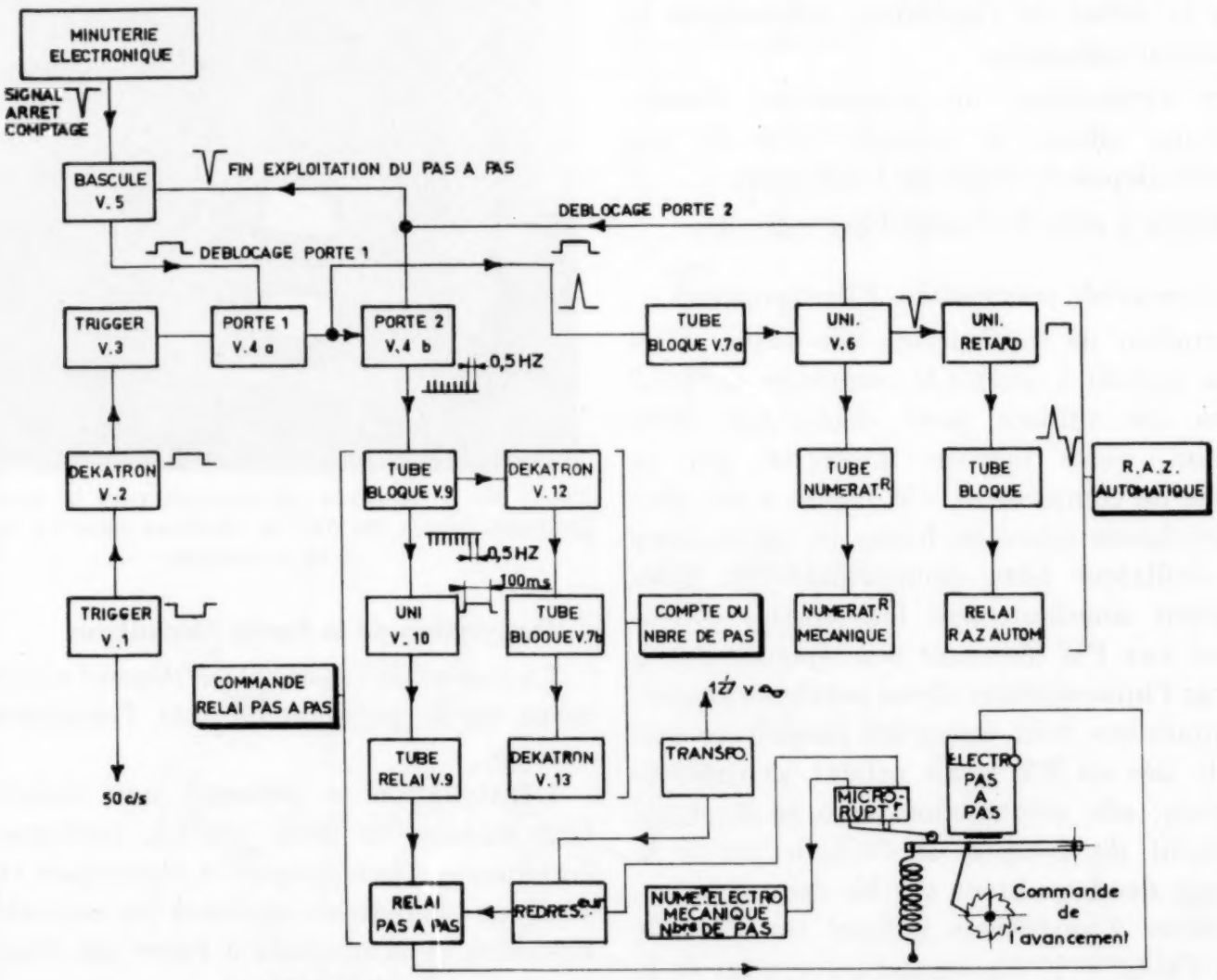

Fig. 2. Bloc diagramme, commande mécanique, compte programme.

Ce bloc a pour fonction:

– avance de la bande irradiée pour la placer dans la position nécessaire au comptage suivant;

– opérer la soustraction d'informations accumulées sur les 2 PM;

– imprimer le résultat de cette soustraction sur une bande de papier.

Il se divise en deux commandes:

(*a*) *Commande mécanique* (fig. 2). Elle comprend:

– l'avance de la bande irradiée par l'intermédiaire d'un pas à pas commandé par des impulsions récurrentes à 0.5 Hz.

– la notation réalisée par V_{12} et V_{13} du nombre de pas effectués pour passer d'une tranche à une autre tranche, deux tranches successives ne pouvant pas être séparées par une distance supérieure à celle correspondant à 40 pas.

– la notation du nombre de mesures effectuées, depuis le début de l'opération affichée sur le numérateur mécanique.

– pour vérification, un numérateur électromécanique affiche le nombre total de pas effectuées depuis le début de l'opération.

– la remise à zéro de l'ensemble du groupe.

(*b*) *Commande soustraction*. Elle comprend:

– l'opération de soustraction elle-même: l'impulsion servant à arrêter le comptage sur les 2 échelles est utilisée pour déclencher cette opération; cette dernière s'effectue par la méthode de complément. On utilise à cet effet des impulsions mises en forme en provenance d'un oscillateur libre (multivibrateur). Elles alimentent simultanément les échelles correspondant aux PM (donnant des réponses $\beta + \gamma$ et γ) par l'intermédiaire d'une entrée auxiliaire. Ces impulsions sont envoyées jusqu'à ce que l'échelle liée au PM γ ait atteint sa capacité maximum; elle affiche alors zéro et le signal épuisement du compte de l'échelle arrête le comptage des impulsions sur les deux échelles. Le nombre d'impulsions indiqué sur l'échelle liée au PM $(\beta + \gamma)$ correspond au résultat de la soustraction désirée.

– le décodeur automatique: le signal d'épuisement du compte de l'échelle γ est également utilisé pour commander le départ du décodeur électromécanique. Ce décodeur analyse alors le compte indiqué par l'échelle liée au PM $(\beta + \gamma)$, décade par décade et actionne le frappe sur la bande de papier.

– une remise à zéro: en fin d'impression, un signal de remise à zéro est appliqué aux deux échelles et l'ensemble complet est prêt à recevoir l'impulsion de synchronisme qui commande le démarrage des échelles de comptage et du compte prédéterminé du "temps de comptage".

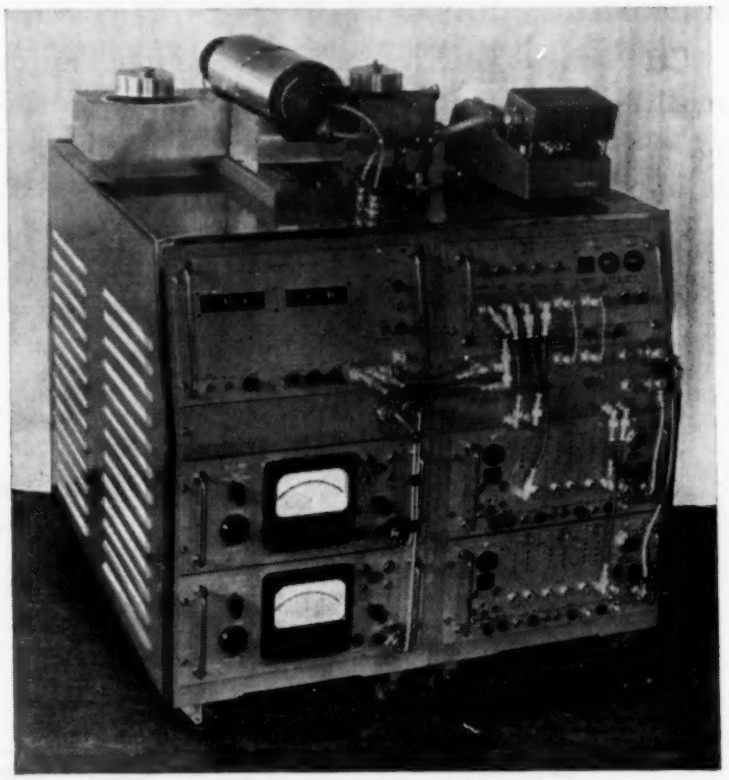

Photo No. 1. Appareil automatique pour la mesure des gradients locaux du flux de neutrons dans un réacteur. Vue d'ensemble.

3. Description de la Partie Mécanique

La valeur de l'installation dépend essentiellement de la précision de tout l'ensemble mécanique.

L'installation se présente sous forme d'un bâti mobile, en deux parties, renfernant les commandes électroniques et électriques et recevant sur son plateau supérieur les ensembles de détection et la machine à écrire qui frappe les résultats (photo No. 1).

Les ensembles de détection se composent essentiellement de deux PM placés dans un blindage cylindrique individuel. Ce blindage contre le rayonnement extérieur est en plomb, chemisé d'aluminium et gainé d'acier inox.

Leur mise en place en profondeur est assuré dans la protection de plomb par un verrouillage lié au bâti.

Les blindages reposent sur des supports en vès. Le PM γ a une position bien définie dans son blindage calé sur son support. Ce dernier comporte tout le dispositif d'avancement du ruban. L'autre PM est placé sur un support se déplaçant sur deux rails (pour des commodités de mise en place de l'ensemble de détection β).

Commande électronique_ Soustraction _ Impression des résultats

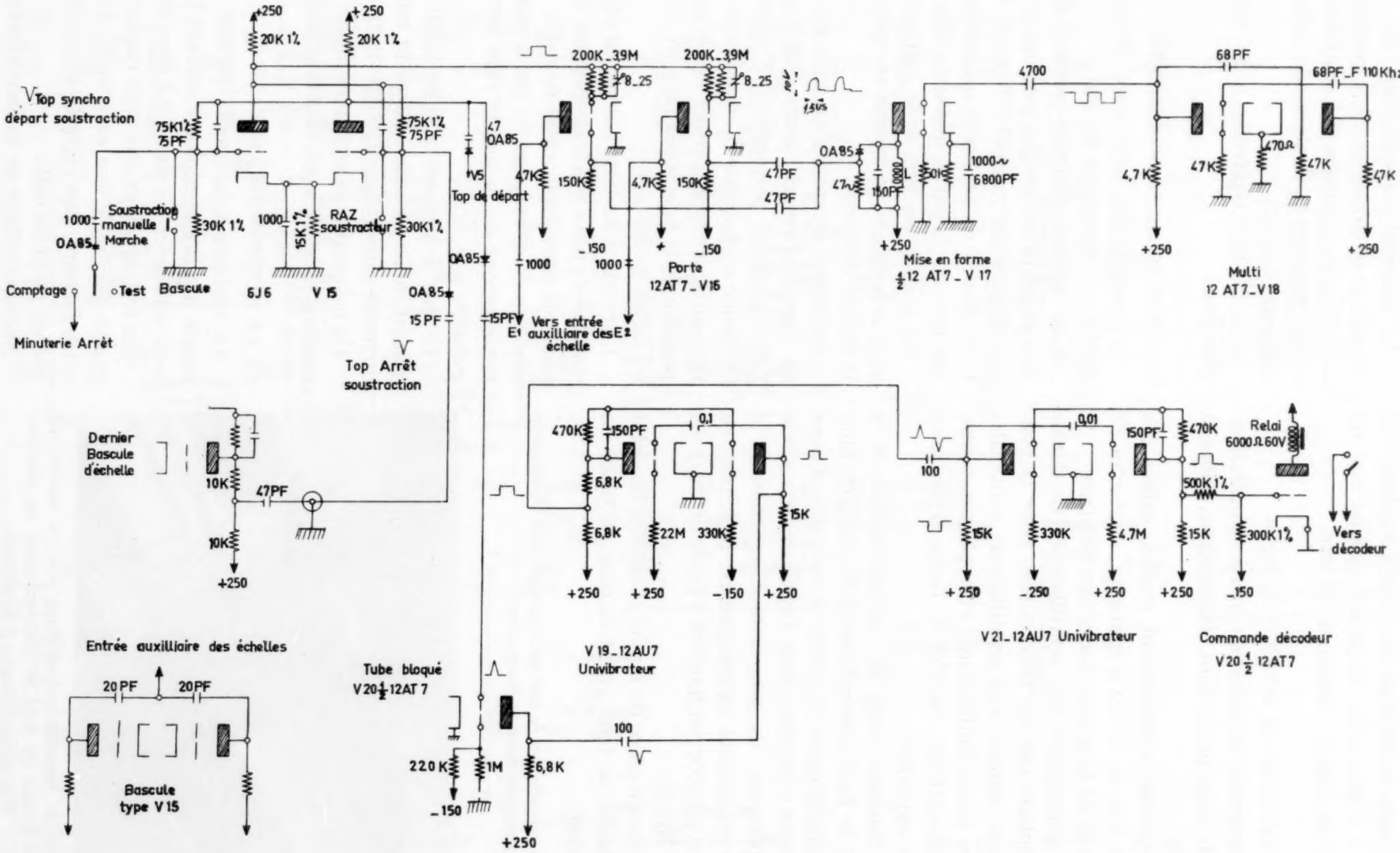

Fig. 3. Commande électronique. Soustraction. Impression des résultats.

La bande métallique irradiée à explorer est collée à l'aide d'un dispositif spécial sur un support de film de cinéma de 35 mm.

3.1. LE SYSTEME DE DETECTION (fig. 3)

Il comprend: scintillateur, porte-scintillateur, guide de film, presse-film, diaphragme, ruban à compter.

Le système actuellement réalisé, utilise des bandes d'or de 2/100 d'épaisseur, de 6 mm de largeur et de longueur maximum 300 mm.

Les dimensions des scintillateurs de forme rectangulaire ont été déterminées pour la configuration utilisée. Ces scintillateurs sont calés dans les porte-scintillateurs et appliqués contre la photo-cathode du PM à l'aide d'un joint optique approprié.

Un fraisage dans le porte-scintillateur γ permet de fixer avec précision le guide de film.

Les diaphragmes en forme de coupelles d'acier inox† sont encastrés dans l'épaisseur du guide et du presseur; ils sont interchangeables et la fenêtre est réalisée en leur centre. Leur mise en place est assurée par fixation à l'aide de deux vis (photo No. 2).

La mise en place du film et le réglage du débit de la bande se font avant la mise en place du PM mobile.

† Des coupelles en or ont été réalisées pour l'utilisation de détecteurs continus de Manganèse.

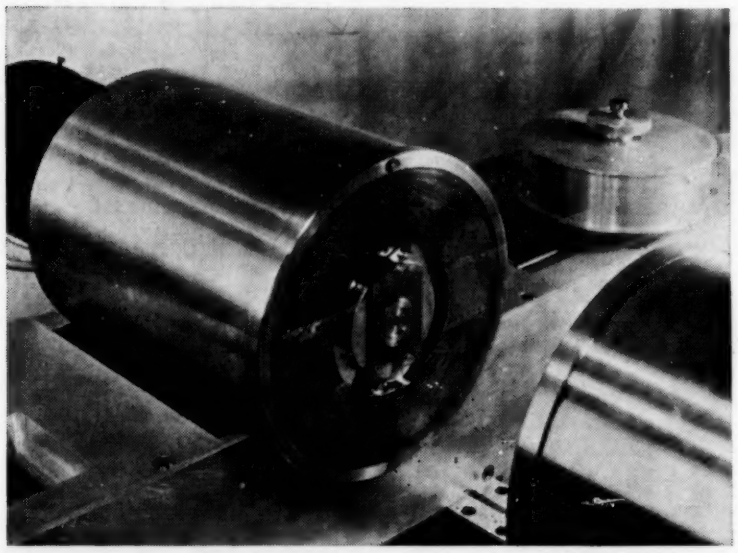

Photo No. 2. Appareil automatique pour la mesure des gradients locaux du flux de neutrons dans un réacteur. Vue du diaphragme β en position.

Au moment du comptage, les deux porte-scintillateurs emboités et le verrouillage assurent:
- un bon parallélisme des scintillateurs
- une distance équivalente du ruban aux scintillateurs
- une distance équivalente du ruban aux diaphragmes.

3.2. LE SYSTEME D'AVANCEMENT

L'ensemble du mécanisme d'avancement est monté sur le support du PM γ.

Une bobine débitrice permet de stocker le film avant la mesure. La position de cette bobine est variable par rapport à l'axe de PM et donne la possibilité de présenter un ruban de longueur 300 mm sur la partie droite du film.

La tension du film et le rattrapage des jeux sont assurés par un ressort en spirale sollicitant la bobine débitrice.

La bobine réceptrice est axée sur une glissière en queue d'aronde commandée par une vis micrométrique permettant d'ajuster le début de bande en fonction du diaphragme utilisé. Un dispositif optique permet de s'assurer de la position de la bande par rapport au diaphragme en début de mesure.

La rotation de cette bobine est obtenue par un système de pas à pas transmettant le mouvement par une démultiplication roue-vis sans fin. Un système de débrayage du pas à pas, permet un facile retour de la bande vers les points déjà mesurés.

Le pas à pas est actionné par un électro-aimant, mais possède également une commande manuelle située dans l'axe de la bobine.

Un numérateur électromécanique enregistre le nombre total de sauts effectués par le pas à pas.

3.3. LE SYSTEME DE COLLAGE

Ce système très simple permet de coller la bande irradiée à explorer suivant l'axe du film avec une précision de $\pm$ 0.2 mm (photo No. 3).

Un fraisage dans une règle en dural permet de guider le film à une extrémité. Dans l'axe de cette fraisure, une réglette reçoit le ruban tenu par un point de colle.

Après encollage de la face externe du ruban,

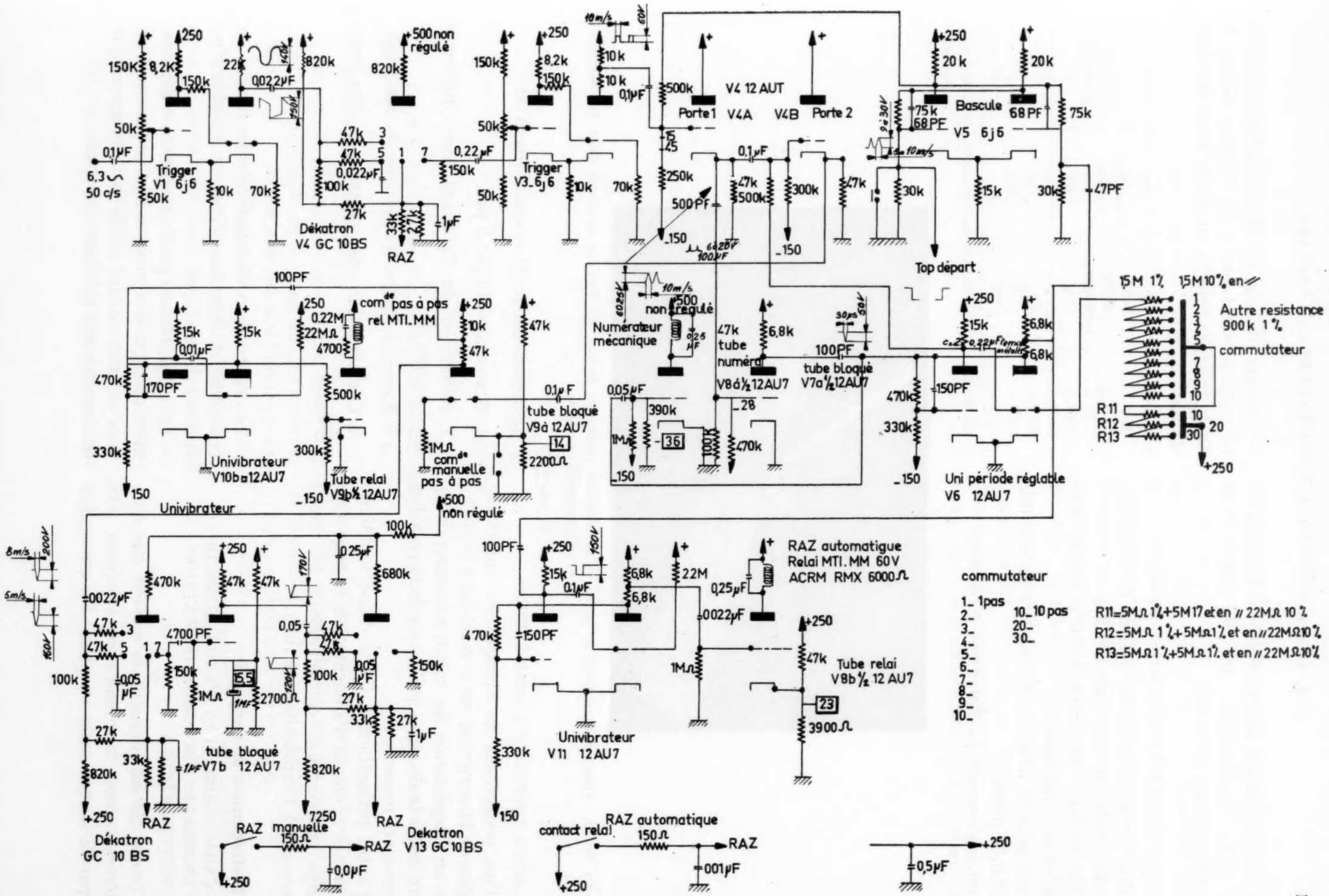

Fig. 4. Commande mécanique, compte programme.

on vient appliquer progressivement le film avec un galet caoutchouté, que précèdent deux roulettes guides de ruban.

3.4. L'ENSEMBLE AINSI REALISE PERMET:

– une bonne symétrie du système de détection,
– une coïncidence des axes des PM
– une distance minimum entre la bande irradiée et les scintillateurs,
– une mise en place rigoureuse et reproductible à chaque mesure,
– un avancement parfaitement déterminé.

les valeurs du seuil de discrimination adoptées ne correspondent pas à des valeurs réelles. A l'indication 0 volt, le bruit de fond est déjà éliminé.

Voies	Haute tension appliquée (V)	Discrimination (V)	Gain du préampli
γ	100	0.17	15
$\beta + \gamma$	1100	0	15

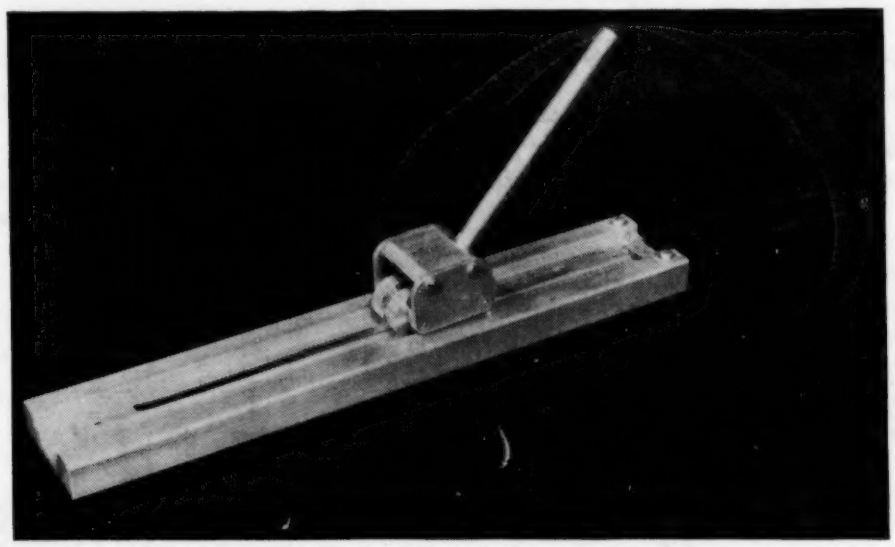

Photo No. 3. Appareil automatique pour la mesure des gradients locaux du flux de neutrons dans un réacteur. Dispositif de collage.

3.5. DEUX DISPOSITIFS SONT PREVUS:

– l'un permettant de changer les caractéristiques de l'inscription sur la machine à écrire au cas où l'exploration du ruban nécessiterait de faire varier la distance qui sépare deux tranches successives mesurées.
– l'autre permettant à l'aide d'une minuterie de couper le circuit d'alimentation au bout d'un temps prédéterminé correspondant au temps nécessaire à l'exploration du ruban.

4. Performances de l'appareil

4.1. CARACTERISTIQUES D'UTILISATION DES ENSEMBLES PHOTOMULTIPLICATEURS-SCINTILLATEURS

Toutes ces caractéristiques doivent être considérées comme nominales et attachées aux appareils actuellement en place. En particulier

Les essais ont porté essentiellement sur:

1. Etalonnage du pas à pas.

2. Résolution de l'appareil avec différents diaphragmes β.

3. Reproductibilité du système de comptage.

4. Compensation des réponses γ des deux voies.

4.2. ETALONNAGE DU PAS A PAS

Le défilement de la bande irradiée devant les ensembles de détection s'effectue à l'aide d'un système de pas à pas.

Les essais réalisés pour déterminer le déplacement de la bande correspondant au passage d'un cran au cran suivant sur le système mécanique ont conduit aux résultats suivants:

No. des essais	Nombre de pas à pas effectués	Longueur de bande débitée (mm)	Valeur sur 1 pas (mm)
1	300	150.7	0.5023
2	300	151.4	0.5046
3	300	150.8	0.5026
4	300	151.0	0.5033
5	300	151.5	0.5050
6	300	151.2	0.5040
7	300	151.2	0.5040
8	300	151.3	0.5040

Nous adopterons comme valeur élémentaire 0.504 $\pm$ 0.001 mm.

coupé perpendiculairement à son axe longitudinal et remplacé sur son support de film une des parties irradiée par une bande non active de même matière et de mêmes caractéristiques géométriques que la bande initiale.

(2) Détermination du taux de comptage β en fonction de la position devant le diaphragme de la transition entre la partie active et la partie inactive. L'avancement était réalisé dixième de mm par dixième de mm à l'aide d'une vis micrométrique associée au support en queue d'aronde de la bobine réceptrice.

La figure 4 représente une des courbes obte-

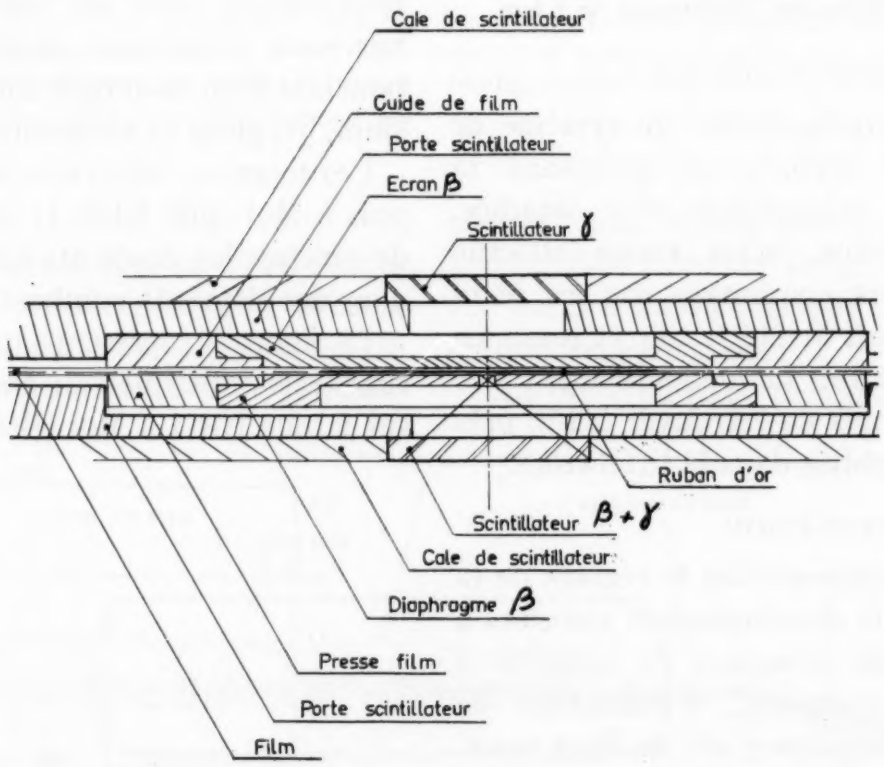

Fig. 5. Système de détection, échelle 4, coupe schématique suivant un plan horizontal dans l'axe des P–M.

4.3. ESSAIS DE RESOLUTION

Ils ont été effectués à l'aide d'une bande d'or irradiée uniformément dans un flux de neutrons de pile.

Une mesure préliminaire réalisée sur le diaphragme de 1 mm nous a permis de déterminer une région de cette bande dans laquelle l'activité induite était constante à 1% près. Cette région a été utilisée de la façon suivante pour étudier le pouvoir de résolution.

(1) Au niveau de la région retenue, nous avons nues. La largeur à mi-hauteur des courbes obtenues par différentiation des précédentes définit la résolution de l'ensemble de détection.

Les résultats sont les suivants:

Diaphragmes (mm)	Résolution mesurée (mm)
0.5	0.5 $\pm$ 0.1
1.0	1 $\pm$ 0.1
2.0	2 $\pm$ 0.1

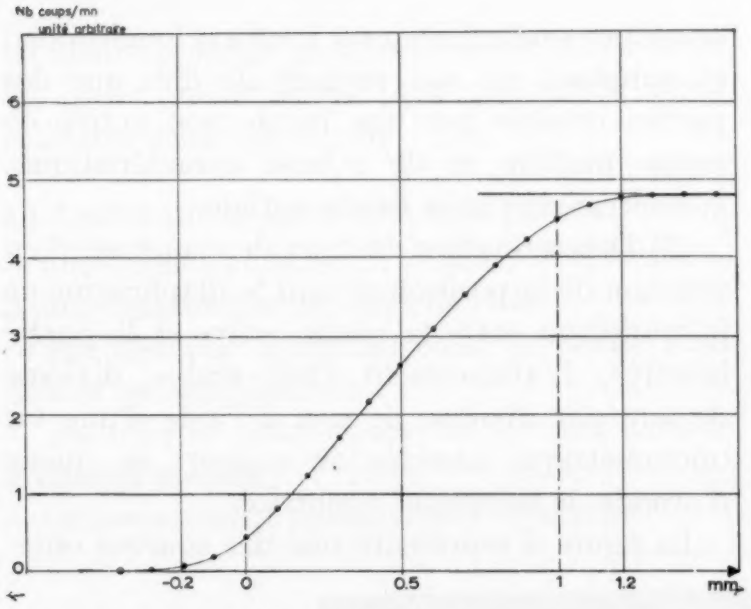

Fig. 6. Pouvoir de résolution, diaphragme de 1 mm.

4.4. ESSAIS DE REPRODUCTIBILITE

Les essais de reproductibilité du système de détection ont été réalisés en analysant la décroissance d'un échantillon d'or irradiée. Pendant une semaine, nous avons effectué chaque jour plusiers comptages sur les deux voies. L'appareil était arrêté le soir et remis en marche chaque matin. Le dépouillement des mesures nous a permis de retrouver à 1% près la période de l'or publiée dans la littérature.

4.5. ESSAIS DE COMPENSATION

Nous appelons compensation le réglage de la haute tension et de la discrimination associées à chaque ensemble de détection de manière à obtenir, dans la géométrie d'utilisation de l'appareil, la même réponse γ sur les deux voies.

Des essais ont été effectués pour vérifier que ce réglage est indépendant:

(1) de la position de la tranche analysée du ruban d'or irradié,

(2) du gradient d'activité au voisinage de la tranche.

† Nous tenons à remercier MM. Vidal et Boyer du Service de la Pile de Fontenay-aux-Roses pour l'aide efficace qu'ils ont bien voulu nous donner dans la réalisation des irradiations nécessaires.

Pour réaliser ces essais, nous avons irradié un ruban d'or sur lequel en trois endroits nous avons placé des petits disques de cadmium pour créer une dépression de flux importante.

Le résultat des mesures fait apparaître une valeur de l'écart des réponses γ des deux voies sans relation apparente avec la position du gradient de l'activité mesurée et toujours inférieure à 1% du taux de comptage β moyen obtenu†.

5. Exemple des Mesures Effectuées

La première application de cet appareil est relative à la mesure du relèvement du flux neutronique créé en intercalant entre deux barreaux d'uranium placés dans une pile un bouchon d'un matériau diffusant tel que magnésium, graphite et aluminium.

Ces mesures, effectuées à Marcoule (Pile G1) puis à Mol (pile EBR-1) (Belgique) ont permis de préciser les gradients axiaux de température dans des éléments combustibles du type G2 [1]).

La figure 7 représente une des courbes expérimentales obtenues au cours d'une expérience sur la pile BR-1 à Mol (Belgique').

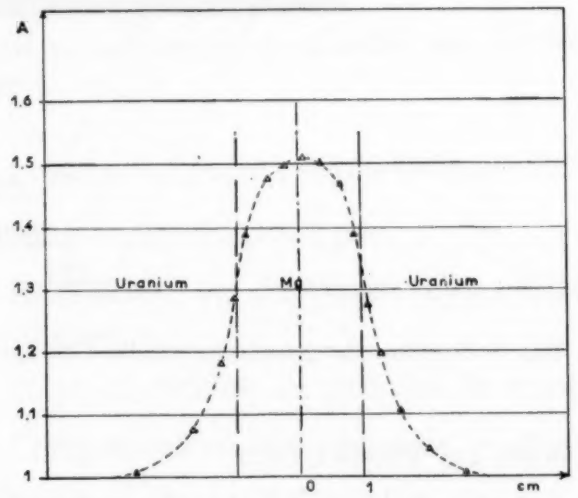

Fig. 7. Relèvement de flux au niveau d'un bouchon de magnésium 20 mm (Mol juillet 1958).

[1]) A. P. Schmitt et A. Teste du Bailler, Note No. 514, SNE/SPM, (12 Nov. 1958).

NUCLEAR INSTRUMENTS AND METHODS 8 (1960) 195–202; NORTH-HOLLAND PUBLISHING CO.

TANDEM ELECTROSTATIC ACCELERATORS

R. J. VAN DE GRAAFF

Massachusetts Institute of Technology

Received 12 August 1959

In this type of accelerator a constant potential is applied to the acceleration of the ion beam, however, not as conventionally with just one voltage application, but instead with a number of applications made in succession by means of a tandem arrangement of high voltage tubes. This number of voltage applications, which is the number of the so-called "stages" of a tandem accelerator, may be two, three, or four, depending on the design chosen. The principles of this type of accelerator are described, and a brief account is given of the design and performance tests of a two-stage accelerator for an output rating of 10 MeV and one-half microampere of protons. Some possibilities for future development are discussed for reaching greater energies by means of three and four-stage tandem arrangements. Preliminary experimental results show the feasibility of operating these by means of the injection of a beam of neutral particles, thus retaining the use of an external ion source at ground potential, as in the present two-stage tandem accelerators.

1. Introduction

In the case of the usual type of electrostatic accelerator, positive ions are produced inside a high-voltage terminal and then accelerated to ground in one stage of acceleration. In the case of the present type of tandem accelerator, negative ions are produced at ground, and then accelerated to a high-voltage positive terminal. Within the terminal the swiftly moving negative ions are stripped of electrons, thus becoming positive ions, which then receive an additional acceleration from the terminal to ground. Thus the particle beam receives two stages of acceleration instead of one.

The principles and techniques used in tandem accelerators have been originated and developed over many years and in various laboratories. It is regretted that lack of space prevents full acknowledgements here. However, reference should at least be made to the following names:

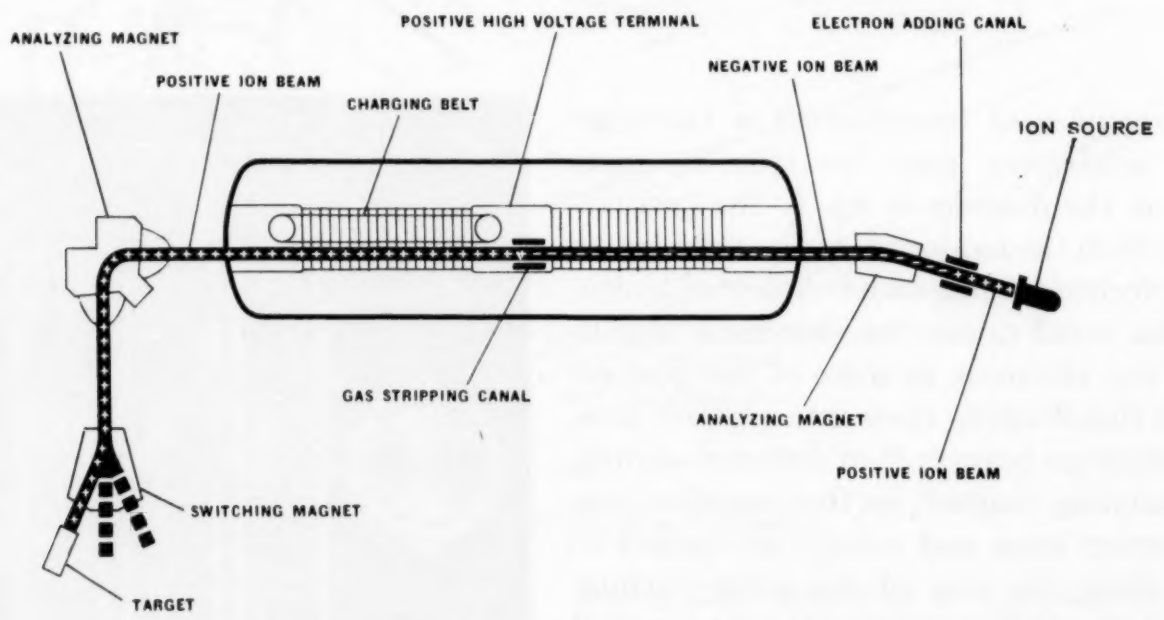

Fig. 1. Two-stage tandem accelerator.

Dempster, Bennett[1]), Kaufman, Alvarez[2]), Marshall, Woodyard, Herb, and Stier.

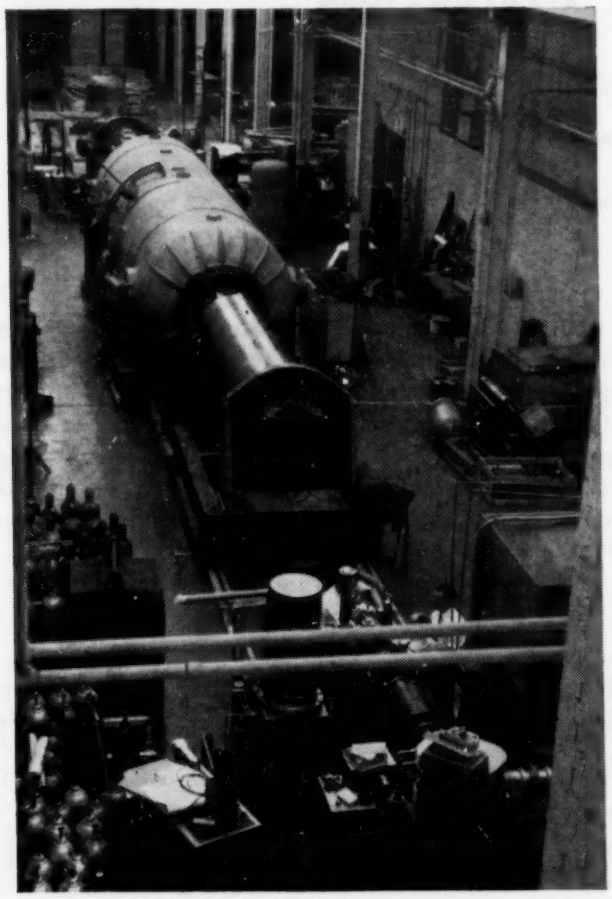

Fig. 2

of its electrons, so that it emerges as a positive-ion beam and is then given its second acceleration which brings it back to ground. The positive-ion beam is then deflected through a 90° analyzing magnet before proceeding through a switching magnet, where it can be directed to any one of three targets.

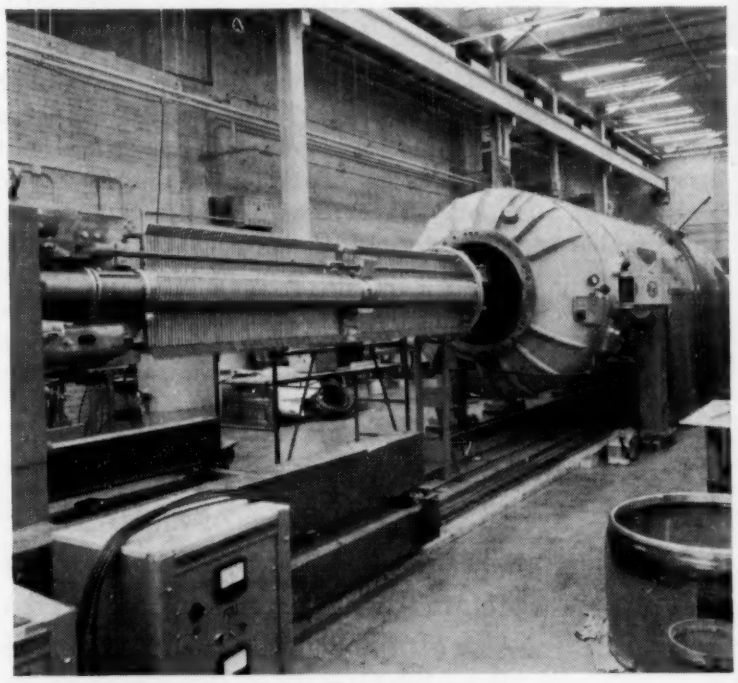

Fig. 3

The principles of operation of a two-stage tandem accelerator may be seen in more detail from the diagram in fig. 1. The positive-ion beam from the ion source at the right passes into the electron adding canal. A flow of hydrogen in this canal causes the successive attachment of two electrons to some of the positive ions, thus transforming these into negative ions. The negative-ion beam is then deflected slightly by an analyzing magnet, so that negative ions of the correct mass and energy are caused to proceed along the axis of the main vacuum tubes, and thus to be accelerated to the terminal which is at a high positive voltage. There the negative-ion beam passes into a second canal, where the presence of gas causes it to be stripped

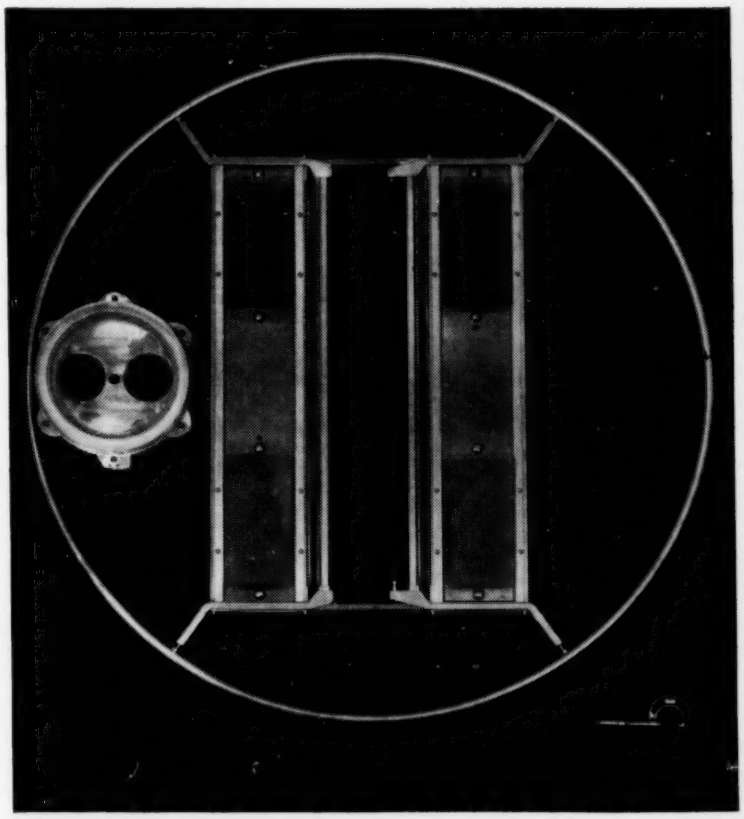

Fig. 4

[1]) W. H. Bennett and P. F. Darby, Phys. Rev. **49** (1936) 97, 422, 881;
W. H. Bennett, U. S. Patent No. 2, 206, 558 (1937);
W. H. Bennett, Rev. Sci. Instr. **24** (1952) 915.

[2]) L. W. Alvarez, Rev. Sci. Instr. **22** (1951) 705.

2. Tandem Accelerator for Chalk River

A two-stage tandem accelerator has been designed and constructed by the High Voltage Engineering Corporation for the Chalk River Laboratory of Atomic Energy of Canada, Limited. After tests in Burlington, it is now in use at Chalk River†. The next three figures are photographs showing the construction of this accelerator.

Fig. 2 shows one column rolled back from its operating position within the tank. Each column has an insulating length of 12 feet, and the tank is 8 feet in diameter and 35 feet long. Fig. 3 is a similar view, but with the equipotential rings removed, so that the acceleration tube and compression members of the column can be seen. Fig. 4 is a photograph of a "cross-section like" assembly of equipotential column parts. The outside ring is 39 inches in diameter. The four glass-block insulators can be seen at

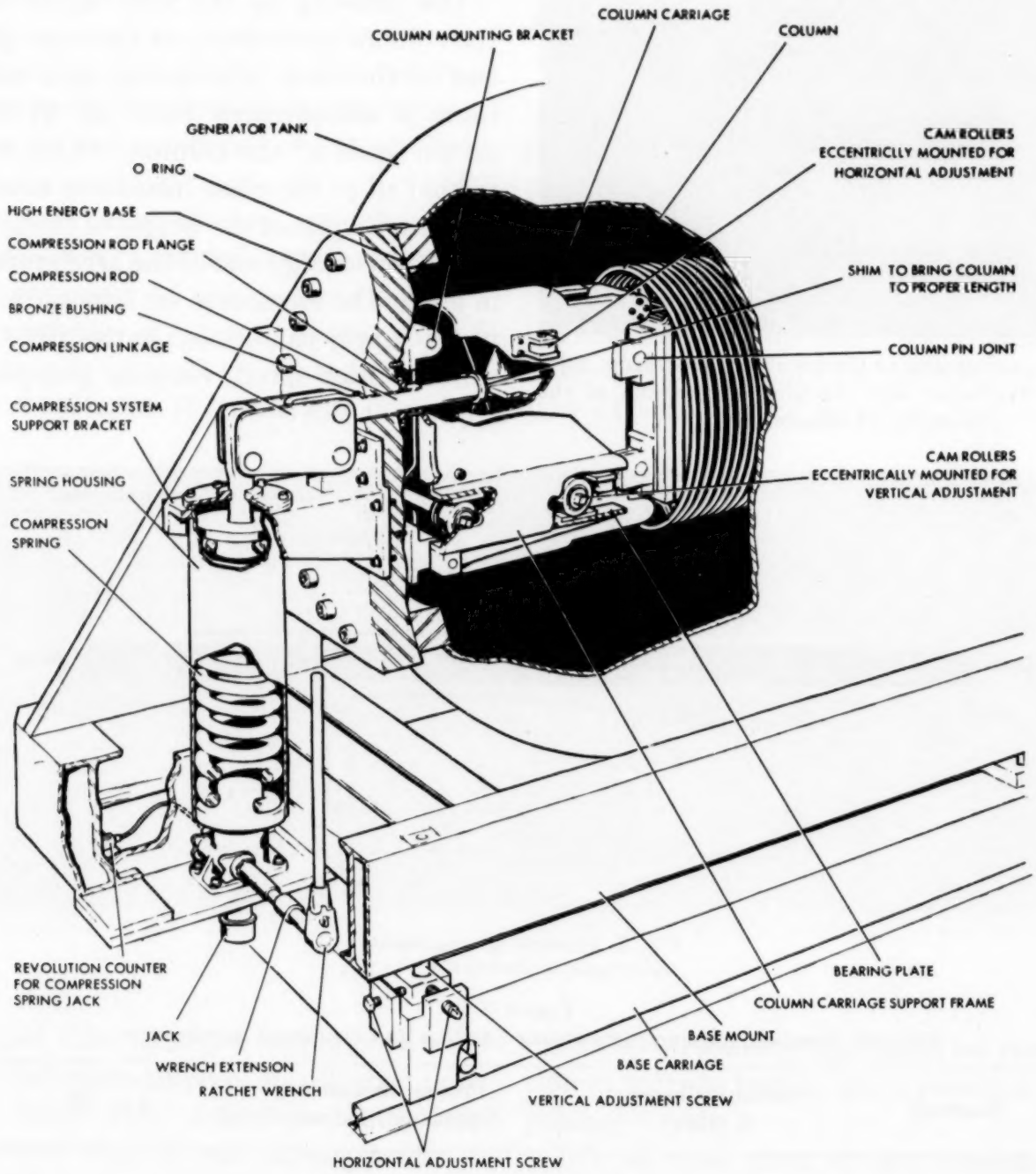

Fig. 5. Column tension adjusting mechanism.

† For additional information regarding this accelerator, reference is made to the following papers: (1) Ten MeV particle accelerator will aid nuclear research at Chalk River, by H. E. Gove, Canadian Electronics Engineering (July 1958). (2) New design makes ten MeV particle accelerator possible, by John L. Danforth, Canadian Electronics Engineering (July 1958).

Fig. 6. Tandem accelerator of University of Wisconsin, fully installated. (Reprinted with the kind permission of the University of Wisconsin.)

the corners of the large rectangle. Space for the belt is provided in the vertical region between the four glass insulators. An acceleration-tube electrode is visible at the left.

The drawing in the next figure shows how the column is mounted on the loose plate at the end of the tank. The spring mechanism maintains a compressive force of 40 000 pounds on the ends of the column, which is sufficient to hold all of the glass insulators firmly in compression in spite of the weight of the column.

The low-energy end of the accelerator is shown in fig. 2. The ion source with its radio-frequency power supply can be seen in the mid-foreground, while a high-speed vacuum pumping system appears at the left.

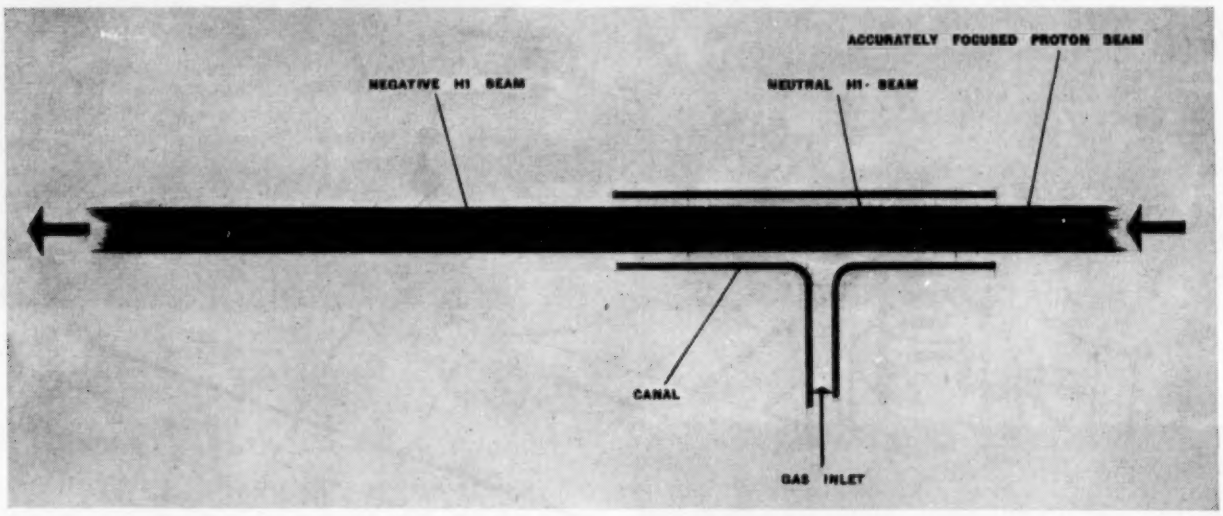

Fig. 7. Present arrangement.

TABLE 1
Neutron threshold measurements using Tandem Van De Graaff Accelerator

Reaction	Threshold energy E (MeV)	Proton resonance frequency f(Mc/sec)	$k \times 10^5$
$Li^7(p,n)$	1.8813 ± 0.0005	9.690 ± 0.010	†2021 ± 3
$B^{11}(p,n)$	3.015 ± 0.003	12.322 ± 0.003	2004 ± 3
$Na^{23}(p,n)$	5.061 ± 0.007	15.950 ± 0.020	2010 ± 4
$Al^{27}(p,n)$	5.798 ± 0.005	17.080 ± 0.010	2009 ± 4
$H^2(O^{16}+5,n)$	14.572 ± 0.030	21.555 ± 0.020	2008 ± 5
$H^2(O^{16}+4,n)$	-14.572 ± 0.030	26.940 ± 0.020	2008 ± 6
	$E(1 + E/2Mc^2) = k f^2 q^2/M$	Average of 5	2008 ± 2
$Ni^{60}(p,n)$	7.028 ± 0.020	18.814 ± 0.010	$k =$ $(2008 \pm 4) \times$ 10^{-5} (assumed)
$Ni^{58}(p,n)$	9.459 ± 0.070	21.840 ± 0.080	

† Corona Stabilizer inoperative for this run.

Fig. 7 shows the ion source, and initial accelerating electrodes, together with the electron-adding canal. A flow of hydrogen maintains this canal at sufficient pressure for charge transfer, so that about 1% of the protons in the beam emerge as negative atomic hydrogen ions.

The stripping canal is located in the terminal between the acceleration tubes. Its diameter is only 0.18 inch, which requires quite accurate beam focussing and alignment.

In the tests of the accelerator, proton beams up to 13.4 MeV were obtained, corresponding to a terminal potential of 6.7 megavolts. After 90-degree analysis, a proton beam of 1.5 microamperes was focussed on the target over a wide range of voltages. These outputs considerably exceeded the specified requirements of 10 MeV and 0.5 microampere. Measurements on the proton beam after deflection by the 90° magnet showed that it was homogeneous in energy to $\pm$ 0.02%.

In some of the tests, negative oxygen ions were injected into the accelerator when the terminal was at four megavolts. Observations at the target showed that some of these negative ions were completely stripped in passing through the terminal, thus reaching an energy of 36 MeV.

While the accelerator was still in Burlington, various tests were made in collaboration with a number of physicists from Chalk River. A number of neutron thresholds were studied and calibration measurements were made for a considerable range of particle energies. Figs. 9 and 10 have been taken from a recent paper† describing this work.

3. Some Possibilities for Future Development

An important feature of the tandem design is that the ion source and initial accelerating and focussing arrangements are situated outside the pressure tank, rather than inside the terminal and tank, as in the usual type of electrostatic accelerator. This external location will greatly facilitate the future development of improved ion sources and injection. It also affords ample space and accessibility for the possible introduction of various new injection devices, such as multiple-ion sources, apparatus for the polarization of particle beams, and equipment for beam pulsing.

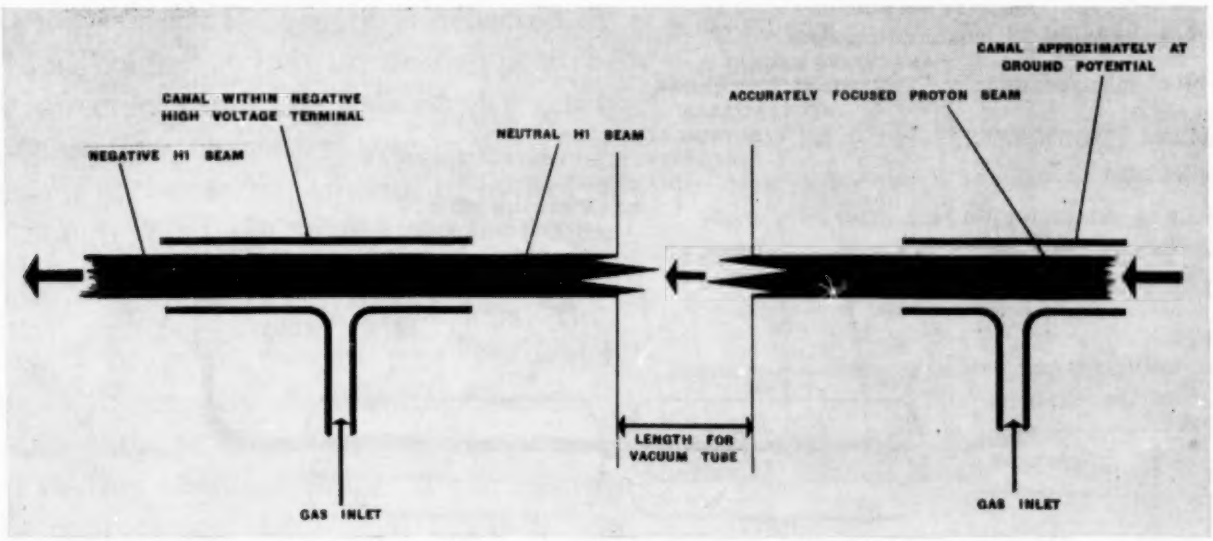

Fig. 8. Proposed arrangement,

Let us now turn to the consideration of future possibilities for the attainment of higher particle energies by tandem acceleration. Obviously, one method is by the use of higher

† Neutron threshold measurements in the proton energy range from 1.8 to 10.5 MeV using the Chalk River Tandem Van de Graaff Accelerator. This paper was read by A. J. Gale at the Vancouver Meeting (August, 1958) of the American Physical Society. Its authors were: E. Almqvist, D. A. Bromley, A. J. Ferguson, H. E. Gove, J. A. Kuehner and A. E. Litherland (Chalk River) and R. Bastide, N. Brooks, R. J. Connor, P. H. Rose (HVEC). Reprints can be obtained from High Voltage Engineering Corporation.

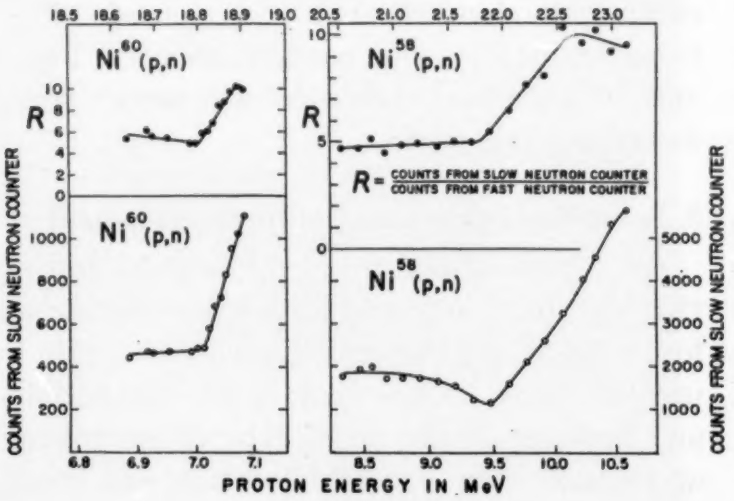
Ni60(p,n)
Ni58(p,n)
R
R = COUNTS FROM SLOW NEUTRON COUNTER / COUNTS FROM FAST NEUTRON COUNTER
COUNTS FROM SLOW NEUTRON COUNTER
PROTON ENERGY IN MeV

Fig. 9
(Reprinted with the kind permission of the Chalk River Group, Atomic Energy of Canada, Ltd.)

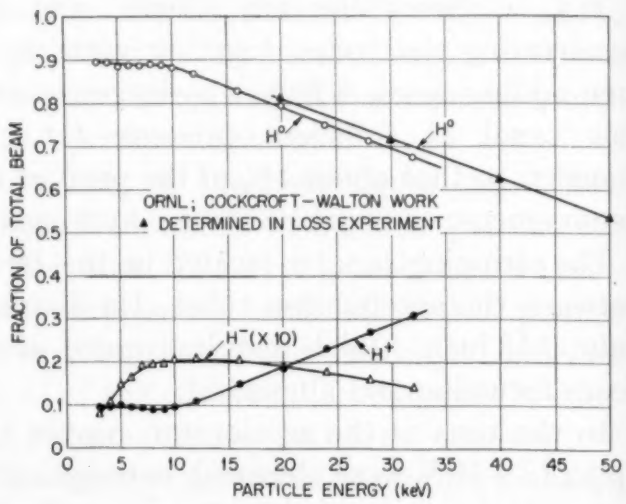

Fig. 10. Fraction of H beam in + 1.0–1 Charge states after passage through "thick" target. H in hydrogen.

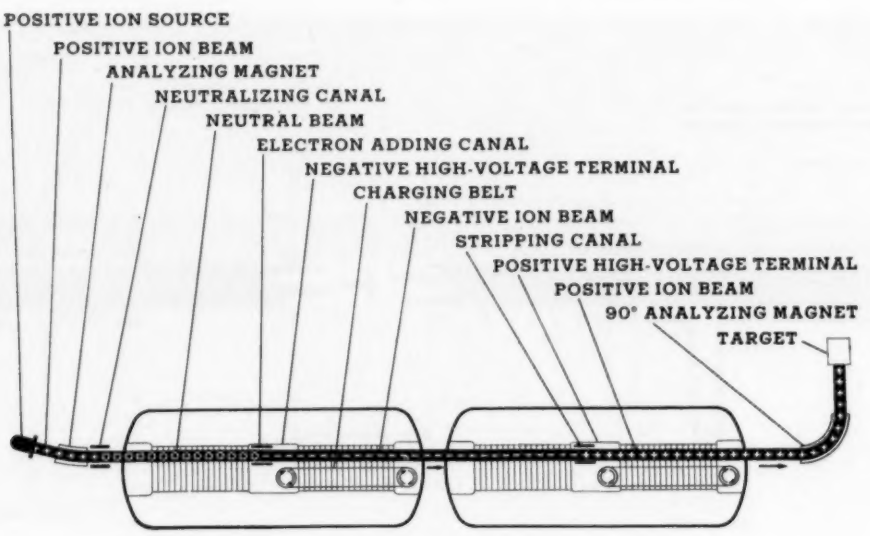

Fig. 11. Three-stage tandem accelerator.

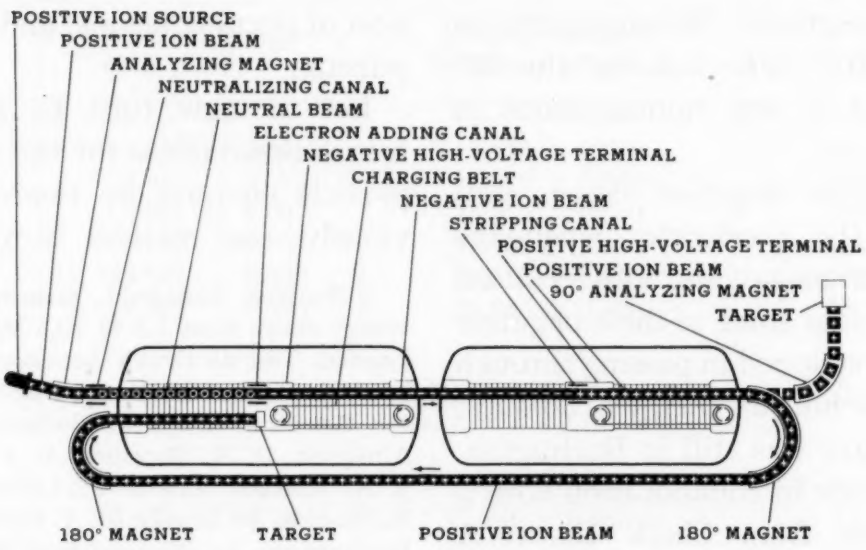

Fig. 12. Four-stage tandem accelerator

terminal potentials. At present the ceiling in this direction is represented by the ONR accelerator at M.I.T. built by J. G. Trump, and used since 1951 by W. W. Buechner for nuclear research at terminal potentials up to 10 megavolts. It is to be expected that in future accelerators there will be continuing increases in the terminal potentials attainable, due not only to growth in the size of accelerators but also to continued progress in high-voltage techniques which will make possible the insulation of still higher voltages in a given size of accelerator.

A more radical method of seeking higher tandem particle energies is by the use of more than two stages of acceleration. Fig. 11 shows a diagram of a possible arrangement for a three-stage tandem accelerator. The positive-ion beam from the ion source at the right is deflected by an analyzing magnet so that the desired positive ions are directed along the axis of the acceleration tubes. In the neutralizing canal, these positive ions encounter an amount of hydrogen which, though relatively small, is nevertheless sufficient to cause the attachment of a single electron to most of the positive ions, thus producing a beam of neutral particles which proceeds to the negative high-voltage terminal. In passing through the electron-adding canal situated in this terminal, some of the neutral particles capture and additional electron and become negative ions. These receive their first main stage of acceleration in passing from the negative terminal to ground, where they are injected into the second pressure tank as a negative-ion beam of considerable energy. In this tank, the beam receives its second and third stages of acceleration.

The operation in this tank is quite similar to that shown in the tank in fig. 1, except that in fig. 11 the injected negative ions are about 100 times more energetic and are correspondingly more homogeneous in energy, so that they can be focussed with great accuracy through the stripping canal in the positive terminal.

It is evident that an alternative arrangement for a three-stage tandem accelerator would be to have the complete apparatus for producing the negative ions installed within the negative high-voltage terminal. However, the use of a neutral particle beam, as indicated in fig. 11, appears more promising, as it would make it possible for the particle injector to be external and at ground, a situation having enormous long-run advantages, some of which have been already mentioned. Obviously such use of a neutral particle beam is practical only if the associated particle scattering is quite small. Some encouraging experimental observations in regard to the scattering effect have been made at HVEC and M.I.T.†.

TABLE 2

Positive-ion energies in MeV for certain possible arrangements of Tandem Accelerators

$V + nV$	(for two-stage tandem)
$2V + nV$	(for three-stage tandem)
$2V + 2nV$	(for four-stage tandem)

Here V = terminal potential in megavolts and n = number of electrons stripped from neutral atom.

TABLE 3

Positive-ion energies in MeV for two different arrangements of Tandem Accelerators

Positive ion	Two-stage	Three-stage
Hydrogen	13.4	20.1
Helium	20.1	26.8
Oxygen	60.3	67.0

Assumptions: Terminal potential = 6.7 megavolts. Complete stripping of positive ions.

It is hoped that some preliminary tests of actual three-stage tandem operation can be made by using the pair of two-stage tandem accelerators now under construction at HVEC.

Fig. 12 shows how a four-stage tandem accelerator could be made by the addition of two 180° deflecting magnets and an additional section of acceleration tube, the target being located inside the negative high-voltage terminal.

Table 2 gives some simple formulas for the positive-ion energies in MeV obtainable with the

† S. F. Philp, Doctorate thesis, 1958.

three different tandem arrangements which have been discussed.

The values for positive-ion energies shown in table 3 were obtained by substitution in the formulas of table 2 for hydrogen, helium and oxygen ions.

In the case of the four-stage tandem it is obvious that the inaccessibility of the target is a serious disadvantage. However, the effect of this difficulty could be much reduced by the development of special techniques and devices. It thus appears possible that four-stage tandems may later find usefulness for certain special types of research needing monoenergetic positive ions in an energy range somewhat higher than otherwise available.

NUCLEAR INSTRUMENTS AND METHODS 8 (1960) 203–210; NORTH-HOLLAND PUBLISHING CO.

CALCULATED SHAPES FOR NEUTRON BURSTS PRODUCED BY PHASED CHOPPER VELOCITY SELECTORS†

NORMAN H. TOLK and ROBERT M. BRUGGER

Phillips Petroleum Company, Atomic Energy Division, Idaho Falls, Idaho

Received 5 May 1960

The burst shapes and transmission probabilities for neutrons passing through a phased chopper neutron velocity selector of the type now being used at the Materials Testing Reactor have been calculated using an IBM-650 computer. Choppers with three types of slits (straight, parabolic, and circular) are considered and burst shapes are presented that show the operating characteristics of such velocity selectors. A function that gives a good fit to many of the burst shapes is presented. The results verify that a circular slit chopper can be used in place of the more exact parabolic slit chopper with only minor distortions in the operating ranges of interest.

1. Introduction

Several authors have considered the problem of finding the probability that a single neutron of particular velocity will pass through a rotating slit. A slit having straight parallel sides[1,2,3]) and a slit having a parabolic shape[4]) have been treated.

The present study adopts and extends this work to make possible a determination of the probability that a neutron will pass through two circular slits a set distance apart rotating with a definite phase relation, which is a geometry similar to that of the Materials Testing Reactor (MTR) phased chopper neutron velocity selector. Calculations of these probabilities for the MTR instrument are needed for a better understanding of the operating conditions, for the adjustment of experimental parameters, and for comparison with experimentally obtained results.

The methods of Marseguerra and Pauli[4]), which apply to calculation of the probability for a single chopper with a slit of parabolic shape, have been modified to fit the case of a slit of circular shape. Since calculations for a single chopper are not easily extended analytically to a double chopper arrangement, an IBM-650 computer program was developed to compute the probability $\theta(v,T)$ that a neutron of velocity v will reach at time T a given position along the beam path of the velocity selector.

The study has produced curves that show the general properties of velocity selectors having choppers with three types of slits: straight, parabolic, and circular.

2. Single Rotating Circular Slit

The procedure for circular slit choppers will be presented to illustrate the method used for all three types of choppers. Fig. 1 is a cross sectional view of the chopper to be considered. The primed coordinates are fixed in the chopper and rotate with it, while the unprimed coordinates are fixed in the laboratory system; z and z' are common to both sets of coordinates. The axis of rotation of the chopper is z. A parallel beam of polychromatic neutrons travels along x toward the right. The chopper of radius R has a slit formed by two surfaces located equal distances from and parallel to the axis of the chopper. The width of the

† Work done under the auspices of the U. S. Atomic Energy Commission.

[1]) R. S. Stone and R. E. Slovacek, Nuc. Sci. Eng. **6** (1959) 466; and KAPL–1499 (1956).

[2]) V. I. Mostovoi, M. I. Pevzner and A. P. Tsitovich, Int. Conf. Proc. Peaceful Uses Atomic Energy (Geneva) **4** (1955) 12.

[3]) P. A. Egelstaff, AERE N/R-1131 (1953); J. Nuc. Energy **1** (1954) 57.

[4]) M. Marseguerra and G. Pauli, Nuc. Instr. and Methods **4** (1959) 140.

slit is h and the chopper rotates counterclockwise with an angular velocity ω. The equations of the upper and lower surfaces that form the sides of the circular slit are

$$y'_u = + (\rho^2 - x'^2)^{\frac{1}{2}} - \rho + \tfrac{1}{2}h$$

and

$$y'_l = + (\rho^2 - x'^2)^{\frac{1}{2}} - \rho - \tfrac{1}{2}h .$$

The radius of curvature of both slit surfaces is ρ. These surfaces are assumed to be perfect absorbers.

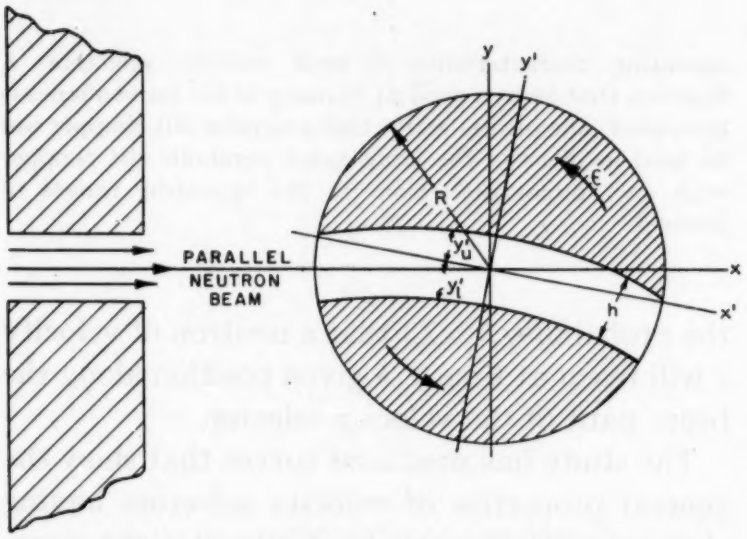

Fig. 1. Single chopper with circular slit. The primed coordinates rotate with the chopper and the unprimed coordinates are fixed in the laboratory frame of reference.

Select a time t associated with each chopper so that $t = 0$ when the rotating coordinate system coincides with the fixed system $x' = x$ and the circular slits are concave toward the negative y direction. (The case with the slit concave toward positive y will not be considered since this orientation is seldom used in curved slit neutron chopper operation.) If h is much smaller than R, and ρ is large compared to R, then the time required for the neutrons to traverse the chopper is small compared to the time for one revolution of the chopper, and it can be assumed that for pertinent values of t, $\sin \omega t = \omega t$. For the slit to be completely closed to very fast neutrons, $R^2 - 2\rho h > 0$. It follows that the equations of the upper and lower surfaces of the slit at time t in the laboratory coordinates are, to a good approximation:

$$y_u = + (\rho^2 - x^2)^{\frac{1}{2}} - \rho + \tfrac{1}{2}h + x\omega t \qquad (1)$$

$$y_l = + (\rho^2 - x^2)^{\frac{1}{2}} - \rho - \tfrac{1}{2}h + x\omega t . \qquad (2)$$

Whether or not the neutrons collide with the surfaces of the slit needs to be known to determine when neutrons are removed from the beam. Consider the front of a plane wave of neutrons traveling in the x direction with velocity v that is at $x = 0$ at time t. Eq. (1) and (2) give the positions of the surfaces of the slit. Let $x = v\tau$ be the position of the wave front when t is changed by an amount τ and the surfaces of the slit are given by eq. (1) and (2) with $t + \tau$ substituted for t. Eliminate τ, to obtain

$$y_u^* = + (\rho^2 - x^2)^{\frac{1}{2}} - \rho + \tfrac{1}{2}h + x\omega t + \omega x^2/v \qquad (3)$$

$$y_l^* = + (\rho^2 - x^2)^{\frac{1}{2}} - \rho - \tfrac{1}{2}h + x\omega t + \omega x^2/v \qquad (4)$$

where y^* gives the magnitude of y for neutrons of velocity v that intersect the upper or lower surfaces of the slit at position x. (See fig. 3 of ref.[4]) for examples of these curves for the parabolic case.) Similar equations can be written for a straight slit and for a parabolic slit[1,4]).

If the neutrons are uniformly distributed in the yz plane before entering the chopper, the greatest number that can possibly pass through the slit is proportional to a y magnitude equal to h. The number of neutrons that actually pass through the slit for a given velocity v and time t is proportional to a y magnitude, $\Delta y^*(v,t) = y_u^*{}_{\min} - y_l^*{}_{\max}$, where $y_u^*{}_{\min}$ is the minimum value of y_u^* for x between $-R$ and $+R$ and $y_l^*{}_{\max}$ is the maximum value of y_l^* for x between $-R$ and $+R$. Thus, the probability $P(v,t)$ that a neutron of velocity v that passes $x = 0$ at time t will pass through the rotating slit is

$$P(v,t) = \Delta y^*(v,t)/h . \qquad (5)$$

The quantity $P(v,t)$ represents the shape of the neutron burst in P, v, and t space that will be passed by a rotating slit. The assumption that $\sin \omega t \cong \omega t$ limits the magnitudes of h and ρ compared to R. For a single chopper, the problem is to determine the values of $y_u^*{}_{\min}$ and $y_l^*{}_{\max}$ from which the transmission probability can be obtained. The maximum probability is obtained for $t = 0$ and $v = 2\omega\rho = v'_0$. The latter is the condition that applies when a circular slit chopper is being designed to transmit neutrons of the desired velocity v'_0.

3. Burst Shape of a Phased Chopper Velocity Selector

Fig. 2 is a schematic diagram of the phased chopper velocity selector[5]) now in use at the MTR[6]). Chopper A chops the neutron beam into bursts of polychromatic neutrons that spread out in time, due to the wide range of velocities of the neutrons, as they travel to chopper B. Chopper B, which spins at exactly the same angular velocity as A and is accurately phased with it, passes only those neutrons that arrive at chopper B in one small time and velocity interval. Thus, the machine acts as a velocity selector, delivering short bursts of monochromatic neutrons.

The MTR neutron velocity selector is designed for scattering experiments[6]). The time for the neutrons to travel from a scattering sample placed 0.5 m distant from chopper B to a detector 2 m from the sample is recorded. A change in energy during scattering can thus be detected. Fig. 2 shows the case where a detector has been placed in the beam 2.5 m from chopper B to correspond in distance to the detector used in the scattering experiment.

IBM-650 programs were written to calculate the transmission probabilities and burst shapes of neutrons passing through such a velocity selector. Since the time t refers to each chopper, a time scale T is selected to relate the angular position of one chopper to the angular position of the second chopper and to determine the time that the neutrons arrive at any point along the beam path. Chopper A starts each timing cycle. Defining time $T = 0$ as the time that the y' coordinate of chopper A is parallel to the laboratory coordinate y, and defining the phase time Δ as the time T at which the y' coordinate of chopper B is parallel to y, the probability and burst shape at any point along the beam is then a function of T. The angular phase difference in degrees is $\omega\Delta 360°/2\pi$. The position of observation along the beam is determined by $D + G$ where D is the distance between choppers and G is the distance from chopper B to the detector. Thus, the position of the detector, which can be moved to any point along the beam path, is the position of the observation. All distances are measured from the centers of the choppers.

In the IBM-650 programs $P(v,t)$ is determined for a single chopper by the calculation of y_u* for a series of x's between $-R$ and $+R$ followed by the selection of the minimum value. Similarly, the maximum value of y_l* is obtained. From

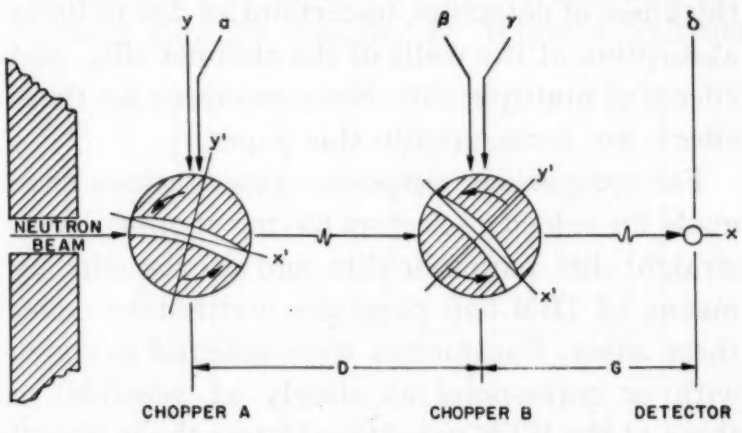

Fig. 2. Phased chopper velocity selector.

these, the probability for velocity v at a given time t can be obtained from eq. (5). The probabilities for neutrons to reach any point along the beam at time T are $P_A(v,t) = P_A(v,t - D/v - G/v)$ and $P_B(v,t) = P_B(v,T - \Delta - G/v)$, where P_A relates to chopper A and P_B to chopper B. P_B is unity for G negative; P_A is unity for D negative Also Δ is greater than or equal to zero so that the phase time is always measured in a positive sense. The probability that a neutron will pass through both choppers is the product of probabilities for the two choppers. The final products are

$$\theta(v,T) = f(v)\, P_A(v,T - D/v - G/v)\, P_B(v,T - \Delta - G/v) \quad (6)$$

and

$$\phi(T) = \int_0^\infty f(v)\, P_A(v,T - D/v - G/v)\, P_B(v,T - \Delta - G/v)\, dv \quad (7)$$

where $f(v)$ is the flux distribution in the incident beam. The quantity $\theta(v,T)$ is the probability, both velocity and time dependent, that a neutron will reach a certain position $G + D$ along the beam of the velocity selector, while $\phi(T)$,

[5]) P. A. Egelstaff, Private Communication; and R. F. Dyer, "Colloquium on Neutron Diffraction and Scattering", AERE M/R-2857 (1958).

[6]) R. M. Brugger, R. E. Schmunk, L. W. McClellan and J. E. Evans, Bul. Am. Phys. Soc. II, **4** (1959) 32.

which is only time dependent, is the quantity actually measured in an experiment, that is, the burst shape in time.

The procedure developed above permits the calculation, at any desired observation point, of the burst shape of neutrons passing through a phased chopper neutron velocity selector. For comparison of the results with experimental data, consideration must be given to the effects of angular divergence of the beam, phase uncertainty, flight path uncertainty due to finite thickness of detectors, uncertainties due to finite absorption of the walls of the chopper slits, and effects of multiple slits. No corrections for these effects are considered in this paper.

For comparison purposes, computations were made for velocity selectors having choppers with straight slits, parabolic slits, and circular slits, by means of IBM-650 programs written to cover these cases. Parameters were selected to agree with or correspond as closely as possible to those of the MTR velocity selector: the radius of the choppers R is 5.08 cm, the slit width of the choppers h is 0.08128 cm, the distance between choppers D is 0 or 2.00 m, the distance from chopper B to detector G is 0 or 2.50 m, the constant n in the Maxwellian distribution is 1.0 neutron/cm^3, and the most probable velocity v_0 of the Maxwellian distribution for a temperature 30.3° C is 2278 m/sec. Since neutron choppers and velocity selectors most often utilize the flux from a thermal reactor as the initial source of neutrons, a Maxwellian flux distribution $(4n/\sqrt{\pi})\ (v^3/v_0^3)\ \exp\ (-v^2/v_0^2)\ dv$ was selected for $f(v)$. The most probable velocity v_0 of the flux from the MTR was used and in all cases n is equal to one neutron/cm^3. This sets the initial flux in the parallel beam to be 2.58×10^5 neutrons/cm^2 sec. To obtain expected intensities from the burst shapes shown in the following figures, the ordinate must be multiplied by the number of bursts per second. To compare these calculated intensities with experimentally obtained ones, it should be remembered that reactor fluxes are quoted for isotropic angular distributions and corrections need to be made for the $1/r^2$ effect.

On several trial passes of the program through the IBM-650 machine, it was found that about twenty steps of x between $-R$ and $+R$ were sufficient; additional steps altered the curve only slightly. The velocity steps and time steps were adjusted for each case. Fig. 7 gives an idea of the number of velocity steps required.

4. Computed Probabilities and Burst Shapes

To better understand the effects of the chopping of the beam by the velocity selector as neutrons pass from chopper A to the detector, the curves shown in fig. 3 through 7 were computed. For illustration, the circular slit

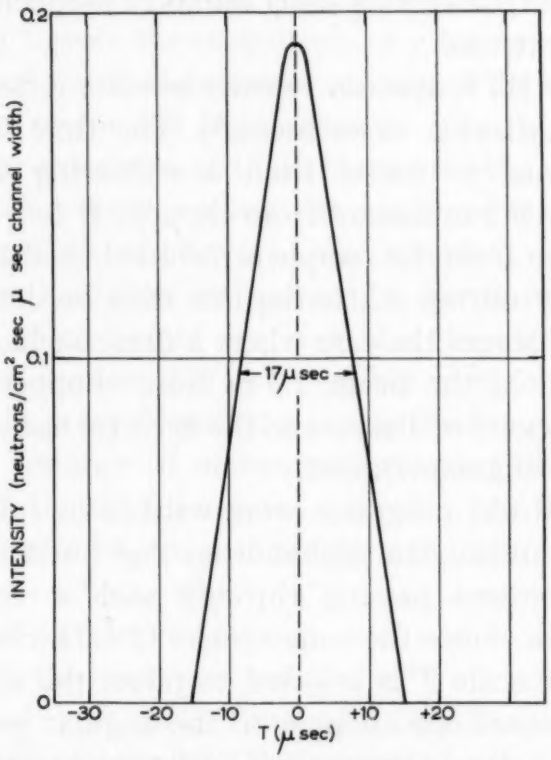

Fig. 3. Burst shape at position α immediately after neutrons are chopped by chopper A.

chopper having a radius of curvature of 211.6 cm was selected. The choppers' angular velocity was 523.6 radians/sec (5000 rpm), which gives maximum transmission for neutrons having a velocity of 2215.6 m/sec. Fig. 3 shows the burst shape $\phi(T)$ immediately after the neutrons have been chopped by chopper A. Since the program considers that the chopping occurs at the center of the choppers, the observation of these neutrons is at position α (see fig. 2) at the center of chopper A. The burst shape is almost a triangle and the base of the triangle is the time required for the periphery of the chopper to move the

width of the slit. The burst is centered at a time that corresponds to that when the circular slit is symmetrical about the y axis. Neutrons having a wide range of velocities are contained within this triangle. The total number of neutrons contained in this burst is much smaller than the initial flux of 2.58×10^5 neutrons/cm² sec because the burst intensity represents one burst per sec.

Fig. 4 shows the burst shape for conditions identical to those of fig. 3 except that the position of observation is at β just before the neutrons are chopped by chopper B. (In this figure the integration is over velocity for each time T: if $\theta(v,T)$ is integrated over all time T for a given velocity, and this result is compared to an unmodified Maxwellian distribution, trans-

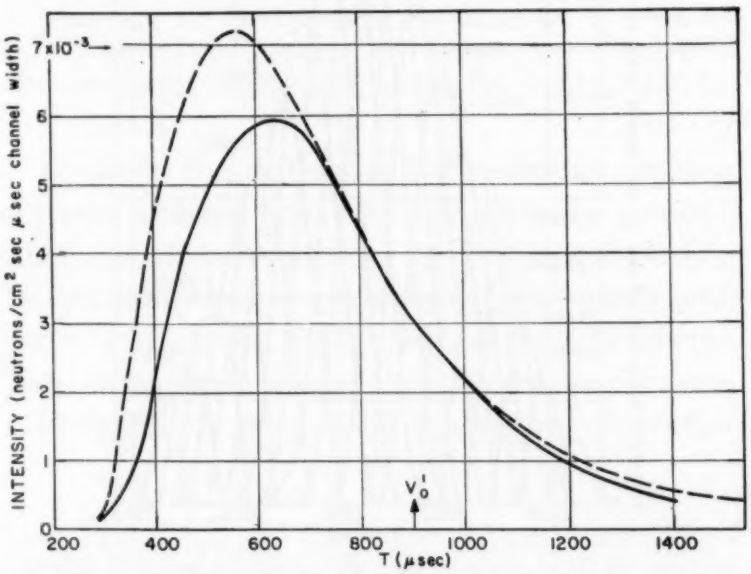

Fig. 4. Neutron distribution (solid line) at position β immediately before neutrons are chopped by chopper B. A Maxwellian distribution (dashed line) that is normalized to the solid curve at 903 μsec is shown for comparison.

mission functions similar to those shown by Stone and Slovacek[1]) are obtained.) The neutrons have spread out in time, the faster ones in the Maxwellian arriving sooner than the slower ones. The shape of the Maxwellian has been modified to some extent by the transmission properties of the curved slit, the transmission at short and long times being suppressed compared to the transmission at $T = 903$ μsec ($v = 2215.6$ m/sec). The integral over time of this curve is the same as the integral of fig. 3.

Fig. 5 shows the burst shape at position γ immediately after the neutrons are chopped by chopper B. The phase time Δ was set at 700 μsec, which allows neutrons near a velocity of 2858 m/sec to pass. Again the burst shape is almost triangular with a half width of 17 μsec and a base width of 31 μsec. This chopper selects a small velocity interval and the total integrated number of neutrons has decreased accordingly.

Fig. 6 is the burst shape at position δ at the detector. The burst, no longer a triangle, has broadened due to the velocity components that passed through chopper B. While a Gaussian

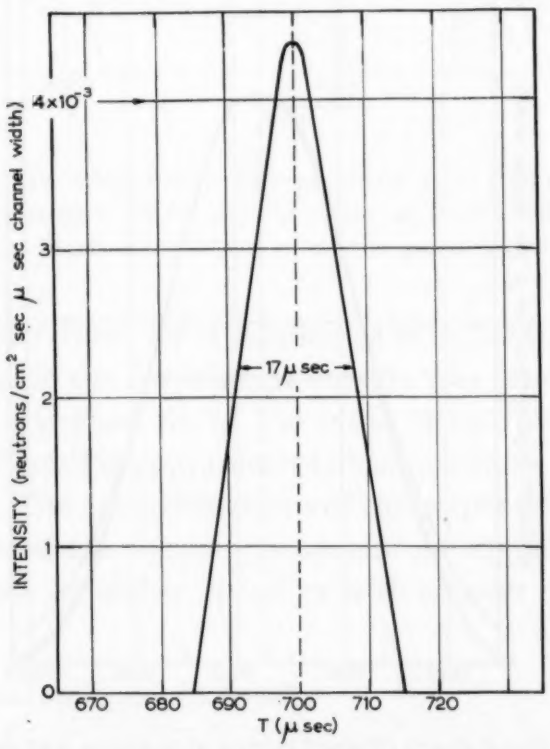

Fig. 5. Burst shape at position γ immediately after neutrons are chopped by chopper B.

with its width at half maximum equal to the half width of the burst shape is a good fit to the shape near the center of the burst, it overestimates the wings. For this particular case, the function

$$f(t) = N_0 \sin^2(\pi t/2\tau)/(\pi t/2\tau)^2 \qquad (8)$$

gives a very good fit. The quantity N_0 is the peak height and τ is the full width at $0.405\,N_0$. Because the initial flux has a Maxwellian distribution, the burst shape is not exactly symmetrical about the time corresponding to the phase setting. The integral of fig. 6 is equal to the integral of fig. 5.

Fig. 7 shows the probabilities $\theta(v,T)$ corresponding to the burst shape $\phi(T)$ of fig. 6 and shows the contributions of the different velocity intervals. Each velocity function has a shape similar to the burst shape directly after chopper B, but the half width is less than 17 μsec. These velocity components add to give the burst shape shown in fig. 6.

Fig. 8 shows a composite of several burst shapes like those of fig. 6 except the phase time Δ is different for each curve. It is seen that the intensity changes rapidly with phase time due

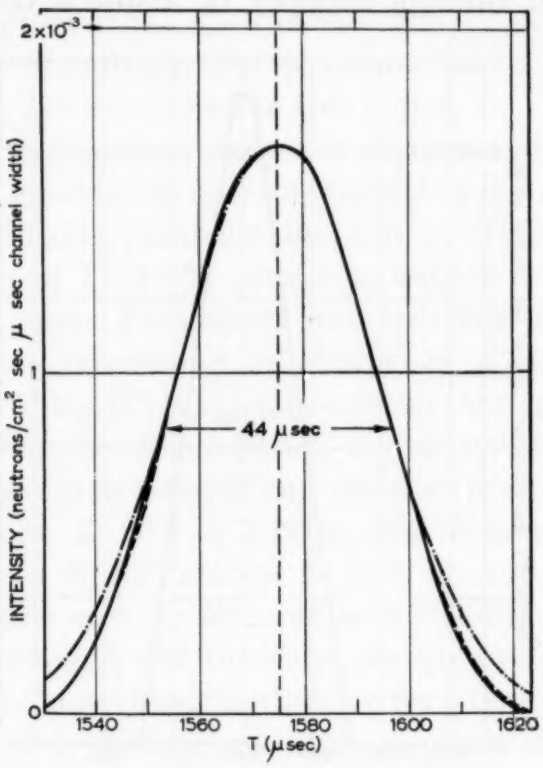

Fig. 6. Burst shape (dashed curve) at position δ at detector. The solid curve is fit of eq. (8) and the dot-dashed curve is a Gaussian distribution.

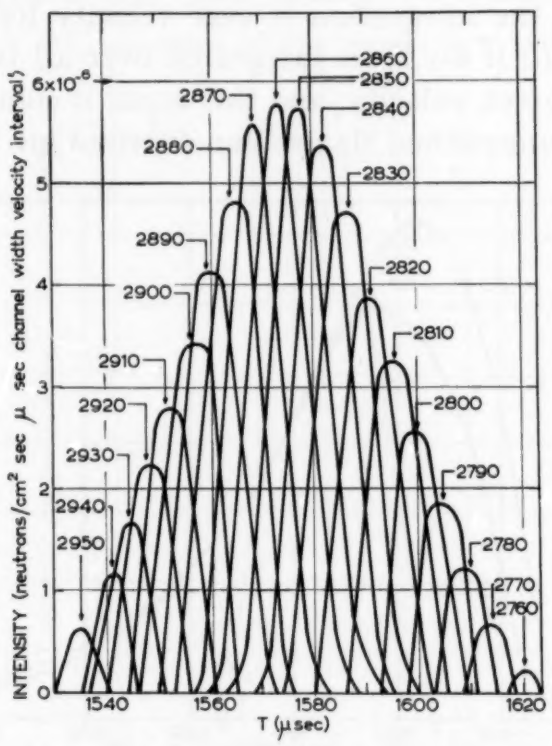

Fig. 7. The probability $\theta(v,T)$ corresponding to fig. 6. Numbers designating individual curves are velocities in m/sec.

both to the Maxwellian flux distribution and the transmission probabilities of the choppers. The program treating parabolic instead of circular slits with $v''_0 = 2\omega\rho$ (where ω and ρ are the same as those used to determine the curves of fig. 3 through 7) gives results that agree with the circular slit case of fig. 8 to better than 0.5%. The constant defining the eccentricity of the parabolic slit[4]) is v''_0/ω where v''_0 is the neutron velocity for maximum transmission.

Also in fig. 8 is shown a composite similar to that for the circular slit case for a velocity selector having straight slit choppers operating at 5000 rpm. The suppression of slower neutrons in this case is very pronounced, and it is evident that curved slits are necessary when slower neutrons are desired. With a straight slit chopper, two bursts per revolution are passed as compared with one burst per revolution for a curved slit chopper. Thus, for maximum intensities at these operating conditions, it is desirable to use the straight slit chopper for neutrons with velocities greater than 4000 m/sec ($\Delta = 500$ μsec) and the circular slit choppers for neutrons below this velocity. Also, it can be seen that the burst shape at the extremes is not symmetrical, this asymmetry being due both to the Maxwellian neutron spectrum and the transmission of the choppers. Table 1 lists some of the changes due to these modifications of the burst shape. The table shows that in some cases there is a difference between the time predicted by the phase time and the time at which the peak of the burst actually appears. For the straight slit this difference appears only at short times. The full width at half maximum is also affected by the Maxwellian flux distribution and the transmission of the choppers. For the circular case

these widths are less at extreme times and also are slightly narrowed at intermediate times. The straight slit burst shape becomes continuously narrower and more distorted at longer times.

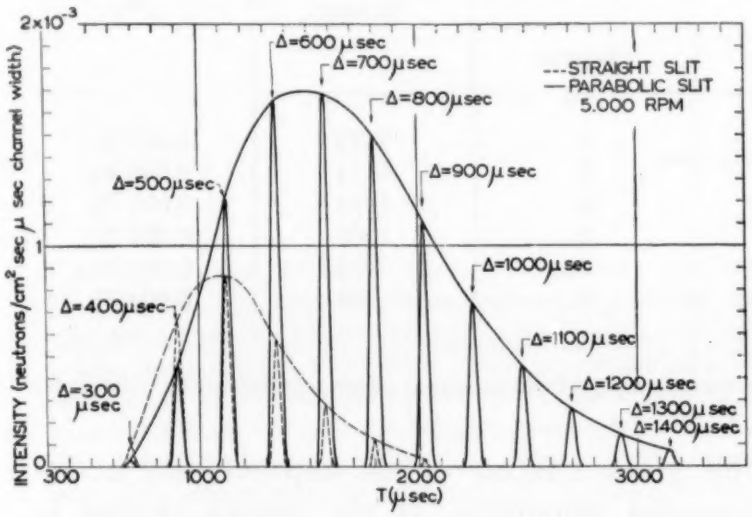

Fig. 8

A composite of burst shapes for parabolic or circular ($\rho = 211.6$ cm) and the straight slit cases at $f = 5000$ rpm. The envelopes were drawn to tie the peaks together.

burst shapes for the two cases are noticeably different, the circular slit case giving higher intensities at the lower velocity end. The total velocity range that can be covered by changing the phase

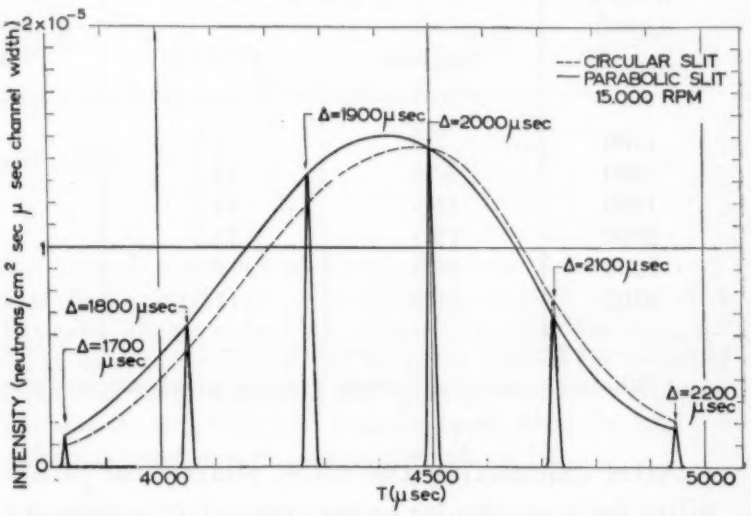

Fig. 9

A composite of burst shapes for parabolic ($v_0'' = 1007$ m/sec) and circular ($\rho = 32.05$ cm) slit cases at $f = 15\,000$ rpm. The envelopes were drawn to tie the peaks together.

To show the difference between the circular slit case and the parabolic slit case, the composite burst shapes shown in fig. 9 were computed. In this computation the frequency is 15 000 rpm and $v''_0 = 2\omega\rho = 1007$ m/sec, or ρ is 32.05 cm. This corresponds to operating conditions for cold neutrons with very good resolution. Now the is smaller than for a similar case at 5000 rpm. Here again the function of eq. (8) was found to be a very good fit to the burst shape. Table 2 gives some of the parameters obtained from these curves. The approximations of this paper will not be valid if the present treatment is applied to choppers at higher speed or with smaller ρ.

TABLE 1

Parameters of burst shapes of fig. 8 for choppers spinning at 5000 RPM

Phase time Δ (μsec)	Full width at half-height of burst shape (μsec)		ΔT (μsec)†		Velocity at peak (m/sec)		Energy at peak (eV)	
	Circular	Straight	Circular	Straight	Circular	Straight	Circular	Straight
300	35	42	+ 6.0	+ 6.0	6607	6607	0.228 182	0.228 182
400	39	42	+ 2.0	+ 2.0	4988	4988	0.130 055	0.130 055
500	43	39	+ 1.0	0	3996	4000	0.083 485	0.083 486
600	44	35	0	— 1.0	3333	3335	0.058 069	0.058 166
700	44	31	0	— 1.0	2857	2858	0.042 667	0.042 726
800	41	22	0	0	2500	2500	0.032 670	0.032 670
900	41		0		2216		0.025 670	
1000	41		— 1.0		2000		0.020 926	
1100	43		— 1.0		1818		0.017 294	
1200	44		— 1.0		1667		0.014 529	
1300	42		— 1.0		1538		0.012 379	
1400	40		— 2.0		1429		0.010 680	

† Where $T - T_0 = \Delta T$ when T is time at which peak actually occurs and T_0 is time at which phase predicts peak will occur.

TABLE 2
Parameters of burst shapes of fig. 9 for choppers spinning at 15 000 RPM

Phase time Δ (μsec)	Full width at half-height of burst shape (μsec)		ΔT (μsec)†		Velocity (m/sec)	Energy (eV)
	Parabolic	Circular	Parabolic	Circular		
1700	7.5	6.5	0	0	1176	0.007 23
1800	12.5	11.5	0	0	1111	0.006 45
1900	14.5	14.0	0	0	1052	0.005 79
2000	13.5	13.5	0	0	1000	0.005 22
2100	14.5	14.5	0	0	952	0.004 74
2200	11.5	11.5	0	0	909	0.004 31

† Where $T - T_0 = \Delta T$ when T is time at which peak actually occurs and T_0 is time at which phase predicts peak will occur.

After calculating the burst shape and probability for a particular experimental arrangement, it is possible to predict the instrument resolution broadening. As an example consider a scattering experiment. If the energy of the scattered neutrons is only slightly changed from the incident energy due to interaction with the sample, the resolution broadening due to the velocity selector is the full width at half height of the burst shape divided by the time for the neutrons to travel from the sample to the detectors. When the velocity selector has circular slit choppers spinning at 5000 rpm and the phase time is 700 μsec, the resolution broadening is $\Delta t/t = 6.3\%$. Since $\Delta t/t = \Delta\lambda/\lambda = 2\Delta E/E$, the uncertainty in the wave length λ is 6.3% and the uncertainty in energy is 12.6%. To improve this resolution the angular velocity can be increased, the distance between the sample and detectors can be increased, or the effect can be observed with colder neutrons. For example, if the angular velocity is increased to 15 000 rpm and the effect can be observed with cold neutrons, the phase time is $\Delta = 2000$ μsec and $\Delta t/t$ is 0.7%. This gives a factor of ten improvement in instrument resolution. If the energy change is large, a more extensive evaluation of the time and velocity components contributing to the probability $\theta(v,T)$ will yield the instrument resolution.

The curves presented in this paper show that the program is very useful in predicting the operating characteristic of the MTR phased chopper velocity selector. These results indicate that small changes occur in the burst widths and in $T - T_0$ that affect the settings of the experimental parameters. Also, eq. (8) is useful for resolution broadening theoretical data before comparing with experimental data. The results verify that a circular slit chopper can be used in place of the more exact parabolic slit chopper with only minor distortions in the operating ranges of interest.

Acknowledgements

The authors would like to acknowledge helpful discussions with Dr. P. D. Randolph and the computational help of Mrs. Carolyn Slayden.

NUCLEAR INSTRUMENTS AND METHODS 8 (1960) 211–216; NORTH-HOLLAND PUBLISHING CO.

HIGH-EFFICIENCY, LONG-LIVED VACUUM COLD TRAP

J. W. BUTLER

Nucleonics Division, United States Naval Research Laboratory, Washington, D.C.

Received 6 April 1960

The construction and performance of a vacuum cold trap for pump oil, "O"-ring, and other vapors are described. The trap has a capacity of 16 liters of liquid nitrogen, and lasts 5 days on one filling when clean. After a period of about 6 months to 1 year of continuous use, the lifetime has dropped to about 3 days. The trap has high pumping speed, and very high trapping efficiency, requiring a minimum of 3 successive cold-surface collisions for a molecule migrating through the trap. The principles of design include the use of very thin re-entrant tubes for mechanical support of the cold reservoir thus minimizing conduction heat transfer, an inner tube for pumping and trapping, shields for reducing radiation heat transfer, and gold-plating for opposing surfaces having different temperatures. Mercury and oil diffusion pump systems are compared.

1. Introduction

Since the liquids used in vacuum diffusion pumps have quite appreciable vapor pressures at room temperatures, the use of these pumps creates a problem of contamination of the vacuum system with the condensed vapor of the pump fluid, oil or mercury. For nuclear reaction particle accelerators, carbon is a particular nuisance because of its high cross sections for the (d,n), (d,p), (He^3,n), (He^3,p), and (He^3,α) reactions and, to some extent, the (p,γ) reaction. In the deuteron and He^3 induced reactions, some of the particle groups lead to excited states in the residual nuclei and hence to intense gamma radiation from the decay of these states. Thus carbon contamination, which is a result of oil vapor condensing on the target and being cracked by the accelerator beam, leads to background particle groups and gamma rays. Furthermore, an appreciable film of contaminant can displace the energy of a reaction resonance or neutron threshold.

Mercury does not lead to appreciable nuclear reaction yields at bombarding energies below 4 MeV (except for coulomb-excited states), but has many disadvantages (discussed below) as a vacuum system contaminant. Similarly, arguments could be made concerning oil and mercury contamination of vacuum systems used for entirely different purposes than for acceleration of charged particles, such as evaporated-target preparation systems, film depositing systems, etc. The problem is therefore to insert some type of vapor trap between the pumps and the vacuum system.

One of the most useful types of such vapor traps is a cold surface, which might be kept cold either by a recycling refrigerant, solid carbon dioxide, or liquid nitrogen. In the past, many different approaches have been used, each possessing certain advantages and disadvantages with respect to the others. In recent years, several aspects of the problem have been discussed by several authors[1]), but within the present author's knowledge, there does not exist a generally satisfactory trap design combining the features of long life, high pumping speed, and high trapping efficiency, except the one described herein. The philosophy of the present design was to obtain as high a degree of the above characteristics as feasible in an a priori manner without the investment of large amounts of time and money in an exhaustive experimental study. The trap built from this

[1]) See, for example, J. R. Ullman, Transactions, Fourth National Symposium on Vacuum Technique (1957);
N. Milleron, Transactions, Fifth National Symposium on Vacuum Technique (1958);
G. H. Miller, Rev. Sci. Instr. **24** (1953) 549; and others.

design has performed in a highly satisfactory manner for over six years. Thus, the present ideas are considered to be more of a contribution to the art of cold-trap design than to the theory.

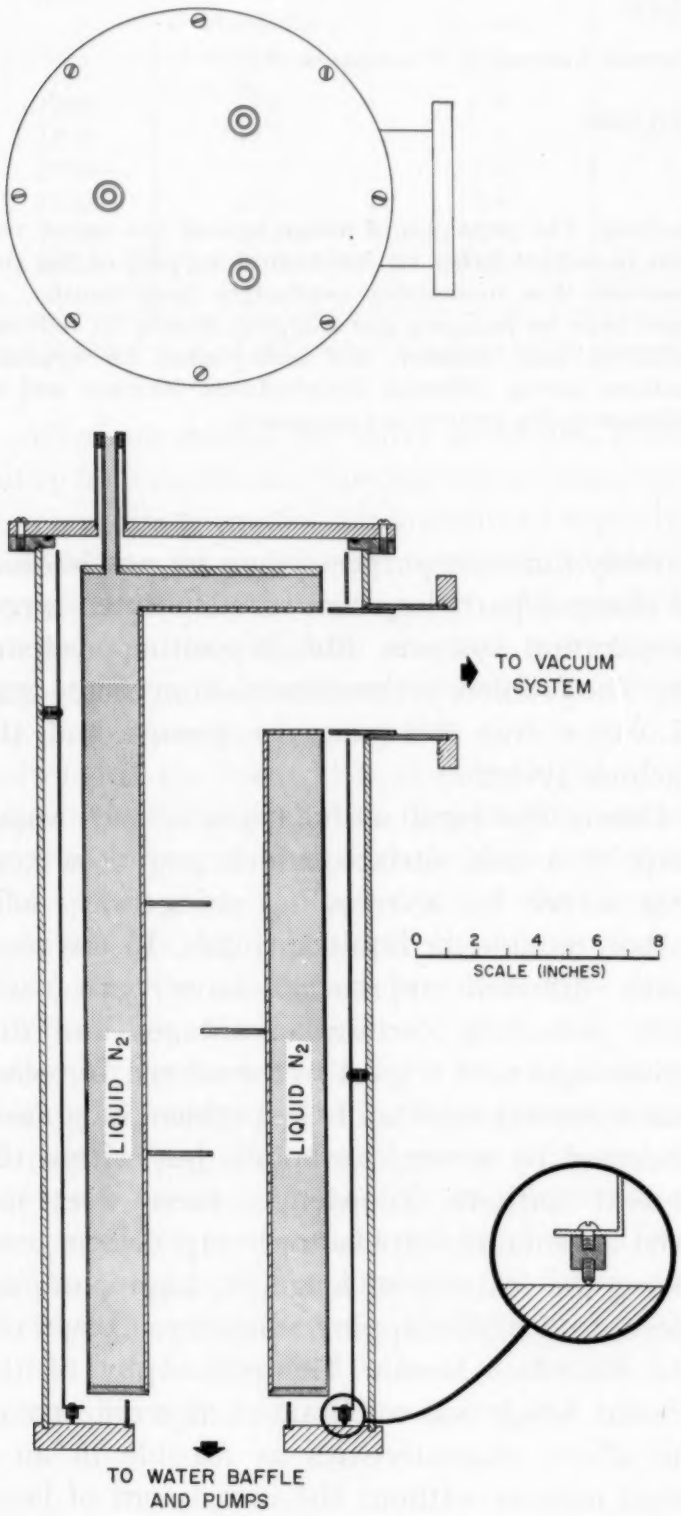

Fig. 1. Cross-section drawing of the cold trap. The shield is supported by two thin sharpened stainless steel screws and porcelain stand-off bushings. The upper two supports are approximately in the middle of the vertical dimension and are included in the drawing even though they are actually in the plane perpendicular to the plane of the drawing. For most vacuum systems, the three approximately semi-circular baffles in the pumping tube are not necessary.

Visiting physicists who have seen the installation described herein have expressed a keen interest in its design and operation. It is therefore felt that a wider dissemination of this information is desirable, and that is the goal of this paper.

2. Description of the Trap

The trap is shown in cross-section form in fig. 1. The outer can is the vacuum retaining wall. The lower flange rests on top of a water baffle, which is in turn on top of a diffusion pump. The inner can, which contains the liquid nitrogen, is supported by three thin stainless-steel tubes (0.006-in. wall) from the top flange. There are no supports on the sides or bottom. Thus the only thermal-conduction path (for practical purposes) between the liquid nitrogen and the outside container is through these thin tubes. Inconel would be slightly better from a thermal conductivity point of view, but the difference between Inconel and stainless steel is quite small. (Other vacuum cold traps which have been built at this Laboratory, smaller than the one described herein, do employ Inconel tubes.)

The tubes are re-entrant at the top in order to increase the length of heat-conduction path from "ground". These protrusions are normally covered by inverted beakers (large enough not to touch anything except the main top flange) in order to minimize heat transfer from the air, and to prevent frosting at the top of the tubes.

The thermal conductivity of a static gas (nitrogen) at atmospheric pressure in the tubes is comparable with the conductivity in the metal tubes. The emanating vapor or gas, however, requires the heat to flow "upstream" against the normal gas flow, thus reducing heat transfer due to this heat path. Moreover, since the cold nitrogen vapor inside the tubes is denser than the outside air, there is essentially no convection heat transfer through this path.

The thermal conductivity of the gas in the vacuum region is considered negligible. Radiation heat transfer between the surface of the liquid-nitrogen reservoir and the outer wall is not negligible, however, and actually constitutes

the major source of heat transfer. Several steps have therefore been taken to minimize this radiation heat transfer.

The trapping action of the system has been limited to the interior surfaces instead of the outer surfaces of the cold reservoir as used in conventional types of cold traps. That is, the pumping action through the trap is through the innermost tube, which is completely surrounded by liquid nitrogen. Thus the trapped foreign matter which coats these surface does not materially affect the radiation heat transfer to the trapping surface, because this "dirty" surface "sees" another surface at the same temperature, thus involving no heat transfer. Trapping action on the outside of the liquid-nitrogen reservoir is minimized by cylindrical baffle inserts (made of glass) at the input and output ends. These baffle inserts do not completely close off access to the outside surfaces, of course, because first, they must not touch the cold surface and thus complete a heat-conduction path to the outside, and second, it is necessary to pump out the region between the outer wall and the liquid-nitrogen can. It might be noted, however, that molecules may not migrate to this region without first striking a cold surface at least once. These baffles also serve as surface barriers in the prevention of the surface creep of the pump fluid.

A slightly modified version of this cold trap, utilizing re-entrant baffling to protect more nearly completely the outer surfaces of the liquid-nitrogen can, has been built for another vacuum system, but this re-entrant baffling appreciably increases radiation heat transfer and construction expense. Therefore, it is believed that for most fairly clean vacuum systems, the simple non-re-entrant baffle inserts are satisfactory.

In order to minimize the radiation heat transfer between the inner (0.006-in.) stainless-steel support tubes and the outer support tubes of the re-entrant sections, these adjacent areas were mechanically buffed†.

The outer wall of the liquid-nitrogen reservoir is made of 0.016-in. stainless steel so that the radiation heat transfer drops somewhat at the lower levels of reserve liquid nitrogen. Under operating conditions, this cylinder is required to stand tensile stress only (inside pressure), so the thinness of the wall is no disadvantage. Moreover, another advantage of the thin wall is the low heat capacity; not much liquid nitrogen is required to cool it from room temperature to liquid-nitrogen temperature.

The innermost tube, however, should remain at the lowest possible temperature regardless of level of reserve liquid nitrogen, because if its temperature rises, trapped vapors will begin to migrate again, and the sticking probability for new molecules striking the surface will decrease. Furthermore, the region where the warming-up would occur (the top) is adjacent to the vacuum system one wishes to protect. Therefore, the innermost tube is made of heavier material, 0.125-in. stainless steel. A simple calculation indicates that less than 2% of the total temperature difference between the liquid nitrogen and the room occurs along the trapping tube, even if the liquid-nitrogen level drops to one inch. The same type metal is used for all parts of the cold reservoir to avoid differential thermal expansion and contraction at the welded junctions. An independent reason for using thicker material for the innermost tube is that this wall has the pressure on the outside, and a very thin wall might therefore collapse. The ends of the can are of thicker ($\frac{1}{4}$-in.) stainless steel because flat surfaces are under greater strain with pressure differentials than curved surfaces.

A radiation shield has been inserted between the two walls to reduce the radiation heat transfer. This radiation shield is made from 0.016-in. stainless-steel sheet, and is supported at the bottom by two thin stainless-steel screws, thermally insulated by porcelain stand-off bushings, and sharpened at the points of contact. Two further supports are near the

† For smaller traps, where mechanical buffing is not feasible, a chemical polishing method, developed by Dr. C. R. Gossett, may be used. This method, utilizing a solution of aqua regia in the inaccessible regions, leaves a bright satin-like finish on the stainless steel.

middle of the vertical dimension and are in the vertical plane perpendicular to the vertical plane containing the other two support points. These supports (shown in fig. 1 in the same plane as the other two support points in order that they be included in the drawing) are from the shield to the outer wall, and consist of screws and porcelain stand-off bushings. Thus the shield is fairly well thermally insulated, and assumes some intermediate temperature between the inner and outer cans, thus reducing the heat transfer to the inner can.

Other shields could be used to decrease further the radiation heat transfer. For example, a second coaxial shield was designed to fit between the inner can and the first shield, but it is not normally used in the installation described here. It could be supported either by the inner can or the first shield. Top and bottom shields could also be used, but their effect is rather small because of the relatively small areas involved. The supports for the shield could also be re-entrant to decrease further the conduction heat transfer from ground.

All appropriate surfaces are plated with gold to reduce heat transfer. These surfaces are the inside of the outer can and flanges, both surfaces of the shield, and the outside of the inner can. The gold was applied using a very inexpensive "paint-on" process and a silica binder†. The binder was removed by baking the parts in an oven, leaving the gold residue which was a reasonably good quality gold plate. It is not easy, however, to achieve a successful plating. It is necessary to have the surface extremely clean before application of the gold mixture.

The innermost tube (pumping tube) was made 4 inches in diameter to provide a high pumping speed. The use of the elbow bend requires a minimum of one cold-surface collision before a molecule can migrate through the trap. (It is assumed that no gas-to-gas collisions occur. At typical cold-trap pressures of a few times 10^{-7} tor, this is a reasonable assumption.) The insertion of the approximately semi-circular baffles raises the minimum number of collisions with the cold surfaces to three successive cold-surface collisions. The baffles are slightly larger than half the pumping-tube cross-sectional area in order to eliminate the possibility of a molecule just barely grazing by all of them. The baffles decrease the pumping speed by about 20%.

For most organic pump oil molecules, the sticking probability is quite high, so for most applications, the baffles shown in the pumping tube are not necessary. (Furthermore, the average number of collisions with a cold surface would be much higher than one, even without the baffles, since one is the minimum.) Most commercially available cold traps do not require even one cold-surface collision for a molecule to migrate through.

3. Experience with the Trap

The trap described has been in continuous use on the 2-MV Van de Graaff Accelerator of the Nucleonics Division at the Naval Research Laboratory since its installation in June, 1953. It is used with a water baffle, an oil diffusion pump of a nominal 500-liter/sec pumping speed, a 100-liter/sec booster pump and a 5-liter/sec forepump. The normal period between cleanings is 6 months to 1 year. When the trap is freshly cleaned, its lifetime is 5 days on one filling of liquid nitrogen. (Since the capacity is 16 liters, the evaporation rate averages slightly over 3 liters per day.) At the end of about a year's continuous use, the lifetime drops to about 3 days, or about 5 liters evaporated per day. Thus, it will normally last over even a long, holiday week end without the necessity of refilling. And no foretrap is necessary.

It is believed that the amount of oil from the diffusion pumps migrating through the cold trap is completely undetectable. When the trap is removed for cleaning, there is always an

† The material used for the gold coating was called "Liquid Bright Gold". The total cost of the plating, including labor, was about $ 50. After this work was done, other materials, using an electroless process, have appeared on the market and our new cold traps are plated with one of them. A good silver plating would also serve as a good reflector (and therefore poor radiator) of infra-red radiation, but would be much more expensive than the processes mentioned above for gold plating.

accumulation of pump oil on the bottom surface of the inner can, and some on the bottom of the two lower baffles. But there is none in the upper part of the vertical pumping tube or on the "ceiling" above the vertical pumping tube. There is also a sizable accumulation of a different type of oil at the end toward the Van de Graaff vacuum system, indicating the removal of appreciable amounts of oil from that system. This oil has a yellow hue and comes from the "○"-rings used with the flanges on the rest of the vacuum system. It is believed that the amount of pump oil migrating through the trap, even without the baffles, would be insignificant compared with the "○"-ring source of oil vapor.

The philosophy which led to the large size of the design can best be expressed in the form of a question. Why store the liquid nitrogen in a separate Dewar flask and therefore lose the liquid nitrogen by evaporation simultaneously in two different vessels when one vessel can perform both functions? Many laboratories solve the nighttime and week-end filling problems by the use of automatic filling systems operating from a supply of liquid nitrogen in a large commercial Dewar flask. Such systems are not only expensive and wasteful of liquid nitrogen, but they are sometimes unreliable. The philosophy in the current design has been therefore to use the same container for both storage and trapping. If no other uses are required for liquid nitrogen, the cold trap could be designed to have a capacity just equal to the size of a commercial Dewar delivery container multiplied by the transfer efficiency, which is fairly high, greater than 85%; and deliveries could be scheduled to coincide with filling needs. If minor, irregular uses occur for liquid nitrogen in other applications, the required amounts may be withdrawn from the trap with no particular difficulty, using a transfer tube similar to the one described below for transferring the liquid nitrogen from the delivery flask to the trap.

Since the present trap has a capacity of 16 liters of liquid nitrogen, a fifteen-liter delivery flask may be used to refill the trap with no wastage when the level of liquid nitrogen drops to the one-fifth mark. If a larger capacity trap is made, the horizontal dimension should be increased to tend to minimize the surface-to-volume ratio, and thus radiation heat transfer. The present trap was designed to fit into an existing vacuum system. Otherwise, the length would have been made somewhat shorter and the diameter somewhat larger in order to increase both pumping speed and lifetime.

Filling the cold trap is a very simple operation. The transfer device consists of a metal tube, long enough to reach to the bottom of the delivery Dewar flask, surrounded at the top by a rubber stopper, with another tube leading to a source of compressed nitrogen, and capable of supplying this pressure to the region outside the first tube, but inside the flask. Thus a pressure of about 10 psi (gage) is applied to the top surface of the liquid in the flask, forcing the liquid up through the metal tube, which has a rubber-tube extension leading through one of the three thin support tubes at the top of the trap. Constant vigilance is not required during the filling operation which takes about 10 minutes if the trap is warm at the start; only about 8 minutes are required if the trap is cold.

Although compressed air could be used for the filling operation, it is not so used at this Laboratory because of the possible hazards associated with the long operating periods of the trap. Since oxygen has a higher boiling point than nitrogen, the use of compressed air would contaminate the liquid nitrogen with oxygen, which would then distill differentially with respect to the nitrogen. That is, the oxygen would tend to accumulate as long as the trap remained cold, perhaps a year or longer. Thus, possible large concentrations of liquid oxygen could build up with possible explosive consequences.

The trap can be cleaned without disassembly, if one allows it to warm up, and torches the outer can; but this procedure is not normally used. The trap is usually disassembled for cleaning, with a small charge of liquid nitrogen still in it. The purpose of retaining the liquid

nitrogen during the disassembly is to keep the trapped material on the inner surfaces until they no longer are adjacent to the other surfaces of the trap, or vacuum system. Cleaning is normally done with standard laboratory cleaning solvents such as trichloroethylene, acetone, and ethyl alcohol.

When the trap is reassembled, it is pumped on a forevacuum (with a glass liquid-nitrogen-filled foretrap next to the forepump) for several hours before filling it. During this period, the outside can is heated to about 60° C by a hand torch. This procedure purges the inner surfaces (of the outer can) of the residue from the previous cleaning process, thus improving their reflectivity. The flanges on each end are not heated quite so much because of the "○"-ring gaskets. The low heat conductivity of the stainless-steel wall allows one to heat the wall quite close to these flanges without actually raising the flange temperature much.

For systems requiring extremely high vacua, metallic gaskets could be installed, and much higher baking-out temperatures could be used; or the system could be completely welded or soldered. Nuclear particle accelerators cannot achieve extremely high vacua because of the leak of ion source gas. Therefore the method described here is satisfactory for such systems.

4. Comparison of Oil and Mercury Systems

Since the use of the cold trap described herein obviates most of the disadvantages in the use of oil diffusion pumps, it is worthwhile to reassess the relative merits of oil diffusion pumps and mercury diffusion pumps. Some disadvantages of mercury pumps are listed, with comments significant to the present discussion.

1. Inability to pump heavy organic molecules, such as forepump oil. Since the mercury atoms (or molecules) are quite light compared with the heavy forepump oil molecules, the mercury pumps cannot prevent the migration of forepump oil through the system.

2. Extra trap required. The above situation necessitates the use of an additional trap, one between the forepump and diffusion pump to prevent this migration. This extra trap is also necessary to prevent the Hg vapor from migrating to the forepump and fouling it.

3. Inconvenience of foretraps. Since the gas pressures between the diffusion pump and forepump are quite high compared to those encountered by a high-vacuum trap, the rate of heat transfer is much higher with consequent shorter life. Thus, keeping foretraps filled over weekends is very inconvenient.

4. Inefficiency of foretraps. Because of the higher heat transfer encountered with foretraps, liquid nitrogen is seldom used. Instead, a combination of solid carbon dioxide and acetone is normally employed, with a consequent lower trapping efficiency. Thus the migration of forepump oil through the diffusion pump is still a possibility.

5. Health hazard. Mercury is a health hazard, especially in case of vacuum system accidents. Mercury is extremely difficult to remove from irregular surfaces because of its high surface tension.

6. Higher initial cost. Oil pumps are less expensive and smaller for equal pumping speeds.

7. Mercury amalgamation. Mercury dissolves many common metals used in vacuum systems. For example, it would not be possible to use gold or silver plating on a cold trap used for mercury. Also mercury dissolves silver solder and fouls ion gages.

8. Shorter cold trap life. In addition to precluding the use of high infra-red reflective coatings, such as silver and gold, on the surfaces of the trap, the mercury vapor which is trapped on the cold surfaces forms a high-heat-transfer "black-body" coating, thus increasing the liquid-nitrogen evaporation rate.

NUCLEAR INSTRUMENTS AND METHODS 8 (1960) 217–220; NORTH-HOLLAND PUBLISHING CO.

ENERGY DEGRADING-FOCUSING OF CYCLOTRON BEAM†

W. J. RAMLER, J. L. YNTEMA and M. OSELKA

Argonne National Laboratory, Argonne, Illinois

Received 24 May 1960

The ANL 60-inch cyclotron is a fixed 10.8 MeV/nucleon accelerator. To increase machine flexibility, it was desired to obtain variable energy projectiles 25—40 feet from the accelerator without severely reducing particle number and beam definition. Sacrificing energy resolution, a focused variable energy beam can be obtained by using the technique of a foil absorption system close coupled with strong focusing provided by quadrupole magnets. The system to be described can readily degrade a deuteron or alpha beam to about 2.5 MeV/nucleon with about 5% of the original particles focused a distance of 35 feet from the accelerator[1]).

1. Focusing and Degrading System

The data to be reported were obtained with the focusing system of fig. 1. Deuterons and alpha projectiles were used with 15% of the total deflected beam focused by the first quadrupole set into a 3 mm diameter concentration at the foil degrader. The beam leaving the acceleration chamber, unit 1, is astigmatic with a total horizontal and vertical divergence of 2° and 0.2°, respectively. Without activating the squeeze coil, unit 3, the cross section of the beam at the entrance to the first quadrupole set, units 5 and 6, is $\frac{1}{2} \times 2$ inches. The inside diameter of the evacuated beam tube is 2 inches and to conserve beam, the lens system first focuses the 2 inch beam dimension. The data to be reported were obtained without the use of the squeeze coil.

Positioning of the focused beam upon the foil degrader to compensate for slight shifts introduced by the machine from day to day is accomplished by unit 7, the first vertical and horizontal deflection magnet[2]). This magnet is an iron core cylinder 12 inches in length, with an I.D. of about 2 inches. Within the inner volume a uniform field whose vector direction (0–360°) and magnitude can be varied to effect beam position.

For the data obtained, the switching coil, unit 8, was not used and the particles were focused on the 0° trajectory. The foil degrader, unit 11, consists of two circular discs, remotely controlled and extensively water cooled. Each disc is independently controlled, and contains 9 apertures to provide a total of 81 absorber steps from 0 to 400 mg/cm² of aluminum. The disc aperture or foil size is one inch with a spacing of 1.5 inches between the foils of the two discs.

The degrader is closed coupled to the second quadrupole set, units 12 and 13, with a distance of $14\frac{1}{2}$ inches between centers of the degrader and unit 12. These quadrupoles function as a 2 inch diameter collecting lens for the degraded and scattered projectiles. Focus currents are adjusted to obtain slightly convergent particle trajectories into the third lens set, units 15 and 16. The dimensions of these units were chosen to be compatible with the required focal lengths and available power supplies.

The third lens set, units 15 and 16, focuses the beam into the experimental tunnel, a distance of 35 feet or more from the cyclotron. The fourth quadrupole set permits beam focusing for distances greater than 35 feet from the cyclotron.

2. Degraded-Focused Beam Currents

Using the described system, deuteron and alpha beams were degraded from 10.8 to about

† Based on work performed under the auspices of the U. S. Atomic Energy Commission.

[1]) W. J. Ramler, Nuclear Science Series Report No. 26, Sector-Focused Cyclotron, p. 266–269.

[2]) R. Benaroya and W. J. Ramler, Unpublished.

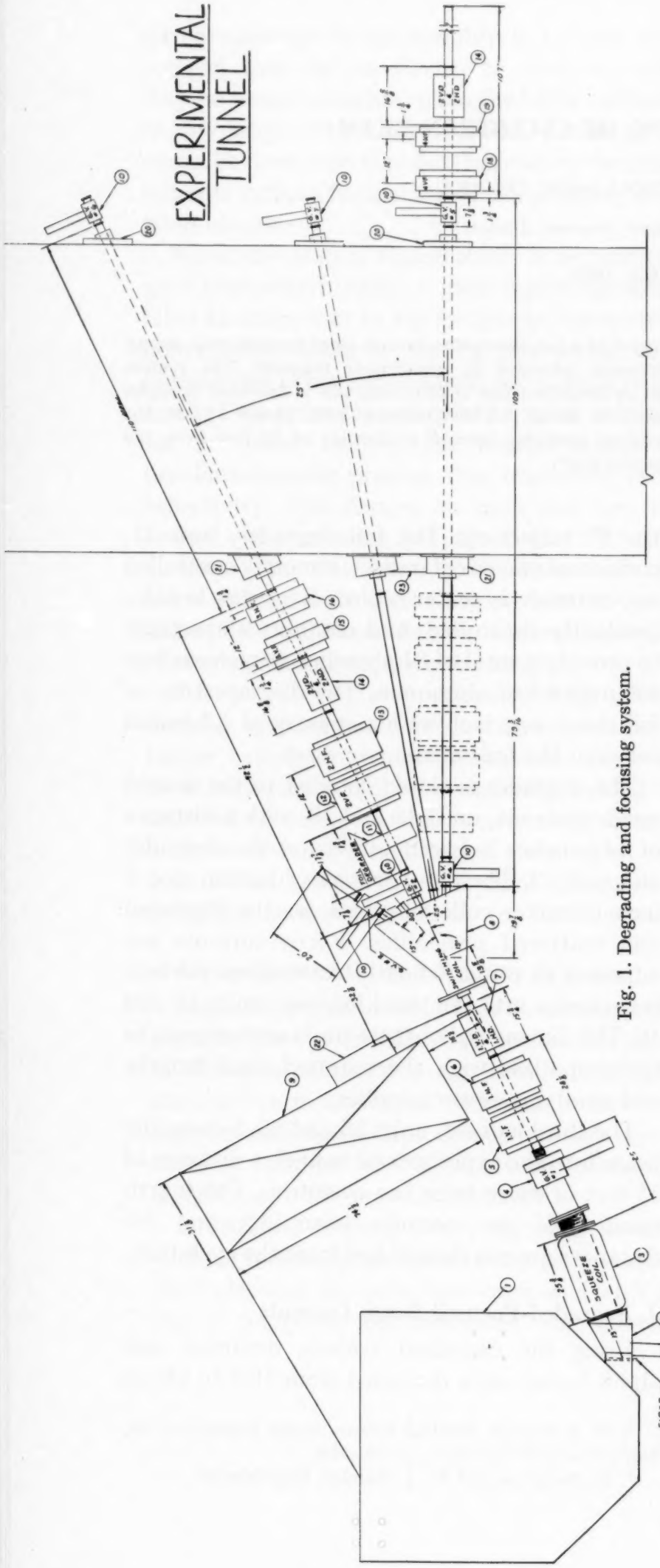

Fig. 1. Degrading and focusing system.

2.5 MeV/nucleon and focused into the experimental tunnel. The beam currents obtained in the tunnel are given by the normalized data of fig. 2. These data were obtained for an input current I_0 of 2.5 μA. Sampling checks at operating currents of $I_0 = 10\ \mu$A, showed that the given curves applied for higher operating levels.

Curve A of fig. 2 relates focused deuteron beam current and energy at a distance of about 20 feet from the degrader. These data were obtained without apertures in the 2 inch I.D. evacuated tube. Beam size was checked at the target by autoradiographing and the resultant pattern was oblong in shape. For the 21.6 MeV beam the cross sectional area was about 0.15 cm^2; 0.5 cm^2 at 15.5 MeV; and 2 cm^2 at 8.8 MeV.

The effect of collimation was determined by the use of two collimator sets, curves B and C. Each system was placed directly in front of the current collecting target. At full energy operation, the target current ratio of the systems, equals the ratio of the aperture areas; 3.5 to 1. The ratio of aperture area to the total unrestricted beam area does not compare favorably with the corresponding target currents. This discrepancy is due to the noncircular beam shape, spatial variation in the particle density, double collimator effects and possible misalignment. From past operating experience, the ratio of I_f/I_0 for the $\frac{1}{8}$ inch collimating system can equal or exceed 5% at full energy as compared to the plotted 1%. Thus, misalignment is quite possible and the plotted aperture curves are pessimistic but certainly representative of what can be obtained from day to day operation.

Alpha beam performance, fig. 2 curve D, exceeds that of deuterons, curve A, for the same geometry. Since the mean scattering angle for these two particles varies approximately with $M^{-\frac{1}{2}}$, it is to be expected that the focusing efficiency be greater for alphas than deuterons. The ratio of alpha to deuteron target current for a given E_f/E_0 compares favorably with calculations[3]) to determine the particle number,

[3]) W. C. Dickinson and D. C. Dodden, A Method for Evaluation of Multiple Scattering Effects in Charged Particle Experiments, L. A. 1182 (Dec. 1, 1950), Unpublished.

alpha or deuterons, accepted by the lens system. For example, for $E_f/E_0 = 0.4$, the ratio of target currents (curves A and D) I_α/I_D is 1.85 as compared to the calculated value of 1.9.

The limitation of the system to efficiently accept and focus low energy projectiles is shown by the break in curve D at $E_f/E_0 = 0.3$ or about 3.2 MeV/nucleon. This limitation is determined by the scattering angle, the distance between the degrader and the collecting lens set and the aperture of the lens. For the mean scattering angle of 3.5 degrees (3.2 MeV/nucleon alpha) and a 2 inch opening, this distance is computed to be about $16\frac{1}{2}$ inches or the approximate distance between the degrader and the center of the unit 12 quadrupole.

The focusing system throughout the collecting of these data performed in a set pattern. The focusing power of the first quadrupole set remained fixed with the given beam focused on to the degrader. For each change in particle energy, the second and third quadrupole sets were optimized for maximum focused particle number. In general, the change of focusing current to each quadrupole was in direct proportion to the change in particle energy.

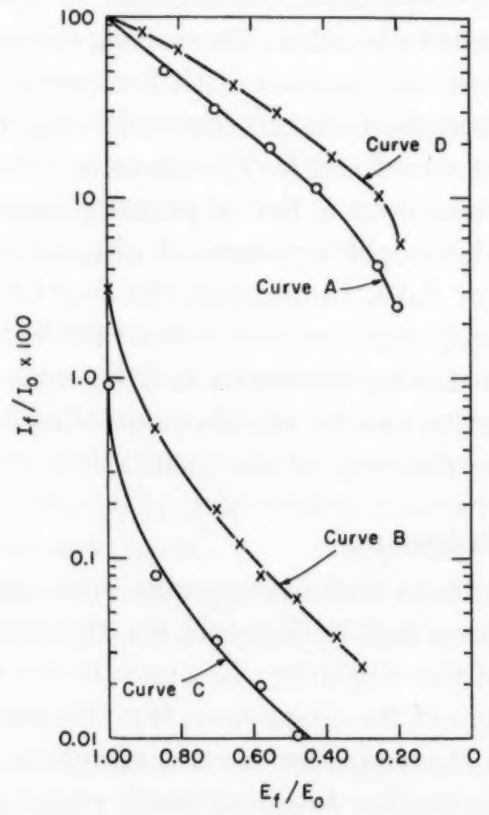

Fig. 2. Focused beam current vs. degraded beam energy. Curve A: deuterons, no collimation; B: deuterons, $2\frac{1}{8}$ inch apertures spaced 30.5 inches apart; C: deuterons, $2\frac{15}{64}$ inch apertures spaced 34 inches apart; D: alphas, no collimators. I_0 and E_0 are the magnitude of current and beam energy prior to degradation. I_f and E_f are the resultant current and beam energy at the target.

3. Energy Spread

To complete the characterization of the system an analysis was performed to determine the energy spread in the degraded deuteron beam. The degraded beam entered the 60 inch scattering chamber through a collimating system of two $\frac{1}{8}$ inch diameter apertures spaced 30.5 inches apart. The incident deuterons were scattered by a Mg target 0.0004 in. thick and the scattered particles were detected by use of a double NaI(Tl) crystal. The first (dE/dx-) crystal was about 0.008 inches thick and the second (E-) crystal was about 0.060 inches thick. Observations were made at two laboratory angles: 30° and 76°.

It is to be recognized that the pulse height distribution in the E crystal has a finite width. The factors contributing to the width are:

(a) The energy spread in the original beam E_0.

(b) The distribution introduced by the absorber in front of the E-crystal (i.e., the dE/dx-crystal).

(c) Statistical fluctuations in the E-crystal and photomultiplier.

Contributions to the distribution due to the finite subtended angle of the detector and the target thickness are negligible in the present case.

The contributions to the energy spread of the first two causes, a and b, are assumed to be constant. The inelastic lines cover a fairly wide energy region and are, in general, sufficiently spaced to be well resolved individually. The separation of the 4.122 and 4.24 MeV doublet is small compared to the observed energy spread. Observation of the deuteron spectrum of deuterons scattered by Mg shows that the line width (i.e., full width and half maximum) of the deuteron peaks is constant for all energies over a range of about 10 MeV. From this, it is concluded that the contribution to the line width of

the fluctuations in the E-crystal photomultiplier system is also a constant.

To determine the energy spread due to the degrader, a sufficient amount of scattering chamber absorber was introduced in the incident beam so that the elastic deuteron peak due to the scattering of the degraded beam coincided with one of the inelastic peaks due to the full energy beam. If the full width at half maximum in the first case is δ_1 and in the second case δ_0, the energy spread due to the absorber is

$$\delta a = \sqrt{\delta_1^2 - \delta_0^2} - 2.36\,\sigma_a \,.$$

For lower energies of the degraded beam, 10 MeV or less, the background problem is less severe and a single crystal was used for detection. For these lower energy data, it is again assumed that the energy distribution due to the inital energy spread in E_0 and to fluctuations of the crystal-photomultiplier system are constant.

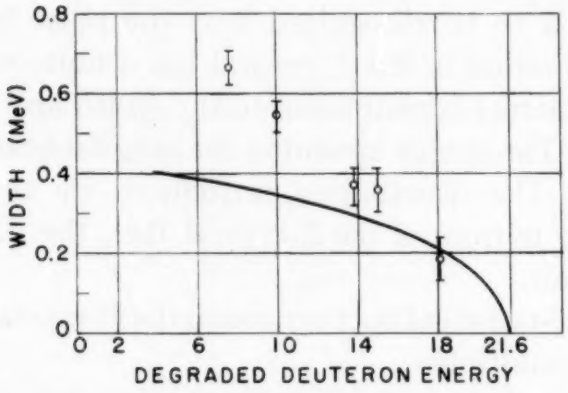

Fig. 3. Degraded deuteron beam energy spread vs. degraded beam energy. The curve has been calculated using the expression from ref. [4]).

The experimental data points given in fig. 3 were obtained by assuming that the distribution curve was normal. It should be noted that, as is to be expected, for large values of X, the distribution curve was skew. These experimental data are compared to calculated beam energy spread given by the solid curve of fig. 3. This calculated curve was obtained for the case of a monoenergetic beam of particles which has been transmitted through a thickness of absorber X. The second moment of the energy distribution of the particles is given, according to Livingston and Bethe[4])

$$(\Delta E)^2 = 4\pi e^4 Z^2 N Z X$$

where eZ is the charge of the incident particle, N the number of atoms per cm^3 of the absorber, Z the atomic number of the absorber and X the path length. This expression can be expected to give fairly good agreement with experiment for small values of X. For absorption up to 8 MeV, or an E_0/E_f of about 0.6, the calculated and experimental data are in good agreement. For larger values of absorption, the experimental points are above the calculated values.

4. Conclusion

The technique described is not limited to the reported projectiles but could be used for protons or other heavy ions. Since the mean scattering angle is approximately proportional to $M^{-\frac{1}{2}}$, the efficiency of focusing will increase with ion mass for degraded particles. The energy spread varies as $M^{\frac{1}{2}}$ and will increase with heavier ions.

The described system provides experimental flexibility to a fixed MeV/nucleon accelerator. If energy resolution is not of primary importance, it provides a quick means of obtaining energy dependent data. In addition the degraded beam can be projected many feet from the accelerator into a low background area and the cross sections of the beam can be readily controlled to maximize the efficiency of the irradiation.

Acknowledgments

The authors wish to recognize the assistance of P. Sorensen and E. Sundahl for the mechanical design of the degrader; E. Sundahl for the construction of the degrader; W. O'Neill for his work on the degrader control circuitry; and R. Benaroya for the design of many components of the external beam focusing system.

[4]) M. S. Livingston and H. A. Bethe, Rev. Mod. Phys. **9** (1937) 245.

NUCLEAR INSTRUMENTS AND METHODS 8 (1960) 221–224; NORTH-HOLLAND PUBLISHING CO.

AN INSTRUMENT FACILITATING THE MEASUREMENT OF SMALL-ANGLE SCATTERING IN NUCLEAR EMULSION

A. G. C. TENNER, B. JONGEJANS and H. WITTEVELD

Natuurkundig Laboratorium der Universiteit van Amsterdam

Received 29 May 1960

The assembly of components constituting the instrument is described. Special attention is paid to the essential features. The wiring diagrams are given. The experience obtained with the instrument in the first months of operation classifies it as a satisfactory new tool in nuclear physics. The principle underlying the instrument can be extended to bubble-chamber film.

1. Introduction

The scattering of an elementary particle by nuclei is a phenomenon of fundamental importance for gaining insight into the interaction between this particle and nuclear matter. With increasing energy of the particle scattering tends to be confined to small angles. The observation of small angles (e.g. < 2 degrees) in emulsion presents special difficulties. The instrument to be described facilitates the measurements of projected angles between 0.2 and 4 degrees. We have named the instrument "Hasem".

2. Description

The instrument consists of a microscope and a mechanical recorder. The main performances should be:

1. Possibility of observation of small kinks in nearly straight lines.

2. High operation speed enabling large quantities of information to be handled in reasonable time.

The microscope is a combination of a microscope head (Leitz Laborlux III) and a lathe bed with carriage. Being of rigid construction, this carriage easily permits coupling of the X-coordinate movement to an electric motor. The range of the X-displacement amounts to 25 cm, that of the Y-movement to 5 cm. The positions in X- and Y-direction can be read on dials with an accuracy of one micron. The position of the stage is reproducible within 5 microns. The mechanical recorder is moved in the X-direction by a direct mechanical joint. In the Y-direction the connection is made by magslips. A view of the instrument is given in fig. 1.

3. Characteristics

The most important features will be discussed now.

a. Requirements for moving the stage:

1. A high speed, resetting stage and recorder into the initial position after having finished a specific track. Stage speed: 8 mm/sec.

2. A low speed adjustable within a certain region. This region comprises an operational speed with a maximum estimated value of 0.16 mm/sec and a minimum speed value slow enough for scrutinizing difficult passages, 0.032 mm/sec.

The extreme values of the velocity are spanned by a special D.C. motor. The motor is coupled to the screw spindle of the microscope stage by means of a cardan joint and a worm gear.

b. The connection of the Y-motion of the microscope stage to the recorder is made by a set of magslips. One magslip is mechanically coupled to the Y-motion of the microscope stage, the other guides the writing lorry. The electric circuit is drawn in fig. 3.

The D.C. component of the double EL 34 ensures

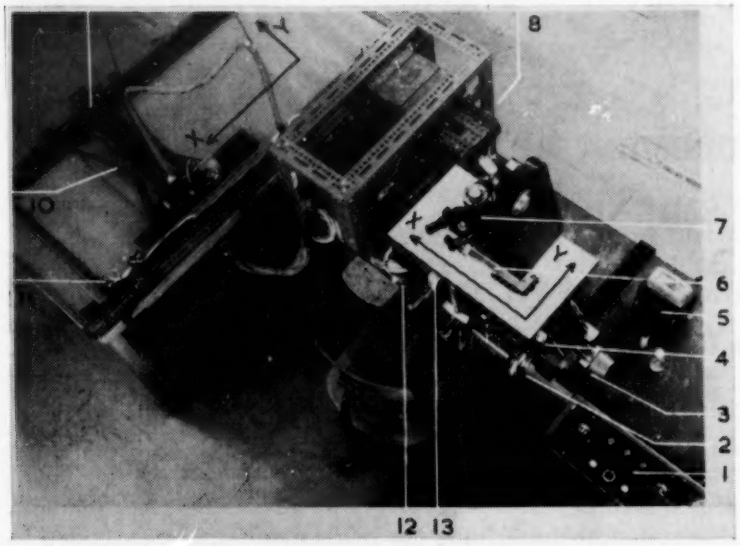

Fig. 1. View of the instrument.

1. Control panel, regulating speed and sense of the motor and locking or unlocking the writing lorry (10).

2. Knob controlling the Y-position of the microscope stage. This knob is fixed to the moving stage.

3. Calibrated disc enabling the reading of the X-position of the stage by indicating parts of the revolutions of the screw spindle.

4. Centimeter lath giving additional information regarding the X-coordinate.

5. Transformer for microscope light. The alarm bell attached to the transformer starts ringing just before the microscope stage reaches its mechanical stops.

6. Microscope stage with an emulsion plate. The plates are provided with copper strips for defining the position.

7. Microscope head. The objective is moved for focussing, the Z-position is therefore read on a dial indicator, also mounted on the head.

8. Electric motor, moving stage and recorder in X-direction. The motor is mounted independently to avoid vibrational disturbances of the microscopic field of view.

9. Recorder on table. On the right-hand side of the recorder the magslip and a 2-phase motor are visible. The latter brings the magslip into the right position.

10. Writing lorry, provided with a ball-point. The ball-point writes under a weight which can be lifted by an electromagnet.

11. One of a series of switches that interrupt the motor current when the instrument reaches the end of its range.

12. Control knob X and Z. With the aid of two hands three directions of motion must be kept under control. Two of them are combined in one hand. The principle will be clear from fig. 2.

13. Dial indicator for reading the Y-position of the stage.

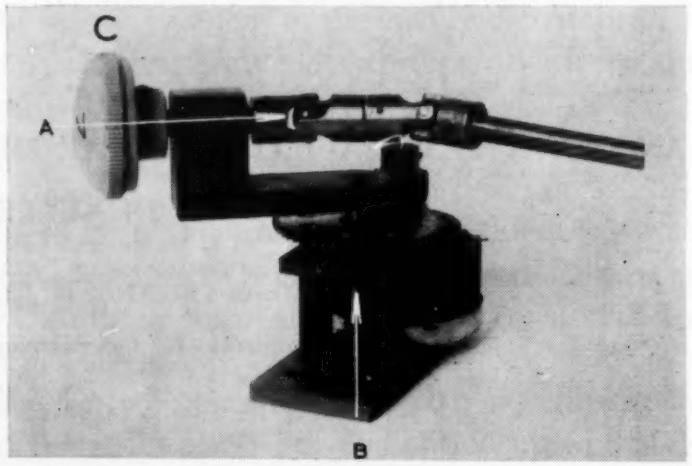

Fig. 2. Sketch of the principle of double rotation. Knob C can be rotated around its axis A; C then governs the focussing device. Knob C can also be rotated about axis B to set a potentiometer regulating the motor speed. The joint bends but still transmits rotations to the microscope.

This resolution is adequate for the purpose of our angle measurements.

c. The backlash in the X-direction between the stage and the recorder amounts to 50 microns. Track-following is always done in one direction so that backlash does not occur in the result. For the Y-direction a mechanical backlash compensation is incorporated into the servosystem. Backlash in Y is not noticed on the recording sheets.

d. The angular amplification is brought in by

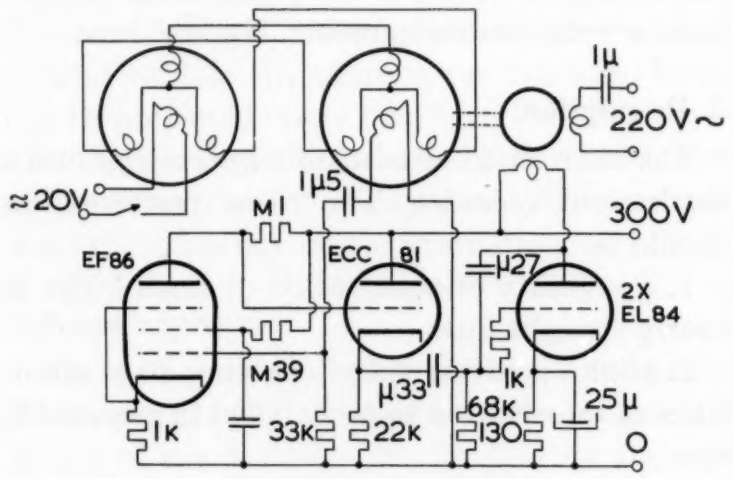

Fig. 3. Diagram of the servosystem.

the necessary damping of the system. The feedback with a capacitor of 0.27 μF decreases the internal resistance of the triodes. The amplification can be regulated by changing the voltage of the anodes of the output triodes. The resolution of the whole system of magslips and writing lorry amounts to 5 microns in the emulsion.

amplifying the X-coordinate by 9.192 and the Y-coordinate by 97.86. Roughly speaking this amounts to an angular amplification of 10.

Exact relations between the various angles involved are easily derived. It will be clear that scattering angles smaller than 2° which up to now presented a stumbling block to emulsion

measurements[1]) are within the scope of this instrument.

4. The Electric Circuit

The diagram of the circuit is shown in fig. 4.

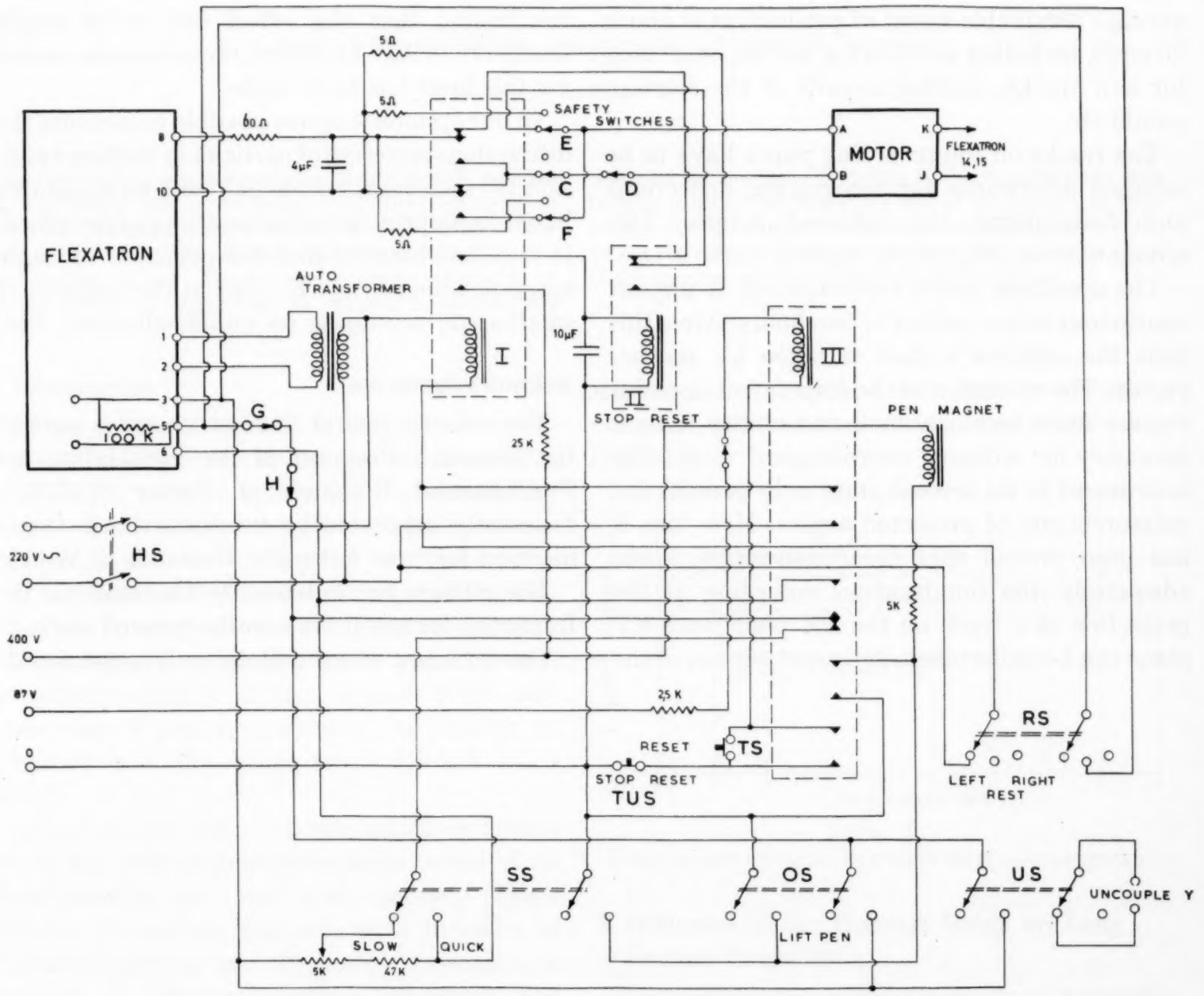

Fig. 4. Diagram of the electric circuit.

Flexatron is a trade name for the feeding unit of the motor. The *RC* circuit of 60 Ω, 4 μF is an additional element to increase speed constancy. Relay I determines the direction of the movement; switches C, D, E and F determine the end of the range of the recorder table. In the *X*-direction (E and F) the motor current is interrupted and the motor shunted for direct stopping. When either E or F is interrupted the motor can at once be operated in the opposite direction. Switches G and H are mounted on the microscope. When they are pushed in, the motor stops. They prevent mechanical damage to the microscope. Relay III operated by TS restores the instrument to the starting position. When this position has been reached, relay II shunts the motor with 5 Ω.

In addition, there are hand switches for the sense of motion (RS), for uncoupling the writing lorry (US), for lifting the ballpoint (OS), for operation at high speed (SS).

[1]) A. Barbaro *et al.*, Nuovo Cimento **9** (1958) 154.

5. Concluding Remarks

The "Hasem" has been operating for several months. Breakdown is becoming rare. The accuracy with which deflections can be measured is 0.06°. This is found by comparing the repeated values of one single measurement. The speed of operation is around 50 cm/h emulsion track. The average attainable speed of production is about 20 cm/h including refollowing tracks, searching for new tracks, making records of the starting points etc.

The tracks on the recording paper have to be scanned afterwards for recognizing deflections and determining the followed length. This amounts to $\approx 20\%$ of the tracing work.

The operation of the instrument is at present continuous over a period of two hours. After this time the observer's place is taken by another person. The operation of the instrument does not require more technical skill and ability than is necessary for ordinary microscopical work. The instrument in its present state only permits the measurements of projected angles. Now that it has been proved that the construction works adequately, the simultaneous recording of the projection of a track on the ZX plane and XY plane can be undertaken. A second version of the instrument incorporating this improvement is under construction.

The angular magnification of 10 now chosen can be easily enlarged because only simple geometrical considerations determine the magnification. The limit of magnification is determined by spurious scattering of the emulsion. We have the feeling that this effect sets in at angles smaller than 0.2°. However, no systematic search for this limit has been made.

In our opinion it seems possible to measure the diffraction scattering of particles in nuclear emulsion up to several tens of GeV with an apparatus based on the principle of the instrument described. It may be observed that the principle of angle magnification can also be used in the analysis of small-angle scattering on bubble-chamber film.

Acknowledgements

The construction of the instrument is part of the Research Program of the Foundation for Fundamental Research of Matter (F.O.M.), financially supported by the Netherlands Organization for Pure Scientific Research (Z.W.O.).

The authors are indebted to Professor G. W. Rathenau for his interest in the present work.

The criticism of our colleagues is appreciated.

NUCLEAR INSTRUMENTS AND METHODS **8** (1960) 225–229; NORTH-HOLLAND PUBLISHING CO.

NEUTRON FLUX MEASUREMENTS FROM 100 keV TO 4 MeV WITH A MODIFIED LONG COUNTER

E. TOCHILIN and R. V. ALVES

U. S. Naval Radiological Defense Laboratory, San Francisco 24, California

Received 23 May 1960

Long counter response to neutrons from a 2-MeV positive ion accelerator was investigated with three instruments which were identical except for the thermal shields within their outer cores. These shields consisted of B_2O_3, Cd, and polyethylene sleeves. For neutron energies ranging from 0.1 to 4 MeV no differences in relative response were observed for the three counters. Measurements made with indium strips placed along the axis of the counter in place of the conventional BF_3 detector showed that the foil technique could significantly extend the intensity range of the counter at no sacrifice in energy response.

1. Introduction

In the course of work at NRDL the Hanson-McKibben long counter has proved invaluable as a simple, reliable instrument for measuring neutron flux[1]). Long counter sensitivity is reasonably uniform with energy for neutrons from 0.02 to 9 MeV. A typical response curve is given in fig. 1[2]). To measure neutron flux one needs only to reproduce the original counter assembly and to calibrate with a neutron source. With adequate care 5 percent accuracy can readily be obtained over the range from 100 keV to 5 MeV[3]).

Although the long counter has found wide use in the field of neutron physics, some of its characteristics are not well defined. These include: (1) energy response as a function of shielding material, and (2) energy response as a function of different thermal detectors. The purpose of this study was to investigate, over a range of neutron energies, the effects produced by varying these parameters. The subsequent findings show that construction of the thermal shield can be simplified and that the intensity range of the counter can be significantly extended.

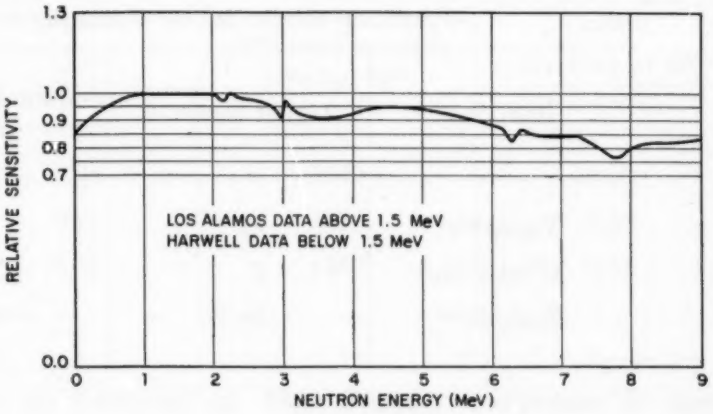

Fig. 1
Long counter efficiency as a function of neutron energy.

2. Influence of the Thermal Shield on Long Counter Response

The original long counter consists of a paraffin cylinder with a $B^{10}F_3$ detector along the axis. This central cylinder is surrounded by a B_2O_3 sleeve and is contained in an additional paraffin sleeve which lowers the response to scattered neutrons. These outer additions are referred to as the "shield". Fig. 2 shows the Precision Long Counter proposed by DePangher[3]). Construction details are similar to those of the Hansen-McKibben counter except that polyethylene rather than paraffin is used to provide better

[1]) A. C. Hanson and J. L. McKibben, Phys. Rev. **72** (1947) 673.

[2]) W. D. Allen and A. T. G. Ferguson, Proc. Phys. Soc. A **70** (1957) 639.

[3]) J. DePangher, Neutron Measurements III: Calibration of Long Counter No. 2 with Radioactive Neutron Sources, Hanford Laboratories Report HW-56199 (1958).

mechanical rigidity and a more uniform density. For calibration checks, the removable rod in the central cylinder is replaced with a PuBe neutron source.

One phase of the present study was to check the effect of the B_2O_3 shield on long counter response. This was of interest for two reasons:

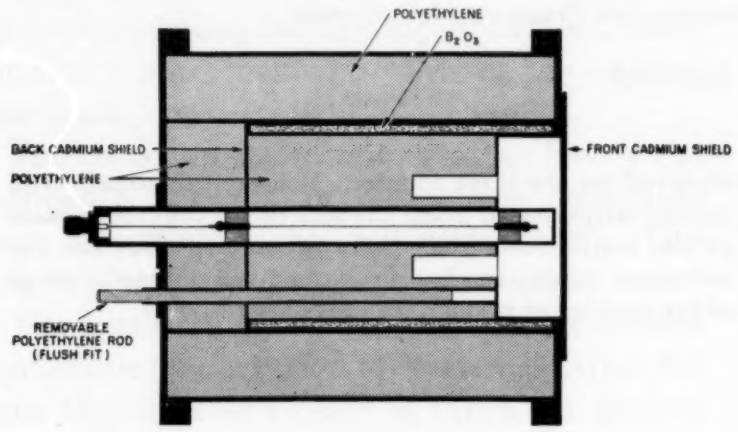

Fig. 2. Precision Long Counter.

comparisons were made between the B_2O_3- and polyethylene-sleeved long counters by simultaneously exposing the Cd counter and either of the other two units to monoenergetic neutrons from a 2-MeV Van de Graaff accelerator. The

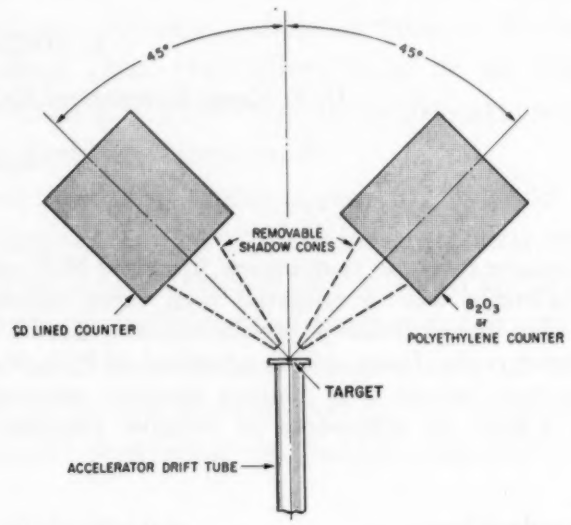

Fig. 3. General view of exposure conditions.

TABLE 1

Operating conditions for obtaining neutrons from the Van de Graaff accelerator

Reaction	Target material	Target thickness ($\mu g/cm^2$)	Particle energy (MeV)	Neutron energy at 45° (MeV)
$T(p,n)He^3$	Zr-T	1000	1.1–1.9	0.06–0.75
$C^{12}(d,n)He^3$	C	171	1.1–1.9	0.77–1.20
$D(d,n)N^{13}$	Zr-D	1902	0.5–1.5	3.0 –4.0

(1) anomalous results obtained by several experimenters have been attributed to the drying out of the B_2O_3 filling, and (2) construction of the thin aluminium shell for the filling material is a delicate machining process which could be eliminated by substitution of a rigid thermal shield such as cadmium.

For this study, two long counters were constructed. One was similar to that of fig. 2 except that the outer shield contained paraffin rather than polyethylene. The B_2O_3 sleeve was removable and could be exchanged for a polyethylene sleeve of identical dimensions. The second counter had a permanent Cd sleeve, 0.020 in. thick, in place of the B_2O_3 filling.

Using the Cd-sleeved counter as a reference, experimental arrangement is shown in fig. 3. Runs were also made with a shadow cone placed between target and inner core. These measurements determined the relative efficiency with which Cd and B shielded the detector from neutrons thermalized outside of the central core.

Monoenergetic neutrons ranging from 0.06 to 4.0 MeV were obtained by using $T(p,n)He^3$, $C^{12}(d,n)N^{13}$, and $D(d,n)He^3$ reactions. Table 1 lists the pertinent data necessary for calculating the available neutron energies. Because the targets made an angle of 45° with the beam, the effective target thickness was $\sqrt{2}$ times the thickness given in Column 3. Neutron energies as a function of laboratory angle and bombarding energies were taken from tables prepared by

Fowler and Brolley for $T(p,n)He^3$ and $D(d,n)He^3$ reactions[4]). The $C^{12}(d,n)N^{13}$ neutron energies were obtained from the data of DePangher[5]). An 80-g PuBe source was used as a neutron standard.

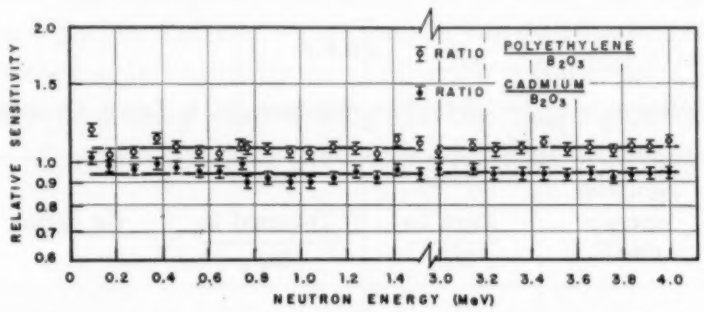

Fig. 4. Relative sensitivity of B_2O_3-, Cd-, and polyethylene-lined counters.

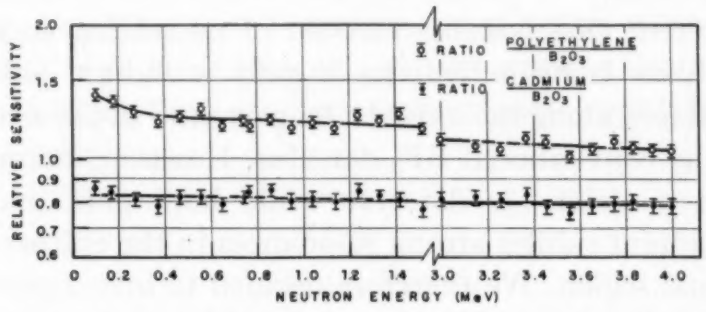

Fig. 5. Relative sensitivity of B_2O_3-, Cd-, and polyethylene-lined counters with shielded central core.

Response of the Cd- and polyethylene-lined long counters relative to the standard B_2O_3 counter is shown in fig. 4. A straight line can be drawn through both sets of data. The relative sensitivities of the Cd- and polyethylene-lined counters to the B_2O_3-lined counter are 0.94 and 1.08, respectively.

Fig. 5 is a similar comparison with the central core shielded by means of a shadow cone as indicated in fig. 3. The Cd/B "shielding" ratio remains reasonably constant at an average value of 0.8. However, the relative sensitivity of polyethylene/B varies with energy, decreasing from 1.4 at 0.1 MeV to 1.05 at 4.0 MeV. This moderate change in shielding efficiency at low energies is not significant since neutrons coming through the shield produce no more than 10 per cent of the total counts.

Table 2 gives data obtained under similar conditions with a PuBe neutron source. Given in Column 4 is the ratio of counts obtained with and without presence of the shadow cone. From 20 to 30 percent of the counter response is from neutrons originating in the outer shield of the detector. For energies from 0.1 to 1.2 MeV, 7 to 12 percent of the Cd-lined counter response was from the outer shield in contrast to 20 percent observed for PuBe neutrons. Column 5 gives the count rate obtained when the counters were rotated 90° so that the tube axis was perpendicular to the source. Column 6 gives the relative sensitivity of the counters for normal vs perpendicular incidence. Despite the impressive mass of moderator surrounding the detector, the shielding properties of the counter to stray neutrons of these energies are poor. Neither the boron nor the cadmium thermal shields had any significant effect on the amount of scattered radiation reaching the detector.

TABLE 2

Primary and secondary response of three long counters exposed to PuBe neutrons

Type of counter lining	Counts per minute		Ratio $\frac{\text{Cone}}{\text{No cone}}$	CPM with counter rotated 90°	Ratio $\frac{\text{Counter at 90°}}{\text{Counter at 0°}}$
	No cone	Cone			
Boron	4033	1008	0.25	2399	0.58
Cadmium	3904	801	0.20	2025	0.53
Polyethylene	4284	1287	0.30	2387	0.56

[4]) J. L. Fowler and J. E. Brolley, Revs. Mod. Phys. **28** (1956) 103.

[5]) J. DePangher, Neutron Measurement II: Operating Points for Obtaining Neutrons from the Hapo Positive Ion Accelerator, Hanford Laboratories Report HW-55085 (1958).

3. Use of Indium Detectors in the Long Counter

There are inherent limitations in the use of a proportional counter device whenever high-intensity or pulsed neutron beams are encountered. One possible method of measuring such fluxes is by activation of gold or indium foils placed along the axis of a long counter in place of the conventional BF_3 detector. However, boron is a strict $1/v$ detector while both gold and indium exhibit strong resonances in the epithermal region. We therefore decided to investigate to what degree foil detectors could reproduce the energy response of a conventional BF_3 counter.

Indium strips, 10.5 in. long, 0.5 in. wide, and 0.020 in. thick, were located in the center of an aluminum shell which simulated the BF_3 tube. This assembly was placed in the long counter so that the foil occupied essentially the same sensitive volume as the original detector. Following exposure, the foils were rolled into a spiral and counted in a 3 in. × 3 in. well-type NaI scintillation counter. A second indium exposure, made in an Al shell wrapped with 0.020 -in. Cd, was used to determine what fraction of the bare foil activity was due to epithermal neutrons. It was assumed that the indium cross section below the Cd cut-off energy of 0.4 eV would cause the foil to behave as a $1/v$ detector in this region. Use of a thick foil also favored the response to thermal neutrons owing to the self-shielding provided by the outer surface in the resonance region.

Table 3 gives the relative indium-to-BF_3 counter response obtained with 0.4-, 1.2- and 4.1-MeV neutrons and with the 80-g PuBe neutron standard. The ratios in Column 2 are for bare indium foils while those in Column 3 are for the thermal response below the Cd cut-off. All ratios are normalized to the PuBe exposures. The beam was monitored with the BF_3 counter from which the average beam level and the neutron-induced foil activity was determined. Column 4 gives the ratio of activity for bare and Cd-shielded foils. Contributions from the epithermal region are seen to be less than 10 per cent which explains why no differences with energy were found in the relative response of the bare and Cd-shielded foils. For PuBe neutrons, the sensitivity of the BF_3 counter and indium detectors were 1.8 counts per n/cm² and 0.042 cpm (at time zero) per n/cm², respectively.

TABLE 3

Relative $\frac{\text{Indium}}{BF_3}$ detector response in a Long Counter

Neutron energy (MeV)	Ratio $\frac{\text{Bare In}}{BF_3}$	Ratio $\frac{\text{Thermal In}}{BF_3}$	Cd ratio
0.4	1.01	1.01	11.5
1.2	0.98	0.98	12.2
4.1	0.99	0.98	13.1
PuBe	1.00	1.00	12.2

The foil technique has subsequently been used to determine fast neutron flux from the University of California 60-in. cyclotron. Earlier measurements were made by (1) measuring fast neutron flux with a sulfur threshold detector utilizing the $S^{32}(p,n)P^{32}$ reaction and (2) measuring spectrum with nuclear track plates[6]). For the simulated fission neutron spectrum obtained from 12-MeV protons and a thick Be target, it was calculated that the sulfur detector, calibrated for 14.1-MeV neutrons, measured fast neutron flux with an efficiency of 28 percent.

To check this value an independent measurement of fast neutron flux was made with a long counter incorporating a gold foil detector. Gold rather than indium was used because of the high beam intensity. Calibration was performed with a PuBe neutron standard. The same effective center and counter sensitivity was assumed for both PuBe and cyclotron neutrons. Comparative values of fast neutron flux obtained with the sulfur-track plates vs long counter measurements agreed to within 4 percent.

4. Summary and Conclusions

Long counter response to monoenergetic neutrons ranging from 0.1 to 4 MeV were observed for three counters which differed only in

[6]) E. Tochilin and G. D. Kohler, Health Physics **1** (1958) 332.

the type of thermal shield used in the outer core. No significant difference in relative response was observed for the three counters. The measurements demonstrate that counter design can be simplified either by replacing the conventional B_2O_3 loaded aluminum shell with a 0.020-in. Cd wrapper or by eliminating the thermal absorber.

Measurements at 0.4-, 1.2-, 4.1-MeV and with PuBe neutrons were also made with indium strips replacing the BF_3 counter. These results showed that foils can be substituted for the BF_3 detector with no sacrifice in energy response. The foil technique is of value whenever high intensities or a pulsed neutron beam preclude the use of proportional counting techniques.

NUCLEAR INSTRUMENTS AND METHODS **8** (1960) 230–232; NORTH-HOLLAND PUBLISHING CO.

ON THE SEPARATION OF π^+ MESONS BY A TIME OF FLIGHT METHOD

G. M. LEWIS, E. GABATHULER and R. E. AZUMA

Department of Natural Philosophy, The University, Glasgow

Received 6 April 1960

A time analysing coincidence unit of short resolving time has been employed to separate photoproduced π^+ mesons from electrons and protons by a time of flight method. The positive pions are additionally identified by their decay characteristics, so that an assessment of the method as a mass discriminator can be made.

1. Introduction

This paper refers to the possibilities of distinguishing low energy π^+ mesons over short flight paths by time of flight methods (cf. fig. 1a). In this method, the reciprocal of the velocity v, and the scintillation response S defining the energy E of the particle in flight, are correlated graphically (cf. fig. 2). The method was developed initially as an alternative to $(dE/dx,E)$ methods of separation in the low energy region, since, in principle, the front crystal need not then be thick enough to give good resolution, but only thick enough to give an indicative time pulse. Reference should be made to the work of Janes and Kraushaar[1]), in the low energy region. Recently, alternative counter methods have been reported on, for the study of low energy π^+ mesons[2,3]).

2. Method and Procedure

The detection system used here is shown schematically in fig. 1a. The evacuated flight path is defined by two plastic scintillation counters; counter 1–1.5 × 1.5 × 0.03 ins., and counter 2–3 × 2 × 1 ins., placed 60 cm apart. Pulses from the collectors of the counters 1 and 2 cut off E180F limiter valves, which generate rectangular pulses 3×10^{-8} sec long. These two pulses overlap and operate the time analysing coincidence unit, illustrated in fig. 1b; this latter unit produces a pulse whose height varies as the time delay representing the time of

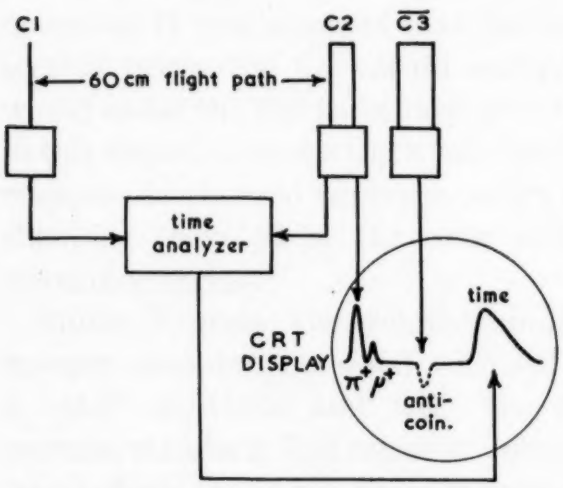

Fig. 1. (a) Detection system and mode of display.

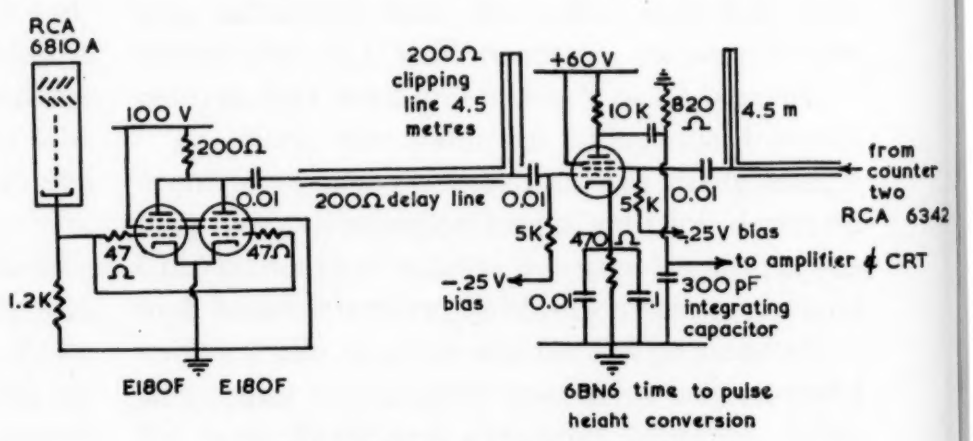

Fig. 1. (b) Time analysing circuit.

[1]) G. S. Janes and W. L. Kraushaar, Phys. Rev. **93** (1954) 900.

[2]) G. M. Lewis and R. E. Azuma, Phys. Soc. **73** (1959) 873.

[3]) J. G. Rutherglen and J. K. Walker, Nucl. Instr. and Methods **8** (1960) 239.

flight[4,5]). This time of flight pulse is used to trigger a Tektronix 517 A oscilloscope, and this pulse is also displayed on the fast time sweep, as a delayed pulse. The individual oscilloscope traces are photographed on film. On this same trace is also displayed the energy pulse from the 7th dynode of counter 2. To increase the power of the device, and to help in the assessment of the method, the dynode pulses from counter 2 lead into 100 ohm cable to give pulses approximately 10^{-8} sec wide. The π^+ particle can then be identified, and properly recorded, as both the π^+ and its 4.15 MeV μ^+ decay pulse are displayed as separate entities on the trace, provided that the particle lives longer than $\approx 10^{-8}$ sec. The time distribution of the π^+–μ^+ separation can also be made and checked with the 2.6×10^{-8} sec π^+ lifetime. Counter 3 serves as an anticoincidence counter for particles which pass right through counter 2. The pulses arising from counter 3 are appropriately delayed and displayed on the trace with inverse polarity, so that traces exhibiting such pulses can be rejected.

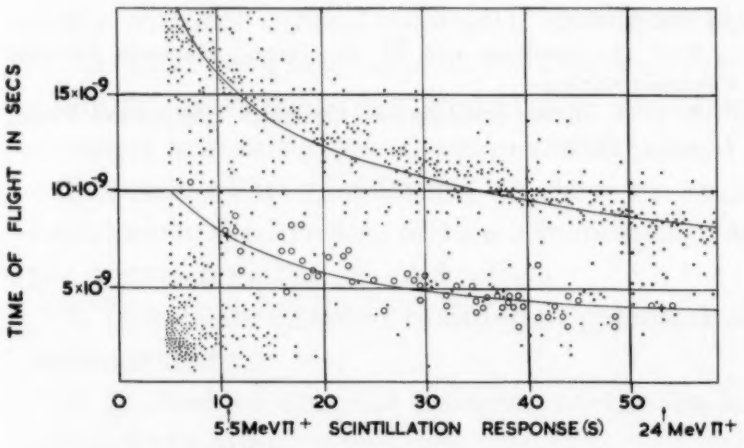

Fig. 2. Experimental results showing time of flight plotted against the scintillation response S, defining the energy E of the particle. This shows the identified π^+ mesons (o) in the meson band, the proton band, and the electron cluster ($\approx 2 \times 10^{-9}$ sec). All particles other than the identified π^+ mesons are represented by ($\cdot$). $+$ indicates the expected values for time of flight for the appropriate energy for π^+ mesons. Curves are shown of the expected time of flight v scintillator response S (cf. text) for a flight path of 60 cm for π^+ mesons and protons.

[4]) G. C. Neilson and D. B. James, Rev. Sci. Instr. **26** (1955) 1018.

[5]) R. E. Azuma and G. M. Lewis, Phil. Mag. **2** (1957) 1325.

An approximate time calibration for fig. 2 was effected with the aid of the more energetic electrons from an In^{114} β-ray source passed into the system, and inserting various lengths of delay cabling between the counters and the time analysing unit. This time calibration, however, when applied to mesons and protons could be uncertain by $\approx 10^{-9}$ sec, because of the variation in pulse rise time as a function of pulse height. A resolving time of 7×10^{-10} sec, (half-width at half-height) was obtained with the system with this indium source, when pulse height selection methods were employed. An electron energy calibration was also made for counter 2 with the 2.6 MeV γ-ray of ThC″. This provided a calibration point and a check on the electron response of the scintillator. Further energy calibrations are discussed below.

The time of flight telescope was set up at approximately 120° to the γ-ray beam of the Glasgow synchrotron, with the front crystal 8 ins. from a $\frac{1}{8}$th in. thick polythene target, viewed approximately end-on.

3. Results

The film record of the individual traces was analysed and the results plotted. The results of one of a series of runs is shown in fig. 2. From this figure it is seen that those mesons, identified positively by the presence of the decay pulses all lie on the lower band, which is distinct and apart from the upper band of particles, which are predominantly protons. The lower band will contain additionally π^+ mesons, which have decayed in such a short time that the μ^+ decay pulse is not distinct from the π^+ pulse (i.e. less than 10^{-8} sec), and also μ^+ mesons. The combined number of these can be expected to be of the same order as that of the identified π^+ mesons. Some μ^- particles will also be expected in this band.

The meson curve is to some extent self-calibrating. The π^+ mesons will have a maximum energy of 24 MeV, corresponding to their maximum range in the 1 in. scintillator. This "cut-off" therefore provides a high energy calibration point. A low energy calibration

point is then found by considering the μ^+ pulse heights which, in $\pi^+ \to \mu^+$ decays, must all be the same size. Since the π^+/μ^+ mass ratio is not very different from unity (viz. 1.33), the pulse height for a π^+ particle of energy $(4.15 \times 1.33) = 5.5$ MeV can be expected to be given by the Seitz relation (cf. Taylor *et al.*[6])) as 1.33 times that of the μ^+ particle. Thus, two energy calibration points are obtained and the times of flight associated with these meson energies calculated. These two check points are indicated in the meson band, they are consistent with the time calibration given earlier.

The scintillation response (S) of NE 102 scintillator for protons has been examined by Evans and Bellamy[7]) and by Gooding and Pugh[8]). $\mathrm{d}S/\mathrm{d}x$ follows closely a relation of form $\alpha(\mathrm{d}E/\mathrm{d}x)\ (1 + 0.01\ \mathrm{d}E/\mathrm{d}x)^{-1}$, where $\mathrm{d}E/\mathrm{d}x$ is in MeV $\mathrm{g}^{-1}\,\mathrm{cm}^2$ and α is a constant (cf. too, Birks[9])). Taking the same relation to hold for π^+ mesons, the upper curve of fig. 2 can be drawn for protons, and the lower curve for π^+ mesons. These curves are consistent with the experimental plots.

4. Discussion

Over the greater part of the energy range, the meson band stands distinct, and the results show that the method has adequate mass discrimination. Further it would seem possible to utilize a shorter flight path which would increase the solid angle subtended by the apparatus at the target. For meson detection from γ-ray machines, it is seen that the difficulties appear increasingly at the lowest energies; the random counts are evident below about 4 MeV in fig. 2. For reliable π^+ meson detection to the lowest energies, with a time of flight system identification by $\pi^+ \to \mu^+$ decay should remain incorporated as an additional criterion.

Acknowledgments

We would like to thank Dr. W. McFarlane and the synchrotron technicians for the use of the synchrotron beam, and Professor P. I. Dee for his interest in this work. We are also grateful to Miss E. Muldoon for help in the film analysis. One of us (E. G.) expresses his appreciation to the Ministry of Education, N.I., for a research grant held during the course of this work.

[6]) C. J. Taylor, W. K. Jentschke, M. E. Romley, F. S. Ely and P. G. Kruger, Phys. Rev. **84** (1951) 1034.

[7]) H. C. Evans and E. H. Bellamy, Proc. Phys. Soc. **74** (1959) 483.

[8]) T. J. Gooding and H. G. Pugh, Harwell, Private Communication.

[9]) J. B. Birks, Scintillation Counters (Pergamon Press, London, 1953).

NUCLEAR INSTRUMENTS AND METHODS 8 (1960) 233–235; NORTH-HOLLAND PUBLISHING CO.

A LOW BACKGROUND BETA COUNTER WITH A PLASTIC SCINTILLATOR ANTICOINCIDENCE SHIELD

J. R. GAT(GUTMANN)† and J. GILAT††

Israel Atomic Energy Commission Laboratories

Received 5 May 1960

The design and performance of a low background beta counter is described. The counter consists of a central gas flow proportional counter surrounded by a large plastic scintillator anticoincidence shield.

1. Introduction

The problem of counting very low beta activities often arises in health physics and in natural radioisotope work. Low background beta counters are required for this purpose. The reduction of the beta counter background to 1 c/m level is usually achieved by surrounding a conventional beta counter by an array of Geiger Mueller tubes, connected in anticoincidence with the central counter[1]). Arrangements of this kind have been applied with success[2,3,4]). Annular or bell shaped multianode shielding counters have also been developed[5,6,7,8]).

The use of a scintillation counter as anticoincidence shield offers certain advantages over the conventional G. M. umbrella:

1. It is easily adapted to different geometrical arrangements.

2. It enables spectral analysis of the background radiation to be made.

3. It eliminates the troublesome fault location so often encountered in multitube shields.

A plastic scintillator seems most suited for such a purpose. A low background counter using a scintillator shield of this type was designed, taking special care to ensure good sensitivity and light collection efficiency.

A previous attempt to use a plastic scintillator in anticoincidence shielding[9]), is reported to have given unsatisfactory results, apparently because of poor geometry and light collection efficiency.

2. Description of Counter

The counter is shown schematically in fig. 1.

An Epon, end window, gas flow counter (Tracerlab Model CE 14P), operating in the proportional region was used as central counter[10]). The anticoincidence shield was made of Nuclear Enterprises NE 102 plastic scintillator, machined to specifications and coated with a diffuse reflecting paint by the manufacturer. Its shape and dimensions were chosen to give maximum sensitivity and efficiency in light collection around the central counter. It was coupled to a 5″, DuMont 6364 photomultiplier. The sample slides and support were made of Perspex. The counters, together with their respective cathode

† Now at Isotope Department, Weizmann Institute of Science, Rehovoth.

†† The work was performed as part of an investigation by this author in partial fulfillment of the requirements for a Ph. D. thesis.

[1]) E. C. Anderson and F. N. Hayes, Ann. Rev. Nucl. Science **6** (1956) 303.

[2]) W. F. Libby, Rev. Sci. Instr. **22** (1951) 225.

[3]) J. L. Kulp and L. E. Tryon, Rev. S. Instr. **23** (1952) 296.

[4]) S. O. Softky, and R. E. Nather, Nucleonics **15**, No. 5 (1957) p. 90.

[5]) W. E. Grummit, R. M. Brown, A. J. Cruikshank and J. L. Fowler, Canadian J. Chem. **34** (1956) 206.

[6]) K. van Dureen, W. K. Hofker and J. Hermsen, Proceedings Second International Conf. on the Peaceful Uses of Atomic Energy, Vol. **14** (1958) 339.

[7]) J. Geiss, C. Gfeller, F. G. Houtermans and H. Oeschger, *ibid.*, cit. Vol. **21** (1958) 147.

[8]) W. Barendsen, *ibid.*, cit. Vol. **21** (1958) 151.

[9]) H. A. May, U.S. AEC Report. ANL 5679 (1957) p. 69.

[10]) Tracerlog No. **81** (1957); No. **92** (1958).

follower preamplifiers, and the sample slide assembly were enclosed in a light-tight brass housing. The entire arrangement was surrounded by a 10 cm thick iron brick shield.

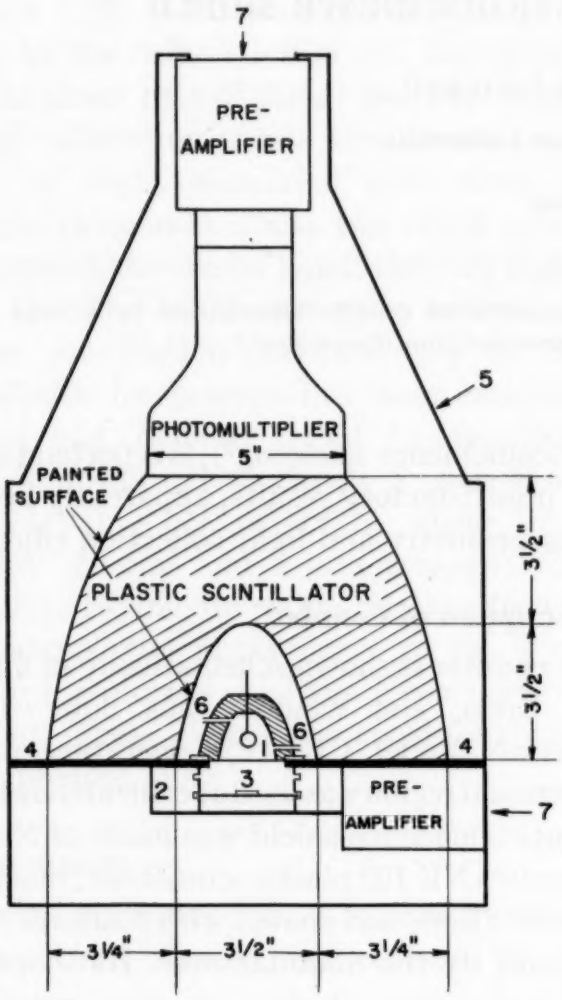

Fig. 1. A scintillator shielded low background β counter, schematic drawing (iron brick shield not shown). 1. Central gas flow counter. 2. Sample slide assembly. 3. Sample. 4. Support plate. 5. Brass housing (light-tight). 6. Gas in- and outlet. 7. Power supply and signal output.

The associated electronic circuitry is shown schematically in fig. 2 †. Pulses from the scintillation counter were recorded on count recording unit A, pulses from the central counter on unit B and the coincidence and anticoincidence counts on units C and D respectively.

The relationship $C + D = B$ was used for checking proper functioning of the equipment. For standardisation and plateau measurements with higher activity samples, the scintillation counter was disconnected, and the output of the RLI8V5 discriminator was connected to recording unit A. The dead time of the coincidence and anticoincidence gates was set at about 3 microseconds ††.

3. Performance

The setup was satisfactorily operated for several months counting Sr^{90}–Y^{90} samples †††.

The performance is summarised by the following data:

Plateau: 4400–4900 volts, slope < 1%/100 volts at a 15 mV sensitivity, (i.e. gain of 2000 and 30 volts discriminator setting).

Efficiency: 40% overall efficiency for a flat 2 cm diameter Y^{90} source, at a distance of 2 mm from the window. (Determined by intercomparison with a standardized beta counter.)

Background: A. Scintillation counter background: 1800 ± 100 c/m, at 1000 volts and 10 mV sensitivity. At this rate the dead time of the instrument is entirely negligible.

B. Proportional counter background: 9.5 ± 0.3 c/m.

C. Coincidence background: 8.7 ± 0.3 c/m.

D. Anticoincidence background: 0.80 ± 0.05 c/m.

The errors indicated on A, B, C include long term variations of the background counting rate during the 6 months testing period. The error in D is the statistical counting error for an overnight count. A detailed analysis showed that the distribution of the counts follows a Poissonian curve.

Increasing the voltage or lowering the discriminator setting of the scintillation counter, caused a steep rise in the scintillation counter background, but had no appreciable effect on the anticoincidence counting rate.

Part of the residual background of 0.8 c/m may be due to scattered and terrestrial radiation

† The scintillation counter discriminator, the coincidence-anticoincidence analyser and the four count-recording units, all installed on a single chassis, were designed and built by Messrs. D. Mydansky and Z. Kamil.

†† Operation of the central counter in the Geiger region, though quite feasible, would necessitate a much longer dead time of the gates.

††† For counting samples of β–γ emitters, a suitable mercury shield should be incorporated between the proportional and the scintillation counter, to eliminate β–γ coincidences.

from below, where no anticoincidence shield was provided. (Removal of the iron bricks beneath the counter increased the anticoincidence background by about 2.5 c/m).

Summary

The feasibility of using plastic scintillators in anticoincidence shielding has been demonstrated by the performance of the counter. A smaller scintillator might possibly be used without sacrificing much of its shielding properties. This would make the entire unit more compact and comparable in price to an array of G. M. tubes.

Acknowledgement

The help of Mr. Sheinin in the assembly and maintenance of the unit is gratefully ackowledged. We would also like to thank Messrs. M. Birk, J. Wolfson and Dr. A. Nir of Nuclear Physics Dept. of the Weizmann Institute for helpful discussions.

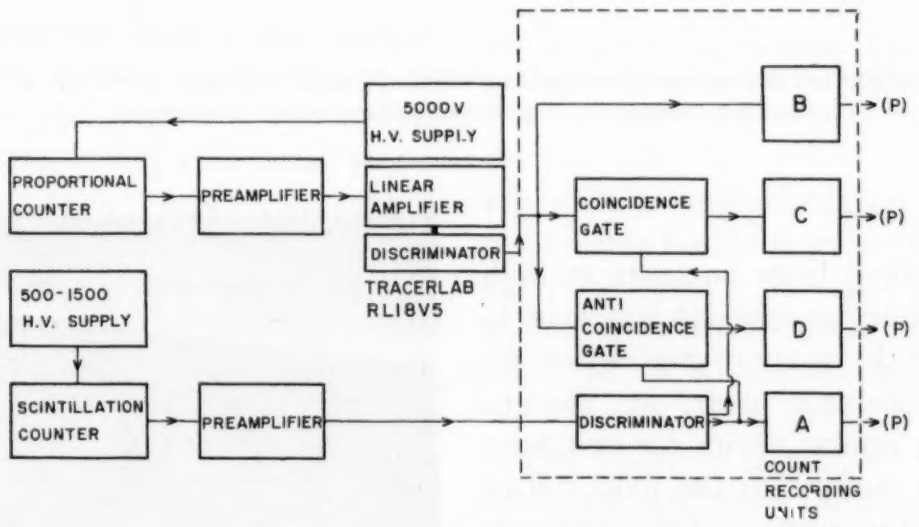

Fig. 2. Block diagram of counter and associated electronic circuits. Count recording Units: A = 2 Philips E1T scaling tubes and mechanical register; B, C, D = Mechanical registers; P = Provision for connection to printing counter.

NUCLEAR INSTRUMENTS AND METHODS **8** (1960) 236–238; NORTH-HOLLAND PUBLISHING CO.

A KILOVOLT, KILOAMPERE LOW PRESSURE SWITCH†

GEORGE J. BRUCKER

United States Signal Corps Laboratories, Fort Monmouth, New Jersey

and

KENNETH C. ROGERS

Stevens Institute of Technology, Hoboken, New Jersey

Received 9 April 1960

A low pressure switch is described that is capable of passing kiloamperes at voltages up to 30 kV. The effect of pressure and gap voltage on the switch closing time is discussed.

1. Introduction

The need for switching large currents at high voltages in thermonuclear research has lead to the development of the vacuum-gap switch[1,2]). The Megatron accelerator work at Stevens Institute requires a similar device for switching the capacitor bank current to the field coil of the Megatron. It is the purpose of this paper to present the design of a practical switch, and the experimentally determined closing time for different gap voltages and pressures.

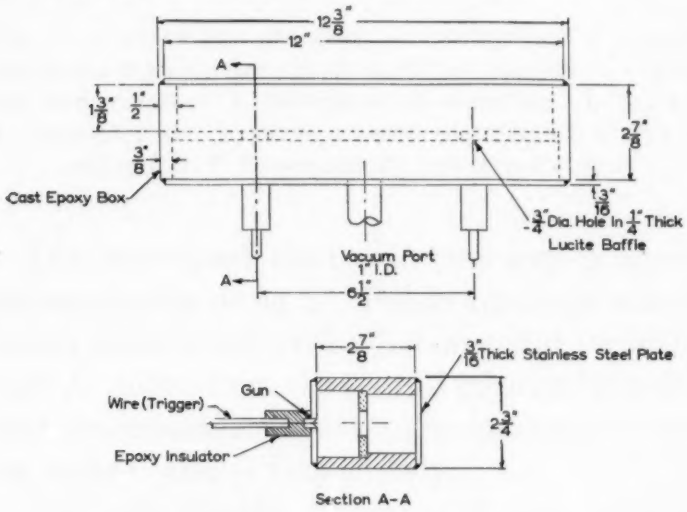

Fig. 1. Details of switch.

† Work performed under the auspices of the United States Army Signal Corps Laboratories, Fort Monmouth, New Jersey and the U.S. Atomic Energy Commission.

†† Twenty-two part of sand, ten parts of Araldite 6050, three parts of Hardener 901 by weight.

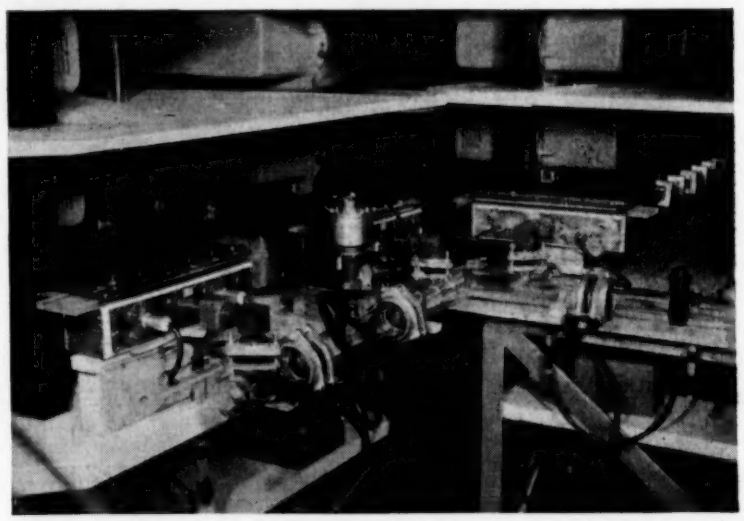

Fig. 2.
View of Stevens capacitor bank showing switches mounted on transmission lines and connected to pumping manifold.

2. Description of Switch

The design of the Stevens capacitor bank[3]) has dictated the rectangular geometry of this switch. Fig. 1 is a drawing of the switch which consists of a rectangular box cast from a mixture of epoxy and sand†† with stainless steel electrodes and a lucite baffle plate. The switch is closed by a plasma burst from a pair of coaxial plasma

[1]) D. C. Hagerman and A. H. Williams, Rev. Sci. Instr. **30** (1959) 182.

[2]) W. R. Baker, Rev. Sci. Instr. **30** (1959) 700.

[3]) K. C. Rogers *et al.*, Megatron Accelerator Progress Report, Signal Corps Contract DA36-039sc-78097 (June 3, 1958).

guns[4]). A high voltage pulse (2 kV to 10 kV) supplied by a hydrogen thyratron (5c22) and a 0.3 μF capacitor fires the guns. A view of the switches mounted on the transmission lines of the capacitor bank is shown in fig. 2.

3. Experimental Procedure

The closing delay time T_d and the "jitter" in T_d were measured for ranges of voltage across the switch V_s, and for vacua from 0.02–3.3 microns Hg. The delay time T_d, is defined to be the length of time from the inception of current flow to the plasma gun to the start of current through the switch. Both rates of current change (dI/dt) were picked up by means of Rogovsky coils, and the integrated signals were presented on a Tektronix 551 dual beam scope. The capacitor bank was prevented from ringing by a resistive load. All pressure readings were made by the same P. I. G. located close to the switch. The data are plotted in figures 3, 4 and 5. Each point is the mean of not less than five separate measurements. The polarity of the applied voltage was varied so that the gun side of the switch was either positive or negative.

4. Discussion of Results

The delay time versus voltage applied across the switch at a constant low pressure (0.02 microns) is shown in fig. 3. At this pressure it is apparent that the delay time, T_d, varies inversely with the applied voltage V_s. If electrons are responsible for closing the switch then reversing the polarity of V_s so that the gun side of the switch is positive should show a longer time delay which is independent of voltage. This is not the case at low pressure.

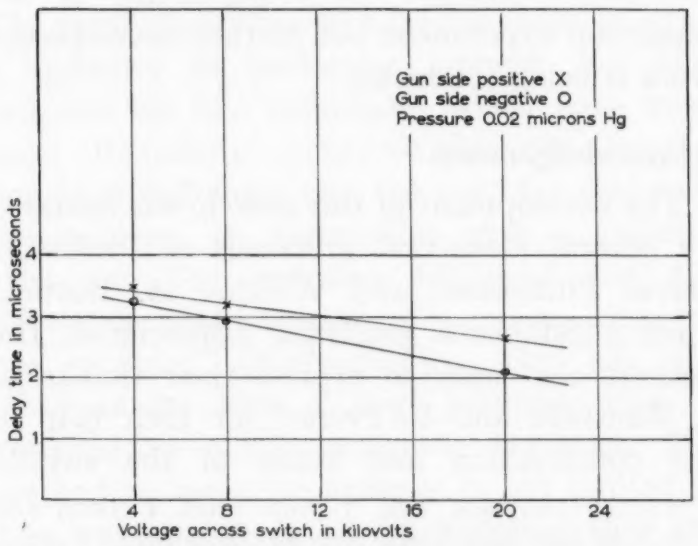

Fig. 3. Switch closing delay time versus voltage across switch for a constant pressure of 0.02 microns Hg and both positive and negative bank voltages.

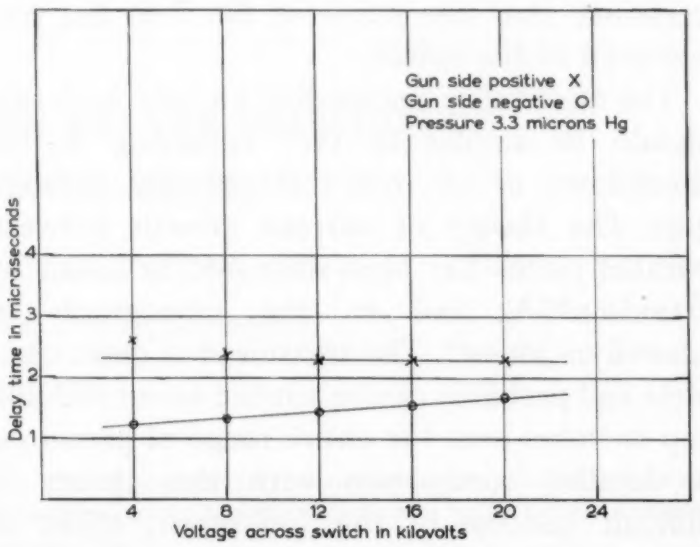

Fig. 4. Switch closing delay time versus voltage across switch for a constant pressure of 3.3 microns Hg and both positive and negative bank voltages.

The evidence in support of the theory that electrons are responsible for switch closure becomes stronger for high pressure operation. Fig. 4 displays this independence of delay time on switch voltage when the gun side of the switch is positive; in this case T_d is comparable to plasma transit time. Reversal of polarity at this pressure (3.3 microns) brings about an increase of T_d with voltage. J. A. Mather[5]), who observed this behavior in a vacuum-gap switch at Los Alamos, has suggested that the increasing delay time is due to the dependence of the electron-atomic ionization cross section $\sigma(v)$ on the applied voltage. The picture does not seem to be this simple as is indicated by fig. 5. The shape of these curves is not explicable on the basis of the ionization cross section voltage dependence, although the precision of this experiment is not sufficient to say with

[4]) K. C. Rogers *et al.*, Megatron Accelerator Progress Report, Signal Corps Contract DA36-039sc-78097 (April 1, 1959).

[5]) J. A. Mather and A. H. Williams, Rev. Sci. Instr. (to be published).

certainty that the curve of fig. 5 is the true behavior of the switch.

The mechanism responsible for switch closure should be similar to that occurring in the breakdown of an over-voltaged low pressure gap. The theory of current growth between parallel plates has been discussed in detail by Davidson[6,7,8]) and in the monograph of Llewellyn-Jones[9]). The treatment is quite complete and probably can be applied to our vacuum gap switches over the entire range of pressures. A detailed comparison with this theory is difficult because of the (unknown) effect of electrode contamination on γ, the second Townsend coefficient. By a more elementary treatment that should apply under low pressure conditions $p \ll 0.1$ microns, the time τ required for the switch to "close" is given by

$$\tau = t_+ + \frac{Mt_+}{1+M} \ln\left(\frac{2M}{M-1}\right).$$

$$M = \gamma\,(e^{\alpha d} - 1)$$

where d: electrode spacing,
α: first Towsend coefficient,
γ: second Townsend coefficient,
t_+: anode to cathode ion transit time.

If the electrodes are of steel and Fe^+ ions are responsible for (secondary) electron liberation at the cathode then for a three inch electrode gap,

$$t_+ = \frac{2.3 \times 10^{-6}}{V_s^{\frac{1}{2}}} \text{ sec},$$

V_s = gap voltage in kilovolts.

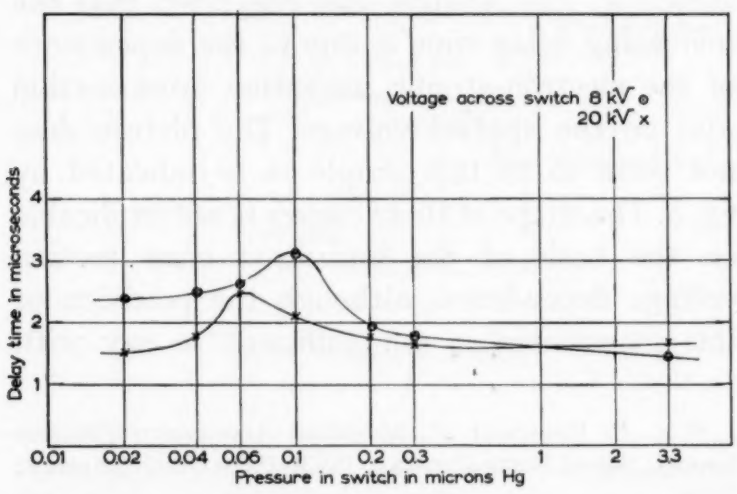

Fig. 5. Switch closing delay time versus pressure for two constant bank voltages with gun side of switch negative.

Clearly the ion transit time determines the time scale. At 20 kV and 0.02 microns pressure $t_+ = 0.5$ microsecond. This requires $M = 1 + 2\,e^{-8}$ if the above expression for τ is used. It is our belief that at all pressures switch closure is triggered by fast electrons from the "plasma gun". Metallic plasma ejected by the gun probably plays a minor role. At low pressures an avalanche is initiated by positive ions liberated from the anode. At high pressures both the anode and the gas in the gap contribute positive ions. Ion bombardment of the cathode releases secondary electrons and breakdown proceeds.

5. Conclusions

The data in fig. 5 points out the desirability of operating the switch at a pressure higher than 0.1 microns. An operating pressure of 0.3 microns would give a switch with a low value of delay time, and one which only depends to a small degree on voltage and pressure. The fluctuation (jitter) in T_d at this pressure is 0.1 μsec. This type of switch was test fired over a 1000 times at 30 kV passing a current of 30 000 amperes. The inductance and resistance of the switch is approximately 20 millimicrohenries and 0.03 ohms respectively. No special voltage conditioning is required. More development work is necessary as the switch is far from optimum, for example decrease of gap spacing will decrease the closing delay time. At this time the switch satisfies the requirements of the Megatron experiment but further development work is being conducted.

Acknowledgements

The development of this switch was initiated by several ideas and proposals of Professors David Finkelstein and Winston H. Bostick. Their assistance is gratefully appreciated. The authors also wish to express their thanks to I. Mansfield and L. Ferrari for their help in the construction and study of the switch.

[6]) P. M. Davidson, Brit. J. App. Phys. **4** (1953) 170.
[7]) P. M. Davidson, Phys. Rev. **99** (1955) 1072.
[8]) P. M. Davidson, Phys. Rev. **103** (1956) 1897.
[9]) F. Llewellyn-Jones, Ionization and Breakdown in Gases (Methuen, London, 1957).

NUCLEAR INSTRUMENTS AND METHODS 8 (1960) 239–243; NORTH-HOLLAND PUBLISHING CO.

A SCINTILLATION COUNTER SYSTEM FOR THE DETECTION OF POSITIVE AND NEGATIVE PIONS

J. G. RUTHERGLEN and J. K. WALKER

Department of Natural Philosophy, University of Glasgow

Received 21 April 1960

A three counter telescope has been developed in which pions are separated from particles of different mass by measurement of dE/dx and E. Identification of positive pions is made by means of the characteristic π^+–μ^+ decay. The arrangements for recording this information both photographically and by means of a pulse height analyser are described.

1. Introduction

The detection and identification of fast charged particles emitted from nuclear reactions is a frequent problem in nuclear physics. It is often necessary to identify particles of a particular mass among a flux of various other particles. This requires, in general, that any technique should consist of a simultaneous measurement of at least two dynamical quantities which have a different dependence on the masses of the particles.

In investigations on the production of pions from nuclei by photons it is necessary to identify pions among a large background of electrons and protons. It is also necessary to have separate identification of the positive and negative pions. The ratio of positive to negative pions is often a quantity of particular interest. For this purpose the two techniques which have been most frequently employed are the nuclear emulsion technique and the use of a magnetic spectrometer in association with a counter telescope. The emulsion technique has the advantage that the positive and negative pions are recorded simultaneously, but has the disadvantage that a large scanning time is required to obtain adequate statistics. The method of magnetic analysis is not limited in this way, but has the disadvantage that the positive and negative pions cannot be counted at the same time.

We have developed a counter telescope system which can be used to count π^+ and π^- simultaneously in a well defined solid angle and energy interval. This system was designed primarily for the measurement of π^-/π^+ ratios, but is also quite satisfactory for the measurement of absolute cross sections.

2. General Method

It can be shown[1,2]) that to a good approximation

$$\frac{dE}{dx} \propto \frac{M^{0.45} Z^{1.1}}{R^{0.45}}.$$

Thus for singly charged particles with the same range R a measure of the specific ionization dE/dx distinguishes particles of different mass. This implies that for mesons, protons and deuterons of the same residual range the dE/dx are in the ratio of 0.4:1:1.3 respectively. This applies to mesons whether they are positively or negatively charged. To make use of this fact three counters were used; the first one to measure dE/dx, the second in which to stop particles and measure the resulting pulse heights E and the third to act as an anticoincidence counter. An automatic plot of dE/dx against E was performed for every particle which stopped in the second counter. The

[1]) B. Wolfe, A. Silverman and J. W. De Wire, Rev. Sci. Instr. **26** (1955) 504.

[2]) J. C. Keck, Phys. Rev. **85** (1955) 410.

resolution was sufficient to give with negligible uncertainty the total number of π^+ and π^- mesons which stopped in the second counter.

To distinguish between π^+ and π^- mesons which stopped in the second counter use was made of the characteristic decay properties of the π^+ meson. The π^+ decays into a μ^+ meson of kinetic energy 4.1 MeV with a half life of 18 mμsec. A delayed coincidence technique for the π^+–μ^+ decay has been used by several experimenters and is described in detail by Imhof *et al.*[3]). A similar system for detecting the π^+–μ^+ decay, with an efficiency of about 50%, has been developed in the present work. In order to determine the efficiency of the delayed coincidence system for detecting the μ^+ it is necessary to use hydrogen as a target from which only π^+ mesons can be photoproduced.

In the general case when there are π^- and π^+ mesons present the knowledge of the efficiency of the delayed coincidence system, together with the number of delayed coincidences recorded, yields the number of π^+ mesons which stop in the second counter. Subtraction of this number from the total number of mesons yields the number of π^- mesons. Thus a simultaneous measurement on both types of charged pion can be performed.

3. Description of Counter Telescope

The telescope consisted of three plastic scintillators (N.E. Type 101) connected by perspex light guides to R.C.A. 6810 A photomultipliers. Scintillators 1, 2 and 3 were 0.25″, 0.75″ and 0.5″ thick and 3″, 3″ and 4″ in diameter respectively. Between counters 1 and 2 there was a perspex absorber 0.25″ thick. Fig. 1 shows the telescope and the associated fast electronics, which was situated close to the counters.

Particles which stop in counter 2 register a $12\bar{3}$ coincidence-anticoincidence in a Bell type coincidence circuit which has a resolving time of 20 mμsec. When such an event occurs it is necessary to measure the pulse heights C_1 and C_2 from the collectors of photomultipliers 1 and 2. This is accomplished by means of the display unit to be described later.

We shall now consider the sequence of pulses for a π^+–μ^+ decay in counter 2. A $12\bar{3}$ event, which may be a π^+ stopping in 2, was made to operate a trigger which produced a gate pulse 80 mμsec long and rise time about 15 mμsec.

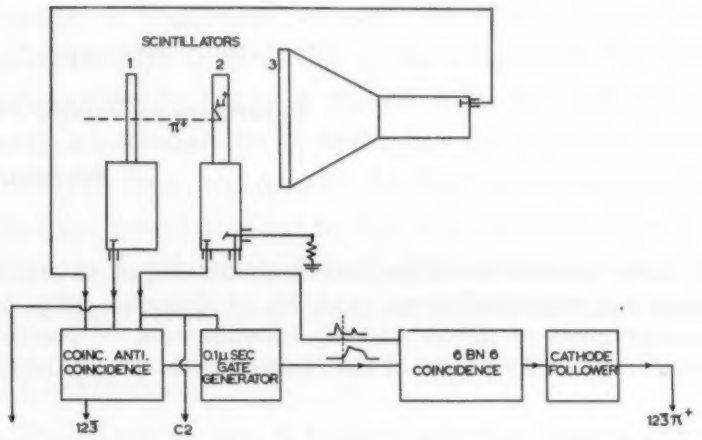

Fig. 1. The scintillation counter telescope and associated fast electronics.

In order to have a faster rise time and to minimise jitter, this pulse was mixed with the limited pulse on the anode of a limiter fed by the collector of photomultiplier 2. This resulted in a gating pulse which had a rise time of about 8 mμsec to 3 volts high and lasted for nearly 100 mμsec. The gate pulse was applied to one grid of a 6BN6 valve. The output pulse from the last dynode of photomultiplier 2 was fed directly on to the other control grid of the 6BN6. A 27″ length of 200 ohm cable was used as a clipping line on this dynode. This line was terminated with an 80 ohm resistor to minimise overshoot[4]). With this arrangement the total width of the pulse was about 15 mμsec. The object of this was to keep the π^+ and μ^+ pulses as distinct as possible. The timing of the pulses on the grids of the 6BN6 was arranged so that the dynode pulse occurred first and the gate pulse was applied to the other grid 15 mμsec later. As the half-life for the π^+–μ^+ decay is 18 mμsec it is clear that something like 50% of π^+–μ^+ decays will be recorded as delayed conincidences. The anode pulse of the 6BN6 was integrated by the stray capacity of the anode. It was found that optimum response was obtained using

[3]) W. Imhof, R. Kalibjian and V. Perez-Mendez, Rev. Sci. Instr. **29** (1958) 476.

[4]) R. Madey, Rev. Sci. Instr. **26** (1955) 971.

— 3 volts bias on both grids of the 6BN6.

The operation of the delayed coincidence circuits ($123\,\pi^+$) could be checked by measurements using the 2.6 MeV gamma ray of ThC^{11}. This was achieved by introducing sufficient 200 ohm delay cable for the dynode pulse to arrive at the grid of the 6BN6 sometime within the gate pulse. The maximum pulse height from ThC^{11} is slightly less than the equivalent light output of the 4.1 MeV μ^+ meson. Thus operation on the maximum pulses of the ThC^{11} gamma ray spectrum was considered adequate for the delayed coincidence system. This was achieved by adjusting the E.H.T. voltage on photomultiplier 2 until the delayed coincidence was just functioning. The E.H.T. voltage on counter 1 was adjusted until the gain was suitable for the display unit to be described.

4. Display Unit

The information from the telescope and its associated fast electronics was fed through 70 ohm cables to the display unit. This information consisted of the pulse heights from the collectors of photomultipliers 1 and 2 (C_1 and C_2) and the pulses from the fast coincidence circuit ($12\overline{3}$) and the delayed coincidence circuit ($12\overline{3}\ \pi^+$). The object of the display unit is to record the above pulses in such a manner as to require a minimum of subsequent analysis.

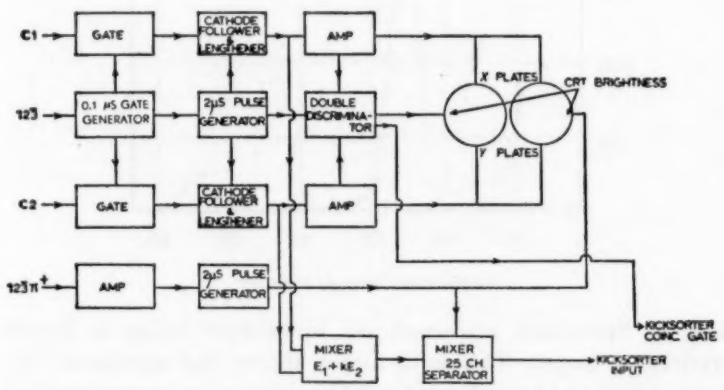

Fig. 2. A block diagram of the electronics in the display unit which records the pulse heights produced in counters 1 and 2 for all particles which stop in the second counter.

A block diagram of the electronics is shown in fig. 2. A pulse signifying a $12\overline{3}$ event was used to trigger a blocking oscillator which produced a 10 V pulse 100 mμsec long. This pulse was used to open gates through which the collector pulses C_1 and C_2 passed to lenghtening circuits, which produced 2 μsec long flat-topped pulses of amplitudes proportional to the amplitudes of the C_1 and C_2 pulses. The lengthened pulses were fed to two paraphase amplifiers whose outputs were connected to the X and Y plates respectively of a cathode ray tube (Mullard Type DB 13/2). Simultaneously the cathode of

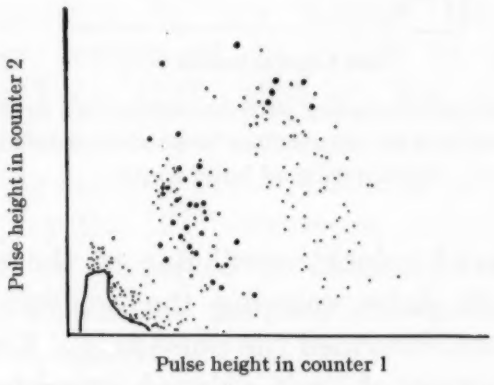

Fig. 3. A spot picture as photographed on the display unit. The target used was hydrogen from which only π^+ mesons may be produced. See text for explanation of large spots.

the C.R.T. was pulsed 40 volts negative for 2 μsec. This produced a spot on the C.R.T. whose coordinates were proportional to the pulse heights C_1 and C_2 from counters 1 and 2. A second C.R.T. whose X and Y plates were connected in parallel with the first was only brightened up when there was a delayed coincidence in counter 2. This was achieved by using the $12\overline{3}\ \pi^+$ pulse to trigger a 2 μsec pulse generator whose 40 volts negative output pulse was fed to the cathode of the second C.R.T. The two C.R.T.'s were photographed simultaneously.

Typical spot pictures are shown in fig. 3 in which the "ordinary" and "delayed coincidence" pictures have been superimposed, the latter being shown by large spots. The three different groups of spots from left to right correspond to electrons, mesons and protons. The number of spots due to electrons is very large and only the outline of the electron region is shown. These pictures were obtained using liquid hydrogen as a target, from which only π^+ mesons can be photoproduced. It is seen that about 50% of the

π^+ mesons have been detected as delayed coincidences. Protons which have produced large pulses in the second counter have produced

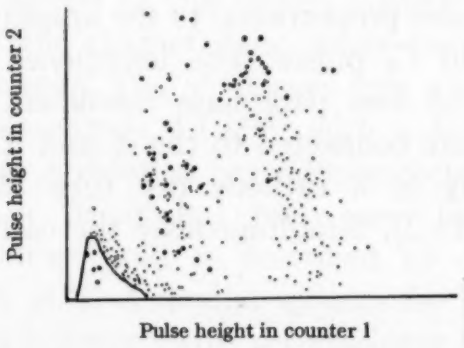

Fig. 4. A spot picture taken with deuterium as a target from which both π^+ and π^- mesons can be produced. See text for explanation of large spots.

"self delayed coincidences" due to the tail of the dynode pulse entering the delayed coincidence gate. Provided the pulse height level for the production of "self delayed coincidences" was higher than the top of the meson region in fig. 3 then no ambiguities could occur. Fig. 3 is the result of a 15 minute run with a 3 cm liquid hydrogen target exposed to a 240 MeV bremsstrahlung beam, and with the telescope about 12″ away from the centre of the target.

When a target other than hydrogen is exposed to the gamma ray beam, π^- as well as π^+ mesons are produced. Fig. 4 shows the result of a 15 minute run using a 3 cm deuterium target. The region between the mesons and protons is now occupied by a few spots. This is due to π^- mesons which stopped in the second counter and produced stars of high energy charged particles, thus increasing the pulse height from counter 2. Although the separation between mesons and protons is not quite so clearly defined as in the case of hydrogen, it was possible to obtain the total number of mesons with good accuracy from an analysis of the spot density. To reduce the probability of fast charged product particles from π^- stars entering the anti-coincidence counter and thus causing a veto, the anti-coincidence counter was situated as far away as possible from the second counter without producing a loss of anticoincidence efficiency.

5. Kicksorter Display

Although analysis of the results was normally performed by counting the spots from the photographs, it is useful in a long experiment to have some means of quickly checking the overall operation of the apparatus. Use was made of a multichannel pulse height analyser for this purpose.

The meson and proton groups on the normal $12\bar{3}$ C.R.T. display are approximately parallel straight lines. Hence if the pulses proportional to C_1 and C_2 are added to form a pulse of height $P \propto C_1 + kC_2$, the spectrum of the pulses P shows well defined peaks corresponding to mesons and protons, when the constant k is correctly adjusted. In fig. 5 such a spectrum, obtained with a liquid hydrogen target, is shown in the first 35 channels.

In order to display the events associated with a delayed coincidence separately, a step pulse of standard height, equivalent to 35 channels on the kicksorter, was added to the corresponding P pulse. The peaks corresponding to π^+ mesons and "self delayed" high energy protons can be seen in channels 40 to 60 in fig. 5.

From the point of view of the dead time of the kicksorter it was desirable to prevent the majority of the large number of electrons from

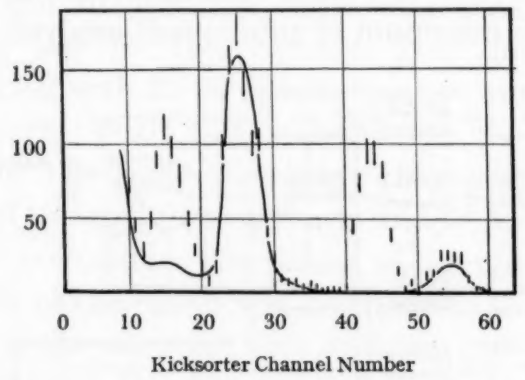

Fig. 5. Spectrum obtained on kicksorter using a liquid hydrogen target. The solid curve shows the spectrum obtained with the target empty. The two groups corresponding to π mesons are well resolved. The upper group contains mesons for which delayed coincidences have been recorded.

being counted by the kicksorter. This was achieved by gating the kicksorter by the output of a double discriminator which was fed by the C_1 and C_2 pulses.

It is seen that the kicksorter display fulfils the requirement of giving an instantaneous assessment of the results and an overall check on the operation of the apparatus at all times.

Acknowledgements

The authors wish to thank Dr. W. McFarlane and the synchrotron technicians for their co-operation, Dr. W. Hogg for use of liquid targets and Professor P. I. Dee for the interest shown in this work. One of us (J. K. W.) expresses appreciation to D.S.I.R. for a maintenance grant held during the course of this work.

Appendix

The energy interval of pions which stop in counter 2 is about 15–25 MeV. With the use of absorbers in front of the telescope, higher energy pions have been studied. However, it is of considerable theoretical interest to study photo-meson production as near as possible to threshold.

To study mesons of kinetic energy 6–12 MeV, a plastic counter, 0.1 inches thick, has been added to the front of the telescope which has been described. The purpose of this counter is to measure the ionization loss of particles which stop in the previous front counter of the telescope. Thus two energy intervals of pions may be studied at the same time.

All the information is displayed in the form of spots on four cathode ray tubes which are photographed by one camera. These four displays correspond to events of the type $12\overline{3}$, $12\overline{3}\,\pi^+$, $123\overline{4}$, $123\overline{4}\,\pi^+$. For continuous monitoring the kicksorter is now used in the following manner. The first 25 channels are used to display the $12\overline{3}$ information and the $12\overline{3}\,\pi^+$ events are displayed in channels 26–50. The second 50 channels are used in a similar way for the $123\overline{4}$ system.

Successful preliminary results have been obtained with the above four counter telescope.

NUCLEAR INSTRUMENTS AND METHODS 8 (1960) 244–248; NORTH-HOLLAND PUBLISHING CO.

THE THEORY AND OPERATION OF THE ROTATING CRYSTAL SLOW NEUTRON CHOPPER

D. A. O'CONNOR

Institute of Nuclear Research, Warsaw†

Received 2 June 1960

The resolution and efficiency of the rotating crystal chopper are derived theoretically as a function of the crystal and collimator parameters. It is shown that the limiting resolution of the device is the same as that of a crystal monochromator. An experimental model chopper is described and its observed resolution compared with the theory.

1. Introduction

In studies on the inelastic scattering of slow neutrons by substances it is necessary to measure the energy distribution of neutrons scattered out of an incident monochromatic neutron beam by a sample. This requires the use of some form of monochromator to produce the incident beam, and some form of spectrometer to measure the energy distribution of neutrons scattered by the sample through some angle. The rotating crystal chopper, together with a time of flight analyzer, is a device which serves simultaneously as a monochromator and as a spectrometer in such experiments. This device was first used and described by Brockhouse[1]).

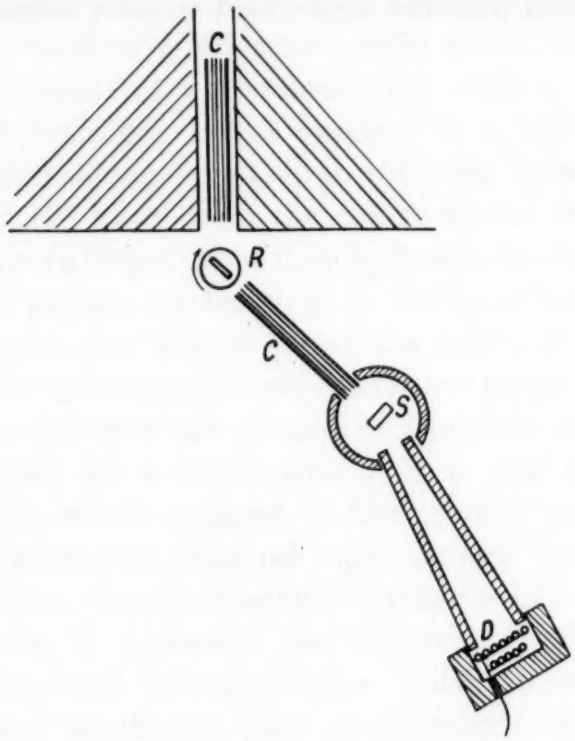

Fig. 1. Arrangement of apparatus for the measurement of the spectra of inelastically scattered neutrons. C = collimators, R = rotating single crystal, S = scattering material, D = neutron detector.

The principle of operation of the crystal chopper will be made clear by fig. 1. A single crystal, rotating continuously about an axis perpendicular to the plane of the diagram, will produce a pulse of neutrons at the collimator exit every time the crystal planes pass through the Bragg position. The mean wavelength of the neutrons will depend on the crystal plane spacing and the angle between the collimators. The energy of the scattered neutrons is found by measuring their time of flight from the sample to the detector.

2. Theory

We are interested here in computing the time duration of the neutron pulse, and the energy resolution of the device when considered as a spectrometer. The effect of the sample on the shape of the pulse will not be considered. Since the beam produced is not ideally monochromatic the pulse duration will vary with

† Present address: Department of Physics, The University, Edgbaston, Birmingham 15, England.

[1]) B. N. Brockhouse, Bull Amer. Phys. Soc. Ser. II, **3** (1958) 233.

distance from the crystal as a result of the spread in neutron velocities, the pulse length being larger than that resulting from purely geometrical considerations.

Using the notation of Borst *et al.*[2]) we write for the collimator transmission functions (assumed equal) $I(\phi) = \exp - \phi^2/\alpha^2$ and for the crystal reflectivity $R(\beta) = R_0 \exp - \beta^2/2\eta^2$ where η is a measure of the mosaic spread of the crystal for the particular planes considered. Consider the moment at which the crystal has its planes at an angle γ to the Bragg position. If $\Delta\theta$ is the deviation of the angle of reflection of an individual ray of the beam from the Bragg angle θ, then we may write for the intensity of neutrons having deviations between $\Delta\theta$ and $\Delta\theta + \mathrm{d}\,\Delta\theta$:

$$P(\Delta\theta,\gamma) = \int I(\phi_1)\, R(\beta)\, I(\phi_2)\, \mathrm{d}\beta \qquad (1)$$

where

$$\phi_1 = \gamma + \beta - \Delta\theta$$

and

$$\phi_2 = \gamma + \beta + \Delta\theta\,.$$

Integration gives:

$$P(\Delta\theta,\gamma) = R_0 \pi^{\frac{1}{2}} \left(\frac{1}{\alpha^2} + \frac{1}{2\eta^2}\right)^{-\frac{1}{2}} \times$$

$$\exp - \left[\left(\frac{\Delta\theta}{\alpha}\right)^2 + \frac{\gamma^2}{\alpha^2 + 2\eta^2}\right]. \qquad (2)$$

If the crystal is rotating with angular velocity ω then the number of neutrons of wavelengths corresponding to the interval $\Delta\theta$, $\Delta\theta + \mathrm{d}\,\Delta\theta$, and emitted at times corresponding to the interval γ/ω, $\gamma/\omega + \mathrm{d}\,\gamma/\omega$, is given by:

$$\frac{1}{\omega} P(\Delta\theta,\gamma)\, \mathrm{d}\gamma\, \mathrm{d}\Delta\theta\,. \qquad (2a)$$

Neutrons of wavelength corresponding to the Bragg angle θ travel a distance L from the crystal in a time T_1 given by

$$T_1 = \frac{2dmL}{h} \sin\theta \qquad (3)$$

where the symbols have their usual meaning. Neutrons of wavelength corresponding to a Bragg angle of $\theta + \Delta\theta$ take a time:

$$T_1 - \Delta T_1 = \frac{2dmL}{h} \sin\theta - \frac{2dmL}{h} \cos\theta \cdot \Delta\theta\,.$$

It follows that the neutrons given by eq. (2) arrive at a point L from the crystal at a time:

$$T + \Delta T = T \pm \frac{\gamma}{\omega} - A\Delta\theta \qquad (3a)$$

where the sign of γ/ω depends on the rotation direction of the crystal and $A = (2dmL/h)\cos\theta$.

Replacing $\mathrm{d}\,\Delta\theta$ in (2) by $(1/A)\,\mathrm{d}\,\Delta T$, we obtain for the number of neutrons arriving at time $T + \Delta T$ to $T + \Delta T + \mathrm{d}\,\Delta T$:

$$P(\Delta T)\, \mathrm{d}\Delta T = \frac{\mathrm{d}\Delta T}{\omega A} \int P(\Delta\theta,\gamma)\, \mathrm{d}\gamma \qquad (4)$$

where $\Delta\theta$ from (3) is given by

$$\Delta\theta = \pm \frac{\gamma}{A\omega} - \frac{\Delta T}{A}\,. \qquad (5)$$

Substituting for $\Delta\theta$ in (4) and integrating we obtain:

$$P(\Delta T) = R_0 \pi 2^{\frac{1}{2}} \alpha^2 \eta\, [\alpha^2 (1 + A^2\omega^2) + 2\eta^2]^{-\frac{1}{2}} \times$$

$$\exp - \left[\frac{(\omega\Delta T)^2}{\alpha^2 (1 + A^2\omega^2) + 2\eta^2}\right].$$

This expression gives the shape of the pulse. The half-width of the pulse is given by:

$$\tau = 2\, (\ln 2)^{\frac{1}{2}} \left[\frac{\alpha^2 + 2\eta^2}{\omega^2} + A^2\alpha^2\right]^{\frac{1}{2}}\,. \qquad (6)$$

The total number of neutrons in one impulse is given by:

$$\int P(\Delta T)\, \mathrm{d}\Delta T = R_0 \pi^{\frac{3}{2}} 2^{\frac{1}{2}} \alpha^2 \eta\, \omega^{-1}$$

and for n impulses per revolution of the crystal the total intensity:

$$n\, (\tfrac{1}{2}\pi)^{\frac{1}{2}} \alpha^2 \eta R_0$$

In the above we have used a very idealised expression for the reflectivity of the crystal. When secondary extinction is strong the $R(\beta)$ function loses its Gaussian shape and can be approximated by an expression of the form

$$R(\beta) \sim 1\,, \qquad |\beta| \leqslant \beta_0$$

$$R(\beta) = 0\,, \qquad |\beta| > \beta_0$$

[2]) L. B. Borst and V. L. Sailor, Rev. Sci. Instr. **24** (1953) 141.

where β_0 depends on the mosaic spread of the crystal and on the reflectivity per unit volume. Using this expression we find that

$$P(\Delta T) = \pi\alpha^2[\operatorname{erf} K(\omega\Delta T - \beta_0) - \operatorname{erf} K(\omega\Delta T + \beta_0)] \quad (8)$$

where

$$K = 2^{\frac{1}{2}}[\alpha(1 + A^2\omega^2)^{\frac{1}{2}}]^{-1}.$$

If, as is often the case, β_0 is smaller than $\alpha(1 + A^2\omega^2)^{\frac{1}{2}}$ then we obtain as an approximation to (8)

$$P(\Delta T) \sim \frac{2\pi^{\frac{1}{2}}\alpha\beta_0}{(1 + A^2\omega^2)^{\frac{1}{2}}} \exp - \left[\frac{(\omega\Delta T)^2}{\alpha^2(1 + A^2\omega^2)}\right]$$

and

$$\int P(\Delta T)\, \mathrm{d}\Delta T \sim \frac{2\pi\alpha^2\beta_0}{\omega}. \quad (9)$$

The half-width of the pulse in this case is

$$\tau = 2(\ln 2)^{\frac{1}{2}}\alpha\left[\frac{1}{\omega^2} + A^2\right]^{\frac{1}{2}}. \quad (10)$$

Expression (9) can also be obtained from (7) by putting the areas of the two $R(\beta)$ functions equal and so obtaining R_0 in terms of β_0 and η.

The expressions (6) and (10) both contain two components which we shall write as

$$\tau = (\tau_a^2 + \tau_b^2)^{\frac{1}{2}}$$

where

$$\tau_a = 2(\ln 2)^{\frac{1}{2}}\frac{\delta}{\omega}$$

$$\tau_b = 2(\ln 2)^{\frac{1}{2}}\alpha A \quad (11)$$

δ will have a value somewhere between α and $(\alpha^2 + 2\eta^2)^{\frac{1}{2}}$ and represents the combined effect of the collimators and the crystal on the angular spread of the pulse. τ_a is dependent on ω as is to be expected. τ_b is independent of ω and is given by the spread in neutron velocities corresponding to the wavelength spread due to the collimator and crystal arrangement when considered as a simple monochromator. As ω increases τ converges to τ_b as a limit. The limiting resolution is given by

$$\frac{\tau_b}{L} = 2(\ln 2)^{\frac{1}{2}}\alpha B$$

where

$$B = \frac{2dm}{h}\cos\theta.$$

Putting in the appropriate constants we obtain

$$\frac{\tau_b}{L} = 8.67 \times 10^{-2}\,\alpha\, 2d\cos\theta \text{ microseconds/metre}$$

where α is in minutes of arc and $2d$ in Å. Thus, as is to be expected the limiting resolution is independent of the length of the flight path (apart, of course, from the effect of the detector thickness and the analyzer channel width).

Comparing the expressions for limiting resolution and the integrated intensity, it is seen that the intensity is inversely proportional to the square of the limiting resolution, which in turn depends on the half-width of the collimator transmission function. On the other hand the intensity is directly proportional to the mosaic spread of the crystal (through η in (7) and β_0 in (9)), which does not appear in the expression for the limiting resolution. It follows that it is desirable to use a crystal with a large mosaic spread. If the speed of the chopper is chosen so that the resolution is close to its limiting value, then the resolution required for a given experiment can be obtained by suitable choice of the collimators.

The fact that the limiting pulse width is due to the separation of neutrons with different velocities, suggests that the rotating crystal chopper could be used as a monochromator of very high resolution. The distribution in time, at the detector, of neutrons of wavelength corresponding to a deviation of $\Delta\theta$ from the Bragg angle, can be found directly from expression (2) by substituting for γ from eq. (5). This gives the number of neutrons of wavelengths between $\Delta\theta$ and $\Delta\theta + \mathrm{d}\,\Delta\theta$ arriving between ΔT and $\Delta T + \mathrm{d}\,\Delta T$:

$$R_0\pi^{\frac{1}{2}}\left(\frac{1}{\alpha^2} + \frac{1}{2\eta^2}\right)^{-\frac{1}{2}} \exp - \left[\frac{\Delta\theta}{\alpha}\right]^2 \times \exp - \left[\frac{\omega^2(\Delta T + A\Delta\theta)^2}{\alpha^2 + 2\eta^2}\right].$$

Thus neutrons of deviation from the mean of $\Delta\theta$ are distributed in time at the detector about $\Delta T = -A\Delta\theta$, and the half-width of their distribution is given by

$$\tau = 2(\ln 2)^{\frac{1}{2}}\frac{(\alpha^2 + 2\eta^2)^{\frac{1}{2}}}{\omega}.$$

This in fact corresponds to τ_a in (11). By increasing ω, τ_a can be made as small as desired compared with τ_b.

3. Experimental Chopper

A rotating crystal chopper has been built in order to test the characteristics of the device.

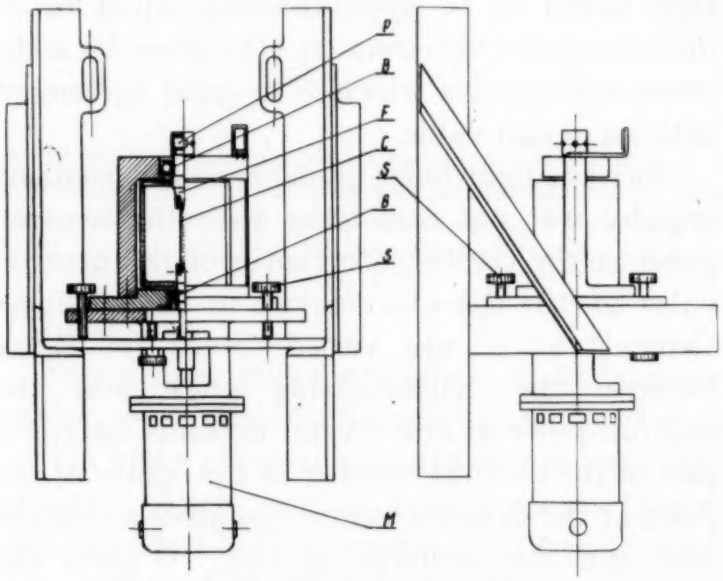

Fig. 2. Drawing of experimental model of chopper. C = single crystal, F = frame holding crystal, B = bearings, M = motor driving crystal, P = glass prisms in lucite cylinder, S = leveling screws.

The design adopted is by no means optimal but is very simple. The mechanical construction will be evident from fig. 2 and the photographs 1 and 2. The crystal in the form of a plate of dimensions 5 × 50 × 50 mm, is mounted in an aluminium frame which rotates about a vertical axis. The crystal plate is cut so that an appropriate crystallographic plane is parallel to the

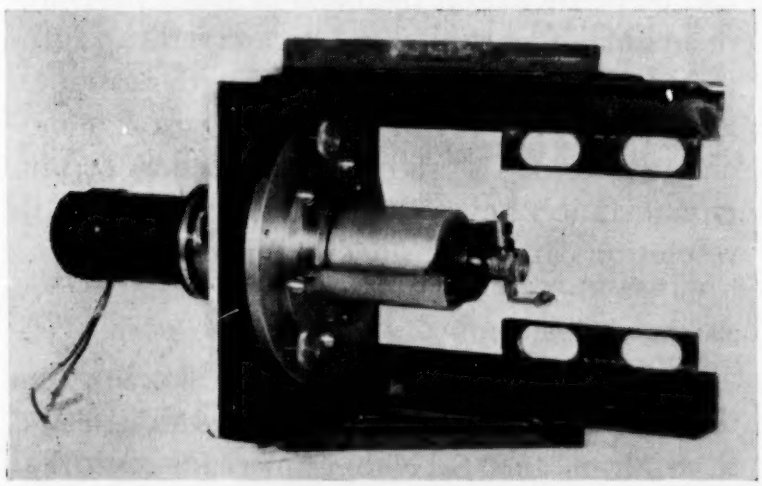

Photograph 1

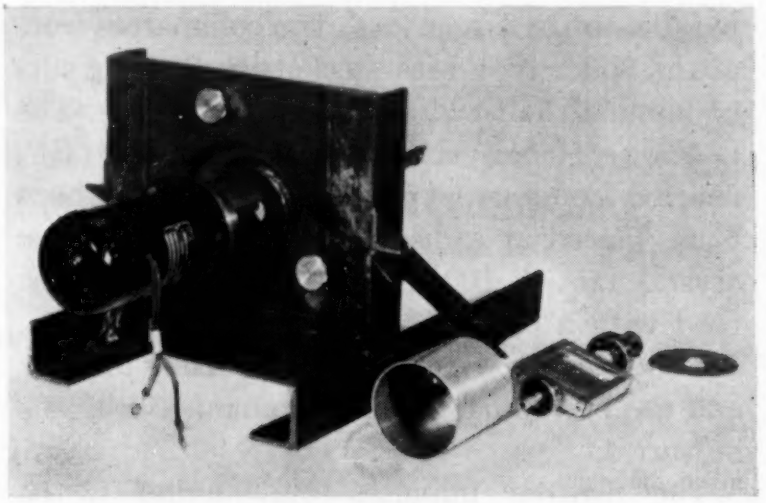

Photograph 2

larger surface of the plate. The crystal and the frame are enclosed in a thin cylindrical aluminium shield to reduce the air resistance in rotation. The crystal is driven by a 100 W series wound electric motor which gives a maximum speed of 15 000 r.p.m. The rotor together with the crystal are very light so that dynamic balancing is not required, care being taken only to ensure that the crystal is mounted symmetrically with respect to the axis.

An electrical impulse for sychronizing the time analyzer is derived from an optical arrangement with a photocell. On the upper end of the rotor axis, two small glass right-angled prisms are mounted with their larger faces pressed together. A narrow light beam when reflected through 90° by the prisms is focussed on a 1 mm slit in front of a photocell at a distance of about 50 cm from the axis. The use of two prisms pressed together ensures that the impulses are 180° apart. The crystal of course gives two neutron pulses, 180° apart, per revolution. The rise time of the light pulse is of the order of microsecond for speeds of rotation as low as 1000 r.p.m.

4. Measurements with the Experimental Chopper

The measurements described below were made at the VVRS reactor in Warsaw. Measurements were made of the width of the neutron pulse as a function of the speed of rotation. The crystal used was zinc cut with its (002) planes

parallel to the larger face. The collimators were of the Soller type with steel strips forming slits of nominal half-width 10 minutes of arc. The neutron detector consisted of a bank of BF_3 neutron counters of effective thickness about 6 cm, placed at a distance of 3.19 m from the crystal axis. A 100-channel time analyzer was used with a channel width of 5 microseconds. The interval between the synchronizing impulse and the beginning of the first channel could be be varied.

The neutron impulses were found to be approximately Gaussian in shape. The counting rate in the analyzer was 250 counts/min at the maximum, and the background counting rate was less than 1% of this value. The half-width of the observed impulses includes contributions due to the channel width and the effective detector width. Thus the total width, τ, will be given by:

$$\tau^2 = \tau_a^2 + \tau_b^2 + \tau_c^2 + \tau_d^2$$

where τ_d is the detector width and τ_c the analyzer channel width. From (11) it is seen that τ_a is proportional to $1/\omega$ so that a plot of τ^2 versus

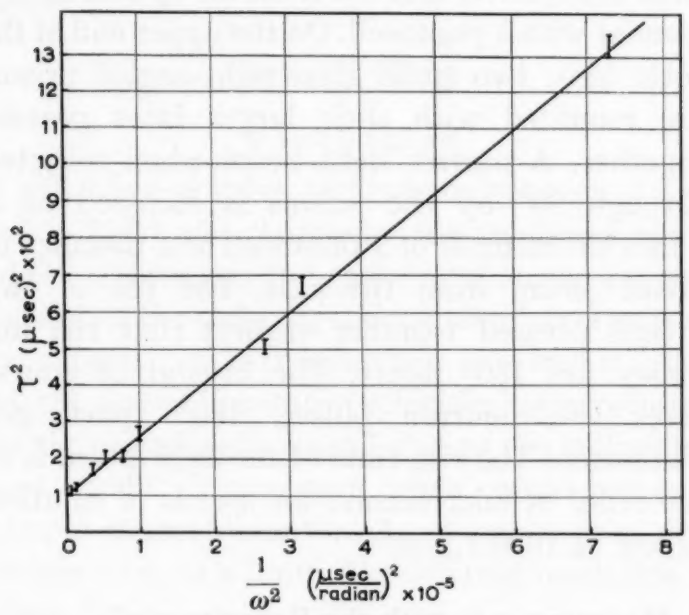

Fig. 3
Plot of τ^2 versus $1/\omega^2$ for experimental model chopper.

$1/\omega^2$ should give a straight line of slope $2\ (\ln 2)^{\frac{1}{2}}\ \delta$ and intercept at $1/\omega^2 = 0$ of $\tau^2 = \tau_b^2 + \tau_c^2 + \tau_d^2$. In fig. 3 there are plotted the observed values of τ^2 as a function of $1/\omega^2$. From the slope δ is found to have the value of 27 ± 1 minutes of arc which is a reasonable value for the collimator and crystal used. The limiting value of τ was found to be 31 ± 1 microseconds. The detector half-width was estimated, on the basis of its thickness and the average neutron velocity, to be 20 microseconds. τ_b is then found to be approximately equal to 22 microseconds which from eq. (11) gives for α the value 9.4 minutes which is in good agreement with its design value.

Since the light pulse giving the synchronizing impulse was not coincident with the neutron pulse at the crystal, the centre of the neutron pulse at the detector moved in the analyzer channels as ω was varied. Since the delay between the synchronizing pulse and the neutron pulse at the crystal depends on $1/\omega$ a plot of the channel number of the centre of the pulse at the detector versus $1/\omega$ gives a straight line, and the intercept at $1/\omega = 0$ gives the channel number of the centre of the pulse corresponding to the true time of flight of the neutrons. In this way the time of flight for the particular Bragg angle used was found to be 1005 ± 5 microseconds which corresponds to a wavelength of 1.28 A. At this wavelength the pulse of second order neutrons given by the crystal was observed to have an amplitude of 2% of the first order pulse.

5. Concluding Remarks

The rotating crystal chopper is a comparatively simple device to build. Its performance can be predicted on the basis of static measurements made on the crystal on a crystal spectrometer. Its normal limiting wavelength resolution is the same as that of a normal crystal monochromator. It is shown that under certain circumstances however, the effective wavelength resolution can be considerably increased.

Acknowledgements

The author wishes to thank K. Skoczek who was responsible for the mechanical design and S. Szafran and S. Nabywaniec for technical assistance.

NUCLEAR INSTRUMENTS AND METHODS 8 (1960) 249–254; NORTH-HOLLAND PUBLISHING CO.

ZUM EINFLUSS DER KRISTALLFORM AUF DAS ENERGETISCHE UND ZEITLICHE AUFLÖSUNGSVERMÖGEN EINER SZINTILLATIONSANORDNUNG

G. LUCK

Jena, Lasallestr. 6

Eingegangen am 25. April 1960

A decrease of the number of reflections of photons in a scintillation crystal leads to smaller fluctuations in time and pulse amplitudes of the output signal. This is possible with special forms of the scintillator. Mainly for great scintillator dimensions and high particle energies this seems of some interest. It is one of the ways to raise the energetical and time resolution of a scintillation arrangement.

1. Einleitung

Neben dem guten zeitlichen Auflösungsvermögen eines Szintillationszählers wünscht man oft ein hohes energetisches Auflösungsvermögen. Mehrere Wege wurden bereits eingeschlagen, um den Szintillationsprozess so zu beeinflussen, damit dieses Ziel erreicht wird. Man entwickelte empfindliche Fotokatoden, verbesserte die Elektronenoptik der Vervielfacher und dergleichen mehr.

Aber kein noch so gut ausgesuchter Szintillator auf der einen und kein noch so optimal gestalteter Multiplier auf der anderen Seite bringen den gewünschten Erfolg, wenn nicht beide gleichzeitig in sinnvoller Weise zum Szintillationszähler vereint werden. Alle Fotonen einer Szintillation sollen möglichst vollzählig zur Fotokatode gelangen. Praktisch entstehen aber Verluste durch die Absorption im Kristall bzw. Lichtleiter und durch die unvollständige Reflexion des umgebenden Reflektormaterials. Die Verlustrate wird umso höher ausfallen, je grösser die Zahl der Reflexionen ist. Die Form des Szintillators hat einen grossen Einfluss darauf.

2. Die Statistik des Szintillationsprozesses

Im wesentlichen besteht der Szintillationsvorgang aus sechs Einzelprozessen[1]):

1. Die Absorption der Kernstrahlung im Szintillator.

2. Die Umwandlung der Energie durch Lumineszenz in Lichtquanten.

3. Der Transport der Fotonen zur Fotokatode.

4. Die Auslösung von Fotoelektronen aus der Fotokatode.

5. Die Elektronenvervielfachung durch die Dynoden des Multipliers.

6. Die Analyse der Ladungsimpulse durch die nachfolgende elektronische Anordnung.

Alle sechs Vorgänge sind statistischer Natur. So hängt die Absorption der Strahlung im Szintillator davon ab, an welcher Stelle sie erfolgt; dasselbe gilt für die Umwandlung in Lichtquanten. Die pro Energieeinheit der einfallenden Strahlung erzeugte Fotonenzahl hängt offensichtlich von der Homogenität der Anregungszentren im Kristall ab. Optische Inhomogenitäten, Sprünge u.s.w. verursachen zusätzliche statistische Schwankungen der Ausgangsimpulse. Ein auf die Katode fallendes Foton kann entweder ein Fotoelektron auslösen oder keines. Die fotoelektrische Empfindlichkeit, die auch mit veränderlicher Fotonenenergie variiert, ist ebenfalls nicht an allen Punkten gleich. So ist diese Umwandlung durch das polychromatische Licht statistisch gesprochen ein aus vielen Einzelprozessen zusammengesetztes "Entweder–Oder" Ereignis. Dasselbe gilt vom Transport der Fotonen zur Katode. Die Chance, überhaupt zur Katode zu gelangen, hängt im wesentlichen von der Zahl der Reflexionen im Kristall und Lichtleiter ab. Nur ein durchschnittlicher Bruchteil f

[1]) Price, Nuclear Radiation Detection (McGraw-Hill, 1958).

der ursprünglichen Fotonenzahl wird ankommen. Da f von der Geometrie der Szintillatoranordnung abhängt – genau wie die einzelnen Umwandlungsgrade von Fotonen in Fotoelektronen –, so bewirkt schon eine einfache Drehung des Vervielfachers gegenüber seinem Szintillator eine veränderte statistische Verteilung der Ausgangsimpulse. Der gesamte Szintillationsvorgang ist ein komplexes statistisches Zusammenspiel aller angeführten sechs Einzelprozesse. Die statistische Durchrechnung wurde bereits weitgehend von Breitenberger[2]) durchgeführt. Daneben existieren noch viele Beiträge anderer Autoren[3–6]), die ebenfalls mehr oder weniger vollständig den gesamten Szintillationsprozess mathematisch statistisch behandelten. An dieser Stelle soll ausführlicher auf den Einfluss der Kristallform und der Verspiegelung der Szintillatorwände eingegangen werden. Es wird sich heraus-stellen, dass der Lichtüberführungsfaktor f auch durch die Form der Kristalle beeinflussbar ist.

Die statistische Behandlung der gestellten Aufgabe erfolgt mit der Methode der "Momente erzeugenden Funktionen" oder kurz "erzeugende Funktionen" (generating functions), wie sie bereits von Laplace und De Moivre eingeführt wurden. Diese Methode erlaubt eine konzentrierte mathematische Behandlung mancher statistischer Probleme.

Es ist das Ziel aller mathematischen Ausführungen, das relative Schwankungsquadrat

$$R^2 = \frac{\delta^2}{\overline{n}^2} \tag{1}$$

zu finden.
Mit der Definition der Generatorfunktion

$$G(x) = \sum_n p_n x^n$$

(x = Hilfsvariable) (2)

folgt an Stelle von (1):

$$R^2 = \frac{G''(1) + G'(1) - [G'(1)]^2}{[G'(1)]^2} \tag{3}$$

(G' = Ableitung nach x)

Für eine vorliegende Problemstellung bleibt nur übrig, die jeweilige Generatorfunktion zu finden, mit deren Hilfe sich dann das relative Schwankungsquadrat nach Formel (3) errechnen lässt.

So findet man für die Erzeugnung der Sekundärelektronen im Vervielfacher eine Generatorfunktion, die sich nur in rekursiver Form ausdrücken lässt. Die Generatorfunktion $G_2(x)$ für die zweite Elektronenkaskade ist

$$G_2(x) = G[G_1(x)] \tag{4}$$

oder allgemein

$$G_{n+1}(x) = G[G_n(x)]\,, \quad \text{mit} \tag{5}$$

$$G_1(x) = G(x) = q + px^m\,. \tag{6}$$

Die Wahrscheinlichkeit m Sekundärelektronen zu erzeugen ist p, der Fall der inaktiven Wahrscheinlichkeit ist $q = 1 - p$.

Die Zahl der Dynoden sei n.

Liegt eine Poissonverteilung (Normalverteilung) vor, so gilt wegen

$$G(x)\, e^{-\lambda(1-x)} \tag{7}$$

nach mehreren Umformungen

$$R_n^2 = \lambda^2 \frac{\overline{m}^{n-1}(\overline{m}^n - 1)}{\overline{m}^{2n}(\overline{m} - 1)} \tag{8}$$

($\overline{m}$ = mittlere Zahl der erzeugten Sekundärelektr.)

mit $\lambda^2 = R^2(X_1)$ und X_1 als Zahl der Elektronen an der ersten Dynode. Für $\overline{m} > 1$ und grössere n ($n \geq 10$) vereinfacht sich Formel (8) zu

$$R_n^2 = \frac{\lambda^2}{\overline{m}(\overline{m} - 1)}\,. \tag{9}$$

Das ist eine Beziehung, die oft im Zusammenhang mit den statistischen Schwankungen eines Szintillationszählers angegeben wird. Die relativen Schwankungen der Elektronen an der ersten Dynode erscheinen am Ausgang um den Faktor $\sqrt{\overline{m}(1/(\overline{m} - 1)}$ verkleinert.

Für grössere Werte von n sind diese Schwankungen von n selbst unabhängig. Eine Erhöhung der Stufenzahl n ändert also nichts an der

[2]) E. Breitenberger, Progress in Nuclear Physics Vol. **4** (1955).

[3]) F. J. Garlick und G. T. Wright, Brit. J. Appl. Phys. **5** (1954) 13.

[4]) G. T. Wright, Phys. Rev. **91** (1953) 1282.

[5]) G. T. Wright, J. of Sci. Instr. **31** (1954) 377.

[6]) W. Feller, Probability Theory and its Applications, (John Wiley, London, 1950).

Schwankungsbreite der Ausgangsimpulse. Es kommt nach Formel (9) nur darauf an, die Zahl der Partikel an der ersten Dynode so hoch wie möglich zu halten, damit die Ausgangsschwankungen klein bleiben. Im λ^2 stehen dann alle statistischen Änderungen verursacht durch unvollständige Lichtüberführung, inhomogen empfindliche Fotokatoden, wechselnde Szintillatorausbeute u.s.w. Um auch diese Einflüsse zu erfassen, wählte Breitenberger einen anderen Ansatz für die Generatorfunktion. Er ging aus von

$$G(x) = E(1 - f) + f \cdot V(x) \qquad (10)$$

mit $V(x)$ als Generatorfunktion der Verstärkung des Vervielfachers, $E(x)$ als Generatorfunktion der Elektronenemission und mit der durchschnittlichen Fotonenüberführungszahl $\bar{f} = \sum_i q_i f_i$.

Als Ergebnis fand er für die relative quadratische Schwankung des Ladungsstosses am Ausgang:

$$R_Q^2 = R_f^2 + \frac{1 + R_v^2}{\bar{E}\,\bar{f}}. \qquad (11)$$

Dieses Ergebnis entspricht dem bereits auf anderem Wege gefundenen Resultat von Garlick und Wright[3]). R_V ist die relative Schwankung, die durch den Verstärkervorgang im Multiplier entsteht, R_f die aus der Fotonenleitung herrührende.

Trägt man nun R_Q^2 als Funktion von $(Ef)^{-1}$ auf, so erhält man eine sehr eindringliche Darstellung (Abb. 1), wie sie bereits Hopkins 1951 vorschlug. Er fand eine Gerade, die um R_f^2 über

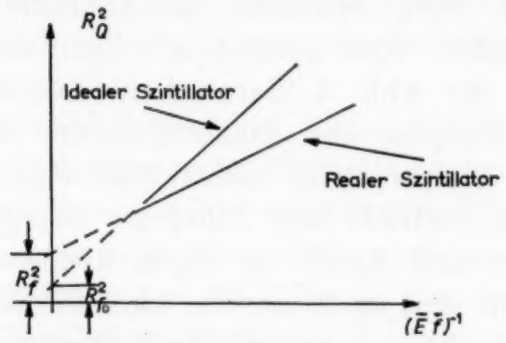

Abb. 1. R_Q^2 als Funktion von $(Ef)^{-1}$.

dem Koordinatenursprung die Ordinate schnitt, genau wie es auch Formel (11) verlangt, wenn f keine Konstante sein soll. Im Falle $f = \text{const.}$, müsste die Gerade durch den Nullpunkt laufen, so wie es sehr oft in der Literatur beschrieben ist. Die Neigung der Geraden ist ein Mass für die Katodenempfindlichkeit des Vervielfachers. Sie verläuft steiler bei grösseren Empfindlichkeiten.

Der Wert von R_f^2 ist offensichtlich davon abhängig, wieviel Schlieren oder sonstige optische

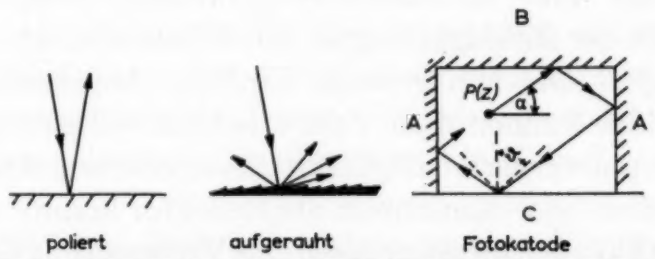

Abb. 2. Schematische Darstellung des Reflektionsvorganges in einem Szintillator. Der Winkelbereich, unter dem keine Totalreflexion auftritt, beträgt 2ϑ.

Fehlstellen der Szintillator besitzt. Jedoch selbst unter der Annahme eines optisch idealen Kristalles, bleibt eine überraschende Tatsache bestehen, dass nämlich R_f^2 mindestens noch in der Grössenordnung 10^{-3} (rel. Schwankung von 3 bis 4%) ist. Namentlich bei guten Szintillationsspektrometern und hohen Quantenenergien ist oft dieser Wert allein verantwortlich für das Gesamtauflösungsvermögen! Zum Beispiel für Gammaenergien grösser als 1 MeV kann man mit einem Szintillator aus NaJ (Tl) $\bar{E}\,\bar{f} > 10^3$ ansetzen und dann ist R_f^2 von merklichem Einfluss. Woher kommt selbst bei optisch idealen Kristallen diese "Grundschwankung" R_{f0}^2? Wie lässt sie sich beeinflussen? Die erste Frage lässt sich dahingehend beantworten, dass selbst optisch ideale Kristalle ein $R_{f0}^2 \approx 10^{-3}$ durch die statistische Zahl der Reflexionen des Lumineszenzlichtes innerhalb des Kristalles erhalten. Das mögen die folgenden Ausführungen und Abbildungen belegen (Abb. 2). Rein anschaulich leuchtet aus der rechten Darstellung der Abb. 2 ein, dass die Anzahl der Reflexionen $r(z)$ davon abhängt, an welchem Kristallort $P(z)$ die Fotonen entstehen und unter welchem Winkel von $P(z)$ gegen die Flächen A, B und C sie emittiert werden. Da das Kristallmedium als optisch sehr gut durchlässig betrachtet werden soll (gilt nicht für Polykristalle und zu kurzwelligen Licht), so tritt beim Auftreten auf die Fläche C sehr oft der Fall einer Totalreflexion ein. Erst wenn das Foton durch eine Störstelle im Szintillator bzw. durch den

Reflektor in eine andere Richtung gelenkt wird, kann es in günstige Winkelbereiche kommen und schliesslich doch zur Fotokatode gelangen. Unter Umständen hat es dabei eine recht erhebliche Zahl von Reflexionen durchgemacht. Nicht nur Kristallinhomogenitäten, sondern auch der Rauhigkeitsgrad der Reflektorwände A und B sind von grossem Einfluss. Angerauhte Wände können diese Zahl erheblich reduzieren. Mit pulverisiertem MgO statt hochpoliertem Magnesium oder Aluminium als Reflektor konnte in der Tat auch messtechnisch eine Verbesserung des Energieauflösungsvermögens erzielt werden[1]).

Durch jede Reflexion treten Verluste an Fotonen im Reflektormaterial auf. Im Endergebnis geben dann Schwankungen der Zahl der Reflexionen eine entsprechende Schwankung der Fotonenzahl. Mit wachsender Zahl der Reflexionen nimmt auch das relative Schwankungsquadrat der Fotonen zu. Vernachlässigt werden Verluste durch die Absorption im Szintillator gegenüber den Verlusten im Reflektormaterial. Quantitativ folgt so für das Quadrat der relativen "Grundschwankung" R_{f0}^2:

$$R^2_{f0} = (1 - \rho)^2 R_r^2 . \qquad (12)$$

Dabei sind ρ der Reflexionsfaktor und R_r die relative Fotonenschwankung auf Grund der Reflexionen. Um R_{f0} klein zu halten, sind ein grosses ρ und nur wenige Reflexionen anzustreben. Für MgO und die in Frage kommenden Wellenlängen um 4000 Å liegt ρ in der Grössenordnung 0.9. Das ist ein ziemlich hoher Wert, wenn man die Skala der Reflexionskoeffizienten fester Körper betrachtet.

Gelingt es nun, die Generatorfunktion des Reflexionsvorganges aufzustellen, so ist R_r^2 bestimmbar und gemäss Formel (12) auch R_{f0}^2. Für den Fall, dass gleichwahrscheinlich ein bis n-Reflexionen auftreten können, findet man als Generatorfunktion folgenden Ausdruck:

$$G_n(x) = \frac{x}{n} \frac{x^n - 1}{x - 1} . \qquad (13)$$

Treten nur einmalige bis doppelte Reflexionen auf, so wird $R_r^2 = 0.11$ und mit $\rho = 0.9$ würde $R_{f0}^2 \approx 10^{-3}$.

Das ist aber genau die Grössenordnung, wie sie bereits für den idealsten Kristall als nicht unterschreitbar angegeben wurde. Zieht man noch die Möglichkeit von Dreifachreflexionen in Betracht, so wächst R_f^2 auf den Wert 0.17 an. Für gleichwahrscheinlich auftretende Reflexionen bis $n = 20$ wirde der Verlauf von R_r^2 als Funktion von n in Abb. 3 errechnet. Man erkennt daraus deutlich, dass besonders stark in Anfangsteil der Kurve ein Anstieg von R_r^2 erfolgt. Eine Ausschaltung aller Drei- bis Mehrfachreflexionen auf nur einfache und doppelte, würde das Auflösungsvermögen um mindestens 20% verbessern.

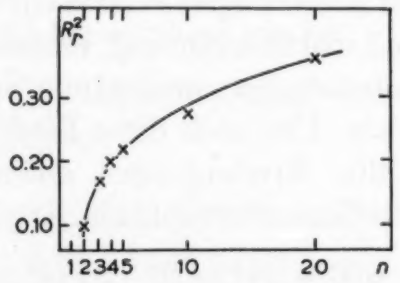

Abb. 3. Das relative Schwankungsquadrat R_r^2 als Funktion der Zahl der Reflexionen n im Szintillator.

Ein Weg dazu wurde bereits angedeutet, nämlich das umgebende Reflektormaterial anzurauhen. Eine andere Möglichkeit wäre eine geeignete Formgebung des Szintillators. Statt zylindrischer Formen sollte man besser konische verwenden. Namentlich bei grossen Flüssigkeitsszintillatoren oder plastischen Phosphoren und hochenergetischen Partikeln, für deren Nachweis ein gutes Auflösungsvermögen gewünscht wird, erscheint die konische Form vorteilhafter. Rein geometrisch kann man sich anhand der Abb. 4 klarmachen, dass mit erhöhter Neigung der Flächen A der Winkelbereich kleiner wird, unter dem eine Totalreflexion auftritt. Das führt zu weniger Reflexionen und damit zu einem kleineren R_{f0}. Natürlich sind auch andere, ähnliche Kristallformen denkbar – etwa ein konisch zugespitzter Zylinder –, bei dem sich ebenfalls die Zahl der Reflexionen herabsetzen liesse.

In der Praxis hat man keine idealen Szintillatoren und ein Teil des R_{f0}-Wertes hat auch andere Ursachen. Das können bevorzugte Lumineszenzgebiete oder durch Nachleuchten der

Kristalle verursachte unnormale Szintillationsänderungen sein. Allerdings nur unter ungünstigen Verhältnissen gewinnen diese Faktoren gegenüber dem Einfluss der Statistik des Reflexionsvorganges vergleichbar Bedeutung.

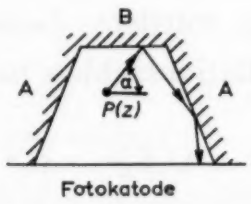

Abb. 4. Durch die konische Form wird der unter dem Winke α emittierte Lichtstrahl (vergl. Abb. 2) nicht mehr tota reflektiert.

3. Grenzen des zeitlichen Auflösungsvermogens

Das Auflösungsvermögen von Koinzidenzanordnungen für ultrakurze Zeiten, zum Beispiel von Chronotons, hängt ab von den zeitlichen Schwankungen der Anstiegszeit der Szintillationsimpulse. Das gilt auch für Koinzidenzanordnungen, die von der Impulsbreite nicht stark abhängig sind, wie die Differentialmethode von Z. Bay[7]).

Das zeitliche Auflösungsvermögen für sehr kurze Zeiten wird durch den Szintillationszähler bestimmt, nicht aber durch die Technik der Koinzidenzkreise. Drei Faktoren sind es, die für die Schwankungen der Anstiegszeit der Szintillationsimpulse verantwortlich sind:

1. Die Fotonenemission des Szintillators erfolgt statistisch.

2. Schwankungen der Sammelzeit der Fotonen durch die endliche Grösse von Szintillator und Lichtleiter.

3. Schwankungen der Fotoelektronen und Sekundärelektronen im Vervielfacher.

Beim Čerenkovzähler entfällt die erstgenannte Ursache. Anstelle dieser Schwankungen treten die Abweichungen der Flugzeit der relativistischen Partikel im Radiator.

R. F. Post und L. I. Schiff[8]) errechneten erstmalig das mittlere Schwankungsquadrat Δt_E^2 für die unter 1) angeführte Schwankungsursache. Sie fanden dafür folgenden Ausdruck:

$$\Delta t_E^2 \approx \frac{t_0^2 q}{q_0^2}\left[1 + \frac{2(q+1)}{q_0}\right]. \qquad (14)$$

Dabei sind t_0 die Abklingzeit des Phosphors, q die Zahl der Elektronen, die mit Sicherheit zur Impulsbildung beitragen und q_0 die durchschnittliche Gesamtzahl der emittierten Fotoelektronen (bei einem angenommenen Überführungsgrad der Elektronen aus der Katode zur ersten Dynode von 100%). Als Beispiel für ziemlich optimale Verhältnisse seien 1 MeV-Elektronen mit einem Umwandlungsgrad von 1% der Fotonen in Fotoelektronen für Terphenyl in Toluol ($t_0 \approx 2.5 \times 10^{-9}$ sec) angenommen. Nur das erste emittierte Elektron möge zur Impulsbildung ausgenutzt werden; also $q = 1$. Dann folgt für $\overline{\Delta t}$:

$$\sqrt{\overline{\Delta t^2}} \approx 3 \times 10^{-11}\,\text{sec}\,.$$

Für Koinzidenzmessungen ist dieser Wert noch mit $\sqrt{2}$ zu multiplizieren.

Diese Grösse von einigen 10^{-11} sec für die Schwankungen der Fotonenemission kann man als Grenzwert ansehen, wie er zur Zeit mit den gebräuchlichen Szintillatoren und Vervielfachern für ultrakurze Zeiten erreichbar ist. Wenn es durch wirksamere Fotokatoden gelänge, den Umwandlungsgrad von Fotonen in Fotoelektronen zu steigern, so würde q_0 anwachsen und man erhält für die Schwankungen der Fotonenemission noch kleinere Zeitwerte. Ein Weg in dieser Richtung stellt die Entwicklung der Multialkali-Katode dar. Sie hat eine etwa 2 bis 3-fach höhere Empfindlichkeit im Vergleich zu den üblichen Fotokatoden vom Typ Cs-Sb.

Auch die Schwankungen $\overline{\Delta t}_V$ der Elektronen der Fotokatode und Dynoden eines Vervielfachers lassen sich bereits in die Grössenordnung einiger 10^{-11} sec bringen. Normalerweise stellen sie mit konventionellen Vervielfachertypen den Hauptanteil der zeitlichen Gesamtschwankungen. Das gilt vor allem für Ausführungsformen mit Jalousie- und Netzdynoden. Speziell für die Kurzzeittechnik entwickelte und im Handel erhältliche Typen, wie zum Beispiel die sowj. Vervielfacher ФЭУ-33 und ФЭУ-36 und der amerikanische RCA 6810 A, erreichen schon Anstiegszeiten – ausgelöst von nur einem bzw.

[7]) Z. Bay, Phys. Rev. **83** (1951) 242.
[8]) R. F. Post and L. J. Schiff, Phys. Rev. **80** (1950) 1113.

weningen Fotoelektronen – von der Grössenordnung 10^{-9} sec und weniger. Der RCA 6810 A ist ein modifizierter RCA 6810, dessen ebene Fotokatode durch ein gewölbte ersetzt wurde, um die Laufzeitschwankungen von der Katode zur ersten Dynode zu verkleinern. Darüber hinaus gibt es noch eine Reihe anderer Massnahmen, um die Laufzeiten der Elektronen im Vervielfacher zu vermindern. Aus der Zahl der Möglichkeiten erwähne ich nur eine interessante Lösung, die RCA beim Typ C 7251 beschritt. Durch Spannungen von alternierendem Vorzeichen an den Dynodenstrecken erreichte man eine schnelle Anfangsbeschleunigung mit anschliessendem raschen Abbremsen der Elektronen kurz vor der nächsten Dynode. Die grossen Streuungen der Anfangsgeschwindigkeiten der Foto- und Sekundärelektronen wurden vermindert und durch das Abbremsen wurde wieder eine Geschwindigkeit hergestellt, wie sie für eine maximale Ausbeute an Sekundärelektronen notwendig ist. Durch dieses Beschleunigungs-Bremsprinzip liessen sich die zeitlichen Schwankungen auf kleiner als 10^{-10} sec herabdrücken!

Bleibt nur noch die Berechnung der Schwankungseinflüsse, wie sie von den verschiedenen Sammelzeiten der Fotonen im Szintillator und Lichtleiter entstehen. Auf Grund der Beziehung

$$\sqrt{\overline{\Delta t_{\mathrm{E}}{}^2}} \approx 3 n_{\mathrm{B}} \sqrt{\overline{\Delta s_{\mathrm{F}}{}^2}} \times 10^{-11} \text{ sec}\,, \qquad (15)$$

mit der mittleren Schwankung $\sqrt{\Delta s_{\mathrm{F}}{}^2}$ (in cm) des Laufweges und n_{B} als Brechzahl des Szintillators für die wirksame Fluoreszenzwellenlänge ist eine Abschätzung dieser Grösse möglich.

Je nach der Zahl der Reflexionen im Szintillator und Lichtleiter werden sich auch die Laufwege voneinander unterscheiden. Die absolute Grösse von $\Delta s_{\mathrm{F}}{}^2$ hängt natürlich von der im Einzelfall benutzten Anordnung ab und ist nicht einfach mathematisch zu erfassen. R. F. Post[9]) gab in erster Näherung für einen zylindrischen Lichtleiter eine Abhängigkeit zwischen Schwankung und Länge des Lichtleiters an.

Prinzipiell steht man jedoch vor der gleichen Frage wie im Falle des energetischen Auflösungsvermögens nicht zu kleiner Partikelenergien: Wie vermindert man im statistischen Mittel die Zahl der Reflexionen? Bereits D. C. Moore[10]) bestätigte messtechnisch den Einfluss einer verbesserten optischen Koppelung zwischen Szintillator und der Fotokatode eines RCA 4646. Die Zeitauflösung wurde eindeutig besser.

Da sich die mittlere Gesamtschwankung $\overline{\Delta t_{\mathrm{G}}}$ eines Szintillationszählers nach Formel

$$\sqrt{\overline{\Delta t_{\mathrm{G}}{}^2}} = \sqrt{\overline{\Delta t_{\mathrm{E}}{}^2} + \overline{\Delta t_{\mathrm{V}}{}^2} + \overline{\Delta t_{\mathrm{F}}{}^2}} \qquad (16)$$

berechnet, und alle Summanden unter der Wurzel mit gleichem mathematischen Gewichtsfaktor auftreten, so dürften unter der Annahme optimaler Verhältnisse der Einflüsse von 1) und 3) die Schwankungen der Sammelzeit der Fotonen im Bereich der Mikromikrosekunden nicht mehr vernachlässigbar sein. So wie es für bestimmte Messungen des energetischen Auflösungsvermögens auf möglichst wenige Reflexionen ankommt, so gilt das gleiche auch für Kurzzeitmessungen. Dabei wird man in Zukunft der Form und Güte des Szintillators und des umgebenden Reflektors mehr Beachtung schenken müssen.

Zusammenfassung

Ausgehend von der Forderung nach einer kleinen relativen statistischen Schwankung der Ausgangsimpuls am Vervielfacher wird gezeigt, dass Schwankungen der Fotonenüberführungszahl eine zusätzliche Verschlechterung des energetischen Auflösungsvermögens bewirken. Dabei hat auch die Kristallform einen Einfluss. Durch günstig gewählte Formen kann man die Zahl der Reflexionen im Szintillator herabsetzen. Namentlich für hohe Teilchenenergien und grosse Szintillatoren erreicht man bessere energetische Auflösungswerte.

Auch das zeitliche Auflösungsvermögen im Bereich von Zeiten kleiner als ca 10^{-11} sec ist nicht mehr von den Schwankungen der Sammelzeit der Fotonen im Szintillator unabhängig. Eine weitgehende Verminderung der Zahl der Reflexionen erscheint dann ebenfalls angebracht.

[9]) R. F. Post, Nucleonics, **10** (1952) 56.

[10]) D. C. Moore, Nucleonics (1955) p. 55, Special Report.

NUCLEAR INSTRUMENTS AND METHODS **8** (1960) 255–258; NORTH-HOLLAND PUBLISHING CO.

LETTERS TO THE EDITOR

IRON-FREE TOROIDAL BETA-BETA COINCIDENCE SPECTROMETER†

MELVIN S. FREEDMAN, FRANK WAGNER, JR., FRED T. PORTER, JOHN TERANDY and PAUL P. DAY

Argonne National Laboratory, Lemont, Illinois

Received 14 March 1960

The first half of a double beta spectrometer, being an iron-free version of the "sliced orange" design of Kofoed-Hansen *et al.*[1]) has been completed. The dual instrument consists of two identical, independent, "back-to-back", plane normal to the axis midway between its detector (D) and the source (S), i.e., the conductors bounding the entrance and exit to the toroidal magnetic field have mirror symmetry, and are precisely formed to have their center

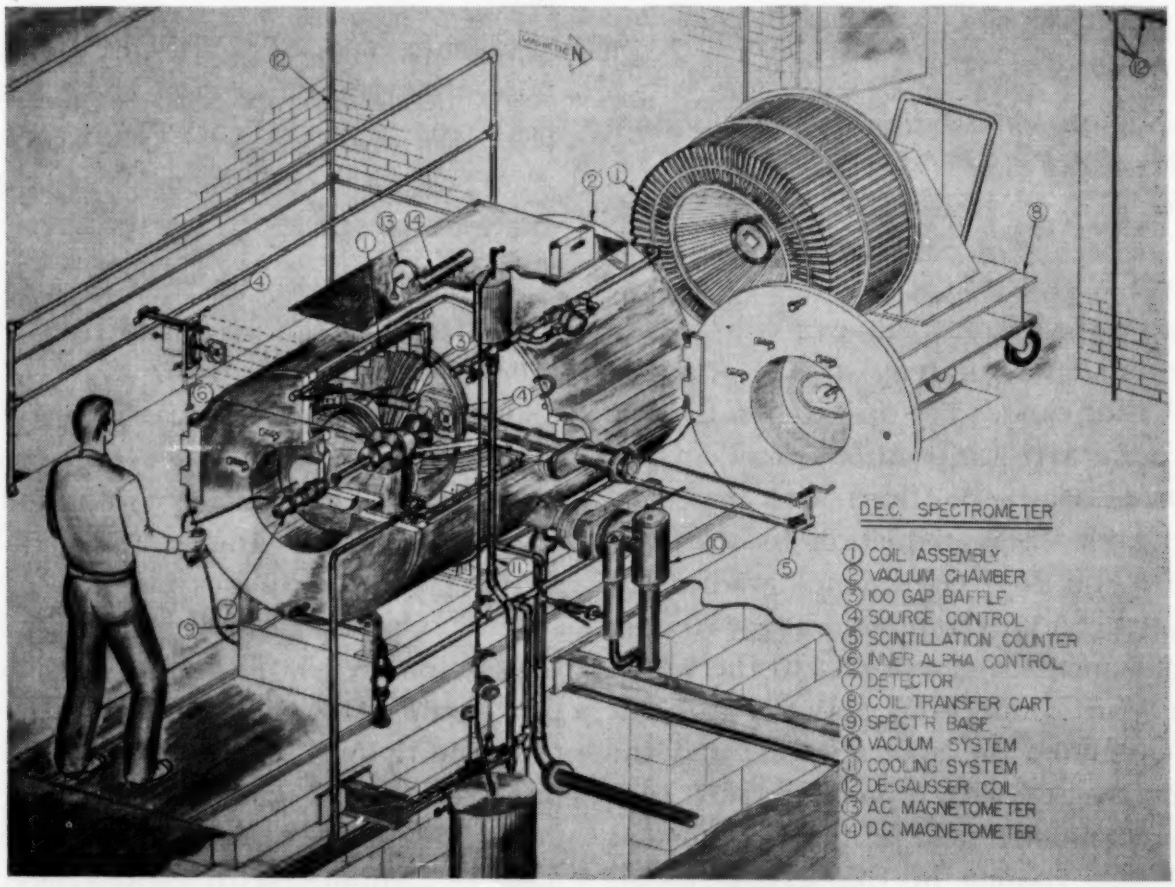

Fig. 1. Isometric projection of double beta spectrometer.
West toroidal coil shown withdrawn from vacuum chamber on coil transfer cart.

100 turn, 100 gap toroidal coils of 1 meter over-all diameter, mounted 12 cm apart in a 1.15 meter diameter, 1.6 meter long vacuum chamber, with the source midway between them on their common axis. Each coil is symmetrical about a lines lie on the focussing curve consistent with the parameter $b^{(1)} = \rho/r = p/A_0 e = 0.59$, where $H = A_0/r$. The performance of the instrument is quite sensitive to the choice of this parameter, owing to the cylindrical lens defocussing effects

† Based on work performed under the auspices of the U. S. Atomic Energy Commission.

[1]) O. Kofoed-Hansen, J. Lindhard and O. B. Nielsen, Det. Kgl. Dansk. Vid. Selsk. **25**, No. 16 (1950).

at the field boundaries[1]). Betas emitted between 30°—70° of the axis can be focussed. The open solid angle in the gaps between the conductors in the range 30°—70° is 20.2%. Distance S—D = 67 cm. E_{max} is 3.5 MeV, requiring 1150 amps at 140 kW, resulting in a maximum rise of 12° C over ambient of the iron-free-water cooled, flattened, tubular conductors ($\frac{1}{8}'' \times \frac{3}{8}''$ cross section). The current supply is a servo controlled motor generator, with series output stage consisting of 240 Delco transistors, type 2N278.

The performance results on the first toroid (transmission T, % of 4π steradians, measured with intensity calibrated sources; resolution, R, full width at half max):

Source Diam	$\frac{1}{8}''$	$\frac{1}{8}''$	$\frac{1}{8}''$	$\frac{1}{4}''$	$\frac{3}{8}''$	1 mm	1 mm
T (%)	19	16	2.8	16	18	13	1.6
R (%)	0.93	0.40	0.21	0.56	0.88	0.30	0.13

One can use the two instruments so as to add their transmissions. As they are rotationally "in phase", they can also be operated in tandem (source at usual detector position, small circular baffle at usual source position) with improved resolution and a large reduction in scattered background. For β—β coincidence studies the efficiency at $R \leq 1\%$ is improved by < 100 over existing instruments. All currents to the toroid and in the series connections between adjacent turns are circulated on coaxial leads, and the coils are constructed with a precision such that the leakage magnetic field at the source and throughout the volume of the second toroid $\leq 10^{-5}$ of the focussing field in the first. Thus 1 keV and 3 MeV betas can be focussed with negligible mutual interference. The construction is entirely non-ferrous, and the instrument is housed in a specially constructed non-ferrous building with all ferrous equipment, generators, motors, pumps, etc., located over 40 feet away from the spectrometer. A 20 foot cubical degaussing coil array surrounding the instrument enables compensation of $H_{earth} \leq 10^{-4}$ oersteds.

Baffles adjustable from outside the spectrometer:

(a) limit exterior and interior conical acceptance angles at source and detector over the range 30°—70°;

(b) intercept axial quantum radiation;

(c) continuously adjust the open width of each gap symmetrically about the gap mid plane;

(d) intercept all multiloop trajectories thus preventing transmission of ghost peaks. (Ghost peak/true peak $\leq 3 \times 10^{-5}$);

(e) select and continuously vary the azimuthal angle into each spectrometer over 360° range.

With this latter baffle β—β angular correlation measurements can be made over the angular range 45°—180° with $T \geq 1\%$. A gamma detector (3″ NaI crystal) can be inserted through a gated side port near the source enabling β—γ coincidences and angular correlation studies. α energy analysis by pulse ion chamber at the source position provides for (α, e^-) coincidence studies. Operation and recording are remote and automatized. Detectors include scintillation counters with provision for cooling the photomultipliers, (no light pipes needed) and proportional end window counters. A port and gate allow source insertion and position adjustment in 1 minute. With various detectors introduced through the side port, triple coincidences ($\beta\beta\beta$), ($\beta\beta\gamma$), ($\beta\beta\alpha$), ($\beta\beta$X) can be observed. A more detailed description of this instrument will be published later.

BANDWIDTHS OF THE EQUAL TIME-CONSTANT AMPLIFIER

J. B. S. WAUGH

Physics Division, Atomic Energy of Canada Limited, Chalk River, Ontario†

Received 8 May 1960

The use of amplifiers with upper and lower pass band limits defined by equal RC time-constants is common in those nuclear physics applications requiring the best signal-to-noise ratio. The relevant noise theory is very well known[1]) but in work on low noise ion chambers[2]) and semiconductor particle detectors[3]) a knowledge of the effective amplifier noise bandwidths was required. Explicit mention of these parameters was not found in the literature and it may be of value to note them.

Consider an ideal amplifier with a level frequency response from zero to infinity and having a voltage gain G_0. The transfer function of such an amplifier when operated with its high frequency response determined by a single (integration) time-constant T_1 and its low frequency response defined by a single (differentiation) time-constant T_2 is $G_0\, pT_1/(1 + pT_1)\,(1 + pT_2)$. When both time-constants equal T, the square of the transfer function or power gain $G(f)$ becomes $4\pi^2 G_0{}^2 f^2 T^2/(1 + 4\pi^2 f^2 T^2)^2$. The maximum gain occurs when $2\pi fT = 1$, thus defining f_c, the centre frequency of the pass band. The overall voltage gain at f_c is 6 db less than that of the flat amplifier. The half-power bandlimit points, $f_{0.5}$, thus occur at 9 db below the original reference and are the roots of the bi-quadratic

$$32\pi^2 f^2 T^2/(1 + 4\pi^2 f^2 T^2)^2 = 1.$$

Hence, $$f_{0.5} = f_c(\sqrt{2} \pm 1)$$

and the half-power bandwidth, $B_{0.5}$, is

$$2f_c = 1/\pi T\,.$$

† Present address: Research School of Physical Sciences, Australian National University, Canberra, A.C.T., Australia.

The effective noise bandwidth B_n evidently differs from the half-power bandwidth since it must be dependent on the actual noise spectral distribution in the region of the pass band. An effective bandwidth can be defined as the width in cps of a rectangular pass band which passes the same noise power. The bandwidth, B_n, so defined[4]) $= (1/G_c)\int_0^\infty G(f)\mathrm{d}f$ where $G(f)$ is the available power gain at the frequency f and $G_c = G(f_c)$ is the power gain at the centre of the pass-band, f_c. This definition supposes that the noise is white, however, if this is not so but the noise has a spectral distribution $P_n(f)\Delta f$, then a bandwidth, containing the same noise power, can be defined from f_c/k to kf_c, i.e.

$$G_0{}^2 \int_{f_c/k}^{kf_c} P_n(f)\,\mathrm{d}f = \int_0^\infty G(f)P_n(f)\,\mathrm{d}f$$

where $G_0{}^2$ is the power gain of the flat amplifier

TABLE 1

Effective amplifier bandwidths for common noise spectral distributions

$P_n(f)$	Bandwidth $= \dfrac{k^2-1}{k} f_c$
f^0, shot noise	$\frac{1}{4}\pi f_c = 0.785\, f_c$
f^{-1}, flicker noise	$2f_c \sinh(\frac{1}{4}) = 0.505\, f_c$
f^{-2}, grid current noise	$\frac{1}{4}\pi f_c = 0.785\, f_c$

1) A. B. Gillespie, Signal, Noise and Resolution in Nuclear Counter Amplifiers (Pergamon Press, 1953).

2) J. B. S. Waugh, A Nuvistor Ionization Chamber Preamplifier, Atomic Energy of Canada Report, CREL-912 (1960).

3) J. M. McKenzie and J. B. S. Waugh, Silicon Junctions as Particle Spectrometers, Proceedings of the 7th Scintillation Counter Symposium, IRE, PGNS (1960).

4) S. Goldman, Frequency Analysis, Modulation and Noise (McGraw-Hill, 1948) p. 254.

assuming equal input and output impedances. Values of the resulting bandwidth, $(k^2 - 1)f_c/k$, are tabled below for the three most common types of noise distributions.

Thus for the "equal time constant amplifier", the half power or 3db bandwidth is twice the centre frequency while the effective noise bandwidth, though dependent on the noise spectral distribution, is also proportional to f_0 in the ratios given above.

The author wishes to acknowledge the assistance of R. E. Bell who read the manuscript and suggested a number of improvements.

BOOK REVIEWS

Experimental Nuclear Physics, Vol. III, Editor E. SEGRÈ, John Wiley and Sons, Inc., New York, Chapman & Hall Ltd., London 1959.

This volume completes the book edited by Professor Segrè. The preceding volumes are already well known standard reference works in the field. The present book deals with Radioactive Decay (E. Segrè), Alpha Radioactivity (G. C. Hanna), Gamma Rays and Beta Rays (Martin Deutsch and O. Kofoed-Hansen) and, Particle Accelerators (E. M. McMillan). The Editor gives in his contribution a very elegant account of the statistical laws governing the radioactive decay and the basic experimental methods used for measurements of decay constants. G. C. Hanna's chapter on Alpha Radioactivity is comparable in scope and magnitude to the recent Handbuch der Physik article by Perlman and Rasmussen. These two surveys of alpha radioactivity will certainly for a long time remain the standard sources of reference. Hanna's paper is perhaps somewhat easier to follow and can be recommended as an introduction into the field. The following two chapters deal with gamma and beta decay. The latter has been revised and brought up to date since the parity nonconservation was discovered. It contains the basic theory and a fairly detailed account of the experimental methods. The chapter on gamma decay on the other hand seems to the reviewer in certain parts somewhat outdated. The compilation of material for this chapter was finished already 1955. For this reason some of the statements in this chapter are no longer valid. But the authors have made several interesting comments and called attention to certain problems worth future studies. The last chapter by Professor McMillan gives a review of the development of particle accelerators from the early days in 1926 when the acceleration of electrons to about 400 keV was achieved by means of high voltage X-ray tubes and up to the CERN and Brookhaven 30 GeV strong focussing machines. The author has managed to cover this vast field in only 150 pages.

It is not necessary to recommend this volume to the readers. T. R. GERHOLM

The Isotope Index, July 1959, International Edition, Editor: J. L. SOMMERVILLE, Scientific Equipment Co, Indianapolis 19, Indiana, $ 5.50.–. This handy booklet is a complete guide to the isotopes, containing information concerning U.S. A.E.C. licensing procedures, isotope supplies, availability, prices, catalogue numbers etc. of labelled compounds, standard sources and sources for radiographic and therapeutic use. Those interested in the industrial and medical applications of labelled compounds of radioactive and stable isotopes will find this Isotope Index very useful. T. R. GERHOLM

NUCLEAR INSTRUMENTS AND METHODS 8 (1960) 259–260; NORTH-HOLLAND PUBLISHING CO.

NEWS ITEMS

ACCELERATOR CONFERENCE

High Voltage Engineering Corporation has organized an accelerator conference to be held in Amsterdam October 4–6, 1960. The conference report will be published in our journal at an early date.

The conference program is the following:

Tuesday, October 4 - Nuclear Physics

Chairman: Prof. H. BRINKMAN,
University of Groningen, The Netherlands

Resonance Reactions—Prof. P. M. ENDT, *University of Utrecht, The Netherlands*

Energy-Angle Distribution of Positrons from a Thick Target Irradiated with Fast Electrons and
Spectrum and Intensity of Photons from Positron Annihilation in Flight—Prof. L. KATZ, *University of Saskatchewan, Saskatoon, Canada*

Coulomb Excitation—Dr. T. HUUS, *Institute for Theoretical Physics, Copenhagen, Denmark*

Experiments using Ultra-Fast Pulse Techniques—Dr. G. GOLDRING, *The Weizmann Institute, Rehovoth, Israel*

Nuclear Lifetimes—Dr. E. COTTON, *Centre d'Etudes Nucléaires de Saclay, Gif-sur-Yvette (S & O), France*

Injectors—Staff member of *Frascati, Italy*

Wednesday, October 5 - Particle Research

Chairman: Prof. H. H. STAUB,
University of Zürich, Switzerland

The Tandem Electrostatic Accelerator—Dr. P. ROSE, *High Voltage Engineering Corporation, Burlington Mass., U.S.A.*

Current Experimentation with the Tandem at the Chalk River Laboratories—Dr. H. GOVE, *Atomic Energy of Canada Ltd., Chalk River, Canada*

Advanced Methods for Nuclear Reactions Research—Dr. K. W. ALLEN, *United Kingdom Atomic Energy Authority, Aldermaston, England*

Polarized Ion Sources—Prof. R. FLEISCHMANN, *University of Erlangen, Germany*

Millimicrosecond Pulsing—Mr. R. CONNOR, *High Voltage Engineering Corporation, Burlington, Mass., U.S.A.*

Recent Advances in High Power Microwave Electron Accelerators for Physics Research—Mr. J. C. NYGARD, *High Voltage Engineering Corporation, Burlington Mass., U.S.A.* and Dr. R.F. POST, *University of California, Livermore, U.S.A.*

Thursday, October 6 - Physics and Radiation Research

Chairman: Prof. K. SIEGBAHN,
University of Uppsala, Sweden

High Intensity Neutron Research—Prof. K. LÜCKE, *Institut für Algemeine Metallkunde, Aachen, Germany*

Reactor Physics with Pulsed Neutron Sources—Dr. K. BECKURTS, *Institute of Neutron Physics, Karlsruhe, Germany*

Isotope Separation—Prof. J. KISTEMAKER, *Laboratorium voor Massaspectrografie, Amsterdam, The Netherlands*

Chairman: Prof. A. CHARLESBY,
Royal Military College of Science, Shrivenham, England

The Use of Electron Bombardment in Solid-State Research—Dr. P. BARUCH, *Ecole Normale Superieure, Paris, France*

Photoactivation and Photoneutron Activation Analysis—Dr. J. W. OTVOS, *Shell Development Company, Emeryville, California, U.S.A.*

High Energy Radiation for Research in Biochemistry and Microbiology—Dr. W. HUBER, *Stanford University, U.S.A.*

Development of Radiation Process Applications—Dr. S. H. PINNER, *B.X. Plastics Limited, England,* and Mr. W. H. T. DAVISON, *Tube Investment Research Laboratories, England.*

Research in Radiation Chemistry—Speaker not known

Future Accelerators: Intense Sources for Processing—Mr. D. A. TRAGESER, *High Voltage Engineering Corporation, Burlington Mass, U.S.A.*

For all information apply to *Mr. Nathan Tufts, Jr.*, High Voltage Engineering Corporation, Burlington, Mass., U.S.A.

SEMINAIRE INTERNATIONAL/INTERNATIONAL SEMINAR

LE CALCUL ANALOGIQUE APPLIQUE A L'ETUDE DES PROCESSUS CHIMIQUES
ANALOGUE COMPUTATION APPLIED TO THE STUDY OF CHEMICAL PROCESSES

Bruxelles 21–22–23 Nov. 1960

Organisé par/Organized by

Institut Belge de Régulation et d'Automatisme

Sous les auspices de/Sponsored by

l'Association Internationale pour le Calcul Analogique et l'Applications Committee of the International Federation of Automatic Control

The papers to be presented will be grouped under four headings:

I. Simulation of kinetic and thermal problems,

II. Simulation of chemical reactors,

III. Automatic control,

IV. Methods of operational research in the chemical industry.

Intending authors are asked to inform the Seminar Secretariat as soon as posible of their desire to present a paper. The address of the Secretariat is 43, Rue de la Science, Brussels 4, Belgium.

NUCLEAR INSTRUMENTS AND METHODS **8** (1960) 261–271; NORTH-HOLLAND PUBLISHING CO.

THE PRETORIA CYCLOTRON

SECOND REPORT

J. J. BURGERJON† and W. WEIDEMANN††

Nuclear Physics Division, National Physical Research Laboratory,
South African Council for Scientific and Industrial Research, Pretoria

Received 15 June 1960

This report deals with improvements to the cyclotron, as well as with the extraction and external focusing of the beam. The various components, in so far as they have been subject to alterations, as well as new components, are described. The properties of both the internal and external beams are discussed in separate chapters. Throughout, reference is made to the first report[1]).

1. General

An audible and visible alarm-system was installed in the cyclotron hall and its entrances, i.e. the waterdoors and the maze-passage from the now completed experimental hall. This alarm is actuated automatically as soon as the cyclotron is potentially dangerous, i.e. when the magnet, the oscillator and the ion-source are in operation simultaneously. It has proved to be a valuable addition to the existing safety measures.

Automatic emergency lighting in all underground halls and passages was installed because of frequent power-cuts on the C.S.I.R. site.

After the completion of the cyclotron experimental hall, it was possible to instal an optical observation system. This makes possible observation of phenomena in the cyclotron hall, and particularly in the vacuum-chamber, through a water window eight feet long and a 4-inch telescope with 25 × magnification, from a radiation-free location.

The polarity of the magnet was reversed to make focusing of the external beam possible at a desired point. For this reason the beam is now accelerated in an anti-clockwise direction.

† From June 1960 at University of Manitoba, Winnipeg, Canada.

†† From August, 1960, at South African Atomic Energy Board, Pretoria.

2. The Magnetic Field

2.1. THOMAS SHIMS

It follows from the previous report that the internal beam position in relation to the geometrical median plane and the internal beam focusing were not of the high quality that would be favourable for successful deflection.

To improve both these properties, new forged pole plates with Thomas shims were fitted[2]). The plates were machined parallel to a thickness of $1\frac{5}{8}''$. This is $\frac{3}{8}''$ thinner than the old ones, to accomodate the Thomas shims, the $\frac{1}{8}''$ Rose shim and the poleface windings. The overall tolerances again are well within the $\pm 0.001''$ limit, while the geometrical positions of the plates and the shims relative to each other and to the pole pieces are fixed within $\pm 0.004''$. No external shims are used, but the $\frac{1}{4}''$ airgaps between poles and plates were filled, after external steering coils proved to be unfeasible. This lowers the generator load by some 6%. In spite of the precise geometry,

[1]) National Physical Research Laboratory. *The Cyclotron of the N. Phys. R. L. First Report.* C.S.I.R. Spec. Techn. Rep. No. E.1., Pretoria, April 1958. A condensed version of this report has been published: J. J. Burgerjon, S. J. du Toit and C. A. J. Kritzinger, The Pretoria Cyclotron., Nucl. Instr. **3** (1958) 323.

[2]) K. Boyer, Los Alamos Scientific Laboratory, U.S.A. Private communication to S. J. du Toit (1957).

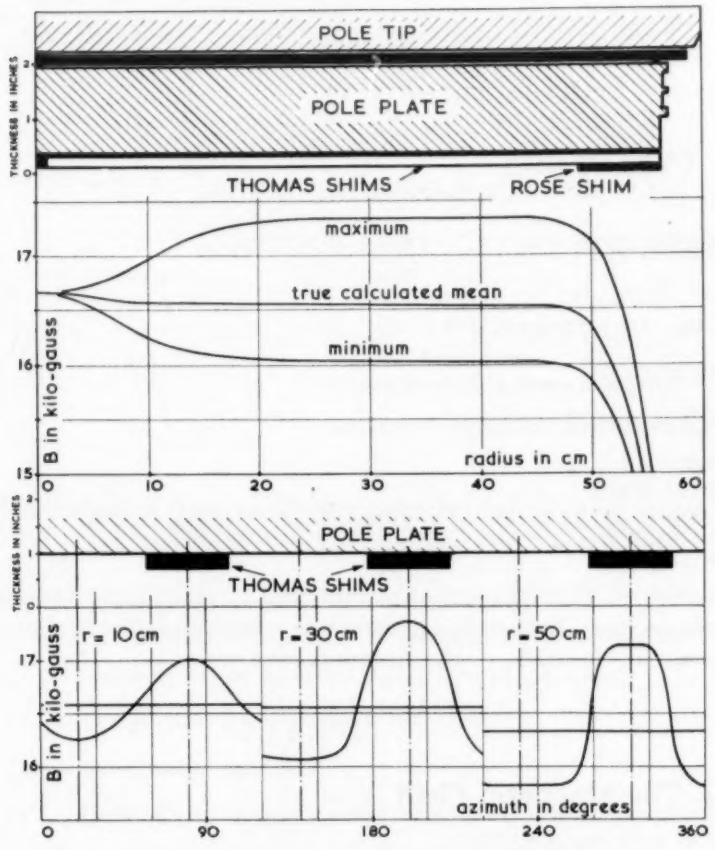

Fig. 1. Radial field plots and azimuthal field curves.

corresponding points of the azimuthally varying field differ by approximately 0.13%.

Fig. 1 shows the shimming, the radial and azimuthal field curves, while fig. 2 shows the various fringing field curves which were measured with a view to extraction calculations. At B in fig. 3 it can be seen that the centre-field versus current plot differs from the previous one because of the alterations.

2.2. POLE FACE WINDINGS

Windings on the interior side of the pole plates were fitted to make possible the choice of any gradient between + 12.7 Gauss/cm and — 14.7 Gauss/cm. As can be seen, working from the centre to the periphery, consecutive areas are surrounded by a diminishing number of turns. By varying the current through the windings it is thus possible to adjust the gradient to any desired value between these limits. The limited number of turns does not appear to have any measurable effect on the smoothness of the radial field plots, which are shown at A in fig. 3.

The water-cooled windings were constructed from $\frac{3}{8}''$ electrolytic copper tubing, flattened to $\frac{1}{8}''$, and insulated by two layers of 0.005″ fibreglass tape. As can be seen on the photograph in fig. 4, they are held in position by grooved polyethylene sectors and the copper linings that cover the whole assembly. At the maximum current of 500 A the waterflow through a coil, slightly increasing with temperature, is approximately 1 l/sec at a pressure of 3 kg/cm². In each coil about 3 kW, supplied by a 6 kW motor-generator set, is dissipated.

2.3. WIRE LOOP CHECK[3])

To determine the radial gradient of an azimuthally homogeneous field that would produce the

[3]) See also G. R. Lambertson, Use of the wire loop in locating the orbital surface of a cyclotron field, U.C.R.L. 3366

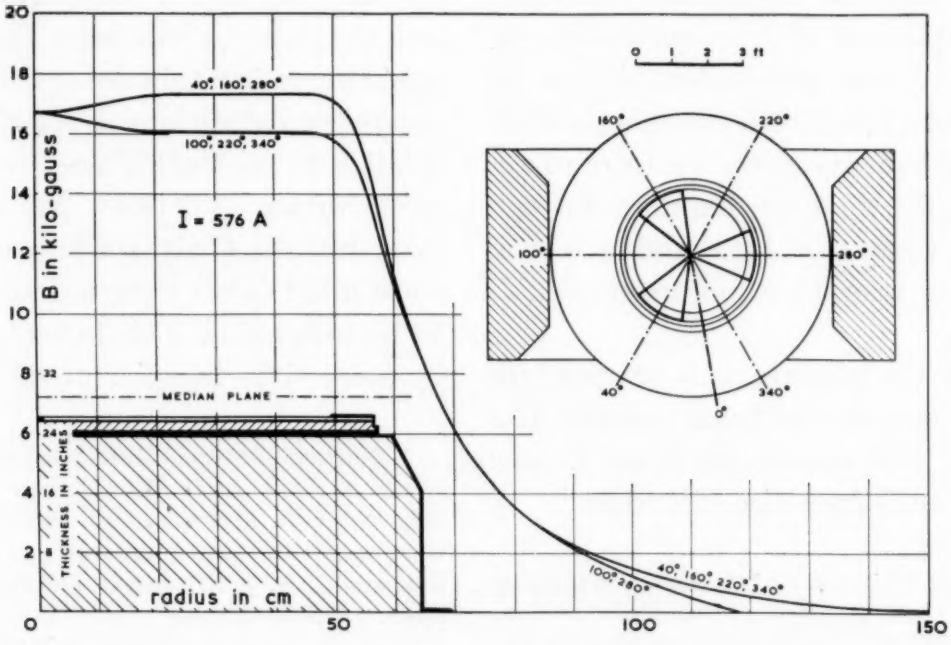

Fig. 2. Fringing field plots.

same focusing effect as the Thomas shims, the following experiment was carried out.

A thin current carrying copper wire loop was suspended by a spring in the vacuum chamber in a position 62 mm above the median plane. As the focusing forces, which act on the beam, act defocusing on the wire, the radial gradient was made focusing for the loop, i.e. positive, and then increased gradually. At a current of 115 A the loop drops, i.e. the focusing radial gradient and the defocusing effect (on the wire) of the Thomas shims are then equal. According to this experiment, the beam-focusing effect of the Thomas shims is roughly equivalent to a radial gradient of 2.2 Gauss/cm.

Fig. 4. Pole plate with Thomas shims, Rose shim and pole face winding.

2.4. STABILIZATION

The galvanometer-type current stabilization of $\pm$ 0.01%, described in the previous report, proved inadequate for successful beam deflection, as the orbit position tends to change together with the degree of resonance. As the current fluctuations of short duration only resulted from voltage fluctuations at the output of the generator, the existing system was augmented by the addition of a short-term voltage stabilizer.

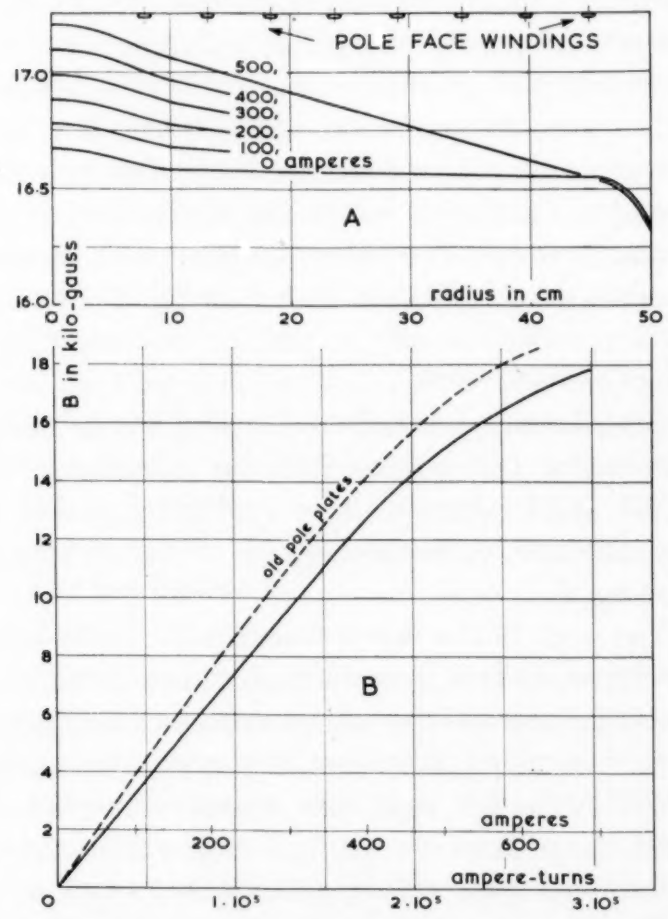

Fig. 3. A. Effect of pole face windings on mean radial field plot; B. Magnetic flux-density versus ampere-turns.

A 10 μF low-loss condensor, connected to the generator terminals through a 1 megohm resistor acts as a reference voltage, with the limitation that only fluctuations which are not long compared to the time constant of 10 seconds, are detected as voltage fluctuations across the resistor. These are amplified by a simple balanced D.C. amplifier, and the output signal is applied to one of the amplidyne field windings. The generator voltage is thus stabilized for short-term fluctuations, while the normal current stabilizer takes care of long-term current variations, due to temperature changes and possible drift of the voltage stabilizer. With this simple stabilizing arrangement, shown as a block-diagram at B in fig. 5, a drift-free stability of $\pm$ 0.002% i.e. 1 in 25 000, is easily achieved, which proved to be more than adequate.

3. The R.F. System

3.1. DEES

Considerable difficulties were experienced with the original dees, as at the time we were not able to acquire the services of a firm that was better qualified to make them. Right from the beginning the dees were not within the required tolerances, while the soldering of the cooling lines was of very poor quality, resulting in leaks.

To remedy the situation, the old dees were sawed off the dee-stems, and new dees of a much-improved design fitted by the C.S.I.R. workshops. As can be seen in fig. 6, these consist

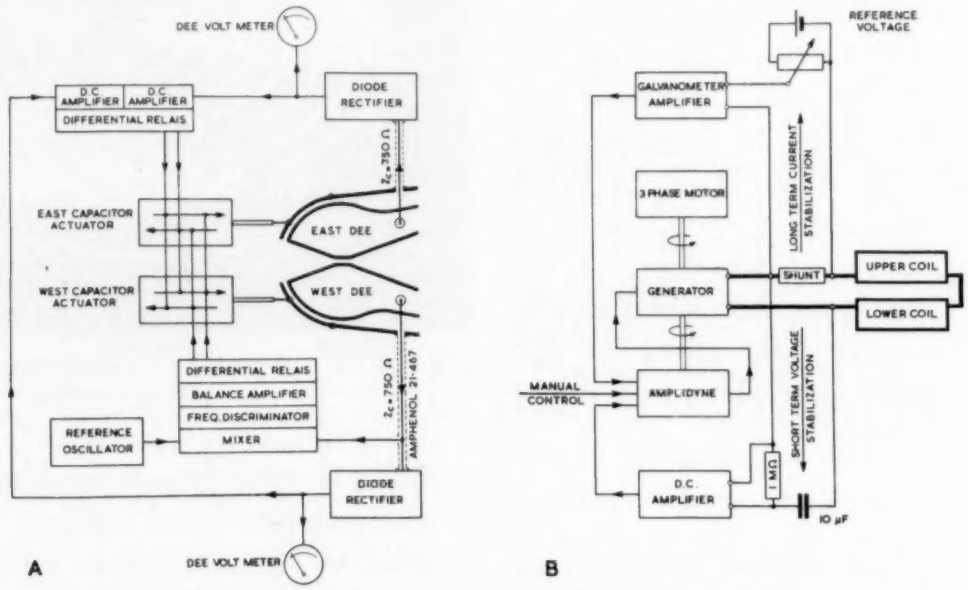

Fig. 5. A. Block diagram of R.F. stabilization; B. Block diagram of magnet stabilization.

of an aluminium backbone, which is secured to the dee-stem by a large number of screws, and onto which in turn the top and bottom lids with their soft-soldered cooling tubes are screwed.

Fig. 6. The dees with the top plates removed.

This makes for superb accessibility to the septum and deflector assembly. Furthermore, the new dees are clad with carbon strips to avoid undue radioactivity. These strips also light up if hit by the beam; this can be observed through the optical system. Tolerances are within $\pm$ 1 mm. Together with the dees the construction of the trimmer condensors was improved and can now effect a frequency change of $\pm$ 1.7%.

To suit the ion source as described in Section 4, vertical feelers were slide-fitted. The first revolution is guided by an extraction plate in the dee opposite the ion source slit, and a further slit in the East dee. The relative positions of the ion source and the slits are shown in fig. 7.

3.2. STABILIZATION

Stabilization was introduced for the R.F. system for the same reason as mentioned on p. 263, and to shorten the warming-up period of the machine. A block-diagram of the system is A in fig. 5.

The ratio of the dee-voltages is stabilized by a combination D.C. amplifier, deriving its signals directly from the dee voltmeters, and actuating both trimming condensors through a differential relay. Although normally equal voltages are used, the ratio of dee voltages can be adjusted at will, and is kept within $\pm$ 0.5%.

The frequency is stabilized by heterodyning the cyclotron frequency with that of a local

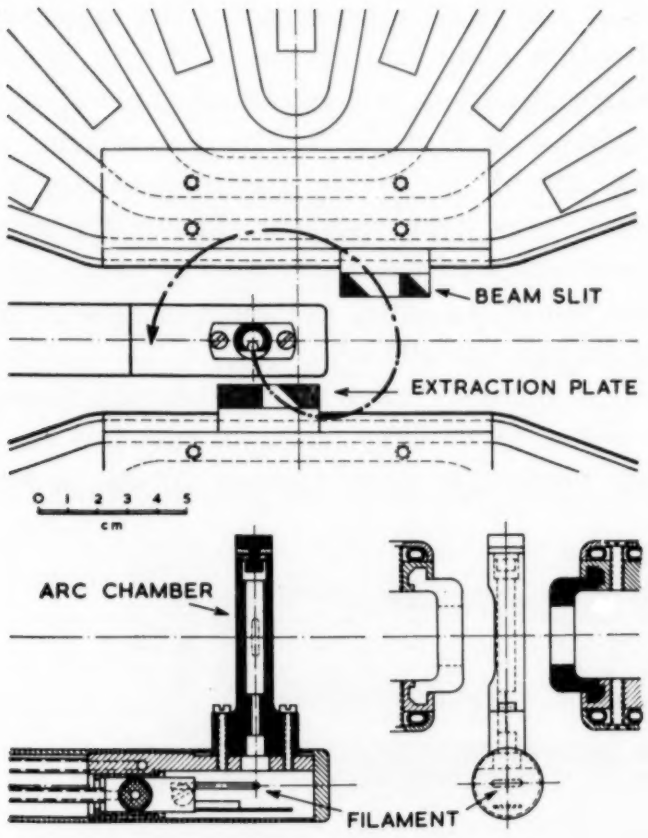

Fig. 7. The ion source and the feelers.

stable Variable Frequency Oscillator. The resultant frequency is amplified and fed into a limiter and discriminator. This F.M. detector drives a D.C. amplifier, and again both condensator plates are actuated through a differential relay. The voltage-ratio stabilizer moves the plates in opposite directions, while the frequency stabilizer moves them together. After some interplay a stable position is reached. To overcome the mechanical overshoot of the actuator motors, D.C. braking is employed. The frequency, which after the warming-up period was normally stable within only $\pm$ 0.01%, is thus also stabilized now within $\pm$ 0.002%.

4. The Ion Source

4.1. ION SOURCE PROPER

A new ion source of more advanced design was installed. The construction is shown in fig. 7, and a photograph can be seen at B in fig. 9.

Teflon insulation was used between the filament holder and the housing, and between the two halves of the filament holder. A silicone-rubber ○-ring was used to seal the water connection between the two halves. The filament holder and housing are made of a tungsten-copper alloy, while graphite was employed for the vertical tube and the reflecting anode, which are insulated from each other by a fused quartz ring.

The filament is made of 2 mm ⌀ tungsten and the reflecting plate underneath of molybdenum. Both vertical tube and filament are of uncomplicated design and can easily be made and replaced when necessary. The vertical chamber has a very long life-expectancy that is mainly limited by accidental breakage.

The filament position can be easily adjusted externally in relation to the $\frac{1}{8}$" ⌀ hole above it. Remote control is possible for the East—West and North—South directions and for tilting of the vertical tube. The output of the source is very sensitive to this last movement.

The ion source normally operates under the following conditions:

Filament Voltage	3 V
Filament Current	124 A
Filament life expectancy	30 hours
Gas flow	0.03 mm 1/sec
Arc voltage	200 V
Arc current	2.2 A .

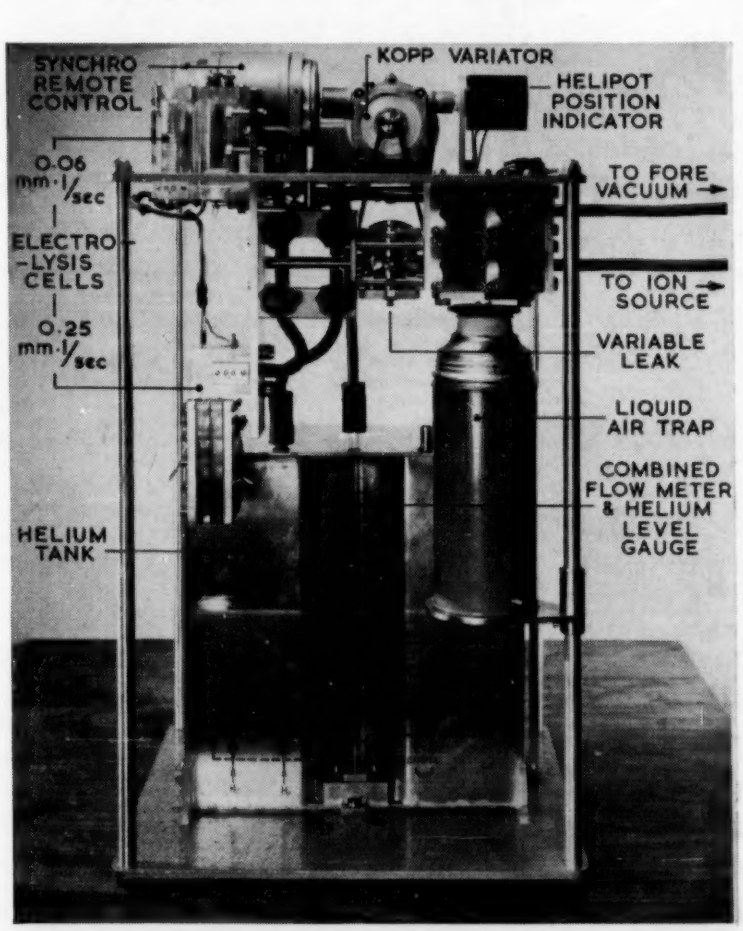

Fig. 8. The ion source gas supply.

The source produces about 2 mA of useful D^+, 1 mA of H_2^+ or 150 μA of He^{++}, as measured after one turn in the cyclotron, guided by the extraction plate in the West dee and the slit in the East dee, under R.F. conditions.

4.2. GAS SUPPLY

Using the principles described in the first report this has been reconstructed for easier maintenance and to facilitate the change-over from deuterium to hydrogen or helium gas. The apparatus is shown in fig. 8.

to suit the relative positions of the ion source, extraction plate and slit, as shown in fig. 7, a number of curves were obtained, three of which are shown at D in fig. 9. This dee-voltage, the most suitable for stable operation of the R.F. system, was kept constant during the entire experiment, and the beam current at the minimum radius, i.e. after one turn of acceleration was adjusted to 500 μA.

The top curve, taken with no current through the pole face windings, shows a very low loss of beam current at radii beyond 20 cm, proving

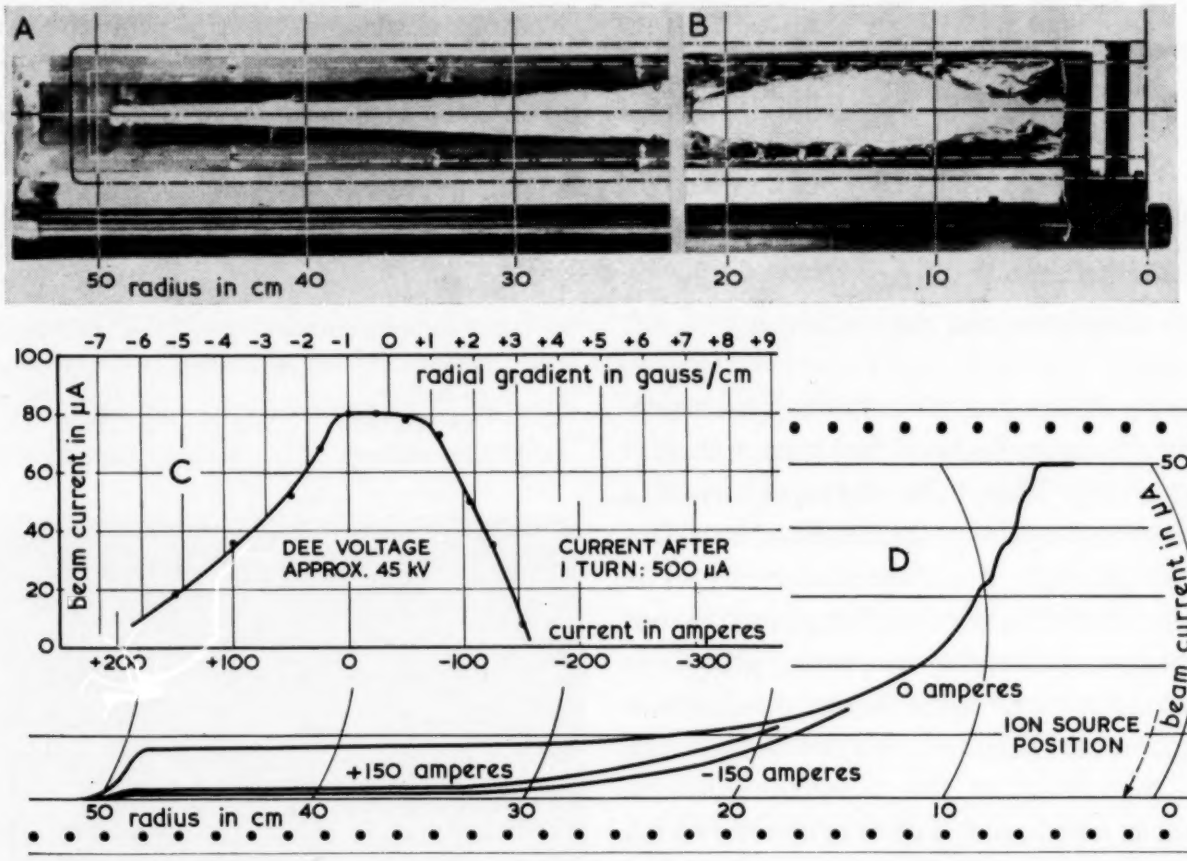
A
B
50 radius in cm 40 30 20 10 0
-7 -6 -5 -4 -3 -2 -1 0 +1 +2 +3 +4 +5 +6 +7 +8 +9
radial gradient in gauss/cm
beam current in μA
100 80 60 40 20 0
C
DEE VOLTAGE APPROX. 45 kV
CURRENT AFTER 1 TURN: 500 μA
current in amperes
+200 +100 0 -100 -200 -300
D
500 400 300 200 100
beam current in μA
0 amperes
ION SOURCE POSITION
+150 amperes
-150 amperes
50 radius in cm 40 30 20 10 0

Fig. 9

A. Beam shape at large radii; B. Beam shape at small radii; C. Effect of the radial gradient; D. Radial beam current plots.

5. The Circulating Beam

5.1. RADIAL BEAM CURRENT CURVES

To obtain more knowledge about the behaviour of the internal beam, a remote controlled sliding probe target was installed in the neutral plane between the dees. In this plane, R.F. pick-up and dee-voltage unbalancing are reduced to a minimum. The target is water-cooled and 4 cm wide to ascertain interception of the total beam even at small radii.

With a dee-voltage of approximately 45 kV, that the magnetic focusing of the Thomas shims is more than adequate at these radii. At the smaller radii, however, the loss of beam is still important, due to insufficient electrostatic focusing, and the experiment indicates that improvements can be expected by placing more beam slits in the proper positions where the beam enters the dees[4]).

The behaviour of the beam is also clearly

[4]) A. H. Morton and W. I. B. Smith, Nucl. Instr. **4** (1959) 36.

illustrated by the two photographs in fig. 9. At A is shown a 0.5 mm thick lead foil that had been placed in the neutral plane between the dees, and which was "burned" away by the beam. The beam is very narrow indeed at the larger radii. The accurate vertical beam distribution at max. radius can be seen in fig. 11 (side view of stationary target). At B is shown a 0.05 mm thick aluminium foil, "burned" away by the beam in the same manner, proving the lack of sufficient focusing at smaller radii.

The photographs also show that the beam is perfectly centred in the geometric median plane between the pole faces. This other great advantage of the Thomas shims is due to the fact that mechanical inaccuracies in the position of the pole plates and shims have a much smaller effect on the position of the orbital plane, as the radii of curvature of the lines of force are orders of magnitude smaller than in a conventional radial gradient field. Thus the "median plane resistor", as described in the previous report, is no longer necessary.

5.2. EFFECT OF THE POLE FACE WINDINGS

From the abovementioned set of curves, the beam currents at maximum radius were plotted as a function of the current through the pole face windings, as shown at C in fig. 9. For positive values of the current, i.e. when this current increases the main field, the radial gradient becomes negative. In this region we observe that the beam current decreases gradually with increase of the negative radial gradient, due to increasing loss of phase of the particles with respect to the constant R.F. voltage. In the region of positive gradient, however, we see a rather abrupt decrease of the beam current, due to defocusing of the beam. It will be noted that this decrease occurs for a value of positive gradient, which was roughly predicted by the wire-loop check (see Section 2).

It is obvious from these experiments that, if this fairly low dee-voltage is used, the cyclotron performs best at approximately zero radial gradient, i.e. with the pole face windings not in use. In fact the cyclotron is always operated under these conditions, and internal currents of over 200 μA (measured calorimetrically) of 16 MeV deuterons can be easily obtained.

5.3. ORBIT POSITIONING COILS

Orbit positioning coils, placed at right angles in the $\frac{1}{4}''$ external shimming gaps, were tried in an effort to facilitate deflection. Each coil was oblong in shape, $15'' \times 25''$ across main diameters, wound of 40 turns of 2×4.5 mm copper, and insulated by polyester-resin impregnated fibreglass. Currents of up to 25 A could be sent through these coils to vary the magnetic field locally by approximately 40 gauss.

While it was possible to move the beam orbits with these coils, a strong horizontal defocusing effect was observed, probably due to the fact that the local field variations have a different effect on particles that leave the ion-source under different phase conditions, thus making a different number of traverses through the regions of stronger or weaker field.

Consequently the orbit positioning coils have been discarded, and orbit positioning is now effected by moving the ion-source only.

6. The Automatic Rotating Target

In the first report, an automatic target and its mode of operation are described. To cope with increasing beam intensities, and to facilitate irradiations where low target temperatures are imperative, a rotating automatic target was designed. This is shown in fig. 10. The mechanism

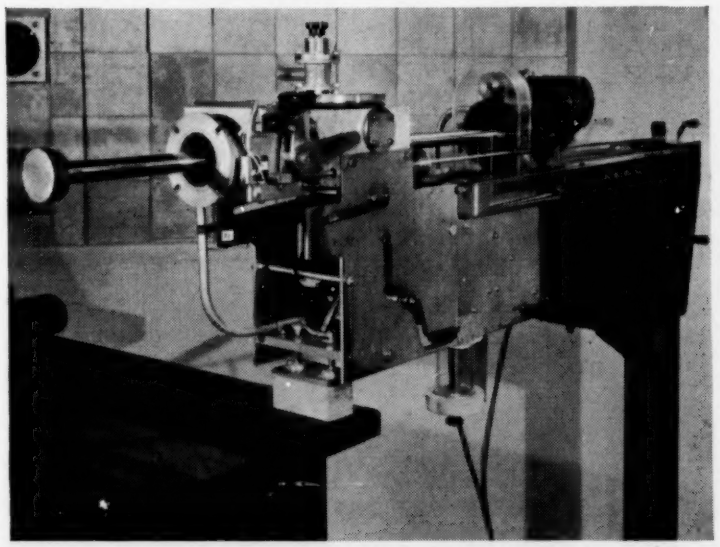

Fig. 10. The automatic rotating target.

operates on exactly the same lines as the previous one, except that the target proper is not sheared, but screwed off by a fork, which then places it in the pneumatic carrier. The blowing-out time of the coolant had to be lengthened, so that the target now reaches the hot laboratory some 80 seconds after the button is pressed.

As can be seen from fig. 11, the distribution of the beam, as measured by the activity of an irradiated target, is much more uniform than is the case with the normal stationary target. Hot spots are thus avoided. For instance, lead of 0.3 mm thickness is not damaged by 80 microamps of 16 MeV deuterons. A non-metal, such as NaCl, is first applied in a thickness of 1 mm to a $\frac{1}{16}''$ copperplate, which is then softsoldered to the target head. This sodium chloride target then can stand up to 25 microamps of 16 MeV deuterons, producing about 30 mC/h of Na^{24}.

7. The Deflecting System

7.1. DEFLECTING CHANNEL

For the first deflection tests, both septum and deflector were carbon-clad. The carbon gave a visible indication when hit by the beam, and prevented undue radioactivity. This safety-measure was welcomed when it was necessary to disassemble the channel frequently because of insulation difficulties. The 20 mm high deflector clears the dee covers by 15 mm, and can stand up to 45 kV without sparking. However, the carbon, useful as it was in the preliminary tests, proved to be unpractical because of the heating of and consequent emission from the deflector.

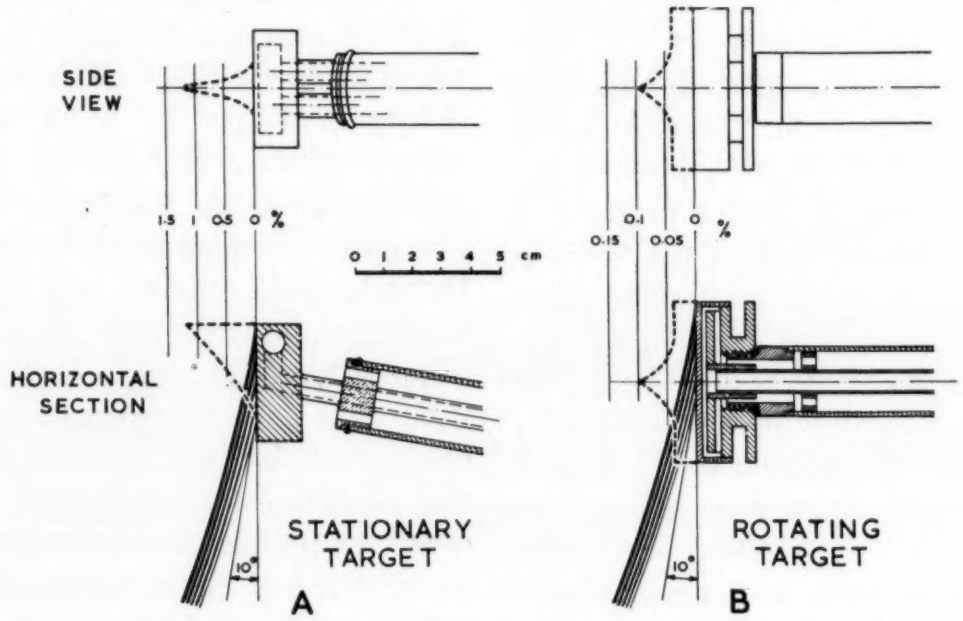

Fig. 11. A. Beam distribution on stationary target; B. Beam distribution on rotating target; The horizontal axes show percents of the *total* activity per mm^2.

The channel was thus replaced by a metal septum and deflector of the same shape.

The deflector entrance and exit and the septum exit are adjustable without breaking the vacuum. The septum entrance can only be adjusted by disassembling the dee. The channel is shown in fig. 6 and its actual position can be seen in fig. 11.

7.2. VOLTAGE SOURCE

An old X-ray rectifier was adapted for this purpose, and can now provide 60 kV at a continuous current of 10 mA. The voltage is variable from the control room, and both current and voltage are measured from there.

The deflector is cooled by water mixed with cutting lubricant, to lubricate the gearpump used for circulating the coolant. This pump and an air-cooled radiator are on a high voltage pedestal, coupled to the drive motor by an insulating shaft. The sole electrical connection between the deflector and the high voltage pedestal is the coolant, which thus acts as a buffering resistor of 50 kΩ, to damp transients initiated by sparks in the vacuum-chamber.

8. The External Beam Focusing System

8.1. FRINGING FIELD WEDGES

As the deflected beam spreads considerably in the horizontal plane, because of the long trajectory in the fringing field, steel blocks were placed in the fringing field to act as sector magnets. Their shape and position can be seen in fig. 12.

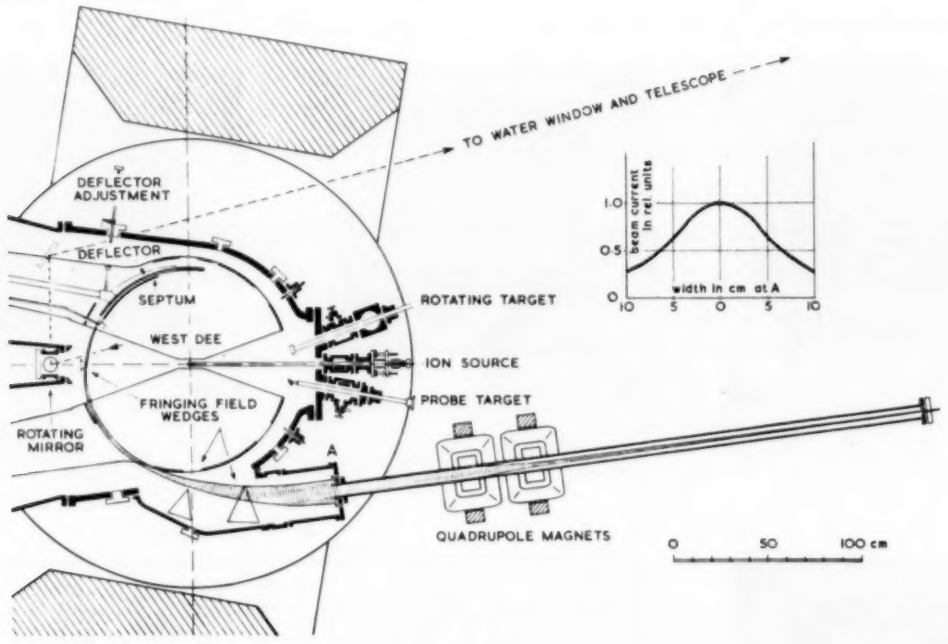

Fig. 12. The beam trajectory.

The first wedges are placed inside the vacuum-chamber and can be moved in and out without breaking the vacuum. They are 35 mm thick and 25 mm apart. The second and third sets of wedges are placed on both sides of the exit-chamber. These wedges are 200 mm thick and 85 mm apart. It is not possible to place the second wedges in the most effective position because of the shape of the exit-chamber.

8.2. QUADRUPOLE MAGNETS[5])

A $2\frac{1}{2}''$ O.D. stainless steel tube leads part of the beam through the quadrupole magnets, which are shown in Figures 12 and 13, thus accepting 60 mm of the horizontally flat beam at the end flange of the exit-chamber extension (A in fig. 12). The beam is focused at a point some 3 m away from this point, where it will be used for experiments.

[5]) See also: W. Weidemann, Nucl. Instr. **8** (1960).

Under operating conditions the magnets consume some 600 watts, which is dissipated through air-cooling at a surface temperature of 80°C. The quality of focus is not affected by varying operating conditions of the cyclotron, and is kept sufficiently constant by a current-stabilization of $\pm$ 0.5%.

9. The Deflected Beam

With the septum entrance at 49.5 cm radius, an entrance gap of 5 mm, and the septum exit at 52.0 cm with an exit gap of 12 mm, and with a deflecting voltage of approximately 40 kV,

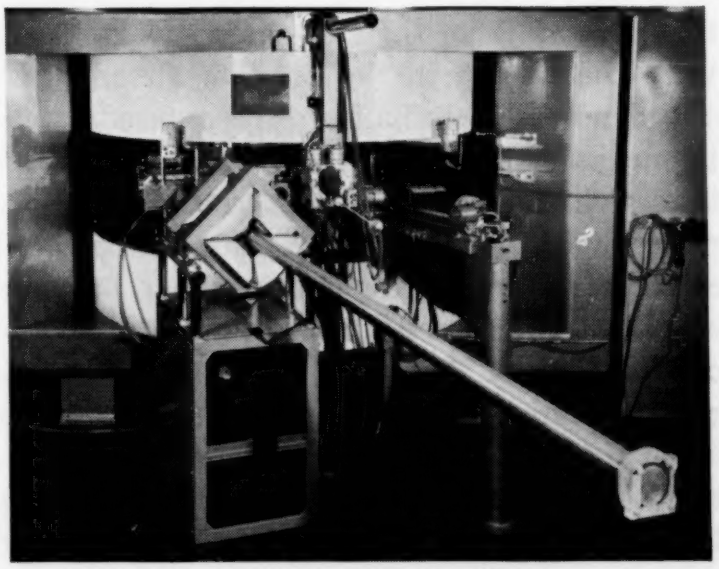

Fig. 13. North view of cyclotron.

about 24% of the beam current at maximum radius can be deflected, as measured on one of the two probes that can be inserted on either side of the rotating mirror. This situation is depicted in fig. 12. If no fringing field wedges are used, the halfwidth of the beam, where part of it enters the pipe leading to the quadrupole magnets, i.e. at point A, is considerably larger than the width of the exit-chamber extension. With the wedges in the position already described, however, the half-width is approximately 13 cm, as can also be seen in fig. 12. This information was obtained from irradiated copper plates and from a ten-target plate which could either be screwed to the exit chamber, or to its extension. Thus practically all of the beam is now confined within the side walls of the exit-chamber extension, and this is about 12% of the beam at maximum radius. Insufficient time was spent on experiments to further reduce the losses in the fringing field region, and it is clear that there is still scope for improvement.

5% of the beam current at maximum radius enters the stainless steel tube and, because of the slight divergence, only 4% enters the first quadrupole magnet, which effects horizontal focusing. Owing to the associated vertical defocusing effect of this magnet, another 1% is lost between the two quadrupole magnets, which leaves approximately 3% of the beam at maximum radius to reach the target onto which the beam is focused.

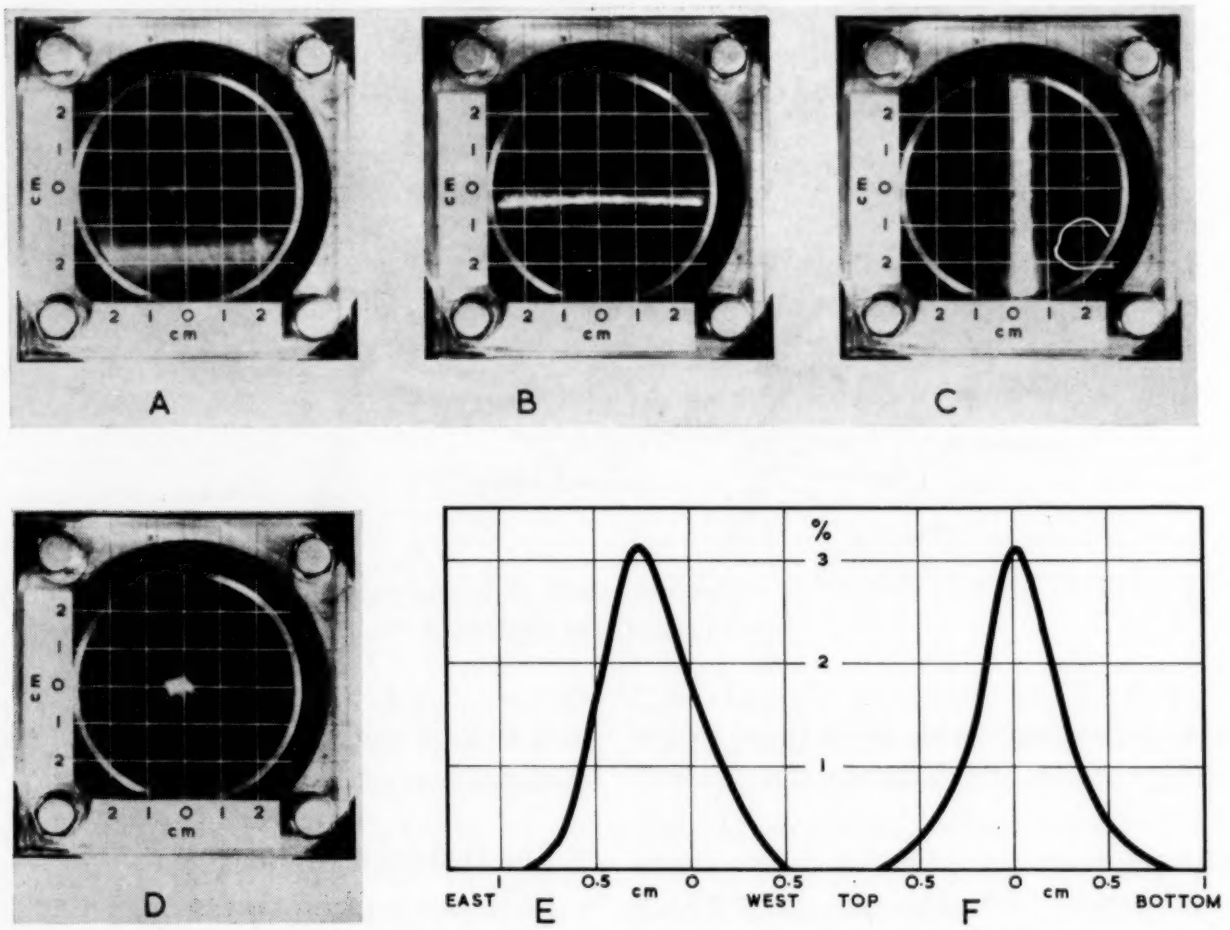

Fig. 14. The focused beam. The vertical axes of E and F show percents of the total beam current per mm².

The quadrupole system, with its nett transmission of 75% confines the beam at the target area to a focus of some 4 by 6 mm, where it would otherwise have spread to approximately 6 cm by 24 cm.

Fig. 14 shows, A: a photograph of part of the unfocused beam directed onto a fused quartz plate, to make the beam shape visible; B: the vertically focused beam; C: the horizontally focused beam; and D: the spot focus, obtained with both quadrupoles in operation. An accurate survey of the beam distribution was made by

irradiating a copper target and measuring its activity distribution, which is shown at E and F in fig. 14.

Acknowledgements

The authors wish to extend their sincere thanks to Dr. S. J. du Toit, for his constant encouragement and interest in the work, while head of the Nuclear Physics Division of the N. Phys. R.L. After his departure in October, 1959, Dr. E. J. Marais, Director of the N. Phys. R.L., added to his already overcrowded schedule the duties of acting head of this department. Thanks are due to him for the admirable way in which he has filled this rôle.

The whole project, of course, would have been impossible without the conscientious and dedicated work of the whole cyclotron group, consisting of Messrs. Z. de Velde Harsenhorst, L. D. Bruins, P. van Vliet, K. Lubbinge and J. Kuiper. In this connection we wish to mention also the sustained and excellent craftsmanship of Messrs. A. Dekter and J. L. Liebenberg of the C.S.I.R. Workshops, who worked for the cyclotron during the period covered by this report.

Finally we would like to express our appreciation to Dr. S. M. Naudé, President of the South African Council for Scientific and Industrial Research for his personal interest in this project.

NUCLEAR INSTRUMENTS AND METHODS 8 (1960) 272–281; NORTH-HOLLAND PUBLISHING CO.

A DOUBLE-DELAY-LINE LINEAR AMPLIFIER EMPLOYING TRANSISTORS I

F. S. GOULDING, R. W. NICHOLSON and J. B. WAUGH

Atomic Energy of Canada Limited, Chalk River, Ontario, Canada

Received 20 June 1960

A transistor amplifier designed mainly for precise scintillation counter spectroscopy is described. Techniques such as double-delay-line pulse shaping and considerable negative feedback result in excellent linearity, gain stability and overload behaviour at high counting rates. An input charge of 2×10^{-13} Coulombs develops a $\pm$ 4V output pulse into a 100 Ω matched cable which feeds the Chalk River kicksorter. With 1 μsec pulse shaping lines the input equivalent R.M.S. noise is 4000 ion-pairs. Lower noise may be achieved by using shorter lines. The amplifier rise-time is 0.2 μsec (10 to 90%). Use of plug-in printed circuit boards increases the versatility of the amplifier and simplifies the adjustment procedures.

1. Introduction

The advantages of double-delay-line pulse shaping and careful control of amplifier limiting action for scintillation counter amplifiers have been appreciated for some time[1,2]) and the use of tube amplifiers employing these techniques has become common wherever high counting rates and large overload pulses are encountered. Work

[1]) E. Fairstein, Rev. Sci. Instr. **27** (1956) 475.
[2]) G. G. Kelly, I.R.E. Nat. Conv. Rec. Pt. **9** (1957) 63.

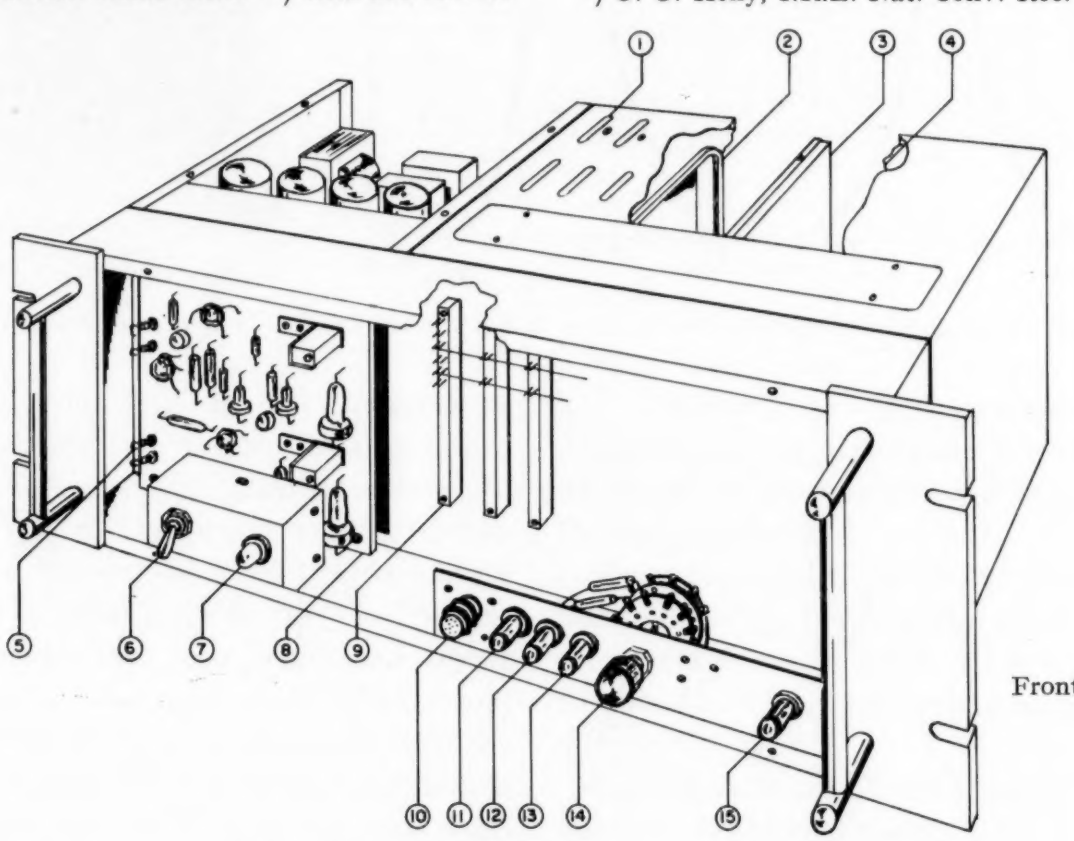

Front panel removed.

Fig. 1. Main amplifier cutaway view.

1. Louvres ventilation and adj. presets;
2. Printed card with handle;
3. Shield;
4. Back cover and card retainer;
5. Power supply to connectors;
6. Mains on/off;
7. Indicator;
8. Printed board (power supply);
9. Printed circuit connectors;
10. To head unit;
11. Input Mix;
12. Input Test;
13. Input Head;
14. Gain control;
15. Output.

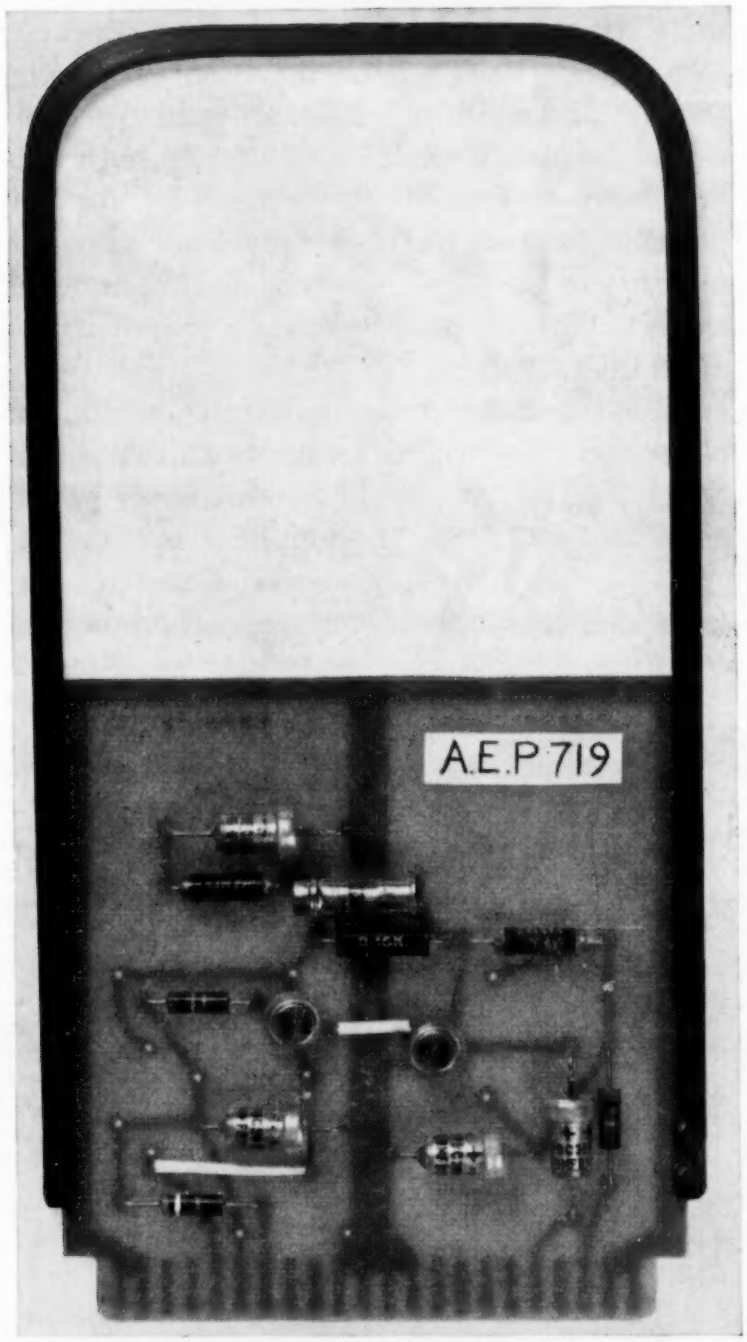

Fig. 2. Typical printed circuit unit.

at Chalk River on transistor amplifiers which started with the use of current fed-back pairs in monitoring instruments[3,4]) and continued with the development of a non-overloading amplifier for proportional counters[5]) has now culminated in the development of a transistor double-delay-line linear amplifier. Apart from the advantages of reliability, small size and low power consumption resulting from the use of transistors this amplifier is much simpler to manufacture and adjust than its tube counterparts.

The complete unit is designed for rack mounting with the head unit containing the scintillation detector, photomultiplier and head amplifier connected to the main unit by not more than 50 feet of cable. A cutaway view of the main unit with its panel removed, shown in fig. 1, illustrates the method of construction. Printed circuit units each containing a basic circuit element (current amplifier, limiter, delay line shaper and output stage) plug into the 8 printed circuit sockets shown in fig. 1. The power supply is contained on the main chassis which also includes separate shielded compartments for each of the plug-in units. Input and output connectors, gain control, power switch and indicator are mounted on a shallow sub-panel behind the main panel.

Experience has shown that the versatility of a plug-in form of construction is invaluable. The present amplifier design has evolved from a methane proportional counter amplifier design using the same base unit described by Waugh[5]) and it is likely that deficiencies which probably will be found to exist in the present design can be easily remedied by simple changes to, or

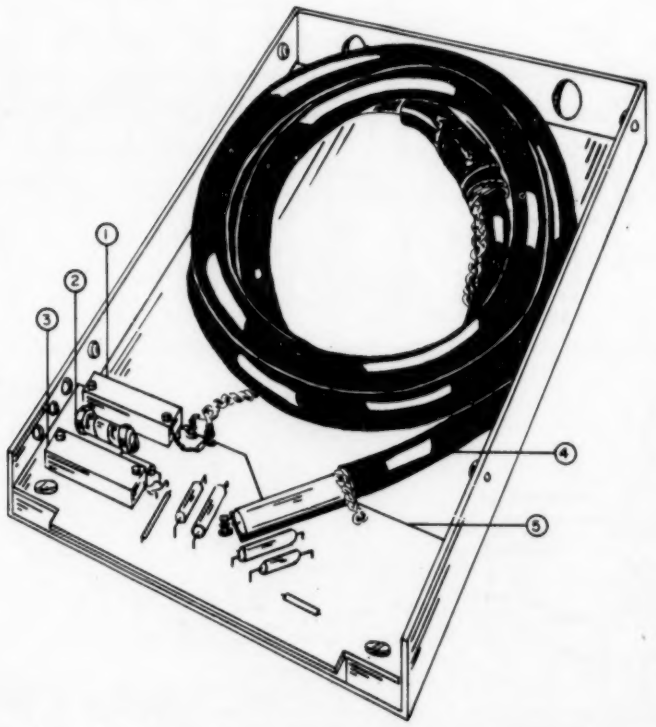

Fig. 3. Delay line pulse shaper. 1. Loss adjustment; 2. High frequency match; 3. Resistive match; 4. HH2000 Delay cable; 5. Printed card copper side down.

[3]) F. S. Goulding, Chalk River Report CREL-741 (1957).
[4]) V. H. Allen, Canadian Electronics Engineering **2** (1958) 22.
[5]) J. B. Waugh, Chalk River Report CREL-828 (1959) (to be published in Nucleonics, July, 1960).

replacement of, plug-in units with no change in the base unit.

A typical printed circuit unit is shown in fig. 2 and fig. 3 illustrates the construction of the delay line pulse shaper. We have employed printed circuits to simplify construction and also to control layout thereby obtaining reproducible results when large quantities of the units are manufactured. The printed circuit pattern is gold plated and the plug portion of the board is palladium plated. These two measures together with the choice of a good printed circuit socket have virtually eliminated dry joints and contact problems.

2. Overall Circuit Design

The amplifier design is based largely on the use of fedback pairs of transistors used as current amplifying sections. Each pair exhibits a low input impedance and high output impedance which lends itself to the inclusion of shaping lines in the outputs of stages. A detailed analysis of the frequency response of the fed-back pair has been performed by Waugh[6,7]); for the present purpose we need only note that the majority of the stages occurring in this amplifier exhibit current gain-bandwidth products of more than 30 Mc/s.

Fig. 4 shows the schematic of the complete amplifier excluding the power supply which is shown in fig. 5. The low ripple power supply which provides $\pm$ 30 V for the amplifier is conventional in design apart from the use of current controlled series transistors for overload protection.

[6]) J. B. Waugh and R. W. Nicholson, Chalk River Report CREL-829 (1959).

[7]) J. B. Waugh and R. W. Nicholson, Chalk River Report CREL-830 (1959).

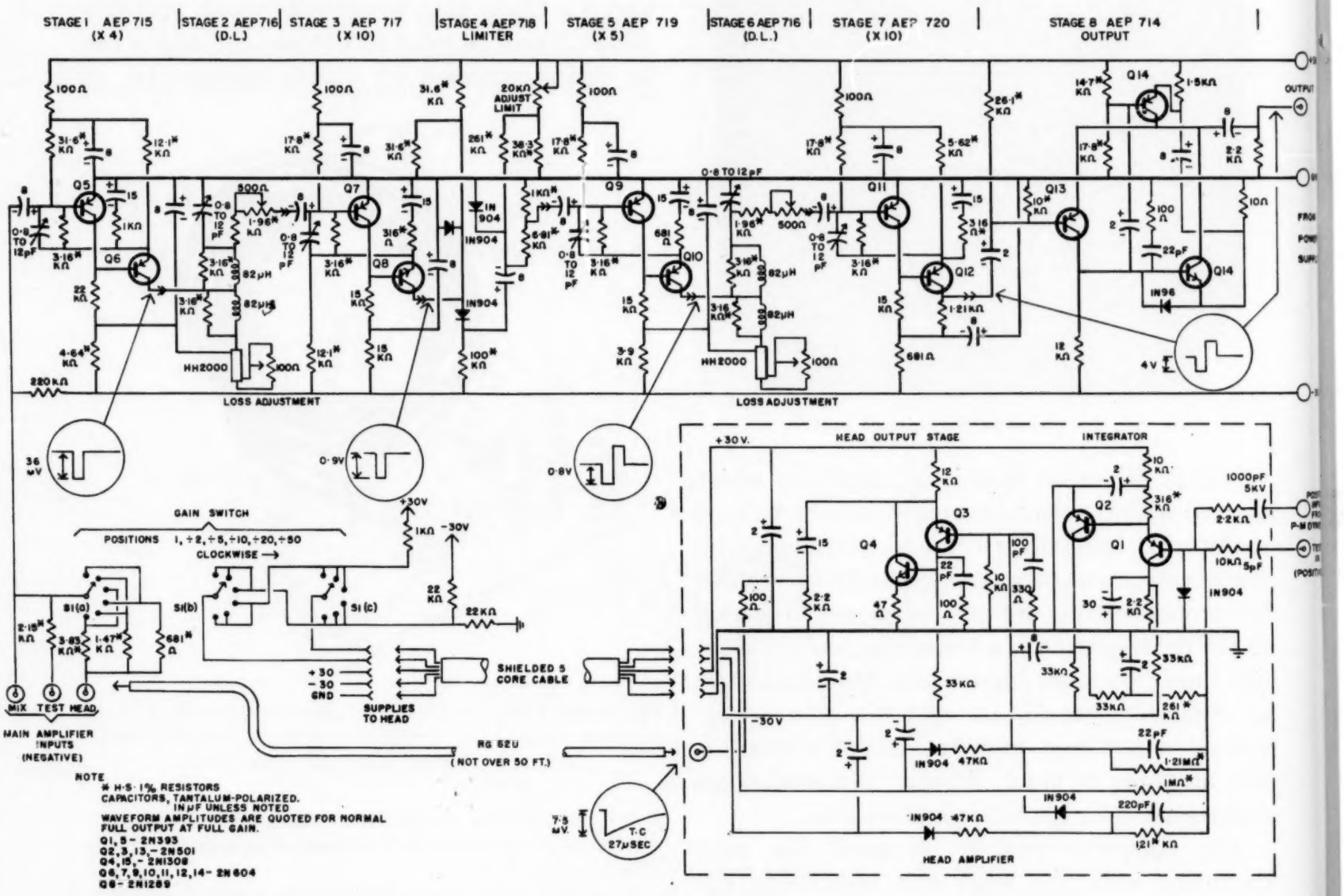
STAGE 1 AEP 715 (X 4)
STAGE 2 AEP 716 (D.L.)
STAGE 3 AEP 717 (X 10)
STAGE 4 AEP 718 LIMITER
STAGE 5 AEP 719 (X 5)
STAGE 6 AEP 716 (D.L.)
STAGE 7 AEP 720 (X 10)
STAGE 8 AEP 714 OUTPUT
LOSS ADJUSTMENT
LOSS ADJUSTMENT
HEAD OUTPUT STAGE
INTEGRATOR
HEAD AMPLIFIER
GAIN SWITCH
POSITIONS 1, ÷2, ÷5, ÷10, ÷20, ÷50
CLOCKWISE →
SHIELDED 5 CORE CABLE
SUPPLIES TO HEAD
MAIN AMPLIFIER INPUTS (NEGATIVE)
RG 62U (NOT OVER 50 FT.)
NOTE
* H·S· 1% RESISTORS
CAPACITORS, TANTALUM-POLARIZED. 1 MF UNLESS NOTED
WAVEFORM AMPLITUDES ARE QUOTED FOR NORMAL FULL OUTPUT AT FULL GAIN.
Q1, 5 – 2N393
Q2, 3, 13, – 2N501
Q4, 15, – 2N1308
Q6, 7, 9, 10, 11, 12, 14 – 2N604
Q8 – 2N1269

Fig. 4. Schematic of amplifier.

The supply is capable of providing up to 150 mA in each voltage line but this capability is not fully used in this amplifier which consumes only 28 mA at $\pm$ 30 V. The design of the power supply will not be discussed further.

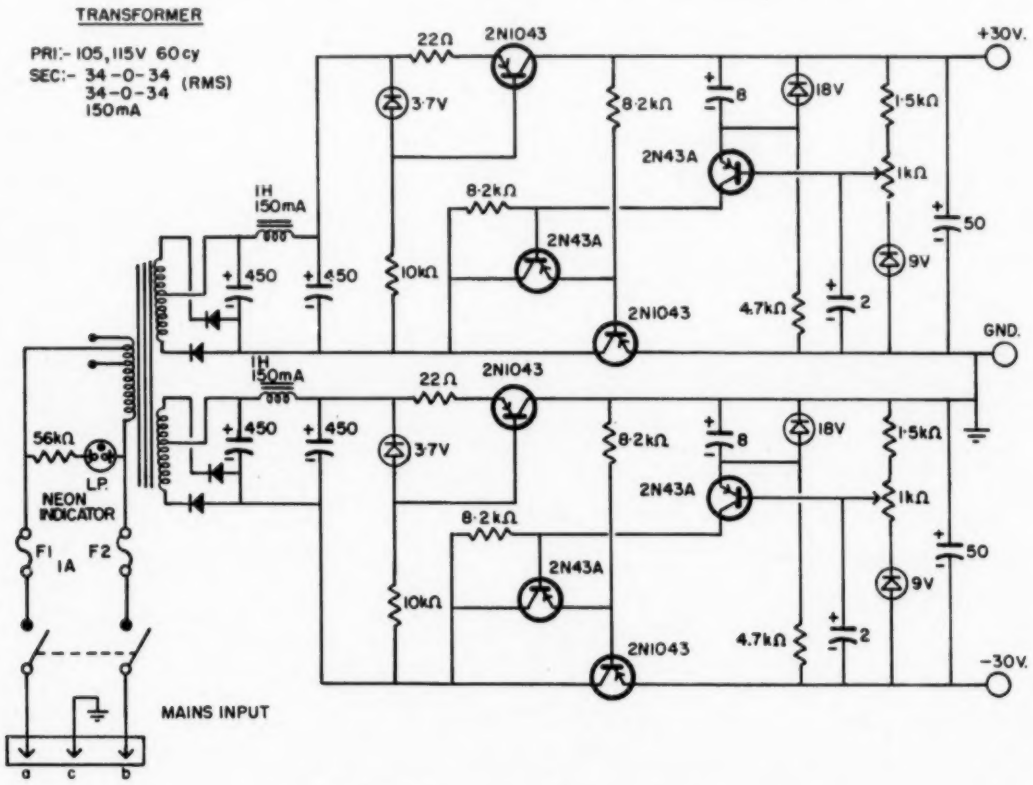

Fig. 5. Power supply schematic.

The block diagram shown in fig. 6 will be used in the following discussion of the general problems involved in the design of the amplifier. Considering the input stages first, a choice must be made between shaping short pulses in the head or integrating the detector charge in the head and feeding long pulses (i.e. with slow decay) into the main amplifier which contains the pulse shaping components. We chose the second alternative partly due to the inconvenience of including shaping lines in the head—which may well be in an inaccessible location where space is at a premium—and also due to the slight reduction in noise obtained when the shaping is done later in the amplifier. The chosen method is not without its difficulties. The greater the number of stages handling long pulses the more severe are problems due to "pile-up" at high counting rates of large overload

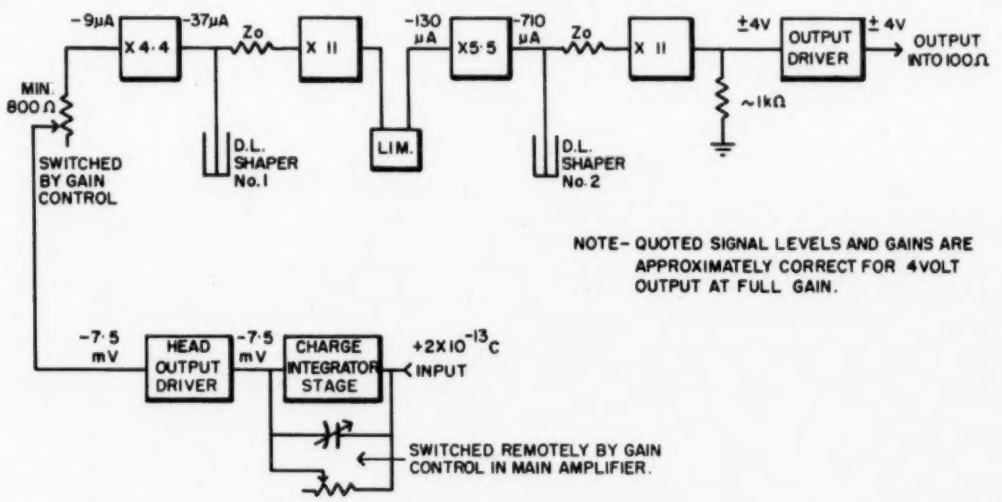

Fig. 6. Amplifier block diagram.

pulses. Also it is difficult to realise long decay times in transistor circuits due to the presence of leakage and drive currents in the input base circuit. This difficulty led to the use of the feedback integrator in preference to a more conventional emitter follower.

The input circuit is designed to accept positive pulses from the dynode of a photomultiplier. This choice was made bearing in mind the increasing use of the final anode (negative pulse) for fast coincidence purposes.

The output signal from the integrator feeds an output driver stage designed to feed 100 Ω cable linking the head to the main amplifier. For most applications where long lengths of cable are not required, matching the cable at the head end only is more satisfactory than terminating in 100 Ω at the amplifier end of the cable. This results from the fact that the driver stage would be called upon to drive a large dc current into the 100 Ω termination in the latter case if a high rate of large overload pulses were applied to the input. If very long lengths of cable are required between head and main amplifiers and if high rates of overload pulses are not present, termination at the main amplifier end of the cable would be preferred.

The signal levels involved in the head amplifier are quite small under normal operating conditions but rise to large values when the main amplifier gain is reduced by attenuation at the input. The design is based on the premise that high counting rates (up to 10^5/sec) of overload pulses equivalent to 50 times the normal maximum operating level may be present. Thus, with no attenuation at the input of the main amplifier (i.e. a series resistor of about 800 Ω) signals levels up to 0.4 V may be produced in the head by these 50 $\times$ overload pulses. At high rates changes in the operating points of the transistors result and, to minimize these, a fixed decay time constant of slightly over 25 μs is built into the integrator. With this time constant and 50 $\times$ overload pulses occurring at 10^5/sec "pile-up" effects may produce up to about 1.5 V temporary shift in operating points in the head. Attenuation at the input of the main amplifier increases this figure and, for this reason, such attenuation is limited to a factor of 5. Further reduction in the overall gain of the system is produced by increasing the value of the integrating capacitor in the head by a factor of 10. This is accomplished by using a diode arrangement in the head switched remotely from the main amplifier by changing a dc level.

The gain and configuration of the main amplifier was determined by the following considerations:

(a) The input stage should present a low impedance at its input. This allows gain to be changed by switching a series resistor and also permits mixing of signals from more than one head and from a test pulse generator.

(b) The first shaping line should be as early as possible in the amplifier.

(c) The only limiting action in the amplifier should occur before the second delay line. This is essential if the area balance of the negative and positive pulses at the output is to be preserved.

(d) The previous consideration implies that the limiter shall not affect linearity and gain in the normal linear range of the amplifier but shall limit sharply slightly above the linear range. A resistor-semi-conductor diode series combination may be shown to exhibit a change from 99% transmission to 99% attenuation (incremental) for a change of output voltage across the diode of about 300 mV. We have therefore chosen to place the limiter diode at a point in the amplifier where the normal maximum linear signal is about 1 V and the diode is biased to produce virtually complete limiting at 1.5 V.

(e) Having fixed the limiter voltage, consideration of the rise-time and stray capacities leads to a choice of resistor value in the limiter ($\sim$ 5 kΩ) and this, in turn, determines the current gain requirements preceding the limiter.

(f) Using easily available very high frequency transistors a simple output stage has been designed capable of feeding up to $\pm$ 6 V into 100 Ω cable. Fixing the normal linear output of the amplifier at $\pm$ 4 V allows the use of this stage. The Chalk River 100-channel analyzer has been modified to accept and analyze these

$\pm$ 4 V signals and we have also designed discriminators with a threshold accuracy of about 0.1% of this signal.

(g) The previous consideration fixes the overall current gain of the amplifier.

(h) Allocation of gain between the head and the main amplifier is affected by various considerations but we have been guided by the desire to keep the noise due to the input circuit of the main amplifier to a small fraction of 1% of the normal operating level at that point in the system.

C_5 decoupling ac signals in this feedback loop. The current in R_{10} or R_{10} and R_{12} combined, depending upon the setting of the gain control in the main amplifier, determines the dc potential at the collector of Q_2. This is chosen to be about — 11 volts. The collector of Q_1 is returned to a low voltage (— 2 V) and its emitter current is kept at a low value (80 μA); these two measures ensure that Q_1 contributes a minimum of noise at the input due to its base current fluctuations. Lowest noise demands a small base current in the input transistor. The type of transistor

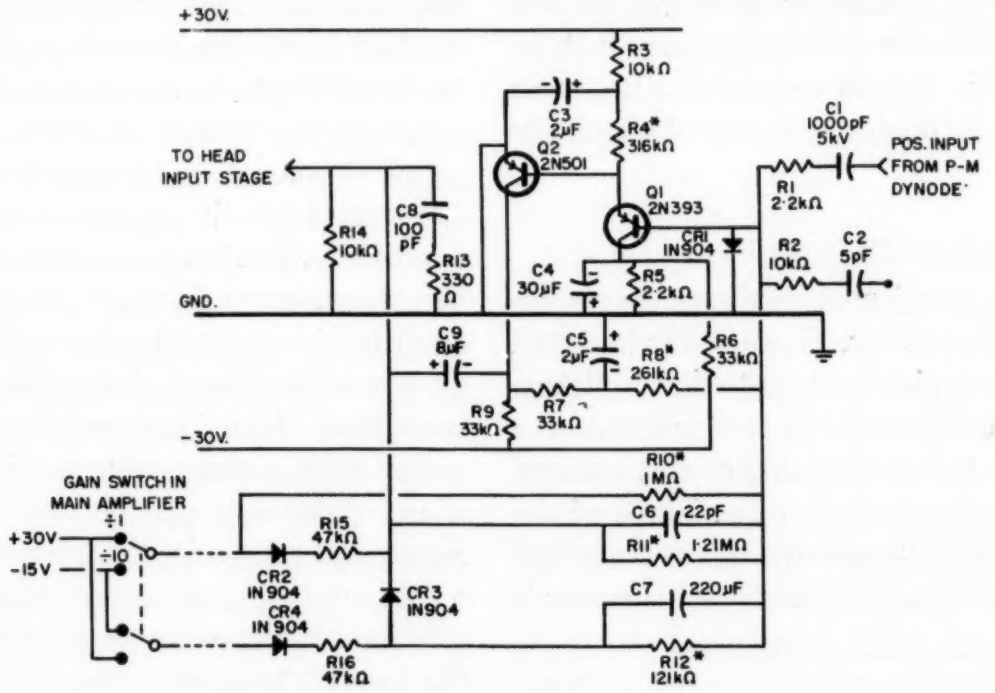

Fig. 7. Integrator-head amplifier.

3. Detailed Stage Design Considerations

In this section a brief description of the circuit of each stage is given together with an explanation of the choice of dc conditions.

3.1. HEAD AMPLIFIER-INTEGRATOR STAGE

Fig. 7 shows the integrator stage in detail and will be used in this description. In discussion of this and the following stages the complete amplifier circuit given in fig. 4 should be used to determine the relationship of any stage to others in the amplifier.

The integrator stage consists of two transistors in cascade, a grounded collector Q_1 driving a grounded emitter Q_2. The dc conditions are determined by feedback through R_7 and R_8 with chosen (2 N393) is the best available type for this position at the present time. Diode CR_1 protects Q_1 from damage when the P-M voltage is applied. It is necessary to use a good quality silicon diode in this position to keep its noise contribution small.

In addition to the input to the head from the dynode of the P-M, a test input is also provided. A voltage step of 40 mV applied to the test input simulates the normal maximum signal under full gain conditions.

When operating under full gain conditions the anode of CR_2 is returned to + 30 V and that of CR_4 is returned to — 15 V. Current therefore flows through CR_2 and R_{15} into R_{14} producing about + 5 V across R_{14}. Diode CR_3 is then

reverse biased since R_{12} connects the anode of CR_3 to the base of Q_1 which is near ground potential. Thus the ac feedback in the integrator is only via C_6, R_{11} while C_7, R_{12} are isolated from the feedback loop. When the gain is to be reduced by a factor of 10 the anode of CR_4 is connected to + 30 V and that of CR_2 to — 15 V. CR_3 then conducts and C_7, R_{12} shunt C_6, R_{11}. In either gain position the decay time constant in the integrator remains near 25 μsec.

3.2. HEAD AMPLIFIER-OUTPUT STAGE

This stage is a transistor analogue of the White cathode follower used commonly in tube circuitry. As the output stage of the main amplifier is similar the design of this stage will be discussed later.

3.3. CURRENT AMPLIFYING STAGES

Four current amplifying feedback pairs are used in the main amplifier. These differ in detail according to the requirements as to dc conditions and gain in different parts of the unit but the basic circuits are the same and the same printed circuit wiring is used in each case. Three of the stages use two p-n-p transistors, but in stage 3 of the amplifier the second transistor of the pair is

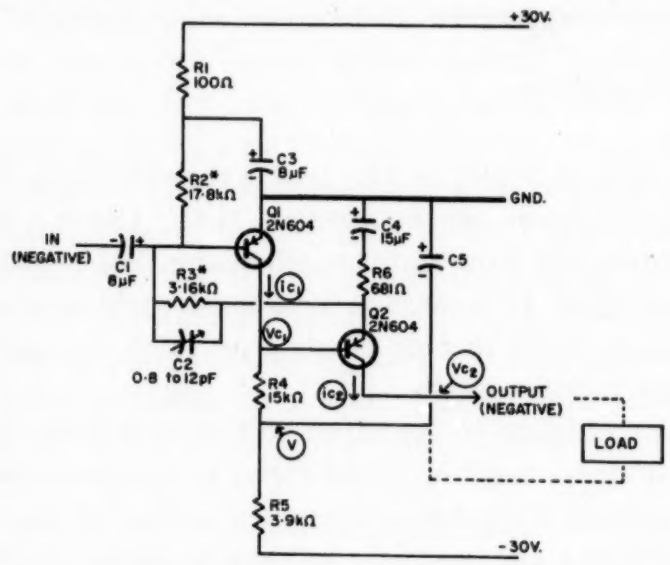

Fig. 8. Typical current amplifying stage.

an n-p-n. This is necessary to avoid overload problems in that particular stage but the basic operation is the same as the other stages. Fig. 8 shows a typical current amplifying stage.

The stage consists of two transistors in cascade, Q_1 being a grounded emitter stage while Q_2 is a grounded collector stage as far as the feedback is concerned. The output is taken from the collector of Q_2 so no phase change occurs in the stage. The current in R_2 flows in R_3 and sets up the dc conditions; thus, in this particular stage, the emitter of Q_2 and collector of Q_1 each resides at about — 5 V with the collector current of Q_1 about 1 mA while that of Q_2 is about 1.5 mA. The ac current gain of the stage is given approximately by $\alpha_2 (R_6 + R_3)/R_6$ where α_2 is the emitter-collector current gain of Q_2. In modern transistors $\alpha_2 \rightarrow 1$ and tests on a number of transistors have shown that α_2 remains constant to within $\pm 0.1\%$ or better for a $\pm 10°C$ change of temperature providing that the transistor is operated under its correct conditions. The low frequency feedback factor of the stage shown in fig. 8 generally exceeds 200 resulting in excellent gain stability and constancy whatever cause of possible gain changes is considered. Transistors may be changed, voltages varied over a reasonable range and the temperature of the unit can be varied over a $\pm 10°C$ range—all producing a total gain change, in the whole amplifier, of considerably less than 1%.

Trimmer capacitor C_2 permits adjustment of the overall frequency response of the stage to produce optimum pulse shape with no overshoots on the edges of the pulse.

The load connected to the amplifying stage output depends upon its position in the main amplifier. The dc conditions in each stage are chosen to permit developing the required signal across the load without either saturating the second transistor or causing it to become

TABLE 1

	V_{c1}	V	V_{c2}	i_{c1}	i_{c2}	Note
Stage 1	— 3	— 12.0	— 12.0	0.35	3.8	
Stage 3	— 5.1	— 17.5	+ 3.2	0.8	— 0.5	n-p-n in second position
Stage 5	— 5.1	— 20	— 20	1.0	1.6	
Stage 7	— 5.1	— 24	— 15	1.20	7.5	

Volts with respect to gnd. Current in mA.

non-conducting. Approximate operating conditions in the various stages shown in fig. 4 are given in table 1 in which the circuit references are the appropriate ones in fig. 8.

3.4. DELAY LINE PULSE SHAPER

Two of these units are included in the main amplifier and lines of different lengths may be plugged in depending upon the decay time of the scintillator being employed. For NaI-Tl, 1 μsec wide pulses are usually shaped. The mechanical arrangement of the delay line shaper is shown in fig. 3 and reference should be made to fig. 4 for the circuit. It is particularly important to terminate the first delay line carefully to avoid both high frequency and low frequency mismatch for, while the normal maximum signal level at the collector of Q_6 is about 40 mV and one channel of a 100-channel kicksorter corresponds to 0.4 mV at this point, 50 times overload signals produce 2 V here. Thus if recovery to less than 1 channel is required the match must be sufficiently accurate that rings, overshoots etc. are kept down to less than 1 part in 500 of the input pulse. Since the second delay line is never subjected to large overloads its matching is less critical but, for convenience, the same adjustments are included with each delay line. These adjustments and their purpose are as follows:

(a) Loss Adjustment

The integrator in the head is arranged to produce a decay time constant of 25 μsec and this waveform when fed to the usual shorted delay line would produce an overswing on the back edge of the shaped pulse. If the shaped length were 1 μsec the overswing would amount to $\frac{1}{25}$th of the pulse amplitude. In order to prevent this happening, a small variable resistance is inserted in place of the usual short circuit in the delay line shaper. Adjustment of this variable resistor alters the loss in the delay line reflected pulse and can be used to eliminate the overswing on the back edge of the shaped pulse. The slight droop on the top of the pulse produced by the 25 μsec decay time-constant is tolerable.

(b) Resistive Match

The usual variable resistor is provided to allow accurate matching at the driving end of the shaper and thereby prevent multiple reflections. Note that we are using current amplifying stages here and the following stage therefore appears in series with the termination, not in shunt as in tube amplifiers.

(c) H.F. Match-Capacity Trimmer

An attempt is made to include a filter network to match the end of the cable despite capacity loading due to the collector of the driving stage. A trimmer capacitor included at the output of the filter is found to permit adjustment to give the best high frequency match.

3.5. LIMITER STAGE

Fig. 9 shows the limiter stage. In the normal operating range diode CR_2 is conducting while CR_1 and CR_3 are reverse biased (see dc potentials shown on the diagram). Input signals appear as pulses of increasing current in the n-p-n transistor which forms the output of the previous stage. In the normal operating range these pulses share between R_1, R_2, R_3, R_6 and the series resistor R_4 feeding the next stage. Since resistor R_4 is of much lower value than the remainder most of the signal from the input of the limiter

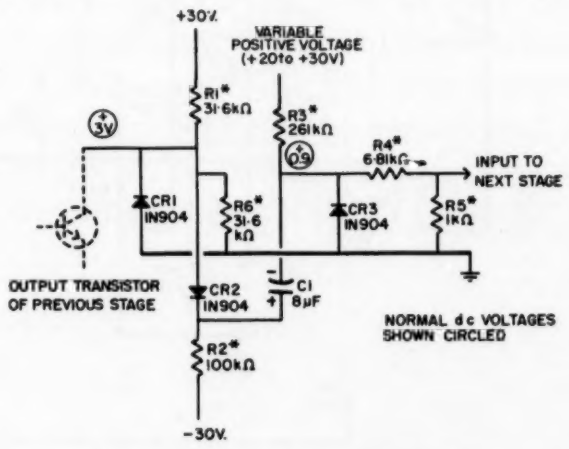

Fig. 9. Limiter stage schematic.

appears at its output. Signals slightly larger than the normal linear range cause CR_3 to conduct and this attenuates the output. As mentioned earlier, the attenuation changes from a negligible amount to a factor of 100 for a change in output

of about 300 mV so, while the circuit is completely linear (i.e. no attenuation due to CR_3) at levels below 1 V of pulse across R_4 (and CR_3), virtually complete limiting is present at 1.5 V. Adjustment of the positive voltage applied to R_3 changes the bias on CR_3 thereby changing the limit level. This adjustment is included to allow for variations between diodes used for CR_3.

When diode CR_3 conducts, CR_2 becomes nonconducting which limits the current charging C_1 during the pulse to that in R_2 (i.e. 340 μA). Were diode CR_2 not present, the largest overload pulses would produce large pulse currents in C_1 and, at high counting rates, a serious shift in the dc voltage across R_4, R_5 would result. Inclusion of CR_2 cuts this dc shift to a tolerable amount. The additional diode CR_1 serves to prevent saturation of the output transistor of the previous stage under the worst overload conditions.

3.6. OUTPUT STAGE

The circuit of the output stage is shown in fig. 10. In order to feed a 100 Ω cable with $\pm$ 6 V pulses the stage must be able to feed $\pm$ 60 mA into the load. To ensure adequate linearity of response the stage must exhibit an output impedance which changes by less than 1 Ω over the operating range. To accomplish these objectives while consuming only a small standing current a transistor version of the well known White cathode follower is used. Transistor Q_1 acts as a difference amplifier between the input and output lines and the amplified signal at the collector of Q_1 is fed to two transistors Q_2 (p-n-p) and Q_3 (n-p-n) in parallel. By using complementary transistors in this manner we ensure that one of these transistors is turned on whichever polarity of input pulse is applied to the circuit. Resistor R_4 defines the standing current in Q_1, R_8 defines the current in Q_2 and the difference between these currents flows in Q_3. Diode CR_1 protects the circuit against very large overload pulses.

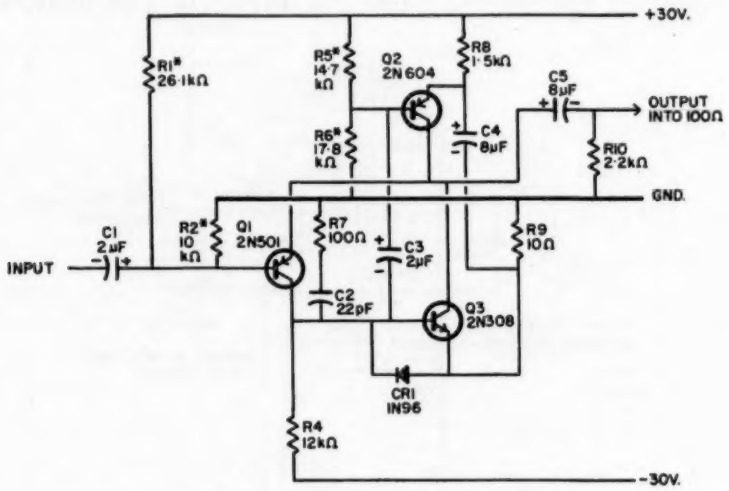

Fig. 10. Output stage schematic.

Loop stability of the circuit does not present severe difficulties as transistor Q_1 appears as a grounded base stage within the loop while Q_2 and Q_3 appear as grounded emitter stages. Since Q_1 is a very high frequency type of transistor the loop response is dominated by the time constant associated with Q_2 and Q_3. To ensure stability under all conditions R_9 is inserted in the emitter circuits of Q_2 and Q_3 thereby increasing the impedance appearing at the collector of Q_1. C_2 and R_7 then shunt this collector to roll off the loop gain at high frequencies.

The head amplifier output stage is similar but, since only negative pulses are to be handled, transistor Q_2 and the associated components are omitted.

4. Performance

4.1. GAIN STABILITY

Varying the ambient temperature over the range 25° C to 45° C produces a change in gain of less than 0.6% and varying the mains input voltage from 105 V to 125 V ac produces no measurable gain change. Gain changes at high counting rates are difficult to measure due to small shifts which occur in the kicksorter used for measurement but counting rates up to 10^5/sec of 15 times overload pulses appear to produce gain changes less than 1%. Less than 0.2% drift in the amplifier gain has been noted over a period of 1 day.

4.2. LINEARITY

The incremental gain of the amplifier (i.e. the slope of an input-output plot) is constant to within 1% over the full 4 V normal range of outputs. We have not detected any departure

from linearity under high counting rate conditions.

4.3. NOISE

The equivalent R.M.S. noise input of each of the two amplifiers tested was about 4000 ion pairs ($\sim$ 30 μV in 20 pF). At full gain this corresponds to a full width at half maximum of less than 1% on an output pulse of 4 V amplitude.

A 0.3 μsec line used in the first shaper and replacement of the second shaper by a network (1 K series, 1 K shunt) coupling from stage 5 to 7 reduced the RMS noise to 1800 ion pairs. For applications requiring low noise and short time resolution (e.g. semi-conductor junction detectors) this mode of operation is preferable to the normal double delay line mode.

4.4. OVERLOAD PERFORMANCE AT HIGH COUNTING RATES

Fig. 11 shows an example of the performance of the amplifier under these conditions. The amplifier fed a 100-channel kicksorter self-gated to reduce wastage of counting time due to noise at low levels and overload pulses at high levels. The system gain was adjusted to observe the Ba^{137} X-ray emitted by a Cs^{137} source. Curves (a) and (b) show the resulting peak under conditions where only the Cs source was present and the total counting rate above 10 keV adjusted to be 10^4 and 5×10^4 counts/second respectively. Curve (c) shows the effect of large overload pulses produced at a rate of about 5×10^4 counts/second by a Co^{60} source added to the 5×10^4 counts/second of Cs^{137}. The peak is broadened somewhat (from 24% to 28%) but there is very little shift in the peak position. A further experiment (not shown in fig. 11) showed a broadening to 32% when observing 10^4 counts/second of Cs^{137} in the presence of 10^5 counts/second of Co^{60}.

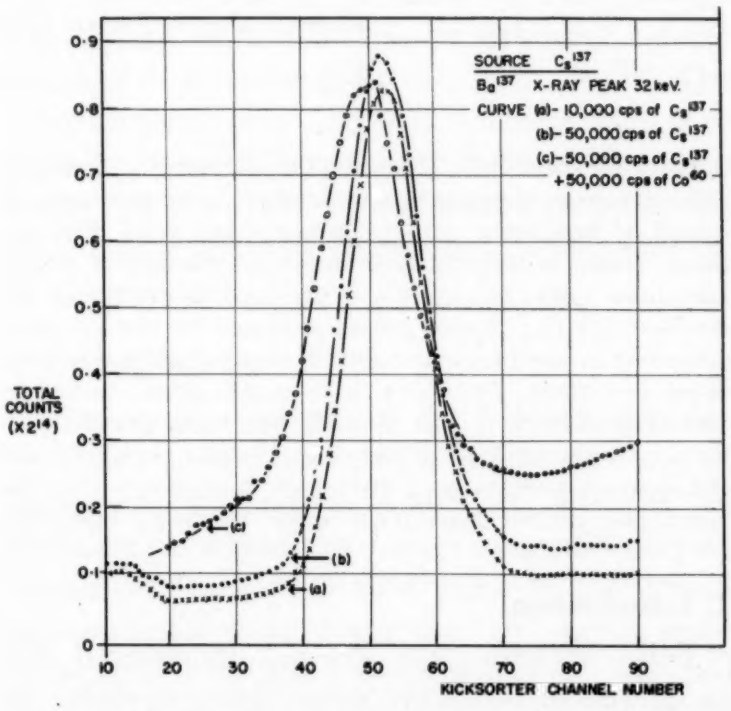

Fig. 11. Spectra at high counting rates.

Acknowledgements

This work was carried out as part of the research programme of the Physics Division of Atomic Energy of Canada Ltd. Our thanks are due to several colleagues who contributed ideas to the design. R. A. McNaught carried out some of the measurements quoted in this paper.

NUCLEAR INSTRUMENTS AND METHODS 9 (1960) 282–296; NORTH-HOLLAND PUBLISHING CO.

A TRANSISTORIZED FAST-SLOW COINCIDENCE AND PULSE AMPLITUDE SELECTING SYSTEM II

F. S. GOULDING and R. A. McNAUGHT

Atomic Energy of Canada Limited, Chalk River, Ontario, Canada

Received 20 June 1960

This paper describes a system developed for fast-slow coincidence experiments in nuclear physics and discusses the design of functional units including a low level discriminator, single or dual-channel analyzer, coincidence circuit and linear gate. The system is designed to use the ± 4 V double-delay-line shaped pulses produced by the amplifier described in the previous paper or equivalent pulses from other amplifiers. Operation with single phase pulses of similar amplitude is also possible but with reduced performance. Uncertainty of the discriminator threshold and the spurious pedestal and disturbances introduced by the linear gate are less than 10 mV under all normal operating conditions. Functional units of the system are constructed on printed circuit boards which plug into a base unit where interconnections are made between them through a programming plug. This arrangement allows the experimenter to change interconnections quickly and makes the whole system extremely versatile. The system also takes advantage of the timing accuracy of the zero cross-over of double-delay-line pulses to give a coincidence resolving time of 40 nsec while using no fast amplifiers or coincidence circuits. A technique of compensating for baseline shift at high counting rates of single phase pulses is also described.

1. Introduction

Bell, Graham and Petch[1]) introduced the technique of fast-slow coincidence systems in 1949 and, since that time, the technique has seen common use in many nuclear physics experiments. The complexity and size of the apparatus required for these experiments is alarming and, for this reason, the development described in this paper was initiated. Apart from the reliability and small size of transistor equipments there appeared to be possible technical advantages over vacuum tube circuits in the small voltage drifts in semi-conductor devices used as voltage discriminators[2]) which would allow the use of relatively low level signals. The system to be described has been designed to accept — 4 V

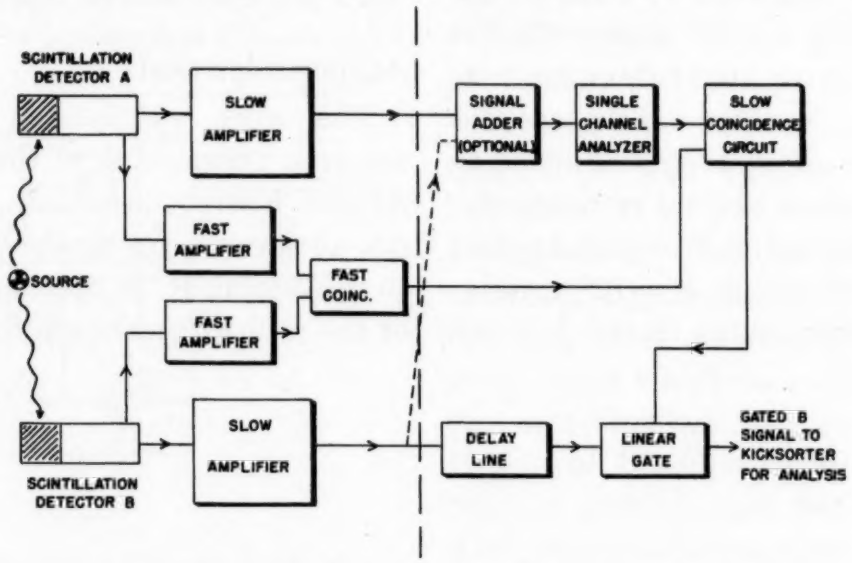

Fig. 1. Typical fast-slow coincidence and amplitude.

[1]) R. E. Bell, R. L. Graham and H. E. Petch, Canadian J. of Physics **30** (1952) 35.

[2]) F. S. Goulding and L. B. Robinson, Chalk River Report CREL-778 (1958).

signals for measurement purposes and the best operation results when ± 4 V signals from a double-delay-line amplifier such as that described in the previous paper are employed. Using these signals the timing accuracy of the zero cross-over of the pulse can be used for fast coincidence purposes[3]) thereby eliminating the need for high frequency chain type amplifiers in all but very short resolving time applications.

The arrangement shown in fig. 1 was chosen as a typical example of a fast-slow coincidence system. It was realised at the outset that many experiments involve more than two signal inputs but nearly all can be built up of dual input blocks such as that in fig. 1. A single unit as described here can accept only two signals for amplitude measurement but connections can be made to other similar units through several connectors provided on the front panel. It was also realised that the experimenter would require many arrangements of interconnections between the functional circuits. To permit this, all required inputs and outputs to and from circuit units are connected to a single programming socket on the front panel of the unit through which interconnections are made. The plug which the experimenter inserts in this socket contains a block diagram of the actual connection system appropriate to that plug.

As an additional aid to versatility of the individual functional circuit units each has been designed to present a reasonably high impedance at the input and, in the case of circuits handling linear signals, the output can drive full signal into matched 100 Ω cable. The circuits which provide logical outputs (i.e. a pulse or no pulse) produce a current output of 10 mA and will develop up to $+12$ V into the load chosen according to the application. Normally these logical outputs are terminated in 100 Ω providing $+1$ V pulses, but it is often convenient to have the higher level output available (e.g. to drive existing scalers).

The mechanical design of the unit is based on the use of a standard form of rack mounting printed circuit board base unit in use at Chalk River. A stable power supply (for the circuit details see ref.[4])) mounts on the chassis while receptacles for up to 14 printed circuit boards occupy the remainder of the chassis. In this particular unit only 8 boards are included and shields are inserted in the remaining positions to reduce electrical interaction between the units. The printed circuit boards insert from the rear of the chassis and access to the sockets for maintenance purposes is available by removing a cover plate over a cut-out in the front panel. The programming plug and discriminator bias controls are mounted on the front panel. Screened leads are used for signal connections to the programme plug to reduce interaction in the low level circuits.

2. Overall Design

The system shown in fig. 1 illustrates the functions to be performed in a fast-slow coincidence system. Signals in the "A" channel are amplitude analyzed by a single-channel analyzer which produces an output pulse to the coincidence circuit only when the "A" input pulse amplitude is within a restricted range. The fast portion of the system determines whether signals in "A" and "B" channels occur within a very short predetermined time of each other and, if so, the fast coincidence circuit feeds a pulse into the slow coincidence unit. If the slow coincidence circuit receives simultaneous inputs from the single-channel analyzer and the fast coincidence circuit it produces an output pulse which opens the linear gate for a defined time allowing the signal in the "B" channel to pass unchanged to a kicksorter for amplitude analysis.

The measurement of pulse amplitude by the single-channel analyzer cannot be completed until the input pulse has reached its peak height. This involves a time delay in measurement and equalizing delays must be inserted in the fast coincidence circuit output and in the "B" channel if the linear gate is to be opened before the "B" signal reaches it. The delay line ac-

[3]) E. Fairstein is believed to have suggested this technique in 1958.

[4]) F. S. Goulding and R. A. McNaught, Canadian Electronics Eng. **3** (1959) 28.

complishes the delay in the "B" channel and fig. 1 assumes that a circuit delay is included in the fast coincidence circuit. The final result of these operations is that the system presents to the kicksorter only those "B" signals coincident within a very short time interval with "A" signals of a selected amplitude. In one common modification of the simple system the single-channel analyzer measures the sum of "A" and "B" channel signals (dotted in fig 1).

while using no fast circuit of the type shown in fig. 1. In this unit we have chosen to limit the resolution to 40 nsec to avoid the need for accurate matching of line lengths in the amplifiers. Faster coincidences can be achieved by feeding a pulse into the unit from an external fast coincidence circuit in the manner shown in fig. 1.

Fig. 2 shows the arrangement employed in the unit. Apart from the delay line and the dual-channel analyzer each functional unit is a single

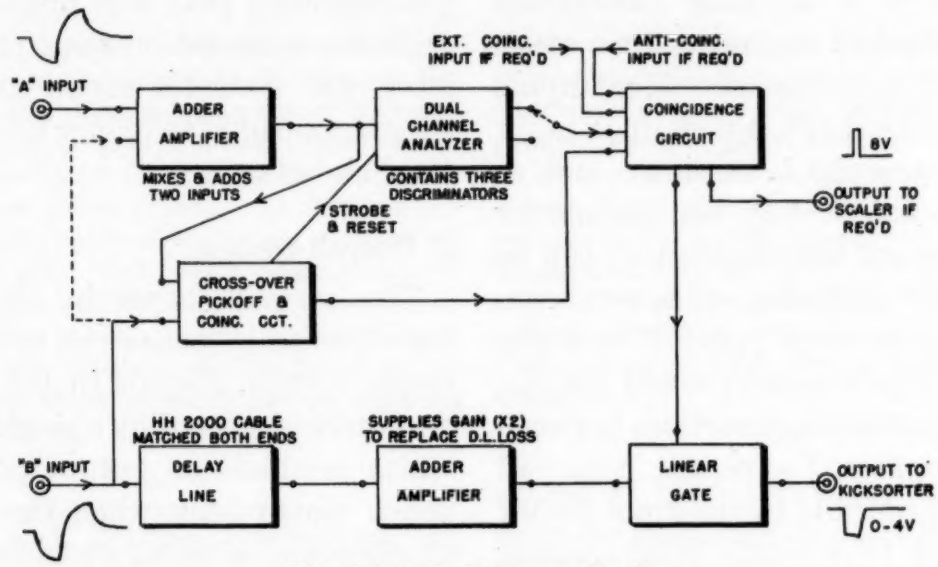

Fig. 2. Block diagram of unit.

In considering the design of a fast-slow coincidence unit the decision was made to omit the fast coincidence circuit shown in fig. 1 from the main unit and regard it as a separate unit. Where very high speed is required it is essential that wiring and construction be more carefully controlled than is possible in a versatile unit of the type to be described. Also, for many applications, no fast coincidence circuits are required to reduce chance coincidence pulses. The decision was therefore made to include circuits in the unit capable of performing functions similar to those to the right of the dotted line in fig. 1.

Use of double delay line pulses suggested the possibility of simply reducing the resolving time of the unit by including circuits capable of determining the zero cross-over of the pulses and taking a coincidence between the zero cross-over in channels A and B. By this technique it is possible to achieve coincidence resolving times of a few nanoseconds on NaI(Tl) scintillation pulses

printed circuit board. The dual-channel analyzer contains 3 discriminator boards while the delay line mounts under the chassis of the base unit. Thus 8 boards are included in the unit. The base unit is wired to bring the inputs and outputs from the boards to the programming socket where connections are made through a programme plug. Fig. 2 illustrates just one way of interconnecting the units. Mounted together with the programme plug is a row of test points which allow monitoring of all waveforms and also permit the connections shown dotted in fig. 2 to be made as required.

3. Details of Functional Circuit Units

3.1. ADDER AMPLIFIER (see fig. 3)

This is a simple circuit designed to provide the facility of algebraically adding two input signals and/or providing gain where required in the system. In fig. 2, one such unit is used in the "A" channel to add signals at input points 14, 15

while, in the "B" channel, a similar unit is used to provide gain × 2 at input 12 to make up for the signal loss due to the delay cable matched in its characteristic impedance at each end.

3.2. COINCIDENCE CIRCUIT (see fig. 4)

This circuit accepts three + 1 V inputs (12, 14, 15) which, if coincident for about 20 nsec normally result in a shaped output pulse + 10 mA,

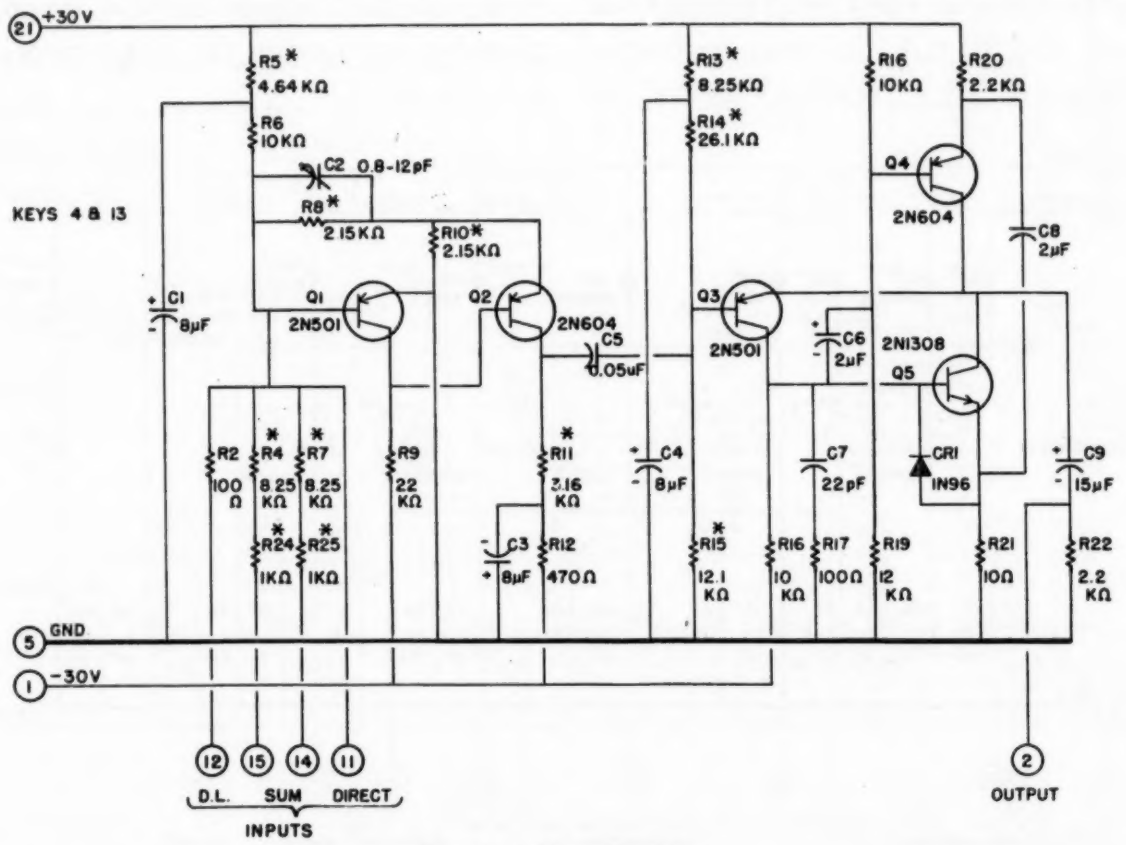

Fig. 3. Adder amplifier.

Transistors Q_1, Q_2 constitute a dc fed-back amplifier with feedback from the emitter of Q_2 to the base of Q_1. The base of Q_1 acts as a virtual ground to provide an adding point for inputs. The collector waveform of Q_2 feeds an output driver containing Q_3, Q_4 and Q_5 which will drive the full signal (up to 6 V) into a 100 Ω load if required to do so. This output stage, which is a transistor complementary-pair analogy to the well known White cathode-follower, was described in the previous paper where a similar stage is used as an output stage in the double delay line amplifier.

The delay line shown in fig. 1 is terminated in 2200 Ω at each end of the cable. The terminating resistors mount directly on the ends of the cable, the input one being *series* fed by the input signal while the *current* in the output resistor is *series* fed to the adder amplifier. Thus no stray capacity is added across the termination of the cable and excellent signal shapes result.

0.4 μsec wide. A + 1 V pulse applied to an anti-coincidence input (22) during the entire time for which the other inputs are coincident inhibits the circuit and prevents an output pulse occurring.

The resistor R_4 provides a nearly constant current of 10 mA into the emitter circuits of transistors Q_1 to Q_5. In the rest condition this current shares between the emitters of Q_2, Q_3 and Q_4 since the bases of these transistors are about 0.5 V negative with respect to the base of Q_1 and 1.6 V negative with respect to the base of Q_5. Thus nearly 10 mA flows in the common collector circuit of Q_2, Q_3 and Q_4 and produces a voltage drop of 3.8 V in R_6. Application of + 1 V input pulses to any one or two of the transistors Q_2, Q_3 and Q_4 causes no change in this situation since if, for example, Q_2 and Q_3 are turned off, Q_4 conducts all the 10 mA current. If, however, simultaneous + 1 V inputs are applied to Q_2, Q_3 and Q_4, Q_1 momentarily conducts the 10 mA, the

collector voltage of Q_2, Q_3, Q_4 falls and the negative voltage swing at these collectors is fed via C_6 to the base of Q_5, Q_5 therefore starts conducting and the positive feedback loop causes a trigger action to ensue at the end of which Q_5 is conducting all the 10 mA, its base potential swinging to about + 13 V (i.e. 1.5 V below the external capacity across pins 8–11 on the printed circuit socket.

The action of a + 1 V anti-coincidence pulse is to prevent Q_1 coming into conduction at the start of the trigger action described earlier, thereby preventing the triggering process from occurring.

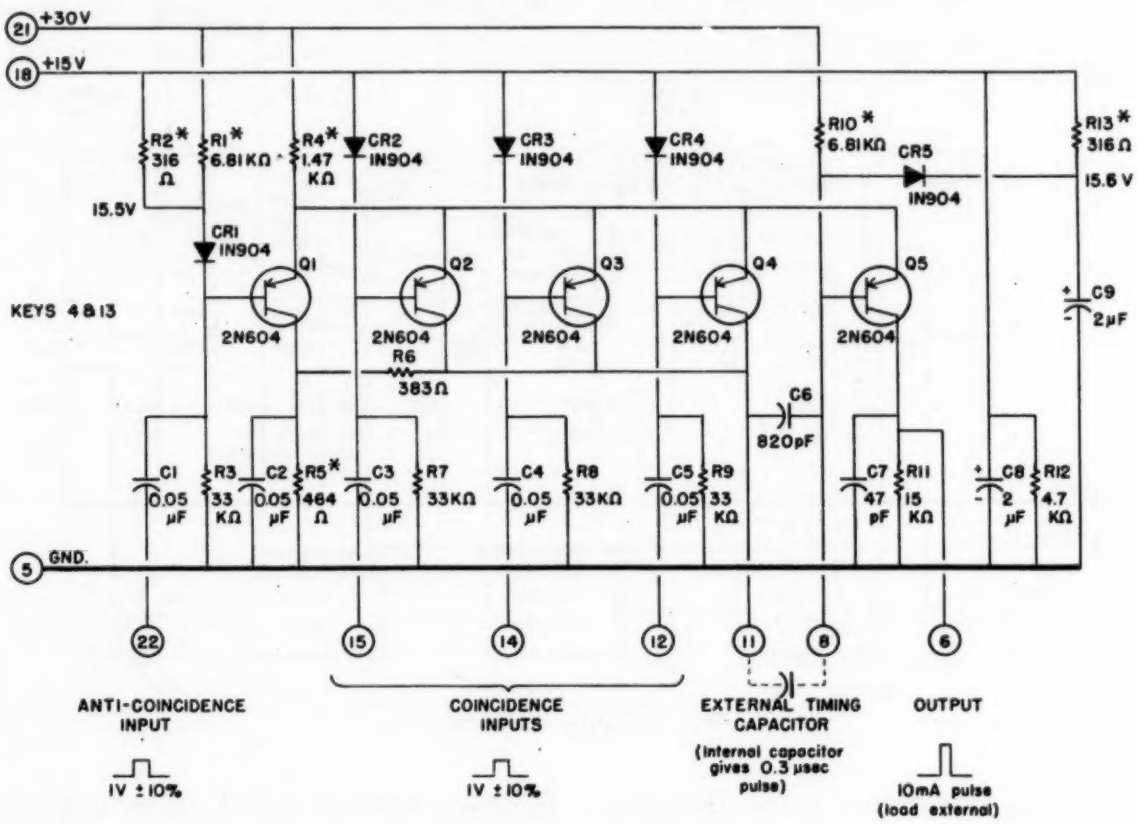

Fig. 4. Coincidence circuit.

base potentials of Q_2, Q_3 and Q_4. The trigger action is extremely fast and occupies only a few nanoseconds.

Following this action, the base of Q_5 rises as C_6 is charged by the current flowing in R_{10}. When the base potential of Q_5 approaches that of Q_2, Q_3 and Q_4 these transistors start to conduct and a regenerative action starts at the end of which the circuit has relaxed back to its rest condition. The output pulse is taken from the collector of Q_5 where a 10 mA pulse is available. This is usually used to produce + 1 V in 100 Ω for other logical units. The small capacitor C_7 prevents rapid changes in the collector voltage of Q_5 thereby reducing the slowing down in triggering which is caused by Miller effect in Q_5. The output pulse width (normally 0.4 μsec) may be increased by adding

The circuit is quite tolerant of variations in input pulse amplitude; both coincidence and anti-coincidence inputs can be varied over the range 0.6 V to 1.5 V with no effect on circuit operation.

3.3. VOLTAGE DISCRIMINATOR (see fig. 5)

The use of low level pulses in a system demands a high degree of stability in the voltage discriminators employed. In the present case we are dealing with a 4 V system and it is reasonable to demand a discriminator with a triggering threshold accuracy of about ± 4 mV under all working conditions. Since the Chalk River kick-sorter operates from negative pulses the discriminator is required to measure the negative pulses of the bi-phase waveform produced by double delay line shaping. A single semi-conductor diode is unable to achieve the required

threshold sensitivity since the voltage drop in such a diode, at constant current, exhibits a temperature coefficient of about — 2.5 mV/° C. For a ± 10° C change of temperature, a reasonable operating range, the change in threshold is

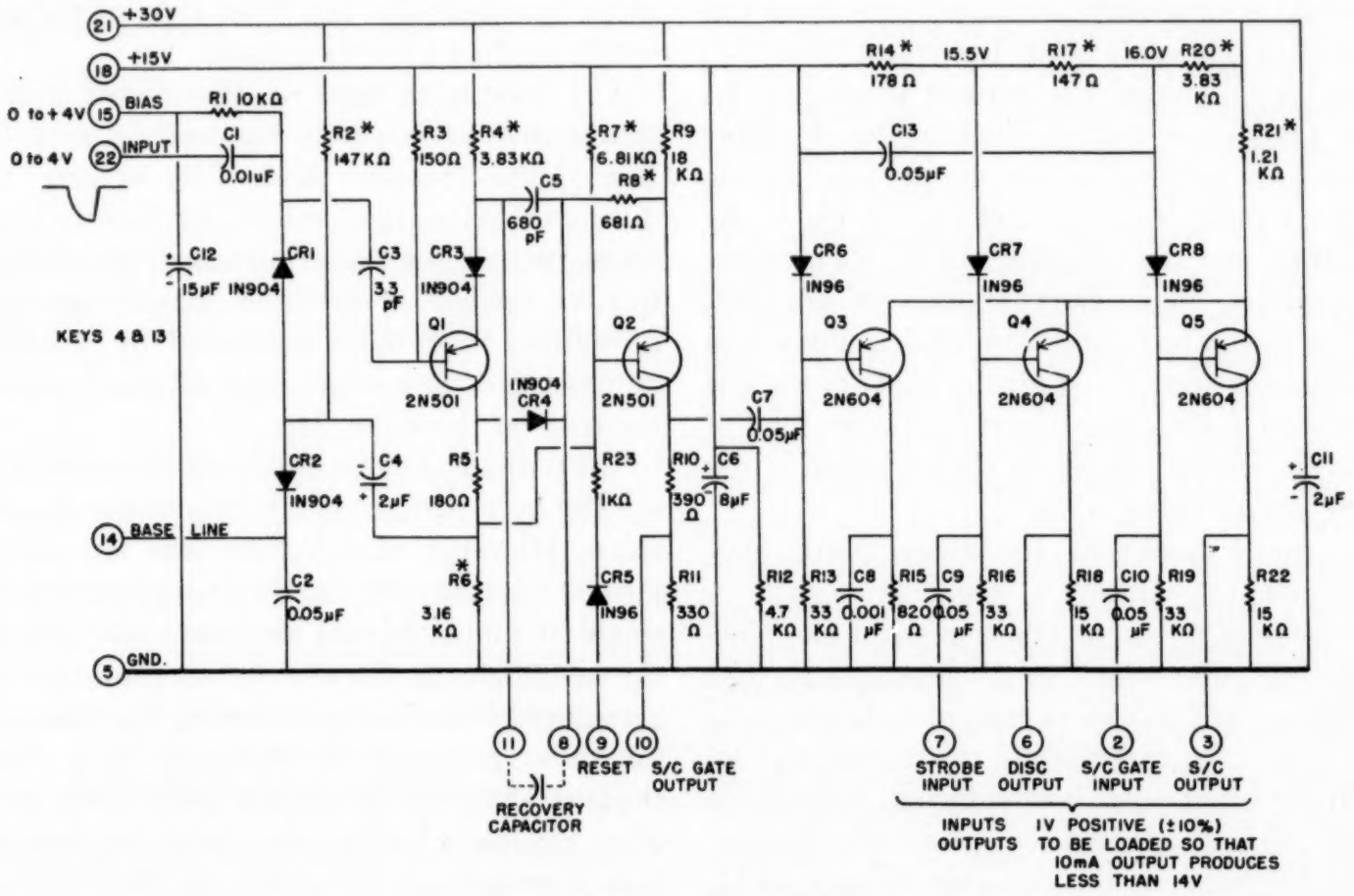

Fig. 5. Voltage discriminator.

± 25 mV. Fortunately, nearly all diodes of a given type exhibit within ± 5% the same temperature coefficient. Therefore, if the drop in one diode is balanced by the drop in another of the same type the temperature coefficient of the pair of diodes will not exceed 250 μV/° C— (i.e. ± 2.5 mV change for ± 10° C).

In the circuit shown in fig. 5, diode CR_1 is the voltage discriminator element while CR_2, operating at constant current, provides the temperature compensation for changes in CR_1. Back bias (0 to + 4V at pin 15) is applied to diode CR_1 and only when the negative pulse applied to the cathode of CR_1 exceeds the bias does CR_1 conduct and a small pulse appear across CR_2.

In a biased diode discriminator of this type a second type of temperature variation occurs. Leakage current in CR_1 flows in R_1 producing a voltage drop in R_1 which changes the effective bias on CR_1. Since the leakage current of the diode is temperature dependant the effective bias depends on temperature. To reduce this effect to negligible proportions a low leakage silicon diode type is selected for CR_1 and the value of R_1 is limited to a value where the temperature coefficient due to leakage current in CR_1 is less than ± 1 mV for ± 10° C change of temperature.

An additional source of change in threshold of a discriminator is base-line shift at the cathode of CR_1 at high pulse rates. This effect is negligible when using double delay line pulses, where the areas of positive and negative pulses are equal, but can be very serious when using single phase pulses. A circuit, to be described later, has been devised which measures the base-line of single phase pulses and the base-line determined by this circuit can be fed into pin 14 on the discriminator board. This minimises the base-line shift at high counting rates of single phase pulses. When using double delay line pulses pin 14 is grounded.

The circuit associated with transistors Q_1 and Q_2 is a trigger circuit of the type described in ref.[2]). With the values shown in fig. 5 the circuit triggers when a negative pulse of about 150 mV appears across CR_2. The triggering threshold is extremely accurate ($\sim \pm 1$ mV) as required in this application. In the rest condition, transistor Q_1 passes the current flowing in R_4 while Q_2 passes that flowing in R_9. Positive feedback is present in the circuit due to the direct coupling from the collector of Q_1 to the base of Q_2 and the coupling via C_5, R_8 between the emitters. Since both transistors are conducting in the rest condition, the circuit would be oscillating were it not for the effect of the low impedance of CR_2 shunting the collector load of Q_1 via Q_4, thereby reducing the loop gain in the trigger circuit below unity.

As seen by diode CR_2, the trigger circuit may be shown to exhibit a negative resistance roughly equal in magnitude to resistor R_8. Thus a negative pulse which feeds through CR_1 and appears across CR_2 causes current to flow into C_4 from diode CR_2; this reduces the current in CR_2 and, if the input pulse is of sufficient magnitude (about 150 mV) across CR_2, the circuit triggers. When this happens the collector voltage of Q_1 drops as Q_1 becomes non-conducting. The 7 V drop at the collector of Q_1 feeds through C_4 to the common anodes of diodes CR_1 and CR_2 holding both diodes out of conduction for the duration of the relaxation period of the trigger circuit.

Capacity feedthrough in CR_1 is partially compensated by the action of capacitor C_3 and resistor R_3. A negative input pulse causes a differentiated negative pulse at the base of Q_1 which tends to prevent the trigger circuit action to the same degree as the capacity breakthrough in CR_1 aids triggering. C_3 has been chosen to make the trigger level almost independent of signal rise time in the range 50 nsec to 0.5 μsec. During the relaxation period the emitter-base junction of Q_1 is reverse biased and C_5 charges due to the current in R_4 flowing into it. At a time determined by C_5 and shunt capacity connected externally across pins 8–11 of the printed circuit socket, Q_1 again conducts and a reverse trigger action occurs. Diode CR_4, which has previously been out of conduction, conducts and capacitor C_5 is rapidly recharged back to its original condition. The recovery time is very short amounting to less than 10% of the pulse width produced by the circuit.

The relaxation time of the circuit may be terminated prematurely by feeding a $+10$ V reset pulse through diode CR_5 at any time during the relaxation period. This facility is used when two or more discriminators are cascaded to give a single or multiple channel analyzer; a common reset pulse generated by a unit to be described then ensures that all discriminators are reset at the same time.

The parts of the discriminator described so far are the only parts required in a single discriminator. However, in a system like the one described here, several discriminators arranged as single or multi-channel analyzers are used and the remaining circuitry in the discriminator unit is required to facilitate cascading discriminators for these purposes. In the case of a single-channel analyzer, an output pulse must result when the lower but not the upper discriminator fires. Furthermore since the rise time of input pulses is not in general very short the two discriminators do not fire at the same time. We therefore arrange to wait until the input pulse is known to have passed its peak amplitude then to sample the condition of the discriminators and finally reset them. The output pulse from the single-channel analyzer which appears during the sampling or strobe period is therefore delayed with respect to the input signal.

An external unit, described later, is used to generate the sample (strobe) and reset pulses. Each discriminator then contains a coincidence circuit similar to that described in the previous section of this paper which accepts inputs from the discriminator itself, from the next highest discriminator in the cascade and also the strobe pulse. The discriminator itself generates a 2.5 V positive pulse which feeds the base of normally conducting transistor Q_3 transferring the current from Q_3 to Q_4. When a ($+1$ V) strobe input

pulse is fed to the base of Q_4 the current transfers to Q_5 unless a + 1 V pulse taken from pin 10 on the next higher discriminator is present at the base of Q_5. In this case Q_4 remains in conduction when the strobe is applied. Thus the + 10 mA output pulse at the collector of Q_5 in a particular discriminator only occurs following a signal

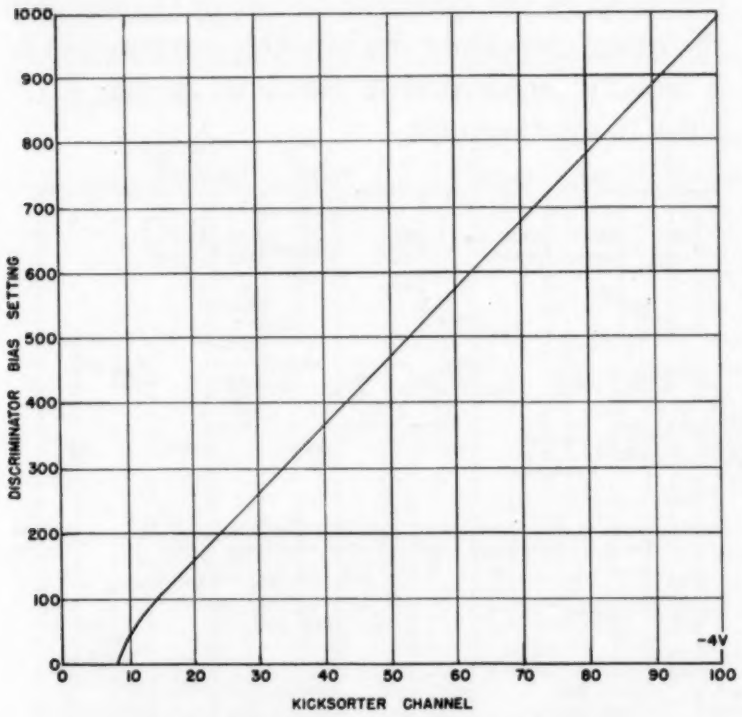

Fig. 6. Discriminator calibration curve.

whose amplitude lies between this discriminator bias and the next one in the cascade. The collector of Q_4 provides a pulse which indicates that the discriminator has fired.

Bias for the discriminators is obtained from helical potentiometers supplied with a stable voltage from a Zener reference element. The potentiometers and the Zener regulating system mount on the front panel of the complete unit. The circuit is shown together with the overall connections for the double-channel analyzer in fig. 9. The linearity of calibration of the discriminator bias control is a matter of some interest. As seen in fig. 6 the calibration is almost linear but the calibration line does not pass through the origin. This is due to the fact that a portion of the current in CR_2 in fig. 5 flows in CR_1 at low bias levels and, when CR_1 is in conduction the sensitivity is mainly determined by the threshold level of the trigger circuit containing Q_1 and Q_2.

3.4. CROSS-OVER PICK OFF AND COINCIDENCE CIRCUIT (see fig. 7)

As mentioned in the previous section cascading several discriminators to produce a multi-channel analyzer requires that a strobe pulse be developed at a time when the input pulse amplitude is known to have reached its maximum value and that a discriminator reset pulse be developed following the strobe pulse. A convenient way of determining a suitable time for the strobe pulse is to measure the zero cross-over of a double delay line pulse (see fig. 2 for pulse shape). One function of the unit to be described is to determine the cross-over of pulses fed to the dual-channel analyzer and to develop strobe and reset pulses for the discriminators in the analyzer. Transistors Q_6, Q_7 determine the cross-over while Q_9, Q_{10} and Q_{11} produce strobe and reset pulses appropriately delayed from the cross-over. Emitter-follower Q_{12} provides the reset pulse with adequate current to reset up to ten discriminators. The cross-over measuring circuit Q_6, Q_7 is duplicated in the "B" channel by Q_1, Q_2 and transistors Q_3, Q_4, Q_5 act as a fast coincidence circuit producing an output pulse at the collector of Q_5 only when crossovers in "A" and "B" channels occur within 40 nsec of each other. The diode circuits in the input of both crossover circuits limit the signal amplitude applied to the transistors to a level where reverse emitter breakdown does not occur.

The operation of the crossover measuring circuit will be described with reference to Q_1, Q_2. Double-delay-line pulses up to ± 6 V in amplitude appear at pin 3 with the negative phase of pulse preceding the positive phase. When no pulse is present the current in R_1 shares between CR_1 and CR_2, approximately 1.25 mA flowing in each. Small negative or positive pulses feed through the two diode impedances in series into the 464 Ω resistor R_4 in the base of Q_1. Large negative signals cut-off the current in CR_2 producing a maximum negative signal of about 0.6 V at the base of Q_1. Large positive signals cut-off CR_1 producing + 0.6 V at the base of Q_1. Thus small input signals appear almost

unchanged at the base of Q_1 but large signals are very effectively limited.

Q_1 and Q_2 constitute a Schmidt type circuit with an accurately controlled amount of backlash (about 150 mV). Q_2 is in conduction in the rest condition and the circuit is triggered into the opposite state when the input negative edge exceeds 150 mV. Due to the voltage movements at the base of Q_2 the retrigger action does not occur until the pulse crosses the baseline at the end of its negative excursion. Preset the base of Q_3. A similar arrangement feeds pulses at the "A" channel crossover from Q_7 to the base of Q_4. Q_3, Q_4 and Q_5 constitute a coincidence circuit of the type described earlier in the paper and, when coincident pulses occur at the bases of Q_3 and Q_4 a shaped square $+10$ mA current pulse 0.25 μsec wide is produced in the collector circuit of Q_5. As with the other coincident circuits this output (pin 6) is usually terminated in 100 Ω to give a $+1$ V pulse in another unit.

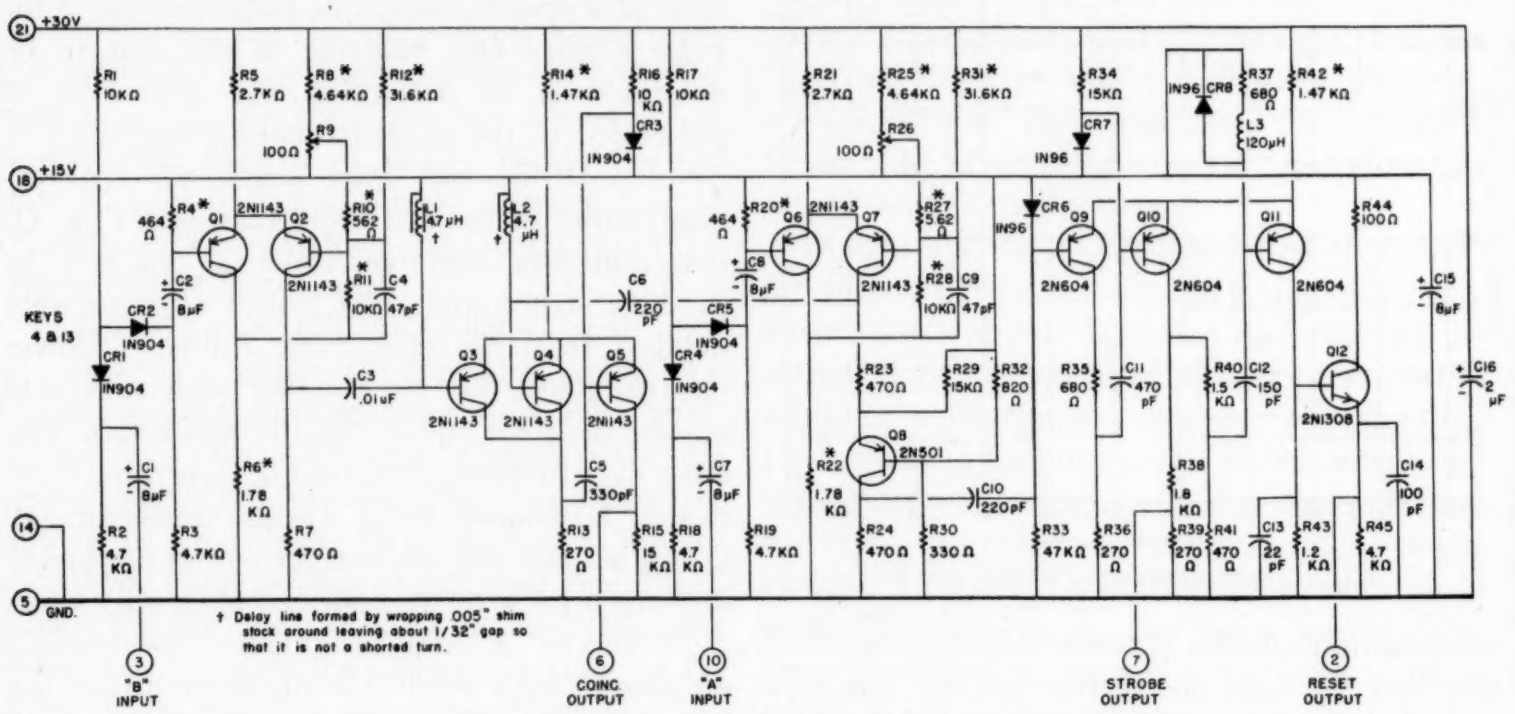

Fig. 7. Cross-over pick off and coincidence circuit.

potentiometer R_9 is provided to allow exact adjustment of the crossover trigger point since the precise trigger level is dependent upon the characteristics of the transistors. Adjustment of R_9 is conveniently carried out by feeding a 300 mV negative pulse having an exponential tail into the input and adjusting R_9 to cause the circuit retrip to occur when the tail reaches 5 mV or so (i.e. or 22 μsec if the pulse tail time constant is 5 μsec). This accuracy of measurement of the crossover ensures timing accuracy of the crossover of $\pm$ 3 nsec on NaI(Tl) pulses for a range of pulse amplitudes from 200 mV to 4 V (the range measured by the discriminators).

When the current in Q_2 turns on at the crossover point, a narrow positive pulse about 1.5 V high is shaped by the shaping network† in

The collector current of Q_7 flows in Q_8 and the back edge of the pulse at the collector of Q_8 is used to trigger a three-transistor trigger circuit which produces strobe and reset pulses for the discriminators. Q_9 is normally in conduction passing all the current (10 mA) in R_{41}. A positive pulse fed from the collector of Q_8 to the base of Q_9 via C_{10} causes Q_{10} to conduct for a period determined by capacitor C_{11} and other components in the base of Q_{10} and collector of Q_9. When Q_9 goes out of conduction its collector voltage falls. This drop in voltage feeds via C_{12} to the base of Q_{11} turning on Q_{11} for a period

† The shaping network is a 4.7 μH "National" choke surrounded by a close fitting grounded shield to give distributed stray capacity from the coil to ground. Its characteristic impedance is about 500 Ω.

determined by its base circuit. This circuit arrangement, which is an adaptation of the coincidence circuit described earlier, allows the generation of a sequence of delayed pulses at a cost of 1 transistor per delay plus 1 triggering transistor. In this case the circuit is used only to produce a + 1 V strobe pulse at pin 7 and a + 10 V reset pulse at the collector of Q_{11} which feeds emitter-follower Q_{12} to drive the output pin 2.

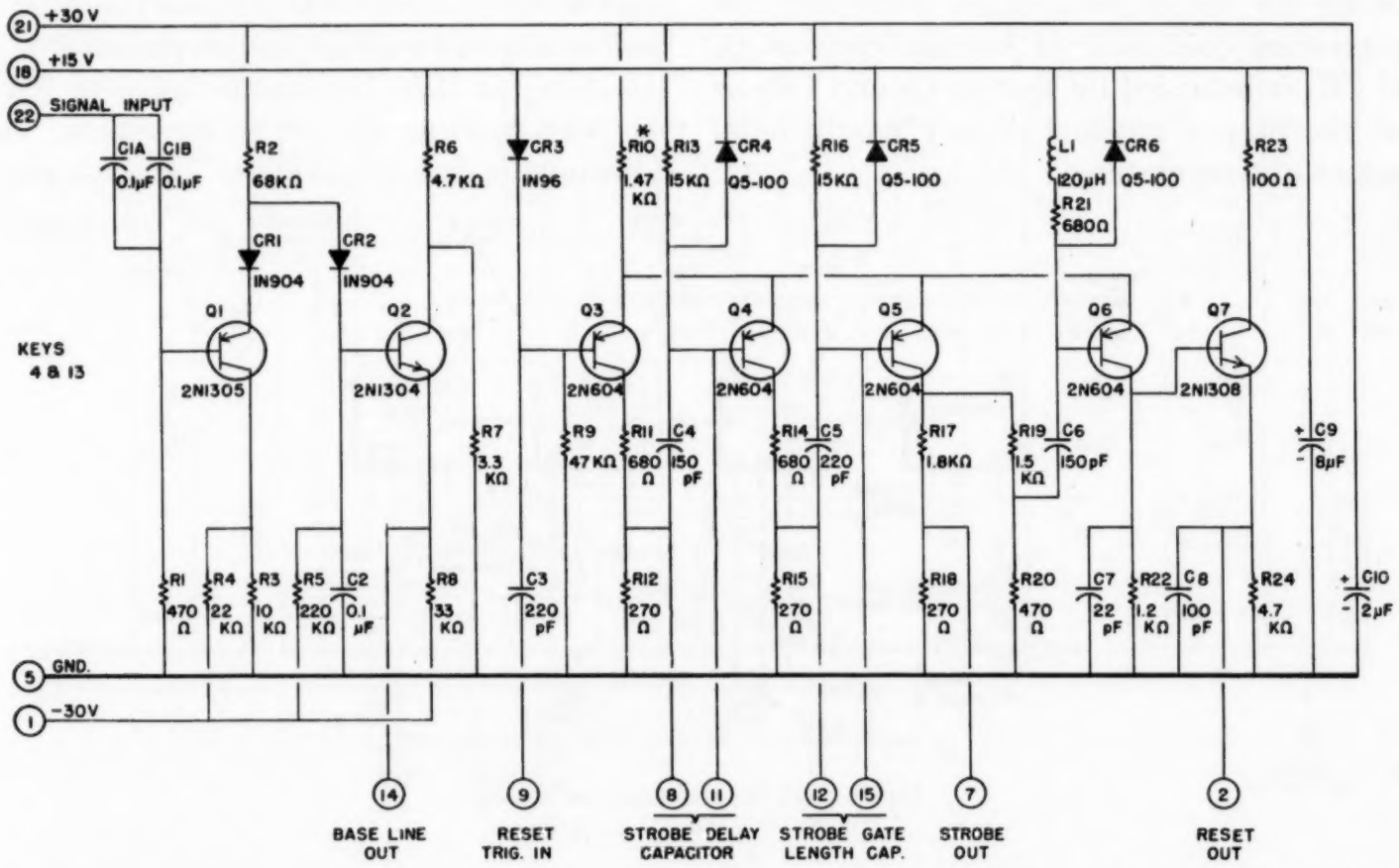

Fig. 8. Base line compensator strobe and reset circuit.

3.5. BASE LINE COMPENSATOR, STROBE AND RESET CIRCUIT (see fig. 8)

Inevitably some applications of the system involve the measurement of single phase as distinct from double delay line pulses. To deal with these cases a unit has been designed which can replace the crossover measurement unit just described in these applications. This unit duplicates the functions of developing strobe and reset pulses as in the crossover pickoff unit but instead of using the input pulse zero crossover as its basic timing mark, the firing of the first discriminator is used for this purpose. A fixed delay then occurs before the strobe pulse is produced. The sequence of delays is produced by the circuits associated with Q_3, Q_4, Q_5, Q_6 in the same way as described in the previous section.

Transistors Q_1 and Q_2 are used to determine the baseline of the input signal pulses. The discriminators then measure the pulse heights from this baseline thereby largely eliminating the baseline shift effects at high pulse rates. Negative input pulses are fed to the base of Q_1 through capacitors C_{1A} and C_{1B} in parallel. At high rates the base of Q_1 moves in a positive direction between pulses since the average current flowing in C_1 must be zero. A negative pulse at the input is emitter-followed by Q_1 and, if the pulse height exceeds about 0.2 V, diode CR_2 is cut off. Capacitor C_2 prevents the cathode of CR_2 falling in potential appreciably during the pulse since C_2 can only be discharged by the small current flowing in R_5. When the negative pulse terminates, CR_2 again conducts, rapidly replacing the charge lost from C_2 during the pulse. It may be seen that a rate of 10^5 pulses/sec each 1 μsec wide causes a change of only about 15 μA in the mean current in the emitter of Q_1, CR_1 and CR_2

as compared with zero input rate. This current change in the three elements produces a total change in voltage across them of only about 5 mV. Thus the voltage across C_2 is a good replica of the baseline of the pulses at the base of Q_1. Q_2 emitter-follows the voltage at its base giving a low impedance output to serve as a baseline for the discriminators. Note that the temperature coefficient of voltage drop in Q_1 and CR_1 is balanced by that in Q_2 and CR_2 so that the output baseline is very nearly independent of temperature.

the bias dial reading is 1000 (i.e. bias control set to maximum bias). A 215 Ω resistor in series with the baseline (pin 14) to discriminator 1 causes the baseline of that discriminator to assume a potential of about + 40 mV (the voltage drop being due to the 200 μA flowing through CR_2 in the discriminator (fig. 5). Adjustable resistors in the equivalent points of the other two discriminators are set to produce the same — 4 V sensitivity in these discriminators as in 1 when the bias controls are set to maximum. These adjustments are required to compensate for

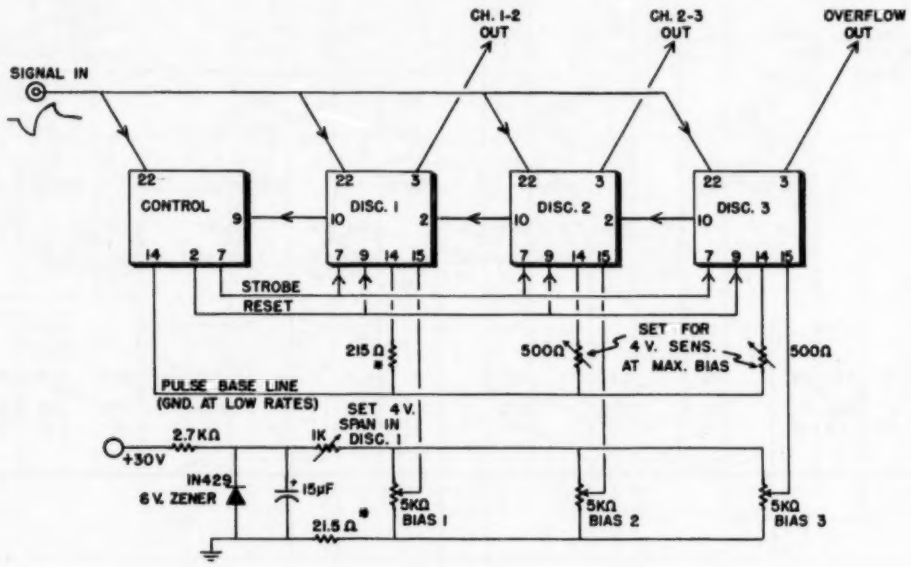

Fig. 9. Dual-channel analyzer wiring.

3.6. DUAL-CHANNEL ANALYZER (see fig. 9)

Many fast-slow coincidence systems use only a single-channel analyzer but occasions do arise when a dual-channel unit is useful and since sufficient space was available a dual-channel analyzer is included in the system. This uses three discriminators each with a bias control and a control unit which generates strobe and reset pulses for the discriminators. If double phase pulses are employed the preferred control unit is the crossover pick-off circuit described in section 3.4, while single-phase negative pulses require the baseline compensator unit described in section 3.5.

The connections shown in fig. 9 are almost self-explanatory. Bias for the discriminators is obtained from a Zener reference element and the 1 kΩ potentiometer in series with the 5 kΩ helical potentiometers serves to adjust the sensitivity of the discriminator 1 to — 4 V when different voltage drops in diodes in the various discriminators. When they are correctly made the discriminators track to within $\pm$ 0.2% of full-scale reading through their entire range.

3.7. LINEAR GATE CIRCUIT (see fig. 10)

The linear gate unit normally permits no input signals to pass through it but, on receipt of a gate trigger pulse, the gate connects signal input to signal output for a predetermined time.

All linear gates are imperfect in that a small pedestal is generated when the gate is open even though no signal is present at the signal input. To illustrate the importance of this many writers use the term "Pedestal-free gate" instead of "Linear gate" as used here. A second defect which occurs is break-through of signals from input to output when the gate is in its non-transmitting condition. These two defects are of

major importance in low level systems and, in a 4 V system as described here, both pedestal and signal breakthrough should be kept down to a few mV.

The block diagram (fig. 11) will be used in the following explanation of the operation of the linear gate. Q_5 and Q_6 are the gating elements; emitter in the non-conducting condition, signals fed to the collector of Q_5 are very highly attenuated by the gate before appearing at the output. Very small spikes appear at the output on fast signal edges but total break-through for 6 V signals is less than 10 mV.

When a gating trigger pulse is fed to its input

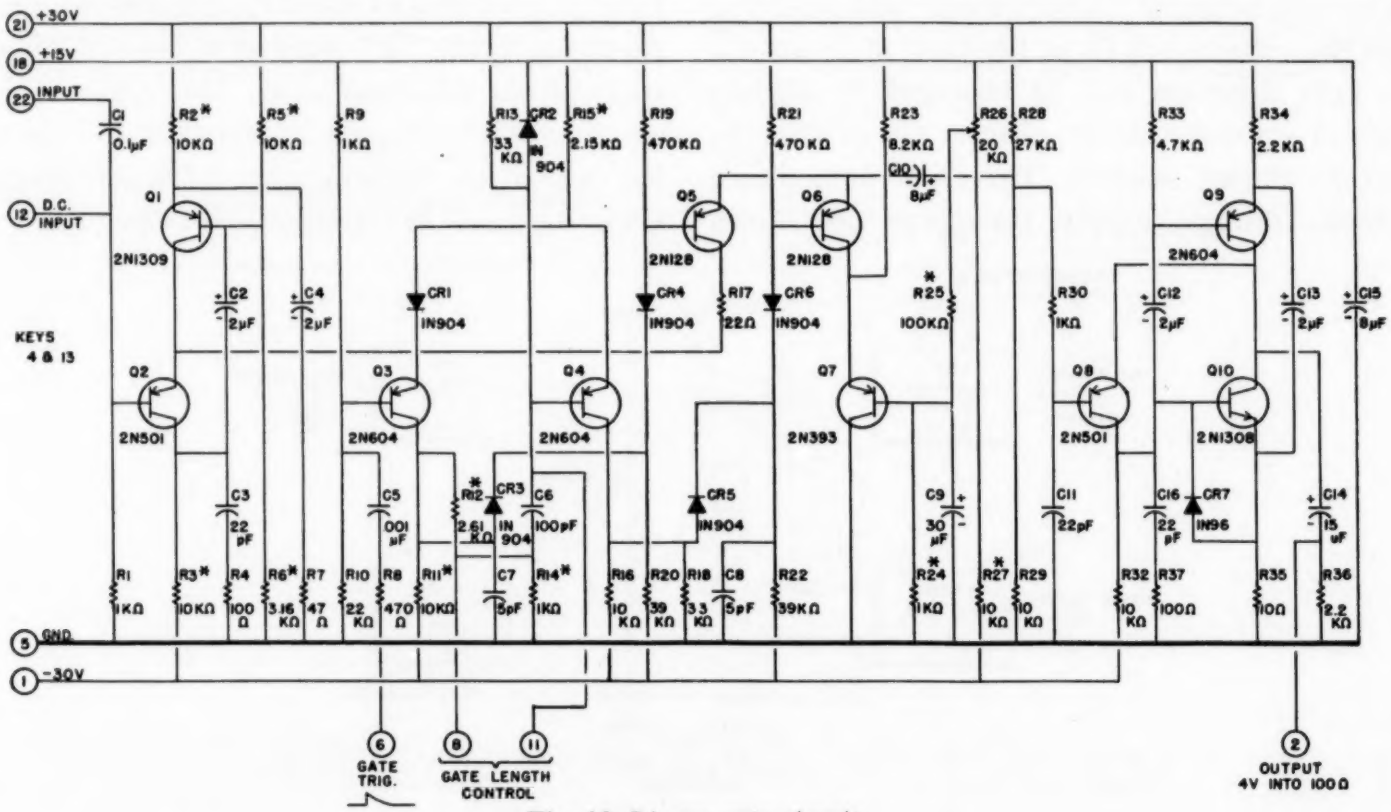

Fig. 10. Linear gate circuit.

the remainder of the circuit is incidental to the operation of the gate. In the rest condition of the circuit diode CR_3 is conducting so that the common cathode of CR_3 and CR_4 is held at + 7 V and, due to the 70 μA flowing in CR_4, the base of Q_5 is at approximately the same voltage. On the other hand CR_5 is non-conducting and CR_6 is passing 0.75 mA. The collector of Q_6 is connected to a low impedance voltage source whose output voltage is very close to ground. The current in CR_6 flows out of the base of Q_6 causing the collector of Q_6 to emit holes into the base and Q_6 acts as an inverted transistor. Since the emitter junction of Q_5 is reverse biased Q_6 is called upon to pass almost no emitter current and its emitter takes up almost the same potential as its collector. The effective impedance seen at the emitter of Q_6 is very low and since Q_5 behaves as a very high impedance between its collector and the gating pulse generator produces a narrow pulse which reverses the situation in transistors Q_5 and Q_6, Q_5 becoming a low impedance between collector and emitter while Q_6 becomes a high impedance. Thus, during the period of the gating pulse, the input signal suffers almost no attenuation in passing through the gate to the output of the unit. Note that a single transistor such as Q_5 or Q_6 with the other transistor replaced by a resistor acts as a good gate and, in fact, this arrangement is used in dc choppers[5]). However, using two transistors improves the transmission-attenuation ratio in the two conditions and also largely eliminates switching transients since one transistor comes into while the other one goes out of conduction.

The low impedance driver feeding the gate is

[5]) G. B. B. Chaplin and A. R. Owens, Proc. I.E.E. **105** B (1958) 258.

needed to prevent the collector current of Q_5 (when conducting) from producing a false signal. The low impedance output driver provides sufficient power to drive 100 Ω cable if required. Both drivers are similar to the output driver described in the previous article on the double delay line amplifier. The gating pulse generator is a normal Schmidt trigger circuit with coupling from the collector of Q_3 to the base of Q_4 via C_6. The gate duration can be changed by adding external capacity from pins 8 to 11 on the printed circuit socket. The low impedance variable voltage supply transistor Q_7 allows

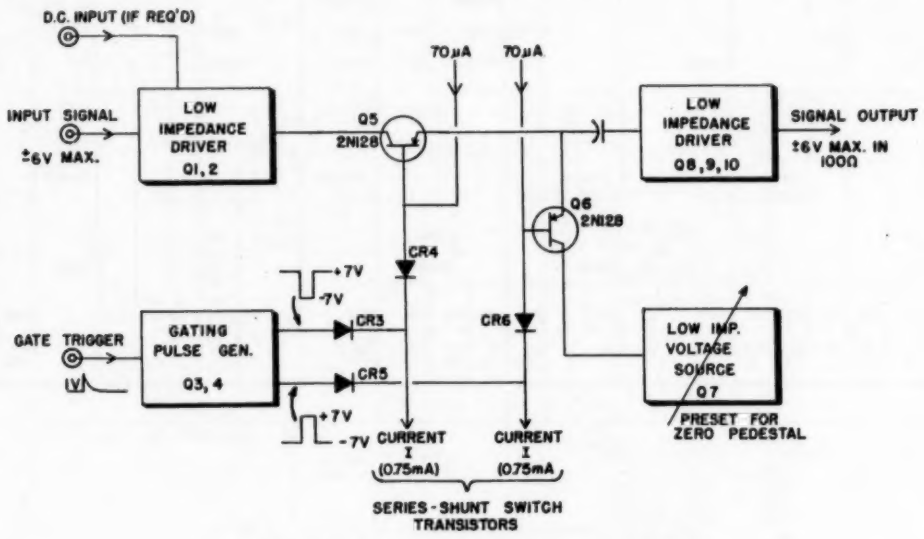

Fig. 11. Block diagram of linear gate unit.

adjustment of the pedestal to zero. The drop in the emitter-base junction of Q_7 compensates for that in the emitter-base junction of Q_2. Note that these voltages temperature compensate each other so that the pedestal is nearly independent of temperature.

Since the linear gate provides a good dc chopper, advantage can be taken of this to produce pulses of defined amplitude. With this in mind a dc input point is provided and application of trigger pulses to the gate generator while a dc potential is fed to the input produces pulses equal in amplitude to the dc input level. This facility is not used in the fast-slow coincidence system but has been used in other applications of the unit.

3.8. TIMING CONSIDERATIONS IN THE SYSTEM

Two cases must be considered according to whether the input pulses are single phase (negative) or double delay line pulses:

(a) *Single Phase Pulses* (using Base Line Compensator Unit)

In this case the triggering of discriminator 1 is used as the basic timing mark. A delay must then be provided to allow for the full rise time of the pulse in the "A" channel before strobing the state of the discriminators. This delay is made equal to the total pulse rise time T to cope with the case where discriminator 1 triggers from the very start of the pulse while the other discriminators may trigger at any point in the rise. Since, on the other hand, discriminator 1 may trigger on a small pulse very close to the end of the rise, the strobe timing can then be between as short as T and as long as $2T$ after the true start of a signal. Thus the linear gate will be instructed to open to allow signals through at any time between T and $2T$ after the start of a signal pulse. The linear gate requires 0.3 μsec to fully open so signals to be gated by it must be delayed by the delay line by a total time $2T + 0.3$ μsec if the gate is to allow through the start of the signal. In practice, the Chalk River kicksorter operates well from 0.3 μsec pulses and the open period of the linear gate need only bracket the signal for this time provided that the signal reaches its full amplitude during the gate open period. Clearly the ideal values of delay line length and of the durations of the various gates

and pulses depend upon the input signals and must be calculated for particular cases. However the following values have been chosen for NaI(Tl) pulses (rise time constant 0.3 μsec) shaped by a single 1 μsec delay line:

Strobe delay: 1.2 μsec
Strobe width: 0.5 μsec
Signal delay in "B" channel: 2 μsec
Gate duration: 2 μsec

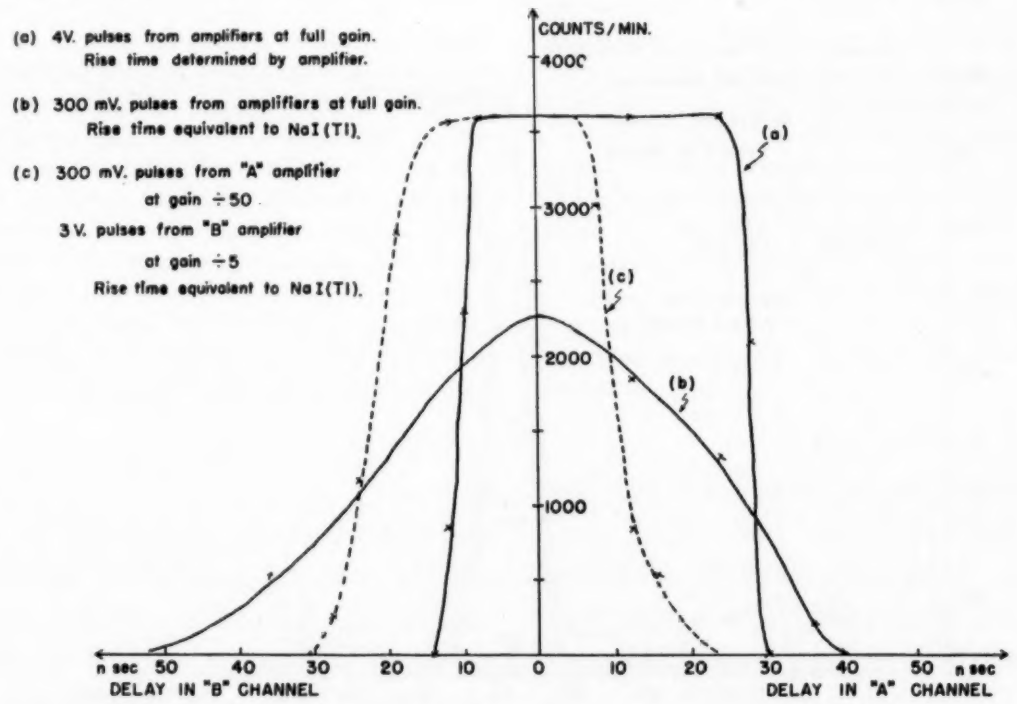
(a) 4V. pulses from amplifiers at full gain.
Rise time determined by amplifier.
(b) 300 mV. pulses from amplifiers at full gain.
Rise time equivalent to NaI(Tl).
(c) 300 mV. pulses from "A" amplifier
at gain ÷50
3V. pulses from "B" amplifier
at gain ÷5
Rise time equivalent to NaI(Tl).
COUNTS/MIN.
4000
3000
2000
1000
(a)
(b)
(c)
n sec 50 40 30 20 10 0 10 20 30 40 50 n sec
DELAY IN "B" CHANNEL
DELAY IN "A" CHANNEL

Fig. 12. Resolution curves for system.

(b) *Double Phase Pulses* (using Crossover Pick-off Unit)

In this case the basic timing mark is the cross-over from negative to positive phase in the pulse. Since this time is absolutely related to the start of the signal and also to the duration of the pulses it is possible to reduce all times as compared with the previous case. The strobe is automatically generated at the crossover time and the following times are suitable for operation with pulse lengths (negative phase) and rise times from 0.4 μsec to 1 μsec.

Strobe width: 0.5 μsec
Signal delay in "B" channel: 1 μsec
Gate duration: 0.5 μsec .

4. Performance

Tests on the instrument have shown that the whole system is quite capable of determining pulse amplitudes at rates up to 10^5 pulses/second and under all normal operating conditions with an accuracy of $\pm$ 5 mV. The time resolution has been measured by the usual method of inserting delay (100 Ω cable) in one channel relative to the other and the resulting resolution curve is seen in fig. 12. These curves were obtained with pulses from a pulse generator feeding two double delay line amplifiers and the remainder of the system. No attempt was made prior to the test to match delays in the two channels.

Curve (a) shows the resolution obtained with full size pulses (i.e. 4 V at the input to the coincidence system) having a rise-time solely determined by the amplifier (0.2 μsec from 10 to 90%). Curve (b) shows the degradation in resolution resulting from operation with small (300 mV) pulses of 0.3 μsec rise-time simulating NaI(Tl) scintillation pulses. Curve (c) is the result of operating with 4 V NaI(Tl) type pulses in the "A" channel and 300 mV similar pulses in the "B" channel. The spread in the resolution curves is entirely attributable to the effect of amplifier noise in producing jitter in the cross-over time of the double-delay-line shaped pulses.

An example of the performance of the instrument used with NaI(Tl) pulses is shown in

fig. 13. The shaping delay lines in the amplifiers were 1 μsec long. The explanatory diagram in fig. 13 shows the set-up. γ-rays from a Cs^{137} source strike both crystals and 180° scattering occasionally occurs from one crystal into the other. The single-channel analyzer in the "A" channel is set to select the 200 keV scattered radiation in detector "A" and the spectrum of events in the photopeak at 660 keV are very prominent. Inclusion of the fast coincidence circuit cuts out nearly all the random coincidences as seen in curve (b). Curve (c) illustrates the effect of inserting 50 nsec delay in the "A" channel thereby eliminating nearly all true coincidences and leaving only the very low rate of chance coincidences at the output.

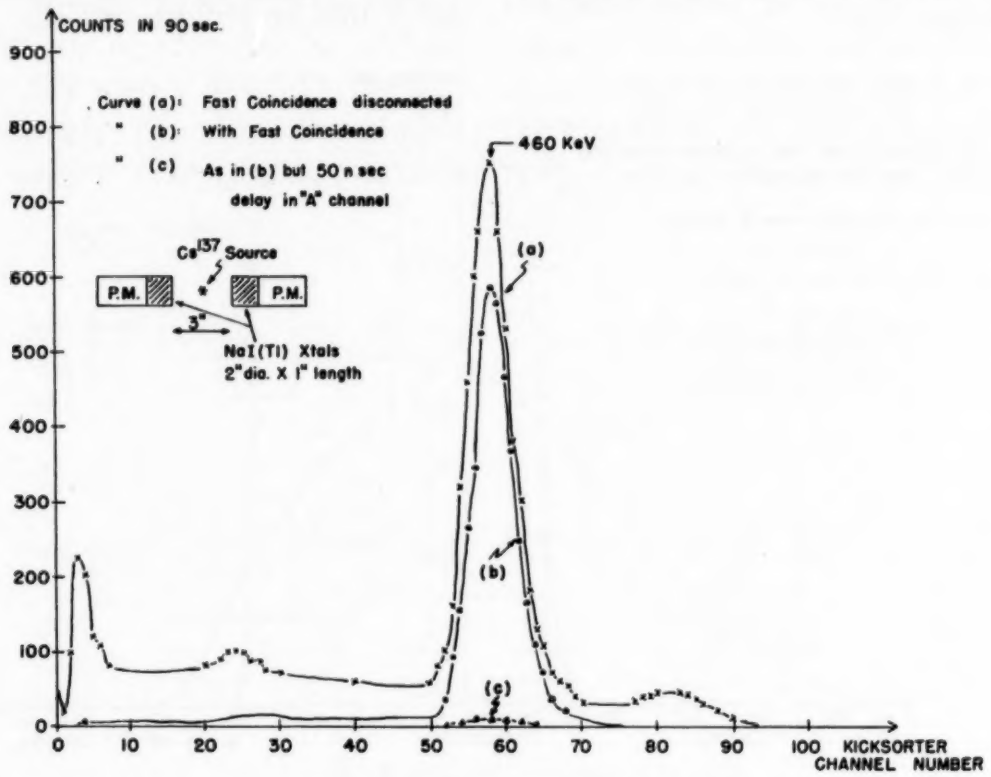

Fig. 13. Spectrum of γ rays in "B" channel in coincidence with 200 keV $\pm$ 20 keV events in "A" detector.

pulses in the "B" detector in coincidence with this is determined by the kicksorter. Curve (a) shows the result when the fast coincidence circuit is not connected. In this case random coincidences occurring in the 0.5 μsec resolution of the slow part of the system produce a general background for the peak and the random coincidences of

Acknowledgements

This work was carried out as part of the research programme of the Physics Division of Atomic Energy of Canada Limited. The authors wish to thank T. K. Alexander and L. B. Robinson for many useful comments and for their interest in this work.

NUCLEAR INSTRUMENTS AND METHODS **8** (1960) 297–303; NORTH-HOLLAND PUBLISHING CO.

A VERSATILE, HIGH EFFICIENCY 4π NEUTRON DETECTOR*†

J. B. MARION, R. J. A. LEVESQUE††, C. A. LUDEMANN and R. W. DETENBECK

Physics Department, University of Maryland, College Park, Maryland

Received 6 May 1960

A high efficiency 4π neutron detector has been constructed which consists of 12 $B^{10}F_3$ proportional counters imbedded in a two-foot cube of paraffin. The response of this detector as a function of neutron energy has been measured in the range 0.1 to 2.5 MeV by observing the yield curves for the T(p,n) and Li^7(p,n) reactions, the absolute total neutron production cross sections for which have been accurately measured by Macklin and Gibbons. These measurements indicate a detection efficiency of approximately 10 per cent and a response which is flat to within ± 5 per cent over the entire energy range studied. The efficiency for the detection of neutrons from a Ra-α-Be source (average neutron energy approximately 5 MeV) was found to be 6.5 per cent. The efficiency was observed to decrease for neutron energies below about 0.1 MeV by measuring the yield from the V^{51}(p,n) reaction. The efficiency for the detection of 50-keV neutrons is approximately 4 per cent. The detector has also been used to detect neutron thresholds for nuclear ground states and excited states by observing the slow threshold neutrons in the forward direction with a Li^6I scintillator surrounded by a B_4C shield. This "closed geometry" technique appears capable of only slightly less sensitivity than the "open geometry" method and is somewhat superior in energy resolution.

1. Introduction

The detection of neutrons in 4π geometry has long been a standard technique for the calibration of neutron source strengths in water-moderated baths containing, e.g., $MnSO_4$. These methods, although capable of high accuracy, require elaborate chemical techniques and therefore are not especially suited for the study of neutron production in nuclear reactions when the energy dependence of the neutron yield is desired. Several detectors have been constructed[1]) for the study of photoneutron processes in 4π geometry; however it appears that only two previous detectors have been designed specifically for the study of total neutron production cross sections from charged-particle induced reactions. The first of these detectors is the 5-foot diameter graphite sphere constructed at the Oak Ridge National Laboratory by R. L. Macklin[2]). This detector has been used extensively for the study of total neutron production cross sections from (p,n) and (α,n) reactions in the light nuclei[3,4]). Johnson, Galonsky, and Ulrich[5]) have constructed a paraffin-moderated assembly and have used this detector in the study of neutron strength functions from (p,n) reactions in the medium weight elements. The present detector was modeled after that constructed by Johnson *et al.*, but was designed to have a somewhat higher efficiency and a response that was more nearly flat with neutron energy. Experiments for which this detector was designed include the study of (α,n) and (p,n) reactions of extremely small cross section. One class of these experiments is the study of (α,n) reactions on the 4n + 1 nuclei (Be^9, C^{13}, O^{17}, and Ne^{21}) which have important astrophysical implications in that several of these reactions are considered to be likely sources of neutrons in stars. These

* Supported in part by the U.S. Atomic Energy Commission.

† A preliminary report of this work was given at the New York Meeting of the American Physical Society, January, 1960: C. A. Ludemann, R. J. A. Levesque and J. B. Marion, Bull. Am. Phys. Soc., Ser. II, **5** (1960) 16.

†† Now at the University of Montreal, Montreal, Quebec, Canada.

[1]) See, for example, R. Nathans and J. Halpern, Phys. Rev. **93** (1954) 437.

[2]) R. L. Macklin, Nucl. Instr. **1** (1957) 335.

[3]) J. H. Gibbons and R. L. Macklin, Phys. Rev. **114** (1959) 571.

[4]) R. L. Macklin and J. H. Gibbons, Phys. Rev. **109** (1958) 105.

[5]) Johnson, Galonsky and Ulrich, Phys. Rev. **109** (1958) 1243.

neutrons undergo capture reactions and thereby contribute to the formation of the heavier elements. Another class of experiments which can be studied with this detector is the investigation of neutron thresholds for nuclear ground states and excited states. The investigation of excited-state neutron thresholds in closed geometry has not previously been attempted.

2. Details of the Detector

2.1. CONSTRUCTION DETAILS

The details of the construction of the detector are shown in fig. 1. The outer shell of the detector is a two-foot cube of $\frac{1}{4}''$ steel plate. Within this steel shell is located an 18″ cube of $\frac{1}{4}''$ Boral (powdered B_4C pressed between 0.040-inch aluminum sheet). Prior to the filling of the shells with paraffin, hollow lucite rods were inserted through the shells for the purpose of supporting the detectors and the beam tube. The region between the steel and the Boral shells constitutes the outer paraffin shield. Neutrons which are incident on the detector from the outside are moderated in this outer shield and are then absorbed by the B^{10} in the Boral. The main paraffin block, which is an 18″ cube, constitutes the detector proper. The lucite rods which position the $B^{10}F_3$ detectors are arranged in two rings each containing 6 detectors. The counters in the inner ring are arranged on a pitch circle diameter of 6″ while the outer ring is on an 8″ diameter circle. This geometry differs from that employed by Johnson *et al.*[5]), in that there are more detectors located at a greater distance from the target position. This design change was made in order to increase the neutron detection efficiency for high energy neutrons. (Johnson's detector showed a decrease in efficiency of approximately 20 per cent between neutron energies of 0.1 and 0.7 MeV.)

The charged-particle beam enters the detector from the left in a beam tube which is inserted in the 1″ diameter hollow lucite cylinder; the target position is at the center of the detector. To the right of the target position is located a 4″ diameter hollow lucite tube. The object placed in this section depends upon the experiment; a polyethylene plug is used when total neutron production cross sections are being measured or a hollow B_4C cylinder is used as a shield for the threshold detector in measurements of neutron thresholds. When the charged-particle beam is on the target, cooling is accomplished by blowing air through the plastic target-cooling tube.

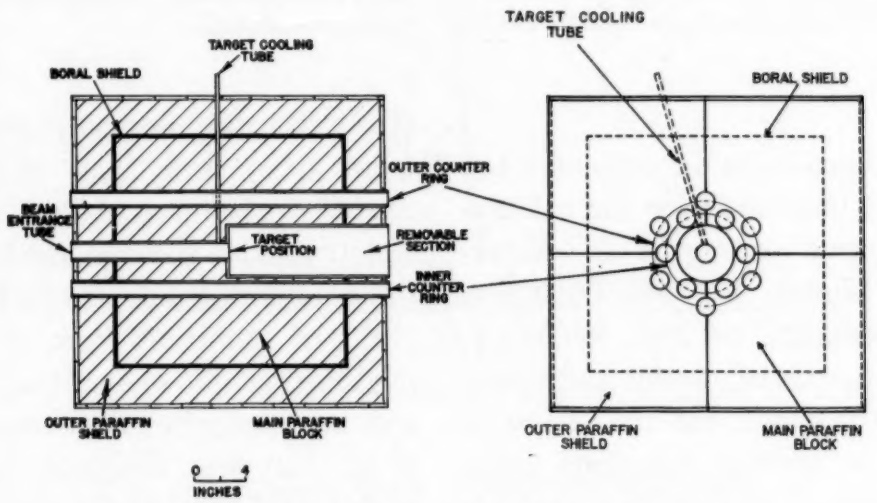

Fig. 1. Construction details of the 4π detecting system.

2.2. $B^{10}F_3$ PROPORTIONAL COUNTERS

The $B^{10}F_3$ proportional counters[6]) which were used in this detector were mounted in the two counter rings as shown in fig. 1. All counters in the inner ring were connected in parallel as were

[6]) Manufactured by Twentieth Century Electronics, Ltd. Croydon, Sussex, England. Distributed in U.S. by Hamner Electronics, Princeton, New Jersey.

all of those in the outer ring. The number of counts in each ring of counters was recorded separately. The pulse-height distribution obtained with six detectors connected in parallel is shown in fig. 2. This curve shows the excellent resolution and gain uniformity exhibited by

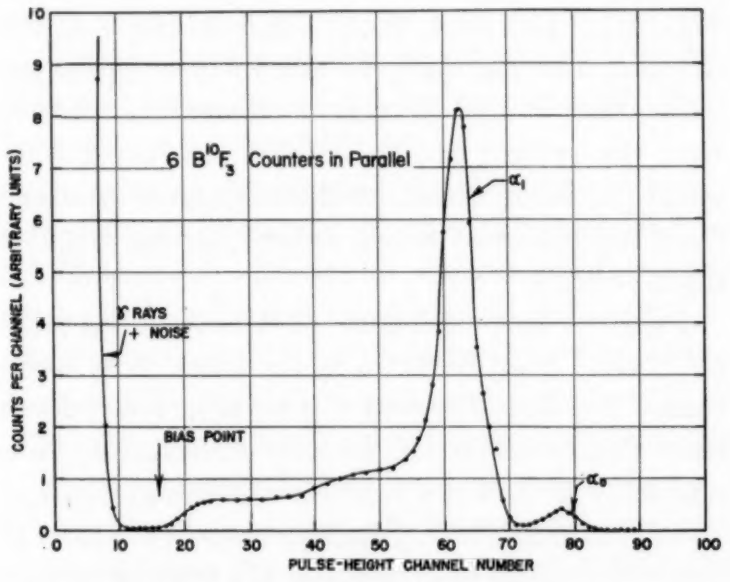

Fig. 2. Pulse-height distribution from 6 $B^{10}F_3$ detectors connected in parallel and irradiated with slow neutrons. The ground-state and first excited-state α-particle groups from the $B^{10}(n,\alpha)Li^7$ reaction are labeled α_0 and α_1, respectively. The resolution of the α_1 peak is 9.0 per cent.

these detectors. No adjustment of the high voltage was used in obtaining this pulse-height distribution; all detectors were connected directly in parallel. The two α-particle groups from the $B^{10}(n,\alpha)$ reaction are clearly resolved (α_0 and α_1 refer to the ground state and first excited state α-particle groups, respectively). Discrimination against γ rays and noise is readily achieved by biasing at channel 16. The detection efficiency of the counters used was found to be almost exactly equal to that of other commercially available detectors of similar size and with the same gas filling pressure[7]); the gain, however, was lower by about a factor of two but the resolution was far superior. When the detectors were operated singly the high voltage used was approximately 1600 volts. With six detectors operating in parallel it was necessary to increase the high voltage to approximately 1900 volts to compensate for the gain loss caused by the increased loading.

2.3. EFFICIENCY CALIBRATION

The efficiency of the detector as a function of neutron energy was measured by observing the yield curves for the $Li^7(p,n)$ and T(p,n) reactions, the absolute total neutron production cross sections for which have been accurately measured by Macklin and Gibbons[4]). The LiF target that was used for the efficiency calibration was obtained from Oak Ridge and was the same target that was used for the measurement of the absolute cross section for the $Li^7(p,n)$ reaction[8]). This target has a measured thickness of 387 ± 5 μg/cm². The tritium target which was used was also obtained from Oak Ridge[9]). During the course of the calibration runs it was found that if beam currents in excess of about 0.02 microamperes were used, then serious jamming of the detectors resulted. It was therefore decided to make the efficiency calibration by using only a single detector in each of the two counter rings. With this procedure, it was possible to use beam currents of approximately 0.2 μA. The use of these larger beam currents minimized instabilities in the regulation of the accelerator and also reduced the inaccuracies in the current integration system. Since all detectors are mounted symmetrically about the beam axis, the total efficiency of each ring was found by multiplying by six the efficiency for a single detector in that ring.

The absolute efficiency of the detector was measured with the Oak Ridge LiF target at a proton bombarding energy of 2.70 MeV. The $Li^7(p,n)$ cross section at this bombarding energy as given by Macklin and Gibbons[4]) is 285 mb. The average neutron energy (i.e., the energy of the neutrons emitted at 90° with respect to the beam axis) at this bombarding energy is 0.58 MeV. At this neutron energy, the detection efficiency of a single counter in the inner ring is

[7]) For example, those manufactured by N. Wood Counter Laboratory, Chicago, Illinois.

[8]) We are indebted to J. H. Gibbons of the Oak Ridge National Laboratory for supplying us with the LiF and V targets which were used in the cross section measurements of the $Li^7(p,n)$ and $V^{51}(p,n)$ reactions.

[9]) Obtained from the Stable Isotopes Division, Oak Ridge National Laboratory, Oak Ridge, Tennessee.

1.05 per cent while the efficiency for a single counter in the outer ring is 0.574 per cent. Therefore, with all twelve detectors connected the total efficiency for the detection of 0.58-MeV neutrons is 9.74 per cent.

A relative yield curve for the $Li^7(p,n)$ reaction was obtained with a target thinner than that used for the absolute calibration. The ratio of this yield curve to that measured by Macklin and Gibbons is shown in fig. 3. The efficiency is plotted as a function of the nominal neutron energy and is normalized to the numbers given

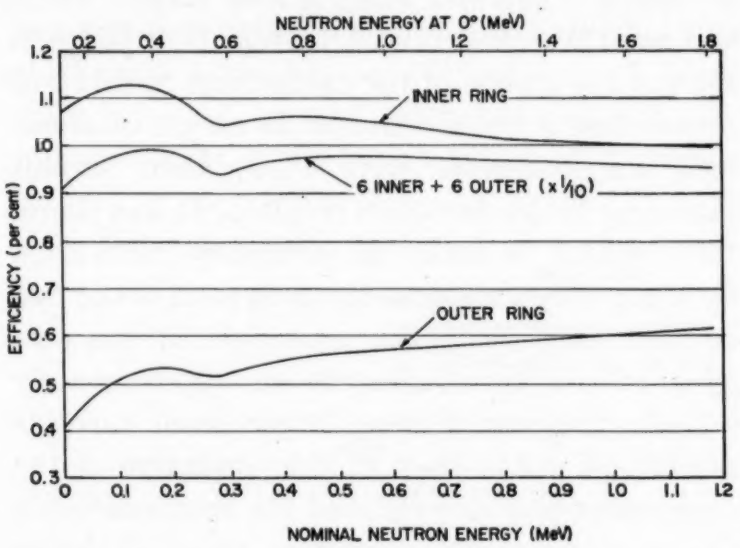

Fig. 3. Ratio of the neutron yield observed from the $Li^7(p,n)$ reaction with the 4π detecting system to that measured by Macklin and Gibbons (ref.[4]). The curves have been normalized at a nominal neutron energy (i.e., energy at 90° to the beam axis) of 0.58 MeV in the manner described in the text. The neutron energy at 0° to the beam axis is given on the upper scale for comparison. The curve marked "6 inner + 6 outer" gives the total detection efficiency of the system.

above for a neutron energy of 0.58 MeV. The curve marked "6 inner + 6 outer" gives the total efficiency of the detector. This curve is seen to exhibit a response which is flat to within about 3 per cent over the nominal neutron energy range from about 0.1 to at least 1.2 MeV.

With the counter geometry used in this detector the efficiency of neutron detection varies with the angle of emission of the neutron from the target relative to the beam axis. Therefore, the response of the detector will be, to some extent, dependent upon the angular distribution of the neutrons being studied. Fig. 3 shows this effect for the case of the $Li^7(p,n)$ reaction. All of the curves show rises and dips in the range of nominal neutron energy up to about 0.4 MeV. The most violent effect occurs between 0.2 and 0.3 MeV which corresponds to the proton bombarding energy range from 2.2 to 2.3 MeV; it is known that the neutron angular distribution changes rapidly with bombarding energy in this region[10]). The fact that large changes in the angular distribution give rise to only a few per cent effect in the detection efficiency indicates that the system can be relied upon to yield accurate total neutron production cross sections even for reactions which exhibit strong angular distributions.

Figure 4 shows the ratio of the measured yield from the T(p,n) reaction to the cross section obtained by Macklin and Gibbons[4]). The curves have been normalized to give a total detection efficiency of 9.74 per cent for a nominal neutron energy of 0.58 MeV. Again a response which is quite flat down to a nominal neutron energy of about 0.1 MeV is obtained. The variation of neutron energy with angle of emission is more rapid for the case of the T(p,n) reaction than for the $Li^7(p,n)$ reaction and at a proton bombarding energy of 3.2 MeV the nominal neutron energy

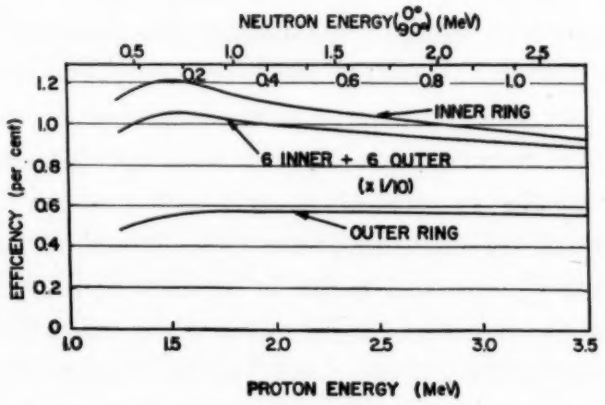

Fig. 4. Ratio of the neutron yield observed from the T(p,n) reaction with the 4π detecting system to that measured by Macklin and Gibbons (ref.[4]). The curves have been normalized at a nominal neutron energy (i.e., energy at 90° to the beam axis) of 0.58 MeV in the manner described in the text.

(i.e., the energy at 90°) is only 1.0 MeV whereas the neutron energy in the forward direction is approximately 2.4 MeV. If the response of the

[10]) R. Taschek and A. Hemmendinger, Phys. Rev. **74** (1948) 373.

detector were such that it decreased rapidly between neutron energies of 1.0 and 2.5 MeV then the response function as determined by measurements on the T(p,n) reaction would show the effect for proton bombarding energies above 3.0 MeV. It is therefore clear that the response cannot change drastically between 1.0 and 2.5 MeV and hence, we may state that the efficiency of the detector is constant to within about 5 per cent over the neutron energy range from about 0.1 to at least 2.5 MeV.

In order to determine the detection efficiency for neutrons of energy outside the range 0.1 to 2.5 MeV two additional measurements were made. A Ra-α-Be source which had been calibrated to an accuracy of better than 4 per cent at the National Bureau of Standards[11]) was used to obtain the efficiency for the detection of neutrons of approximately 5 MeV; a value of 6.5 per cent for the total detection efficiency was obtained. This confirms the previous statement that the efficiency cannot fall off rapidly as the neutron enrgy is increased in the 1.0 to 2.5 MeV. range. In order to obtain some indication of the response for low energy neutrons a measurement was made of the yield from the 1.607-MeV resonance in the $V^{51}(p,n)Cr^{51}$ reaction. The neutron energy at this resonance is 50 keV and the yield has been measured by Gibbons, Macklin and Schmitt[12]). A detection efficiency of approximately 4 per cent was obtained for 50-keV neutrons[8]).

When all of the uncertainties in the various measurements are taken into account it is considered that the absolute detection efficiency of this system is known to within 8 per cent for the neutron energy range from 0.1 to 5 MeV, and that the response is flat to within about 5 per cent over the neutron energy range from 0.1 to 2.5 MeV.

3. Threshold Measurements

The counter ratio method for the detection of thresholds for nuclear ground states and excited states was introduced by Bonner and Cook[13]) and has recently been summarized in detail[14,15]). The method utilizes two detectors mounted in tandem and in line with the charged-particle beam. The detector located nearer the target is designed to have a response function peaked for low energy neutrons while the second detector has a more or less flat response. The ratio of the counting rate in the slow neutron detector to

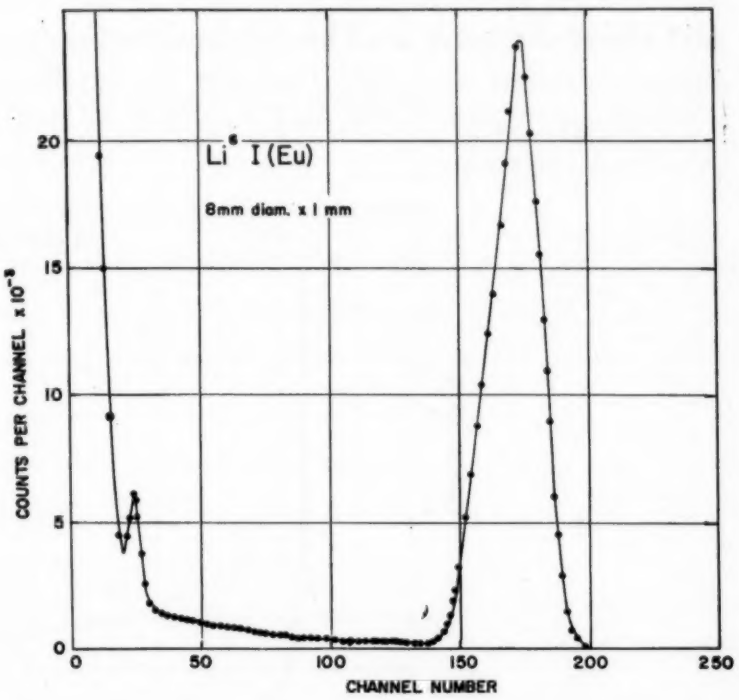

Fig. 5. Pulse-height distribution in the $Li^6I(Eu)$ crystal when irradiated with slow neutrons.

that in the fast neutron detector shows rapid increases when neutron threshold energies are reached. The geometry utilized in the detection of neutron thresholds with the 4π detecting system differs from the "open geometry" employed by the Rice group[13]) in that the fast neutron detector is replaced by the 4π system. The slow neutron detector employed in the present measurements consists of a $Li^6I(Eu)$ crystal (8 mm diam. $\times$ 1 mm thick) mounted on DuMont 6291 photomultiplier tube. This

[11]) We are indebted to the Neutron Physics Division of the National Bureau of Standards for supplying us with this calibrated source.

[12]) Gibbons, Macklin and Schmitt, Phys. Rev. **100** (1955) 167.

[13]) T. W. Bonner and C. F. Cook, Phys. Rev. **96** (1954) 122.

[14]) T. W. Bonner, in Nuclear Spectroscopy, ed. F. Ajzenberg-Selove (Academic Press, New York, 1960) Part A, p. 477.

[15]) J. B. Marion and T. W. Bonner, in Fast Neutron Physics, eds., J. B. Marlon and J. L. Fowler, (Interscience Publishers, Inc., New York, to be published 1960) Part II.

assembly is mounted at 0° with respect to the charged-particle beam. In order to supress detection of slow neutrons moderated in the paraffin of the 4π detector, the Li^6I crystal is mounted in a B_4C shield which is placed in the removable section indicated in fig. 1. The B_4C shield is a hollow cylinder of outside diameter 4″ and inside diameter 2″. The slow neutron detector is located within this cylinder and at a distance of approximately 2″ from the target. A $\frac{1}{8}$″ thick piece of paraffin is placed between the target and the Li^6I crystal in order to thermalize the forward neutrons and increase the detection efficiency of the crystal. This paraffin also serves to smooth out the intrinsic efficiency function of the Li^6I detector which otherwise would show a maximum at a neutron energy of 0.25 MeV due to the resonance in the $Li^6(n,\alpha)T$ reaction at that energy. Therefore, with a forward counter sensitive only to low energy threshold neutrons and with the 4π detector having a response sensitive to the fast neutron component, the basic requirements of the counter ratio method are met. The response to slow neutrons of the Li^6I crystal used as the slow detector is shown in fig. 5. It is evident that the $\alpha + T$ peak from the $Li^6(n,\alpha)T$ reaction is clearly resolved and that discrimination against γ rays and noise is relatively easy. The peak-to-valley ratio of the $\alpha + T$ peak is 100:1. As an illustration of the capabilities of this "closed geometry" system in the investigation of neutron thresholds fig. 6 shows the results for the first two thresholds (ground state and first excited state) in the $Li^7(p,n)Be^7$ reaction. The ratio of the yield in the forward counter to that in the 4π detector shows the peak at 1.881 MeV corresponding to the ground-state threshold energy for this reaction. The energy region near this threshold is shown in more detail in fig. 7. The ratio curve falls to half value in ap-

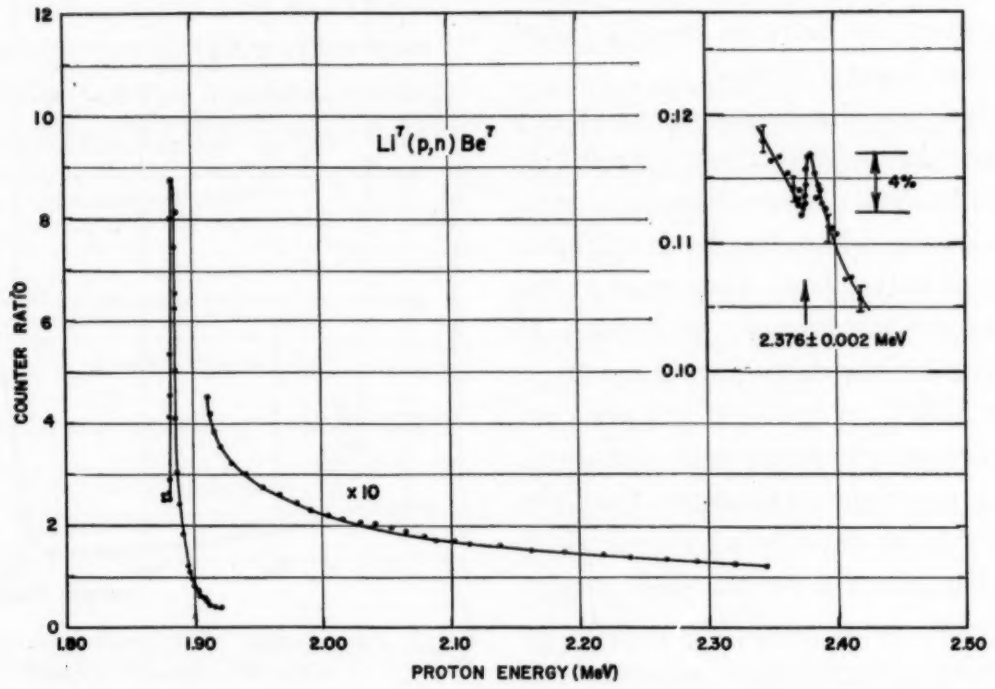

Fig. 6. Ratio of counting rate in the forward detector (Li^6I crystal) to that in the 4π system for the $Li^7(p,n)Be^7$ reaction.

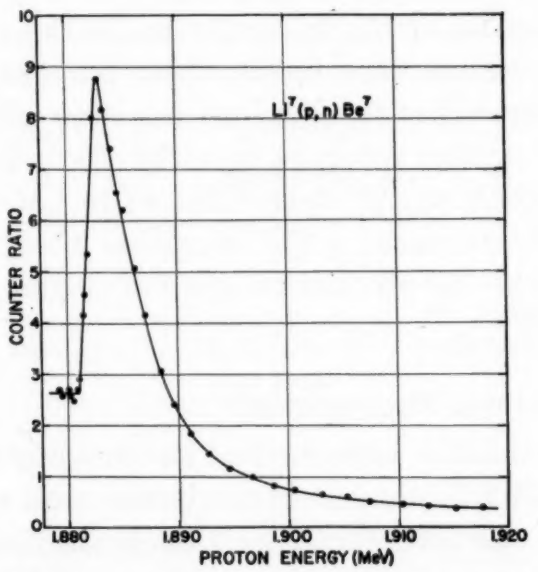

Fig. 7. Low energy region of fig. 6 for the $Li^7(p,n)Be^7$ reaction. The fall-off distances are given in the text.

proximately 5 keV and to 0.1 of the peak value in approximately 17 keV. The energy resolution as determined by these fall-off distances is superior to that obtained in open geometry experiments[16]) where the corresponding energy values are 20 and 200 keV, respectively. The threshold for the first excited state neutron group is extremely weak but is clearly shown in the ratio curve at a proton energy of 2.376 ± 0.002 MeV. (This gives as the energy for the first excited state of Be^7 433 ± 2 keV.) The magnitude of the effect observed at this excited-state threshold with the closed geometry system shows that this method is at present not as sensitive as the open geometry technique. The present results indicate a 4 per cent rise at the first excited state threshold whereas the Rice group[16]) has observed an 8 per cent effect. It is anticipated that by utilizing a somewhat larger Li^6I crystal and by placing this detector at a greater distance from the target the sensitivity can be materially increased.

[16]) T. W. Bonner and F. Gabbard; (1958) unpublished results.

NUCLEAR INSTRUMENTS AND METHODS 8 (1960) 304–312; NORTH-HOLLAND PUBLISHING CO.

H.F. POWER METER FOR OPERATION AT 2.5 MW PULSED POWER

E. ZACCHERONI†

CERN, *Proton Synchrotron Division, Geneva*

Received 11 February 1960

A description is given of an oil-cooled dummy load specially constructed to measure the output power of the 2.5 MW pulse amplifier of the CERN linear accelerator. The equipment can be used both as a dummy load and as a calorimetric power meter. Arrangements have been made to use it also as an attenuator of more than 30 db.

1. Introduction

The construction and the operation of the 2.5 MW pulsed power amplifier[1,2]) of the CERN linear accelerator raise the problem of dissipation and measurement of the output power.

The characteristics of the power pulse are as follows:

maximum pulsed power	2.5 MW
pulse length	200 μsec
radio-frequency	202.6 MHz
repetition frequency	1 pulse/sec .

A dummy load is needed which can withstand the high voltage corresponding to a 2.5 MW pulse and dissipate a mean power of the order of 500 W. It will be used both for the final installation and laboratory work. For installation a simple load is required. It will be connected to the power divider inserted between the drive stage and the final amplifier of the H.F. chain (fig. 1). The use of the power divider[3]) will not be discussed here. It is sufficient to note that the power divider regulates the drive to the final amplifier without affecting the output loading of the drive stage.

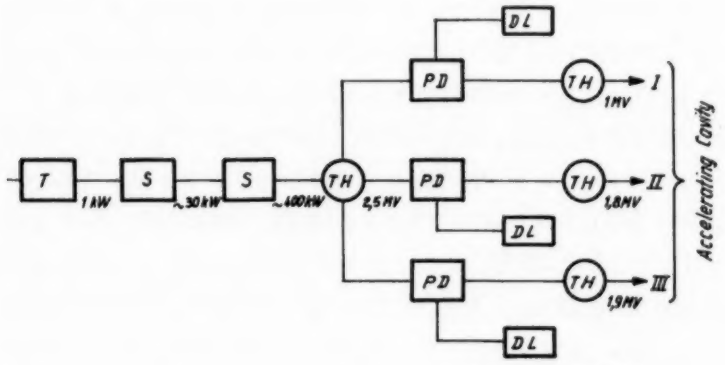

Fig. 1. T: transmitter (crystal controlled); S: pre-amplifiers; T.H.: drive and final amplifiers; P.D.: power dividers; D.L.: dummy loads.

The regulation is done by dividing the output power of the drive stage between the dummy load and the input to the final stage in any required ratio. If necessary the power can be diverted completely into the dummy load. The distribution of power can be measured by power flow monitors[4]), and no absolute power meter is required. For laboratory work, however, it is desirable to have a power meter of reasonable

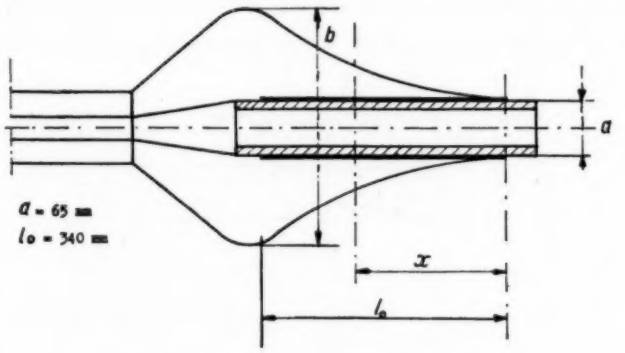

Fig. 2. $a = 65$ mm; $l_0 = 340$ mm.

† Present address: International Atomic Energy Agency, Vienna.

[1]) I. Afanassieff, Générateur à impulsion de 2 M.W. crête, Revue Technique CFTH (24.12.1956) p. 21.

[2]) E. Zaccheroni, The 2.5 M.W. amplifier of the CERN linear accelerator, CERN 58-22 LINAC/RF Group (September 1958).

[3]) P. Bramham, A coaxial line variable power divider and phase shifter for high power, CERN/PS Report (in preparation).

[4]) E. Zaccheroni, Power flow monitors for the LINAC H.F. system, CERN/PS report.

accuracy for checking the amplifier performance and calibrating the power flow monitors. The oil-cooling proposed for the dummy load suggested the idea of using the equipment also for calorimetric power measurement.

2. Coaxial Resistor Dummy Load

A "lossy line" consisting of a cylindrical resistor in a suitable outer conductor (fig. 2) has been used as reflection-free termination of the 50 Ω output line of the amplifier. The high peak

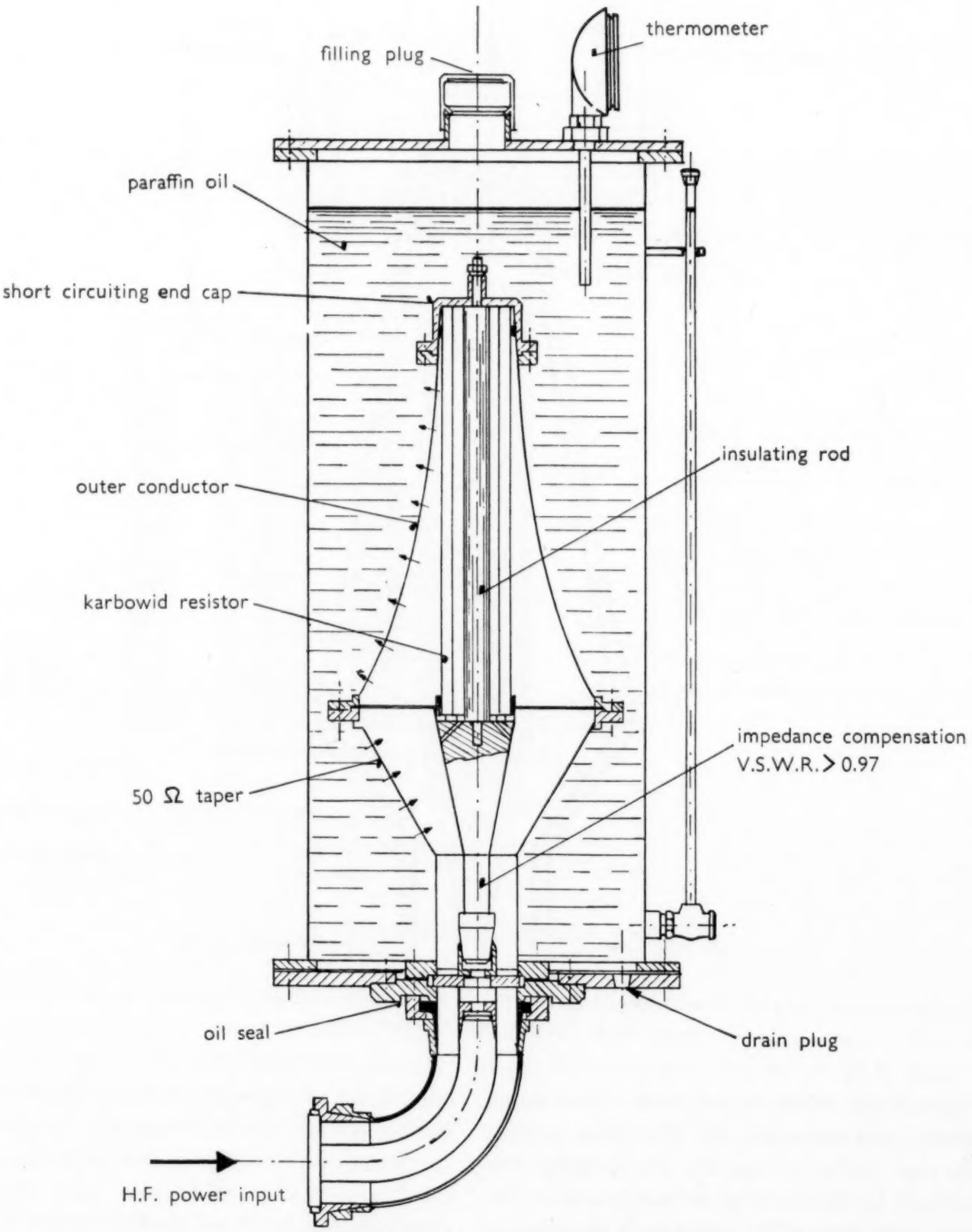

Fig. 3. Coaxial resistor dummy load.

power level raises surface breakdown problems on the inner conductor and fixes a minimum length for the resistor. The resistor used is the carbon coated Siemens Karbowid 50 ohm, 100 watt type. It stands easily the voltage corresponding to the 2.5 MW peak power if the pulse but it increases considerably the mean dissipation of the resistor.

The fixed frequency of operation makes it possible to choose between different shapes of outer conductor. The simplest form would be a cylindrical sleeve of any reasonable diameter

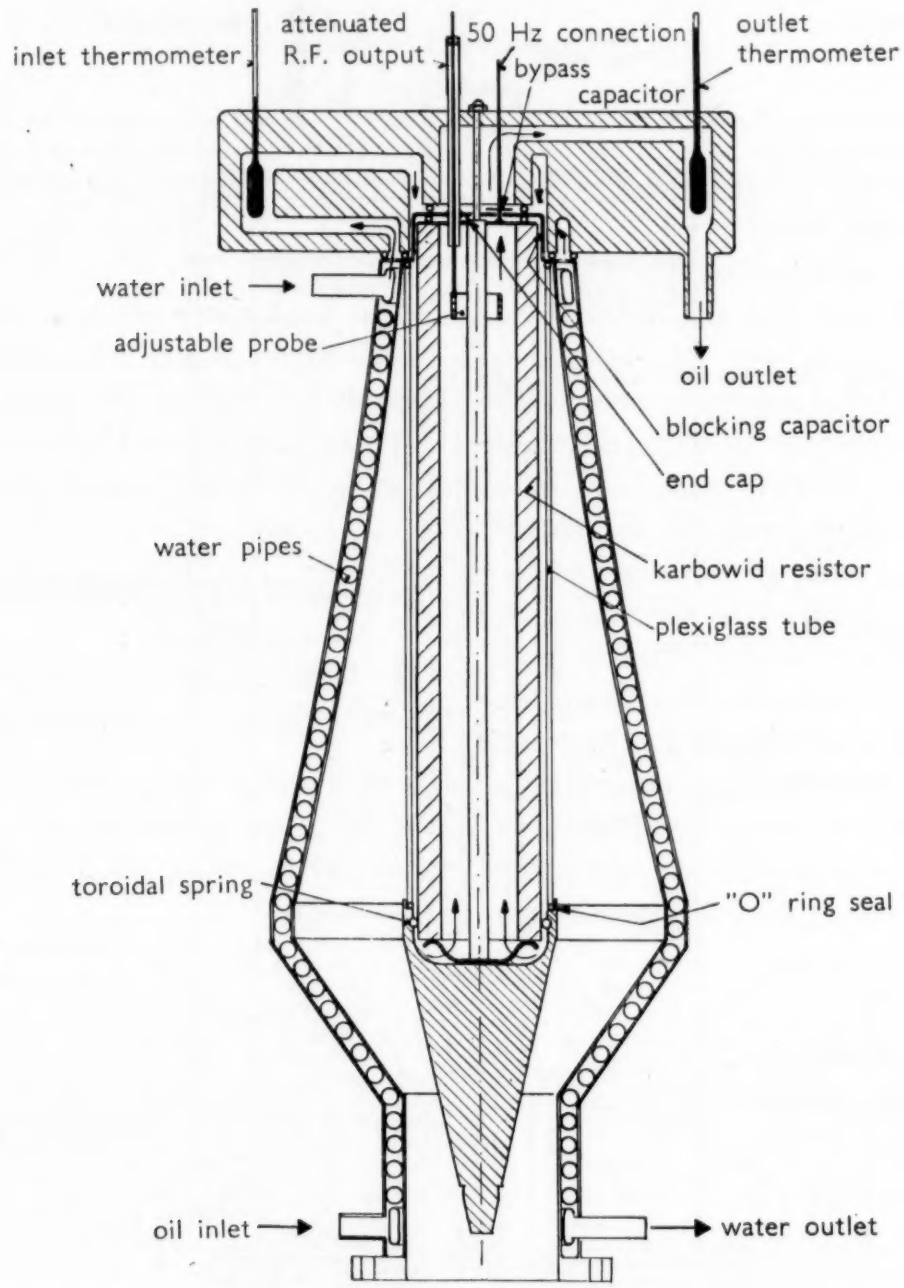

Fig. 4. Dummy load for power meter.

immersed in oil; when tested with water some breakdown was experienced. The heat during the 200 μsec pulse is carried away from the carbon layer by the ceramic former, so that the rise in temperature of the carbon at the end of the pulse is less than 150° C.

Oil cooling does not help appreciably during connected at one end to the resistor. It is easy in fact at any given frequency to compensate the reactive part of the load impedance and to transform the resistive part into the wanted value. However, the standing wave inside the dummy load and in the coaxial transformer cannot be avoided and the increased voltage at

the antinodes might cause trouble. Moreover the power is not uniformly dissipated along the carbon film. All these difficulties may be avoided by using an outer conductor of exponential shape.

It is shown in the Appendix that the input impedance of such a dummy load is equal to the resistance of the inner resistor and is independent of its length. The distribution of current along the resistor is uniform and no reflection will occur inside the dummy load. In principle, no coaxial transformer is needed. In practice, there may be some mismatch on the line; it will, however, be so small that the increase in voltage is negligible, and a very simple matching transformer can be used.

As illustrated in fig. 3 the outer conductor is connected to the extremity of the inner resistor by means of a brass cap. An insulating rod running along the axis fixes the inner conductor of the tapered line at the other end of the resistor. The impedance compensation is provided by adjusting the diameter of the inner conductor in the line that precedes the taper. The whole structure is contained in a box filled with paraffin oil (dielectric constant $\varepsilon = 2.17$), holes being provided in the outer shell to allow free circulation of the oil.

The maximum temperature reached during operation is about 50° C. The dielectric constant does not appreciably change over this range of temperature.

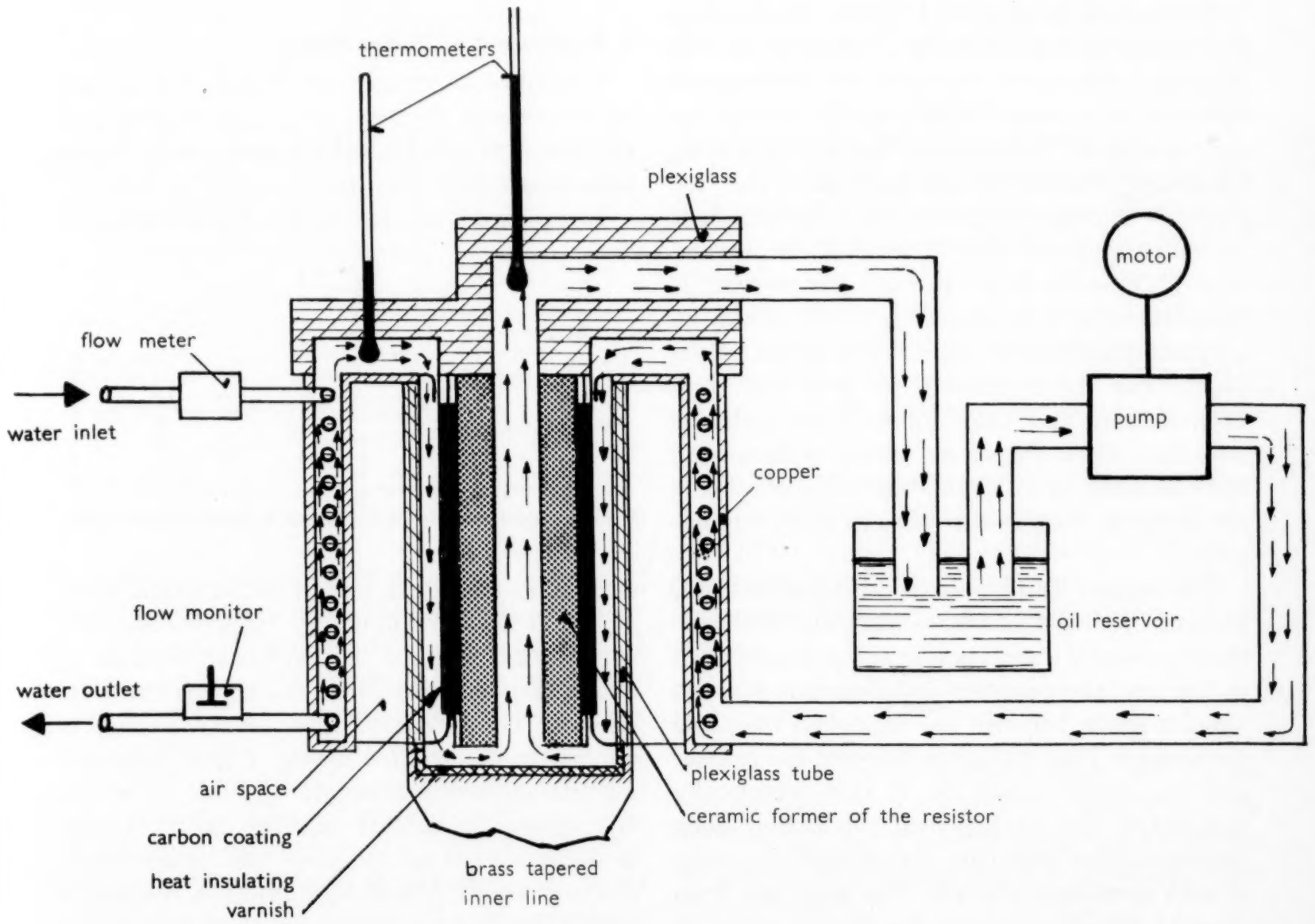

Fig. 5. Oil circulation of the power meter.

3. Dummy Load for Power Meter

The apparatus described above can work, in principle, as a calorimeter for measuring the power dissipated in the dummy load, if some precautions are taken to avoid heat leakage. The measurement, however, would be very inconvenient, because the heat capacity of the volume of oil is large and so the temperature rise would be very slow. In order to avoid this difficulty, the oil is confined by a plexiglass cylinder to a 2 mm annular space around the resistor (fig. 4). Sufficient cooling is obtained by circulating the oil at constant flow, and the power is calculated by measuring the difference in temperature of the oil between output and input. Constant flow through the system is maintained by a reciprocating pump driven by a synchronous motor (fig. 5). The stroke of the pump can be regulated to give any flow between zero and three l/min. Heat exchange with the surroundings is decreased by choosing a suitable sense of oil circulation and by keeping the mean oil temperature near to room temperature.

The dummy load is surrounded by an external jacket in which the oil flows from the bottom to the top around water cooling pipes. It goes then to the first thermometer and descends through annular space between the plexiglass tube and the resistor. Heat exchange between the resistor and the outer conductor is thus practically eliminated. The residual heat conduction along the end cap has been made very small by covering it with insulating varnish. The same has been done at the other end of the resistor along all the surface of the tapered line, which is in contact with the oil.

A further reduction in heat exchange has been obtained by adjustment of the oil flow so as to give a temperature difference of only a few degrees.

With $\Delta T = 1$ or 2° C the error in reading the thermometers becomes appreciable; a compromise has been reached by allowing a rise of the order of 5 degrees for 2.5 MW power. Arrangements have also been made to stir up the oil before it reaches the second thermometer so as to have a stream of uniform temperature. Air bubbles must be carefully avoided, because they can affect the measurements. The closed circuit of oil and the submerged pump produce a stream completely free of bubbles. Nevertheless valve points are provided to eliminate bubbles which may occur during filling.

4. Calibration of Power Meter

To calibrate the meter, 50 Hz power is applied to the resistor through an a.c. wattmeter and the power level adjusted by means of a Variac auto-transformer (fig. 6).

In principle, one calibration would suffice to determine once and for all the function $W = f(\Delta T)$ at constant flow (fig. 7). Nevertheless a substitution method is preferred because it allows the performance of the equipment to be checked continuously. The 50 Hz power is applied to the resistor during a time sufficient for the oil temperature to stabilise, then the H.F. power is applied and the 50 Hz power is decreased so as to keep the temperature rise unchanged. When equilibrium is reached a second reading of 50 Hz power is taken, the difference in reading giving the H.F. power applied. The H.F. and 50 Hz power are dissipated in the same part of the circuit with the same distribution, so errors due to heat exchange are avoided. Application of 50 Hz power to the resistor at the same time as H.F. power has been made possible by replacing the direct short circuit of the end piece by a capacitor of

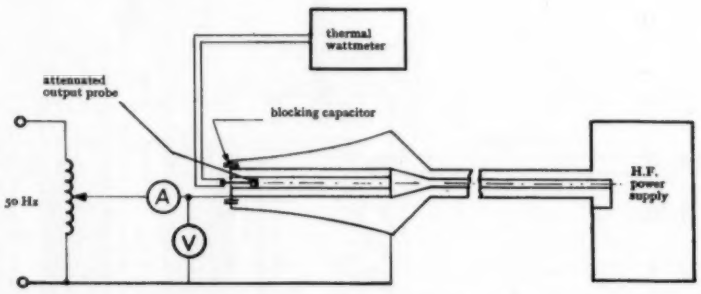

Fig. 6. Application of 50 Hz and H.F. power to the load.

[5]) J. K. Murray, U.H.F. Power meter for operation in the 200 Mc/s Communication Band, Electronic Engineering (May 1958) p. 345.

[6]) M. Geiger and E. Zaccheroni, A gated pulse voltmeter, CERN/PS Report LRF, 3 (March 1957).

negligible reactance (fig. 6). The capacitor consists of a 0.1 mm polyester film covering the silvered terminal of the cylindrical resistor and clamped under a copper strip fixed to the outer

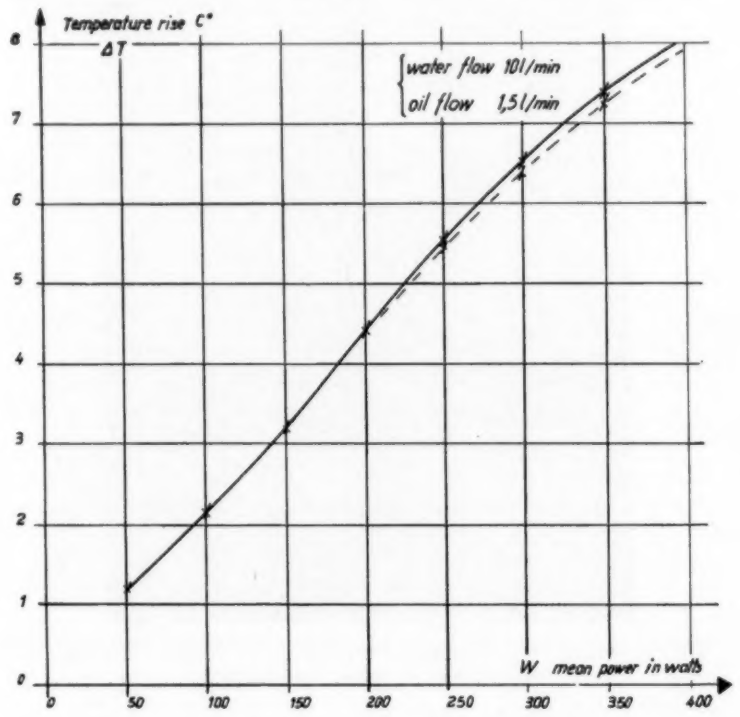

Fig. 7. Calibration curve of the power meter.
Broken line: check of calibration curve three months later.

conductor. The 50 Hz circuit is completed through the loop of the H.F. supply.

Accuracy of the measurement depends only on the accuracy of reading a fixed temperature rise from the two thermometers and the mean power on the a.c. wattmeter. Facilities are provided for connecting an external voltmeter and ammeter if higher precision is required. An accurate measurement by the substitution method takes about 40 minutes. A faster method using the dummy load as an attenuator has been developed, as described below.

5. Dummy Load as Attenuator

A fixed proportion of the power dissipated in the load can be measured directly by low-power equipment. As the frequency is fixed, the frequency sensitivity of the divider is not important, so that a single probe situated inside the resistor can be used. The coupling can be varied by adjusting the depth of insertion of the probe. The coupling must be loose enough not to affect the impedance matching of the dummy load. A 60 ohm coaxial line carries the attenuated power to a thermal wattmeter, the position of the probe being chosen to give a power ratio of 2000/1 (— 33 db). Five minutes is sufficient for a good measurement.

6. Conclusion

As already stated, the mean output power of the 2.5 MW pulse amplifier can be measured in three different ways:

(a) by observing temperature rise and reading the power from the calibration curve.

(b) By substitution of 50 Hz power for the H.F. power to be measured. The difference in reading of an a.c. wattmeter with and without the H.F. gives the amount of H.F. power.

(c) By reading on a low-power thermal wattmeter when the attenuation is known.

The most accurate of the three methods is (b). It forms the basis of the calibration for methods (a) and (c).

On the contrary the most practical is method (c) which allows a fairly accurate measurement in quite a short time. Once the mean power is measured, the pulse power can be calculated if the pulse length τ and repetition time τ' are known,

$$W_{\text{pulse}} = \frac{\tau'}{\tau} W_{\text{m}} .$$

If the pulse is rectangular there will be no uncertainty in measuring its length on the oscilloscope, but if the rise and fall times are not negligible the effective length is calculated from the expression

$$\tau = \frac{\int v^2(t)\, \mathrm{d}t}{V^2}$$

where V is the amplitude of the flat top.

The amplitude stability can be monitored with the accuracy of 0.5% by a "gated pulse voltmeter" connected to a power flow monitor.

The overall accuracy of the apparatus can be

[7]) D. R. Crosby and C. H. Pennypacker, R.F. resistor as uniform transmission lines, Proc. IRE **34** (1946) 62.

[8]) C. T. Kohn, The design of a radio frequency coaxial resistor, I.E.E. Proc. IV, 101 (1954) 146.

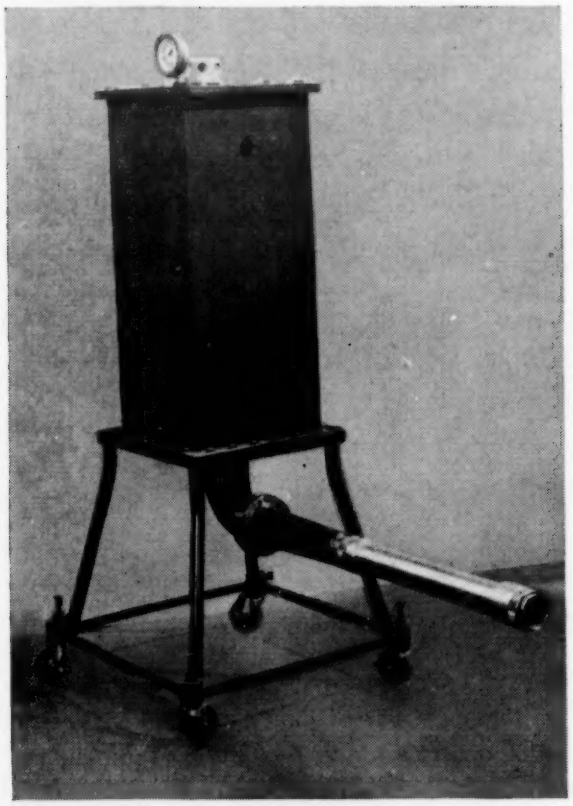

General view of coaxial resistor dummy load.

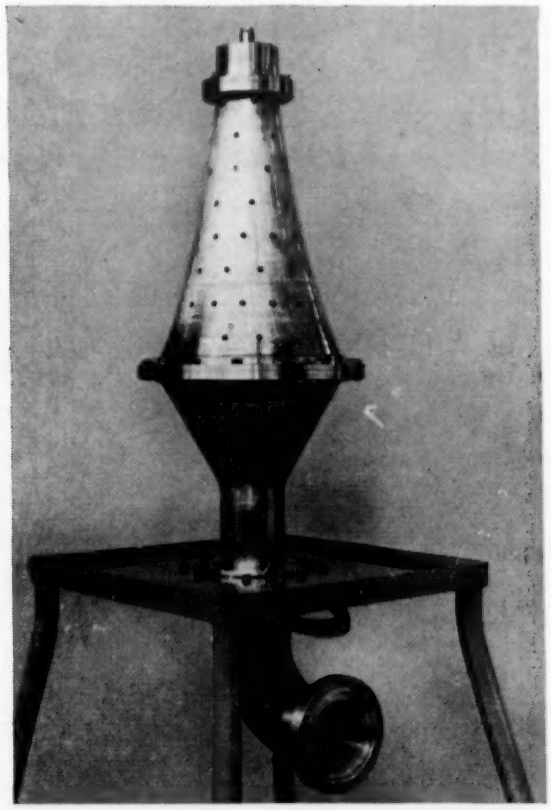

View of the dummy load partially opened, showing the exponential outer conductor.

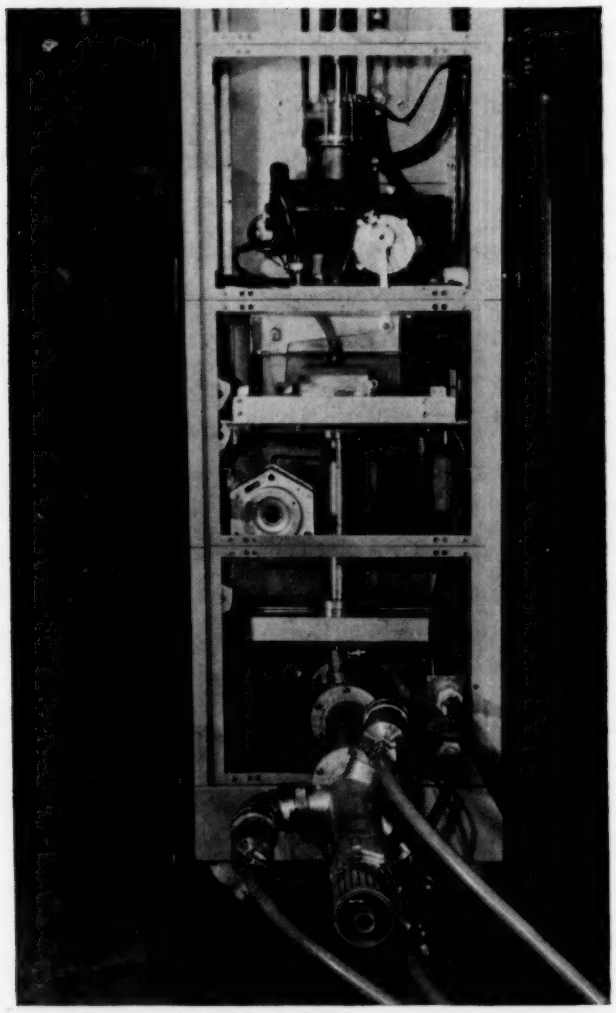

Rear view of power meter, showing the H.F. input, power flow monitor and constant flow pump.

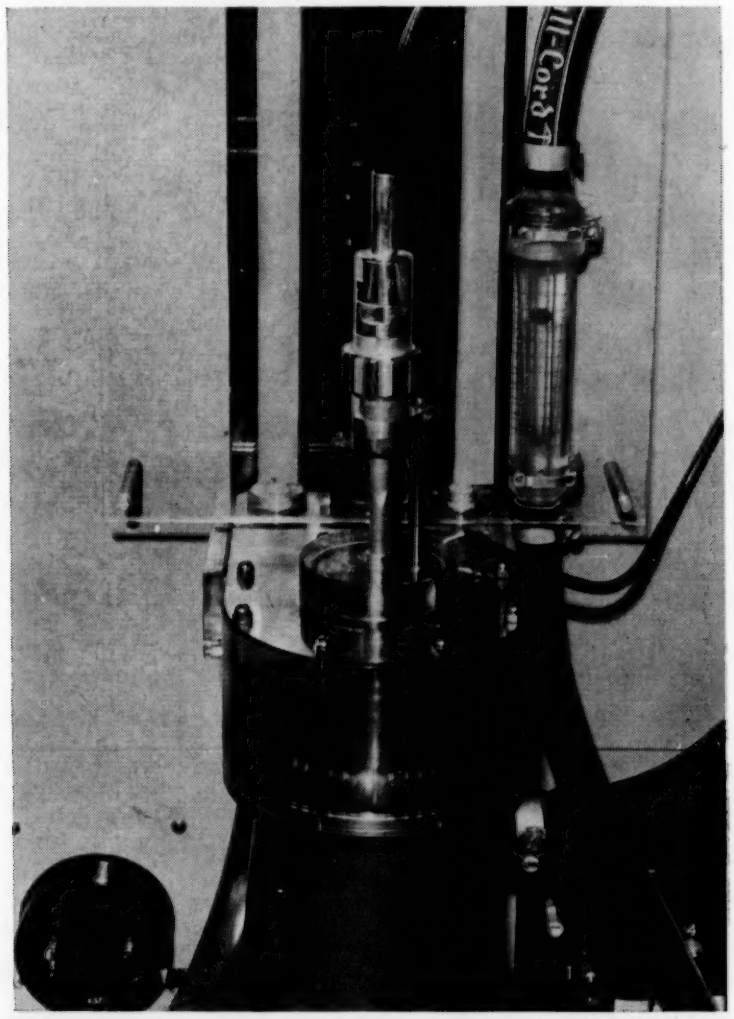

Head of dummy load for power meter, with thermometer holes, attenuated output probe and 50 Hz power input connexion.

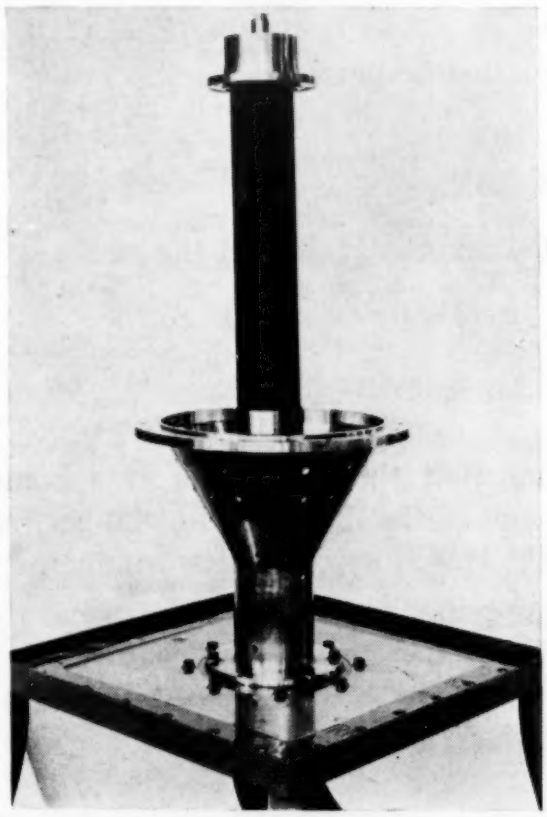

Coaxial resistor and tapered outer conductor.

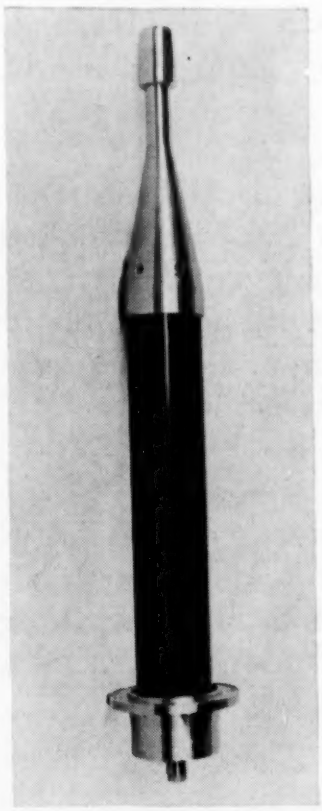

Brass end cap, coaxial resistor and tapered inner conductor.

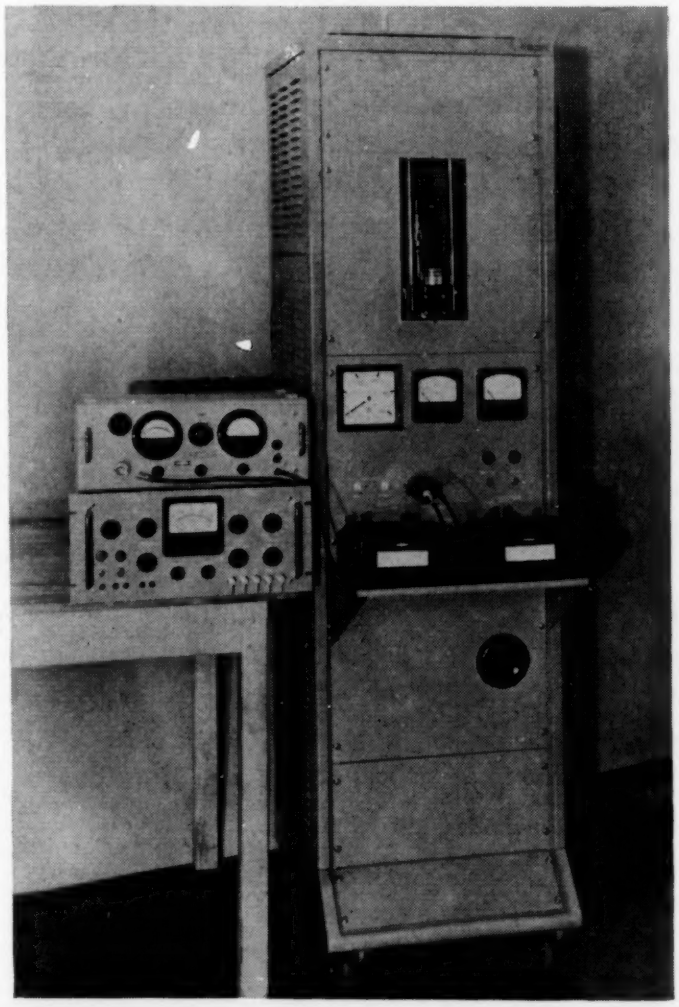

Front view of power meter with gated pulse voltmeter, thermal wattmeter and a.c. meters.

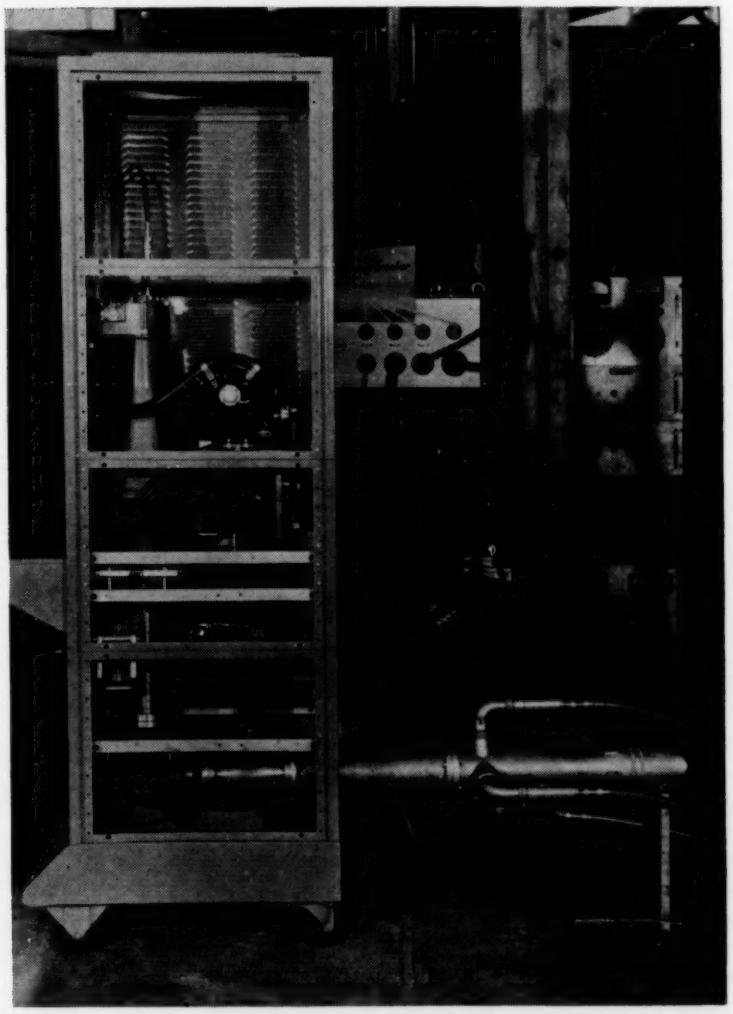

Side view of power meter.

kept better than 3% over the range from 100 kW to 2.5 MW by suitable choice of oil flow and attenuation.

I would like to thank Mr. Dind for his help in the design and construction of the dummy load, and I am particularly indebted to Mr. Stierlin for having adapted the original experimental design of the power meter to a convenient final construction.

Appendix[9])

Let us consider a coaxial line with a resistive inner conductor whose length is not negligible compared with the wave length (fig. 2). We can write the well-known transmission line equations:

$$\frac{\mathrm{d}I}{\mathrm{d}x} = (g + \mathrm{j}\omega c)\, V$$

$$\frac{\mathrm{d}V}{\mathrm{d}x} = (r + \mathrm{j}\omega l)\, I \qquad (1)$$

where r, l, g, c are the line constants and $I = I(x,t)$, $V = V(x,t)$ are the current and the voltage at a point x from the end of the line. Let Z be the characteristic impedance at the point x. From $Z = V/I$ it follows:

$$\frac{\mathrm{d}Z}{\mathrm{d}x} = \frac{1}{I}\frac{\mathrm{d}V}{\mathrm{d}x} - \frac{V}{I^2}\frac{\mathrm{d}I}{\mathrm{d}x} = (r + \mathrm{j}\omega l) - (g + \mathrm{j}\omega c)\, Z^2 . \qquad (2)$$

In this case we can assume $g = 0$. It follows that

$$\frac{\mathrm{d}Z}{\mathrm{d}x} = r + \mathrm{j}\omega\,(1 - cZ^2) . \qquad (3)$$

[9]) C. G. Montgomery, Technique of microwave measurements, Vol. II, MIT, Ch. 12, p. 721.

If we choose $cZ^2 = 1$, that is $Z = \sqrt{1/c}$ the above equation becomes:

$$\frac{\mathrm{d}Z}{\mathrm{d}x} = r , \qquad Z = rx + k . \qquad (4)$$

If the line is short circuited at the end

$$Z_{x=0} = 0 , \qquad \text{then} \qquad k = 0$$

and

$$Z = rx .$$

This means that the impedance at a point x from the end of the line should equal the resistance of the length x of the inner conductor.

But, as specified above $Z = \sqrt{1/c}$, so that the dimensions of the line in any point must be those of a non-dissipative line of impedance Z. It follows then, from the familiar

$$Z = \frac{60}{\sqrt{\varepsilon}} \ln \frac{b}{a}$$

and eq. (5) that

$$b = a \exp\,(rx\,\sqrt{\varepsilon}/60) .$$

The inner diameter a being constant, b must vary exponentially. At the point $x = l_0$, where l_0 is the length of the inner conductor,

$$Z = rl_0 = R .$$

The resistance R can be chosen to be equal to the characteristic impedance of the feeding line so that the dummy load can match the line directly. Although in this case it is not important it is worth noting that, if $cz^2 = 1$, the dummy load impedance is independent of frequency.

NUCLEAR INSTRUMENTS AND METHODS **8** (1960) 313–319; NORTH-HOLLAND PUBLISHING CO.

THE SPHERICAL CONDENSER AS A HIGH TRANSMISSION PARTICLE SPECTROMETER

II. DISC SOURCE

R. D. BIRKHOFF, J. M. KOHN†, H. B. ELDRIDGE and R. H. RITCHIE

Health Physics Division, Oak Ridge National Laboratory††, Oak Ridge, Tennessee

Received 10 May 1960

The inverse square electric field between the plates of a charged spherical condenser provides a focussing of charged particles leaving a source on the inner sphere. Part I of this paper dealt with the characteristics of such a spectrometer for the case where the source may be considered concentrated at a point on the axis of the instrument. The present analysis is concerned with the line profile, the transmission, and the resolution of the spectrometer for a distributed source. Where high transmission is important, a source on the inner sphere having a radius 30% of the radius of the inner sphere provides a transmission of 16% at an energy resolution of 7.7%.

In Part I of this paper[1]) the trace equation was considered of a non-relativistic charged particle in an inverse square electric field such as exists between two charged concentric spheres. It was shown that particles emitted isotropically from a point on the inner sphere may experience a focussing action after rotating through an angle ϕ ($> \frac{1}{2}\pi$) about the center of the spheres. (See Fig. 1.) An annular slit at the angle ϕ allows those particles in a certain radial band to pass into a region where they may be counted. The dependence of the transmission versus energy relation on the position and size of this annular slit has been examined. Very high transmissions are attainable in such a device without undue sacrifice of energy resolution, e.g., 25% transmission at 6% energy resolution is possible.

The present discussion concerns the effect of distributing the source over a spherical cap on the inner sphere centered about the instrument axis. The trace equation is obtained for a particle leaving the source off the axis, and the effect on the transmission-energy profile is examined in the small angle approximation used in Part I.

For generality we consider a source point P′ which is displaced from the on-axis point P a distance ξr_m parallel to the line OP, and a distance ηr_m perpendicular to this direction (see fig. 2). Here r_m is the radius of the inner sphere. The velocity vector $\bar{v}$ of a particle originating at

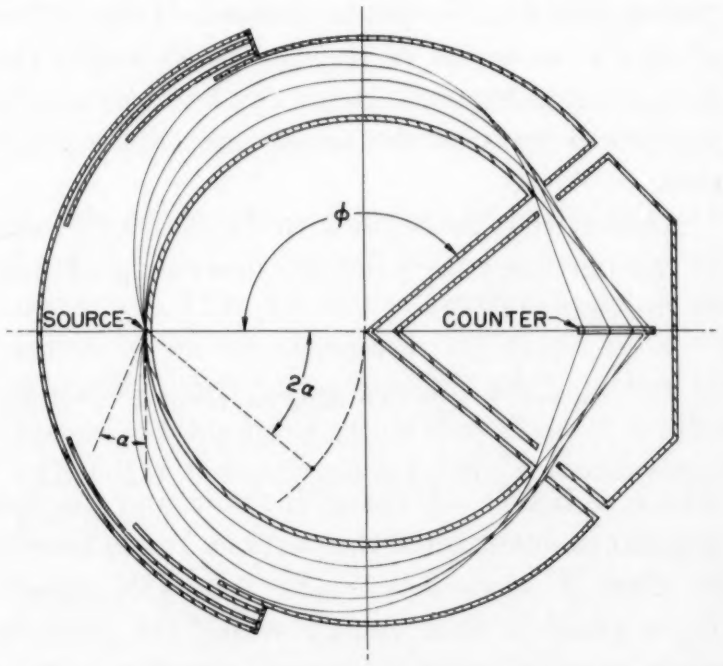

Fig. 1. Schematic of spherical condenser spectrometer with point source on the axis.

P′ is referred to a system of polar coordinates (θ', ψ') having polar axis parallel to the OP′ direction and to an unprimed system (θ, ψ) with polar axis parallel to OP. In both systems the aximuthal angles ψ and ψ' are measured from the

† Retired.

†† Operated by Union Carbide Corp. for the U.S. Atomic Energy Commission.

[1]) See Nuclear Instruments **6** (1960) 157–163.

plane containing the points O, P, and P′. We define $\alpha = \frac{1}{2}\pi - \theta$ and $\alpha' = \frac{1}{2}\pi - \theta'$. Suppose that after emission from the point P′, the charged particle travels in a focussing electric field and enters the plane of the selector gap at the point Q. The angle of rotation φ' is measured from the line OP′ in the plane containing OP′Q while the angle φ is measured from the line OP in the plane containing OPQ.

where we put $E = (1 + \delta)E_0$ as before. The constants A and B are evaluated from the given initial conditions (a) $[r]_{\phi' = 0} = r_m(1 + \xi)$; and (b) $[\mathrm{d}/\mathrm{d}\phi'\ (1/r)]_{\phi' = 0} = -[r_m(1 + \xi)]^{-1} \tan \alpha'$. One finds

$$(1 + \varepsilon) = \frac{(1 + \delta)(1 + \xi)^2 \cos^2 \alpha'}{1 - \cos \varphi' + (1 + \delta)(1 + \xi) \cos \alpha' \cos (\varphi' + \alpha')} \tag{3}$$

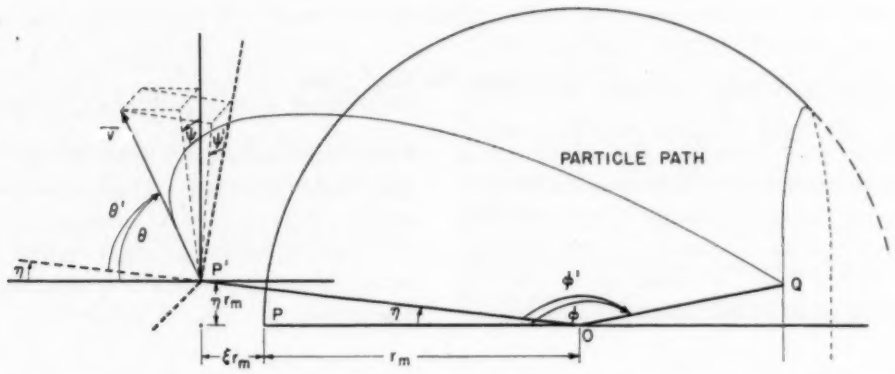

Fig. 2. Quantities describing the displacement of a point source off the axis of symmetry and inner sphere.

An orbit equation referring to the primed angles α' and φ' and containing the displacement parameters ξ and η will be derived. If one writes α' and φ' in terms of the unprimed angles the transmission-energy relation can be expressed in analytical form in the small-angle approximation.

As in Part I, we begin with the standard form of the particle path equation describing motion in the plane OP′Q:

$$u = \frac{1}{r} = \frac{mk}{l^2} + A \sin \varphi' + B \cos \varphi' \tag{1}$$

where, as before, r is the orbit radius and l is the angular momentum of the particle. It was shown in Part I that $k = 2r_m E_0$ (eq. (3)) where $E_0 = \frac{1}{2}mv_0^2$ is that energy which the particle must have in order to execute circular motion about O with radius r_m given the proper initial conditions. Also, the angular momentum l is given by $l = mv\, r_m(1 + \xi) \cos \alpha'$ if we assume $\xi \ll 1$. Then

$$u = \frac{1}{r} = \frac{1}{r_m(1 + \delta)(1 + \xi)^2 \cos^2 \alpha'} + \\ + A \sin \varphi' + B \cos \varphi' \tag{2}$$

where $\varepsilon = r/r_m - 1$. We now write the relations between the primed and unprimed angles from fig. 2. Assuming $\eta, \xi \ll 1$, we have the following relationship from the vectors $\bar{v}$, $\overline{OP}$, and $\overline{OP'}$ (fig. 2).

$$\cos \theta' \cong \cos \theta + \eta \sin \theta \cos \psi \cong \cos (\theta - \eta \cos \psi)$$

or

$$\alpha' = \alpha + \eta \cos \psi \tag{4}$$

since $\alpha = \frac{1}{2}\pi - \theta$ and $\alpha' = \frac{1}{2}\pi - \theta'$. From the vectors $\overline{OP}$, $\overline{OP'}$ and $\overline{OQ}$, one finds

$$\cos \varphi \sim \cos \varphi' - \eta \sin \varphi' \cos \psi'$$

$$\varphi \sim \varphi' + \eta \cos \psi' \tag{5}$$

or

$$\chi = \chi' - \eta \cos \psi'$$

where χ and χ' are the supplementary angles of ϕ and ϕ' respectively.

The relation between ψ' and ψ may be seen from fig. 2 to be

$$\tan \psi' \cong \frac{\sin \theta \sin \psi}{\sin \theta \cos \psi - \eta \cos \theta}$$

or

$$\cos \psi' \cong \cos \psi - \psi \tan \alpha \sin^2 \psi\,.$$

Since we shall retain only first order terms in η we may write

$$\alpha' = \alpha + \eta \cos\psi \qquad (4')$$

$$\chi' = \chi + \eta \cos\psi \,. \qquad (5')$$

We now return to the trace equation (eq. (3)) and expand it retaining only first powers of ξ, δ and η and up to second powers in α' and χ' $(= \pi - \varphi')$. We find

$$\varepsilon = 2\delta + 3\xi + \chi'\alpha' - 2\alpha'^2 \,.$$

Inserting the expression for α' and χ' from eqs. (4') and (5'), we have

$$\varepsilon = 2\delta + 3\xi + \alpha(\chi - 3\eta\cos\psi) + \chi\eta\cos\psi - 2\alpha^2 \,. \qquad (6)$$

From eq. (6) the radial displacement of the trace, ε, depends to a much smaller extent on the tangential displacement of the source point, η, than on the radial displacement ξ. That is, the coefficient of the former, $(\chi - 3\alpha)\cos\psi$, is always less than unity and tends to become smaller still when the integration over the azimuthal angle ψ is performed. In contrast the coefficient of the latter, 3, is obviously not reduced in this integration. Thus it appears advantageous to let $\xi = 0$ in the remainder of the calculation in the hope that the desirable characteristics found for a source on the axis will not be adversely affected by tangential displacements of the source. The trace equation may be transformed by the relations

$$d = \delta/\chi^2 \,, \qquad e = \varepsilon/\chi^2 \,, \qquad h = \eta/\chi \,,$$

$$a = \alpha/\chi \,, \qquad c = \xi/\chi^2$$

to eliminate the explicit dependence on χ and eq. (6) becomes

$$e = 2d + 3c + a\,(1 - 3h\cos\psi) + h\cos\psi - 2a^2 \,. \qquad (7)$$

The case $c = 0$ will be treated below.

In Part I the effect of varying the position and width of the energy-selecting annular gap at the angle φ for the on-axis source was examined. The optimum transmission-energy characteristic was obtained by choosing the inner gap radius r_i equal to r_m and the outer gap radius r_0 to be equal to $r_m(1 + \frac{1}{8}\chi^2)$ (see fig. 2 of Part I). Fig. 3 shows a plot of the relation between reduced energy d and reduced takeoff angle $a(= \alpha/\chi)$ for intercept with the outer gap radius, corresponding to $e = \varepsilon/\chi^2 = \frac{1}{8}$, as curve A. The intercept with the inner gap radius at $e = 0$ is shown as curve B. Particles emitted from the source in the range $a < 0$ are immediately intercepted by the inner sphere and need not be considered further. Particles emerging from the source at angles $a > \frac{1}{2}$ were assumed to intercept the outer sphere after rotating through a central angle φ of approximately $\frac{1}{2}\pi$ radians. The energy dependence

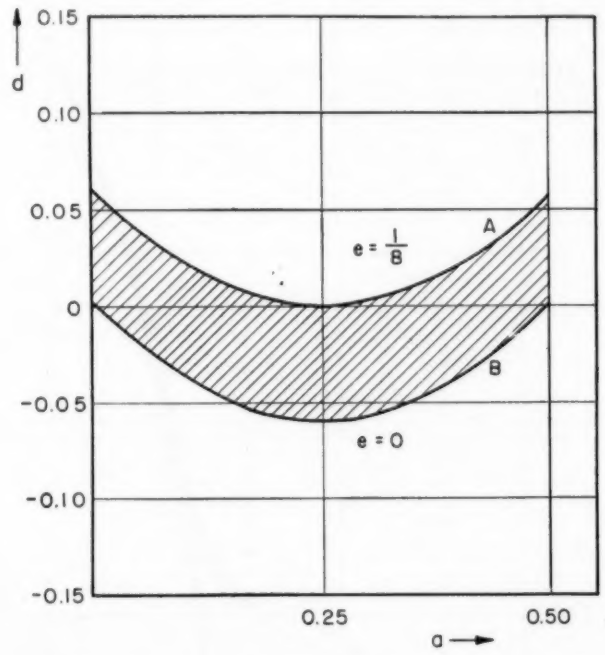

Fig. 3. Allowed region for take-off angles and energies for point source on the axis and inner sphere.

in this outer sphere interception was derived in Part I (eq. (16)), but for $\chi \ll 1$ it may be neglected. Thus the allowed region in fig. 3 was taken to be the cross-hatched area. Since the transmission is proportional to the length of the horizontal line lying inside this area at a given value of d, the expression for the transmission in this case is

$$T_{h=0}(d) = \tfrac{1}{4}\chi\sqrt{1 + 16d} \qquad 0 > d > -\tfrac{1}{16} \qquad (8)$$

$$= \tfrac{1}{4}\chi\,(1 - 4\sqrt{d}) \qquad \tfrac{1}{16} \geqslant d > 0 \qquad (9)$$

$$= 0 \qquad \tfrac{1}{16} \leqslant |\,d\,| \,. \qquad (10)$$

Comparison of this $T(d)$ relation obtained using the small angle approximation with that found from an exact orbit calculation showed very good agreement even for $\chi \approx 1$.

The case $h \neq 0$, $c = 0$ will now be considered

under the assumption that the inner and outer gap radii have the values chosen before, i.e., $r_1 = r_m$ and $r_0 = r_m(1 + \frac{1}{8}\chi^2)$.

Analytical expressions for the transmission at given values of the azimuthal angle ψ, the displacement h and the energy d may be derived easily if one assumes that the inner sphere and outer sphere intercepts are unchanged by the displacement of the source from the axis. This is clearly a good assumption if $\chi \ll 1$. Then, as before, the transmission at a given value of d is proportional to the horizontal intercept lying inside the area bounded by the lines $a = 0$, $a = \frac{1}{2}$, and the parabolas

$$2a^2 - a(1 - 3h\cos\psi) + \tfrac{1}{8} - h\cos\psi - 2d = 0 \quad (11)$$

and

$$2a^2 - a(1 - 3h\cos\psi) - h\cos^2\psi - 2d = 0\,. \quad (12)$$

The first of these parabolas represents the intercept of the trace with the outer gap radius while the second corresponds to the inner gap radius intercept.

The evaluation of the transmission now is considerably more complex than for the source on the axis, and the details are given in the appendix. It may be seen that the transmission at an azimuthal angle ψ, source displacement h, and energy d, may be expressed by various functions of the quantities $(h\cos\psi)$ and d appropriate to the values of these parameters. One may define the transmission $t(h\cos\psi, d)$ with the understanding that the functional dependence of t on its arguments will be given by the equations in the Appendix. Then the average over ψ is given by

$$\bar{t}\,(h,d) = \frac{1}{\pi}\int_0^\pi t(h\cos\psi,d)\,d\psi\,. \quad (13)$$

Fig. 4 shows a plot of $\bar{t}(h,d)$ as a function of d for various values of h. These calculations of $\bar{t}(h,d)$ as well as those described below were made using an IBM-704 computer.

The transmission for a disc source of radius h_0 is given by

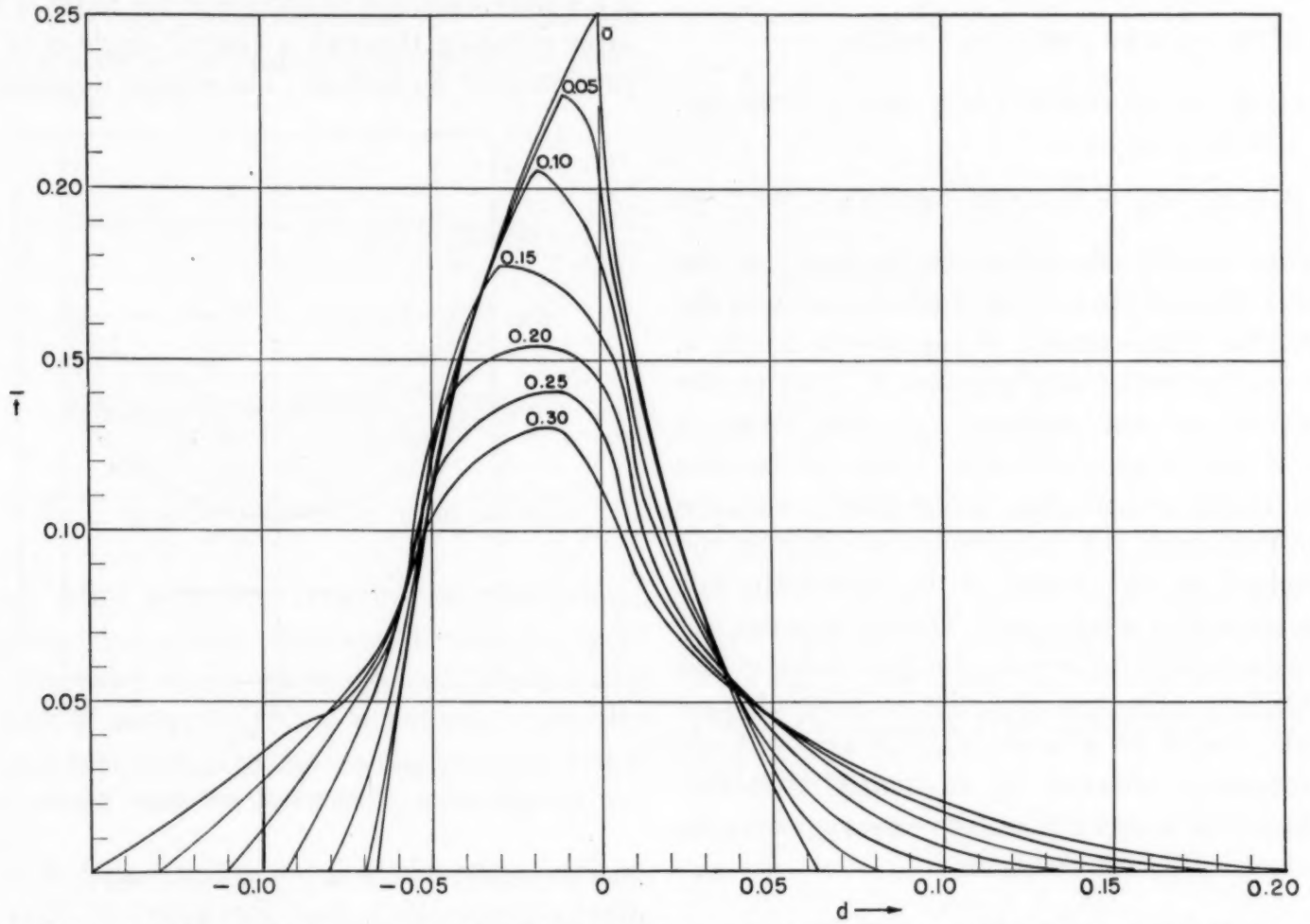

Fig. 4. Line profiles for a point source on the inner sphere but off the axis of symmetry. Numbers on curves are values of $h = \eta/\chi$ where η is the displacement of the source point from the axis of symmetry in units of the radius of the inner sphere.

$$\bar{t}_D(h_0,d) = \frac{2}{\pi h_0^2}\int_0^{h_0} h\,dh \int_0^{\pi} t(h\cos\psi,d)\,d\psi \quad (14)$$

where the factor $2/h_0^2$ normalizes the total source intensity to unity. This may be simplified by setting $h = h_0 y$, and $y\cos\psi = \cos\omega$. One finds

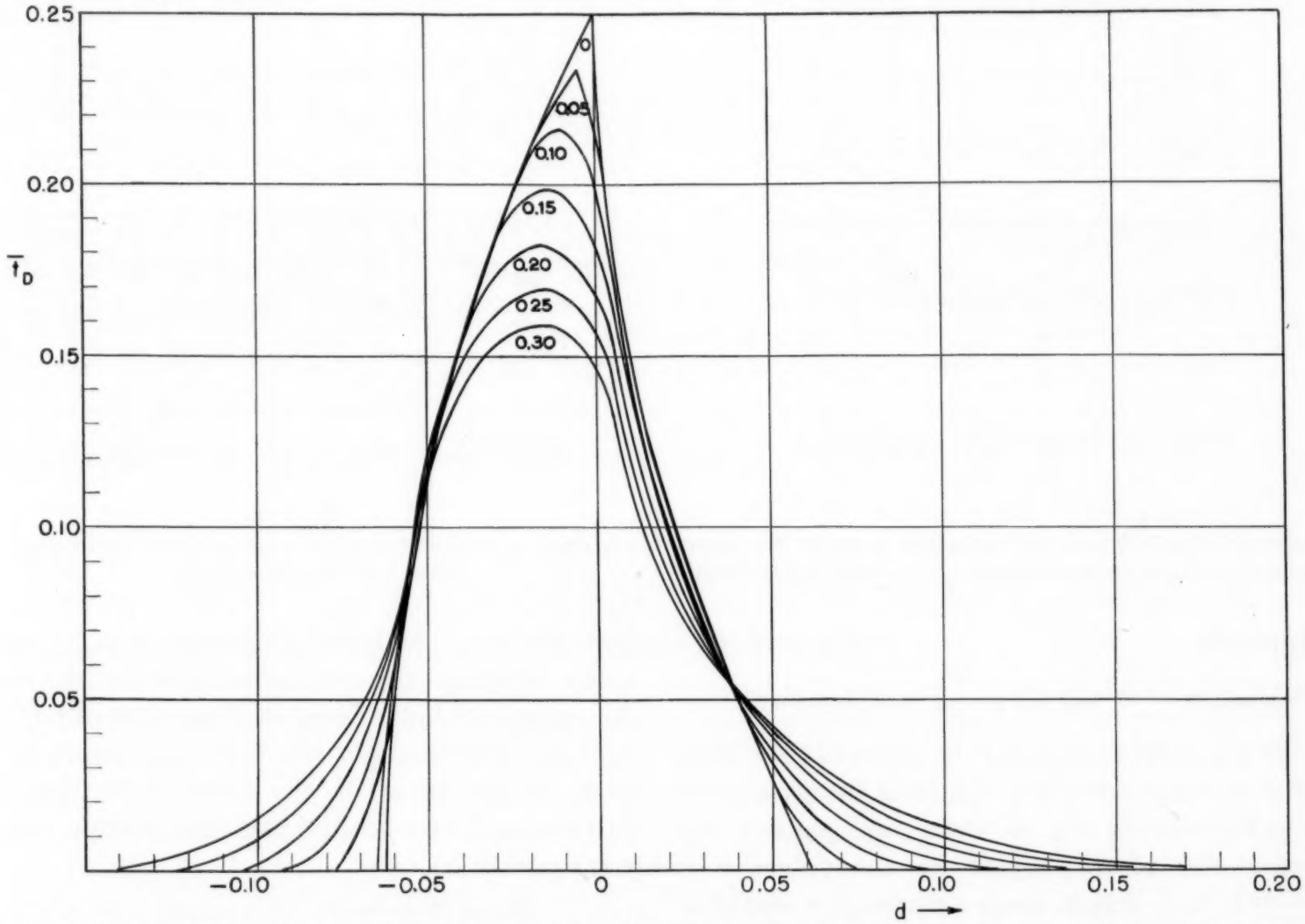

Fig. 5. Line profiles for a disc source on the inner sphere. Numbers on curves are values of $h_0 = \eta_0/\chi$ where η_0 is the source radius in units of the radius of the inner sphere.

$$\bar{t}_D(h_0,d) = \frac{2}{\pi}\int_0^1 y\,dy \int_{\cos^{-1}y}^{\cos^{-1}(-y)} t(h_0\cos\omega,d)\,\frac{\sin\omega\,d\omega}{\sqrt{y^2-\cos^2\omega}} \quad (15)$$

which may be further simplified by inverting the order of integration. The final result is

$$\bar{t}_D(h_0,d) = \frac{2}{\pi}\int_0^{\pi} \sin^2\omega\; t(h_0\cos\omega,d)\,d\omega\,. \quad (16)$$

Fig. 5 shows a plot of $\bar{t}_D(h_0,d)$ as a function of d for various values of h_0.

A calculation of instrument performance for the case of the largest source ($h = 0.3$) and highest transmission ($\chi = 1$) will serve to illustrate the use of the curves of fig. 5. It should be borne in mind that these values represent the extremes of the calculation where some error is inevitably present due to the small angle approximations used. In light of the good agreement between the calculations and graphical methods in Part I, it is thought that here also these calculations for large sources and angles will be very nearly correct. The above values of h and χ yield a source radius η of 0.3 in units of the radius of the inner sphere. The transmission and resolution are, from fig. 5, 0.16 and 0.077 respectively as compared with the corresponding values for the point source on the axis of symmetry of 0.25 and 0.063. Thus the transmission is reduced to 64% of its value for the point source and the resolution is impaired by the factor 1.22. Thus the ratio of transmission to resolution is reduced by about about a factor of two, a remarkably small change for a source radius which is 30% of the radius of the inner sphere. Use of such a large diameter source will permit a spreading of the radioactive material thinly enough to avoid

serious self-absorption problems. For use as a low-energy X-ray spectrometer, the spherical condenser instrument should allow use of broad beams of X-rays and extremely thin photoelectric radiators.

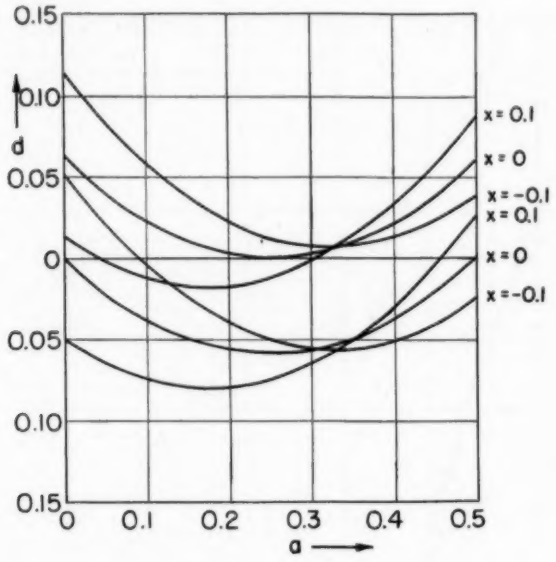

Fig. 6
Allowed region for take-off angles and energies for representative values of source displacement and azimuthal angle.

parameter x. The line $l_{\min}$ represents the variation with x of the position of the minimum of the lower parabola while l_0, and $l_{\frac{1}{2}}$ show the variation of the intercept of the lower parabola with the lines $a = 0$ and $a = \frac{1}{2}$, respectively, as a

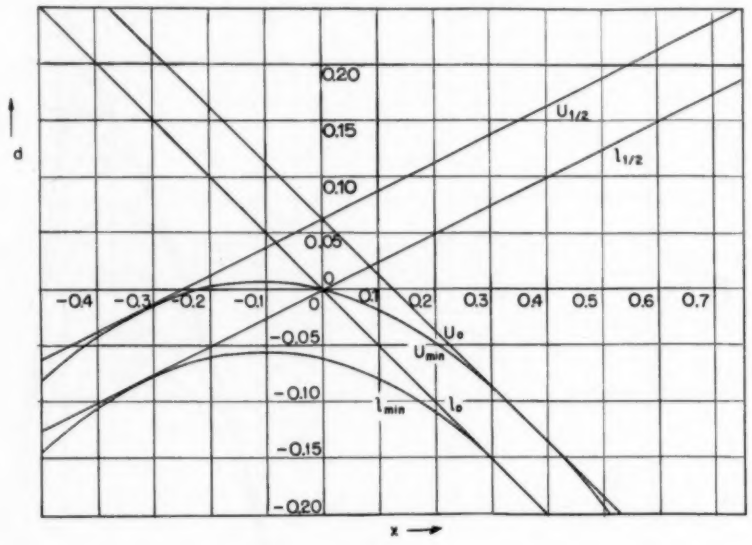

Fig. 7
Variation of critical boundary points with source displacement and azimuthal angle.

Appendix

Derivation of the $t(x,d) = \frac{1}{\chi} T(x,d)$ *relation*

It is helpful to consider the shape of the region of acceptance for a few values of the parameter $x = h \cos \psi$. In fig. 6 there are plotted the boundaries of this region for the values $x = (-0.1, 0, +0.1)$ in the d-a plane. One sees that as x increases in the positive direction, the region is depressed toward negative values of d in the left side of the region and raised toward larger positive values on the right side and that this skewing is reversed for decreasing values of x.

In obtaining the length of the horizontal intercept which lies inside the region of acceptance one must consider several different cases when $x \neq 0$; e.g., the intercept is clearly zero when d lies below the minimum in the lower parabola. Likewise, when d increases to the point where the value of a on the parabola is either greater than $\frac{1}{2}$ or less than zero one must change analytic representations for the length of the intercept.

Fig. 7 shows a plot of the variation in the position of these critical points in d versus the function of x. The lines designated by $u_{\min}$, u_0, and $u_{\frac{1}{2}}$ represent the corresponding quantities on the upper parabola. From an inspection of fig. 7 one may immediately write down expressions for $t(x,d)$. If one lets $a^l_{\pm}$ be the value of the larger $(+)$ or smaller $(-)$ solution of the equation (the lower parabola)

$$a^2 - \tfrac{1}{2}(1 - 3x)\, a - \tfrac{1}{2}(x + 2d) = 0$$

and $a^u_{\pm}$ be the larger $(+)$ or smaller $(-)$ solution of

$$a^2 - \tfrac{1}{2}(1 - 3x)\, a + \tfrac{1}{2}(\tfrac{1}{8} - x - 2d) = 0$$

then the transmission $t(x,d)$ may be written for the general case as

$$t(x,d) = \frac{1}{x} T(x,d) = \tfrac{1}{2}\Big[\{ \operatorname{Min}(\tfrac{1}{2}, a^l_+) - \operatorname{Max}(0, a^l_-) \} \operatorname{St}[-\operatorname{Im}(a^l_+)] - \{ \operatorname{Min}(\tfrac{1}{2}, a^u_+) - \operatorname{Max}(0, a^u_-) \} \operatorname{St}[-\operatorname{Im}(a^u_+)] \Big]$$

where

$$\operatorname{St}(z) \equiv 1 \qquad (z \geqslant 0)$$
$$\equiv 0 \qquad (z < 0)$$

and $\operatorname{Im}(z)$ is the imaginary part of the complex number z. Explicit representations for t may be written down as follows. When $x > 0$

$t = 0$ $\quad (d \leqslant -\frac{1}{16} - \frac{1}{8}x - \frac{9}{16}x^2)$

$t = t_1 = \frac{1}{4}\sqrt{(1-3x)^2 + 8(x+2d)}$ $\quad (-\frac{1}{16} - \frac{1}{8}x - \frac{9}{6}x^2 \leqslant d \leqslant -\frac{1}{2}x)$

$= t_2 = \frac{1}{8}\{(1-3x) + \sqrt{(1-3x)^2 + 8(x+2d)}\}$ $\quad (-\frac{1}{2}x \leqslant d \leqslant -\frac{1}{8}x - \frac{9}{16}x^2)$

$= t_3 = \frac{1}{8}\{(1-3x) + \sqrt{(1-3x)^2 + 8(x+2d)} - 2\sqrt{(1-3x)^2 + 8(x+2d) - 1}\}$ $\quad (-\frac{1}{8}x - \frac{9}{16}x^2 \leqslant d \leqslant \operatorname{Min}\{\frac{1}{4}x, [\frac{1}{16} - \frac{1}{2}x]\})$

$= t_4 = \frac{1}{4}\{1 - \sqrt{(1-3x)^2 + 8(x+2d) - 1}\}$ $\quad (\frac{1}{2}x \leqslant d \leqslant \frac{1}{16} - \frac{1}{2}x)\ (x \leqslant \frac{1}{12})$

$= t_5 = \frac{1}{8}\{\sqrt{(1-3x)^2 + 8(x+2d)} - \sqrt{(1-3x)^2 + 8(x+2d) - 1}\}$ $\quad (\frac{1}{16} - \frac{1}{2}x \leqslant d \leqslant \frac{1}{4}x)\ (x \geqslant \frac{1}{12})$

$= t_6 = \frac{1}{8}\{1 + 3x - \sqrt{(1-3x)^2 + 8(x+2d) - 1}\}$ $\quad \operatorname{Max}[(\frac{1}{16} - \frac{1}{4}x), \frac{1}{4}x] \leqslant d \leqslant \frac{1}{16} + \frac{1}{4}x$

$= 0$ $\quad (\frac{1}{16} + \frac{1}{4}x \leqslant d)$

For the case $x \leqslant 0$, the transmission takes a slightly different form

$t = 0$ $\quad (d \leqslant -\frac{1}{16} - \frac{1}{8}x - \frac{9}{16}x^2)$

$= t_1$ $\quad (-\frac{1}{16} - \frac{1}{8}x - \frac{9}{16}x^2 \leqslant d \leqslant \frac{1}{4}x)$

$t = \frac{1}{8}\{(1+3x) + \sqrt{(1-3x)^2 + 8(x+2d)}$ $\quad (\frac{1}{4}x \leqslant d \leqslant -\frac{1}{8}x - \frac{9}{16}x^2)$

$= \frac{1}{8}\{(1+3x) + \sqrt{(1-3x)^2 + 8(x+2d)} - 2\sqrt{(1-3x)^2 + 8(x+2d) - 1}\}$ $\quad (-\frac{1}{4}x - \frac{9}{16}x^2 \leqslant d \leqslant \operatorname{Min}[\frac{1}{2}x, (\frac{1}{16} + \frac{1}{4}x)])$

$= t_4$ $\quad (-\frac{1}{2}x \leqslant d \leqslant \frac{1}{16} + \frac{1}{4}x),\ (-\frac{1}{12} \leqslant x)$

$= t_5$ $\quad (\frac{1}{16} + \frac{1}{4}x \leqslant d \leqslant -\frac{1}{2}x),\ (x \leqslant -\frac{1}{12})$

$= \frac{1}{8}\{(1-3x) - \sqrt{(1-3x)^2 + 8(x+2d) - 1}\}$ $\quad \operatorname{Max}(-\frac{1}{2}x, [\frac{1}{16} + \frac{1}{2}x]) \leqslant d \leqslant \frac{1}{16} - \frac{1}{2}x$

$= 0$ $\quad (\frac{1}{16} - \frac{1}{2}x \leqslant d)$

NUCLEAR INSTRUMENTS AND METHODS **8** (1960) 320–326; NORTH-HOLLAND PUBLISHING CO.

CONTINUOUS MONITORING OF URANIUM LEACH SOLUTIONS

G. G. EICHHOLZ

Physics and Radiotracer Section, Mineral Sciences Division, Mines Branch, Department of Mines and Technical Surveys, Ottawa, Canada

Received 12 May 1960

A method for the determination of uranium content in leach solution by scintillation alpha-ray detection has been developed for possible application to the continuous monitoring and control of breakthrough in ion exchange colomns. The radioactive solution flows through a circular cell containing several thin disks of a plastic scintillation phosphor which respond to bombardment by alpha particles from uranium atoms in the solution. The fluorescence produced in the phosphor is observed and amplified by means of standard scintillation counter techniques. Breakthrough curves have been obtained by this method, and correlation with various alpha emitters has been attempted by the use of an alpha-ray spectrometer. Positive detection of activity to levels down to 0.2 g/l equivalent uranium content in solution seems possible on a continuous basis.

1. Introduction

In leach processes for the extraction of uranium from its ores and in subsequent chemical purification steps it would be advantageous if the actual uranium content of the various solutions could be monitored and recorded instantaneously and continuously. Such monitors might then be adapted to control the particular extraction process or to warn of excessive contamination in waste solutions. For this purpose it is tempting to turn to the radioactivity of uranium. The practical difficulty that one encounters, however, is that purified uranium with all its daughter elements removed emits only alpha particles. Though quite energetic (4.18 MeV), these particles have a short range in air and are easily absorbed in all solids and liquids, so that their range in water is only of the order of 25 microns.

For this reason attempts to monitor the uranium content of solutions continuously have not been very successful so far. The continuous monitoring of streams for fission products and other gamma emitters can be done fairly easily. (Wilson[1]), Wingfield[2]), and others), but for alpha emitters it has become customary to monitor by sampling the solution or stream automatically at fixed intervals. From these samples the uranium is extracted as an insoluble compound which is deposited on disks or filters and then counted with a zincsulphide scintillation counter. Such methods have been described by Smales *et al.*[3]), Le France *et al.*[4]), and Wingfield[5]). The only equipment which has been described in the literature for direct continuous monitoring of alpha emitters in solution is that of Taylor and Abson[6]). Their apparatus consisted essentially of a rotating drum which dipped into the liquid and pulled up a thin liquid film by surface tension. This film passed under a zinc sulphide scintillation counter, in close proximity but without contact, and the alpha emission from the solution was thus determined. This ingenious method, however, did not work out too well in practice, as it was difficult to maintain

[1]) J. N. Wilson, Nucleonics **17**, No. 11 (1959) 140.

[2]) E. C. Wingfield, A Gamma Monitor for Liquid Streams, E. I. du Pont de Nemours and Co., Savannah River Laboratory, Report DP-342 (1958).

[3]) A. A. Smales, L. Airey, J. Woodward and D. Mapper, The Monitoring of Effluent for Alpha Emitters, A.E.R.E. Harwell Report C/R 2223 (1957).

[4]) J. D. LeFranc, P. Pottier and G. Roux, Énergie nucléaire **2**, No. 3 (1958) 195.

[5]) E. C. Wingfield, An Alpha Monitor for Waste Streams, E. I. du Pont de Nemours and Co., Savannah River Laboratory, Report DP-197 (1957).

[6]) D. Taylor and W. Abson, Proc. I.E.E. **98**, Part II (1951) 762.

uniform films on the drum under operating conditions and the sensitivity proved to be insufficient.

The work at the Mines Branch, Ottawa, arose principally from a desire to monitor the breakthrough of uranium in ion exchange columns used for the extraction of uranium in acid leach circuits, but the system developed may well have wider applications. Its main principle consists of detecting the alpha particles continuously by placing the detector in contact with the liquid. To compensate for the low sensitivity attainable, and because it is only the surface layer of the detector which responds to the alpha particles, it is important to increase the surface area used to detect the alpha particles. A further difficulty arises from the acidity of the leach solutions which attack unprotected inorganic scintillators and this requires careful design of the detector cell.

A first approach to this problem was attempted in 1951 by applying a thin coating to zinc sulphide films, the usual scintillating detector for alpha particles, to protect the zinc sulphide against corrosion from the solution[7]). This protective coating had to be uniform and free of pinholes, yet thin enough to permit easy passage of the alpha particles, while being fully resistant to strong sulphuric acid solutions. These requirements seemed to be mutually exclusive and this approach was abandoned in favour of one using thin plastic scintillation phosphors which at that time had just been developed[8,9]).

The advantage of the plastic scintillators lies in the fact that they may be made of polystyrene and are acid resistant and easy to manufacture in any desired shape or thickness. As plastic scintillators are also sensitive to gamma-rays, it is important to make them as thin as practicable to minimize counts from radium daughters and cosmic-ray background. The scintillation flashes produced by alpha particles are much smaller in plastic scintillators than in zinc sulphide, and good optical coupling is important. The remainder of the detection equipment consists of standard photomultiplier tubes, a pre-amplifier, a ratemeter and a recorder.

2. Description of Apparatus

For test purposes, work with different detectors was carried out inside a large light-tight box which permitted maximum flexibility in changing detector types and configurations. The photomultiplier was supported vertically within its shield inside the box, and a detector cell rested on the light-sensitive photocathode of the photomultiplier. Depending on the nature of the tests either the scaler or the ratemeter was used as the count indicator.

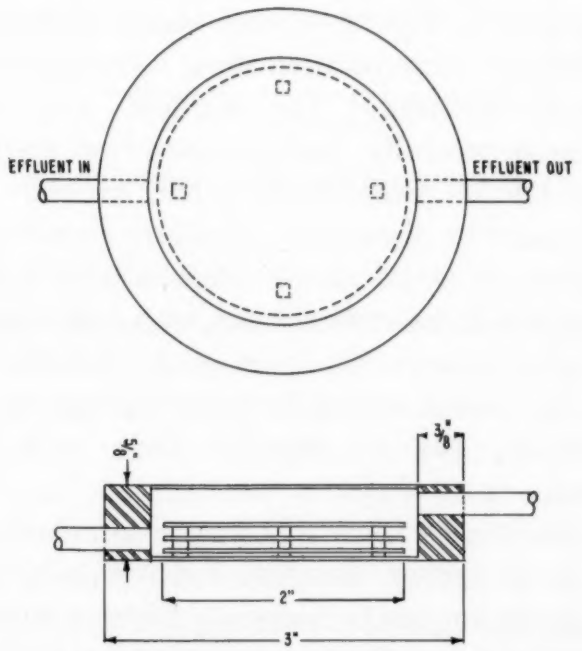

Fig. 1. Details of detector cells.

A 5-inch photomultiplier tube was used in some tests, but most of the test work was done with the cheaper 2-inch photomultiplier tube, type 6292, since, contrary to expectations, no appreciable increase in sensitivity and performance was obtained with either of two 5-inch photomultipliers, type 6364, which were tried.

The most critical operation is the preparation of the detector cells. Their assembly is presented diagrammatically in fig. 1 which shows an

[7]) J. E. Wilson, Mines Branch Internal Report IR-42/51, Mines Branch, Department of Mines and Technical Surveys, Ottawa, Ont. (unpublished, 1951).

[8]) G. G. Eichholz and J. L. Horwood, Rev. Sci. Instr. **23** (1952) 305.

[9]) G. G. Eichholz, Phys. Rev. **89** (1953) 912.

all-plastic cell. All the plastic disks are made of scintillating plastic sheet having polystyrene beads as spacers. A similar cell was made with a stainless steel case, with the same type of plastic disk window and inner assembly. The stainless steel was painted with white Tygon paint to act as a light reflector.

The scintillator sheets were made on a laboratory press with polystyrene powder hot-moulded under pressure[8]). The hot platens were covered with aluminium foil and the thickness of the film could be adjusted by surrounding the powder with spacer rings of the appropriate thickness. Various scintillators were tried; a typical mixture would consist of 10g polystyrene (Dow No. 666), 400 mg p-terphenyl and 10 mg tetraphenyl butadiene. Diphenyl hexatriene was also used as a wave length shifter. For mechanical strength, slightly thicker sheets were chosen for the cell windows than those used in the inner detector assembly. The windows had to be mounted carefully since in operation they are subjected to considerable liquid pressure, and leaks could be disastrous. Absolute cleanliness is essential to avoid grease films on the detector disks. The disks were cut out with a sharp point around a heavy cylindrical guide. Similar commercial plastic scintillator sheets can also be employed, but no detailed tests have been carried out on these.

Calibration was carried out by circulating solutions of known uranium content in a closed circuit by means of a Sigma finger pump. All runs with test solutions from the ion exchange column were done with gravity feed only. It was found important to maintain the pH of the test solutions low, as in some early tests at near neutral pH a dense solid layer precipitated out on the plastic cell, which was later identified as silica from the leach solutions.

The photomultiplier was usually run at a potential of around 1100 volts. The ratemeter threshold level served as the only effective pulse height discriminator. Background levels were low, provided that the disk thicknesses were small enough to minimize gamma-ray detection.

3. Test Results

Owing to the intermittent nature of this project over the years 1954–1959, conditions varied from test to test and only typical results will be quoted here.

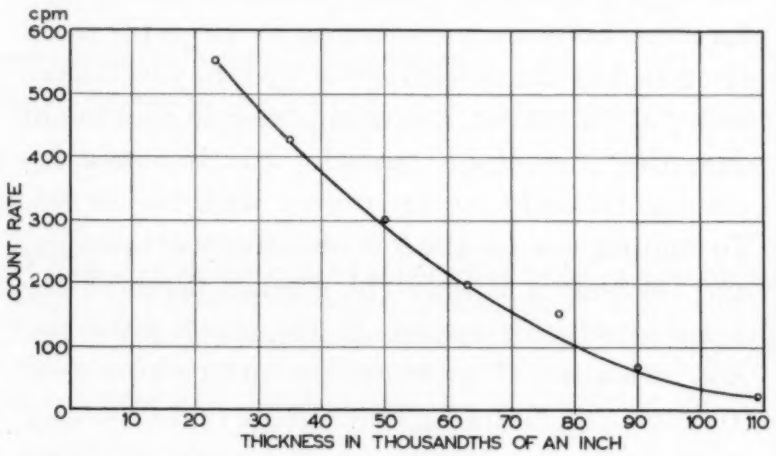

Fig. 2. Effect of phosphor thickness of alpha-ray detection.

3.1. DETECTOR TESTS

Experiments were carried out with various detector configurations and have been described more fully in a previous report[10]). Only the main conclusions will be summarized here. Fig. 2 shows the effect of scintillator thickness on count rate. It is seen that for thicker films there is considerable self-absorption of the fluorescent light, probably due to internal light scattering in the

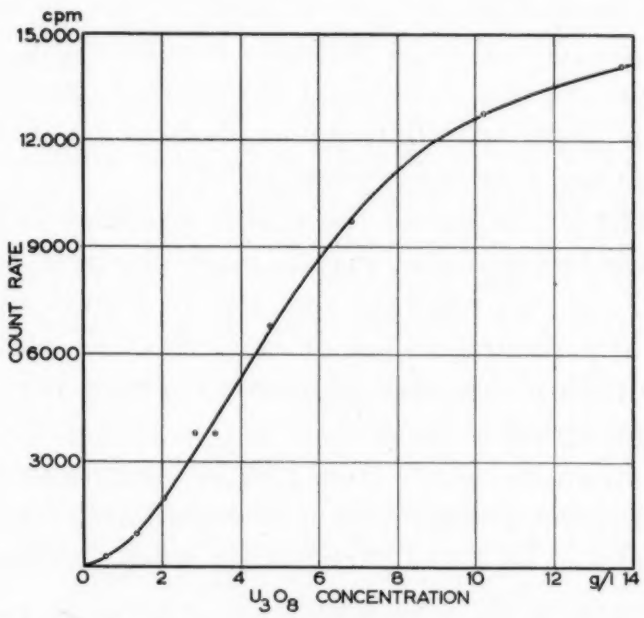

Fig. 3. Effect of uranium concentration on count rate.

[10]) H. H. Schwartz, Mines Branch Internal Report IR-219/56, Mines Branch, Department of Mines and Technical Surveys, Ottawa, Ont. (unpublished, 1956).

films. In practice, detector sheets were kept well below 15 mils.

Fig. 3 shows the response curve obtained with high grade solutions in a four-disk detector cell. The response is seen to be linear over most of the range. At the upper end it appears to level off, but this effect is ascribed to loss of light in passing through the solution, which was noticeably yellow at the higher concentrations. This light loss sets an upper limit to the total thickness of solution sampled, and hence to the number of disks that can usefully be employed. Table 1 presents results obtained in a typical case with different numbers of detectors, for a U_3O_8 concentration of 5 g/l.

TABLE 1

Effect of varying the number of detector disks (in a 7 cm diameter cell)

Number of detectors	Count rate (cpm)
1	3 437
2	7 345
3	11 958
4	14 743

It is seen that the count rate goes up steadily for all disk assemblies shown. In practice, four or five disks have been used for convenience. Larger assemblies pose problems in parallel mounting.

3.2. CALIBRATION

The system was calibrated by circulating synthetic uranium solutions through it. The solutions contained between 0.1 and 2 g/l U_3O_8, and fig. 4 is the corresponding calibration curve. It was seen that with the ratemeter time constant used, 0.1 g/l U_3O_8 is almost indistinguishable from background and represents the practical limit for the particular detector cell used. The recorder trace can be smoothed out by using a longer time constant in the ratemeter, and this is satisfactory when no abrupt changes in uranium content of the effluent are anticipated. The results shown in fig. 4 were obtained at a much later date and with a different detector cell than those shown in fig. 3, and this accounts for the better low-level discrimination obtained.

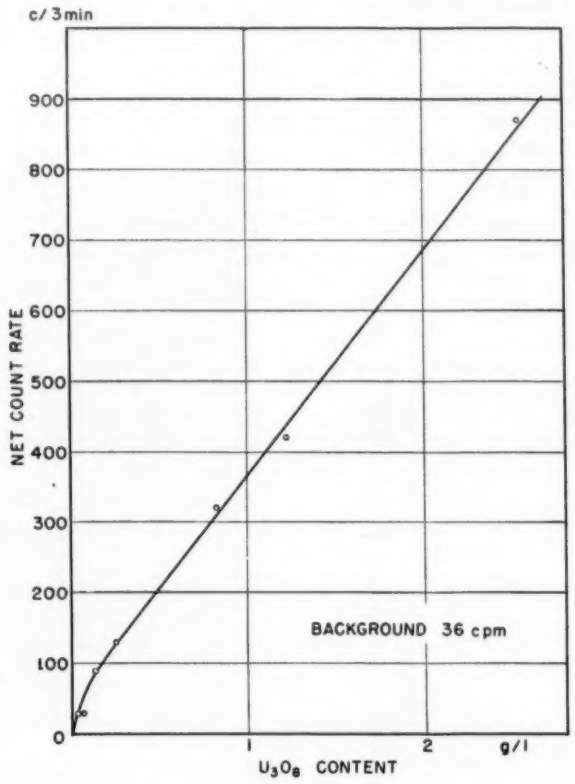

Fig. 4. Calibration for uranium solutions.

3.3. ION EXCHANGE EFFLUENT TESTS

Numerous tests were carried out on effluents from ion exchange columns for various pregnant uranium liquors. They all demonstrated plainly the steady rise in uranium content of the effluent and the absence of any abrupt change which could be pin-pointed as a definite breakthrough point. This is contrary to the experience gained by chemical determinations, where it was found that a fairly sharp increase in uranium content is observed in the effluent as the resin is loaded and breakthrough occurs. The difference may in part be due to the presence of other alpha emitters, and in part to a difference in scale. Most chemical loading curves pay little attention to the pre-breakthrough region. Fig. 5 shows a plot of the readings from two typical recorder traces for two different test runs. Some of the assays corresponding to these samples marked on run B are tabulated in table 2. This liquor contained some iron as well, and the iron assays are tabulated too, to show that the changes observed are not connected with the iron content.

TABLE 2
Solution monitor run B (Sept. 1959)

Sample number	U_3O_8 assay (g/l)	Fe assay (g/l)
Head sample	1.96	1.65
9	0.006	1.82
10	0.006	1.80
11	0.005	1.80
12	0.022	1.80
13	0.068	1.77
14	0.14	1.82
15	0.21	1.62

height analyser. This equipment is shown in fig. 7.

Figs. 8 and 9 show the alpha-ray spectra corresponding to some of the samples listed in table 2. According to the usual, arbitrary criterion used in uranium leach work, breakthrough was considered to take place when the uranium content in the effluent exceeded 0.1 g/l, i.e. between samples No. 13 and 14. Fig. 8 compares the alpha-ray spectrum of sample No. 12 with two spectrum curves obtained with pure uranium standards. It is seen that sample No. 12 consists almost entirely of thorium-230 with a peak at 4.68 MeV, clearly resolved from the uranium peaks at 4.76 MeV for uranium-234 and 4.18 MeV for uranium-238.

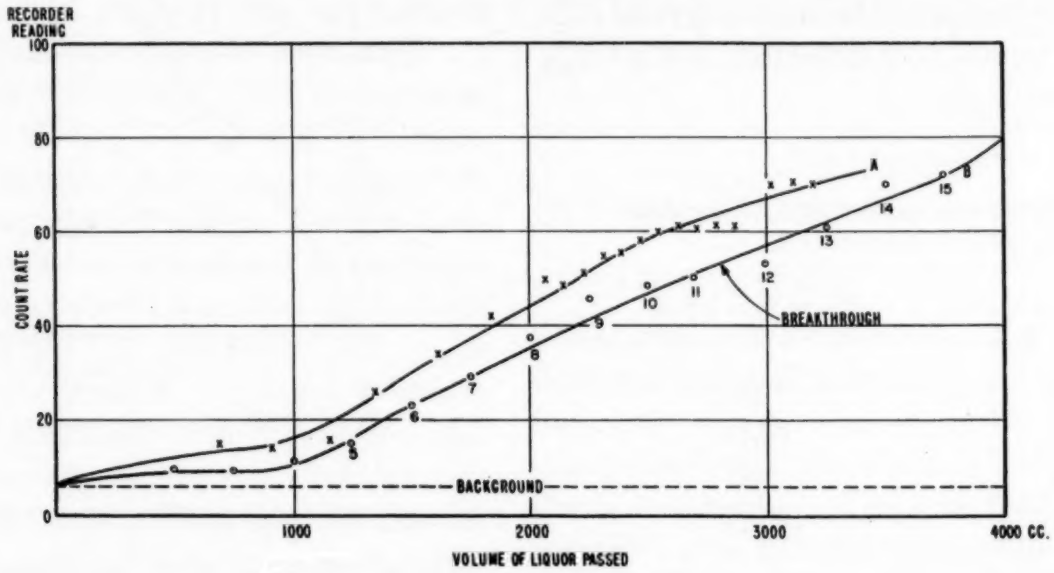

Fig. 5. Plot of typical ratemeter readings for two uranium leach liquors (ion-exchange column effluents). Feed rate 13 ml/min.

3.4. IDENTIFICATION OF EMITTING ISOTOPES

Some early runs with different pregnant leach liquors were characterised by a surprisingly rapid rise in detector indication. This is shown in fig. 6, in which the monitor indications for typical leach liquor effluents are plotted. The early rise was ascribed to the appearance of ionium (Th-230), which is replaced by uranium on the ion exchange resin. This was reportedly one of the difficulties encountered with Taylor and Abson's equipment[6]). To investigate this point, an alpha-ray spectrometer was set up as an aid in the identification of the alpha emitters in the various samples. The alpha-ray spectrometer consists of an ionization chamber of the type described by Harvey *et al.*[11]), followed by a linear amplifier, AEP type 1444, and a Marconi six-channel pulse

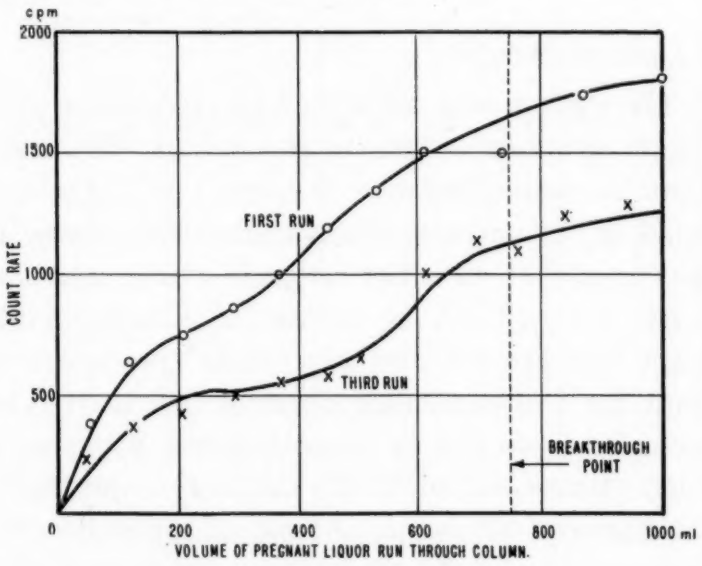

Fig. 6
Monitor indication of uranium content in two different test runs. (Breakthrough point determined colorimetrically.)

[11]) B. G. Harvey, H. G. Jackson, T. A. Eastwood and G. C. Hanna, Can. J. Phys. **35** (1957) 258.

Fig. 9 shows the progressive change in the alpha-spectra from sample to sample. It illustrates how thorium is adsorbed on the ion exchange resin first, to be replaced by uranium as in the effluent and on the monitor records is linked so closely with the occurrence of breakthrough for uranium that it cannot be considered objectionable.

Fig. 7. Alpha-ray spectrometer.

breakthrough is approached, until for sample No. 16, long after breakthrough, uranium clearly predominates in the effluent. In this particular case, therefore, the appearance of ionium (Th-230)

3.5. OTHER URANIUM SOLUTIONS

To test the usefulness of the equipment in other applications, carbonate solutions from the leach plant of Eldorado Mining and Refining

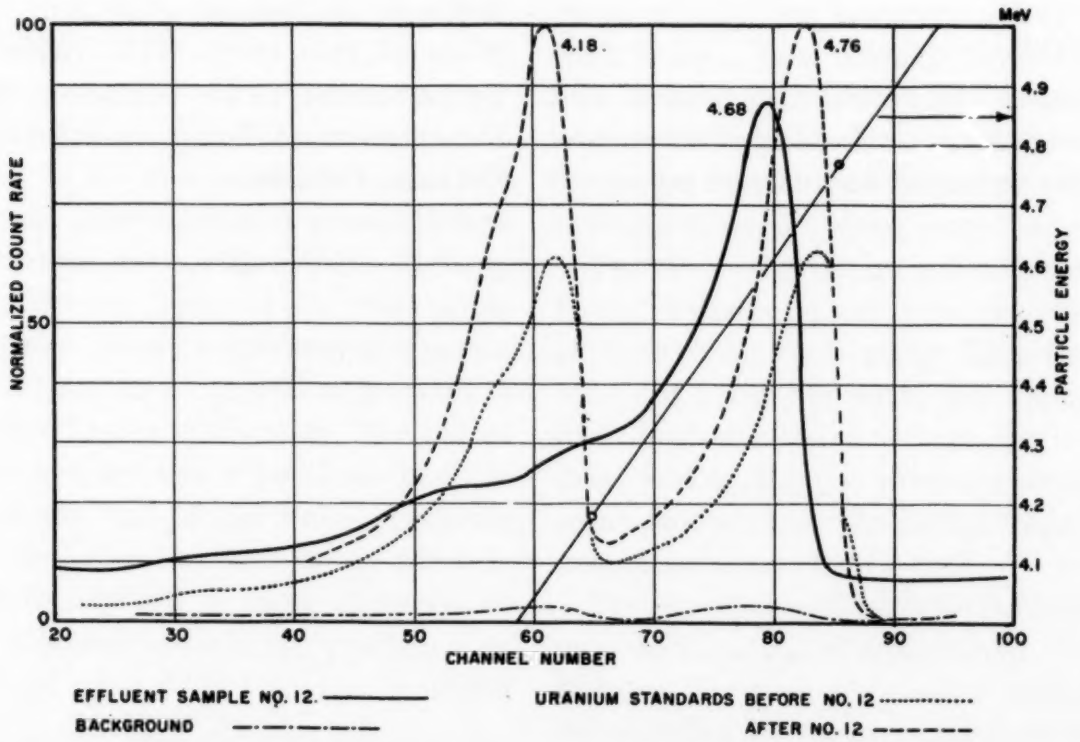

Fig. 8. Alpha-ray spectra of effluent samples (from Monitor Run B).

Limited at Beaverlodge, Sask., were run through the system. It was found that satisfactory monitor indications were obtained, provided that the liquors were filtered to remove all solid residues, for uranium contents above 0.15 g/l.

4. Conclusions

The tests indicate that it is possible to monitor uranium-bearing solutions continuously by the use of a plastic scintillator detector cell. While this method is less sensitive than methods using intermittent sampling and radiochemical purification, it is faster and more convenient. The limit in sensitivity for a given detector is set by the spontaneous fluctuations in count rate, which in turn depend on the time constant of the ratemeter. Where a slow response is adequate, a longer time constant of the order of 50 seconds, may be used to give a smoother output indication. For a sensitive, rapid response the fluctuations are too great and the variation in count rate too slow to permit actual control of the ion exchange column by breakthrough indication. However, the monitor can serve as a useful indicator of improper operation of the column or of premature breakthrough. It may also be useful in plutonium plants and in uranium refining.

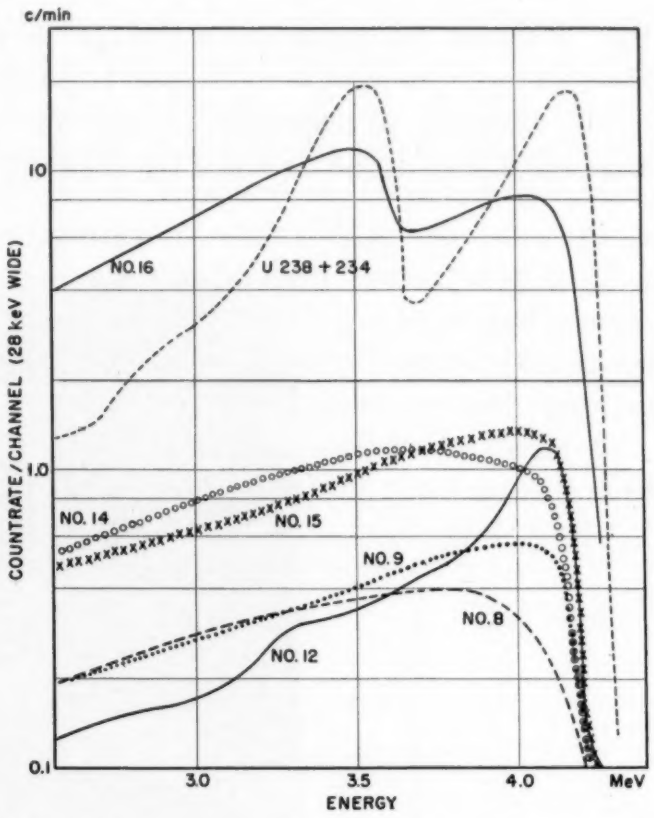

Fig. 9. Alpha-ray spectra of effluent samples showing uranium breakthrough.

Acknowledgments

It is a pleasure to record the patient and persevering assistance of J. M. Lefebvre who prepared all the detectors and carried out much of the test work, and the contributions of H. H. Schwartz and R. A. Wilkinson. Dr. J. D. Keys set up the alpha-ray spectrometer and C. McMahon and J. L. Horwood obtained the spectra. This project was suggested by the late Dr. E. A. Brown and the author owes much to discussions with him on various aspects of this work. This paper is published by permission of the Director, Mines Branch, Department of Mines and Technical Surveys, Ottawa, Canada.

NUCLEAR INSTRUMENTS AND METHODS 8 (1960) 327–330; NORTH-HOLLAND PUBLISHING CO.

DRIFT VELOCITIES OF ELECTRONS IN ARGON, NITROGEN AND ARGON MIXTURES

T. NAGY, L. NAGY and S. DÉSI

Central Research Institute for Physics, Budapest

Received 7 June 1960

Drift velocities of electrons produced by fission fragments in a parallel-plate ionization chamber have been measured in argon, nitrogen, and mixtures of gases, such as argon-nitrogen, argon-carbon dioxide and argon-methane. The results obtained are compared with data reported in the literature.

1. Introduction

For the operation of electron pulse ionization chambers it is necessary to know the drift velocities of electrons in the filling gas. In pure argon the drift velocity depends considerably on the presence of impurities and that is why the most careful purification of the gas is required in order to obtain reproducible results. This fact explains the discrepancies between data reported on this gas in the literature.

We repeated the experiments in pure argon and furthermore, measured the electron drift velocities in argon mixed with small amounts of contaminating gas.

2. Method of Measurement

Our measuring method was similar to that employed by Klema and Allen[1]) and Colli and Facchini[2]), that is we measured the collection times of electrons produced in a parallel-plate ionization chamber. But while these authors measured the collection times of electrons produced by α particles, in our experiments the rise times of pulses produced by fission fragments were photographed for investigation. The use of fission fragments instead of α particles has the advantage that the end of the pulse rise time becomes more definite. The end of the pulse is determined by the arrival of those electrons at the collecting electrode which are produced at the beginning of the track by the ionizing particle. As the specific ionization of the fission fragments is the greatest at the beginning of the track, that is the density of the electrons here is great, the rise of the pulse stops abruptly (fig. 1). The α particles on the other hand,

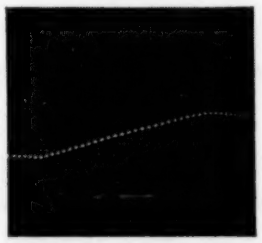

Fig. 1. Photograph of a pulse produced by a fission fragment. The marker has a duration of 0.5 μsec.

produce only few electrons at the beginning of their tracks, thus making determination of the end of the rise rather more uncertain than in case of fission fragments. A further advantage is the larger amplitude of pulses produced by fission fragments as compared with that of α particles.

The electrodes of the ionization chamber were 16 cm in diameter and were placed at a distance of 5 cm from each other. The 1 mg/cm^2 thick uranium layer deposited on the negative electrode had a diameter of 5 cm. With these dimensions and at the gas pressure applied, the electrons produced by the fission fragments move in a homogeneous electric field.

The chamber and a Po-Be neutron source were mounted in a paraffin container. By varying the distance between the source and the chamber, the number of fissions could be varied within wide limits.

[1]) E. D. Klema and J. S. Allen, Phys. Rev. **77** (1950) 661.
[2]) L. Colli and U. Facchini, Rev. Sci. Instr. **23** (1952) 39.

The chamber was connected to a purifying furnace 15 cm long and 5 cm in diameter containing 100 g of calcium chips. A motor was used to help the circulation of gas due to convection and in the case of gas mixtures also the mixing process. The rotor was provided with blades and the stator was mounted outside the gas system separated from the former by a glass tube.

Argon was purified as follows. The whole system was evacuated to 10^{-4} mm Hg pressure, then the furnace was heated up to 500° C in order to outgas the calcium. When the pressure decreased again below 10^{-4} mm Hg, the argon was let in through a trap containing liquid nitrogen.

Prior to the addition of molecular gases to the purified argon, the furnace was cooled in order to prevent the absorption of the small amounts of molecular gases by the calcium.

Gas pressures in the experiment ranged from 1000 to 2000 mm Hg, the potential difference between the electrodes could be varied from 0.1 to 7.5 kV.

In the course of each measurement the pressure was kept at a constant value, whereas the electrode potential was varied. The voltage pulses coming from the chamber were fed through a preamplifier and an amplifier to the vertical deflecting system of a synchroscope. The upper frequency limit of the amplifier chain was about 4 Mc/s, the clipping time 150 μsec. The pulses were fed from the amplifier to the synchroscope through a delay line in order to render visible the whole rising edge of the pulse, while the horizontal deflecting system was triggered by the non-delayed pulse.

The pulses were photographed as follows: the shutter of the camera was kept open until the appearance of a pulse. Since the camera was mounted on the synchroscope, the presence of the pulse was observed on the screen of a second synchroscope. A 25/10 DIN speed Agfa Rapid film and a lens with a relative opening of 1:1.5 was used.

The pulses obtained in the chamber were of various amplitudes depending on energies and directions of fission fragments. For a given pressure and field strength, however, the rise times are independent of the amplitudes.

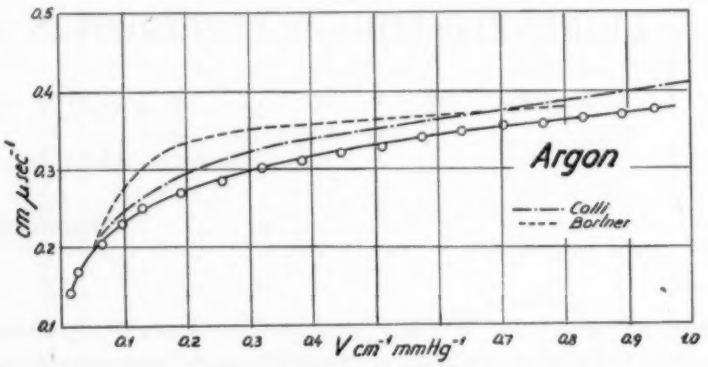

Fig. 2. Electron drift velocities in argon.

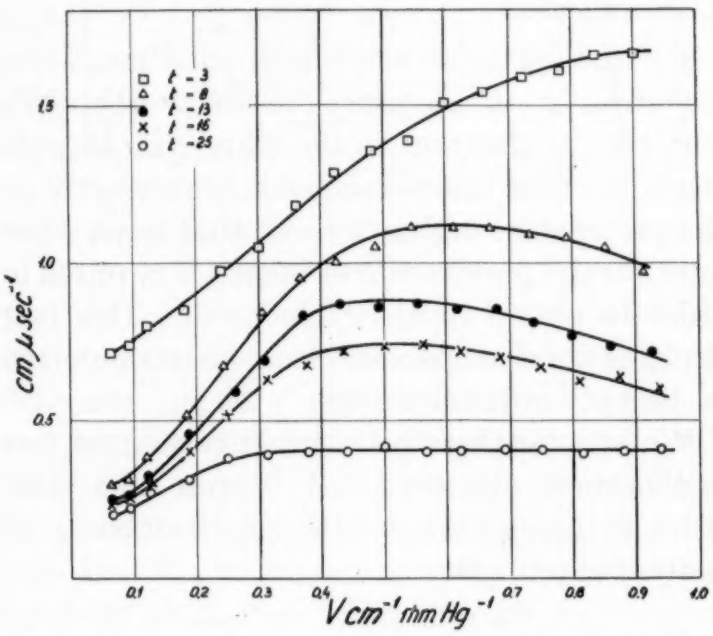

Fig. 3. Variation of electron drift velocity in argon with the time of purification if calcium was not outgassed. t denotes the purification time in hours.

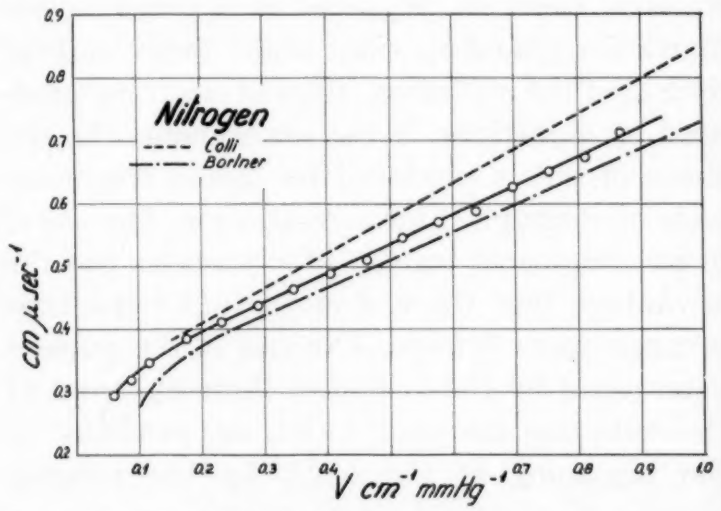

Fig. 4. Electron drift velocities in nitrogen. Our experimental points are marked by circles.

3. Results

3.1. ARGON

The results of our measurements of electron drift velocities in pure argon are shown in fig. 2, where the experimental points are marked by circles.

For comparison, the values obtained by Colli and Facchini[2]), and Bortner *et al.*[3]) were also plotted. These curves agree fairly well with our results. Nearly the same values were obtained by Nielsen[4]), Kirshner and Toffolo[5]). Several authors obtained much higher values for the drift velocity. This is probably due to the inadequate purity of the argon.

The purity of the tank argon used in our experiment was 99.7%. Using the above purifying procedure, the purification process was completed within 1–2 hours after the gas had been introduced. If the calcium was not outgassed, the purifying process was extremely retarded. For the latter case the values of the drift velocity are shown in fig. 3 with the purification time as parameter.

3.2. NITROGEN

The results obtained for nitrogen are seen in fig. 4. These data agree fairly well with those obtained by Klema and Allen[1]), Colli and Facchini[2]) and Bortner *et al.*[3]). The purity of the nitrogen used was better than 99.9% and for purification only a liquid nitrogen trap was used.

3.3. ARGON-NITROGEN GAS MIXTURES

The results are plotted in figs. 5 and 6. In the former we have shown also our curve for pure argon. It can be seen that even a small — 0.1%-nitrogen contamination considerably affects the value of the drift velocity. In both figures results of other authors are shown too.

In order to avoid overcrowding neither the curves of Colli and Facchini[2]) for 1% N_2 contamination nor those of English and

[3]) T. E. Bortner, G. S. Hurst and W. G. Stone, Rev. Sci. Instr. **28** (1957) 103.

[4]) R. A. Nielsen, Phys. Rev. **50** (1936) 950.

[5]) J. M. Kirshner and D. S. Toffolo, J. Appl. Phys. **23** (1952) 594.

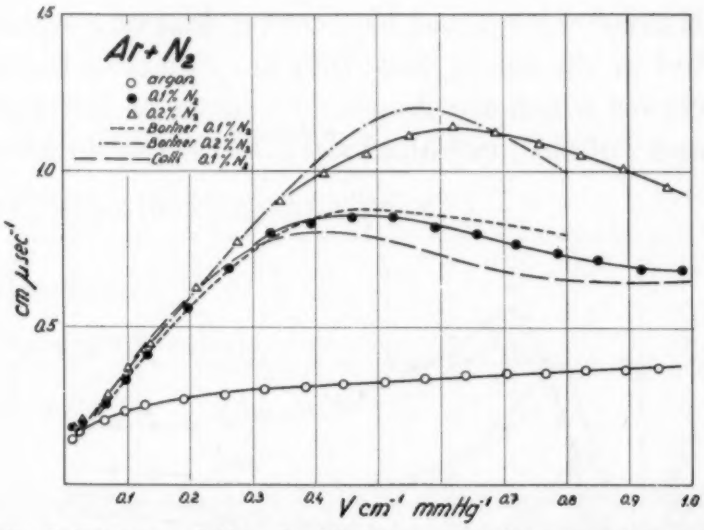

Fig. 5. Electron drift velocities in argon-nitrogen mixtures.

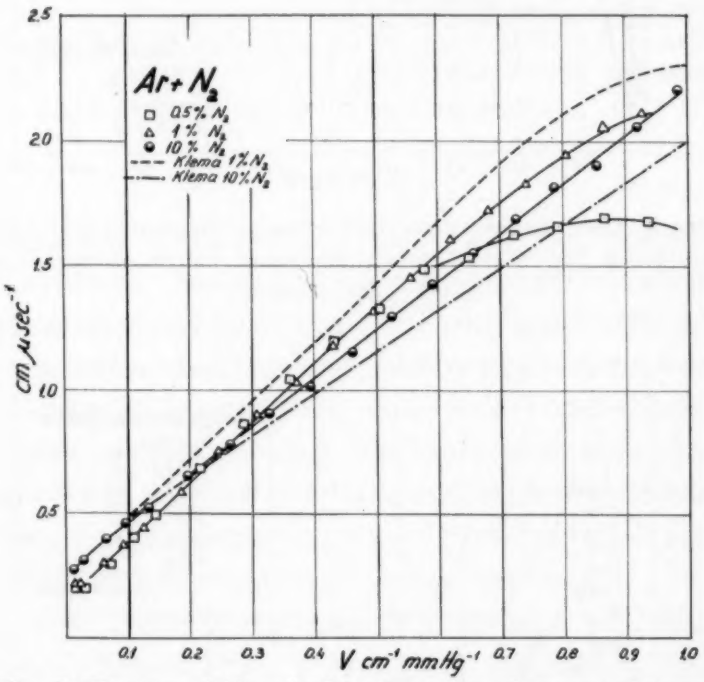

Fig. 6. Electron drift velocities in argon-nitrogen mixtures.

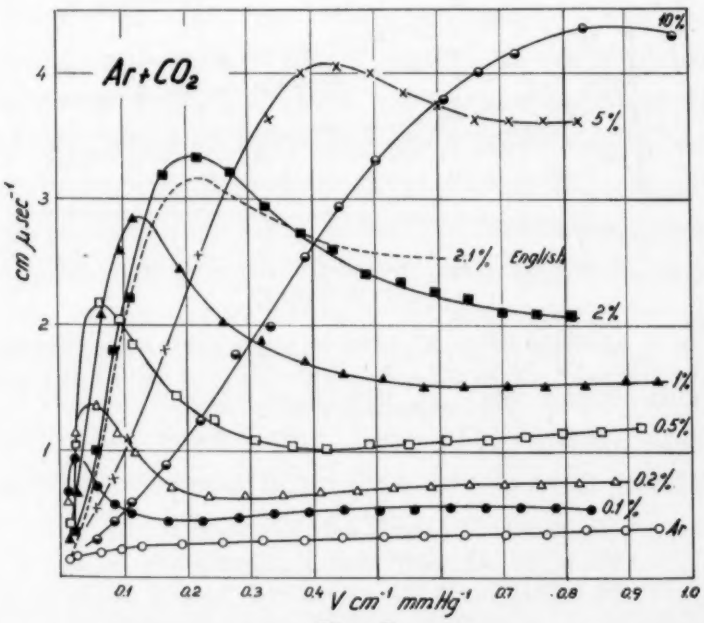

Fig. 7
Electron drift velocities in argon-carbon dioxide mixtures.

Hanna[6]) for 1% and 10% contamination are plotted in the figure, since they lie quite close to the curves which are shown. The curve of Kirshner and Toffolo[5]) obtained for 0.7% contamination which is not shown in the figure, lies much lower than our curve for 0.5% N_2, even lower than that of Bortner *et al.*[3]) for 0.2% N_2 contamination which incidentally shows a good agreement with our results.

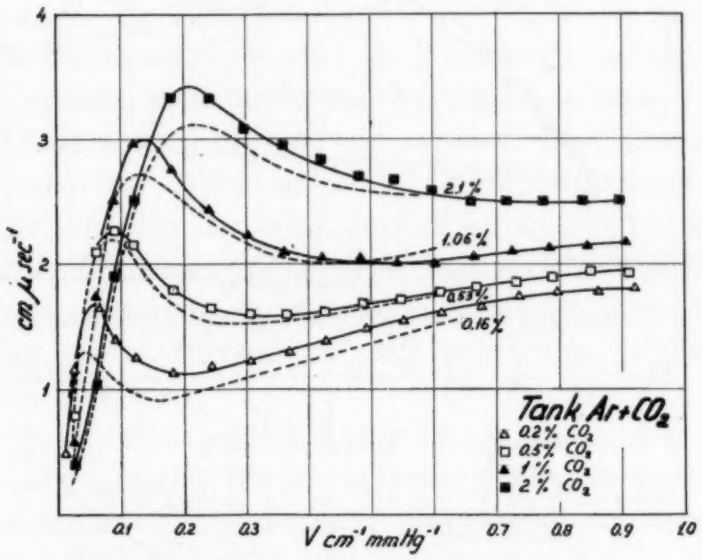

Fig. 8. Electron drift velocities in tank argon-carbon dioxide mixtures. The dashed curves represent values obtained by English and Hanna[6]).

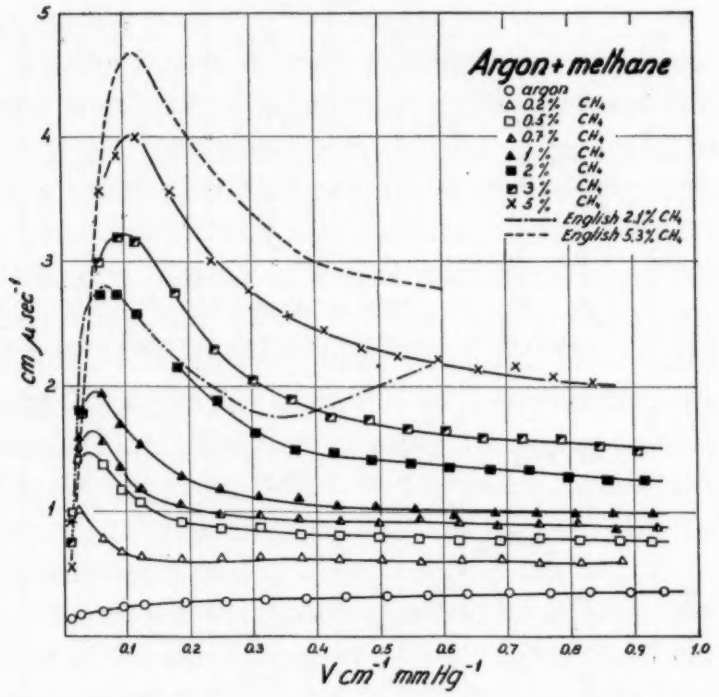

Fig. 9. Electron drift velocities in argon-methane mixtures. The asterisk* marks the coincident points of the 0.2, 0.7 and 2% contamination curves.

3.4. ARGON-CARBON DIOXIDE MIXTURES

In fig. 7 the drift velocities measured in purified argon slightly contaminated with various amounts of CO_2 are shown. For comparison, we have plotted English and Hanna's[6]) result obtained for argon with 2.1% CO_2 added. In their experiment, however, argon had not been purified and therefore, owing to the presence of some nitrogen contamination the tails of their curves show a stronger increase. The purity of argon used by the latter authors was 99.6%, thus nearly the same as that of our tank argon gas.

For comparison, measurements were carried out with a mixture of unpurified argon and carbon dioxide. The results are shown in fig. 8 and agree fairly well with those of English and Hanna[6]). From figs. 7 and 8 it is seen that the maxima of the curves obtained in both experiments lie nearly at the same abscissa value and for higher percentage contamination are shifted to the right.

The carbon dioxide was purified by repeated solidification and simultaneous desorption.

3.5. ARGON-METHANE GAS MIXTURES

Our results for pure argon to which some methane had been added are to be seen in fig. 9. For the purification of methane we used the same procedure as for carbon dioxide. For comparison, we plotted again results of English and Hanna[6]), however, as in the former case these authors here also used unpurified argon.

[6]) W. N. English and G. C. Hanna, Can. J. Phys. **31** (1953) 768.

NUCLEAR INSTRUMENTS AND METHODS **8** (1960) 331–338; NORTH-HOLLAND PUBLISHING CO.

EIN UNIVERSELLES VERFAHREN ZUR STABILISIERUNG VON SZINTILLATIONS-SPEKTROMETER-ANORDNUNGEN†

S. HAUN und D. KAMKE

Physikalisches Institut der Universität Marburg/L

Eingegangen am 22. Mai 1960

The gain of a scintillation-spectrometer can be held constant for long measuring times by including the spectrometer in a regulation circuit. All devices of this kind which have been described as yet are dependent on specific features of the spectrum and many situations arise where none of them can be used. The introduction of a pulsed source of light makes such stabilization devices universally applicable. This paper describes a light source and a suitable stabilization circuit with which a stability better than 0.5 per cent has been achieved for a 14 hour period, starting immediately after turning on the electronic circuits. The static and dynamic regulation properties are given as well as a method for evaluating all the effects due to the statistical character of the pulse height distribution produced by the light source and the photomultiplier.

1. Einleitung

Die Analyse eines elektrischen Impulshöhenspektrums, wie man es beim Szintillationsspektrometer mit Hilfe von Szintillationssubstanz und Photokathode (Photomultiplier) aus dem Energiespektrum einer Kernstrahlung herleitet, erfordert mit Amplituden-, Einkanal- oder Mehrkanaldiskriminator in vielen Fällen längere Messzeiten. Gutes energetisches Auflösungsvermögen genügt infolgedessen nicht, um mit einer bestimmten Apparatur zuverlässige Messergebnisse zu erhalten. Zusätzlich muss sichergestellt sein, dass man eine beliebige Energie innerhalb der untersuchten Kernstrahlung stets an derselben Stelle der Diskriminatorskala registriert. Dazu reichen elektronische Stabilisierung aller Versorgungsspannungen und Gegenkopplung im Impulsverstärker vielfach nicht aus.

Da die auftretenden Instabilitäten in erster Linie von Änderungen des Verstärkungsfaktors zwischen Photokathode und Verstärkerausgang herrühren, lässt sich folgendes Regelverfahren anwenden: Eine geeignete Stelle innerhalb des zu untersuchenden Impulshöhenspektrums wird ständig so kontrolliert, dass jede Verschiebung dieser Stelle gegenüber der Analysatorskala (und nur eine solche) eine entgegenwirkende Änderung der Hochspannung am Photomultiplier und damit der Gesamtverstärkung hervorruft.

Alle Stabilisierungseinrichtungen, die bisher nach diesem Prinzip praktisch ausgeführt wurden[1]), setzen eine hinreichend intensive Linie innerhalb des zu untersuchenden Energiespektrums voraus, deren Intensität oder Gestalt sich in einigen Fällen während der Messzeit nicht ändern darf. Bei vielen Messaufgaben, insbesondere bei allen Arbeiten an Beschleunigungsmaschinen, ist diese Voraussetzung nicht erfüllt. Der gelegentlich vorgeschlagene Ausweg, der zu untersuchenden Strahlungsquelle ein radioaktives Präparat hinzuzufügen, um die Stabilisierungseinrichtung an eine Linie innerhalb des Spektrums dieses Präparates anzuschliessen, kann nur selten beschritten werden,

† Eine ausführliche Beschreibung aller angestellten Untersuchungen findet man in No. 35 der "Rundberichte über unveröffentlichte Arbeiten aus dem Gebiete der Kernphysik und kosmischen Höhenstrahlung, herausgegeben im Auftrag des Fachausschusses für Kernphysik und kosmische Höhenstrahlung im Verband Deutscher Physikalischer Gesellschaften e.V. und der Kommission für Atomphysik". Sonderdrucke dieses "Rundberichtes" sind bei den Autoren der vorliegenden Arbeit verfügbar.

[1]) D. H. Wilkinson, J. Sci. Instr. **27** (1950) 36;
G. F. von Dardel, J. Sci. Instr. **32** (1955) 302;
H. de Waard, Nucleonics **13**, No. 7 (1955) 36;
U. Cappeller und R. Klingelhöfer, Z. f. Physik **150** (1958) 375.

ohne gleichzeitig das zu untersuchende Spektrum unerwünscht zu verändern.

Dagegen werden alle in der Literatur beschriebenen Stabilisierungsverfahren uneingeschränkt anwendbar, wenn man die benötigte scharfe Spektrallinie dadurch herstellt, dass man zugleich mit dem Fluoreszenzlicht der Szintillationssubstanz das Licht einer äusseren Impulslichtquelle (ILQ) auf die Photokathode nur in genau bekannter Weise verändert (besonders wertvoll bei der Untersuchung intensitätsschwacher Spektren).

Allerdings werden Schwankungen, die von Änderungen der Fluoreszenzausbeute der Szintillationssubstanz herrühren, von einer derartigen Stabilisierungseinrichtung nicht erfasst. Instabilitäten dieser Art gehen jedoch meistens mit erheblichen Änderungen der Szintillator-

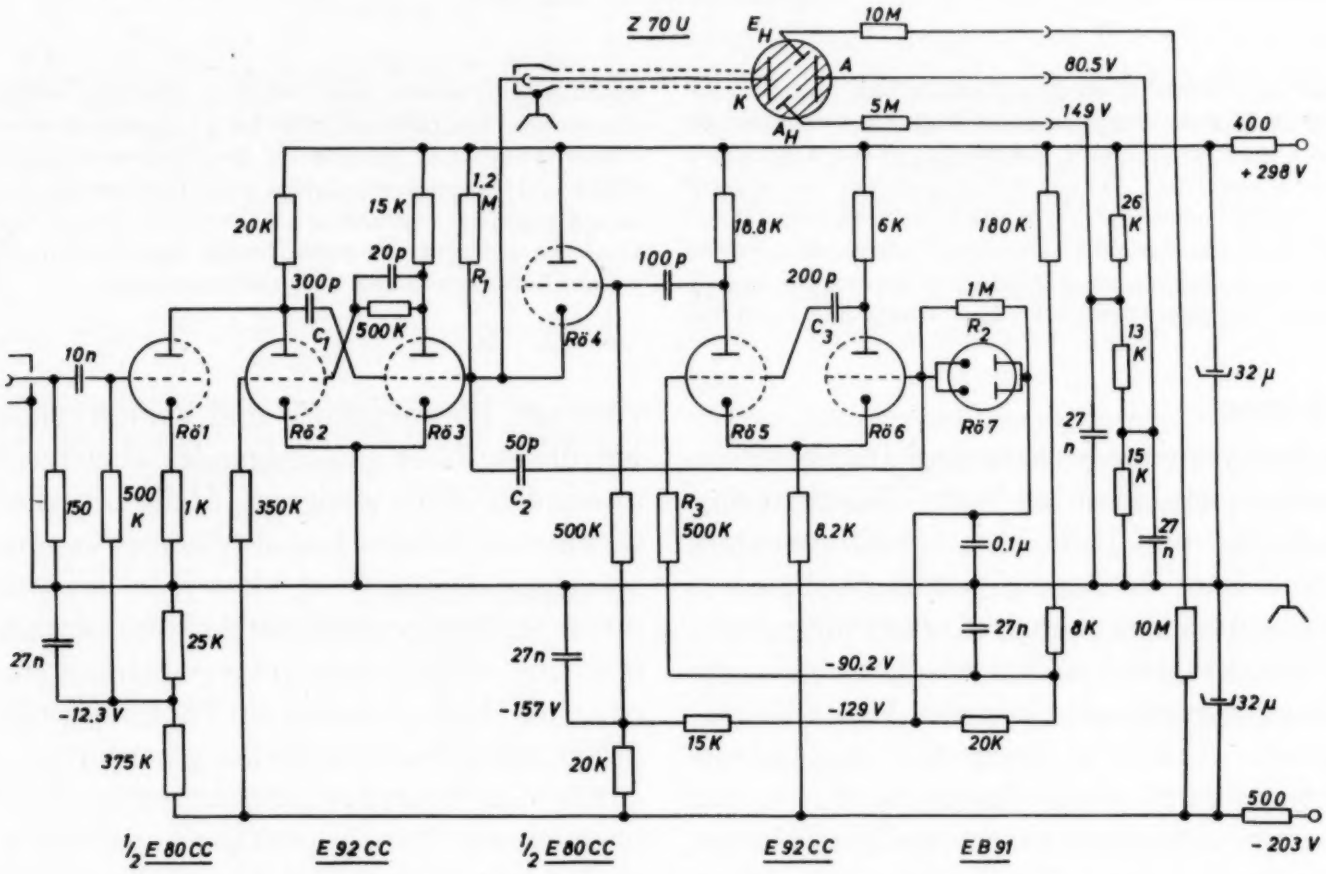

Fig. 1. Vollständiges Schaltbild der ILQ (Relaisröhre Z 70 U mit Zündgerät).

einfallen lässt. Dieses Verfahren bietet folgende Vorteile:

1. Die Lage der künstlichen Spektrallinie ("Lichtlinie") innerhalb des Spektrums (d.h. die Höhe der zugeordneten elektrischen Impulse) ist durch eine mechanische Blende vor der ILQ leicht einstellbar.

2. Eine solche Spektrallinie ist sehr scharf; daher sind Verschiebungen des Spektrums an ihr besonders deutlich wahrzunehmen.

3. Die Zahl der Lichtimpulse je Zeiteinheit ist beliebig wählbar und streut nicht statistisch. Dadurch wird das zu untersuchende Spektrum

eigenschaften einher, die ohnehin zum Abbruch der Messung zwingen.

2. Die Impulslichtquelle

Eine Impulslichtquelle (ILQ) zur Stabilisierung einer Szintillationsspektrometer-Anordnung muss folgende Eigenschaften besitzen:

1. Sie muss klein genug sein, um sich am Kopfteil eines Szintillations-Strahlungsdetektors mechanisch leicht anbringen zu lassen.

2. Sie soll Lichtimpulse liefern,

a. deren "Farbe" (Spektrum) mit der des Fluoreszenzlichtes der Szintillationssubstanz möglichst übereinstimmt;

b. deren Dauer von der Grössenordnung 1 μs ist;

c. die mit konstanter Frequenz (höchstens einige $10^2\,s^{-1}$) einander folgen;

d. deren Photonenzahl pro Impuls mit möglichst geringem mittlerem Schwankungsquadrat um einen Mittelwert streut; dieser Mittelwert muss über längere Messzeiten hinweg (10–20 Stunden) konstant bleiben.

Nach Vorversuchen mit einem Thyratron, der Gastriode EC 50[2]), wurden diese Eigenschaften schliesslich durch Verwendung der Röhre Z 70 U (Valvo), einer Relaisröhre mit kalter Kathode, erreicht. Diese Röhre bietet einige besondere Vorteile:

1. Sie ist ausserordentlich klein (10 mm ø, 25 mm Länge).

2. Ihr Entladungsleuchten ist sehr gut sichtbar.

3. Durch eine zusätzliche Hilfsentladung ist ihre Zündkennlinie von der äusseren Beleuchtung unabhängig, insbesondere arbeitet die Röhre auch in völliger Dunkelheit zuverlässig.

4. Bei der Konstruktion dieser Röhre ist besonderer Wert auf geringe Exemplarstreuung und gute Konstanz der Zündkennlinie während der – im übrigen sehr langen – Lebensdauer gelegt worden.

Figur 1 zeigt die Schaltung, mit der die Z 70 U als ILQ betrieben wird. Ihre wesentlichen Bestandteile sind zwei Univibratoren U_1 (Rö 2 und Rö 3) und U_2 (Rö 5 und Rö 6); beim Umklappen in den metastabilen Zustand bewirkt U_1 die Zündung, U_2 die Löschung der Relaisröhre. Die Schaltung hat folgende besondere Eigenschaften:

1. Die Frequenz der Lichtimpulse wird durch eine von aussen zugeführte Folge positiver Triggerimpulse bestimmt, deren Form und Höhe (etwa 6 V) nicht kritisch sind (vgl. Abschn. 5).

2. Zwischen zwei aufeinanderfolgenden Lichtimpulsen liegt an der Hauptentladungsstrecke der Z 70 U stets nur eine Spannung von rund 80 V, d.h. 33 V weniger als die minimale Brennspannung. Dadurch werden unbeabsichtigte Zündungen der Röhre sicher verhütet.

[2]) S. Haun und D. Kamke, Physikal. Verhandlgn. **9**, No. 2 (1958) 21.

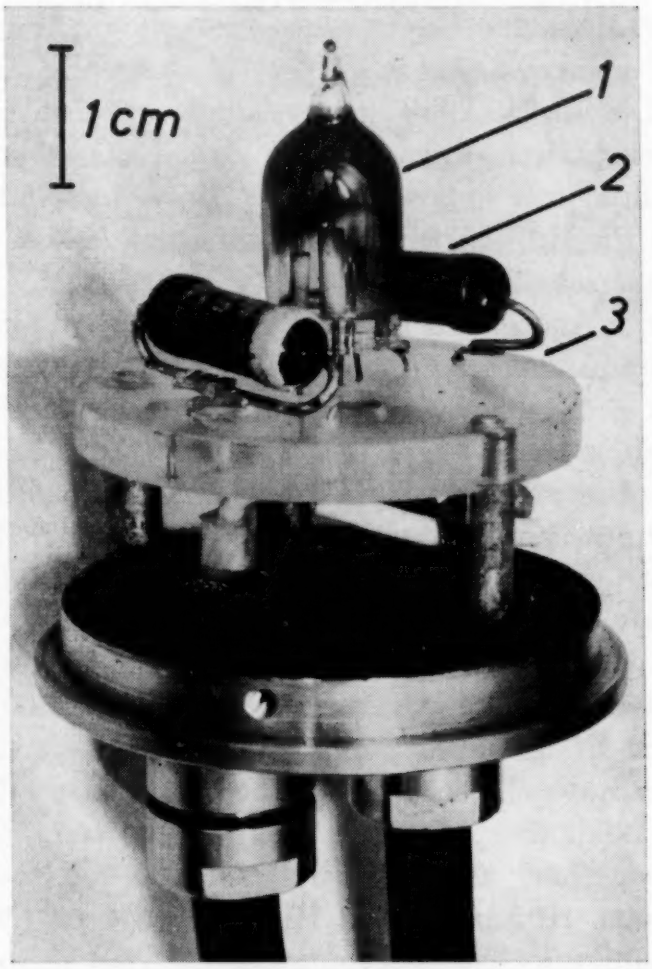

Fig. 2. Halterung der Relaisröhre im Innern des ILQ-Gehäuses.

3. Der Löschvorgang setzt erst ein, wenn Strom durch die Entladungsröhre fliesst. Dadurch wird ein Ausbleiben einzelner Zündungen trotz möglicher Zündverzögerung unmöglich gemacht.

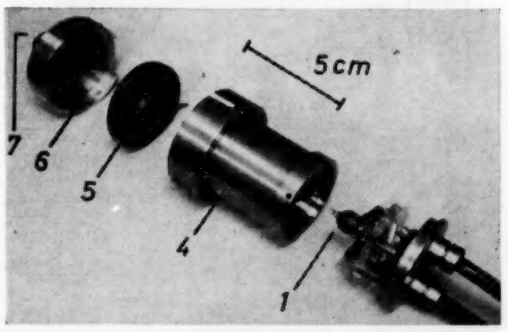

Fig. 3. ILQ, in ihre Einzelteile zerlegt.

4. Die je Lichtimpuls durch die Röhre fliessende Ladung, die die emittierte Lichtmenge bestimmt, hängt nur von wenigen Schaltelementen ab, nämlich im wesentlichen von Kondensator C_1 und der Differenz der Gitterpotentiale von Rö 5 und Rö 6.

Den mechanischen Aufbau dieser ILQ zeigen die Figuren 2 und 3.

Die Relaisröhre (1) besitzt anstelle von Sockelstiften etwa 32 mm lange Anschlussdrähte, mit denen sie neben Vorwiderständen (2) für Hilfselektrode und Hilfsanode auf einer Isolierscheibe (3) aus Plexiglas befestigt ist. Die ganze Anordnung befindet sich im Innern eines zylindrischen, lichtdichten Gehäuses (4), welches vor der Spitze der Entladungsröhre durch eine Irisblende (5) abgeschlossen wird. Die Fassung (6) dieser Blende läuft in einen Schraubansatz (7) aus, mit dem das ganze Gehäuse von der Seite in die Eisenabschirmung des Photomultipliers eingeschraubt wird, und zwar dort, wo ein Plexiglas-Lichtleiter den optischen Kontakt zwischen der Photokathode und dem Szintillator herstellt. Mit ihrem Zündgerät ist die Relaisröhre durch zwei 30 cm lange Kabel verbunden: Ein Koaxialkabel stellt die Verbindung zur Kathode her, ein dreiadriges Kabel versorgt Anode, Hilfsanode und Hilfselektrode mit den benötigten Gleichspannungen.

Die Figur 4 zeigt die bei den hier zu beschreibenden Untersuchungen ausschliesslich benutzte

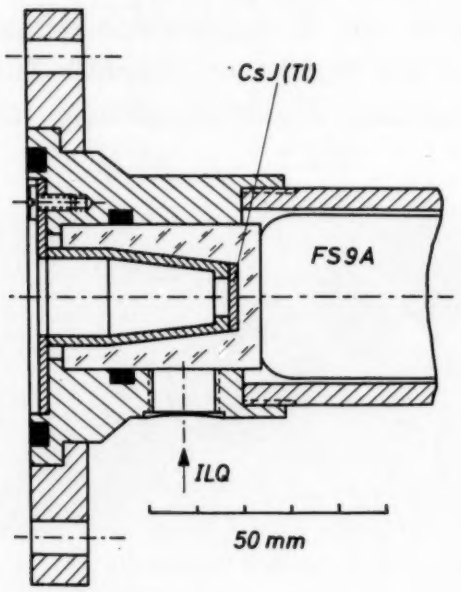

Fig. 4. Kopfstück des Strahlungsdetektors mit Gewindebohrung für die ILQ.

Anordnung im Kopfstück des Strahlungsdetektors: CsJ (Tl) als Szintillationssubstanz vor einem FS9A-Multiplier; der Lichtleiter (Plexiglas) führt das Licht der von unten einzuschraubenden ILQ der Photokathode zu und dient zugleich als Vakuum-Abschluss.

3. Der Regelkreis

Die *Regelstrecke* besteht aus Photomultiplier und Impulsverstärker des normalen Szintillationsspektrometers. Der Mittelwert V des für jeden Impuls anzugebenden Verhältnisses

$$\frac{\text{Höhe des elektrischen Ausgangsimpulses}}{\text{auf die Photokathode eingefallene Photonenzahl}}$$

stellt die Regelgrösse dar.

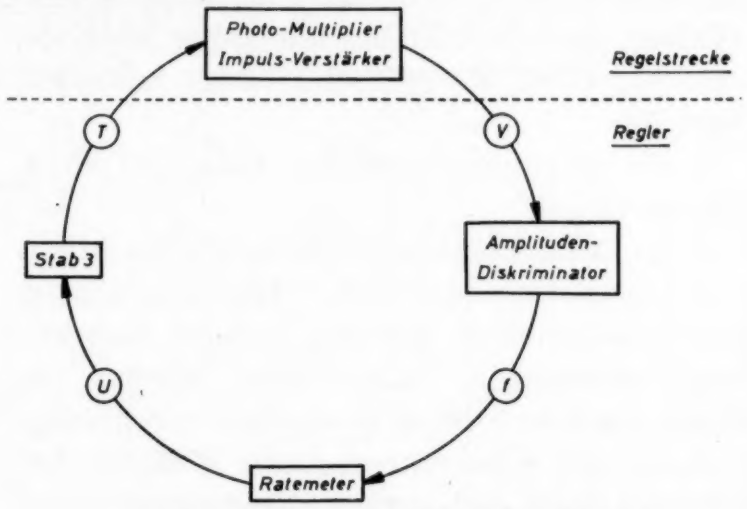

Fig. 5. Blockschaltbild des Regelkreises.

Der *Regler* setzt sich folgendermassen zusammen: An den Verstärker ist ein Amplitudendiskriminator (Schmitt-Trigger) angeschlossen. Ist die Irisblende vor der ILQ so eingestellt, dass die Lichtimpulse am Verstärkerausgang nur zu höheren Spannungsimpulsen führen als die Szintillationen des durch eine Kernstrahlung angeregten Szintillationskristalles, so ist bei passender Schwelleneinstellung des Diskriminators dessen Ausgangszählrate f eindeutig der Regelgrösse V zugeordnet (solange der Mittelwert der je Lichtimpuls auf die Photokathode einfallenden Photonenzahl sowie die Höhe der Diskriminatorschwelle unverändert bleiben). f wird daher als Mass für die Regelgrösse einem Ratemeter zugeführt, dessen Ausgangsspannung U die Multiplier-Hochspannung T und damit die Regelgrösse V beeinflusst.

Als Ratemeter dient eine gebräuchliche Zusammenstellung von Impulsformerstufe, *RC*-Integrierglied und Röhrenvoltmeter; zur Regulierung der Hochspannung wird "Stab 3" des

"Marburger Geräteprogrammes" verwendet, ein Hochspannungs-Stabilisierungsgerät (Differenzverstärker mit Querregelröhre), welches gestattet, die vorstabilisierte Hochspannung T mit Hilfe der Gleichspannung U kontinuierlich zu verändern.

Das statische Regelverhalten dieses Kreises ist durch den *Regelfaktor* zu beschreiben: Eine bestimmte Störung möge die Regelgrösse bei geöffnetem, also unwirksamem, Regelkreis um S, bei geschlossenem Regelkreis dagegen um q verändern. Dann wird das Verhältnis

$$\frac{S}{q} = \eta \qquad (1)$$

als Regelfaktor bezeichnet.

Um die Beiträge der einzelnen Kreisglieder zum Regelfaktor zu erkennen, ist für jedes Glied die Beziehung zwischen Änderungen von Eingangs- und Ausgangsgrösse aufzustellen. Solange diese Änderungen klein bleiben, sind sie bei jedem Glied einander proportional; dann ist der Regelfaktor im wesentlichen das Produkt aller Proportionalitätskonstanten. Insbesondere ist er der Intensität der "Lichtlinie" (Zahl der Lichtimpulse je Zeiteinheit) direkt und ihrer relativen Halbwertsbreite indirekt proportional.

Eine direkte Messung des Regelfaktors wurde folgendermassen ausgeführt: Durch Änderung der Verstärkungseinstellung am Impulsverstärker wurde eine bekannte Störung S innerhalb der Regelstrecke verursacht und die resultierende Änderung q der Regelgrösse bestimmt, indem ein einfaches Szintillationsspektrum mit einem zweiten Amplitudendiskriminator (parallel zum Diskriminator des Regelkreises angeschlossen) verfolgt wurde (Beschreibung der Apparatur siehe Abschnitt 5). Die Frequenz der Lichtimpulse betrug dabei $100\ s^{-1}$, die relative Halbwertsbreite der "Lichtlinie" 3%.

Aus der erhaltenen Kurve (Figur 6) ist der Regelfaktor als Koordinatenverhältnis jedes Kurvenpunktes zu entnehmen. Man liest für kleine Störungen $\eta = 35$ ab, ferner eine rasche Abnahme des Regelfaktors für Störungen $|S| > 5.5$ db.

Um das Verhalten des Regelkreises gegenüber zeitabhängigen Störungen zu untersuchen, wurden die Übergangsfunktionen aller Kreisglieder

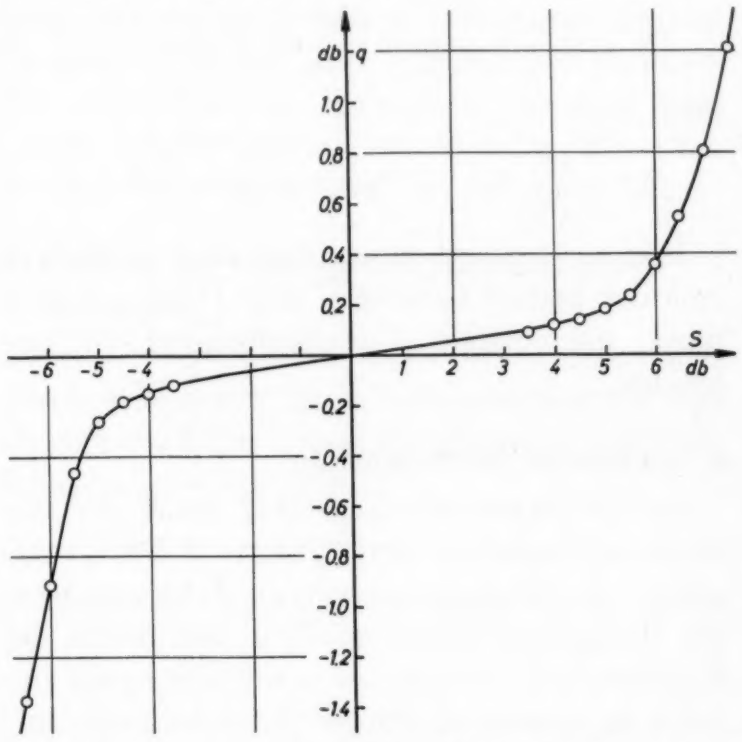

Fig. 6. Messung des Regelfaktors und des Regelbereiches.

ermittelt. Während bei Regelstrecke und Diskriminator die jeweilige Ausgangsgrösse einer Änderung der Eingangsgrösse spontan folgt, verlaufen die Ausgangsgrössen von Ratemeter und Stab 3 nach sprunghafter Änderung der Eingangsgrösse um K_f bzw. K_U nach Exponentialfunktionen. Diese Funktionen wurden oszillographisch aufgezeichnet und photographiert. Sie werden beschrieben durch die Ausdrücke

$$\Delta U(t) = -a\left(1 - \exp\left(-\frac{t}{D}\right)\right) K_f\,, \qquad (2)$$

$$\frac{\Delta T(t)}{T_0} = b\left(1 - \exp\left(-\frac{t}{d}\right)\right) K_U \qquad (3)$$

für $t \geq 0$ mit

$D = 17.6\ s\,, \qquad d = 2.15\ s\,, \qquad a > 0\,, \qquad b > 0\,.$

(T_0 ist der zu $U = 0$ gehörige Wert von T.)

Daraus kann die Übergangsfunktion des geschlossenen Regelkreises nach bekannten Regeln ausgerechnet werden. Man findet, dass sich die Regelgrösse nach einer sprunghaft eingetretenen Störung K_V, die innerhalb des linearen Teils der Kurve von Figur 6 bleibt, gemäss einer gedämpften Sinusschwingung auf den neuen Regelzustand einstellt:

$$\Delta V(t) = \frac{K_V}{\eta}$$

$$\left[1 + (\eta - 1)\left(\cos \omega t + \frac{\delta}{\omega} \sin \omega t\right) \exp(-\delta t)\right] \quad (4)$$

mit

$$\delta = \frac{1}{2}\left(\frac{1}{d} + \frac{1}{D}\right), \qquad \omega = \sqrt{\frac{1}{dD}\eta - \delta^2}\,.$$

Hieran ist zu erkennen, dass man wenigstens eine der beiden Grössen d und D klein halten muss, um längere Einschwingdauer zu vermeiden.

4. Statistische Betrachtungen

Bei geschlossenem Regelkreis führt der statistische Charakter der Zählrate f (Ausgangsgrösse des Diskriminators) zu Schwankungen der Multiplier-Hochspannung T und damit der Regelgrösse V, so dass das zu untersuchende Impulshöhenspektrum auf der Skala des Analysiergerätes (Amplituden- oder Kanaldiskriminator) ständig um eine mittlere Lage hin und her wandert. Der Einfluss dieser Erscheinung auf die Genauigkeit, mit der das Spektrum einer Kernstrahlung ausgemessen werden kann, ist zu untersuchen.

Man denke sich bei fester Einstellung des Analysiergerätes dessen Ausgangsimpulse wiederholt eine bestimmte Zeit τ lang ausgezählt. Sind die Verschiebungen des Impulshöhenspektrums so klein, dass die Krümmung seiner Integral- bzw. Differentialkurve (je nachdem, ob ein Amplituden- oder Kanaldiskriminator als Analysiergerät dient) nicht spürbar ist, so streuen die Zählergebnisse ξ_i der einzelnen Zählperioden um denselben Mittelwert $\bar{\xi}_i$, wie es der Fall wäre, wenn das Spektrum seine mittlere Lage ständig beibehielte; jedoch ist das mittlere Schwankungsquadrat $\overline{(\xi_i - \bar{\xi}_i)^2}$ geändert. Man findet für diese Grösse †:

$$\overline{(\xi_i - \bar{\xi}_i)^2} = \bar{\xi}_i + \overline{\left(\frac{\mathrm{d}n}{\mathrm{d}T}\int_0^\tau \delta T(t)\,\mathrm{d}t\right)^2} \quad (5)$$

oder umgeformt:

$$\overline{(\xi_i - \bar{\xi}_i)^2} = \bar{\xi}_i + 2\left(\frac{\mathrm{d}n}{\mathrm{d}T}\right)^2 \int_0^\tau \mathrm{d}t \int_t^\tau \overline{\delta T(t)\cdot\delta T(t')}\,\mathrm{d}t' \,. \quad (6)$$

† Einzelheiten siehe "Rundbericht No. 35".

Hierin drückt $\mathrm{d}n/\mathrm{d}T$ die Abhängigkeit der Ausgangszählrate n von der Mulitplier-Hochspannung T aus; diese Grösse hängt vom verwendeten Multiplier, von der gewählten Beobachtungsstelle innerhalb des Spektrums und vom Analysiergerät ab. Mit $\delta T(t)$ ist die Abweichung der Hochspannung von ihrem Mittelwert $\overline{T}$ zum Zeitpunkt t bezeichnet gemäss der Beziehung

$$T(t) = \overline{T} + \delta T(t) \quad \text{mit} \quad \overline{\delta T(t)} = 0\,. \quad (7)$$

Der Querstrich schliesslich deutet Mittelbildung über viele Zählperioden von gleicher Länge τ an.

Treten dagegen grössere Verschiebungen des Impulshöhenspektrums auf, so streuen die Zählergebnisse ξ_i um einen anderen Mittelwert, als es bei konstanter Hochspannung $T(t) = \overline{T}$ der Fall wäre: Jede Spektrallinie wird verbreitert, das energetische Auflösungsvermögen der Spektrometer-Anordnung herabgesetzt. Für eine Spektrallinie, die bei konstanter Hochspannung $\overline{T}$ die relative Halbwertsbreite B hat, findet man, wenn die Hochspannung mit dem mittleren relativen Schwankungsquadrat $\overline{(\delta T/\overline{T})^2}$ um $\overline{T}$ als Mittelwert schwankt, die relative Halbwertsbreite B':

$$B'^2 = B^2 + c^2\overline{\left(\frac{\delta T}{\overline{T}}\right)^2}\, 8 \ln 2\,. \; [3] \quad (8)$$

Darin ist c die den Multiplier kennzeichnende Proportionalitätskonstante zwischen relativen Änderungen von Hochspannung und Verstärkungsfaktor. Es bleiben also das mittlere relative Schwankungsquadrat einer einzelnen Hochspannungsablesung, sowie die Korrelation zweier um eine bestimmte Zeitspanne getrennter Ablesungen bei geschlossenem Regelkreis zu bestimmen. Dazu geht man folgendermassen vor:

Zunächst wird aus den Übergangsfunktionen von Ratemeter und Stab 3 berechnet, welche Veränderung der Hochspannung T ein einzelner Impuls hervorruft, der zum Zeitpunkt t_i in das Ratemeter des Regelkreises einläuft. Man findet für Zeiten $t \geq t_i$:

[3]) E. Breitenberger, Progress in Nucl. Phys., Vol. **4**, (Pergamon Press, 1955) 56.

$$\Delta T(t) = A\left(\exp\left(-\frac{t-t_i}{d}\right) - \exp\left(-\frac{t-t_i}{D}\right)\right) \quad (9)$$

oder abgekürzt:

$$\Delta T(t) = A \cdot W(t-t_i)\,. \quad (10)$$

Hiermit lässt sich die Grösse $\delta T(t)$ als Summe der Wirkungen von Impulsen angeben, die vor dem Zeitpunkt t in das Ratemeter eingelaufen sind. Da am geschlossenen Regelkreis die Zahl der während eines kurzen Zeitintervalles Δt aus dem Amplitudendiskriminator in das Ratemeter einlaufenden Impulse um einen Mittelwert streut:

$$Z_i = \bar{f}\cdot\Delta t_i + \nu_i\,, \qquad \bar{\nu}_i = 0\,, \quad (11)$$

führt man $\delta T(t)$ auf frühere Zahlen ν_i zurück:

$$\delta T(t) = A \sum_{t_i<t} \nu_i W(t-t_i)\,. \quad (12)$$

Durch Quadratur und Mittelbildung ist hieraus die gesuchte Grösse $\overline{(\delta T)^2}$ zu finden. Diese Berechnung wird allerdings erschwert durch die den geschlossenen Regelkreis kennzeichnende Rückwirkung der in das Ratemeter einlaufenden Impulsfolge auf sich selbst. Diese Rückwirkung äussert sich in einer statistischen Abhängigkeit der Zahlen ν_i voneinander: Jede der Zahlen ν_i wird sowohl von statistischen Prozessen bei der Impulsbildung in ILQ und Photomultiplier als auch von der gerade herrschenden Hochspannung bestimmt, welche ihrerseits von früheren Zahlen ν_i abhängt. Für die Berechnung der Grösse $\overline{\nu_i^2}$, die bei der Quadratur des Summenausdruckes für $\delta T(t)$ auftritt, ist ausserdem zu beachten, dass die ILQ im Gegensatz zu jedem radioaktiven Strahler eine regelmässige Impulsfolge liefert. Es gelingt, alle diese Einflüsse exakt zu berücksichtigen, die auftretenden Integralgleichungen durch einfache Exponentialansätze zu lösen und schliesslich $\overline{(\delta T)^2}$ auszurechnen†. Die Grösse $\overline{\delta T(t)\cdot\delta T(t')}$ ergibt sich im Verlaufe dieser Rechnung. Das numerische Endergebnis steht in bester Übereinstimmung mit der direkten Beobachtung; man findet

$$\sqrt{\overline{\left(\frac{\delta T}{\bar{T}}\right)^2}} = 0.25 \times 10^{-3}\,.$$

† Vgl.: Rundbericht No. 35.

Das bedeutet, dass die beschriebene Stabilisierungseinrichtung keine merkliche Verringerung des energetischen Auflösungsvermögens verursacht, jedoch unter ungünstigen Umständen die statistische Genauigkeit einzelner Messungen spürbar vermindern kann, so dass man die Messzeit entsprechend zu verlängern hat.

5. Prüfung der stabilisierten Spektrometer-Anordnung

Die stabilisierte Spektrometer-Anordnung wurde durch Messungen des α-Teilchenspektrums von Po geprüft. Figur 7 zeigt das Blockschaltbild der vollständigen Apparatur.

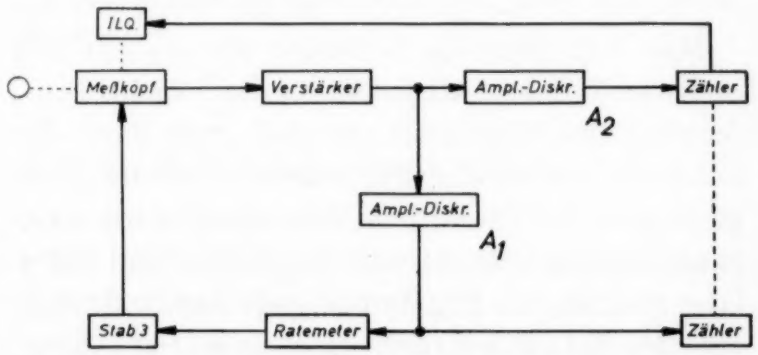

Fig. 7. Blockschaltbild der stabilisierten Spektrometer-Anordnung. Die gestrichelt gezeichnete Verbindung der beiden Zähler deutet synchrone Steuerung der Zählperioden an.

Der Aufbau des Messkopfes ist aus Figur 4 zu ersehen. An den Impulsverstärker (zweistufiger gegengekoppelter Pentodenverstärker mit zwei gleichen, parallel geschalteten Ausgangsstufen) sind die Regelkreisglieder und ein Amplitudendiskriminator A_2 als Messanalysator angeschlossen. Die Ausgangsimpulse der beiden Diskriminatoren A_1 und A_2 werden von zwei gleichen Berkeley "Eput and Timer"-Geräten gezählt. Eines dieser Geräte liefert unabhängig von seiner Funktion als Zähler an einem besonderen Ausgang eine quarzgesteuerte Impulsfolge, die gleichzeitig zur Zündung der ILQ und zur synchronen Festlegung der Zählperioden an beiden Zählern dient.

Die Messungen selbst wurden folgendermassen ausgeführt: Man wählt zunächst an der Irisblende der ILQ die je Lichtimpuls auf die Photokathode einfallende Lichtmenge so, dass im elektrischen Impulshöhenspektrum die "Lichtlinie" etwas höher liegt (dem Absolutbetrag der

Impulshöhe nach) als die 5.3 MeV-Linie des Po-α-Teilchenspektrums. Figur 8 zeigt die Photographie des Oszillographenschirmbildes dieses Impulshöhenspektrums; seine Analyse mit einem Amplitudendiskriminator liefert die entsprechende Integralkurve.

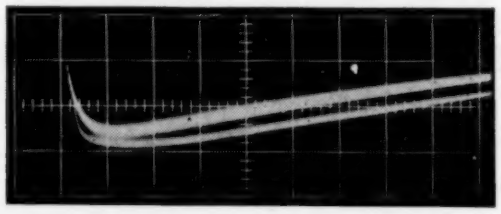

Fig. 8. Po-α–Spektrum mit "Lichtlinie" am Ausgang des Messkopfes; Massstab vertikal 0.5 V/Einheit, horizontal 2 μs/Einheit.

Man legt jetzt die Schwelle von A_1 auf den steilsten Teil der Integralkurve der "Lichtlinie", schaltet den Regelkreis ein und stellt dann die Schwelle von A_2 auf den steilsten Teil der Integralkurve der Po-α-Linie. Nun werden die Ausgangsimpulse von A_1 und A_2 fortlaufend 100 s lang gezählt, die Ergebnisse gedruckt und nach 10 s Pause automatisch eine neue 100 s-Zählperiode begonnen. Aus den Mittelwerten der beiden Zahlenfolgen, die man auf diese Weise erhält, lassen sich Änderungen des Verstärkungsfaktors von Multiplier und Impulsverstärker um 0.1% sicher erkennen. Gegensinnige oder verschieden starke Änderungen beider Mittelwerte deuten auf Einflüsse hin, denen Po-α- und "Lichtlinie" nicht in gleicher Weise unterliegen, denen die Regelung daher nicht entgegenwirken kann.

Zunächst wurde das Verhalten einzelner Teile der Apparatur gegenüber Änderungen der Umgebungstemperatur untersucht. Es zeigte sich, dass Änderungen von 5°–10° C nur dann die Po-α-Linie um mehr als 0.5% ihrer mittleren Impulshöhe verschieben, wenn sie die Photokathode treffen. Diese Erscheinung ist durch die Temperaturabhängigkeit der spektralen Empfindlichkeit der Photokathode zu erklären[4]), die sich deshalb in dieser Weise bemerkbar macht, weil die spektrale Zusammensetzung des Lichtes der ILQ (die Z 70 U ist mit reinem Neon gefüllt) wesentlich von der des Fluoreszenzleuchtens von CsJ[5]) abweicht. Daher wurden zusätzliche Vorkehrungen getroffen, um Temperaturänderungen von der Photokathode fernzuhalten: Durch eine Rohrschlange um den Abschirmzylinder des Multipliers strömt ständig die Badflüssigkeit eines Thermostaten. Mit dieser Anordnung wurde schliesslich erreicht, dass sich der Verstärkungsfaktor während 14 Stunden um weniger als 0.5% änderte, und zwar *vom Zeitpunkt des Einschaltens an* (d.h. ohne ein Anwärmen der Apparatur abzuwarten) und trotz Anstiegs der Raumtemperatur um 4° C.

Mit diesem Ergebnis ist die prinzipielle Grenze der Wirksamkeit einer solchen Stabilisierungseinrichtung erreicht. Entsprechende Versuche zeigten nämlich, dass langsame Schwellenverschiebungen an Amplitudendiskriminatoren und Instabilitäten, die nicht durch Veränderung des Verstärkungsfaktors auszugleichen sind, in derselben Grössenordnung liegen.

Wir danken Herrn Professor Walcher für das dieser Arbeit entgegengebrachte Interesse sowie für die Bereitstellung von Messgeräten der Deutschen Forschungsgemeinschaft und des Bundesministeriums für Atomkernenergie und Wasserwirtschaft.

[4]) N. Schaetti, W. Baumgartner, Helv. Phys. Acta **24** (1951) 614.

[5]) H. Knoepfel, E. Loepfe und P. Stoll, Helv. Phys. Acta **30** (1957) 521.

NUCLEAR INSTRUMENTS AND METHODS **8** (1960) 339–343; NORTH-HOLLAND PUBLISHING CO.

AN IMPROVED ANTI-COINCIDENCE SHIELD FOR USE IN LOW BACKGROUND COUNTING

R. P. PARKER

Physics Department, Institute of Cancer Research, Royal Cancer Hospital, London

Received 12 May 1960

A liquid scintillator is used as an anticoincidence shield for eliminating the cosmic ray component of the background of a Geiger-Müller (G.E.C. Type GM 4 LB) counter. The apparatus is described and its performance compared with that of a shield of Geiger counters. A reduction in background from approximately 0.8 cpm (as measured with the Geiger shield) to approximately 0.45 cpm, as measured with the scintillator shield, was obtained. Evidence is presented which suggests that the reduction is due to the detection of cosmic ray induced reactions in the material surrounding the counter.

1. Introduction

There are four main causes of the background counting-rate of a Geiger counter, namely external radiation from the environment, radiation from the counter itself, spurious counts and the contribution from cosmic rays. The first two effects may be reduced by careful choice of shielding and constructional materials (see, for example, Grummitt[1]). Good design of the counter and its associated electronic apparatus, with especial regard to avoiding pick-up of external electrical interference, should eliminate spurious counts. Whilst the primary soft cosmic ray component may be absorbed by approximately 15 cm lead or its equivalent[2]) it is not economically possible to shield against the hard component, which largely consists of the very penetrating μ-mesons. It is therefore normal to use a shield of cosmic ray counters in anticoincidence with the sample counter. An alternative method is to use a scintillation counter, as described below.

The properties required of an anticoincidence shield are

a. 100% efficiency to cosmic ray particles.
b. Complete screening of the sample counter.
c. Long life.
d. Reliability and robustness.
e. High efficiency to γ-radiation.

2. Types of Anti-Coincidence Shields

Cosmic-ray shields are normally made up from a number of Geiger counters, but proportional counters have also been used[3]).

In the Geiger counter shield the sample counter is surrounded by about twenty tubular cosmic ray counters arranged in such a manner that there is no gap between their active volumes. Such counters are very efficient detectors of the μ-meson component of cosmic rays[4]) but have a very low γ-efficiency. This system has the advantage that a number of different sample counters may be accommodated under one shield, but Geiger counters have a restricted life (approximately 10^8 counts) and need repeatedly checking to see that all the counters are operating on their respective plateaux. Thus the maintenance cost is quite high.

The use of scintillation counters both as cosmic-ray detectors[5,6]) and as anti-Compton shields suggested that they might form the basis

[1]) H. W. E. Grummitt, R. M. Brown, A. J. Cruikshank and I. L. Fowler, Canad. J. Chem. **34** (1956) 206.
[2]) B. Rossi, Rev. Mod. Phys. **20** (1948) 537.
[3]) A. Moljk, R. W. P. Drever and S. C. Curran, Proc. Roy. Soc. A **239** (1957) 433.
[4]) K. Greisen and N. Nereson, Phys. Rev. **62** (1942) 316.
[5]) M. M. Brennan, Nuovo Cimento **6** (1957) 216.
[6]) C. H. Millar, E. P. Hincks and G. O. Hanna, Canad. J. Phys. **36** (1958) 54.
[7]) C. C. Trail and Sol. Taboy, Rev. Sci. Instr. **30** (1959) 425.

of an anti-coincidence shield for a Geiger counter. It was decided to use a liquid luminophor since this has the advantage of being readily adaptable to any required shape. Such a technique also has the advantages of simplicity, reliability and robustness. The apparatus may be readily adapted to portable apparatus or to use as an anti-Compton screen in γ-spectrometry.

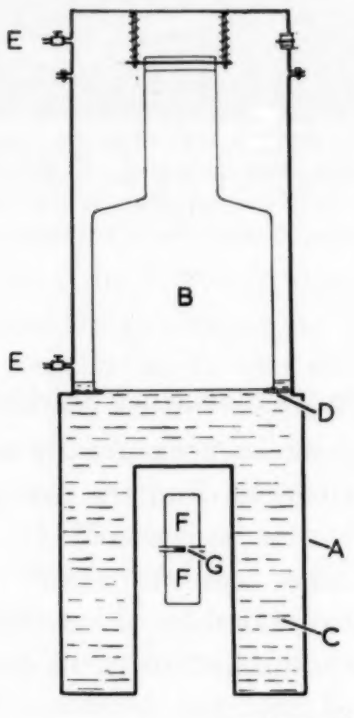

Fig. 1

Furthermore, any failure or change in efficiency of the system is immediately made apparent by monitoring the scintillator counting rate, whereas failure of one counter from a ring of twenty separate counters connected together could go unnoticed for some time.

The apparatus is shown in fig. 1 and consists of a vessel (A) made of commercial copper in the form of an inverted well, coated with "Group 37 enamel" pigmented with rutile titanium dioxide (by Courtesy of International Paints Ltd) to improve the reflectance of the wall surface. The photomultiplier (B) (EMI type 6099 B) dips into the luminophor (C) in order to obtain good optical contact, and is supported by polythene rods (D). This configuration does not give equal response for radiation incident from different directions, but has the advantage of greater detection efficiency in the vertical direction. In order to preserve the properties of the scintillator for long periods the space above it was filled with nitrogen by means of the gas taps (E). Sample counters (F), together with the sample (G), are contained in a perspex holder which can be inserted from below without disturbing the scintillator tank.

The liquid scintillator used was a solution of 3 g 2, 5-diphenyloxazole per litre of "Analar" toluene. The sample counter was surrounded by at least 5 cm of luminophor in order to provide a reasonable γ-efficiency. Since μ-mesons suffer an energy loss of 2.0 MeV cm^{-1} during passage through toluene they can be detected with 100% efficiency.

The whole assembly was surrounded by 5 cm of aged lead and placed on the floor of a pit excavated 2 metres deep into chalk, which has a low natural radioactive content and therefore serves as a good shielding material[8,9]). In later experiments the counters had the additional shielding of one metre of chalk directly above.

The photomultiplier was connected via a cathode follower to an amplifier and discriminator (Isotope Developments Ltd. Type 652). An EHT of 1700 V was used, with the discriminator set to approximately 100 keV. For a routine apparatus it is not necessary for the amplifier to be linear, and with a 13-stage photomultiplier any amplifier with a gain of approximately 30 db. would be suitable. The discriminator bias level need not be very stable, enabling a very simple circuit to be used.

The output pulse was lengthened to 200 μsec. and used as the blanking-off pulse in the anti-coincidence circuit. The sample pulse was delayed by 100 μsec, enabling the anti-coincidence circuit to be made simple and stable, with a coincidence resolving time of 200 μsec.

The total background counting rate of the sample counter (G.E.C. type GM4 LB) before

[8]) J. Vennart, Brit. J. Rad. **30** (1957) 55.

[9]) W. V. Mayneord, W. Anderson, R. E. Bentley, L. K. Burton, J. O. Crookall and N. G. Trott, Nature **182** (1959) 1473.

anti-coincidence cancellation was approximately 5 cpm, of which approximately 4.5 cpm are due to μ-mesons, and thus represent true coincidences. Only 0.5 cpm can cause random coincidences, and with a typical scintillator counting rate of 1000 cpm it follows that the random coincidence rate is only 0.002 cpm, which is negligible.

The long resolving time also avoids the necessity of an amplifier with good overload characteristics. Although a wide range of pulse heights has to be handled the amplifier is unlikely to be paralysed for more than 200 μsec following overload.

3. Results

The stability of the apparatus was checked by a series of 43 consecutive background readings of a GM 4 LB counter, carried out over a period of one month. Only one reading deviated from the mean value by more than two standard deviations. In two cases the interval distribution of the pulses was recorded and on analysis found to be exponential, indicating very few spurious pulses.

Owing to its height it has only recently become possible to place the apparatus under the chalk and not merely on the pit floor. A comparison with an orthodox Geiger counter shield has therefore to be made indirectly, and the results of different shielding arrangements are given in tables 1–3. The Geiger counter shield used was made up from twenty glass-wall counters (20th Century Electronics Type G 24). Unless otherwise stated 5 cm of aged lead was used as additional shielding.

4. Discussion

Table 1 indicates that the anticoincidence counting rate of a single GM4 LB end-window Geiger counter (General Electric Co.Ltd) is reduced by 0.2–0.3 cpm when the scintillator shield is used as opposed to the Geiger shield, even when the latter has the advantage of better shielding above the counter. This additional shielding of 1 metre of chalk is seen (table 2) to reduce the anticoincidence rate by a further 0.13 cpm presumably due to better shielding from environmental γ-radiation. Thus with identical shielding arrangements the anticoincidence rate with the Geiger shield is approximately 0.8 cpm (table 1) and with the liquid scintillator shield approximately 0.4 cpm (table 2).

From the last column of table 2 it is apparent that with the Geiger shield the rate of coincidence between the shield and the sample counter is unaltered by the addition of chalk shielding above the counters. This is to be expected if the coincidences are due to μ-mesons which are not appreciably attenuated by the chalk.

When the liquid scintillator is used (table 2, lower section) the additional chalk shielding again reduces the anticoincidence rate by 0.13 cpm, as with the Geiger shield. However, the performance of the scintillator shield is different in that the coincidence rate on the pit floor is

TABLE 1

Comparison between liquid scintillator shield on pit floor and Geiger shield under the chalk

Counter (GM4 LB)	Anticoincidence rate (cpm)			Coincidence rate† (cpm)		
	Geiger shield under chalk	Liquid scintillator on pit floor	Reduction	Geiger shield under chalk	Liquid scintillator on pit floor	Increase
A	0.86 ± 0.01	0.57 ± 0.01	0.29	4.38 ± 0.03	4.62 ± 0.02	0.24
B	0.81 ± 0.01	0.57 ± 0.01	0.24	3.24 ± 0.03	4.09 ± 0.02	0.85
C	0.77 ± 0.01	0.50 ± 0.01	0.27	3.18 ± 0.03	3.96 ± 0.02	0.78

† Corrected to 760 mm Hg atmospheric pressure.

TABLE 2
Counting rates on pit floor and under the chalk

Counter	Shield	Anticoincidence rate (cpm)			Coincidence rate† (cpm)		
		Pit floor	Under chalk	Reduction	Pit floor	Under chalk	Reduction
Pair of GM4 LB	Geiger	1.35 ± 0.01	1.05 ± 0.01	0.15††	6.96 ± 0.03	6.96 ± 0.03	—
Pair of GM4 LB	Geiger	1.29 ± 0.01	1.06 ± 0.01	0.12††	7.18 ± 0.03	7.22 ± 0.03	—
Single GM4 LB	Geiger	0.82 ± 0.01	0.60 ± 0.01	0.22	4.06 ± 0.03	4.04 ± 0.03	—
Single GM4 LB	Scintillator	0.50 ± 0.01	0.37 ± 0.01	0.13	3.75 ± 0.03	3.42 ± 0.03	0.33
Single GM4 LB	Scintillator	0.53 ± 0.01	0.40 ± 0.01	0.13	3.78 ± 0.03	3.45 ± 0.03	0.33

† Corrected to 760 mm Hg atmospheric pressure.
†† For a single GM counter.

now 0.33 cpm higher than it is under the chalk (table 2, right-hand column).

These results suggest that the scintillator shield is an efficient detector of a component of the background radiation which is inefficiently detected by the Geiger shield. This component is attenuated by the chalk, as shown in the last column of table 2. Various suggestions as to its nature may be considered.

(i) *Environmental γ-radiation.* This is improbable, since the reduction in anticoincidence rate by the chalk is approximately the same with each type of shield (table 2, column 5). Furthermore, the chalk is known to have a radioactive content of 1.2×10^{-12} α-ray curies g^{-1} [10]) and 6×10^{-8} $g^{40}K$ g^{-1} [11]). A calculation based on these values suggests that the environmental component of the background is approximately 0.3 cpm for the counter when shielded by chalk only. The addition of 5 cm aged lead would reduce this to less than 0.1 cpm. These figures agree with table 3, which indicates that an additional 5 cm aged lead shielding reduces the anticoincidence rate from 0.72 cpm to 0.37 cpm.

(ii) *Cosmic ray neutrons.* These are known to contribute to the background of the large counters used in ^{14}C estimation[12]). It is unlikely that the detection of secondary processes originating from these neutrons contribute significantly to the background of a small counter. Also, the anticoincidence rate (as measured with a Geiger shield) of these end-window counters shows no significant variation with atmospheric pressure. Such a variation would be expected if the component was due to neutrons, since the neutron flux in cosmic rays at sea-level varies

[10]) R. C. Turner, Private communication.
[11]) J. Vennart, Private communication.
[12]) Hl. de Vries, Nuclear Physics **1** (1956) 477.

TABLE 3
Counting rate of a GM4 LB counter in the liquid scintillator shield with various shielding arrangements

Shielding	Anticoincidence rate (cpm)	Coincidence rate† (cpm)
1 metre chalk all round	0.72 ± 0.01	3.60 ± 0.03
As above, but 5 cm Pb around sides	0.42 ± 0.01	3.54 ± 0.03
5 cm Pb + 1 metre chalk all round	0.37 ± 0.01	3.42 ± 0.03

† Corrected to 760 mm Hg atmospheric pressure.

inversely with barometric pressure to the extent of 1% per mm mercury pressure[13]).

(iii) *Other cosmic ray effects.* It is probable that the increased efficiency of the scintillator shield over the Geiger shield is due to the detection of the products of cosmic ray produced reactions in the material surrounding the counter, such as μ-meson decay, collision and capture processes. Presumably the products of a reaction outside the scintillator shield are detected by the sample counter, whilst the originating particle does not pass through the shield. The detection efficiency of the scintillator shield to low energy γ-radiation is much greater than that of a Geiger shield[5]), especially if the radiation is incident in the vertical direction, (as is probable if formed in a cosmic ray shower), due to the increased path length in the scintillator.

Independent evidence that a component of the background is due to the detection of uncharged radiation in the wall of the counter is given by Dixon *et al.*[14]) who detected strong characteristic X-radiation from the wall material of a proportional counter.

Acknowledgements

The author wishes to acknowledge the guidance and encouragement of Professor W. V. Mayneord throughout this work, and Dr. R. E. Bentley for many profitable discussions.

[13]) J. A. Simpson, W. Fonger and S. B. Treiman, Phys. Rev. **90** (1953) 934.

[14]) D. Dixon and A. Mcnair, Phil. Mag. **45** (1954) 1099.

NUCLEAR INSTRUMENTS AND METHODS **8** (1960) 344–347; NORTH-HOLLAND PUBLISHING CO.

A NEW METHOD OF MASS DISCRIMINATION

G. HREHUSS

Central Research Institute of Physics, Budapest, Nuclear Physics Laboratory

Received 14 May 1960

Emission spectra of CsI(Tl) scintillation crystals bombarded by heavy as well as light particles have been investigated. The results show the number of photons of shorter wavelength to be relatively higher in the case of excitation by light particles. This fact offers a new possibility for mass discrimination.

Mass discrimination with the use of scintillation detectors for the study of nuclear reactions is made possible by the recent discovery of the shape dependence of light pulses of scintillators on the mass of the exciting particles. Previous experiences in this field may be summarized as follows[1,2]).

The fluorescence of scintillators in general use is composed of two exponential components with half-lives differing from each other by about unit order of magnitude. Now, whereas the longer lived component is independent of the mass of the exciting particle, the component with a shorter half-life may show a difference in decay rate up to a factor of two depending on whether the excitation is induced by electrons or by α particles. For CsI(Tl) crystals the mean life of the longer lived component is 7 μsec, while that of the mass-dependent part is 0.43 μsec and 0.7 μsec for excitations initiated by α and β particles, respectively. For organic scintillators the case is similar with the difference, however, that for the latter the mean life is in general much shorter and also the mass-dependent component is faster for β-excitation. In the following, however, we shall restrict our considerations to the inorganic scintillator CsI(Tl).

Assuming that the mass-dependent component is due to the de-excitation of metastable states, it may be supposed that particles of different mass generate different metastable states with different probabilities, that is the emission spectra obtained from light particles can be expected to differ from those produced by heavy particles. If there is an appreciable difference, this will give a relatively simple method of mass discrimination: We have only to insert a colour filter between the photomultiplier and the phosphor permitting the transmission of either the spectrum range characteristic for the heavier or that for the lighter particles.

In order to verify this assumption the following measurements were performed:

1. Glass colour filters with known transmission characteristics were inserted between a CsI(Tl) scintillator 2.0 cm high and 3.0 cm in diameter (Harkovkij Zav. Chimreaktivov product) and an RCA 6342 photomultiplier. The phosphor was excited by Po α rays which struck the phosphor with an energy of 5.0 MeV, and by an annihilation radiation of 0.52 MeV as well as by direct γ radiation of 1,28 MeV from Na^{22}. By means of a single-channel amplitude analyzer the α and γ spectra were measured by using various colour filters. For both sources the number of scintillations was found to be about 10^3 sec^{-1}.

If the time constant of the anode circuit is sufficiently large, a voltage pulse proportional to the number of photons of the light pulse coming from the crystal is produced on the load resistance of the multiplier. Denoting now the number of photons per unit wave length by $f(\lambda)$,

[1]) R. S. Storey, W. Jack and A. Ward, Proc. Phys. Soc. (London) **72** (1958) 1.

[2]) R. B. Owen, Nucleonics **17** (1959) 92.

the function of spectral sensitivity of the multiplier by $\sigma(\lambda)$ and the transmission function of the colour filter by $\tau(\lambda)$, the voltage pulse of the multiplier for given particle energy is

$$S = K \int_{-\infty}^{+\infty} \tau(\lambda') \cdot \sigma(\lambda') \cdot f(\lambda') \, \mathrm{d}\lambda' \, .$$

The transmission function of the colour filters is given by

$$\tau(\lambda') \approx \begin{cases} 0 \text{ for } \lambda' < \lambda \\ \text{constant for } \lambda' > \lambda \, . \end{cases}$$

Using the symbol Λ for denoting the red limit of the multiplier, we have

$$S = K' \int_{\lambda}^{\Lambda} \sigma(\lambda') \cdot f(\lambda') \, \mathrm{d}\lambda'$$

and the spectral properties of the phosphor both for β and α excitation can be characterized by the ratio

$$s(\lambda) = \frac{S_\beta}{S_\alpha} = \frac{\int_{\lambda}^{\Lambda} \sigma(\lambda') \cdot f_\beta(\lambda') \, \mathrm{d}\lambda'}{\int_{\lambda}^{\Lambda} \sigma(\lambda') \cdot f_\alpha(\lambda') \, \mathrm{d}\lambda'} \, .$$

The measured ratios are shown in fig. 1 approximated by a straight line fitted to the points by the method of least squares. For each filter the α as well as the γ spectra were measured without altering the multiplier voltage. For better evaluation the photopeaks and the α peak were shifted to a convenient point of the measuring range of the amplitude analyzer by using the previously calibrated attenuator of the amplifier. Also an experiment was carried out to see whether saturation effect of the multiplier did not affect linearity and it was found that even within the applied voltage range (1000–1370 V) the deviation from linearity was less than 2.5%.

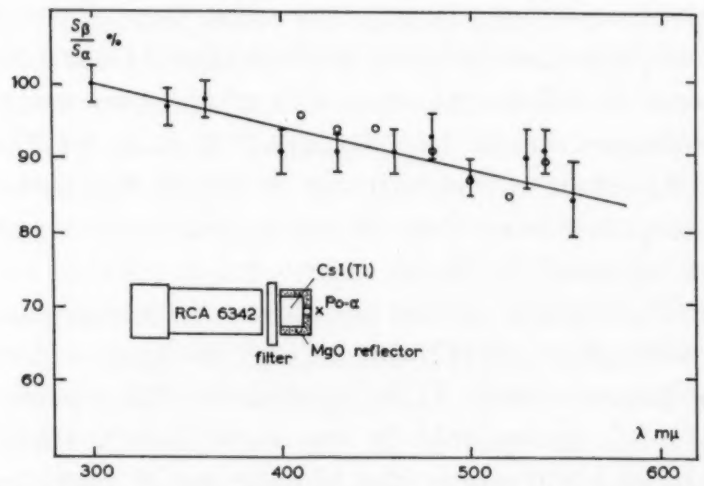

Fig. 1. The ratio of amplitudes S_β and S_α obtained with colour filters. The circles denote values of S_β/S_α calculated from the spectrographic measurements.

A similar effect may be caused also by a possible selective absorption of the CsI(Tl) crystal, for the path length of photons induced by α particles is longer than that of photons produced by β particles. Therefore the crystal was examined by means of a spectrophotometer, however, apart from surface reflection no wave length-dependent effects were found in the 400–600 mμ range and the surface reflection is negligible in this case.

2. The emission spectra of CsI(Tl) crystals excited successively by light and heavy particles were investigated by means of the arrangement shown in fig. 2. Since a continuous spectrum was expected, it was sufficient to use a spectroscope of low resolution in these experiments. The spectra were photographed by a Contax D camera on Agfa Isopan F film. The surface of the 1 mm thick crystal was about 1 cm² and a lucite wedge applied thereto directed the light to the spectroscope slit. The surface exposed to bombardment was covered by a 0.25 mg/cm² thick aluminium foil held down by a wire grid which served at the same time to carry away the charge collecting on the surface.

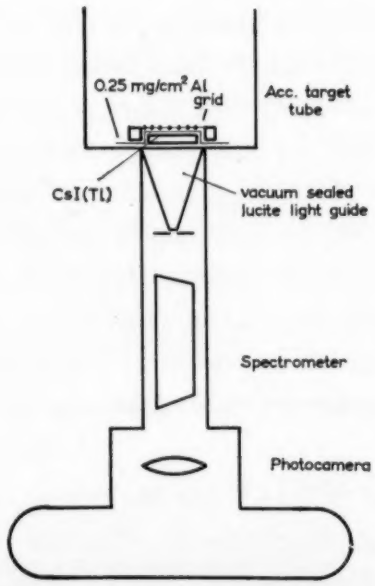

Fig. 2. Experimental arrangement for direct investigation of spectra.

To induce excitation by electrons we made use of the 1 MeV Van de Graaf accelerator operating in our Institute. The bombarding electron beam passed through a 20 mg/cm² fredal foil, continued its flight through air for a distance of about 2 cm and then struck the crystal with an energy of 400 keV, the current density being about 1 μA/cm².

For heavy-particle bombardment the crystal was placed into the vacuum system of the 600 keV ion accelerator of the Institute in a way to be struck directly on the surface covered by the Al foil and the grid. It was bombarded by deuterons and α particles having energies of 300 keV and 500 keV for He^{++} ions and 250 keV for He^{+} ions, respectively. Taking into account the stopping power of the Al foil, the excitation energies were estimated to be 180 keV and 250 keV, respectively, while that produced by He^{+} ions was negligibly small. Current density on the crystal surface was invariably about 1 μA/cm².

After irradiation no damage could be observed on the crystal surface. The photographs of the spectra provided with a calibrated scale of wavelengths as well as with normal blackening were evaluated by MΦ-4 microphotometer after development. The spectra obtained and normalized to the same number of photons in the 410–580 mμ wave length range are seen in fig. 3.

Conclusion

In order to compare the results of the measurements performed by means of colour filters with those made by using a spectrometer the spectra obtained in the second experiment were analyzed as follows:

The ratios

$$\frac{\int_{\lambda}^{580} n_{\beta}(\lambda')\,\mathrm{d}\lambda'}{\int_{\lambda}^{580} n_{\alpha}(\lambda')\,\mathrm{d}\lambda'}$$

were computed for various values of λ within the range $410 < \lambda < 580$ mμ. Here $n_{\beta}(\lambda')$ and $n_{\alpha}(\lambda')$ mean the number of photons registered per unit wave length interval in the case of bombardment with β and α particles, respectively. Since in the given wave length range the colour sensitivity of the photomultiplier as well as that of the film were of about the same shape, the two measurements could be compared. Results of the comparison are seen in fig. 1, where the ratios computed from data of the second experiment are marked by circles.

Thus it is seen that the shape of the emission spectrum of CsI(Tl) depends on the mass – light or heavy—of the exciting particles. The number of photons emitted in the wave length range $410 < \lambda < 500$ mμ is the highest for β particle-induced excitation and decreases with increasing mass number.

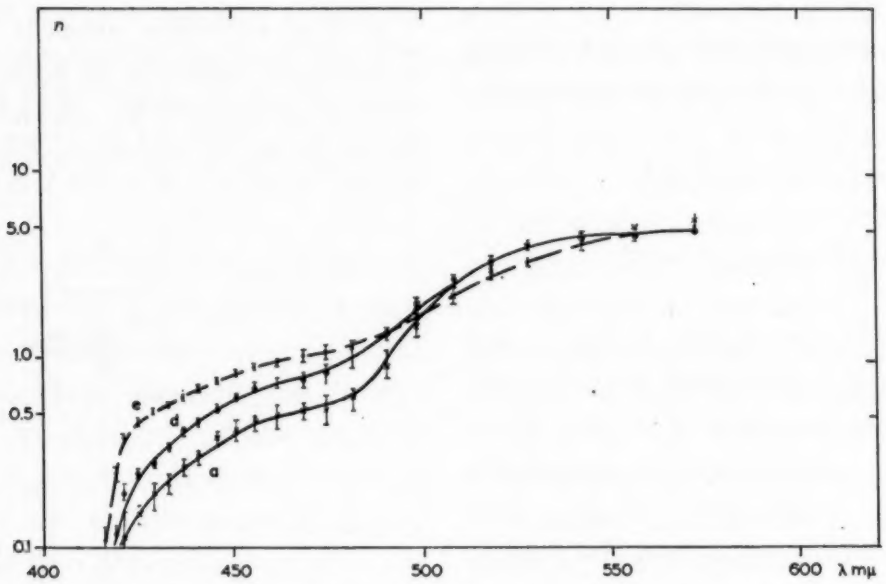

Fig. 3. Emission spectra of CsI(Tl) bombarded by electrons deuterons and α particles, not corrected for colour sensitivity of film.

The effect investigated above has been used for mass discrimination purposes in the following way. Two photomultipliers (DuMond 6292) equipped with a yellow ($\lambda_{rf} > 500$ mμ) and a blue colour filter ($\lambda_{rf} < 500$ mμ), respectively were attached to a CsI(Tl) scintillation crystal (1″ by ½″). The total gain of each channel consisting of the photomultiplier and a non-overloading amplifier was adjusted in order to obtain the same pulse amplitude for an α particle of given energy at the output of both amplifiers. The pulses of both channels were transmitted to an analyzer each, and a coincidence circuit—scaler system counted the coincident pulses of the analyzers, which in addition were provided with a common bias. In the ideal case only the α particles can produce coincidences in such an arrangement for the response-energy functions of the two counters would be different for β particles according to the previous measurements.

Energy distributions of α and β particles, respectively are shown in fig. 4 measured by means of the method described. The energy of α particles emitted by a Po source was reduced in order to make the α spectrum comparable to the γ spectrum of Na^{22} serving as background by the use of thin Al absorption foils. Because of these foils the shape of the α spectrum became of course deformed.

Fig. 4 shows the pure α energy distribution without background, the α and β energy distributions obtained when the crystal was irradiated by α particles and at the same time γ radiation from Na^{22} was also present. The last two were obtained by means of the new mass discrimination method applied to α and β particles, respectively. The latter is at the same time the background of the α spectrum. We can see from these spectra that the background decreases by about an order of magnitude for α energies of less than 0.7 MeV and a mass discrimination of practically 100% can be achieved above 1.7 MeV. The lower limits of these energy values are determined by the

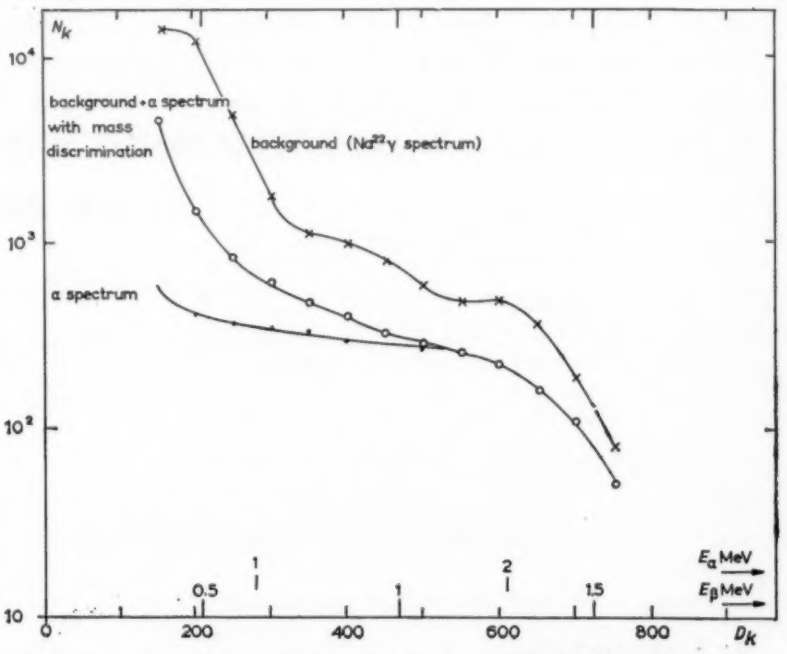

Fig. 4. α and β energy distributions measured by means of spectral mass discrimination.

statistical amplitude fluctuation of the multiplier pulses. In the case of low energy particles—because of the low number of photons produced—this amplitude fluctuation can be so big that the pair of analyzers adjusted for detecting only α particles detects β particles as well.

In order to illustrate the linearity of the effect made use of above the pulses of the yellow-and the blue-sensitive multipliers were—as usual—transmitted to the horizontal and vertical plates of an oscillograph. The shape of the impulses thus obtained can be seen on the photograph reproduced in fig. 5.

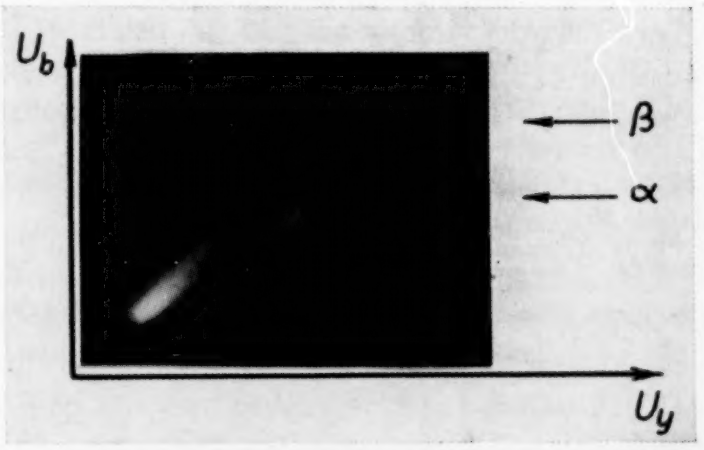

Fig. 5. The spacing and linearity of spectral mass discrimination for β and α particles, respectively.

NUCLEAR INSTRUMENTS AND METHODS **8** (1960) 348–353; NORTH-HOLLAND PUBLISHING CO.

AN IMPROVED INSTRUMENT FOR NUCLEAR EMULSION TRACK PHOTOMETRY

S. v. FRIESEN and B. PERSSON

Department of Physics, University of Lund, Lund

Received 3 June 1960

A description is given of a semi-automatic nuclear emulsion track photometer of high precision.

1. Introduction

A nuclear emulsion track photometer developed at Lund has been described in a number of papers[1–6]). The instrument has proved to be very useful in the determination of the masses of slow particles in nuclear emulsions. Recently, very satisfactory results have also been obtained in charge determinations on relativistic or nearly relativistic particles of the primary cosmic radiation[7–9]). The present paper describes an improved version of the photometer.

In the former instrument the mean track width, MTW, was determined by means of a modified Leitz microscope of type B. A Ks 100 objective combined with the lower lens of an eye-piece produces an image of the track. The tube length has been chosen in such a way as to give a magnification of exactly 100 times. At the position of the image there is a slit 3.0 × 0.25 mm². After passing through the slit the light falls on the cathode of a photomultiplier tube. The amplified output of the multiplier operates a Speedomax recorder. The recorded value x measures the amount of light which passes through the slit when it covers a section of the image of the track. This can be moved out of the slit by turning a plane parallel glass plate in the light path inside the tube. We now record a value y, which represents the amount of light passing through the slit when it is empty. When multiplied by the width of the slit, $(1 - x/y)$ gives the MTW of that segment of the track which is being measured. The MTW values which are obtained in this way must be corrected for depth in the emulsion, since with increasing depth the amount of scattered light increases. Also the effect of uneven development must be taken into account. We have always measured y on both sides of the track. This involves three measurements, three readings of the Speedomax chart and the calculation of $1 - x/y$.

A considerable gain in speed would be obtained if the three measurements could be made simultaneously and the calculations performed automatically. Such an arrangement would also to a large extent eliminate errors due to mistakes in reading the chart and in the calculations.

The new instrument includes the suggested improvements. It delivers directly an output voltage proportional to $(1 - x/y)$, which can be recorded by means of a digital voltmeter and a digital printer on a strip of paper.

[1]) S. v. Friesen and K. Kristiansson, Arkiv för Fysik **4** (1952) 505.

[2]) K. Kristiansson, Arkiv för Fysik **8** (1954) 311.

[3]) S. v. Friesen, Arkiv för Fysik **8** (1954) 305.

[4]) S. v. Friesen and L. Stigmark, Arkiv för Fysik **8** (1954) 121.

[5]) K. Kristiansson, Arkiv för Fysik **10** (1956) 447.

[6]) T. Johansson and K. Kristiansson, Arkiv för Fysik **11** (1957) 467.

[7]) B. Waldeskog and O. Mathiesen, Arkiv för Fysik **17** (1960) 427.

[8]) K. Kristiansson, O. Mathiesen and B. Waldeskog, Arkiv för Fysik **17** (1960) 455.

[9]) K. Kristiansson, O. Mathiesen and B. Waldeskog, Arkiv för Fysik **17** (1960) 485.

2. Description of the Instrument

Fig. 1 shows the principle of the photometer. The objective B and the lens C form an image of the track A on the middle one of three parallel

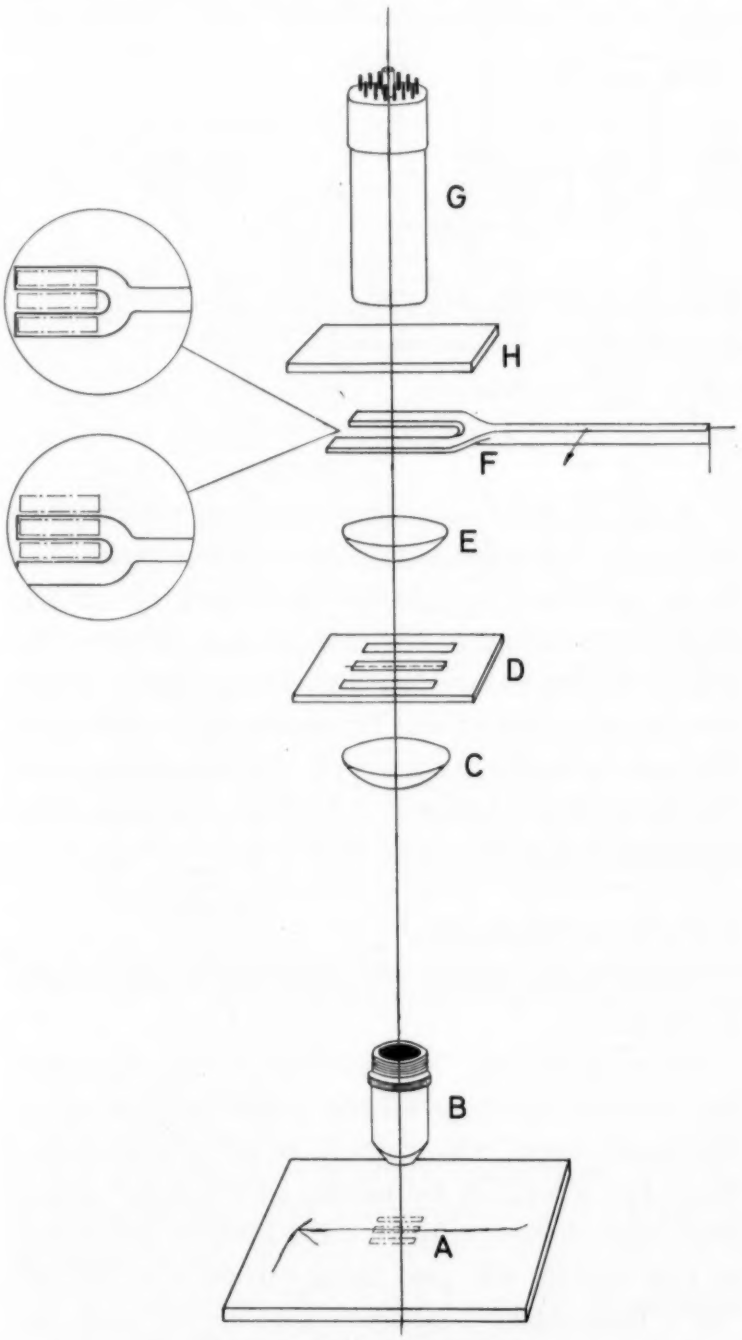

Fig. 1. Schematic diagram of the track photometer showing among other details the forked shutter, which lets the photomultiplier see either the track itself or the empty emulsion on both sides of the track.

slits at D. A second lens E produces a magnified image of the slits at the position F. A forked shutter normally covers the two outer slits, so that the photomultiplier G sees only a region of the emulsion defined by the middle slit and containing the track. By means of an electromagnet the shutter can be moved to a new position where it covers the middle slit and leaves the outer ones free. The photomultiplier now sees one region of the emulsion on each side of

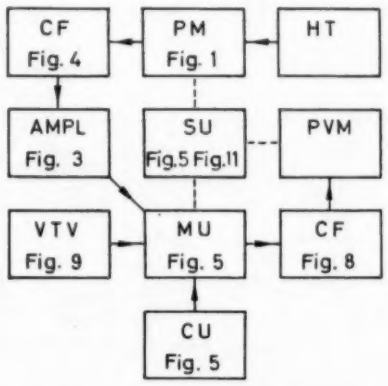

Fig. 2. Block diagram of the complete instrument. H.T. = High tension supply; P.M. = Photometer; C.F. = Cathode follower; Ampl. = Amplifier; M.U. = Main unit; S.U. = Steering unit; C.U. = Calibration unit; V.T.V. = Vacuum tube voltmeter; P.V.M. = Printing voltmeter.

the track and at the same depth in the emulsion. H is a milk glass plate which distributes the light more evenly over the cathode of the photomultiplier tube.

We thus measure two voltages x and $2y$, and need some means of comparing them in order to find $(1 - x/y)$. This can be achieved by means of an arrangement shown in fig. 2.

A perforated disc rotating in front of the microscope lamp gives 500 cycle AC output from the Du Mont 6467 photomultiplier. The AC goes to an amplifier (fig. 3) via a cathode follower (fig. 4). The final stage of the amplifier consists of another cathode follower. A built-in rectifier produces a DC voltage proportional to the amount of light hitting the photo cathode. Let x and $2y$ be the voltages which correspond to the middle slit (with the track) and the two outer slits, respectively. These voltages are used to charge the capacitors C_1 and C_2 to the voltages x and y (figs. 5 and 6a). In order to find the difference $-(y - x)$, we then disconnect point b and connect point c to ground (fig. 6b). The voltage $-(y - x)$ determines the input grid voltage of a Schmitt trigger circuit (fig. 7). Next we connect a resistor R across C_2, which starts to discharge, operating the trigger when its input grid reaches zero potential i.e. when $y = x$. At

exactly the same moment as we apply R across C_2 we also begin to charge a third capacitor C_3 through a circuit having the same time constant RC_2. The trigger impulse discontinues the charging of C_3, which has now reached a voltage U. The supply from which we charge C_3 gives U_0 volts. We call the discharging time T and get the following expressions:

$$x = y\, e^{-T/RC_2},$$

$$U = U_0\,(1 - e^{-T/RC_3}),$$

and

$$U = U_0\,(1 - x/y).$$

When multiplied by the width of the slit the voltage U, which is proportional to $(1 - x/y)$, measures the mean width of the track.

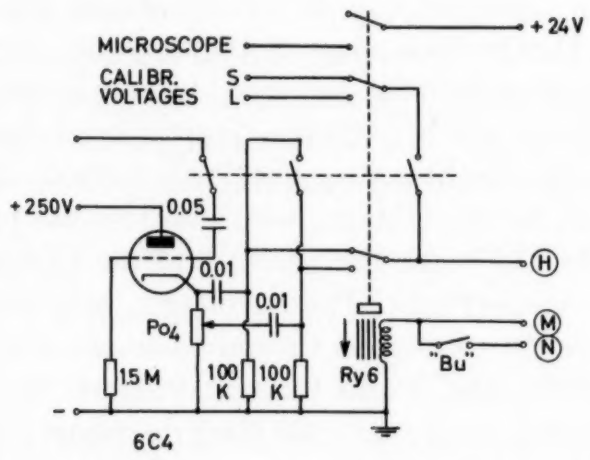

Fig. 4. Cathode follower operating on the input side of the amplifier.

The voltage U across C_3 goes to a cathode follower shown in fig. 8. The output of the cathode follower operates a Hewlett-Packard model 405 AR automatic DC digital voltmeter and a model H03-561 B digital recorder. In this way the MTW values come out of the instrument printed on a paper strip ready for analysis.

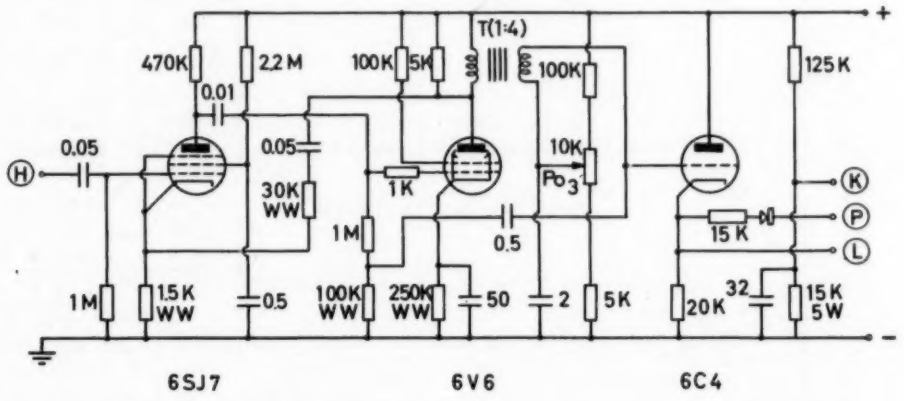

Fig. 3. Amplifier for the charging of the capacitors C_1 and C_2 (fig. 5).

A special calibration unit (fig. 10) which gives 500 cycle signals in accurately known ratios, has been provided to enable the checking of the correct operation of the instrument. It gives the choice between two fixed ratios or ratios which can be adjusted at will by means of a calibrated Helipot potentiometer. For the adjustment of the instrument there is a built-in vacuum tube voltmeter (fig. 9).

3. Cycle of Operation

In the following an activated relay will be said to be closed.

On pushing the "start" button (fig. 5), relay Ry 1 closes, whereas all the others remain open. The instrument is now ready to receive information. The operator by means of a mirror and a lens (not shown) adjusts and focuses the track in the middle slit and then pushes the button "M". This starts a synchronous motor and the cycle of operation begins. The motor operates a number of micro switches MS 1–5 in a predetermined sequence by means of a series of cams on a shaft. MS 1 and MS 2 connect the capacitors C_1 and C_2, one after the other, to the output of the amplifier (fig. 3). MS 3 operates Ry 6 (fig. 4) so that the capacitors get the charge which corresponds to the correct position of the forked shutter. When C_1 and C_2 have reached their equilibrium voltages x and y MS 4 causes Ry 5 (fig. 5) to close. This results in the following:

1. Breaking of the ground connection of Ry 1, which opens this relay. The grid of the Schmitt trigger valve 6 SJ 7 (fig. 7) gets the potential $-(y-x)$ (too low to trigger).

2. After a short delay Ry 2 closes:

All this accomplished, Ry 5 opens. Meanwhile the discharging of C_2 continues to the point where $y = x$, i.e. until the trigger input gets zero potential. Triggering takes place and Ry 3 closes. The result will be that:

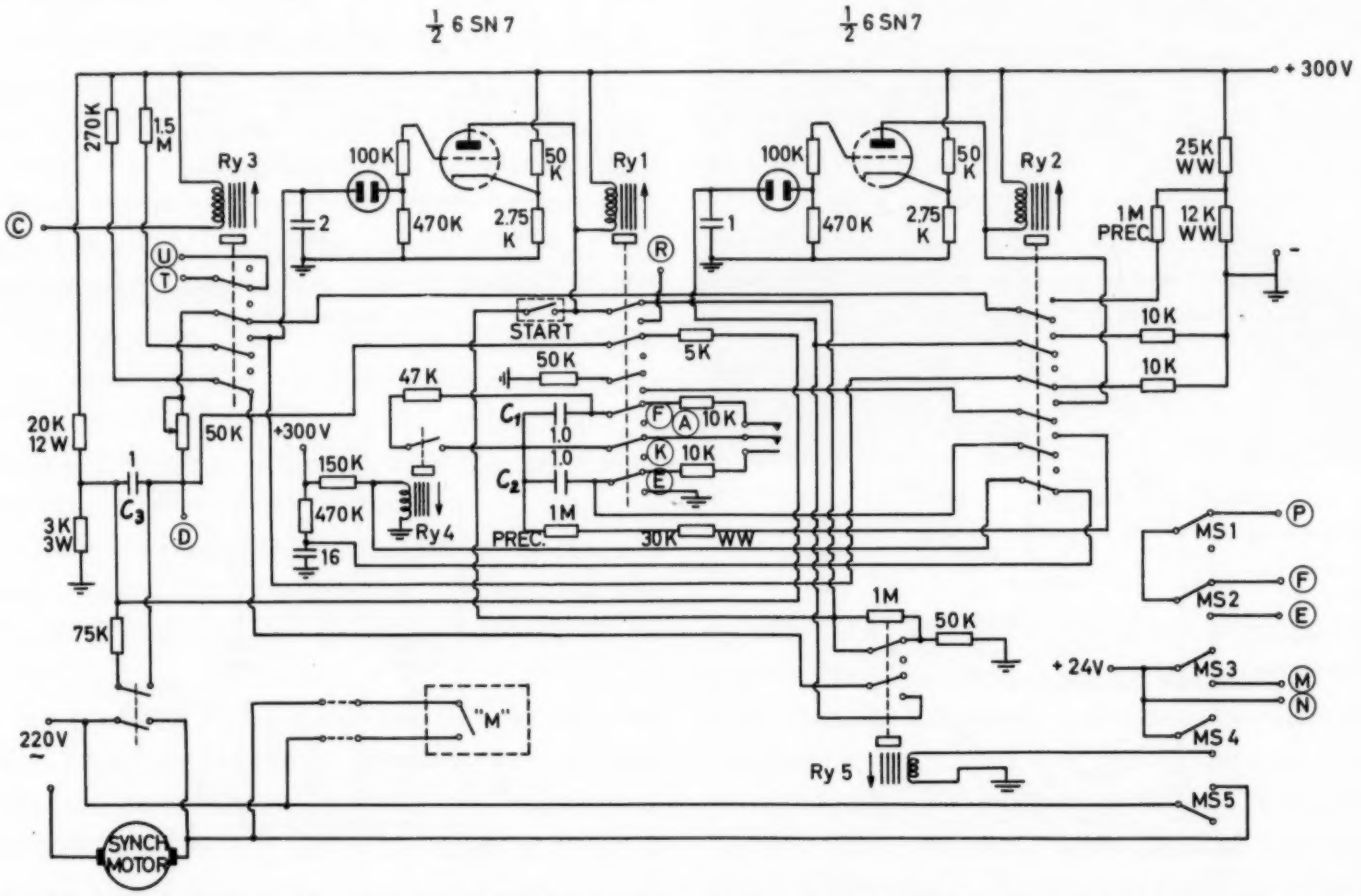

Fig. 5. Main unit including cam-operated microswitches and relays, which determine the cycle of operation and the arrangement including capacitors C_1, C_2, and C_3, which computes the mean track width.

(a) discharging C_2

(b) charging C_3

(c) breaking the ground connection of the 6 NS 7 circuit, which operates Ry 1, after a suitable delay.

(d) connecting that 6 SN 7 circuit to ground which operates Ry 2 and finally

(e) breaking the short circuit between the coil of Ry 4 and the 16 μF capacitor causing it to charge to 300 volts.

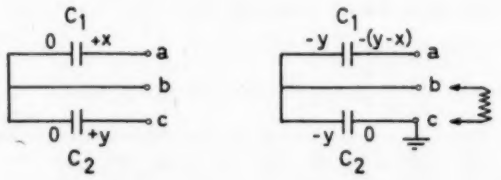

Fig. 6. The diagrams show the connection of the capacitors C_1 and C_2 a) being charged b) discharging.

(a) the charging of C_3 ceases.

(b) Ry 1 closes with a certain delay, discharging C_3 and opening Ry 2.

In its new position Ry 2 connects the 6 SN 7 circuit of Ry 1 to ground. It also makes the 16 μF capacitor discharge through the coil of

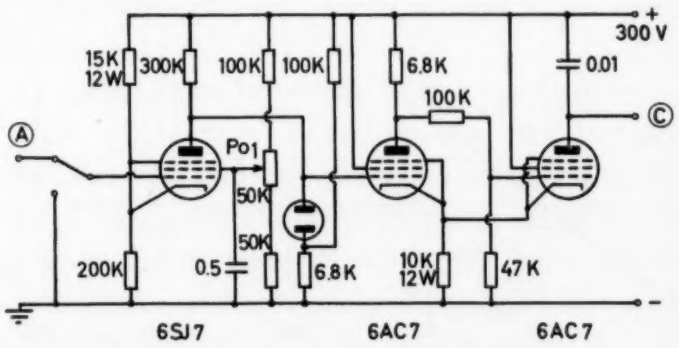

Fig. 7

Schmitt trigger circuit controlling by means of relays the discharging of the capacitors C_1 and C_2 and the charging of C_3.

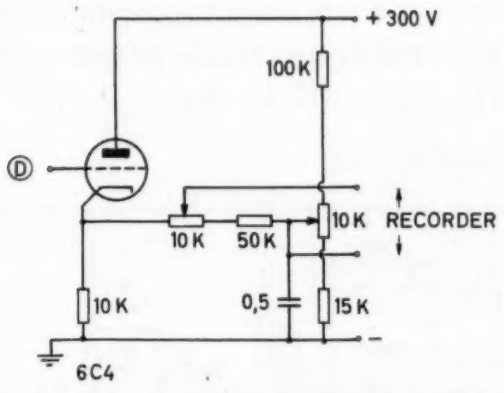

Fig. 8. Cathode follower on the output end of the main unit, feeding the printing voltmeter.

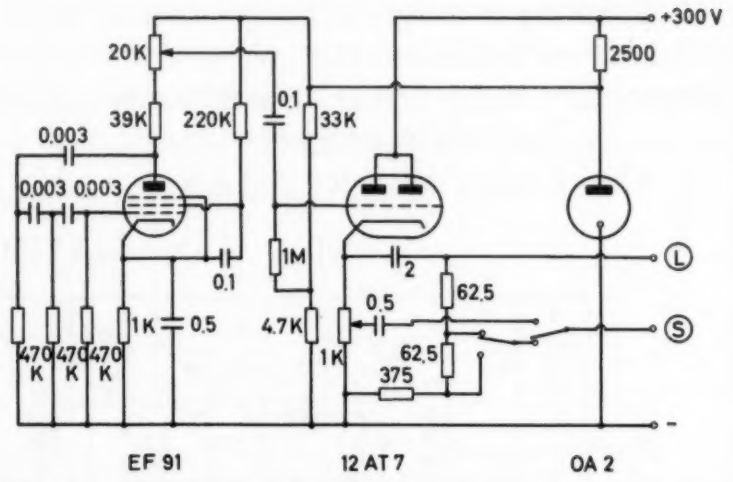

Fig. 10. Calibrating unit giving 500 c/s A.C. voltages in known ratios.

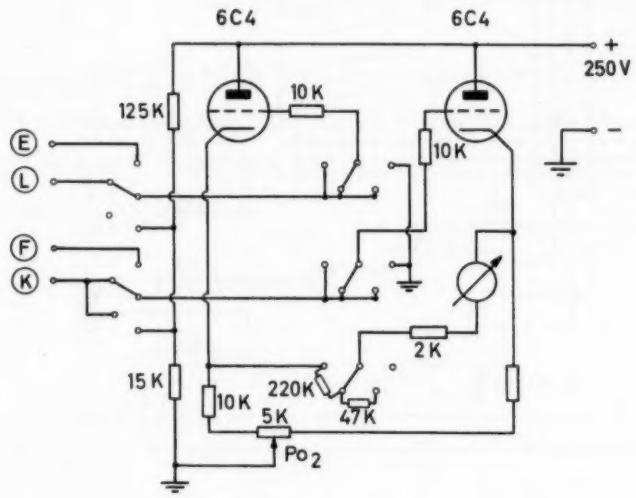

Fig. 9. Vacuum tube voltmeter for the adjustment of the instrument.

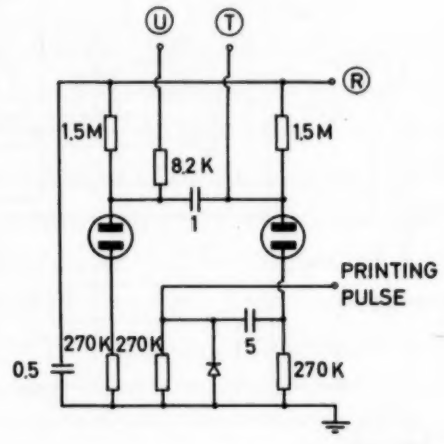

Fig. 11. Neon bulb circuit, which gives a printing pulse to the printing voltmeter at the correct time. The left hand neon bulb ignites at a lower voltage than the other one.

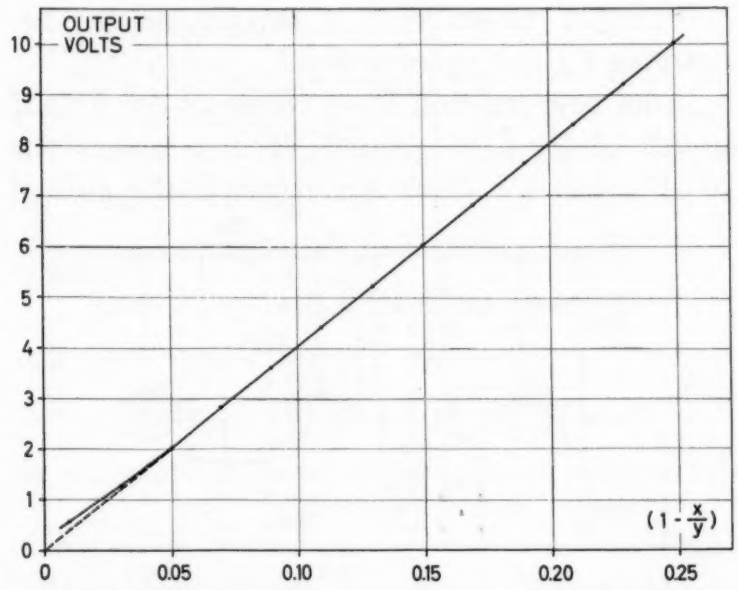

Fig. 12. Diagram showing the linearity of the relation between track width – slit width ratio ($1 - x/y$) and the output voltage of the instrument.

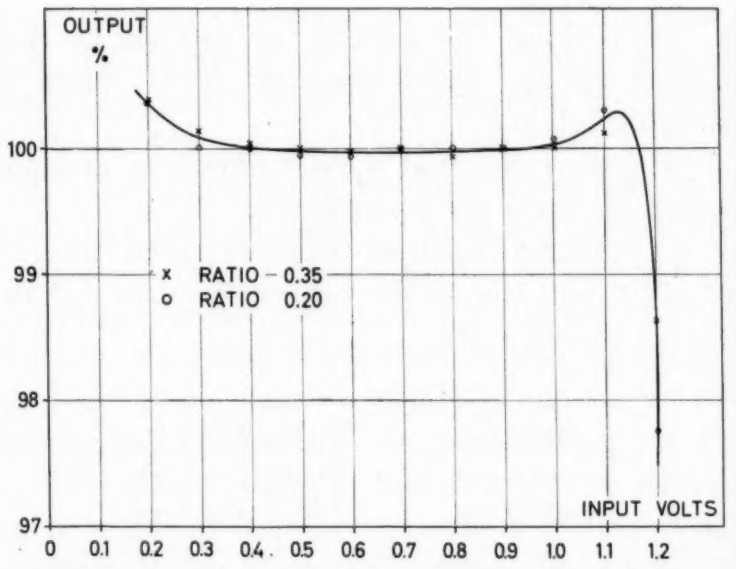

Fig. 13. Diagram showing that the output of the main unit is independent of the input voltage in the region 0.3–1.0 volts.

Ry 4 making this relay close temporarily to discharge C_1.

We are now back at the beginning of the cycle and ready for a new measurement.

4. Adjustments

In order to facilitate the adjustments a built in vacuum tube voltmeter has been provided (fig. 9).

The necessary adjustments are the following:

1. With the input grid of the Schmitt trigger grounded the 6 SJ 7 screen voltage is adjusted by means of the potentiometer Po_1 so that the circuit just triggers.

2. The vacuum tube voltmeter is set to read zero by means of the potentiometer Po_2.

3. The points K and L (fig. 3) are brought to the same potential by means of the potentiometer Po_3.

4. The level of the incoming signals is given a suitable value by varying the voltage on the photomultiplier or the intensity of the light source.

5. By pushing the button Bu (fig. 4) one can switch rapidly between observation of the middle slit and the outer slits, and adjust the potentiometer Po_4 for the same reading in both positions.

For each adjustment the VTV is connected to the proper circuit by means of a selector switch. During the measurements the VTV should be disconnected.

Fig. 14 shows the photometer and its auxiliary equipment.

5. Performance

The relation between $(1 - x/y)$ and the output of the instrument is shown in fig. 12. The linearity is good down to a value of $1 - x/y$ equal to 0.05. By choosing the width of the slit in a suitable way it will always be possible to work inside the linear region. Fig. 13 shows that the output of the machine is independent of the input voltage to better than one tenth of one per cent in the region from 0.3 to 1.0 volt.

The instrument has been in use for many months and has been proved to work in a very satisfactory manner. One of the tests made on slow singly charged particles in Ilford G 5 emulsions consisted in measuring an ending proton track 6000 microns in length. The average MTW value was calculated for 250 micron sections of the track. The sum of these averages was also calculated. One month later the same track was remeasured. It is obvious that the position of the track on the photometer cannot have been identical on the two occasions. Certain individual grains may have fallen at one time in a certain 31 micron section the next time in an adjacent section. The average diameter of a grain is 0.6 microns. The track being curved, due to scattering in the emulsion, its position in a direction at right angles to the slit must also have varied to some extent.

In spite of this the mean of the absolute values of the differences between the MTW-values found for the 250 micron sections amounted to only 0.88%, and the difference between the totals was not more than 0.13%. This error is inside the accuracy of $\pm$ 0.2% given by the manufacturer of the digital voltmeter.

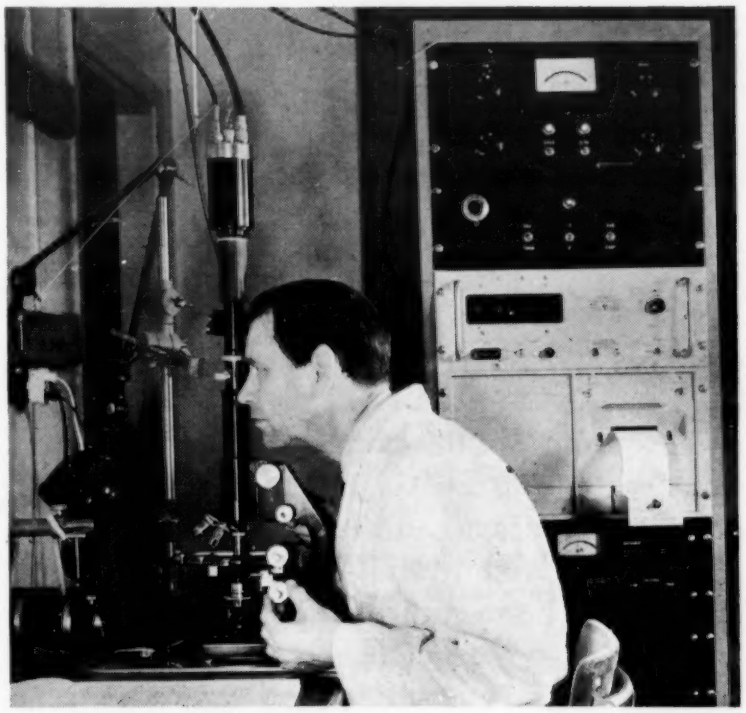

Fig. 14
Semi-automatic nuclear emulsion track photometer in use.

NUCLEAR INSTRUMENTS AND METHODS 8 (1960) 354; NORTH-HOLLAND PUBLISHING CO.

LETTER TO THE EDITOR

A METHOD FOR THE SEPARATION OF GOLD IRRADIATED MERCURY ISOTOPES

W. PARKER

Institute of Physics, University of Uppsala, Uppsala, Sweden

Received 6 July 1960

The purpose of this note is to make known the constructional details of an apparatus developed for the separation and consequent deposition of Hg isotopes from irradiated Au. The apparatus, which may be seen in the figure, functions as a vacuum evaporator and can be put together in a few hours by a machine shop and, when complete, may be relied upon to give reproducible results. Part of the apparatus forms a dewar flask constructed by placing a small brass cup, A, within a larger one, B. Cup A has a diameter of 40 mm's, the larger cup, B, 70 mm's. The bottom of A is drilled and tapped to take a threaded rod, C. Hard soldered to B are two half inch standard vacuum connections E and D. The male counterpart of D is fitted with a quartz tube, F, fastened by means of thermal cement† G, while the second vacuum connection E, is for evacuating the system.

The operating procedure is as follows: Part or all of the Au target is placed in the quartz tube. A gold spot, the diameter of which will depend on the source requirements, is vacuum deposited onto a suitable piece of mylar. The unthreaded end of the rod is smeared with vacuum grease and brought into contact with the uncoated side of mylar, the surplus mylar being pleated along the sides of the rod. The rod and quartz tube can now be screwed into their respective positions. After pumping for some minutes the rotary pump is isolated by means of a valve and the dewar filled with either dry ice and alcohol or liquid air. A bunsen burner is suitable as a heat source and only a small flame necessary.

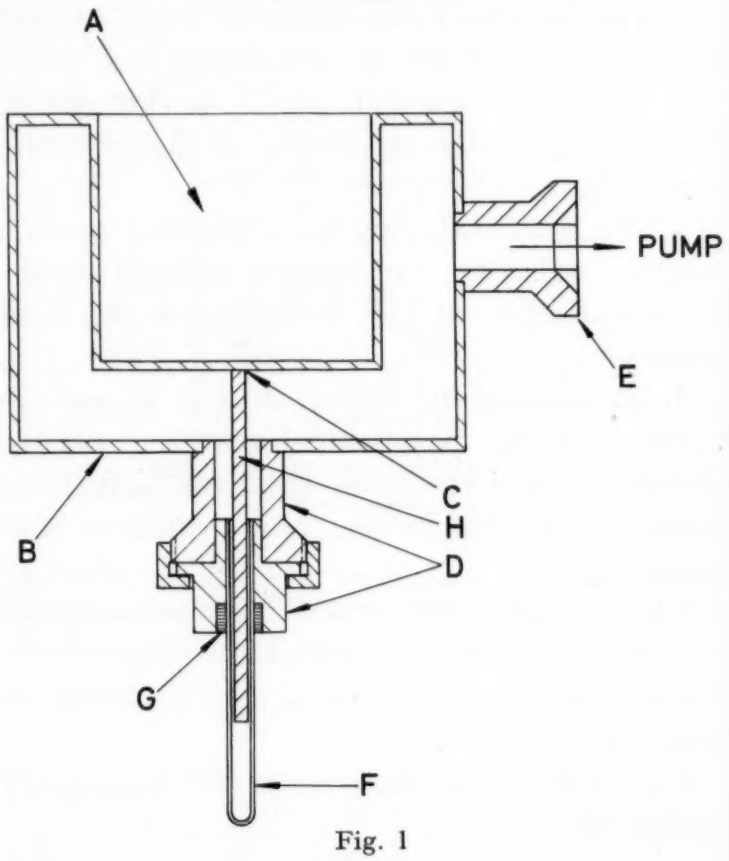

Fig. 1

Deposition times were from 15 to 60 minutes after which the mylar was removed and stretched over a suitable holder. Using the described apparatus efficient depositions have been carried out, and when necessary, 100% separation achieved.

† Alumina Thermal Cement.

AUTHOR INDEX

ALVES, R. V. *see* TOCHILIN
AMSEL, G., P. BARUCH et O. SMULKOWSKI, Détecteur de particules lourdes a jonction n-p au silicium . 92
AZUMA, R. E., *see* LEWIS

BARUCH, P., *see* AMSEL
BATCHELOR, R., W. B. GILBOY, A. D. PURNELL and J. H. TOWLE, Improvements in the fast neutron time of flight technique using pulse shape discrimination in an organic phosphor 146
BERGSTRÖM, I., E. C. O. BONACALZA, A. JECH, M. PEREZ and P. THIEBERGER, The oscilloscope method of measuring nuclear half-lives 151
BIRKHOFF, R. D., J. M. KOHN, H. B. ELDRIDGE and R. H. RITCHIE, The spherical condenser as a high transmission particle spectrometer II. Disc source 313
BLANKENSHIP, J. L., *see* HALBERT
BONACALZA, E. C. O., *see* BERGSTRÖM
BRAAMS, C. M. and P. B. SMITH, The Utrecht 850kV cascade generator. I. Beam deflection and energy control 27
BRINI, D., A. GANDOLFI and G. L. TABELLINI, Transistorized apparatus for accumulation and binary-decimal conversion 46
BRUCKER, GEORGE J. and KENNETH C. ROGERS, A kilovolt, kiloampere low pressure switch 236
BRUGGER, ROBERT M., *see* TOLK
BUCZKÓ, M., *see* CSIKAI
BURGERJON, J. J. and W. WEIDEMANN, The Pretoria cyclotron, Second Report 261
BUTLER, J. W., High-efficiency, long-lived vacuum cold trap 211

CSIKAI, J. and M. BUCZKÓ, The effect of gamma-background on the BF_3 proportional counter 73

DAY, P. PAUL, *see* MELVIN S. FREEDMAN
DÉSI, S., *see* NAGY
DETENBECK, R. W., *see* J. B. MARION
DE VRIES, C. and A. H. WAPSTRA, A Siegbahn-Edvarson type ironfree double focusing beta-ray spectrometer 121
DUCROS, G., *see* SARAZIN
DUNAITZEV, A. F., YU. D. PROKOSHKIN and TANG SYAO-WEI, π^- star detector 11

EICHHOLZ, G. G., Continuous monitoring of uranium leach solutions 320
ELDRIDGE, H. B., *see* BIRKHOFF
ENGELHARDT, H., I. HAUSER and U. KRECKER, Apparatus and laboratory for processing nuclear emulsion stacks. 55

FREEDMAN, MELVIN S., FRANK WAGNER, JR., FRED T. PORTER, JOHN TERANDY and PAUL P. DAY, Iron-free toroidal beta-beta coincidence spectrometer (Letter to the editor) 255

GABATHULER, E., *see* LEWIS
GANDOLFI, A., *see* BRINI
GAT (GUTMANN) J. R. and J. GILAT, A low background beta counter with a plastic scintillator anticoincidence shield 233
GIANNELLI, G. and L. STANCHI, Nonlinear operations on pulses by means of p-n junctions 79
GILAT, J., *see* GAT (GUTMANN)
GILBOY, W. B., *see* BATCHELOR
GOULDING, F. S., R. W. NICHOLSON and J. B. WAUGH, A double-delay-line linear amplifier employing transistors I 272
GOULDING, F. S. and R. A. MCNAUGHT, A transistorized fast-slow coincidence and pulse amplitude selecting system II 282

GUNNERSEN, E. M. and G. JAMES, On the efficiency of the reaction $H^3(d,n)He^4$ in titanium tritide bombarded with deuterons. 173

HALBERT, M. L. and J. L. BLANKENSHIP, Response of semiconductor suface-barrier counters to nitrogen ions and alpha particles 106
HAUN, S. und D. KAMKE, Ein universelles Verfahren zur Stabilisierung von Szintillations-Spektrometer-Anordnungen 331
HAUSER, I., *see* ENGELHARDT
HREHUSS, G., A new method of mass discrimination . 344

JAMES, G., *see* GUNNERSEN
JECH, A., *see* BERGSTRÖM
JONGEJANS, B., *see* TENNER

KAMKE, D., *see* HAUN
KOHN, J. M., *see* BIRKHOFF
KRECKER, U., *see* ENGELHARDT

LEVESQUE, R. J. A., *see* J. B. MARION
LEWIS, G. M., E. GABATHULER and R. E. AZUMA, On the separation of π^+ mesons by a time of flight method 230
LUCK, G., Zum Einfluss der Kristallform auf das energetische und zeitliche Auflösungsvermögen einer Szintillationsanordnung 249
LUDEMANN, C. A., *see* J. B. MARION

MARION, J. B., R. J. A. LEVESQUE, C. A. LUDEMANN and R. W. DETENBECK, A. versatile, high efficiency 4π neutron detector 297
MAYER-KUCKUK, T. und R. NIERHAUS, Über die Bestimmung der zufälligen Koinzidenzen in Schnell-Langsam-Koinzidenz-Anordnungen . . 76
MCNAUGHT, R. A., *see* GOULDING
MOAK, C. D., Space-charge effects in cylindrical beams with uniform acceleration 19

MULOT, P., R. POUSSOT, A. P. SCHMITT et C. P. ZALESKI, Appareil automatique pour la mesure des gradients locaux du flux de neutrons dans un réacteur 185

NAGY, L., *see* NAGY
NAGY, T., L. NAGY and S. DÉSI, Drift velocities of electrons in argon, nitrogen and argon mixtures 327
NICHOLSON, R. W., *see* GOULDING
NIERHAUS, R., *see* MAYER-KUCKUK

O'CONNER, D. A., The theory and operation of the rotating crystal slow neutron chopper 244
OSELKA, M., *see* RAMLER

PARKER, R. P., An improved anti-coincidence shield for use in low background counting 339
PARKER, W., A method for the separation of gold irradiated mercury isotopes (Letter to the editor) 354
PEREZ, M., *see* BERGSTRÖM
PERSSON, B., *see* v. FRIESEN
PORTER, FRED T., *see* MELVIN S. FREEDMAN
POUSSOT, R., *see* MULOT
PROKOSHKIN, YU. D., *see* DUNAITZEV
PURNELL, A. D. *see* BATCHELOR

RAIMBAULT, P., *see* SARAZIN
RAMLER, W. J., J. L. YNTEMA and M. OSELKA, Energy degrading-focusing of cyclotron beam 217
RITCHIE, R. H. *see* BIRKHOFF
ROGERS, KENNETH C., *see* BRUCKER
RUTHERGLEN, J. G. and J. K. WALKER, A scintillation counter system for the detection of positive and negative pions 239

SAKAI, MITSUO, Optimum conditions for double focusing beta ray spectrometers 61
SAMUELI, J., *see* SARAZIN
SARAZIN, A., J. SAMUELI, G. DUCROS et P. RAIMBAULT, Circuit allongeur d'impulsons rapides 70
SCHMITT, A. P., *see* MULOT
SMITH, P. B., *see* BRAAMS
SMITH, P. B., *see* SMULDERS
SMULDERS, P. J. M. and P. B. SMITH, The Utrecht 850kV cascade generator. II. The beam integrator and galvanometer. 40
SMULKOWSKI, O., *see* AMSEL
STANCHI, L., *see* GIANNELLI
STOKER, P. H., On the construction and long-term performance of medium pressure BF_3 proportional counters used for cosmic-ray recording . 23

TABELLINI, G. L., *see* BRINI
TANG, SYAO-WEI, *see* DUNAITZEV
TENNER, A. G. C., B. JONGEJANS and H. WITTEVELD, An instrument facilitating the measurement of small-angle scattering in nuclear emulsion . . . 221
TERANDY, JOHN, *see* MELVIN S. FREEDMAN
THIEBERGER, P., *see* BERGSTRÖM
TIEMEYER, J. C., A stabilizing system for a 700 kV cascade generator 117
TOCHILIN, E., and R. V. ALVES, Neutron flux measurements from 100 keV to 4 MeV with a modified long counter 225
TOLK, NORMAN, H. and ROBERT M. BRUGGER, Calculated shapes for neutron bursts produced by phased chopper velocity selectors 203
TOWLE, J. H. *see* BATCHELOR

VAN BLADEL, J., Fields excited by beam currents in circular accelerators 1
VAN DE GRAAFF, R. J., Tandem electrostatic accelerators 195
v. FRIESEN, S. and B. PERSSON, An improved instrument for nuclear emulsion track photometry . 348

WAGNER, JR., FRANK, *see* MELVIN S. FREEDMAN
WALKER, J. K., *see* RUTHERGLEN
WAPSTRA, A. H., *see* DE VRIES
WAUGH, J. B. S., Bandwidths of the equal time-constant amplifier (Letter to the editor) 257
WAUGH, J. B., *see* GOULDING
WEIDEMANN, W., *see* BURGERJON
WITTEVELD, H., *see* TENNER

YNTEMA, J. L., *see* RAMLER

ZACCHERONI, E., H. F. power meter for operation at 2.5 MW pulsed power 304
ZALESKI, C. P., *see* MULOT

BOOK REVIEWS

SEGRÉ, E. (Editor), Experimental Nuclear Physics, Volume III (T. R. GERHOLM) 258
SOMMERVILLE, J. L. (Editor), The Isotope Index, July 1959, International Edition (T. R. GERHOLM) . . 258

SUBJECT INDEX

Accelerators and Reactors

Fields excited by beam currents in circular accelerators, J. VAN BLADEL 1
Space-charge effects in cylindrical beams with uniform acceleration, C. D. MOAK 19
The Utrecht 850 kV cascade generator I. Beam deflection and energy control, C. M. BRAAMS and P. B. SMITH . . . 27
The Utrecht 850 kV cascade generator II. The beam integrator and galvanometer, P. J. M. SMULDERS and P. B. SMITH 40
A stabilizing system for a 700 kV cascade generator, J. C. TIEMEYER 117
Appareil automatique pour la mesure des gradients locaux du flux de neutrons dans un réacteur, P. MULOT, R. POUSSOT, A. P. SCHMITT et C. P. ZALESKI 185
Tandem electrostatic accelerators, R. J. VAN DE GRAAFF 195
Energy degrading-focusing of cyclotron beam, W. J. RAMLER, J. L. YNTEMA and M. OSELKA 217
The Pretoria cyclotron, Second Report, J. J. BURGERJON and W. WEIDEMANN 261
H.F. power meter for operation at 2.5 MW pulsed power, E. ZACCHERONI 304
Continuous monitoring of uranium leach solutions, G. G. EICHHOLZ 320

Detectors

π-star detector, A. F. DUNAITZEV, YU D. PROKOSHKIN and TANG SYAO-WEI 11
On the construction and long-term performance of medium pressure BF_3 proportional counters used for cosmic-ray recording, P. H. STOKER 23
The effect of gamma-background on the BF_3 proportional counter, J. CSIKAI and M. BUCZKÓ 73
Détecteur de particules lourdes a jonction n-p au silicium, G. AMSEL, P. BARUCH et O. SMULKOWSKI 92
Response of semiconductor surface-barrier counters to nitrogen ions and alpha particles, M. L. HALBERT and J. L. BLANKENSHIP 106
Neutron flux measurements from 100 keV to 4 MeV with a modified long counter, E. TOCHILIN and R. V. ALVES . 225
A low background beta counter with a plastic scintillator anticoincidence shield, J. R. GAT (GUTMANN) and J. GILAT 233
A scintillation counter system for the detection of positive and negative pions, J. G. RUTHERGLEN and J. K. WALKER 239
Zum Einfluss der Kristallform auf das energetische und zeitliche Auflösungsvermögen einer Szintillationsanordnung, G. LUCK 249
A versatile, high efficiency 4π neutron detector, J. B. MARION, R. J. A. LEVESQUE, C. A. LUDEMANN and R. W. DETENBECK 297
Drift velocities of electrons in argon, nitrogen and argon mixtures, T. NAGY, L. NAGY and S. DÉSI 327

Instruments and Methods for Nuclear Spectroscopy

Optimum conditions for double focusing beta ray spectrometers, MITSUO SAKAI 61
A Siegbahn-Edvarson type ironfree double focusing beta-ray spectrometer, C. DE VRIES and A. H. WAPSTRA . . . 121
Improvements in the fast neutron time of flight technique using pulse shape discrimination in an organic phosphor, R. BATCHELOR, W. B. GILBOY, A. D. PURNELL and J. H. TOWLE 146
The oscilloscope method of measuring nuclear half-lives, I. BERGSTRÖM, E. C. O. BONACALZA, A. JECH, M. PEREZ and P. THIEBERGER 151
Calculated shapes for neutron bursts produced by phased chopper velocity selectors, NORMAN H. TOLK and ROBERT M. BRUGGER 203
On the separation of π^+ mesons by a time of flight method, G. M. LEWIS, E. GABATHULER and R. E. AZUMA . . . 230
The theory and operation of the rotating crystal slow neutron chopper, D. A. O'CONNOR 244
The spherical condenser as a high transmission particle spectrometer II. Disc source, R. D. BIRKHOFF, J. M. KOHN, H. R. ELDRIDGE and R. H. RITCHIE 313
Ein universelles Verfahren zur Stabilisierung von Szintillations-Spektrometer-Anordnungen, S. HAUN und D. KAMKE 331
An improved anti-coincidence shield for use in low background counting, R. P. PARKER 339
A new method of mass discrimination, G. HREHUSS 344

Instruments and Methods for High Energy Physics

On the construction and long-term performance of medium pressure BF_3 proportional counters used for cosmic-ray recording, P. H. STOKER 23
Apparatus and laboratory for processing nuclear emulsions stacks, H. ENGELHARDT, I. HAUSER and U. KRECKER 55
An instrument facilitating the measurement of small-angle scattering in nuclear emulsion, A. G. C. TENNER, B. JONGEJANS and H. WITTEVELD 221
An improved instrument for nuclear emulsion track photometry, S. v. FRIESEN and B. PERSSON 348

Letters to the Editor

Iron-free toroidal beta-beta coincidence spectrometer, MELVIN, S. FREEDMAN, FRANK WAGNER, JR., FRED T. PORTER, JOHN TERANDY and PAUL, P. DAY 255
Bandwidths of the equal time-constant amplifier, J. B. S. WAUGH 257
A method for the separation of gold irradiated mercury isotopes, W. PARKER 354

News Items

Accelerator Conference, sponsored by High Voltage Engineering Corporation, Amsterdam, Octorber 4–6, 1960 . . 259
Seminaire Internationale, International Seminar, organized by Institut Belge de Regulation et d'Automatisme, Brussels, November 21–23, 1960 260

Nuclear Electronics

Transistorized apparatus for accumulation and binary-decimal conversion, D. BRINI, A. GANDOLFI and G. L. TABELLINI 46
Circuit allongeur d'impulsions rapides, A. SARAZIN, J. SAMUELI, G. DUCROS et P. RAIMBAULT 70
Über die Bestimmung der zufälligen Koinzidenzen in Schnell-Langsam-Koinzidenz-Anordnungen, T. MAYER-KUCKUK und R. NIERHAUS 76
Nonlinear operations on pulses by means of p-n junctions, G. GIANNELLI and L. STANCHI 79
A double-delay-line linear amplifier employing transistors I, F. S. GOULDING, R. W. NICHOLSON and J. B. WAUGH 272
A transistorized fast-slow coincidence and pulse amplitude selecting system II, F. S. GOULDING and R. A. MCNAUGHT 282

Miscellaneous

On the efficiency of the reaction $H^3(d,n)He^4$ in titanium tritide bombarded with deuterons, E. M. GUNNERSEN and G. JAMES 173
High-efficiency, long-lived vacuum cold trap, J. W. BUTLER 211
A kilovolt, kiloampere low pressure switch, GEORGE J. BRUCKER and KENNETH C. ROGERS 236